Conference Proceedings of the Society for Experimental Mechanics Series

Alfred Wicks *Editor*

Structural Health Monitoring, Volume 5

Proceedings of the 32nd IMAC, A Conference and Exposition on Structural Dynamics, 2014

SEM

Springer

Conference Proceedings of the Society for Experimental Mechanics Series

Series Editor

Tom Proulx
Society for Experimental Mechanics, Inc.,
Bethel, CT, USA

For further volumes:
http://www.springer.com/series/8922

Alfred Wicks
Editor

Structural Health Monitoring, Volume 5

Proceedings of the 32nd IMAC, A Conference and Exposition on Structural Dynamics, 2014

Springer

Editor
Alfred Wicks
Department of Mechanical Engineering
Virginia Polytechnic Institute
and State University
Blacksburg, VA, USA

ISSN 2191-5644 ISSN 2191-5652 (electronic)
ISBN 978-3-319-04569-6 ISBN 978-3-319-04570-2 (eBook)
DOI 10.1007/978-3-319-04570-2
Springer Cham Heidelberg New York Dordrecht London

Library of Congress Control Number: 2014933800

Printed on acid-free paper

Springer is part of Springer Science+Business Media (www.springer.com)

Preface

Structural Health Monitoring, Volume 5 represents one of the eight volumes of technical papers presented at the 32nd IMAC, A Conference and Exposition on Structural Dynamics, 2014 organized by the Society for Experimental Mechanics, and held in Orlando, Florida, February 3–6, 2014. The full proceedings also include volumes on Dynamics of Coupled Structures; Nonlinear Dynamics; Model Validation and Uncertainty Quantification; Dynamics of Civil Structures; Special Topics in Structural Dynamics; Topics in Modal Analysis I; and Topics in Modal Analysis II.

Each collection presents early findings from experimental and computational investigations on an important area within structural dynamics. Structural Health Monitoring is one of these areas. Topics in this volume include:

Structural health monitoring
Damage detection
Energy harvesting

The organizers would like to thank the authors, presenters, session organizers, and session chairs for their participation in this track.

Blacksburg, VA, USA

Alfred Wicks

Contents

Chapter 1
Assessment and Localization of Active Discontinuities Using Energy Distribution Between Intrinsic Modes

Reza Mohammadi Ghazi and Oral Buyukozturk

Abstract A method for localization and severity assessment of structural damages is proposed. The algorithm works based on nonlinear behavior of certain type of damages such as breathing cracks which are called active discontinuities in this paper. Generally, nonlinear features are more sensitive to such damages although their extraction is sometimes controversial. A major controversy is the imposition of spurious modes on the expansion of the signal which needs to be addressed for an effective application and robustness of the method. The energy content of Intrinsic Mode Functions (IMFs), which are the resultants of Empirical Mode Decomposition (EMD), and also the shape of energy distribution between these modes before and after damage, are used for localization and severity assessment of the damages. By using EMD, we preserve the nonlinear aspects of the signal while avoiding imposition of spurious harmonics on its expansion without any assumption of stationarity. The developed algorithms are used to localize and assess the damage in a steel cantilever beam. The results show that the method can be used effectively for detecting active structural discontinuities due to damage.

Keywords Structural health monitoring • Active discontinuity • Nonlinearity • Normalized Cumulative Marginal Hilbert Spectrum • Energy transfer

1.1 Introduction

Structural Health Monitoring (SHM) can play a significant role in improving the safety of structures as well as extending their life time. Greater complexity, aging, higher operational loads, and severe environmental effects result in more attention to this field. However, after more than 30 years of research, SHM has not been vastly applied in real world structures. Non-unique solutions of inverse problems, complexity, and variety of systems in the real world are the most important reasons that slow down the progress of SHM from research level to application. For instance, several methods have been proposed to detect breathing cracks such as mode shape curvature [1], model updating [2], energy method [3], and nonlinearities [4–7]. All of the aforementioned methods were shown to be effective in a specific problem; however, this does not guarantee their generality. Methods which use numerical models suffer from difficulties of providing a precise model to monitor a system. Most other methodologies are not generalizable since they have been tested on a very specific structure. Moreover, the approach of these papers, typically, is proposing a metric, called a damage index (DI), and then verifying its sensitivity to a certain type of damage. Applicability of the methods with the mentioned approach is possible only after answering the following questions: Is the proposed DI sensitive to the same type of damage, but in different structures? Is the physics behind the DI the best possible representative of damage in the system? If not, how can we improve the method for application in

R.M. Ghazi
Department of Civil and Environmental Engineering, Massachusetts Institute of Technology, 77 Massachusetts Avenue, Bldg 5-336, Cambridge, MA 02139, USA
e-mail: rezamg@mit.edu

O. Buyukozturk (✉)
Department of Civil and Environmental Engineering, Massachusetts Institute of Technology, 77 Massachusetts Avenue, Bldg 1-281, Cambridge, MA 02139, USA
e-mail: obuyuk@mit.edu

A. Wicks (ed.), *Structural Health Monitoring, Volume 5: Proceedings of the 32nd IMAC, A Conference and Exposition on Structural Dynamics, 2014*, Conference Proceedings of the Society for Experimental Mechanics Series, DOI 10.1007/978-3-319-04570-2_1,

real structures? Is comparing the values of DIs sufficient for characterization of a structure as intact or damaged? A damage detection algorithm is not applicable unless all these questions are answered.

We address the first three questions in this study by proposing several DIs based on nonlinearities due to damage. Other questions will be addressed in future studies. The proposed algorithm in this paper is suitable for detection of a certain type of damage called an active discontinuity. As defined in [8], active discontinuities, such as breathing cracks, are regarded as additional degrees of freedom whose effects on response of the system are above the noise floor. Obviously, activation of a discontinuity depends on the input energy and characteristics of excitation, meaning that the effect of discontinuity on the response of the system may not be discernible from noise under a specific excitation and hence, not activated. Note that even if the discontinuity is activated, it may or may not be detectable using a certain DI depending on its sensitivity to damage and/or how the damage affects the system response. For example, fundamental frequencies of a beam are not changed more than 2 % in presence of a breathing crack with the depth of around 20 % of the beam's cross section [4], so it turns out to be quite difficult to detect small breathing cracks using a DI based on fundamental frequencies. The problem can be ameliorated by capturing nonlinear effects of damage since nonlinear features of structural response are generally more sensitive to damage [4–7]. On the other hand, a DI should not demonstrate a very high sensitivity to changes in a signal since the results of the algorithm are highly affected by noise and hence, not reliable. Several methods have been proposed based on different types of nonlinearities such as [4–7]. Most of the mentioned DIs suffer from one of these two shortcomings: (1) there is no solid physical interpretation behind the damage index such as those which aim to capture changes in the geometry of signal, (2) subjectiveness which makes it very difficult to use the DIs in complex structures and large sensor networks.

In this paper we try to capture nonlinear effects using an energy-based method. The algorithm not only is sufficiently sensitive to active discontinuities, but also has a concrete physical interpretation behind each DI related to the concept of energy transfer between vibrating modes. There are two requirements essential for retaining the validity of the method; the first is preservation of nonlinearities and the second, prevention of energy leakage of any kind in signal processing. By the use of Empirical Mode Decomposition (EMD) [9], all nonlinearities are preserved in the expansion of a signal in terms of its Intrinsic Mode Functions (IMFs). In addition, there is no leakage of energy due to imposing spurious harmonics on such an expansion, and hence, both requirements are satisfied. The efficacy of the algorithm has been experimentally verified on different structures. The results show that the method can effectively detect active discontinuities due to damage in all cases. In this paper, we present the results only on one simple case which is a cantilever beam consists of three elements.

1.2 Active Discontinuities and Energy Transfer Between Vibrating Modes

As defined in [8], an "Active Discontinuity" is a type of damage which can affect response of the system such that its effect is discernible from the sensor noise floor. Activation of a discontinuity mostly depends on the severity of damage as well as characteristics of the excitation. It implies that a discontinuity which is activated under a certain excitation may not be activated, and therefore detectable, under a different excitation. Such damage, if activated, generates new modes of vibration or amplify some existing ones. In other words, the damage results in transfer of energy between existing modes or from them to newly generated ones. Based on experiments, this phenomenon showed more sensitivity to damage compared to frequency shift while there is no controversy on the definition of frequency in this concept. In fact, the behavior of active discontinuities is nonlinear and the generated modes by their activation are mostly of high frequency. These high frequency modes change the energy content of other existing ones although they do not affect the dominant response of the system unless the damage is very severe. That is the reason that the energy based method with consideration of nonlinearities is more preferable than other methods which try to capture any kind of change only in frequency response of a system assuming linearity. However, there is a requirement which needs to be satisfied in order to make use of the strengths of the energy method. The requirement is to prevent leakage of energy in any form. Immediately, one can conclude that this condition cannot be always completely satisfied in the Fourier domain, especially in presence of noise, because of spurious harmonics which are imposed on the expansion of the signal. Note that the argument is about the accuracy of method and does not mean to totally disregard Fourier transformation for energy methods. In this paper, we use EMD as the signal processing tool to expand a signal into a set of nonlinear IMFs without any spurious modes and hence, prevent energy leakage. It is also noteworthy that by the "energy of a signal" we mean the norm of the signal or mode function. The norm is the actual energy only if the signal is displacement time history.

Two assumptions are required for development of the algorithm in the simplest form. First, that the input energy and frequency content of excitations are consistent before and after damage. This implies that the algorithm has not been developed for damage detection using arbitrary excitations. There is always a baseline required, but the baseline is calculated using the structure itself without any theoretical assumptions. Secondly, the presence of damage is the only difference between the intact and damaged structure. This assumption is equivalent to consistency of environmental effects.

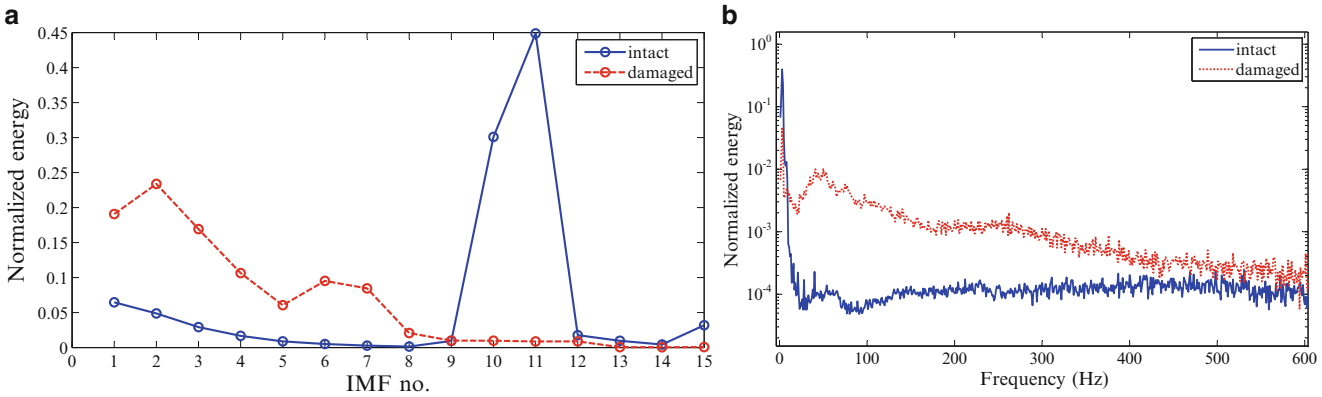

Fig. 1.1 Different energy distribution curves for same sensor data, (**a**) MHS, (**b**) energy distribution between IMFs

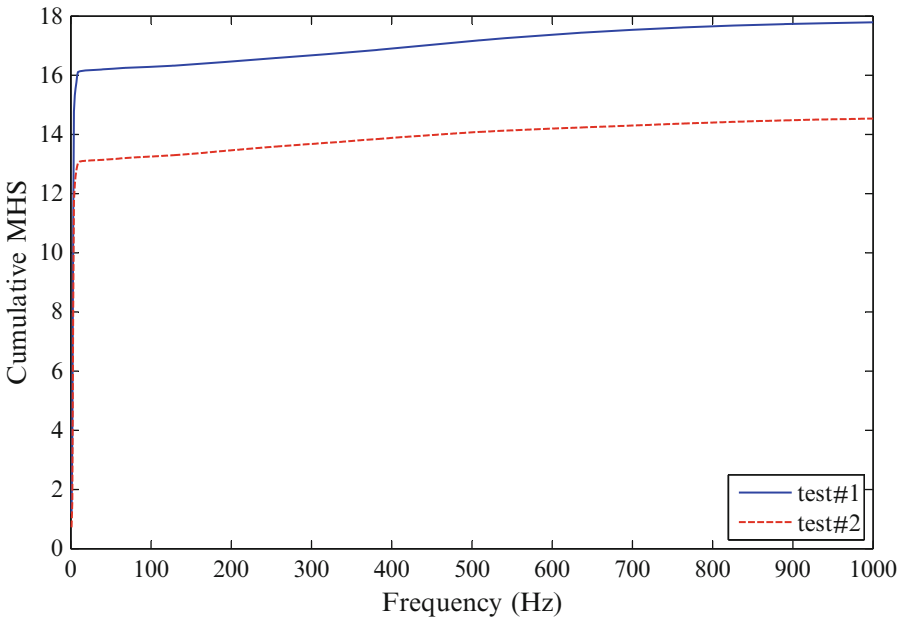

Fig. 1.2 Cumulative MHS for an empirical data of two tests on an intact structure (same sensor)

1.2.1 Normalized Cumulative Marginal Hilbert Spectrum (NCMHS)

With energy methods, we need to express the distribution of energy with respect to a physical quantity. If this quantity is frequency in the sense of Fourier transformation, the distribution is called Power Spectral Density (PSD). Same concept can be defined using EMD and Hilbert Huang Transformation (HHT) and the distribution is called Marginal Hilbert Spectrum (MHS) in this domain. Energy distribution can also be expressed with respect to each IMF as defined in [8]. The latter is useful only if the IMFs are monocomponent. It is less accurate compared to the MHS but computationally more efficient. Figure 1.1 shows different energy distributions for empirical data.

Working with the non-smooth functions shown in Fig. 1.1 is not mathematically preferable. Smoothing can be regarded as solution for this problem, but the true physics may be lost. Instead of modifying the curves by smoothing, we propose a more elegant way of solving the non-smoothness problem which is using the cumulative energy distributions rather than the distribution itself. The cumulative function is strictly increasing, smooth, and therefore easy to use, and preserves all physics without imposing any approximation on the problem. In Fig. 1.2 the cumulative MHS for two tests' data from same sensor on the same structure vibrating under similar excitations are shown. It should be noted that smoothness is used for functions and not sampled data. If we assume that the MHS can be represented as a continuous function, meaning that all frequencies in a specific range have some contribution, then its cumulative summation will be smooth.

Although the cumulative distributions are smooth and monotonically increasing, they still need modification before comparison. As shown in Fig. 1.2, there is a considerable deviation between two curves although they obtained from the

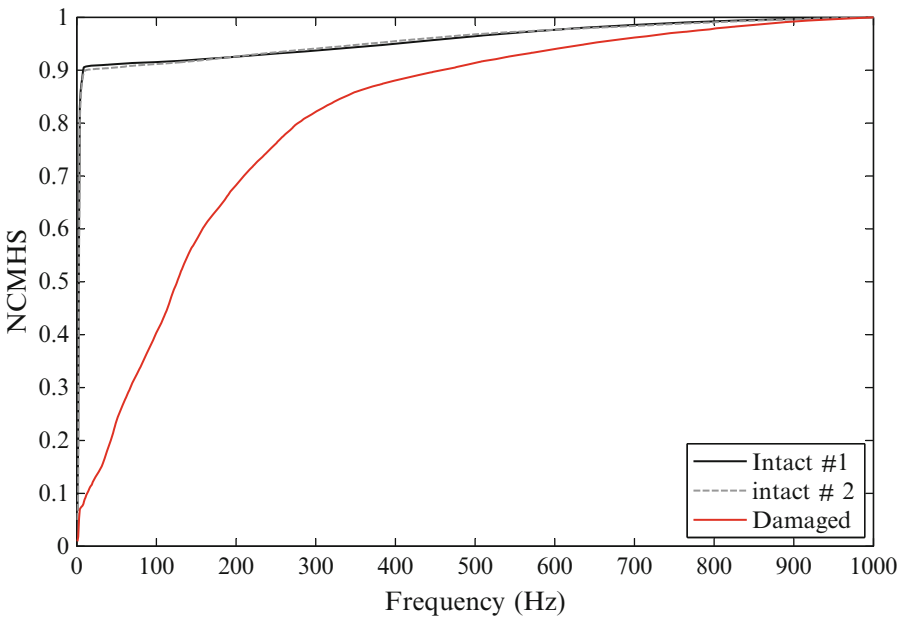

Fig. 1.3 NCMHS of empirical data consists of two tests on an intact structure and one test on the same structure with damage (same sensor)

intact structure. The reason is that the total input energies of the tests are different. As a result, comparing these two curves may lead us to a totally wrong deduction which is classifying an intact structure as damaged. Of course, it depends on the comparison methodology; for instance, if we focus only on the pattern of the distribution, they may be consistent. On the other hand, if we measure some other quantity such as the area under the curves the result of the algorithm will be wrong. In order to solve this problem we use the first basic assumption which is the consistency of spectrum and input energy of excitations in all tests. The consistency means that the difference between input energy does not affect the response of the structure; therefore, the effect of this difference can be neglected. As a result, we disregard the difference between input energy and normalize the cumulative function with respect to total input energy. The result is the Normalized Cumulative Marginal Hilbert Spectrum (NCMHS), examples of which are shown in Fig. 1.3. In this figure, the NCMHS for a set of empirical sensor data consisting of two tests on an intact structure and one for the same structure with damage are illustrated. In contrast to cumulative curves, the difference between Normalized Cumulative curves of the intact structure is not significant while the deviation between the damaged and intact structures is quite obvious. This procedure is generalizable to any other energy distribution such as the PSD to obtain the Normalized Cumulative PSD (NCPSD) or to energy distribution between IMFs as well, provided the assumption is satisfied.

1.3 Damage Indices

In previous section, it was shown that the NCMHS can be regarded as a reliable signature for the intact state of a structure under excitations with consistent spectra and input energies. In addition, it was shown that the NCMHS for the certain type of damages, active discontinuities, deviates from that signature due to the change in the pattern of energy distribution. Some, out of many, possible ways of quantifying this deviation are presented in this paper. We also do not restrict ourselves to use only the normalized cumulative curves since some quantities, such as the mean frequency, make sense only if the original curves are used. The first DI is defined as

$$DI_1 = \frac{\sum_i |A_i|}{A_{BL}} \tag{1.1}$$

where A_i is each portion of the area between NCMHS of the structure we are testing and the baseline NCMHS (Fig. 1.4); A_{BL} is the area under the baseline NCMHS. In this study, we defined the baseline using median of tests on intact structure, using only the sensor data and without any theoretical assumption. The median is chosen because of its robustness with

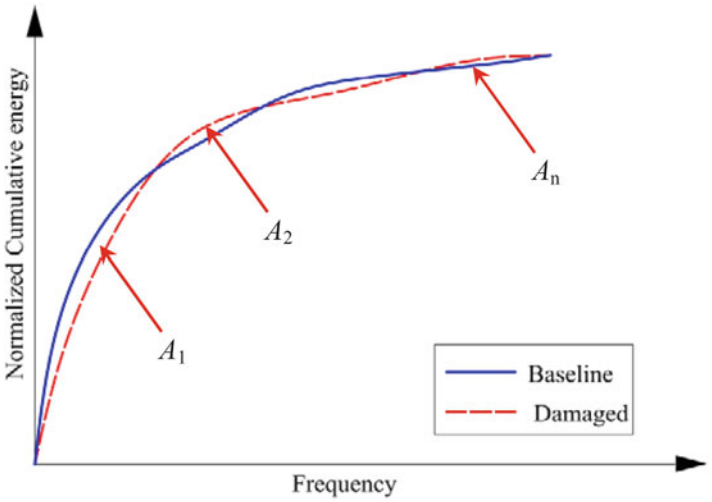

Fig. 1.4 Parameters for comparing NCMHS

respect to outliers. The numerator in Eq. (1.1) is the absolute value of the whole area between two curves and its physical interpretation is the total energy transfers between different modes. The denominator is only for normalization which provides a dimensionless DI in the range of zero to one. Similarly, another measure of energy transfer can be defined as

$$DI_2 = \frac{\left|\sum_i A_i\right|}{A_{BL}} \tag{1.2}$$

In this DI, some of the A_is are cancelled out if one curve oscillates around the other. Indices for comparing these curves are not restricted to Eqs. (1.1) and (1.2). Other possible methods are the ones which are used for comparing cumulative probability distributions. Of course, some of them cannot be interpreted physically even if they work well. For instance, Kolmogorov–Smirnov distance can be used and it shows a good sensitivity to damage; however, it has no solid physical interpretation.

As it mentioned before, some DIs should be defined using the original MHS. Again, based on the assumption for consistency of input energy, we can normalize the MHS to make a more meaningful comparison. Using normalized MHS one can define

$$DI_3 = \frac{\overline{F}}{\overline{F}_{BL}} \tag{1.3}$$

where the $\overline{F}$ is the mean frequency of MHS, $\overline{F}_{BL}$ is the mean frequency of baseline MHS. This DI can be interpreted as a measure of change of fundamental modes (frequencies), but not in Fourier domain. It tells us where the accumulation of energy is.

1.4 Severity Assessment

After localization of damage, the same concept of energy transfer between modes can be used for severity assessment of the active discontinuity. Stiffness reduction and generation of nonlinear high frequency vibrating modes are two main effects of such damages on the behavior of structure. The first effect dominates when the damage severity is low. In this case, the rigidity of the structure around the damage is high enough such that it prevents the generation of higher modes; therefore, the fundamental frequencies shift due to the energy transfers into low frequency modes. If the severity is high, the later effect dominates and the energy of high frequency modes will be increased.

Capturing this phenomenon is easier if the distribution of energy between IMFs is used rather than the MHS. In fact, the high resolution discretization of frequency bands in the MHS hides these tiny effects. As shown in Fig. 1.5, the cumulative

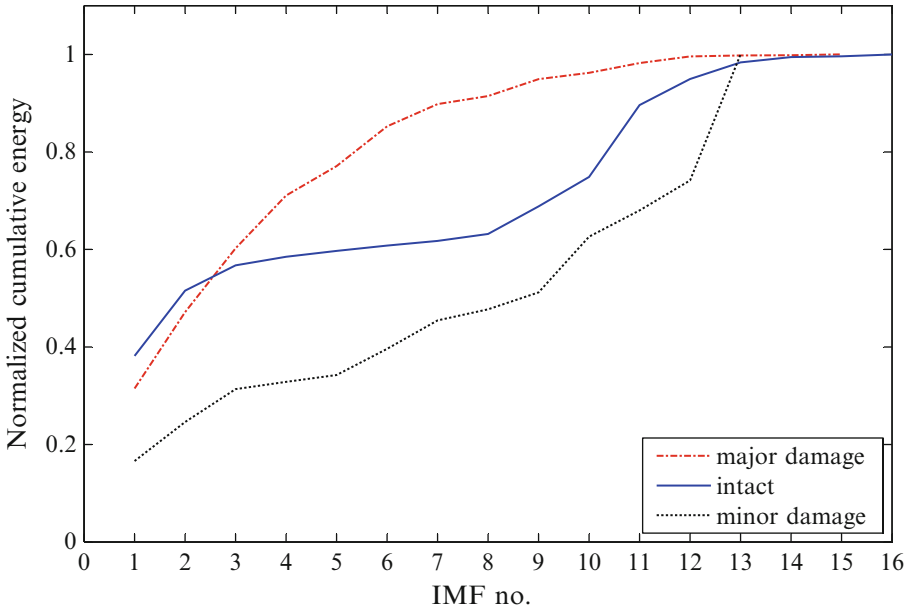

Fig. 1.5 Comparison of normalized cumulative distribution of energy between IMFs

Table 1.1 Different damage scenarios

Damage scenario	Description
1	Minor damage at node #2
2	Major damage at node #2
3	Minor damage at node #3
4	Major damage at node #3

energy distribution in the case of major damage lays above the intact case. The reason for the high slope of the curve near the high frequency IMFs in the damaged case is the accumulation of energy in these modes. For the minor damage, on contrary, the slope of the curve is high near the low frequency IMFs and hence, it is below the baseline.

1.5 Experimental Setup

In this study, we try to capture some nonlinear phenomena which are very difficult to simulate numerically. Therefore, experimental tests have been chosen as a more rigorous way of verification of the algorithm. The algorithm has been verified for different structure and the one which is presented in here is a cantilever beam consisting of three elements bolted together as shown in Fig. 1.6. The bolts are completely tightened in the intact structure such that the end plates of the elements are clamped. A triaxial accelerometer also is attached in the vicinity of each connection. Free vibration is chosen as the excitation in order to reduce the complications of dealing with different excitations and focus only on the efficacy of the algorithm.

The structure was tested under four damage scenarios which are listed in Table 1.1. In the case of minor damage, two bolts removed in one side of the connection while two other bolts were completely tightened. For the major damage, all four bolts were slightly loosened such that the structure did not lose stability. The sampling rate was chosen to be 3 kHz in order to capture the higher modes as precisely as possible.

1.6 Results

The sensor data in z direction (Fig. 1.6), perpendicular to the discontinuities, was analyzed. To assess the sensitivity of the algorithm to data length, two signal lengths were investigated: 5 s of data, and 2 s of data for comparison. In this paper, only the results of the later one are shown because there is no considerable difference between them. Moreover, multiple tests were conducted for each damage scenario, but, because the results are similar, for the sake of brevity only one of them is illustrated.

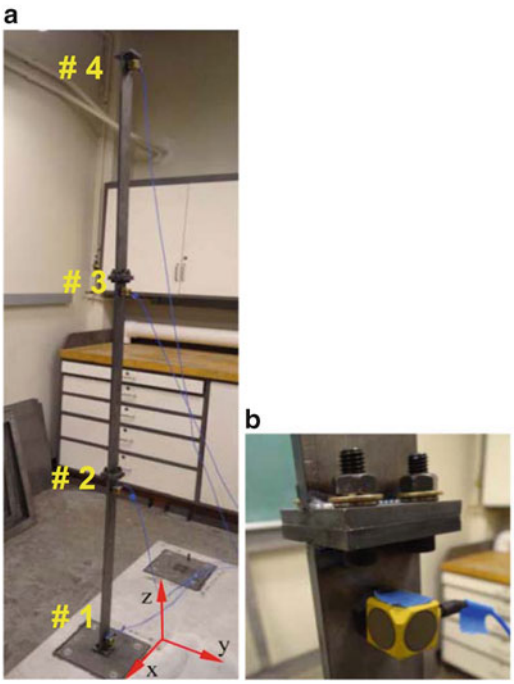

Fig. 1.6 Experimental setup; (**a**) cantilever beam consists of three elements; (**b**) accelerometer attached near a connection

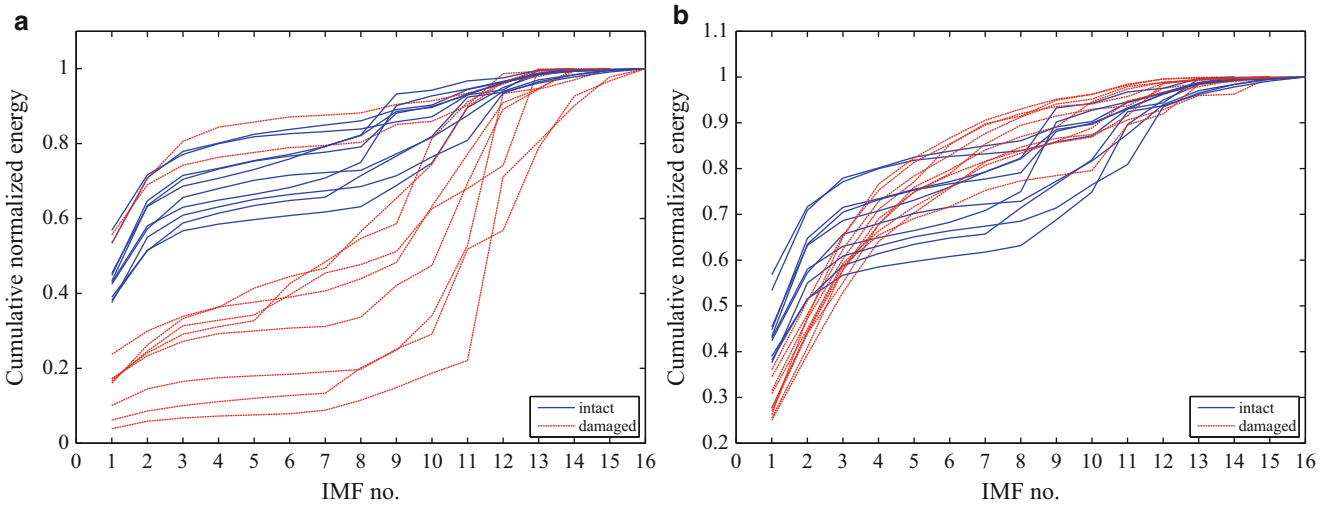

Fig. 1.7 NCMHS for the sensor at node #3; (**a**) minor damage; (**b**) major damage

The NCMHS for all tests and both minor and major cases are shown in Fig. 1.7. As expected, the curves are above the intact case in the case of major damage due to transfer of energy to high frequency modes and vice versa for minor damages. The damage index in all cases, which is shown in Fig. 1.8, has the highest value for the sensor at the node adjacent to the damage. It should be noted that for minor damage, the two end plates of elements in the connection where the damage presents are completely clamped in one side and there is no visible gap. However, the algorithm can effectively detect and also assess the severity of damage by considering nonlinearities in a very simple way.

1.7 Conclusions

In this study, an algorithm for localization and assessment of certain type of damages named active discontinuities was proposed. Breathing cracks and loosened bolts in a connection are examples of this type of damage. Activation of such discontinuities results in the generation of new vibrating modes which are nonlinear and mostly have high frequency content.

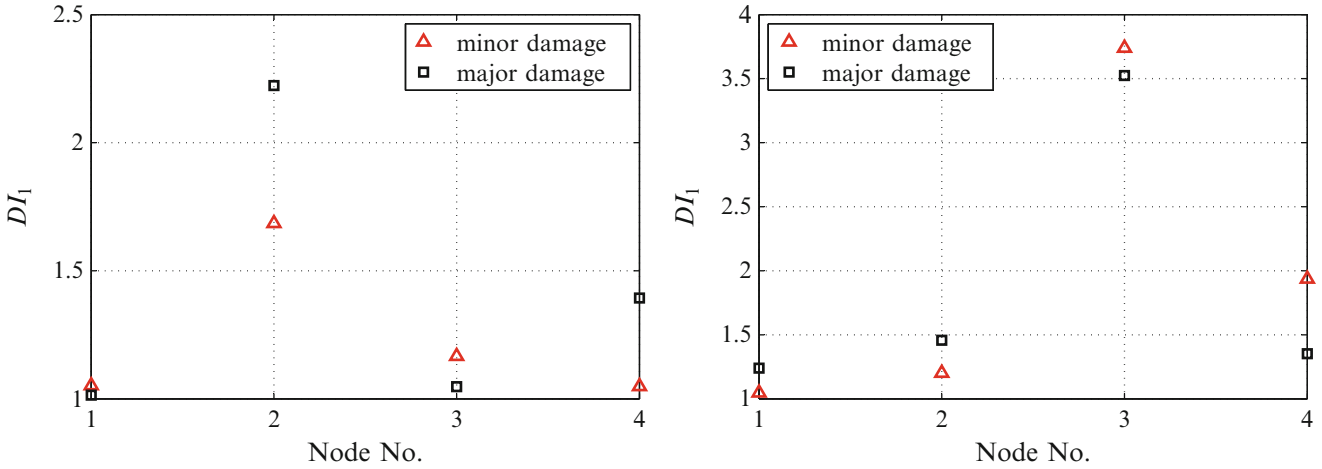

Fig. 1.8 DI_1 for (**a**) damages at node #2 and (**b**) damages at node #3

Assuming the same excitations for both intact and damaged structures, the distribution of input energy between the modes of vibration is changed due to damage. In other words, active discontinuities result in energy exchange between existing modes and newly generated modes due to damage. In order to capture this effect, several conditions should be satisfied. First, the spectrum and input energy of the excitation for both intact and damaged structures should be consistent. Second, any leakage of energy should be prevented for the method to be reliable. By using EMD for the decomposition of a signal, nonlinearities are preserved and all requirements for the second aforementioned condition is satisfied. To capture the nonlinearities after decomposition, we use the distribution of energy between different modes of vibration which can be expressed in different ways. MHS and distribution of energy between IMFs are examples of such distributions. Two modifications are accomplished on the energy distribution to make it easier to analyze them. The modifications are, first using cumulative energy distribution and the second, normalization with respect to total input energy. These modifications give us well-behaved monotonically increasing curves, named the NCMHS if the MHS is used as the original distribution, which can be regarded as a signature for the system by preserving all physics.

Among several methods of comparing the normalized cumulative curves, we used the area between NCMHSs for the damaged structure and the baseline. This index, in contrast to other pure mathematical indices, has a solid physical interpretation which is the total transferred energy between modes. Stiffness reduction and generation of nonlinear high frequency modes are two important effects of active discontinuities. These effects, which manifest themselves in the shape of the energy distribution, can be used for severity assessment of the damage. The energy distribution between IMFs, because of low resolution, magnifies the accumulation of energy in certain frequency band and hence, more appropriate for severity assessment. In the case of major damage, the energy is transferred to high frequency modes and the corresponding curve lays above the baseline. The opposite is true for the minor damages.

The efficacy of the algorithm is experimentally verified by testing a cantilever beam consisting of three elements which are bolted together under four damage scenarios. The results show that the algorithm can effectively detect and localize active discontinuities and also assess their severity even in the case of minor damages. The algorithm provides quantitative damage indices by capturing nonlinearities in a simple and effective manner.

Acknowledgments The authors acknowledge the support provided by Royal Dutch Shell through the MIT Energy Initiative, and thank chief scientists Dr. Dirk Smit and Dr. Sergio Kapusta, project manager Dr. Yile Li, and Shell-MIT liaison Dr. Jonathan Kane for their oversight of this work. Thanks are also due to Dr. Michael Feng and his team from Draper Laboratory for their collaboration in the development of the laboratory structural model and sensor systems. Sincere appreciation is given to Justin Chen for his help in collecting experimental data and editing the paper.

References

1. Pandey AK, Biswas M, Samman MM (1991) Damage detection from changes in curvature mode shapes. J Sound Vib 145(2):321–332
2. Lam HF, Katafygiotis LS, Mickleborough NC (2004) Application of a statistical model updating approach on phase I of the IASC-ASCE structural health monitoring benchmark study. J Eng Mech 130(1):34–48

3. Cornwell P, Doebling SW, Farrar CR (1999) Application of the strain energy damage detection method to plate-like structures. J Sound Vib 224(2):359–374
4. Peng ZK, Lang AQ, Billings SA (2007) Crack detection using nonlinear output frequency response functions. J Sound Vib 301:777–788
5. Nochols JM, Todd MD, Seaver M, Virgin LN (2003) Use of chaotic excitation and attractor property analysis in structural health monitoring. Phys Rev 67:016209
6. Nichols JM, Trickey ST, Todd MD, Virgin LN (2003) Structural health monitoring through chaotic interrogation. Meccanica 38:239–250
7. Yin SH, Epureanu B (2006) Structural health monitoring based on sensitivity vector fields and attractor morphing. Philos Trans A Math Phys Eng Sci 364:2515–2538
8. Mohammadi Ghazi R, Long J, Buyukozturk O (2013) Structural damage detection based on energy transfer between intrinsic modes. In: Proceedings of ASME 2013 conference on smart material, adaptive structures and intelligent systems (SMASIS), September 2013, No. 3022
9. Huang NE, Shen Z, Long SR, Wu MC, Shih HH, Zheng Q, Yen N, Tung CC, Liu HH (1998) The empirical mode decomposition and the Hilbert spectrum for nonlinear and non-stationary time series analysis. Proc R Soc A Math Phys Eng Sci 454:903–995

Chapter 2
Wave Analyses in Structural Waveguides Using a Boundary Element Approach

Stefan Bischoff and Lothar Gaul

Abstract Wave-based SHM concepts are widely used for an efficient evaluation of the state of a structure. In order to localize defects in waveguides, an exact knowledge of the propagation properties of ultrasonic waves is required.

Within this work, a boundary element formulation for modeling 3D waveguides is presented by which wave numbers as well as mode shapes of wave modes can be analyzed. In a BE modeling process, a segment of the periodic waveguide is considered. The collocation method, in which the boundary integral equation is solved at discretized nodes, is used to set up the corresponding system matrices. Applying a periodicity condition, the solution of the resulting eigenvalue problem provides both propagating and non-propagating modes of the waveguide. The model is verified by comparing the numerical results with theoretical considerations.

Additionally, a SHM application is demonstrated in order to characterize defects. The numerical accuracy of the simulation results are validated by an energy balance criteria.

Keywords Boundary elements • Periodic structural waveguide • Structural health monitoring • Crack detection

2.1 Introduction

In civil engineering, multi-wire strands are frequently used as stay cables of cable-stayed bridges, or overhead transmission lines. Generally, these structures are exposed to the ambient environmental conditions, and thus subjected to wind-induced vibrations, corrosion etc. As sight inspection techniques are limited to the detection of surface flaws, automated monitoring schemes such as vibration-based methods are developed in order to detect failure in multi-wire strands [5].

This work focuses on active wave-based approaches for damage localization and characterization. Considering elongated structures such as pipes, railroad rails and multi-wire strands ultrasonic waves are preferably used as they may travel over long distances with little decay and therefore allow for long range inspections. An example for power cables of overhead transmission lines is depicted in Fig. 2.1. Ultrasonic waves are excited in the monitored multi-wire strand and are partially reflected and transmitted at discontinuities. Reflections are measured by a sensor and damage detection algorithms evaluate whether a defect exists.

The work is structured as follows. First, a theoretical description of guided waves in waveguides is presented. As the use of analytical models is restricted to relatively simple geometries, a more general approach based on Boundary Element (BE) formulations is applied. A brief theoretical background of the classical BE method is given, and subsequently extended to the Waveguide BE method by modeling a waveguide segment with a periodicity condition. In the forth section, the method is applied to waveguides with circular and Z-shaped cross-section. Several numerical results, e.g. circular wavenumbers, showing convergence of the numerical results to the analytical solution, are presented. Section 2.5 illustrates a Structural Health Monitoring (SHM) application of ultrasonic guided waves in order to characterize defects in waveguides. Herein, the Waveguide BE method is used in combination with the classical BE method to predict scattering phenomena induced by surface opening defects of various depths. Based on measured reflection coefficients, the inverse problem of defect classification is possible. Conclusions complete this article.

S. Bischoff (✉) • L. Gaul
Institute of Applied and Experimental Mechanics, University of Stuttgart, Pfaffenwaldring 9, 70550, Stuttgart, Germany
e-mail: bischoff@iam.uni-stuttgart.de; gaul@iam.uni-stuttgart.de

A. Wicks (ed.), *Structural Health Monitoring, Volume 5: Proceedings of the 32nd IMAC, A Conference and Exposition on Structural Dynamics, 2014*, Conference Proceedings of the Society for Experimental Mechanics Series, DOI 10.1007/978-3-319-04570-2_2,

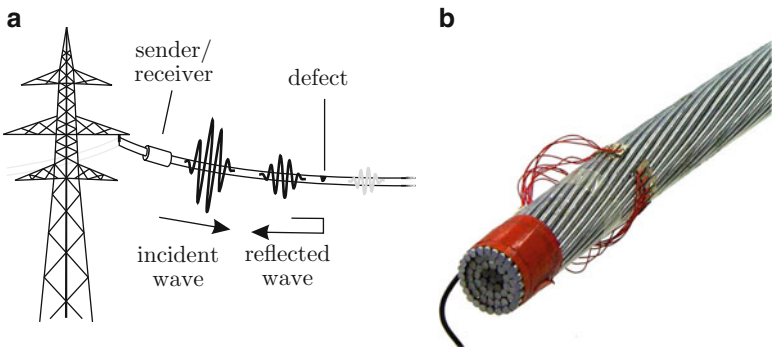

Fig. 2.1 (**a**) Scheme of SHM concept for overhead transmission lines. Piezoelectric transducers (**b**) attached at surface wires are used as actuators and sensors being able to generate and measure guided ultrasonic waves in power cables

2.2 Wave Propagation in Waveguides with Circular Cross-Section

Guided waves appear in elongated structures where internal disturbances are totally reflected at the lateral boundary. As a result, standing waves are formed in the cross-section propagating in axial x_3-direction. In the following, the analytical solution describing wave propagation in cylindrical wires is presented briefly—for further information see e.g. [1, 9].

The governing partial differential equation for a homogeneous isotropic elastic domain is the Lamé Navier equation of the displacement field $\boldsymbol{u}$. Neglecting body forces, the wave equation can be expressed as

$$(\lambda + \mu)\nabla(\nabla \cdot \boldsymbol{u}) + \mu\nabla^2\boldsymbol{u} = \rho\ddot{\boldsymbol{u}} \tag{2.1}$$

with the Lamé constants, λ and μ, and the density ρ. Application of the Helmholtz theorem connected with the potential technique leads Eq. (2.1) into two uncoupled wave equations for the scalar and vector potential functions, Φ and $\boldsymbol{H}$,

$$\nabla^2\Phi = \frac{1}{c_1^2}\frac{\partial^2\Phi}{\partial t^2} \qquad \text{and} \qquad \nabla^2\boldsymbol{H} = \frac{1}{c_2^2}\frac{\partial^2\boldsymbol{H}}{\partial t^2} \tag{2.2}$$

with the extensional and shear wave velocities, c_1 and c_2, for an infinite media. The solution of these wave equations can be found by applying the technique of separation of variables, arriving at the following general complex form for the displacement field $\boldsymbol{u}$

$$\boldsymbol{u}(\boldsymbol{x}, t) = \hat{\boldsymbol{u}}(x_1, x_2)\, \mathrm{e}^{\mathrm{j}(kx_3 - \omega t)} \tag{2.3}$$

with the circular wavenumber k and the angular frequency ω. The characteristic mode shapes are described by displacement fields, $\hat{\boldsymbol{u}}(x_1, x_2)$. For waveguides with circular cross-section, three types of waves may propagate: longitudinal, flexural and torsional waves [1]. Using common nomenclature, these waves are abbreviated as L(0,m), F(n,m) and T(0,m) with order n and sequential numbering m.

Solving the characteristic equations for each mode type is complex. As the use of analytical models is also restricted to relatively simple geometries, such as waveguides with circular cross-section, various numerical techniques have been developed in order to analyze waveguides with arbitrary cross-sections. Mace et al. [12] introduced a wave-based approach for analyzing guided waves in arbitrarily shaped waveguides. Based on Floquet's principle only a Finite Element (FE) discretized waveguide segment is considered using periodic boundary conditions.

In the following, an alternative approach, namely the Waveguide BE method, is introduced for modeling 3D waveguides of arbitrary cross-section. The method requires a BE discretization of a waveguide segment and a periodicity condition that allows harmonic wave motion in direction of propagation. Instead of discretizing the waveguide segment with Finite Elements, the BE method can be employed effectively as the boundary data are of primary interest. Furthermore, the problem dimension is reduced by one and as the method is based on fundamental solutions which analytically fulfil the field equations [7], high accuracy is obtained. Unfortunately, the BE method usually leads to fully populated system matrices, in contrast to sparse matrices which are often associated with FE approaches.

Below, the Waveguide BE method for 3D elastodynamics is outlined and thereafter applied to various different periodic waveguides with different cross-sections.

2.3 Waveguide Boundary Element Method

At the beginning, a theoretical background of the BE method in the elastodynamics is given. By applying the collocation technique, a system of linear algebraic equations is obtained. Taking into account the given constraints, the system of equations is transferred into an eigenvalue problem, whereas the solutions are obtained in terms of circular wavenumbers and mode shapes.

2.3.1 Elastodynamic Boundary Element Formulation

The process of deriving the boundary integral equation (BIE) for the unknown field quantities is well known from the standard BE literature (see e.g. [3, 6]) and is therefore only briefly outlined here.

The elastodynamic BIE of a boundary model may be derived from Cauchy's equation of motion through a weighted residual statement [7] as follows

$$c_{ij}(\xi)u_j(\xi) + \fint_\Gamma T_{ij}(x,\xi)\,u_j(x)d\Gamma = \int_\Gamma U_{ij}(x,\xi)\,t_j(x)d\Gamma\,,\ \xi \in \Gamma\,, \tag{2.4}$$

where $\fint$ denotes a Cauchy principal value (CPV) integral and c_{ij} is the free term coefficient at $\xi \in \Gamma$. The physical quantities introduced in Eq. (2.4) are the displacement and traction components, u_j and t_j, on the boundary Γ. U_{ij} and T_{ij} are the displacement and traction fundamental solutions at the field point x when a unit load is applied at the load point ξ in i direction.

The numerical implementation of Eq. (2.4) requires a discretization of the boundary into finite boundary elements $\Gamma^{(e)}$, see Fig. 2.2a. By means of shape functions Φ^n and nodal values, $\breve{u}_j^n$ and $\breve{t}_j^n$, the field quantities, u_j and t_j, are approximated as follows

$$u_j^{(e)} = \sum_n \Phi^n \breve{u}_j^n \qquad \text{and} \qquad t_j^{(e)} = \sum_n \Phi^n \breve{t}_j^n\,. \tag{2.5}$$

Applying the collocation technique to Eq. (2.4), one gets a system of algebraic equations in matrix form

$$\boldsymbol{H}\breve{\boldsymbol{u}} = \boldsymbol{G}\breve{\boldsymbol{t}}\,, \tag{2.6}$$

where the matrices $\boldsymbol{H}$ and $\boldsymbol{G}$ contain the boundary integral terms of the traction and displacement fundamental solutions, while the displacement and traction vectors on the boundary are given by $\breve{\boldsymbol{u}}$ and $\breve{\boldsymbol{t}}$, respectively.

In these formulations, the numerical integration of the regular integrals over the boundary elements is performed by Gaussian quadrature. The weak singularities are solved by regularising the transformation to polar coordinates [11], while strongly singular integrals are carried out by means of traction-free rigid body motion used for elastostatic singular integration in combination with regular Gaussian quadrature [7].

2.3.2 Boundary Element Analysis of Periodic Structures

A periodic waveguide segment is shown in Fig. 2.2b. The structural models required for the BE formulation are created with the aid of a universal preprocessor, such as HyperMesh of Altair Computing Inc. Thereby, the segment of the periodic structure is meshed with an equal number of nodes on their left and right cross-section. According to Sect. 2.3.1, the dynamics of the waveguide segment is given as $\boldsymbol{H}\boldsymbol{u} = \boldsymbol{G}\boldsymbol{t}$. Partitioning of degrees of freedom with respect to the external surface, Γ_E, as well as the left and right cross-section, Γ_L and Γ_R, lead to

$$\begin{bmatrix} \boldsymbol{H}_{\mathrm{LL}} & \boldsymbol{H}_{\mathrm{LE}} & \boldsymbol{H}_{\mathrm{LR}} \\ \boldsymbol{H}_{\mathrm{EL}} & \boldsymbol{H}_{\mathrm{EE}} & \boldsymbol{H}_{\mathrm{ER}} \\ \boldsymbol{H}_{\mathrm{RL}} & \boldsymbol{H}_{\mathrm{RE}} & \boldsymbol{H}_{\mathrm{RR}} \end{bmatrix} \begin{bmatrix} \boldsymbol{u}_\mathrm{L} \\ \boldsymbol{u}_\mathrm{E} \\ \boldsymbol{u}_\mathrm{R} \end{bmatrix} = \begin{bmatrix} \boldsymbol{G}_{\mathrm{LL}} & \boldsymbol{G}_{\mathrm{LE}} & \boldsymbol{G}_{\mathrm{LR}} \\ \boldsymbol{G}_{\mathrm{EL}} & \boldsymbol{G}_{\mathrm{EE}} & \boldsymbol{G}_{\mathrm{ER}} \\ \boldsymbol{G}_{\mathrm{RL}} & \boldsymbol{G}_{\mathrm{RE}} & \boldsymbol{G}_{\mathrm{RR}} \end{bmatrix} \begin{bmatrix} \boldsymbol{t}_\mathrm{L} \\ \boldsymbol{t}_\mathrm{E} \\ \boldsymbol{t}_\mathrm{R} \end{bmatrix}\,. \tag{2.7}$$

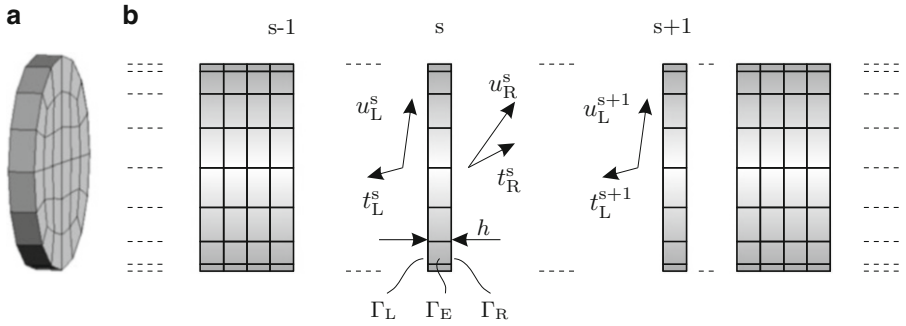

Fig. 2.2 (**a**) Boundary element waveguide model as well as (**b**) integrated segment s of a cylindrical waveguide with displacement and traction fields on the left and right cross-section, Γ_L and Γ_R

Elimination of displacements $\boldsymbol{u}_E$ by the boundary condition of vanishing tractions, $\boldsymbol{t}_E = 0$ at Γ_E, yields the dynamic stiffness relation

$$\boldsymbol{D} \begin{bmatrix} \boldsymbol{u}_L \\ \boldsymbol{u}_R \end{bmatrix} = \begin{bmatrix} \boldsymbol{t}_L \\ \boldsymbol{t}_R \end{bmatrix} , \tag{2.8}$$

which allows for coupling with neighboring waveguide segments at the interfaces, Γ_L and Γ_R. Depending on the total number of external degrees of freedom, the order of the dynamic stiffness matrix $\boldsymbol{D}$ may reduce drastically.

Considering periodic continuation of the waveguide segments, continuity of displacements and equilibrium of tractions at the cross-sections between neighboring segments, s and $s+1$, yields,

$$\boldsymbol{u}_L^{s+1} = \boldsymbol{u}_R^s , \quad \boldsymbol{t}_L^{s+1} = -\boldsymbol{t}_R^s . \tag{2.9}$$

Combining Eqs. (2.8) and (2.9) one obtains the so called transfermatrix $\boldsymbol{T}$ relating the displacements and tractions in the cross-sections of subsequent segments

$$\boldsymbol{T} \begin{bmatrix} \boldsymbol{u}_L^s \\ \boldsymbol{t}_L^s \end{bmatrix} = \begin{bmatrix} \boldsymbol{u}_L^{s+1} \\ \boldsymbol{t}_L^{s+1} \end{bmatrix} \tag{2.10}$$

where the single partitions of the transfermatrix are given as

$$\boldsymbol{T} = \begin{bmatrix} -\boldsymbol{D}_{LR}^{-1}\boldsymbol{D}_{LL} & \boldsymbol{D}_{LR}^{-1} \\ -\boldsymbol{D}_{RL} + \boldsymbol{D}_{RR}\boldsymbol{D}_{LR}^{-1}\boldsymbol{D}_{LL} & -\boldsymbol{D}_{RR}\boldsymbol{D}_{LR}^{-1} \end{bmatrix} . \tag{2.11}$$

Assuming harmonic wave propagation the displacements and tractions of neighboring cross-sections can be linked by a complex phase shift λ, defined as $\lambda = e^{jkh}$ with the length h,

$$\boldsymbol{u}_L^{s+1} = \lambda \boldsymbol{u}_L^s , \qquad \boldsymbol{t}_L^{s+1} = \lambda \boldsymbol{t}_L^s . \tag{2.12}$$

Inserting Eq. (2.12) into Eq. (2.10) results in a eigenvalue problem

$$\boldsymbol{T} \begin{bmatrix} \boldsymbol{u}_L^s \\ \boldsymbol{t}_L^s \end{bmatrix} = \lambda \begin{bmatrix} \boldsymbol{u}_L^s \\ \boldsymbol{t}_L^s \end{bmatrix} . \tag{2.13}$$

Using eigenvalues and eigenvectors, the guided wave propagation characteristics such as wavenumbers k and mode shapes for displacement and traction fields, $\hat{\boldsymbol{u}}$ and $\hat{\boldsymbol{t}}$, respectively, can be derived. On the basis of wavenumbers, guided waves can be classified as propagating and non-propagating modes.

The logarithm of a complex eigenvalue $\lambda = |\lambda| e^{j\theta}$ with $\theta \in [-\pi, \pi)$ is generally defined as

$$\mathrm{Ln}(\lambda) = \ln(|\lambda|) + j(\theta + 2\pi m) , \quad m = 0, 1, 2, 3, \ldots \quad . \tag{2.14}$$

In order to ensure precise results and unique solutions, the wave analysis is restricted to modes whose wavenumbers, $k = -\frac{j}{h}\mathrm{Ln}\lambda$, fulfill the condition

$$-\frac{\pi}{h} \leq \mathrm{real}\{k\} < \frac{\pi}{h} . \tag{2.15}$$

In general, the Waveguide BE solutions are obtained in a stable manner, and thus do not require the root searching algorithms used in analytical formulations.

2.4 Numerical Results

In this section, the performance of the Waveguide BE method for various periodic waveguides with different cross-sections and with respect to the mesh density is analyzed. Boundary models are built with HyperMesh, simulations are performed using MATLAB.

2.4.1 Waveguide with Circular Cross-Section

First, the Waveguide BE method is applied for uniform rods with circular cross-section. As aluminium is well known for its high electrical conductivity and is therefore frequently used in power cables, the analysis is conducted for aluminium [EN AW-6082 T6] wires of radius $r = 2\,\text{mm}$.

A waveguide segment of length $h = 0.5\,\text{mm}$ is truncated from the cylindrical structure and meshed using quadratic boundary elements. Each segment is exactly one element long. The accuracy of the Waveguide BE solution depends on both the discretization of the waveguide cross-section and the order of the used interpolation function. Figure 2.3 shows the relative wavenumber error of all propagating wave modes at a frequency of 200 kHz, calculated for different discretizations. The benefit of improved accuracy must be carefully weighted against the increased computational effort due to the higher number of elements. As the relative wavenumber error for BE meshes with 726 DOF's is below 1 %, the waveguide cross-section is discretized in the further course with 32 quadratic elements (entire waveguide segment is meshed with 80 quadratic elements) avoiding high computational effort for determining the system matrices.

Additional outcomes of the Waveguide BE method are displacement and traction fields. The in-plane displacement fields for the basic wave modes are shown in Fig. 2.4. In agreement with theory, the longitudinal mode L(0,1) is axially symmetric, whereas the torsional wave T(0,1) contains only rotational components. Also note that the flexural wave F(1,1) is arbitrarily oriented and occurs in pairs of equal wavenumbers due to the cross-sectional symmetry. In the same way, higher order modes can be analyzed.

For a specific frequency, the Waveguide BE method allows for an efficient determination of wave modes. While an analytical determination of the propagating modes is possible for waveguides with circular cross-section, the Waveguide BE results also obtain nonpropagating modes, which are especially important when analyzing guided wave interaction at defects in SHM applications.

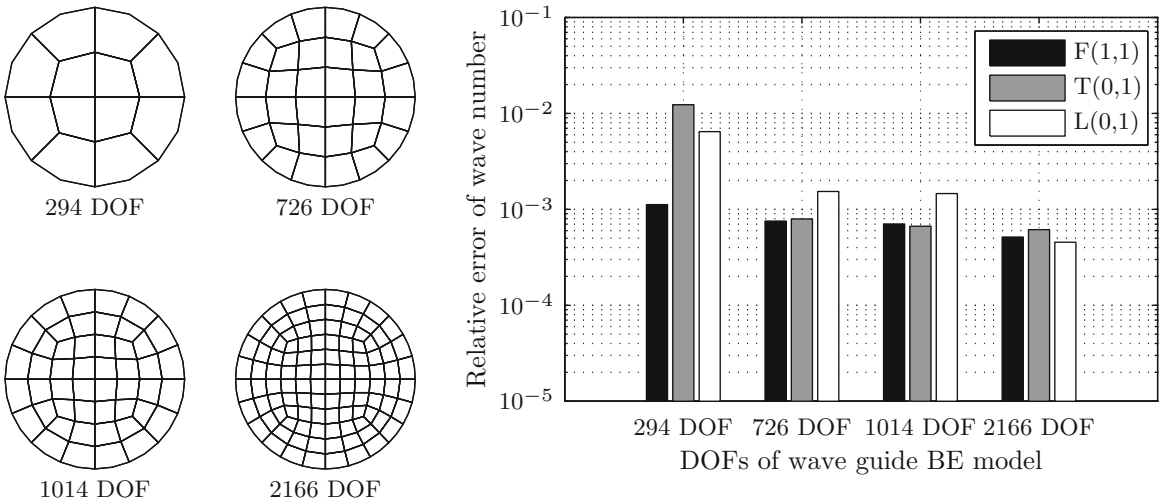

Fig. 2.3 Relative error between analytically derived and numerically calculated wavenumbers for various discretizations

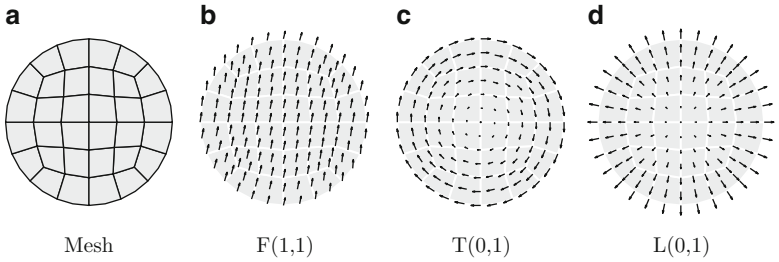

Fig. 2.4 Meshed waveguide with circular cross-section as well as in-plane displacements of the basic propagating modes. (**a**) Mesh, (**b**) F(1,1), (**c**) T(0,1), (**d**) L(0,1)

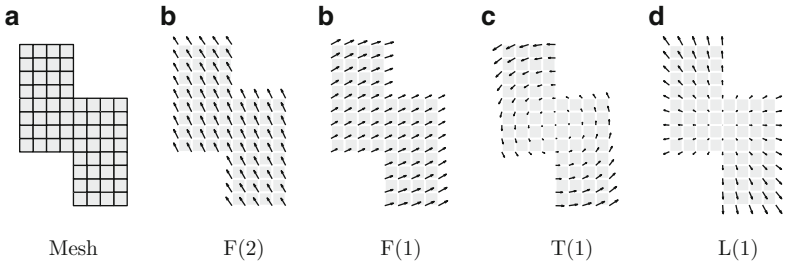

Fig. 2.5 (**a**) Meshed waveguide with Z-shaped cross-section as well as (**b**)–(**e**) in-plane displacements of the basic propagating modes

2.4.2 Waveguide with Z-Shaped Cross-Section

Bridge cables are typically composed of two types of twisted wires. Cylindrical wires form the core of those structures, while Z-shaped wires are frequently used in the outer layers [13]. Due to its geometrical complexity, an analytical theory characterizing guided wave propagation in Z-shaped wires is not available.

Therefore, the Waveguide BE method, described in the previous section, is applied to a Z-shaped aluminum [EN AW-6082 T6] waveguide that is horizontally and vertically bounded by 4 mm and 6 mm, see Fig. 2.5a. Similar to waveguides with circular cross-section, mode shapes and circular wavenumbers can be calculated. Figure 2.5b–e illustrate the in-plane displacement fields for the basic modes. The results are similar to the results for cylindrical wires. Beside a longitudinal and a torsional wave mode one can also recognize two independent flexural wave modes with different wavenumbers. Since the previously defined nomenclature is only valid for waveguides with circular cross-sections, the basic wave modes are referred to as L(1), T(1) and F(1) and F(2), respectively.

2.5 SHM Application

In many SHM applications, guided waves are used to detect and characterize defects in elongated structures. General, mode conversion occurs if an incident guided wave hits an defect. The portion of energy scattered by the particular modes is described by scattering coefficients, which depend on the type and size of the defect as well as on the frequency. Determination of these coefficients is possible by means of a variety of methods, e.g. [4, 10].

The classical BE method in combination with the Waveguide FE method has been used in [2, 8] for modeling the interaction of guided waves with defects in 3D waveguides. The Waveguide FE model was constructed using 32 SOLID95 elements in ANSYS, whereas each segment is one element long. The total number of degree of freedom is 801. The BE modeling process involved in this approach has been discussed in detail in [2]. In the current study, an aluminum wire of diameter 4 mm is modeled with a vertical notch. The depth of the notch ranges from 0 to 100 % of to the diameter, while the notch width is 1 mm. The dynamic behavior of the corresponding boundary model (including the defect, see Fig. 2.6a) is determined by applying the classical BE method. Interface boundary conditions between the BE model and the semi-infinite sections on each side of the waveguide are implemented as a modal sum of all permitted wave modes. The scattered wavefields contain all propagating modes as well as evanescent modes with the lowest imaginary part of the wavenumber.

In the following, an alternative approach is developed by extending the classical BE method with the Waveguide BE method described in Sect. 2.3. For convenience, the material properties for aluminum [ENAW-6082T6] are used in all simulations. WBE-BE results of five simulations (marked by $*$) with notch depths from 20 to 80 % are shown in Fig. 2.6b and compared to WFE-BE results. Using the basic longitudinal wave L(0,1) as incident wave, a good agreement between the scattering coefficients resulting from both methods is observed. Furthermore, results of both methods are compared in terms of energy conservation. In the absence of external forces, the energy conservation concept can be applied in order to validate

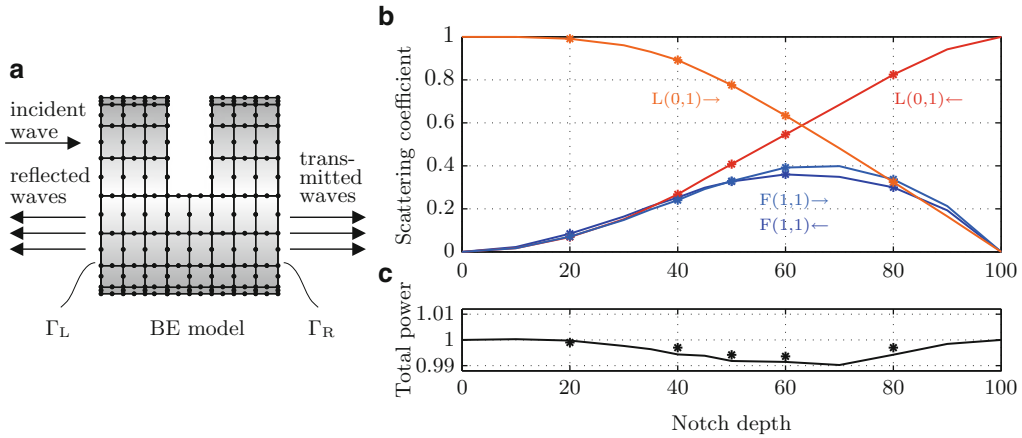

Fig. 2.6 (**a**) Scheme of a BE model with scattered wavefields as interface boundary conditions and (**b**) scattering coefficients for a incident L(0,1) wave at $f = 200$ kHz for variable notch depth based on BE-WFE (*solid lines*) and on BE-WBE method (marked by *) as well as (**c**) corresponding total scattering power. ← denotes reflected, → denotes transmitted propagation modes

the numerical accuracy. Figure 2.6c shows the cumulative power of all scattered waves for both methods. As it can be seen, the use of the Waveguide BE method gives only a marginal improvement compared to the numerical results based on the WFE-BE method.

2.6 Conclusions and Outlook

The wave propagation in waveguides is multimodal and dispersive, depending on the frequency range. In order to predict elastic wave propagation in 3D periodic waveguides with arbitrarily shaped cross-section a Waveguide BE method was introduced. With this numerical tool, circular wavenumbers and mode shapes for waveguides with circular cross-section were calculated and compared with analytical results. Similar simulations were also conducted for waveguides with Z-shaped cross-section. The method allows for an accurate computation and visualization of waveguide modes. Additional, a SHM application of the method was presented in order to investigate mode conversion at defects.

In the future, the authors plan to implement online SHM concepts for multi-wire systems. Especially the wave propagation in power cables composed of twisted wires with local contact shows complex coupling behavior. These aspects have to be considered in order to develop new feasible damage detection concepts.

References

1. Achenbach J (1987) Wave propagation in elastic solids. North Holland, Amsterdam. ISBN 0720403251
2. Bischoff S, Gaul L (2013) Simulation of guided wave interaction with defects in rope structures. In: Allemang R, De Clerck J, Niezrecki C, Wicks A (eds) Special topics in structural dynamics, vol 6, Conference proceedings of the society for experimental mechanics series. Springer, New York, pp 603–609. ISBN 978-1-4614-6545-4
3. Brebbia C, Dominguez J (1992) Boundary elements: an introductory course. WIT Press, Southampton
4. Cho Y, Rose JL (1996) A boundary element solution for a mode conversion study on the edge reflection of Lamb waves. J Acoust Soc Am 99(4):2097–2109
5. Farrar CR, Doebling SW (1998) Damage detection II: field applications to large structures. In: Proceedings of modal analysis & testing conference, NATO Advanced Study Institute, Sesimbra, pp 427–443
6. Gaul L, Schanz M (1999) A comparative study of three boundary element approaches to calculate the transient response of viscoelastic solids with unbounded domains. Comput Methods Appl Mech Eng 179(1–2):111–123
7. Gaul L, Kögl M, Wagner M (2003) Boundary element methods for engineers and scientists. Springer, Berlin
8. Gaul L, Sprenger H, Schaal C, Bischoff S (2012) Structural health monitoring of cylindrical structures using guided ultrasonic waves. Acta Mech 223:1–12
9. Graff KF (1991) Wave motion in elastic solids. Dover, New York
10. Gregory RD, Gladwell I (1983) The reflection of a symmetric Rayleigh-Lamb wave at the fixed or free edge of a plate. J Elast 13(2):185–206

11. Lachat JC, Watson JO (1976) Effective numerical treatment of boundary integral equations: a formulation for three-dimensional elastostatics. Int J Numer Method Eng 10(10):991–1005
12. Mace BR, Duhamel D, Brennan MJ, Hinke L (2005) Finite element prediction of wave motion in structural waveguides. J Acoust Soc Am 117(5):2835–2843
13. Siegert D, Brevet P (2005) Fatigue of stay cables inside end fittings: high frequencies of wind induced vibrations. Bull Int Organ Study Endurance Ropes 89:43–51

Chapter 3
Spectral Element Based Optimization Scheme for Damage Identification

M.I. Albakri and P.A. Tarazaga

Abstract Due to its simplicity, impedance-based structural health monitoring (SHM) has gained a lot of interest in the SHM community. Impedance measurements have proved to be very effective in detecting the presence of damage. Damage identification, on the other hand, can hardly be done with a single impedance measurement, and an array of sensors is normally required to identify damage location and severity. However, impedance measurements contain valuable information about the fundamental frequencies of the structure, and when combined with modelling, more quantitative information on structural damages can be extracted. In this study, a single impedance measurement is used for damage detection and identification in a beam. Spectral element model is developed to calculate the structural impedance of the damaged beam, and then damage defining parameters, which are damage location, width and severity, are updated through an optimization scheme. The proposed technique is computationally efficient, as it requires solving a very small system of equations with only three optimization parameters.

Keywords Structural health monitoring • Electromechanical impedance • Spectral element method • Damage identification • Optimization

3.1 Introduction

Impedance-based structural health monitoring has emerged as a promising non-destructive tool for real-time structural damage assessment. Being an active health monitoring technique, Impedance-based SHM uses piezoceramic (PZT) materials as collocated sensors and actuators. The direct and converse piezoelectric effects are utilized to simultaneously excite the structure and measure its response [1]. It has been shown that the electrical impedance of the PZT material can be directly related to the mechanical impedance of the host structural [2, 3]. This allows for the evaluation of the host structure's health through the measured electrical impedance.

The sensitivity of vibration-based SHM techniques in detecting damage is closely related to the frequency range at which the structure is being interrogated [4]. To sense incipient-type damage, it is necessary for the wavelength of excitation to be smaller than the characteristic length of the damage to be detected [5]. Therefore, impedance-based SHM is carried out at high frequencies, typically in the range of 30–400 kHz. This ensures high sensitivity to incipient damage, but on the other hand, it introduces several modelling-related challenges.

The theoretical basis for impedance-based SHM was first proposed by Liang et al. [2], where the dependence of the piezoelectric impedance on the host structure's mechanical impedance was developed. Later studies extended this concept to include two and three dimensional PZT-structure interactions [6, 7]. These models were mainly semi-analytical in nature, and utilized the finite element method to evaluate the mechanical impedance of the host structure. These models where successfully applied for monitoring structures at relatively low frequencies. However, the FE solutions become increasingly inaccurate as the frequency range increases. The accuracy of the FE approximation can be improved by mesh refinement, and higher order basis functions, but this results in a more computationally expensive model.

M.I. Albakri (✉) • P.A. Tarazaga
Centre for Intelligent Materials Systems and Structures, Virginia Tech, 310 Durham Hall, Blacksburg, VA 24061, USA
e-mail: malbakri@vt.edu; ptarazag@vt.edu

A. Wicks (ed.), *Structural Health Monitoring, Volume 5: Proceedings of the 32nd IMAC, A Conference and Exposition on Structural Dynamics, 2014*, Conference Proceedings of the Society for Experimental Mechanics Series, DOI 10.1007/978-3-319-04570-2_3,

The spectral element method (SEM) provides a more efficient solution for modelling high frequency structural vibrations. Unlike conventional FEM, SEM uses frequency dependent shape functions to construct a dynamic stiffness matrix. This eliminates the need for discretising the structure into elements, and hence, the structure can be represented by a minimum number of degrees of freedom [8, 9]. This has attracted many researches to utilize SEM for high frequency impedance modelling and damage identification. Peairs et al. [10] used SEM with piezoelectric models and electric circuit analysis to model electromechanical impedance. Park et al. [11] developed an integrated methodology to detect and locate structural damages in rods by monitoring impedance measurements and tracking changes in the frequency response function data. Similar work was presented by Guo and Sun [12]. They utilized SEM, optimization techniques, and impedance measurements for damage identification in rods. In these studies, damage identification was performed by discretizing the structure under consideration into a finite number of spectral elements, and then solving for the change in the local wave number in each individual element, corresponding to changes in mass and stiffness at damage location. This approach increases the number of spectral elements required to model the structure, thus increasing computational cost and greatly hampering the advantage offered by the spectral element method. Furthermore, the accuracy to which the damage can be identified, in terms of location and width, is limited by the resolution of the spectral element mesh.

In this paper, a semi-analytical model for electromechanical impedance is first developed. Spectral element method is utilized for evaluating the mechanical impedance of the host structure. The structure examined in this study is a beam undergoing both axial and flexural vibrations. For damage identification, a single open, non-propagating crack is considered. Damage defining parameters, which are damage location, width and severity, are updated through an optimization scheme. The proposed technique is computationally efficient, as only four spectral elements are used to fully describe the damaged beam.

3.2 Modeling

A semi-analytical model for electromechanical impedance is developed in this section. Following Liang et al. [2], an analytical model for the electrical impedance is first presented in Sect. 3.2.1. A spectral element model for evaluating the mechanical impedance of the host structure is then derived in detail in Sect. 3.2.2.

3.2.1 Electromechanical Impedance Model

Figure 3.1a shows a PZT patch attached to a host beam that undergoes both longitudinal and flexural vibrations. Due to the coupled electromechanical characteristics of piezoceramics, the measured electrical admittance of the PZT patch depends on both the dynamic characteristics of the PZT itself and the mechanical impedance of the host structure, denoted by Z_{St} [2]. Assuming linear piezoelectricity, the constitutive equations of the PZT patch operating in 1–3 mode are [13]

$$\begin{aligned} \varepsilon_{11} &= d_{13} E_3 + \overline{s}_{11}^{E} \sigma_{11} \\ D_3 &= \overline{e}_{33}^{\sigma} E_3 + d_{31} \sigma_{11} \end{aligned} \tag{3.1}$$

where ε_{11} is the mechanical strain, σ_{11} is the stress, D_3 is the electric displacement, E_3 is the electric field, d_{31} is the piezoelectric coupling coefficient, $\overline{s}_{11}^{E} = s_{11}^{E}(1 - i\eta)$ is the complex mechanical compliance of the material measured at zero

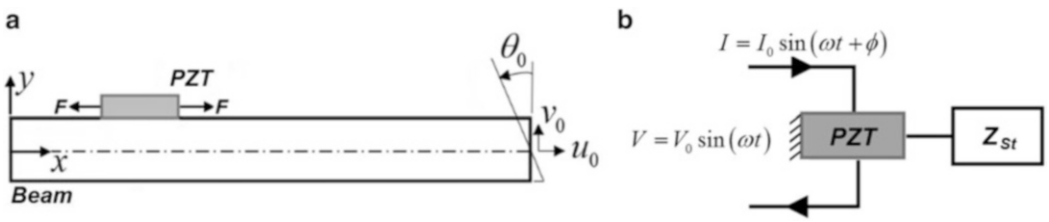

Fig. 3.1 (**a**) A beam with a single PZT patch, (**b**) Liang's model

electric field, $\overline{e}_{33}^{\sigma} = e_{33}^{\sigma}(1 - i\delta)$ is the complex permittivity measured at zero stress, η and δ are the mechanical loss factor, and the dielectric loss factor, respectively.

If the PZT patch is perfectly bonded to the host structure, shear lag effects are negligible, and assuming that the dimensions of the PZT patch are much smaller than those of the host structure, such that both PZT ends experience the same value Z_{St}. The electrical admittance of the PZT actuator can be described as [2]

$$Y(\omega) = \frac{I}{V} = i\omega \frac{w_a l_a}{h_a}\left[\overline{e}_{33} - d_{31}^2 \overline{Y}^E + \frac{Z_a}{Z_{st} + Z_a} d_{31}^2 \overline{Y}^E \frac{\tan(k l_a)}{k l_a}\right] \tag{3.2}$$

where $Z_a = \frac{w_a h_a \overline{Y}^E}{i\omega l_a} \cdot \frac{k l_a}{\tan(k l_a)}$ is the PZT short circuit impedance, $k = \left(\omega^2 \rho_a / \overline{Y}^E\right)^{1/2}$ is the wave number, ρ_a is the density of the PZT material, w_a, h_a, and $2l_a$ are the PZT width, thickness and length, respectively.

3.2.2 Structural Impedance Model

The PZT actuator exerts an eccentric force on the host structure, resulting in both longitudinal and flexural vibrations, as shown in Fig. 3.1a. The displacement at any point in the beam can be defined by the longitudinal and lateral components, denoted by $u(x, y, t)$ and $v(x, y, t)$, respectively

$$\begin{aligned} u(x, y, t) &= u_0(x, t) + y\theta_0(x, t) \\ v(x, y, t) &= v_0(x, t) \end{aligned} \tag{3.3}$$

where u_0 and v_0 denote the axial and transverse displacements of the beam's neutral axis, respectively. θ_0 is the rotation angle of the normal to the neutral axis. With small strains and deformations, the state of strain at any point in the beam is given by

$$\begin{aligned} \varepsilon_{11}(x, y, t) &= \frac{\partial u(x, y, t)}{\partial x} = \frac{\partial u_0(x, t)}{\partial x} - y\frac{\partial \theta_0(x, t)}{\partial x} \\ \varepsilon_{12}(x, y, t) &= \frac{1}{2}\left(\frac{\partial u(x, y, t)}{\partial y} + \frac{\partial v(x, y, t)}{\partial x}\right) = \frac{1}{2}\left(\frac{\partial v_0(x, t)}{\partial x} - \theta_0(x, t)\right) \end{aligned} \tag{3.4}$$

The total potential energy functional, U, kinetic energy functional, T, and the work done by external forces, W, are

$$\begin{aligned} U &= \frac{1}{2}\int_V \sigma^T \varepsilon \, dV = \frac{1}{2}\int_0^L \left\{ \overline{Y}_B A\left(\frac{\partial u_0}{\partial x}\right)^2 + Y_B I\left(\frac{\partial \theta_0}{\partial x}\right)^2 + GAK_1\left(\frac{\partial v_0}{\partial x} - \theta_0\right)^2 \right\} dx \\ T &= \frac{1}{2}\int_V \rho\left(\dot{u}^2 + \dot{v}^2\right) dV = \frac{1}{2}\int_0^L \left\{\rho A\left(\dot{u}_0^2 + \dot{v}_0^2\right) + \rho I K_2 \dot{\theta}_0^2\right\} dx \\ W &= F_x u|_0^L + F_y v|_0^L M\theta|_0^L \end{aligned} \tag{3.5}$$

where Y_B is the beam's young modulus of elasticity, G is the beam's modulus of rigidity, ρ is the beam's density. K_1 and K_2 are Timoshenko's shear and inertia correction factors, respectively. Applying Hamilton's principle yields

$$\rho A \frac{\partial^2 u_0}{\partial t^2} - Y_B A \frac{\partial^2 u_0}{\partial x^2} = 0$$
$$\rho A \frac{\partial^2 v_0}{\partial t^2} - GAK_1 \frac{\partial}{\partial x}\left(\frac{\partial v_0}{\partial x} - \theta_0\right) = 0$$
$$\rho I K_2 \frac{\partial^2 \theta_0}{\partial t^2} - Y_B I \frac{\partial^2 \theta_0}{\partial x^2} - GAK_1\left(\frac{\partial v_0}{\partial x} - \theta_0\right) = 0 \tag{3.6}$$

External forces and moments are given by

$$F_x = Y_B A \frac{\partial u_0}{\partial x}.$$
$$F_y = GAK_1\left(\frac{\partial v_0}{\partial x} - \theta_0\right)$$
$$M = Y_B I \frac{\partial \theta_0}{\partial x} \tag{3.7}$$

From Eq. 3.6, it could be noted that axial and flexural deformations are completely uncoupled, which allows for solving them separately. Separation of variables yields

$$u_0(x,t) = \widehat{u}(x)e^{i\omega t} = \left(A_1 e^{ik_0 x} + A_2 e^{-ik_0 x}\right) e^{i\omega t}$$
$$v_0(x,t) = \widehat{v}(x)e^{i\omega t} = \left(B_1 e^{-ik_1 x} + B_2 e^{-ik_2 x} + B_3 e^{-ik_3 x} + B_4 e^{-ik_4 x}\right) e^{i\omega t}$$
$$\theta_0(x,t) = \widehat{\theta}(x)e^{i\omega t} = \left(R_1 B_1 e^{-ik_1 x} + R_2 B_2 e^{-ik_2 x} + R_3 B_3 e^{-ik_3 x} + R_4 B_4 e^{-ik_4 x}\right) e^{i\omega t} \tag{3.8}$$

where k_0 is the wave number for the axial deformations given by: $k_0 = (\omega^2 \rho / Y_B)^{1/2}$, $k_1, \ldots, k_4$ are the two pairs of wave numbers associated with flexural deformations calculated by solving the following characteristic equation

$$\det\left(\begin{bmatrix} \rho A\omega^2 - GAK_1 k^2 & iGAK_1 k \\ -iGAK_1 k & \rho I\omega^2 K_2 - Y_B I k^2 - GAK_1 \end{bmatrix}\right) = 0 \tag{3.9}$$

$R_1, \ldots, R_4$, are the amplitude ratios of lateral deflections and their corresponding rotations given by

$$R_n = i\frac{\rho A\omega^2 - GAK_1 k_n^2}{GAK_1 k_n} \tag{3.10}$$

From Eq. 3.8, nodal displacements can be written as

$$\boldsymbol{d} = H(\omega)\,\mathbf{A} \tag{3.11}$$

where $\boldsymbol{d} = \left[\widehat{u}_1\ \widehat{v}_1\ \widehat{\theta}_1\ \widehat{u}_2\ \widehat{v}_2\ \widehat{\theta}_2\right]^T$ is the vector of nodal displacements, $\boldsymbol{A} = \left[A_1\ A_2\ B_1\ B_2\ B_3\ B_4\right]^T$ is the vector of unknown coefficients, and $H(\omega)$ is given in Appendix. Similarly, nodal forces can be written as

$$\boldsymbol{F} = G(\omega)\,\mathbf{A} \tag{3.12}$$

where $\boldsymbol{F} = \left[F_{x1}\ F_{y1}\ M_1\ F_{x2}\ F_{y2}\ M_2\right]^T$ is the vector of nodal forces and moments, and $G(\omega)$ is given in Appendix. Thus, the dynamic stiffness matrix, $K_D(\omega)$, relating nodal forces and displacements is calculated

$$\boldsymbol{F} = G(\omega)\,H^{-1}(\omega)\,\boldsymbol{d} = K_D(\omega)\,\boldsymbol{d} \tag{3.13}$$

from which the structural impedance seen by the actuator can be calculated as

$$Z_{st} = \frac{F}{\dot{u}\left(x_1, \frac{1}{2}h_b, t\right)} = \frac{F}{i\omega\widehat{u}\left(x_1, \frac{1}{2}h_b\right)} \tag{3.14}$$

It is worth noting that the results obtained from spectral element method are readily available in frequency domain, which allows for direct comparison with electromechanical impedance measurements. Moreover, only frequencies of interest are solved for with this method.

3.3 Damage Modeling and Identification

In this study, a single, open and non-propagating crack is considered; a beam with such a crack is shown in Fig. 3.2a. It is assumed that this type of structural damage can be represented by a reduction in axial and bending stiffness of the beam, which in turn changes the local wave number in the element where the crack is located. This is a common assumption in damage detection studies and inverse analysis [11, 14]. With this assumption, the damage can be completely described by determining three parameters, which are crack location, crack width, and stiffness reduction, denoted by x_a, x_b and α, respectively. For simplicity, it is also assumed that the crack is located to the right of the PZT patch, as shown in the Fig. 3.2a. Thus, the cracked beam can be fully described with four spectral elements, as shown in Fig. 3.2b. Element number 3 in the figure is where the crack is located, and its stiffness is reduced by a factor α, such that $\alpha \in (0,1]$. This damage will affect the driving point impedance measured at node number 2, which is the structural impedance seen by the PZT patch. This in turn reflects on the PZT's electrical impedance calculated by Eq. 3.2.

Minimizing the difference between the "measured" electrical impedance and the simulated one, the variables x_a, x_b and α, can be determined, and damage can be located and quantified. Therefore, the inverse problems of damage identification is rendered as an optimization problem. The objective function to be minimized can be formulated as

$$\begin{aligned} &Min.J = 1 - Corr\left(\, Z\left(x_a, x_b, \alpha\right), Z_{measured}\right) \\ &Subject\ to\ x_a > x_1 \\ &x_a + x_b < L - x_1 \\ &0 < \alpha \leq 1 \\ &x_a, x_b, \alpha \geq 0 \end{aligned} \tag{3.15}$$

Since the correlation between the measured and simulated admittances is always ≤ 1, the global minimum is reached when the value of the objective function approaches zero. This is only achievable when the simulated admittance matches the experimentally measured one. The first two constraints are imposed to avoid having elements of zero or negative length. Several optimization techniques could be implemented to solve this problem, most of them are heuristic in nature. In this study, a simplified particle swarm optimization is applied, the details of which is out of the scope of this paper.

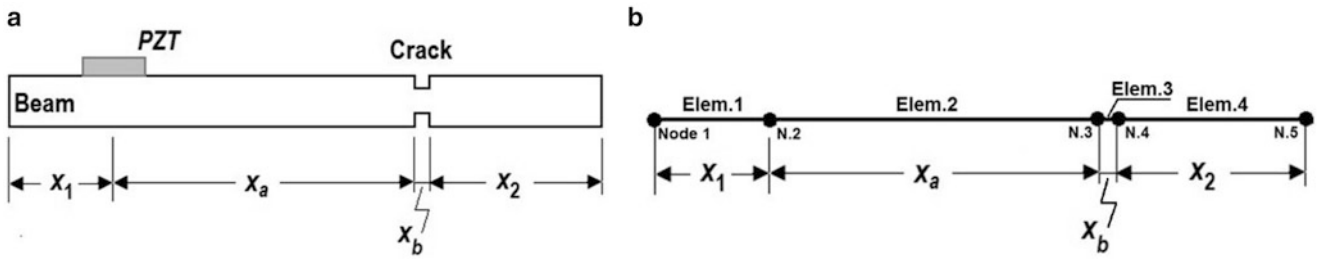

Fig. 3.2 (**a**) Cracked beam with a PZT patch, (**b**) spectral element model

3.4 Simulation Results

Three case studies are presented in this section. In each case, three damage scenarios are considered where either crack location, crack width, or crack severity is varied. The beam addressed in this study is 545 mm long, 25.4 mm wide and 3.175 mm thick aluminium beam fixed at the left end ($x = 0$). For the first case study, relative stiffness reduction is varied while keeping location and with unchanged. Table 3.1 summarizes the different damage scenarios. Figure 3.3 shows the frequency response functions of the longitudinal and transverse vibrations for case study 1. These are the driving point FRFs as seen by the PZT patch.

In general, damage reduces the effective stiffness of the structure, which results in a shift in the FRF towards lower frequencies, in other words, resonant and anti-resonant frequencies shift to the left. The nature of this shift depends on the analysed frequency range, damage location and severity. For instance, the longitudinal displacement anti-resonant frequency originally located at 40,988 Hz, seen in Fig. 3.3a, almost remains unaffected by the introduced damage, with less than 0.03 % change. On the other hand, the other two anti-resonance frequencies shown in Fig. 3.3a are much more sensitive to damage progression. This highlights the importance of selecting a suitable frequency range for impedance-based SHM where high damage sensitivity can be achieved. Simulation results can aid the process of frequency range selection for optimum damage detectability.

The change in structural mechanical impedance affects the PZT's electrical impedance, as suggested by Eq. 3.2. This change in measured electrical impedance can be directly used for damage detection. Impedance signature can also be used for damage identification by minimizing the objective function in Eq. 3.15. However, it has been found that the estimated electrical impedance is very sensitive to the material properties of the PZT patch, in particular complex permittivity and damping coefficient. Accurate values of these parameters is necessary to get a realistic estimate of the piezoelectric impedance. Bhalla and Soh [15] showed that the actual material properties can significantly deviate from what is reported by the manufacturer, and the free–free impedance signature of the PZT patch needs to be examined in order to get the actual values of these parameters. Therefore, PZT electrical impedance will not be presented in the current study, and damage identification will be carried out based on the changes in FRFs rather than impedance signature.

The FRFs of the transverse vibrations for the damage scenarios in case studies 2 and 3 are shown in Fig. 3.4. It could be noted that crack width has a similar impact on FRFs as the relative stiffness reduction. Damage location on the other hand has

Table 3.1 Damage scenarios considered in this study

	Case study 1			Case study 2			Case study 3		
	Damage 1	Damage 2	Damage 3	Damage 1	Damage 2	Damage 3	Damage 1	Damage 2	Damage 3
Stiffness reduction (%)	25	50	75	50	50	50	50	50	50
Damage width (mm)	2	2	2	1	3	5	2	2	2
Damage location (mm)	300	300	300	300	300	300	150	250	350

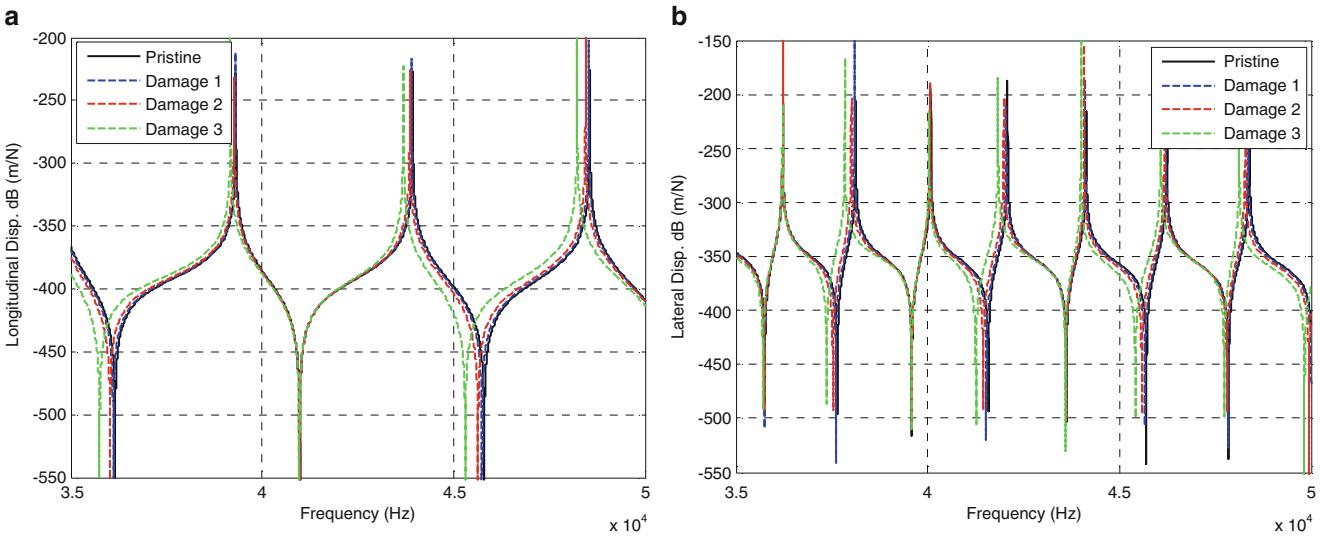

Fig. 3.3 (**a**) Longitudinal displacement FRF, (**b**) lateral displacement FRF for case study 1

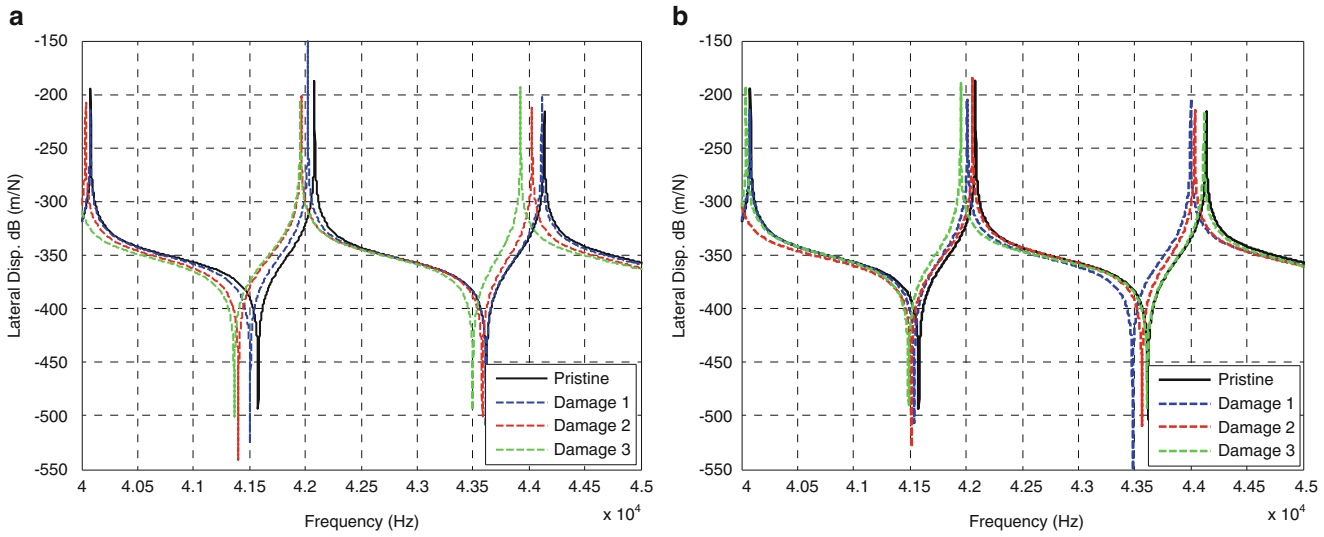

Fig. 3.4 Frequency responses for damage scenarios considered in (**a**) case study 2, and (**b**) case study 3

Table 3.2 Damage identification results

	Case study 1		Case study 2		Case study 3	
	Actual reduction (%)	Estimated reduction (%)	Actual width	Estimated width	Actual location	Estimated location
Damage 1	25	25	1	1	150	150
Damage 2	50	50	3	3	250	250
Damage 3	75	75	5	5	350	350

a completely different effect. While the shifts in FRFs monotonically increase with crack width and severity, damage location has dissimilar effects on different parts of the FRF. For instance, damage location 1 results in a larger shift for the resonance peak located initially at 44,115 Hz, however, for the 40,080 Hz peak, damage location 2 has the most profound effect. At low frequency ranges, the effect of damage location on the FRF can be interpreted through the mode shape associated with each fundamental frequency. However, this task gets more complicated at the high frequency ranges typically encountered with impedance-based SHM. The trends of FRFs dependence on each of the damage defining parameters can be utilized to develop a smart optimization scheme, where the search direction is updated based on the relative shifts in resonance and anti-resonance frequencies. Such an optimization algorithm is currently under development (Table 3.2).

Finally, for each damage scenario in the three case studies presented in this section, the inverse problem is addressed. Damage identification is carried out by minimizing the objective function in Eq. 3.15 with FRFs replacing impedance signatures, the results are summarized in Table 3.2. Due to their monotonic effects on FRFs, very few iterations where needed to determine the optimal values of damage width and relative stiffness reduction. Finding the optimal value for damage location is relatively more complicated, and more iterations are required. The trends discussed earlier can be implemented in the optimization algorithm so as to improve its efficiency.

3.5 Summary

Although modelling is not needed for the basic damage detection when using impedance based SHM, modelling provides valuable insights to this technique. Modeling becomes a necessity when performing more advanced SHM tasks such as damage identification and remaining life estimation (prognosis). In this study, a single impedance measurement is used for damage detection and identification in a beam. Spectral element method is utilized to calculate the high frequency structural impedance of the damaged beam. Damage defining parameters, which are damage location, width and severity, are then updated through an optimization scheme. The proposed technique is computationally efficient, as it requires solving a very small system of equations with three optimization parameters.

The efficiency of the optimization algorithm can be further improved by incorporating the trends of FRFs dependence on each of the damage defining parameters. Experimental validation of this method, including noise effects on damage identification capabilities, will be investigated in a later study.

Appendix

Matrices $H(\omega)$ and $G(\omega)$ appearing in Eqs. 3.11 and 3.12 are

$$H(\omega) = \begin{bmatrix} e^{ik_0x_1} & e^{-ik_0x_1} & 0 & 0 & 0 & 0 \\ 0 & 0 & e^{-ik_1x_1} & e^{-ik_2x_1} & e^{-ik_3x_1} & e^{-ik_4x_1} \\ 0 & 0 & R_1e^{-ik_1x_1} & R_2e^{-ik_2x_1} & R_3e^{-ik_3x_1} & R_4e^{-ik_4x_1} \\ e^{ik_0x_2} & e^{-ik_0x_2} & 0 & 0 & 0 & 0 \\ 0 & 0 & e^{-ik_1x_2} & e^{-ik_2x_2} & e^{-ik_3x_2} & e^{-ik_4x_2} \\ 0 & 0 & R_1e^{-ik_1x_2} & R_2e^{-ik_2x_2} & R_3e^{-ik_3x_2} & R_4e^{-ik_4x_2} \end{bmatrix}$$

$$G(\omega) = \begin{bmatrix} iY_BAk_0e^{ik_0x_1} & -iY_BAk_0e^{-ik_0x_1} & 0 \\ 0 & 0 & -GAK_1(ik_1+R_1)e^{-ik_1x_1} \\ 0 & 0 & -iY_BIk_1R_1e^{-ik_1x_1} \\ iY_BAk_0e^{ik_0x_2} & -iY_BAk_0e^{-ik_0x_2} & 0 \\ 0 & 0 & -GAK_1(ik_1+R_1)e^{-ik_1x_2} \\ 0 & 0 & -iY_BIk_1R_1e^{-ik_1x_2} \end{bmatrix} \times$$

$$\begin{bmatrix} 0 & 0 & 0 \\ -GAK_1(ik_2+R_2)e^{-ik_2x_1} & -GAK_1(ik_3+R_3)e^{-ik_3x_1} & -GAK_1(ik_4+R_4)e^{-ik_4x_1} \\ -iY_BIk_2R_2e^{-ik_2x_1} & -iY_BIk_3R_3e^{-ik_3x_1} & -iY_BIk_4R_4e^{-ik_4x_1} \\ 0 & 0 & 0 \\ -GAK_1(ik_2+R_2)e^{-ik_2x_2} & -GAK_1(ik_3+R_3)e^{-ik_3x_2} & -GAK_1(ik_4+R_4)e^{-ik_4x_2} \\ -iY_BIk_2R_2e^{-ik_2x_2} & -iY_BIk_3R_3e^{-ik_3x_2} & -iY_BIk_4R_4e^{-ik_4x_2} \end{bmatrix}$$

References

1. Park G, Sohn H, Farrar CR, Inman DJ (2003) Overview of piezoelectric impedance-based health monitoring and path forward. Shock Vib Dig 35(6):451–464
2. Liang C, Sun FP, Rogers CA (1994) Coupled electro-mechanical analysis of adaptive material systems — determination of the actuator power consumption and system energy transfer. J Intell Mater Syst Struct 5(1):12–20
3. Giurgiutiu V, Zagrai AN (2000) Characterization of piezoelectric wafer active sensors. J Intell Mater Syst Struct 11(12):959–976
4. Peairs DM, Tarazaga PA, Inman DJ (2007) Frequency range selection for impedance-based structural health monitoring. J Vib Acoust 129(6):701
5. Nokes JP, Cloud GL (1993) The application of interferometric techniques to the nondestructive inspection of fiber-reinforced materials. Exp Mech 33(4):314–319
6. Yang Y, Xu J, Soh C (2005) Generic impedance-based model for structure-piezoceramic interacting system. J Aerosp Eng 18(2):93–101
7. Annamdas V, Soh C (2007) Three-dimensional electromechanical impedance model. I: formulation of directional sum impedance. J Aerosp Eng 20(1):53–62
8. Lee U, Kim J, Leung AY (2000) The spectral element method in structural dynamics. Shock Vib Dig 32(6):451–465
9. Doyle JF (1997) Wave propagation in structures: spectral analysis using fast discrete Fourier transforms. Springer, New York
10. Peairs DM, Inman DJ, Park G (2007) Circuit analysis of impedance-based health monitoring of beams using spectral elements, Struct. Health Monit., 6(1):81–94
11. Park G, Cudney HH, Inman DJ (2000) An integrated health monitoring technique using structural impedance sensors. J Intell Mater Syst Struct 11(6):448–455
12. Guo Z, Sun Z (2011) Spectral element modeling based structure piezoelectric impedance computation and damage identification. Front Archit Civ Eng China 5(4):458–464

13. Leo DJ (2007) Engineering analysis of smart material systems. Wiley, Hoboken
14. Dilena M, Morassi A (2009) Structural health monitoring of rods based on natural frequency and antiresonant frequency measurements. Struct Health Monit 8(2):149–173
15. Bhalla S, Soh C (2004) Structural health monitoring by piezo-impedance transducers. II: applications. J Aerosp Eng 17(4):166–175

Chapter 4
Nonlinear Dynamic Behavior of Cantilever Piezoelectric Energy Harvesters: Numerical and Experimental Investigation

P.S. Varoto and A.T. Mineto

Abstract It is known that the best performance of a given piezoelectric energy harvester is usually limited to excitation at its fundamental resonance frequency. If the ambient vibration frequency deviates slightly from this resonance condition then the electrical power delivered is drastically reduced. One possible way to increase the frequency range of operation of the harvester is to design vibration harvesters that operate in the nonlinear regime. The main goal of this article is to discuss the potential advantages of introducing nonlinearities in the dynamics of a beam type piezoelectric vibration energy harvester. The device is a cantilever beam partially covered by piezoelectric material with a magnet tip mass at the beam's free end. Governing equations of motion are derived for the harvester considering the excitation applied at its fixed boundary. Also, we consider the nonlinear constitutive piezoelectric equations in the formulation of the harvester's electromechanical model. This model is then used in numerical simulations and the results are compared to experimental data from tests on a prototype. Numerical as well as experimental results obtained support the general trend that structural nonlinearities can improve the harvester's performance.

Keywords Energy harvesting • Piezoelectric materials • Nonlinear vibrations • Electromechanical models • Energy scavenging

4.1 Introduction

Energy harvesting is commonly defined as a process where a certain amount of non electrical energy is transformed and stored into electrical energy for future use, mainly to power small electronic equipments such as wireless sensors in a remote network. Piezoelectric vibration energy harvesting fits in this context since it employs piezoelectric materials in the conversion of ambient structural vibration signals into usable electrical energy. Most of literature works have focused on the power harvested when the response behavior can be adequately characterized as a linear oscillator with harmonic excitation [1, 2]. The early studies about energy harvesting from piezoelectric material began in the 1990s with the work of Starner [2], and Umeda et al. [4, 5]. The piezoelectric cantilever is a key structure for energy harvesting applications. Erturk and Inman have recently published a series of papers on energy harvesting using the cantilever model and their work provide a broad coverage of several important modeling aspects that were validated with experimental data [6–9].

Recently, Erturk and Inman [7–10] proposed several mathematical models of beams to analyze the efficiency of cantilever beams used as piezoelectric energy harvesters. Anton and Sodano [11] presented a comprehensive review on relevant contributions on piezoelectric energy harvesting. Although there is a fairly large amount of publications on linear piezoelectric energy harvesting, in recent years nonlinear energy harvesting has received special attention from researchers. The main advantage of using nonlinear models over the common linear approach is the possibility of increasing the frequency range of operation of these harvesters. One of the most common mechanism to introduce nonlinear effects on a typical cantilever beam harvester is by magnetic materials to generate nonlinear magnetic forces that will in turn generate nonlinear elastic forces acting on the system magnetic [12–14]. The inherent material nonlinearities arising for example

P.S. Varoto (✉) • A.T. Mineto
Department of Mechanical Engineering, School of Engineering of Sao Carlos, University of Sao Paulo,
Av. Trabalhador Saocarlense 400, Sao Carlos, SP 13566-560, Brazil
e-mail: varoto@sc.usp.br

A. Wicks (ed.), *Structural Health Monitoring, Volume 5: Proceedings of the 32nd IMAC, A Conference and Exposition on Structural Dynamics, 2014*, Conference Proceedings of the Society for Experimental Mechanics Series, DOI 10.1007/978-3-319-04570-2_4,

from piezoelectric constitutive equations also has influence on the energy harvester and it was first studied by Wagner and Hagedorn [15]. Later, Mann [16] highlight the importance of modeling inherent piezoelectric nonlinearities in energy harvesters.

The main goal of this article is to discuss the potential benefits of introducing nonlinearities in the dynamics of a typical piezoelectric vibration energy harvester. The device is essentially a cantilever beam partially covered by piezoelectric material with a magnet tip mass. We also consider the nonlinear constitutive piezoelectric equations to improve the harvester performance. Governing equations of motion are derived for the harvester considering the excitation applied at its fixed boundary. The nonlinear electromechanical nonlinear model is used in numerical simulations.

4.2 Harvester's Electromechanical Model

This section highlights some key features of the electromechanical model used to investigate the effects and potential benefits of nonlinearities on the output power generated by the energy harvesting system shown in Fig. 4.1. As seen the harvesting device consists of a cantilever metallic beam usually denoted as the substructure and partially covered by piezoelectric ceramic on both sides and carrying a lumped mass at its free end. The piezoceramic layers are connected in series to a load resistor R_1 and the input to the system consists of a base input harmonic acceleration that is applied at the harvester's grounded side. The tip mass consists of a neodymium magnet that is rigidly attached to the substructure's free end and that oscillates in the vicinity of a second magnet. A repulsive or attractive nonlinear force can be then generated at the beam's free end, depending on the magnetic polarity of these magnets. This contactless interaction between the magnetic fields of the tip magnets introduces a nonlinear force on the bimorph beam what in turn can generate nonlinear oscillations of the harvesting device.

Motion and voltage equations of motion for the system shown in Fig. 4.1 can be obtained by employing Lagrange's equations for electromechanical systems [17]

$$\begin{aligned} \frac{d}{dt}\left(\frac{\partial Lg}{\partial \dot{\eta}}\right) - \frac{\partial Lg}{\partial \eta} &= -c_f \dot{\eta} \\ \frac{d}{dt}\left(\frac{\partial Lg}{\partial \dot{\lambda}}\right) - \frac{\partial Lg}{\partial \lambda} &= -\frac{\dot{\lambda}}{R1} \end{aligned} \tag{4.1}$$

where L_g is the so called Lagrangian operator that in the case of the system shown in Fig. 4.1 can be written as

$$L = T_v + T_p + T_m - U_v + U_p + U_m \tag{4.2}$$

where T and U are the harvester's kinetic and potential energies. Subscripts v, p, and m in Eq. (4.2) refer to substrate, piezoelectric material and magnets, respectively. The beam's dynamic $w(x, t)$ deflection relative to the moving boundary is approximated by the single mode and can be written in terms of the mode shape $W(x)$ and modal coordinate $\eta(t)$

$$w(x,t) = W(x)\eta(t) \tag{4.3}$$

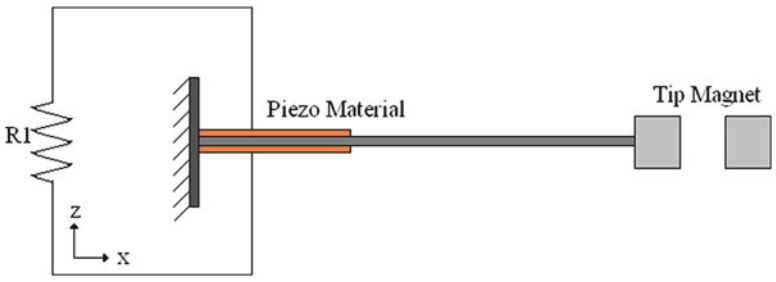

Fig. 4.1 Piezomagnetoelastic vibrational energy harvester model

4.2.1 Kinetic Energy

Derivation of the system's kinetic energy of the substrate and piezoelectric layers can be obtained from

$$T_{v,p} = \frac{1}{2}\rho_{v,p} A_{v,p} \int_0^L (\dot{w}(x,t) + \dot{z}(t))^2 dx \tag{4.4}$$

where the $(\cdot)$ indicates a time derivative, ρ_v and ρ_p are the density of the beam and the piezoelectric material, respectively. Constants A_v and A_p denote the cross sectional area of the beam and the piezoelectric material, respectively. The time dependent variable $z(t)$ is the base motion and L_p is the length of piezoelectric layer. A similar expression to Eq. (4.4) is used to account for the kinetic energy of the lumped magnetic mass m_m attached to the beam's end

$$T_m = \frac{1}{2} m_m [\dot{w}(L,t) + \dot{z}(t)]^2 \tag{4.5}$$

Combination of Eqs. (4.4)–(4.6) leads to the following expression for the harvester's total kinetic energy

$$T = \left[\frac{1}{2}\rho_v A_v W_0^{2L} + \rho_p A_p W_0^{2Lp} + \frac{1}{2} m_m W(L)^2\right] \dot{\eta}(t)^2 + \left[\rho_v A_v W_0^{L} + 2\rho_p A_p W_0^{Lp} + m_m W(L)\right] \dot{\eta}(t)\dot{z}(t) + \\ + \frac{1}{2}\dot{z}(t)^2 \left[m_m + m_v + 2m_p\right] \tag{4.6}$$

Constants m_v, m_p are the total mass of the beam and of the piezoelectric layers, respectively.

4.2.2 Potential Energy

The total potential energy of the system is found by adding the potential energy of the beam, the piezoelectric material and the tip mass. The potential energy distributed along the length of the beam is:

$$U_v = \frac{1}{2} Y_v I_v \int_0^L \left[w''(x,t)\right]^2 dx \tag{4.7}$$

where Y_v is the Young's modulus of the beam material and I_v is the area moment of inertia of the beam about its geometric center. Considering the nonlinearities from the piezoelectric material, the following constitutive equations are used to the compute of the potential energy of the piezoelectric material:

$$\begin{aligned} T_1 &= c_{11} S_1 + c_{111} S_1^2 + c_{1111} S_1^3 - e_{31} E_3 - e_{311} S_1 E_3 - e_{3111} S_1^2 E_3 \\ D_3 &= e_{31} E_3 + e_{311} S_1 E_3 + e_{3111} S_1^2 E_3 + \varepsilon_{33}^s E_3 \end{aligned} \tag{4.8}$$

where T_1 and S_1 are the stress and strain along the length of the beam while D_3 and E_3 indicate the electric displacement and electric field that develops through the thickness of the piezoelectric laminates. The material constants c_{11}, c_{111} and c_{1111} and e_{31}, e_{311} and e_{3111} are the second, third and fourth order elastic and electro-elastic tensor components, respectively.

The potential energy distributed along the length of the piezoelectric material is:

$$U_p = \frac{1}{2} \int_{Vp} (T_1 S_1 - D_3 E_3)\, dV_p \tag{4.9}$$

The potential energy associated to the magnetic force is given as [18, 19]

$$U_m = -\frac{A}{2} W(L)^2 \eta(t)^2 + \frac{B}{4} W(L)^4 \eta(t)^4 \tag{4.10}$$

Thus, the total potential energy of the system is given as

$$U = \left(b + \frac{B}{4}W(L)^4\right)\eta(t)^4 + \left(a - \frac{A}{2}W(L)^2 + \frac{1}{2}Y_v I_v D^2 W_0^{2L}\right)\eta(t)^2 - c\frac{\dot{\lambda}(t)}{2}\eta(t) - d\frac{\dot{\lambda}(t)}{2}\eta(t)^3 - e\dot{\lambda}(t)^2 \tag{4.11}$$

where

$$a = \frac{1}{2}c_{11}b_w\left(\frac{1}{12}h_v^3 + \frac{1}{2}h_v^2 h_p + h_v h_p^2 + \frac{2}{3}h_p^3\right)D^2 W_0^{2lp} \tag{4.12}$$

$$b = \frac{1}{2}c_{1111}b_w\left(\frac{1}{80}h_v^5 + \frac{1}{8}\,h_v^4 h_p + \frac{1}{2}h_v^3 h_p^2 + h_v^2 h_p^3 + h_v h_p^4 + \frac{2}{5}h_p^5\right)D^2 W_0^{4Lp} \tag{4.13}$$

$$c = \frac{1}{2}e_{31}b_w\left(h_v + h_p\right)D^2 W_0^{Lp} \tag{4.14}$$

$$d = \frac{1}{2}e_{3111}b_w\left(\frac{1}{4}h_v^3 + \frac{3}{4}h_v^2 h_p + h_v h_p^2 + \frac{1}{2}h_p^3\right)D^2 W_0^{3Lp} \tag{4.15}$$

$$e = \frac{1}{2}\varepsilon_{33}^s b_w\left(\frac{h_v}{4h_p^2} + \frac{1}{2h_p}\right)L_p \tag{4.16}$$

4.2.3 Lagrangian

Once all energy quantities are determined, the Lagrangian can be found by substitution of all expressions into Eq. (4.2) with further algebraic manipulation. The following expression is then found

$$\begin{aligned} Lg = {} & \left(\frac{1}{2}\rho_v A_v W_0^{2L} + \rho_p A_p W_0^{2Lp} + \frac{1}{2}m_m W(L)^2\right)\dot{\eta}(t)^2 + \left(\rho_v A_v W_0^{L} + \rho_p A_p W_0^{Lp} + m_m W(L)\right)\dot{\eta}(t)\dot{z}(t) + \\ & \frac{1}{2}\left(m_m + m_v + 2m_p\right)\dot{z}(t)^2 - \left(b + \frac{B}{4}W(L)^4\right)\eta(t)^4 - \left(a - \frac{A}{2}W(L)^2 + \frac{1}{2}Y_v I_v D^2 W_0^{2L}\right)\eta(t)^2 + \\ & c\frac{\dot{\lambda}(t)}{2}\eta(t) + d\frac{\dot{\lambda}(t)}{2}\eta(t)^3 + e\dot{\lambda}(t)^2 \end{aligned} \tag{4.17}$$

where c_f is the damping coefficient of the mechanical spring and $\dot{\lambda} = V$ is the voltage of the system. Performing the derivations in Eq. (4.1) and dividing the resulting equations for the modal mass of the system we achieve the following result for the dynamic equations of the energy harvester nonlinear.

$$\begin{cases} \ddot{\eta} + \tilde{c}_f\dot{\eta} + \tilde{k}\eta + \tilde{b}\eta^3 - \tilde{c}V - \tilde{d}V\eta^2 = -\dfrac{F}{m_t}cos\left(\omega t\right) \\ \dot{V} + \dfrac{V}{2R1e} = -\dfrac{c}{4e}\dot{\eta} - \dfrac{3d}{4e}\eta^2\dot{\eta} \end{cases} \tag{4.18}$$

The coefficients appearing in the system of Eq. (4.18) are given by:

$$\tilde{m} = \rho_v A_v W_0^{2L} + 2\rho_p A_p W_0^{2Lp} + m_m W(L)^2 \tag{4.19}$$

$$\widehat{m} = \frac{\rho_v A_v W_0^{L} + 2\rho_p A_p W_0^{Lp} + m_m W(L)}{\tilde{m}} \tag{4.20}$$

$$\tilde{b} = \frac{4b + BW(L)^4}{\tilde{m}} \tag{4.21}$$

$$\tilde{c} = \frac{c}{2\tilde{m}} \tag{4.22}$$

$$\tilde{c}_f = \frac{c_f}{\tilde{m}} \tag{4.23}$$

$$\tilde{d} = \frac{3d}{2\tilde{m}} \tag{4.24}$$

$$\tilde{k} = \frac{\left(2a - AW(L)^2 + Y_v I_v D^2 W_0^{2L}\right)}{\tilde{m}} \tag{4.25}$$

The sign of the stiffness constant k can be positive or negative. The positive sign corresponds to low intensity magnetic forces and in this situation occur the position of static equilibrium and the system is a nonlinear mono-stable oscillator. The natural frequency of the system is given by:

$$\omega_n = \sqrt{\tilde{k}} \tag{4.26}$$

The electromechanical coupled equations given by system of Eq. (4.18) can be solved numerically, solving the initial value problems for ordinary differential equations. In this work it is used the explicit iterative method Runge–Kutta 4,5 in Matlab® for the simulation of Eq. (4.18) for the approximation of solutions of ordinary differential equations.

4.3 Numerical Simulations

In order to investigate potential benefits of introducing nonlinear effects on the performance of the energy harvesting system shown in Fig. 4.1 in terms of output voltage generation a series of numerical simulations were performed with Eq. 4.18 described in the previous section. Numerically simulated results employed the geometrical data and material properties shown in Table 4.1 below. A beam made of spring steel ($130 \times 0.0254 \times 0.000635$ mm) was used as the substructure. It was partially covered by two layers of piezoelectric material in a bimorph configuration. It should be emphasized that the numerical simulations considered the nonlinear effects from the piezoelectric material as defined in the constitutive equations from analytical model. Table 4.1 also shows the main characteristics of the magnetic tip mass used in the simulations. All numerically simulated results presented in this section were obtained with the harvester of Fig. 4.1 operating in the so called mono stable condition, that considers the magnetic gap between the tip masses larger than a given threshold, as previously pointed in [18, 20].

Table 4.1 Dimensions and properties of beam, PZT and tip mass

Parameter	Values
Beam (steel):	
Length L	0.127 m
Width t	0.0254 m
Thickness h_v	0.000635 m
Density ρ_v	7,850 kg/m^3
Young's Modulus Y_v	210 GPa
PZT-5H:	
Length L_p	0.0381 m
Width t	0.0254 m
Thickness h_p	0.5×10^{-4} m
Density ρ_p	7,500 kg/m^3
Piezoelectric constant e_{31}	-16.6 C/m^2
Permittivity $\in_{33}$	1,500 $\in_0 \in_0 = 8.85 \times 10^{-12}$ F/m
c_{1111}, Stanton et al. [14]	-3.6673×10^{17} GPa
e_{3111}, Stanton et al. [14]	1.7212×10^8 C/m^2
Tip mass:	
Length L_t	0.0127 m
Width t	0.0127 m
Thickness h_t	0.0127 m

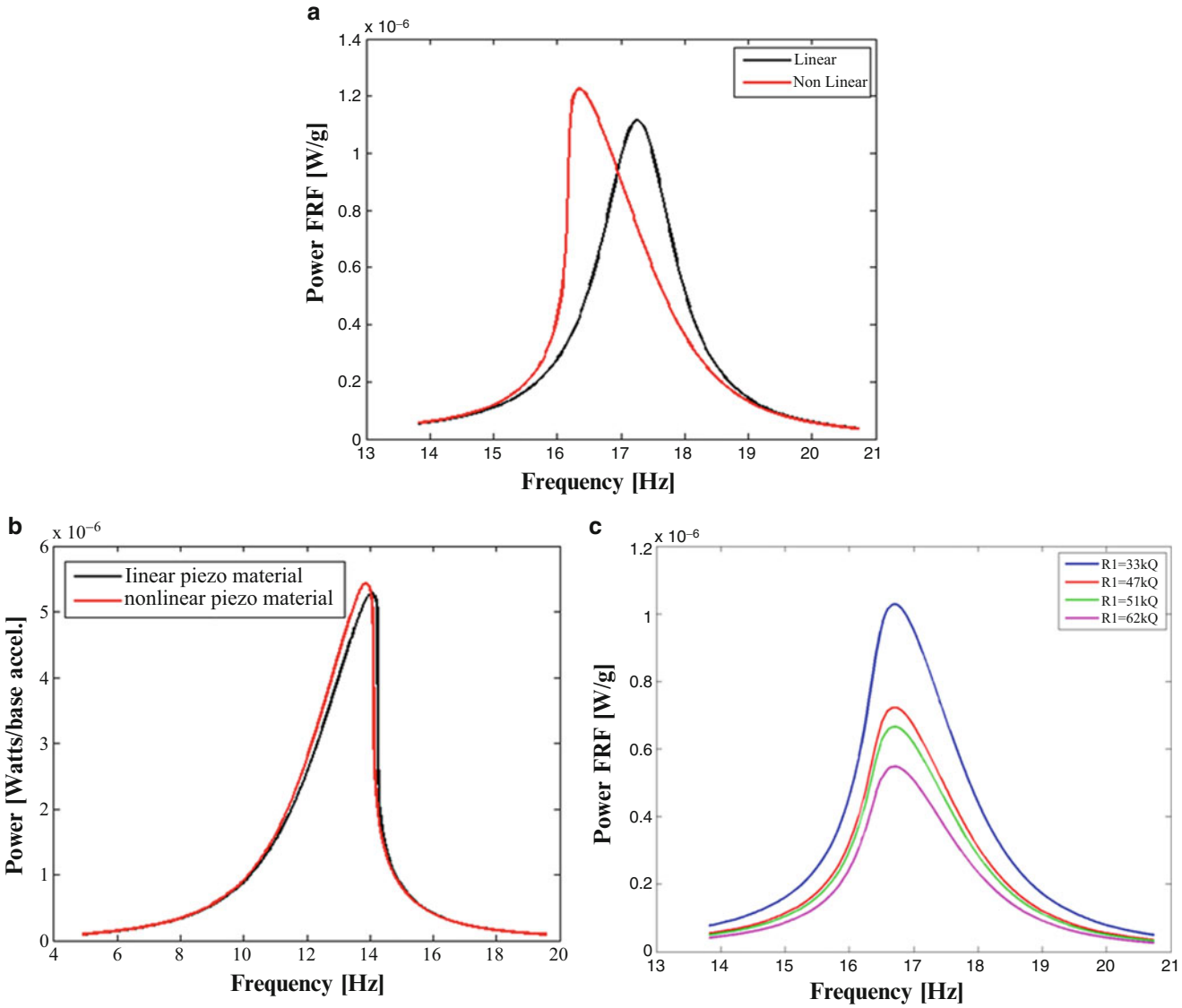

Fig. 4.2 Influence of piezoelectric material nonlinearities: (**a**) linear model versus nonlinear model; (**b**) comparison between linear material and nonlinear associated to hardening effect; (**c**) Influence of load resistance on nonlinear material behavior

Figure 4.2a shows the results of a numerical simulation where the effect of the nonlinearity coming from the piezoelectric material was considered. In this case all magnetic effects were absent and the only nonlinear effects from material properties were considered. Figure 4.2a shows the output power FRF, given as the ratio of the harvester's electrical output to the input base acceleration for case where coefficients c_{1111} and e_{3111} are employed in the constitutive analytical model. When compared to the result from the linear model it is noticed that the presence of piezoelectric material nonlinearities introduce a softening behavior on the resulting output power FRF since the curve slightly bends to the left as the excitation frequency increases. It is also noticed that the nonlinear frequency response has higher amplitude in the vicinity of the harvester's natural frequency than the corresponding linear result. Additionally, the base of the nonlinear power FRF is slightly wider than the linear one suggesting that the material nonlinearity can also contribute to increase the range of working frequencies for the harvester.

The result shown in Fig. 4.2b shows numerical results for the case where a repulsive magnetic nonlinear effect was introduced in the numerical model in addition to the nonlinearity effect coming from the piezoceramics. The result is a hardening behavior as the power FRF bends to the right as the excitation frequency increases. It is noticed that the benefits of the material nonlinearities in this case are slightly more significant in comparison to the linear material assumption since the

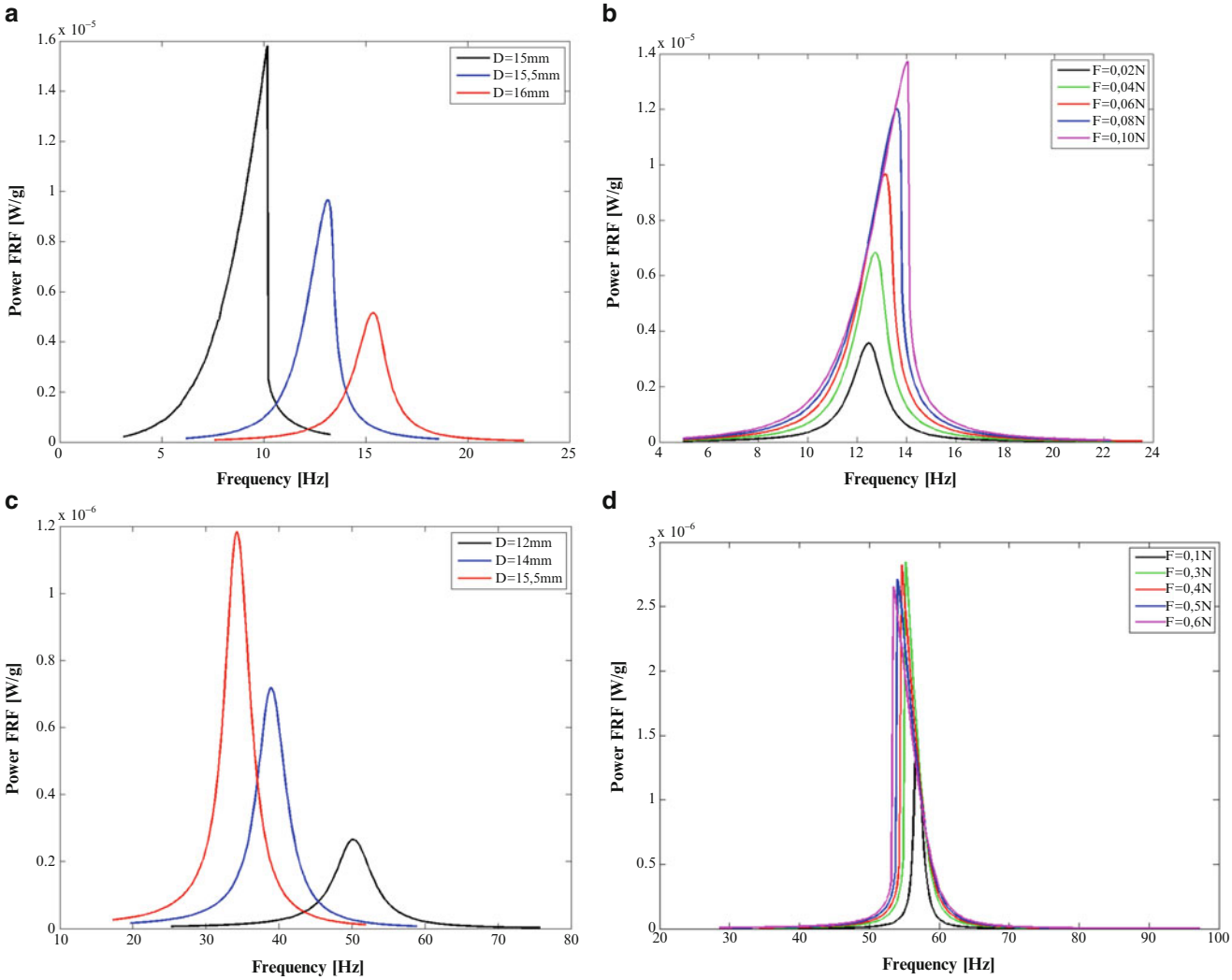

Fig. 4.3 Influence of magnets on power FRF: (**a**) variation of magnet distance, repulsive; (**b**) variation of magnetic force, repulsive; (**c**) variation of magnetic force, attractive; (**d**) variation of magnet distance, attractive

hardening effect from the magnetic field presents a dominant effect. Figure 4.2c shows the effects of the load resistance R1 on the power generation of the mono stable harvester. It is seen that as R_1 increases the amount of electrical power decreases thus suggesting an optimal value for the load resistance R_1 leads to the best performance of the device in terms of power generation.

Next, the effects of the gap between the tip magnets is considered in two situations, repulsive and attractive magnetic forces. Figure 4.3 shows the numerical results obtained in both cases. Figure 4.3a shows the results for the output power FRF when the distance between magnets is varied and a repulsive magnetic force is present. It is noticed that as the magnet gap is increased the value of the natural frequency significantly increases and the output power decreases. Thus the repulsive magnetic force tends to introduce a hardening behavior on the harvesting system associated to also causing a variation in the equivalent stiffness and power FRF amplitude. Figure 4.3b shows numerical results where a constant magnet distance was used and the amplitude of the repulsive magnetic force was varied. As expected as the magnetic force increases, higher values of the peak amplitude are obtained.

The results for the numerical simulations using attractive magnetic forces are shown in Fig. 4.3c, d. Figure 4.3c indicates that as the gap between the attractive magnets is increased the value of the natural frequency decreases and more power is generated. Similar behavior is found for the output power FRF for increasing values of the magnetic attractive force.

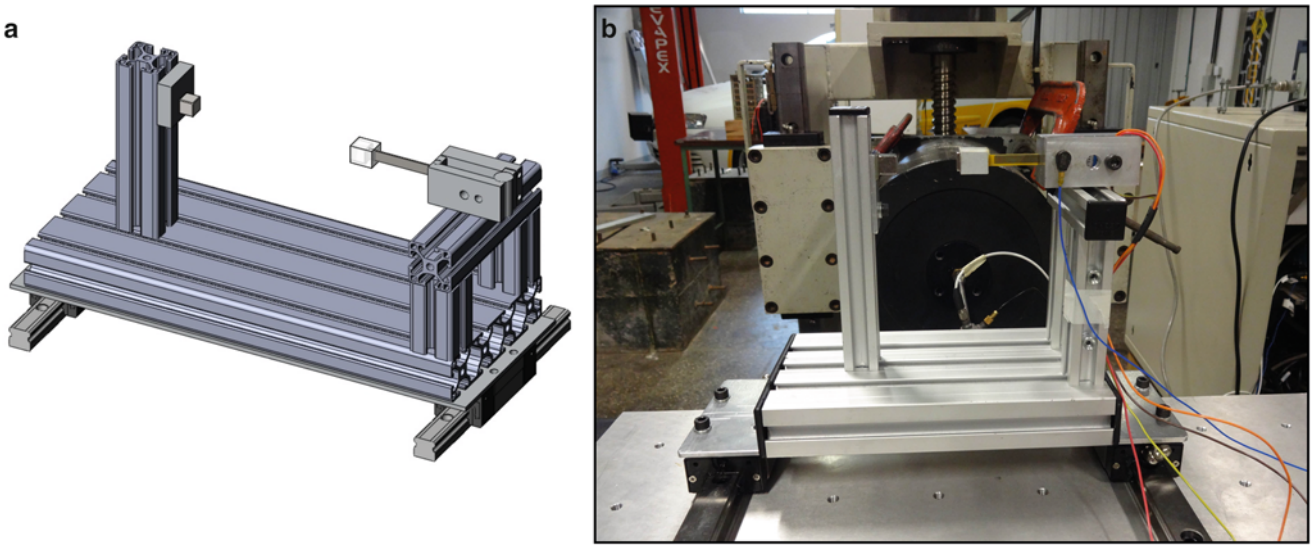

Fig. 4.4 Experimental setup used in tests: (**a**) illustration; (**b**) actual testing apparatus

4.4 Experimental Results

In order to validate some of the results from the numerical simulations presented in the previous section, an experimental analysis were performed on an energy harvesting system. As depicted in Fig. 4.4 a special fixture was constructed in order to test the harvesting device in both linear and nonlinear testing configurations. Figure 4.4a shows an illustration of the testing apparatus and Fig. 4.4b shows the actual device used in the experimental work. A MIDÉ Volture V22BL energy harvester was used in the tests. The sensor is attached to the test fixture through a clamping device that is used to simulate the cantilever boundary condition. A neodymium magnet is attached to the harvester's free end and a second magnet is mounted on a vertical tower that part of the fixture as shown in Fig. 4.4. The magnet gap between the tip and fixed magnet can be varied by moving the vertical tower along the longitudinal axis of the test fixture. The test fixture assembly is mounted on the top of linear tracks and attached to the armature of the vibration exciter that in turn will provide the excitation signals to the harvesting system. Table 4.2 shows the characteristic of the harvester used in the tests. All material properties available were obtained from the manufacturer data sheet.

In relation to the instrumentation used in the tests, an B&K 4808 electromagnetic vibration exciter with B&K 2712 power amplifier was used to provide the excitation signals to the system. The tip velocity of the energy harvester was measured by a Polytec PDV 100 laser vibrometer and the input base acceleration on the harvester clamp fixture was measure by a tear drop PCB 352A24 (101.5 mV/g) piezoelectric accelerometer along with a PCB 482A16 power unit. All signals were acquired by an four channels SignalCalc ACE 104 PCMCIA spectrum analyzer from Data Physics Corporation. Two types of tests were performed on the system shown in Fig. 4.4, namely the Linear Test and the Nonlinear Test. In the linear tests no magnetic force of any nature was introduced since the main goal of conducting linear tests is to identify basic characteristics of the energy harvesting system such as the damped natural frequency. Therefore the linear tests were conducted in the absence of the magnet located on the vertical tower shown in Fig. 4.4. For the nonlinear tests, the second magnet was introduced and several testing conditions were experimentally examined, as it will be further discussed.

4.4.1 Linear Tests Results

Experimental results for linear tests were obtained by applying a random input excitation signal to the test system. A low amplitude excitation signal was used throughout the linear tests. Linear test results are shown in Fig. 4.5. Figure 4.5a, b show the voltage and electrical power FRF relating the harvester's output voltage to the input base acceleration measured by the reference accelerometer located on the harvester's base respectively. These results were obtained by employing several load resistors. It can be noticed that an increasing value for the load resistor leads to higher values of the harvester's output voltage

Table 4.2 Properties of the energy harvester

Geometrical parameters	Beam	Piezo
Length, L (mm)	27.65	24.13
Width, b_w (mm)	6.17	6.17
Thickness, h (mm)	0.69	0.035
Material properties:		
Mass density, ρ (kg/m^3)	–	7,800
Young Modulus, Y (GPa)	–	67
Piezo constant, e_{31} (C/m^2)	–	−190
Permittivity, ε_{33}^S (F/m)	–	−0.9

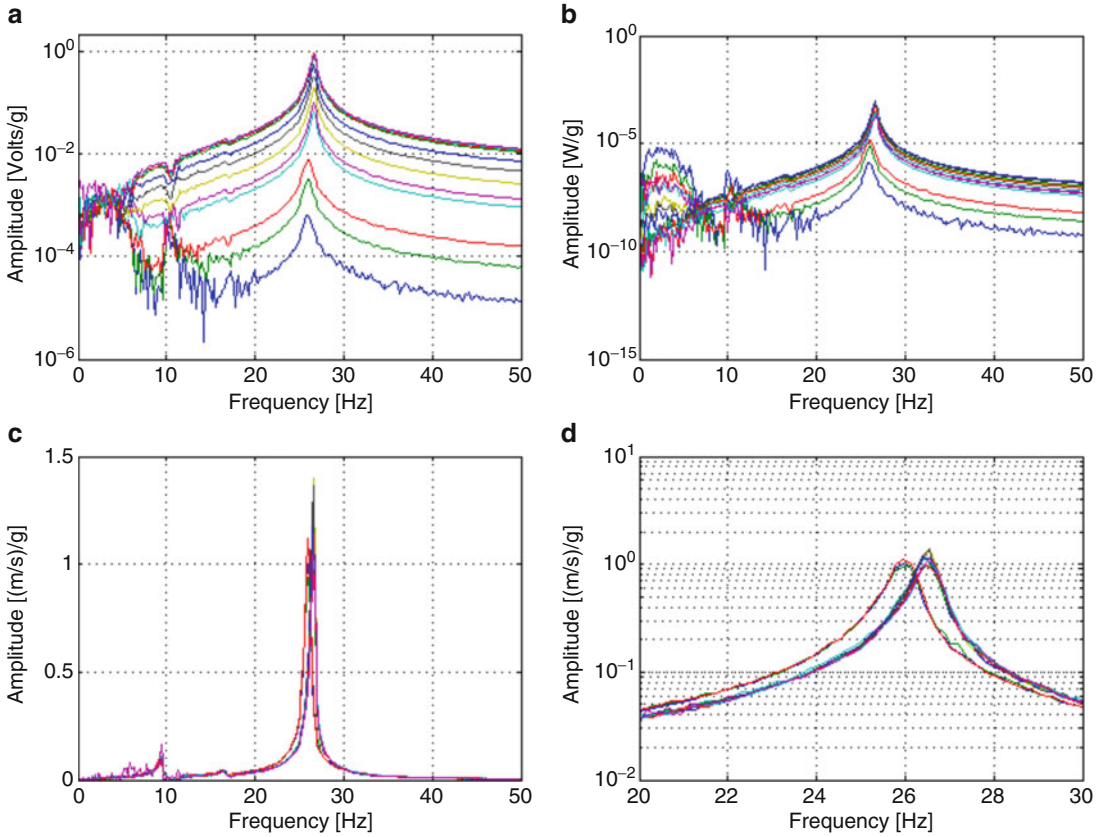

Fig. 4.5 Experimental results from linear tests: (**a**) output voltage FRF; (**b**) output power FRF; (**c**) tip velocity; (**d**) tip velocity in zoom mode

(Fig. 4.5a) and consequently for the output power (Fig. 4.5b). Figure 4.5c, d show the measured tip velocity obtained through the laser signal for all values of load resistors employed. Similar behavior to the results shown in Fig. 4.5 were previously observed [7–10].

4.4.2 Nonlinear Tests Results

Nonlinear tests were performed by applying a sinusoidal excitation of variable frequency (sine sweep) to the test apparatus of Fig. 4.4. For both the repulsive and attractive configuration of the tip magnets two testing scenarios were analyzed. First the amplitude of the input excitation signal was varied and the output harvested voltage was measured. Second, the magnet distance between the magnets was varied and the corresponding output voltage was also measured. Figures 4.6 and 4.7 show

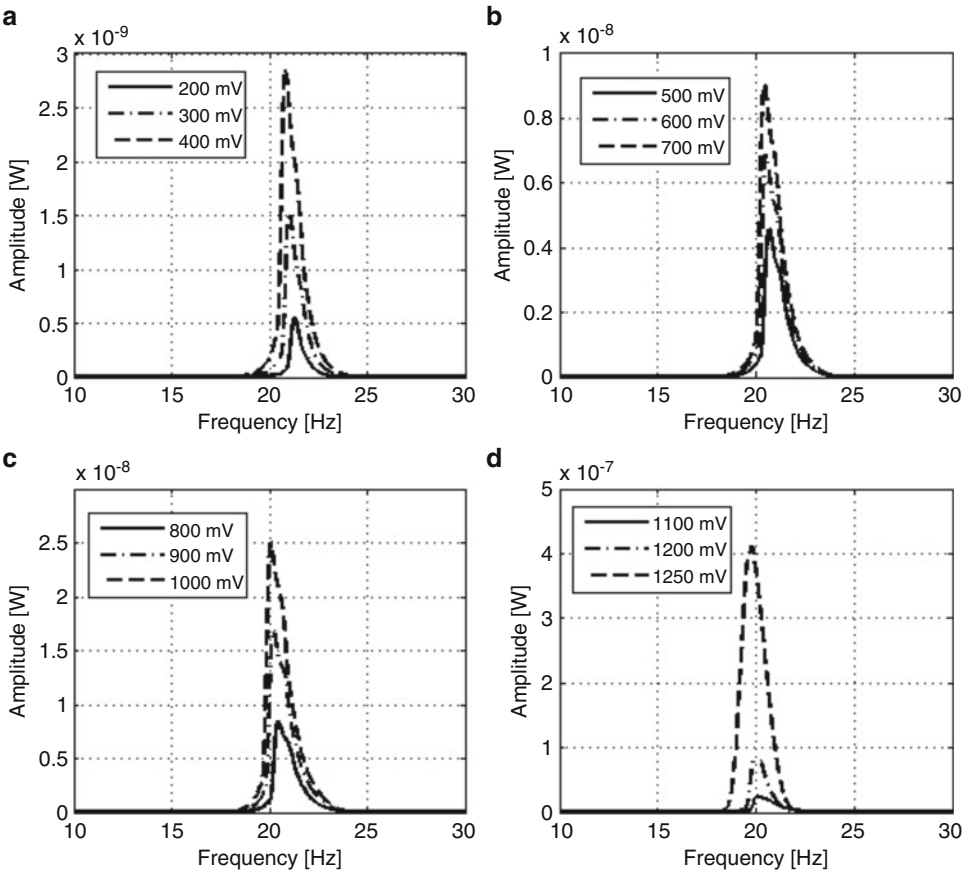

Fig. 4.6 Test results for repulsive tests for several input acceleration levels

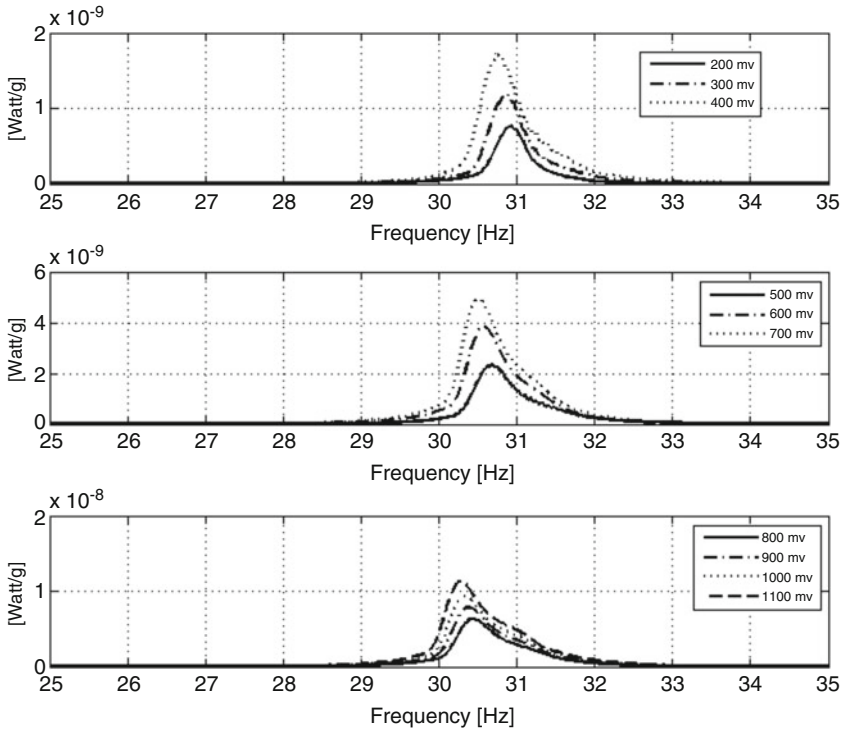

Fig. 4.7 Test results for repulsive tests for several input acceleration levels

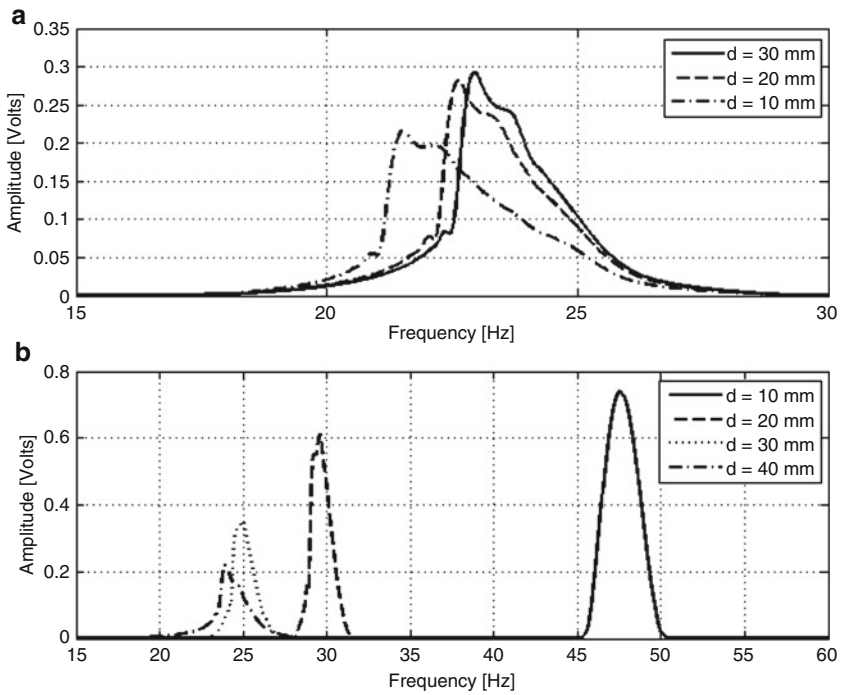

Fig. 4.8 Test results for variable magnet spacing: (**a**) repulsive; (**b**) attractive

the results for the repulsive and attractive configurations of the tip magnets when the input excitation voltage is varied. It can be noticed in both cases that increasing values of the input voltage leads to an increase in the harvester's output voltage. However, for the repulsive case in Fig. 4.6 as the input voltage increases the FRF narrows what is clear indication of a reduction on the harvester working frequency range. For the case of attractive magnets it is seen from Fig. 4.7 that increasing values of the excitation signal leads to more electrical output power being generated and the working bandwidth of the harvester also tends to increase, what in principle points to an advantage over the repulsive configuration. Finally, Fig. 4.8 shows experimental results obtained when the distance between the tip magnet and the fixed magnet is varied, for both repulsive and attractive testing scenarios. It is observed that in the case of repulsive magnet force, Fig. 4.8a as the magnet distance increase the harvester natural frequency and power peak amplitude are affected. Similar results were obtained for the attractive case, as shown in Fig. 4.8b.

4.5 Concluding Remarks

In this paper we presented the modeling and the analytical investigation of a nonlinear piezoelectric energy harvester. The device consisted of a cantilever beam partially covered by piezoelectric material with a magnetic tip mass. In this model was considered the nonlinearity inherent comes from the piezoelectric constitutive equations besides the nonlinearity comes from the magnetic tip mass. The electromechanically coupled equations were solved numerically, through the initial value problems for ordinary differential equations. The electrical power output was investigated varying the amplitude of the base acceleration, the distance between the magnets and the load resistor. We also concluded that the parameters investigated influence in the frequency range of operation of the device and the nonlinear effects present on the energy harvester extend the useful frequency range of studied device. Experimental data supported the results obtained from numerical simulations.

Acknowledgements Authors are grateful to CAPES (*Coordenação de Aperfeiçoamento de Pessoal de Nível Superior-Brazil*) for the financial support received through graduate scholarships and to EESC-USP for the laboratory support received.

Appendix

The following expressions were used in Eqs. (4.6) and (4.11) [18, 20]

$$W_0^{2L} = \int_0^L W^2(x)dx \qquad D^2W_0^{2Lp} = \int_0^{Lp} W''(x)^2dx$$

$$W_0^{L} = \int_0^L W(x)dx \qquad D^2W_0^{2L} = \int_0^L W''(x)^2dx$$

$$W_0^{2Lp} = \int_0^{L_p} W^2(x)dx \qquad D^2W_0^{Lp} = \int_0^{Lp} W''(x)dx$$

$$W_0^{Lp} = \int_0^{L_p} W(x)dx \qquad D^2W_0^{4Lp} = \int_0^{Lp} W''(x)^4dx$$

$$D^2W_0^{3Lp} = \int_0^{Lp} W''(x)^3dx$$

References

1. Williams CB, Yates RB (1996) Analysis of a micro-electric generator for microsystems. In: Transducers95/Eurosensors 9, pp 369–372
2. Starner T (1996) Human-powered wearable computing. IBM Syst J 35:618–629
3. Umeda M, Nakamura K, Ueha S (1996) Analysis of transformation of mechanical impact energy to electrical energy using a piezoelectric vibrator. Jpn J Appl Phys 35:3267–3273
4. Umeda M, Nakamura K, Ueha S (1997) Energy storage characteristics of a piezo-generator using impact induced vibration. Jpn J Appl Phys 35:3146–3151
5. Beeby SP, Tudor MJ, White NM (2006) Energy harvesting vibration sources for microsystems applications. Meas Sci Technol 13:175–195
6. Lin JH, Wu XM, Ren TL, Liu LT (2007) Modeling and simulation of piezoelectric MEMS energy harvesting device. Integr Ferroelectr 95:128–141
7. Erturk A, Innam DJ (2008) Issues in mathematical modeling of piezoelectric energy harvesters. Smart Mater Struct 17:065016
8. Erturk A, Innam DJ (2008) A distributed parameter electromechanical model for cantilevered piezoelectric energy harvesters. J Vib Acoust 130:041002
9. Erturk A, Innam DJ (2008) On mechanical modeling of cantilevered piezoelectric vibration energy harvesters. J Intell Mater Syst Struct 19:1311–1325
10. Erturk A, Innam DJ (2009) An experimentally validated bimorph cantilever model for piezoelectric energy harvesting from base excitations. J Vib Acoust 18:025009
11. Anton SR, Sodano HA (2007) A review of power harvesting using piezoelectric materials (2003–2006). Smart Mater Struct 16:R1–R21
12. Erturk A, Hoffmann J, Inman DJ (2009) A piezomagnetoelastic structure for broadband vibration energy harvesting. Appl Phys Lett 94:254102
13. Stanton S, Mcgehee C, Mann B (2009) Reversible hysteresis for broadband magnetopiezoelastic energy harvesting. Appl Phys Lett 95, 3 pp
14. Stanton S, Mcgehee C, Mann B (2010) Nonlinear dynamics for broadband energy harvesting: investigation of a bistable piezoelectric inertial generator. Physica D 10:640–653
15. Wagner UV, Hagedorn P (2002) Piezo-beam systems subjected to weak electric field: experiments and modelling of nonlinearities. J Sound Vib 256(5):861–872
16. Mann B (2009) Energy criterion for potential well escapes in a bistable magnetic pendulum. J Sound Vib 323(3–5):864–876
17. Preumont A (2006) Mechatronics: dynamics of electromechanical and piezoelectric systems. Springer, Dordrecht
18. Karami MA, Varoto PS, Inman DJ (2011) Experimental study of the nonlinear hybrid energy harvesting system. In: Proceedings of the SEM international modal analysis conference, IMAC-XXIIIX, Jacksonville
19. Daqaq MF (2010) Response of uni-modal Duffing-type harvesters to random forced excitations. J Sound Vib 329:3621–3631
20. Mineto AT (2013) Energy harvesting from nonlinear structural vibration signals. Ph.D. Thesis, University of Sao Paulo, Sao Paulo (in Portuguese)

Chapter 5
Nonlinear Dynamics of a Hybrid Piezo-Electromagnetic Vibrating Energy Harvester

S. Mahmoudi, N. Kacem, and N. Bouhaddi

Abstract The nonlinear dynamics of a novel hybrid piezo-electromagnetic vibrating energy harvester is modeled and investigated. The proposed concept takes advantage of the mechanical elasticity of a sandwich PZT/Steel/PZT beam to perform a vertical guidance for a vibrating magnet while combining electromagnetic and piezoelectric transduction techniques at large displacement. We follow the extended Hamilton principle in order to derive the multiphysics continuum problem and discretize it into a finite system of nonlinear ordinary differential equations in time domain using the Galerkin method. The resulting reduced order model is solved numerically using the harmonic balance method coupled with the asymptotic numerical continuation technique. Several numerical simulations have been performed showing that the performances of a classical vibrating energy harvester can be significantly enhanced up to 100% in term of power density and up to 10% in term of frequency bandwidth.

Keywords Energy harvesting • Nonlinear dynamic • Hybrid harvester • Magnetic levitation • Piezoelectric generator

5.1 Introduction

Energy harvesting from ambient energy aims at realizing electromechanical generators to supply autonomous microsystems from energy of their local environment. The research motivation in energy harvesting is related to the willingness to measure, monitor, and process data from a hostile environment, and be able to communicate in a completely autonomous way. Also, it is due to the reduced power requirement of these small harvester components. On this concept, vibration energy harvesting provides an efficient solution to implement self-sustained low-power microelectromechanical systems or MEMS. In order to make this mechanical energy of ambient vibration usable and turn it into useful electrical energy, there are several types of electromechanical transduction, where the most common transduction modes are electromagnetic [1] and piezoelectric [2].

Conventional linear vibration energy harvesters are usually designed to be resonantly tuned to the ambient dominant frequency. When the system's resonance and excitation frequency do not coincide, the linear harvesting devices are known to under perform. Also, for these kind of devices, the energy from multi-frequency or broad-band excitation may be not suitably captured. So, to increase the widening of the bandwidth and to have more harvested power, researches are oriented towards the study of nonlinear systems. Ferrari et al. [3] proposed a nonlinear piezoelectric harvester that exploit stochastic resonance with white-noise excitation. For instance, Mann et al. [4] took into consideration in their device, magnetic nonlinearity writing the magnetic force as a combination of linear and nonlinear stiffness. They demonstrated that the insertion of the system nonlinearity can result in relatively large oscillations over a wide frequency-band, i.e. the potential improvement of the ability to exploit ambient energy. Recently, new models of energy harvesting, called hybrid harvesters have been developed. These new devices use both transduction techniques, piezoelectric and electromagnetic explained previously. Vinod et al. [5] have developed a hybrid harvester and concluded that the total power is the sum of power produced the magnetic and the piezoelectric ways. Karami et al. [6] analyzed the influence of mechanical and electrical damping on the harvester power. They investigated also the effects of multiphysics coupling of a nonlinear hybrid harvester.

S. Mahmoudi • N. Kacem (✉) • N. Bouhaddi
Applied Mechanics Department, FEMTO-ST - UMR 6174, University of Franche-Comté-24, rue de l'Épitaphe, 25000 Besançon, France
e-mail: saber.mahmoudi@femto-st.fr; najib.kacem@femto-st.fr; noureddine.bouhaddi@univ-fcomte.fr

A. Wicks (ed.), *Structural Health Monitoring, Volume 5: Proceedings of the 32nd IMAC, A Conference and Exposition on Structural Dynamics, 2014*, Conference Proceedings of the Society for Experimental Mechanics Series, DOI 10.1007/978-3-319-04570-2_5,

In this paper, the nonlinear dynamics of a novel hybrid piezo-electromagnetic vibrating energy harvester is modeled and investigated. The proposed concept takes advantage of the mechanical elasticity of a sandwich PZT/Steel/PZT beam to perform a vertical guidance for a vibrating magnet while combining electromagnetic and piezoelectric transduction techniques at large displacements.

The extended Hamilton principle is applied to the considered system in order to derive the equation of motion describing the vertical vibrations of the moving magnet while taking into account the geometric and magnetic nonlinearities. The Galerkin discretization procedure was used in order to transform the mutiphysics continuum problem into a finite system of nonlinear ordinary differential equations in time. The reduced order model is solved numerically by the harmonic balance method coupled with the asymptotic numerical continuation technique. Based on the proposed concept, several numerical simulations have been performed showing that the performances of a particular vibrating energy harvester [4] can be significantly enhanced in terms of power density and bandwidth.

5.2 Design and System Modeling

The concept of the proposed design (Fig. 5.1) is inspired from energy harvesters based on magnetic levitation as described in [1,4]. The main drawback of such electromagnetic harvesters is the large mechanical damping caused by the direct contact of the moving magnet with the inner surface of the tube which reduces the amplitude oscillation, i.e. diminishes the harvested power. This requires the maintenance of the harvester by lubricants. Moreover, these electromagnetic harvesters have a limited band-width since the magnetic nonlinearity is quite low.

To overcome this damping effect and to have a large bandwidth, we propose the design depicted in Fig. 5.1. Two piezoelectric layers are connected in parallel by a middle layer of steel, having a length L, to reinforce the stiffness of the beam. A center magnet *(M)* is attached to the middle of the beam and inserted between the two fixed magnets *(T)* and *(B)* respectively at the top and the bottom. The three magnets are placed vertically in such a way that all opposed surfaces have the same pole. A wire-wound copper coil is wrapped horizontally around the separation distance between the magnet *(M)* and the two other magnets *(T)* and *(B)*.

This axi-symmetric configuration is chosen to ensure that the position of the neutral axis is defined at $y = 0$. The piezoelectric layers are subjected alternatively to tension and compression, when a harmonic excitation $\tilde{Y}(t) = \tilde{Y} sin(\tilde{\Omega}\tilde{t})$ is applied at the device base. The proposed system has a geometric symmetry with respect to the Δ axis as shown in Fig. 5.1. Thus, for simplification reasons, the dynamic study can be limited to a single symmetric part considering the beam clamped at $\tilde{x} = 0$ and guided at $\tilde{x} = L$ and a rigid body along the length L_c.

The continuum multiphysics problem is derived including the equation of motion of the moving magnet at large displacements and the two transduction equations. A variational approach, based on the extended Hamilton principle is applied to the considered dynamical system as follows:

$$\delta I = \int_{t_1}^{t_2} (\delta \mathcal{L} + \delta \mathcal{W}_{nc})\, d\tilde{t} = 0 \tag{5.1}$$

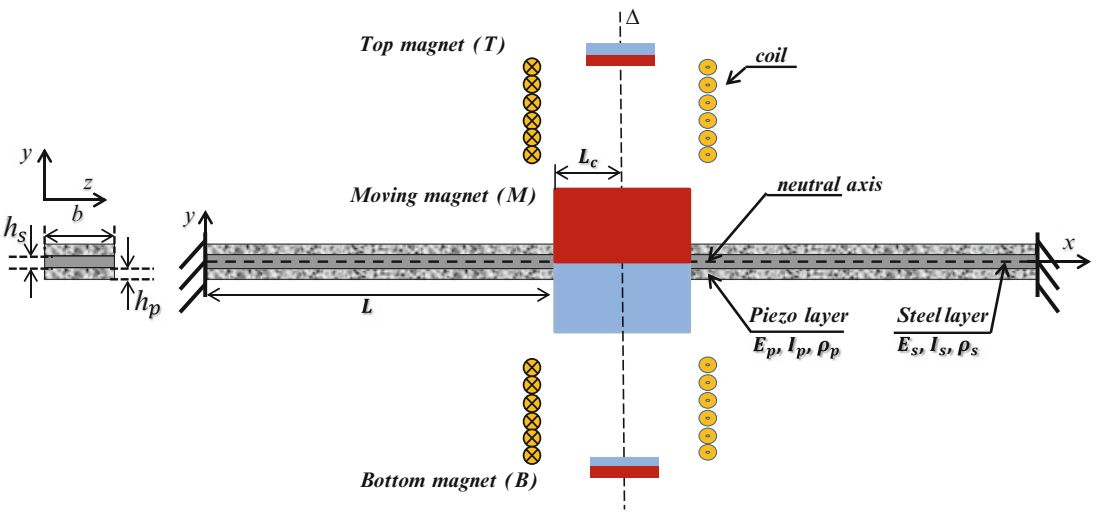

Fig. 5.1 Design of the hybrid piezo-electromagnetic vibrating energy harvester

where $\mathcal{W}_{nc}$ denotes the work of the non-conservative and external forces and $\mathcal{L}$ is the Lagrangien of the system. Doing so, we obtain the following equation of motion,

$$\begin{aligned}&\left[(\rho_s S_s + 2\rho_p S_p)\ddot{\tilde{v}} + (E_s I_s + E_p I_p)\tilde{v}^{(4)} + \tilde{c_m}\dot{\tilde{v}} - N(\tilde{x})\tilde{v}''\right] H_1(\tilde{x}) \\ &+ \left[\tilde{F_m} + \frac{\tilde{c_e}}{L_c}\dot{\tilde{v}}\right] H_2(\tilde{x}) = -\left[(\rho_s S_s + 2\rho_p S_p)H_1(\tilde{x}) + \frac{M}{L_c}H_2(\tilde{x})\right]\ddot{\tilde{Y}}\end{aligned} \tag{5.2}$$

with the associated boundary conditions:

$$\begin{aligned}&\tilde{v}(0,\tilde{t}) = 0 = \tilde{v}'(0,\tilde{t}) \\ &\tilde{v}'(L,\tilde{t}) = 0 = (E_s I_s + E_p I_p)\tilde{v}'''(L,\tilde{t}) - M\ddot{\tilde{v}}(L,\tilde{t})\end{aligned} \tag{5.3}$$

where (I_p,E_p, ρ_p, S_p) and (I_s,E_s, ρ_s, S_s) are the second moment of inertia, the Young's modulus, the density and the cross section , respectively, of the two piezoelectric layers and the steel layer. H_1 and H_2 are two Heaviside functions defining the elastic part along the length L and the rigid one along L_c. $\tilde{F_m}$ is the magnetic force applied to the moving magnet having M as mass, $\tilde{c_m}$ and $\tilde{c_e}$ are respectively the mechanical and electrical damping. $N(\tilde{x})$ is the nonlinear mechanical term due to the beam mid-plane stretching. The piezoelectric layers are connected to a resistance R_p. So the current flowing through this resistance is equal to $\frac{V}{R_p}$, where V is the total generated voltage [7]. Therefore, the governing equation for the piezoelectric transduction is:

$$\frac{V}{R_p} = 2b\, e_{31}\int_0^L \frac{\partial\tilde{v}}{\partial\tilde{x}}\frac{\partial\dot{\tilde{v}}}{\partial\tilde{x}}d\tilde{x} - b\, e_{31}(h_s + h_p)\int_0^L \frac{\partial^2\dot{\tilde{v}}}{\partial\tilde{x}^2}d\tilde{x} - \frac{b\, L\epsilon_{33}}{2h_p}\dot{V}(\tilde{x},\tilde{t}) \tag{5.4}$$

For the electromagnetic transduction, the magnetic field variation in the separation zone gives rise to an induced current $i(\tilde{t})$ respecting Lenz's Law.

$$i(\tilde{t}) = -\left(\frac{\alpha}{R_{load} + R_{int}}\right)\dot{\tilde{v}}|_{\tilde{x}=L} \tag{5.5}$$

where α is an electromagnetic coupling coefficient expressed as $\alpha = NBl$, where N is the number of turns, B the residual magnetic field and l is the coil length.

5.3 Solving

For convenience and equation simplicity, the following nondimensional variables are introduced:

$$v = \frac{\tilde{v}}{r};\quad Y = \frac{\tilde{Y}}{r};\quad t = \frac{\tilde{t}}{\tau};\quad x = \frac{\tilde{x}}{L};\qquad \tau = L^2\sqrt{\frac{\rho_s S_s + 2\rho_p S_p}{E_s I_s + E_p I_p}} \tag{5.6}$$

Then a reduced-order model is generated by modal decomposition transforming the continuum multiphysics problem into a finite degree-of-freedom system consisting of ordinary differential equations in time. Undamped linear bending mode shapes $\phi_i(x)$ of the considered structure are used as basis functions in the Galerkin procedure. Therefore, the deflection is expressed as $v(x,t) = \sum_{i=1}^{n} a_i(t)\phi_i(x)$, where $a_i(t)$ is the ith generalized coordinate. The mode shapes $\phi_i(x)$ are normalized such that $\int_0^1 \phi_i\phi_j dx = \delta_{ij}$. The magnetic force is expanded in a Taylor series up to the third order. Assuming that the first mode is the dominant one and considering that the mechanical damping is structural expressed as $c_m = 2\xi\omega_1$, we obtain the following system of three coupled equations representing piezo-electro-mechanical effects in which the motion of the mechanical structure follows a non-linear Duffing equation,

$$\ddot{a_1} + c\dot{a_1} + \omega_1^2 a_1 + \beta_3 a_1^3 = -F_1\ddot{Y} \tag{5.7}$$

$$\frac{V}{R_p} = I_{elast} - C_p \dot{V} \tag{5.8}$$

$$i(t) = -\frac{\alpha\, r\, \phi_1(1)}{(R_{load} + R_{int})\tau} \dot{a}_1 \tag{5.9}$$

and the boundary conditions are:

$$\begin{aligned} &\phi_i(0) = \phi_i'(0) = 0 \\ &\phi_i'(1) = \frac{E_s I_s + E_p I_p}{L^3} \phi_i'''(1) + \frac{M}{\tau^2} \omega_i^2 \phi_i(1) = 0 \\ &\phi_i(x) = \phi_i(1) \;\; \forall \; 1 \leq x \leq 1 + \frac{L_c}{L} \end{aligned} \tag{5.10}$$

The linear stiffness involves mechanical and magnetic contributions. For this type of harvester, the Duffing term is enhanced by the significant contribution of the nonlinear cubic elastic stiffness. In addition, the overall dissipation is represented by a global coefficient c in Eq. (5.7) which includes a modal and an electrical damping.

The numerical resolution is done by the harmonic balance method coupled with the asymptotic numerical continuation technique [8]. The harvested power is the sum of the two powers transduced piezoelectrically P_p and electromagnetically P_m.

$$P = P_p + P_m = \left(\frac{\omega_1 \frac{2b\, e_{31} r^2}{L\tau} A_1^2 \int_0^1 \phi_1'^2(x) dx}{\sqrt{(2\omega_1 C_p)^2 + \frac{1}{R_p^2}}} \right)^2 \frac{1}{R_p} + R_{load} \left(\frac{\alpha\, r\, \phi_1(1) A_1 \omega_1}{(R_{load} + R_{int})\tau} \right)^2 \tag{5.11}$$

where A_1 is the frequency response amplitude.

5.4 Results and Discussion

Several numerical simulations have been performed in order to highlight the roles of the elastic guidance and the hybrid transduction in terms of bandwidth and harvested power enhancement. The considered geometric and physical properties of the bimorph beam are given in Table 5.1.

Table 5.1 Physical and geometric properties of the bimorph cantilever beam

b	Beam width (m)	8×10^{-3}
L	Beam half-length (m)	50×10^{-3}
L_c	Moving magnet length (m)	10^{-2}
E_s	Effective Steel's Young modulus (GPa)	230.77
E_s^*	Steel's Young modulus (GPa)	210
E_p	Effective piezoelectric's Young modulus (GPa)	69.7
E_p^*	Piezoelectric's Young modulus (GPa)	63
ν_s	Steel's Poisson ratio	0.3
ν_p	Piezoelectric's Poisson ratio	0.31
ρ_s	Steel density (kg/m^3)	7,800
ρ_p	Piezoelectric density (kg/m^3)	7,500
e_{31}	Piezoelectric coupling coefficient (C/m^2) ou (N/V.m)	-13.87
ϵ_{33}	Piezoelectric permittivity (F/m)	1,500 ϵ_0
ϵ_0	Vacuum permittivity (F/m)	8.854×10^{-12}

Table 5.2 Magnetic parameters

Magnet type	NdFeB (N35)
Residual magnetic flux density B (T)	1.18
Coercive force (KA/m^3)	860
Magnet density(Kg/m^3)	7,400
Dimension of the moving magnet (x,y,z) (m)	(0.01,0.01,0.01)
Coil material	copper
External load resistance R_{load} (Ω)	10^3
Internal resistance R_{int} (Ω)	188
Separation distance r (m)	0.005
Total length of the coil l (m)	0.01

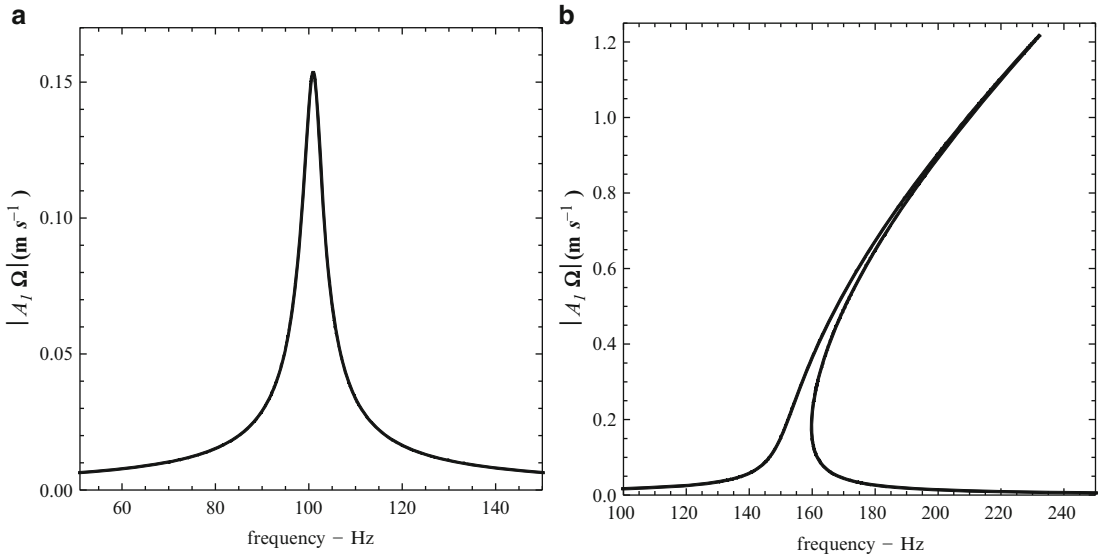

Fig. 5.2 Relative velocity response at excitation amplitudes $F_1\ddot{Y} = 0.9\,g$. (**a**) Case of pure magnetic levitation and (**b**) case of elastic guidance

Table 5.3 Characteristics of some energy harvesting designs based on magnetic levitation

Refs	Bandwidth (Hz)	Acceleration (g)	Volume (cm^{-3})	Density Pmax per g (μWcm^{-3}g^{-1})
Sari [9]	4200–5000	50	1.4	0.0057
Xiang [10]	369, 938, 1184	0.76	9.504	0.44
Nguyen [11]	520–580	0.19	0.0271	29.52
Abu Riduan [1]	7–10	0.5	40.18	104.04
Current work	153–198	0.9	31.2	932

5.4.1 Performance Enhancement by Elastic Guidance

The case of nonlinear electromagnetic VEH is investigated in order to demonstrate the importance of the elastic guidance. To do so, the two piezoelectric layers are removed from the device described in Fig. 5.1 reducing it to the steel beam having a thickness $h_s = 0.75\,10^{-3}$ m , the moving magnet (M) and the other two fixed magnets (B) and (T).

In this case, the motion equation of the resulting system can be deduced from the general equation (5.7) by canceling all piezoelectric terms (ρ_p, E_p, h_p).

Using the magnetic parameters of Table 5.2, the velocity responses of the system with magnetic levitation and with elastic guidance are depicted in Fig. 5.2. The proposed nonlinear VEH is compared to an electromagnetic harvester based on magnetic levitation [1, 4] having the same magnetic properties for which the maximum power density is approximately 587 mW and the bandwidth is around 1.9%. Interestingly, Fig. 5.2 shows that the mechanical nonlinearity due to the beam mid-plane stretching generates large velocities over a wider range of excitation frequencies and consequently an important harvested power. Indeed, the proposed design provides 27 mW in harvested power, 932 μW/cm^{3}g in power density and 29% in bandwidth for a structural damping factor $\xi = 0.25\%$. The remarkable performances of the proposed device with pure electromagnetic transduction are highlighted in Table 5.3 with respect to existing magnetic harvesters.

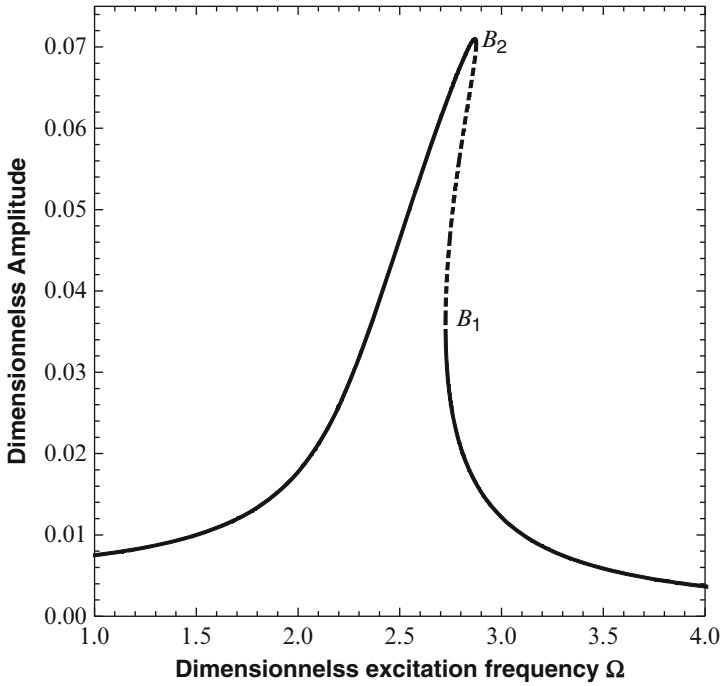

Fig. 5.3 Numerical frequency response of the hybrid VEH with the exception of the quality factor $Q = 50$. *Solid line* denotes stable periodic solutions and a *dashed line* represents unstable periodic solutions

Table 5.4 Thickness of the bimorph beam and magnetic intensities of magnets

Parameter		Value
h_s	Thickness of the steel layer (m)	0.3×10^{-3}
h_p	Thickness of the piezoelectric layer (m)	0.16×10^{-3}
Q_T	Magnetic intensity of the magnet T (Am)	5.37
Q_B	Magnetic intensity of the magnet B (Am)	5.42
Q_M	Magnetic intensity of the magnet M (Am)	86

5.4.2 Performance Enhancement by Hybrid Piezo-Electromagnetic Transduction

The two transduction techniques are combined into a hybrid VEH with piezo-magneto-coupling as depicted in Fig. 5.1. The VEH is excited at its base by a harmonic excitation $\tilde{Y}(\tilde{t}) = \tilde{Y}\sin(\tilde{\Omega}\,\tilde{t})$ where $\tilde{Y} = 5 \times 10^{-5}$ m. The frequency response of the mechanical structure is plotted in Fig. 5.3.

In this configuration, the two transduction techniques are combined into a hybrid VEH and the structural damping has been introduced via a quality factor Q for sandwich materials [12]. The total rigidity of the bimorph beam is amplified which increases the primary resonance frequency of the structure up to $f = 93$ Hz. A slightly nonlinear frequency response of the considered mechanical structure is plotted numerically in Fig. 5.3, using the data in Tables 5.1 and 5.2 as well as the physical and geometrical parameters of Table 5.4. Remarkably, the elastic part of the harvested energy by the piezoelectric transduction is nil when the beam vibrates linearly. Therefore, it is necessary to reach large displacements to take advantage of the PZT layers. In practice, the external excitation at the device base must be significantly high. Numerical simulations show that the device bandwidth and the density power can reach 10% and 1190 $\mu W/cm^3 g$ respectively.

5.5 Conclusion

The non-linear dynamics of a hybrid piezo-electromagnetic vibrating energy harvester (HVEH) was modeled including the main sources of non-linearities. The continuum mutiphysics problem was derived thanks to the extended Hamilton principle. The modal Galerkin decomposition method was used in order to obtain a reduced order model consisting of a nonlinear Duffing equation of motion coupled with two transduction equations. The resulting system was solved using the harmonic balance method coupled with the asymptotic numerical continuation technique.

Several numerical simulations have been performed to highlight the performance of the proposed HVEH. Particularly, the power density and the bandwidth can be boosted up to 60 and 29% respectively compared to the case of a VEH with a pure magnetic levitation thanks to the nonlinear elastic guidance. Moreover, the hybrid transduction permits the enhancement of the power density up to 100% (44% transduced piezo-electrically and 56% harvested magnetically).

Future work will include the optimization of the performances of the proposed nonlinear HVEH when the piezoelectric layers are replaced by PZT patches close to the clamped extremities of the beam.

References

1. Foisal ARM, Hong C, Chung GS (2012) Multi-frequency electromagnetic energy harvester using a magnetic spring cantilever. Sens Actuators A Phys 182(0):106–113
2. Zhou L, Sun J, Zheng XJ, Deng SF, Zhao JH, Peng ST, Zhang Y, Wang XY, Cheng HB (2012) A model for the energy harvesting performance of shear mode piezoelectric cantilever. Sens Actuators A Phys 179(0):185–192
3. Ferrari M, Ferrari V, Guizzetti M, Ando B, Baglio S, Trigona C (2010) Improved energy harvesting from wideband vibrations by nonlinear piezoelectric converters. Sens Actuators A Phys 162(2):425–431
4. Mann BP, Sims ND (2009) Energy harvesting from the nonlinear oscillations of magnetic levitation. J Sound Vib 319(1–2):515–530
5. Challa VR, Prasad MG, Fisher FT (2009) A coupled piezoelectric-electromagnetic energy harvesting technique for achieving increased power output through damping matching. Smart Mater Struct 18(9):095029
6. Karami MA, Inman DJ (2011) Equivalent damping and frequency change for linear and nonlinear hybrid vibrational energy harvesting systems. J Sound Vib 330(23):5583–5597
7. Buchberger G, Schoeftner J (2013) Modeling of slender laminated piezoelastic beams with resistive electrodes-comparison of analytical results with three-dimensional finite element calculations. Smart Mater Struct 22(3):032001
8. Cochelin B, Damil N, Potier-Ferry M (1994) Asymptotic-numerical methods and pade approximants for non-linear elastic structures. Int J Numer Method Eng 37(7):1187–1213
9. Sari I, Balkan T, Kulah H (2008) An electromagnetic micro power generator for wideband environmental vibrations. Sens Actuators A Phys 145–146:405–413
10. Yang B, Lee C, Xiang W, Xie J, He JH, Kotlanka RK, Low SP, Feng H (2009) Electromagnetic energy harvesting from vibrations of multiple frequencies. J Micromech Microeng 19(3):035001
11. Nguyen DS, Halvorsen E, Jensen GU, and Vogl A (2010) Fabrication and characterization of a wideband MEMS energy harvester utilizing nonlinear springs. J Micromech Microeng 20(12):125009
12. Abdelkefi A, Najar F, Nayfeh AH, Ben Ayed S (2011) An energy harvester using piezoelectric cantilever beams undergoing coupled bending-torsion vibrations. Smart Mater Struct 20(11):115007

Chapter 6
Numerical Modeling of Steel-Framed Floors for Energy Harvesting Applications

Joshua A. Schultz, Christopher H. Raebel, and Aaron Huberty

Abstract Pedestrian movement on lightweight steel-framed floor systems can excite several vibration modes in the frequency range from 0 to 30 Hz. Although structural engineers are able to design floor systems that minimize annoying vibrations due to human activities, the frequency modes may be targeted for secondary applications such as low-demand energy harvesting. The techniques of modal analysis are useful in determining the parameters of these floor systems, with the goal of targeting resonant frequency modes for energy harvesting.

Advances in vibration analysis and energy harvesting technology combined with an increasing need for sustainable energy generation have inspired recent development of intermediate scale harvesters for floor vibration. These devices necessitate accurate numerical modeling strategies for coupled steel-framed floor and harvester device systems. An accurate numerical model of a coupled floor-harvester system can provide analysis resulting in optimized and efficient designs for harvesting ambient floor vibrations suitable for energizing low demand applications.

Numerical analysis of an existing experimental floor system is presented. The existing floor system was selected for analysis because its frequencies, damping ratios and mode shapes were previously obtained, allowing for focus on the numerical model. Optimization, limitations and extensions of the numerical model and a modeling protocol is discussed.

Keywords Energy harvesting • Floor vibration • Resonance • Coupled systems • Numerical analysis

6.1 Introduction

Lightweight, steel framed building floor systems are susceptible to occupant-induced vibrations. If the fundamental frequency of the floor system is approximately 7 Hz, the vibrations may be objectionable to those occupying the building [1]. Building design engineers have the capabilities to design a floor system that minimizes annoying vibrations due to walking and other occupant activities.

If floor vibrations are not within the objectionable range, they may be beneficial. Recent advancements in micro-electrical mechanical systems (MEMS) have uncovered their ability to harvest energy from low frequency vibration content [2–5]. The techniques of modal analysis are useful to determine the vibration characteristics of these floor systems [6, 7]. Once identified, building engineers may be able to harvest energy from occupant-induced vibrations in order to power low demand applications such as LED lighting, motion sensors and the like.

This paper describes numerical modeling techniques suitable for determining parameters for harvesting energy from a steel framed floor system. The specimen considered is an existing experimental floor with known dynamic properties [6, 7]. A parametric study of the dynamic properties of a generalized harvesting device is conducted to determine efficient stiffness and mass magnitudes for optimized power output under existing space constraints. The coupling of the device and floor

J.A. Schultz
Skidmore, Owings & Merrill, L.L.P., Chicago, IL 60604, USA
e-mail: joshua.schultz@som.com

C.H. Raebel (✉) • A. Huberty
Department of Civil and Architectural Engineering and Construction Management,
Milwaukee School of Engineering, Milwaukee, WI 53202, USA
e-mail: raebel@msoe.edu; hubertya@msoe.edu

A. Wicks (ed.), *Structural Health Monitoring, Volume 5: Proceedings of the 32nd IMAC, A Conference and Exposition on Structural Dynamics, 2014*, Conference Proceedings of the Society for Experimental Mechanics Series, DOI 10.1007/978-3-319-04570-2_6,

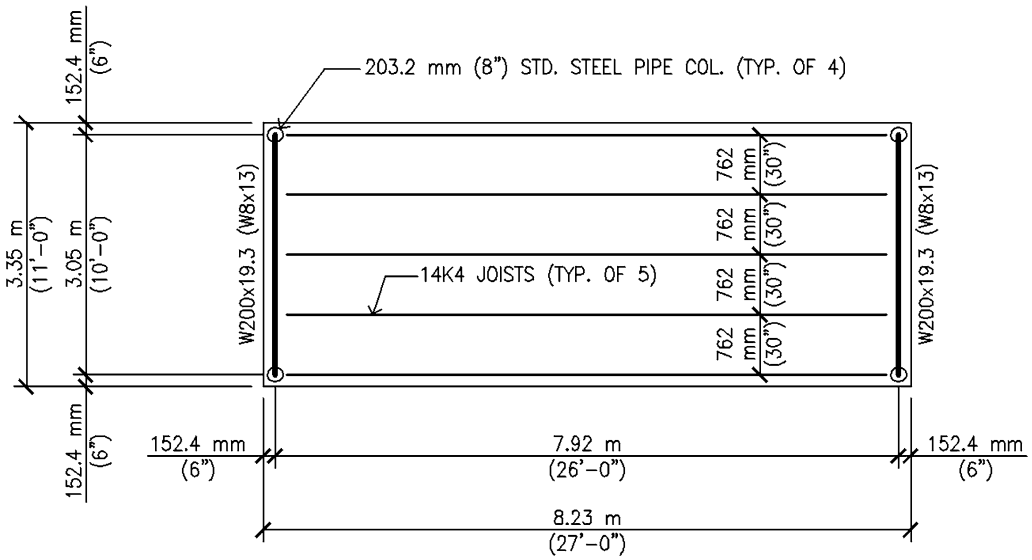

Fig. 6.1 Plan of experimental floor

system results in optimization complexities in which changing one part of the system impacts the vibrational response of the whole. Accordingly, adjusting the stiffness and mass of the device affects the dynamic properties of the host system [8] and can either improve or detract from performance. This dependency is investigated numerically for the mass and stiffness parameters of the system.

6.2 Description of the Experimental Floor

The subject of analysis is an experimental floor designed to be susceptible to walking vibrations. The floor under consideration has been used for past research, including the development of an experimental protocol for vibration assessment [6, 7] and preliminary energy harvesting studies [9]. Although the experimental floor is limited to one bay, the system was designed and constructed to be similar to floor systems typically found in office buildings. The past research was successful in determining modal parameters such as frequencies, damping ratios and mode shapes.

The experimental floor system, illustrated in plan view in Fig. 6.1, consists of a 63.5 mm (2-1/2 in.) thick floor slab comprised of concrete over 25.4 mm (1 in.) deep type "C" form deck. The deck was screwed to 14K4 open web steel joists spaced at 762 mm (30 in.) center to center with a 8.23 m (27 ft) total length. The open web steel joists are supported by W200 × 19.3 (W8 × 13) steel beams with a distance of 3.05 m (10 ft) from center to center of supports. Standard 203.2 mm (8 in.) diameter pipe columns support the beams, and the pipe columns are anchored to a concrete slab-on-grade. Figure 6.2 shows a section cut through the W200 × 19.3 (W8 × 13) steel beam, illustrating the relationship between the deck, steel joist, steel beam and column.

6.3 Modal Properties of the Floor System

Modal properties of the experimental floor system were extracted as part of a prior research initiative [6, 7]. Normalized mode shapes are shown in Fig. 6.3, and the magnitudes of frequency and damping as a percent of critical are shown. The frequencies and damping ratios were measured from a 30 Hz chirp excitation generated from a mechanical shaker. Other excitation types (heel drop, instrumented hammer) produced very similar results, yet slight differences were observed.

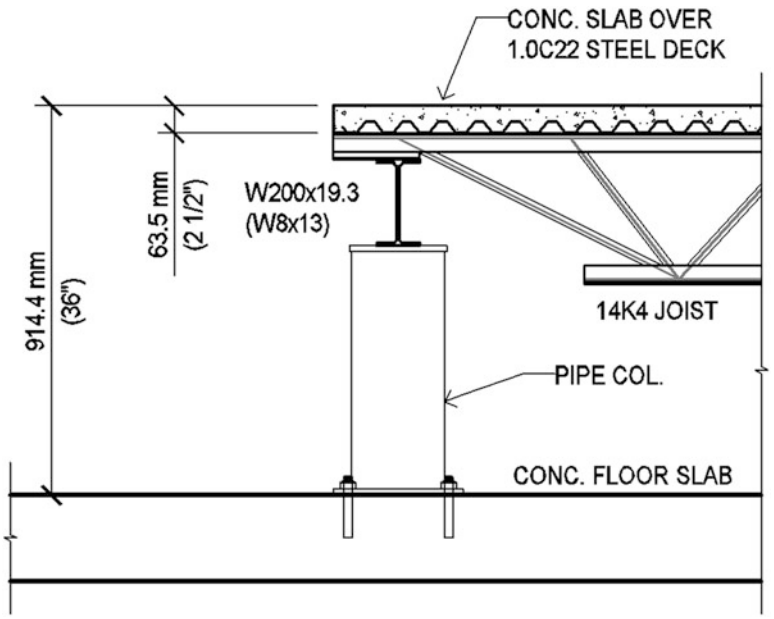

Fig. 6.2 Section cut through W200 × 19.3 (W8 × 13) beam

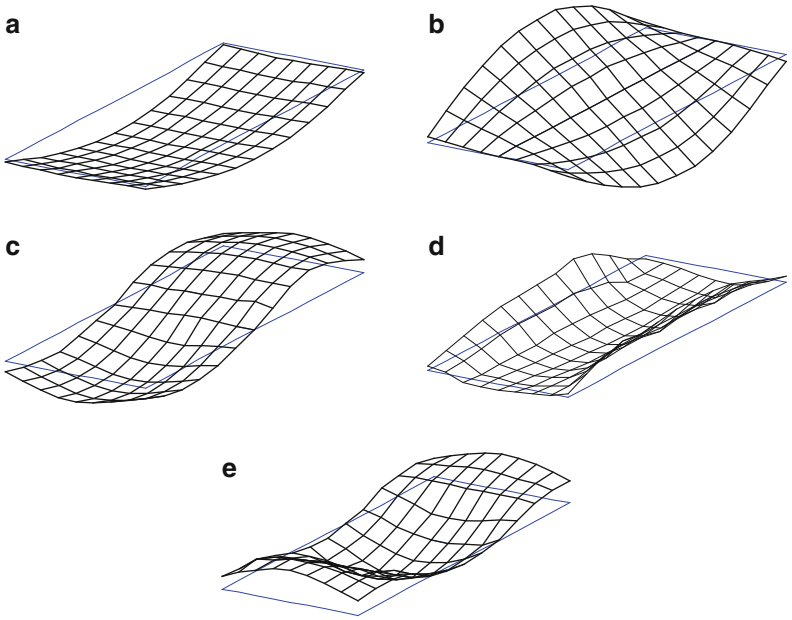

Fig. 6.3 Normalized mode shapes, frequencies and damping ratios for modes 1–5 (found experimentally). (**a**) Mode 1 (7.06 Hz; 0.27 % damping), (**b**) Mode 2 (8.86 Hz; 0.28 % damping), (**c**) Mode 3 (19.36 Hz; 0.42 % damping), (**d**) Mode 4 (23.91 Hz; 0.60 % damping), (**e**) Mode 5 (29.55 Hz; 0.35 % damping)

6.4 Mathematical Model of Floor System

The floor system may be modeled mathematically using a lumped-parameter model possessing "m" modal (normal) and "n" spatial coordinates [10]. This type of model is convenient when attempting to target vibration modes for energy harvesting. The general form of this model is

$$M^*\ddot{Z} + C^*\dot{Z} + K^*Z = \Psi^T F(t) \tag{6.1}$$

$$\dot{Y} = \Psi\dot{Z}; \quad Y = \Psi Z \tag{6.2}$$

where $\ddot{Z}$, $\dot{Z}$, Z are the modal acceleration, velocity and displacement vectors, respectively, each containing *m* elements; *m* is the number of orthogonal modes of vibration included in the model; $\dot{Y}$, Y are the spatial velocity and displacement vectors, respectively, each containing *n* elements; n is the number of spatial coordinates included in the model; and F(t) is

the input force vector containing n elements.

$$\Psi = \begin{bmatrix} \Psi_{11} & \Psi_{12} & \cdots & \Psi_{1m} \\ \Psi_{21} & \Psi_{22} & \cdots & \Psi_{2m} \\ \vdots & \vdots & \ddots & \vdots \\ \Psi_{n1} & \Psi_{n2} & \cdots & \Psi_{nm} \end{bmatrix} = \begin{bmatrix} \Psi_1 \\ \Psi_2 \\ \vdots \\ \Psi_n \end{bmatrix} = \text{modal transformation matrix} \tag{6.3}$$

$$M^* = \begin{bmatrix} 1 & 0 & \cdots & 0 \\ 0 & 1 & \cdots & 0 \\ \vdots & \vdots & \ddots & \vdots \\ 0 & 0 & \cdots & 1 \end{bmatrix}_{mxm} = \text{modal mass matrix} \tag{6.4}$$

$$C^* = \begin{bmatrix} 2\zeta_1\omega_1 & 0 & \cdots & 0 \\ 0 & 2\zeta_2\omega_2 & \cdots & 0 \\ \vdots & \vdots & \ddots & \vdots \\ 0 & 0 & \cdots & 2\zeta_m\omega_m \end{bmatrix} = \text{modal damping matrix} \tag{6.5}$$

where ζ_i is the modal damping coefficient for the i^{th} mode and ω_i is the circular natural frequency for the i^{th} mode.

$$K^* = \begin{bmatrix} \omega_1^2 & 0 & \cdots & 0 \\ 0 & \omega_2^2 & \cdots & 0 \\ \vdots & \vdots & \ddots & \vdots \\ 0 & 0 & \cdots & \omega_m^2 \end{bmatrix} = \text{modal stiffness matrix} \tag{6.6}$$

The mathematical model above illustrates that the parameters required in the analysis of a specific floor system are the circular natural frequencies (ω_i), the modal damping coefficients (ζ_i) and the modal transformation matrix (Ψ) for a prescribed number of vibration modes and spatial coordinates.

6.5 Numerical Model of Floor System

A numerical model was developed using SAP2000 Advanced software [11]. This software is often used by structural engineers for general structural analysis. The program has the capability to perform dynamic analyses of regular systems such as the experimental floor.

The numerical model was intentionally kept simple. Prior studies [6, 7] have shown that relatively accurate floor models can be constructed with commercially available structural analysis software. It is reasonable to believe that floor-harvester system can also be sufficiently modeled with commercially available software.

The SAP2000 model was constructed using plate elements for the concrete slab and beam elements for the open web steel joists, steel beams and columns. In an effort to match the driving point and modal results from the experimental analysis, the model was discretized using a "dense" accelerometer grid of 117 points [6]. Meshing of the plate elements was performed manually in order to maintain control of the mesh. The model was constructed using the dimensions shown in Fig. 6.1, including the overhangs on each edge of the floor.

The concrete slab was modeled as a solid thin plate with a 50.8 mm (2 in.) thickness. This thickness accounts for the solid concrete atop the steel deck plus an equivalent concrete thickness to account for the concrete within the steel deck flutes. The material model for the concrete consisted of a modulus of elasticity of 28,144 MPa (4,082 ksi) and Poisson's ratio of 0.19. The compressive strength used for the concrete was 25.9 MPa (3.75 ksi). These values match the properties measured for the experimental floor [6]. The open web steel joists were modeled using properties from a database internal to SAP2000, and the moment of inertia was adjusted to include the composite properties of the joist. Calculation of the composite moment of inertia is standard practice in floor vibration evaluation and is discussed in detail in reference [1]. The wide flange girder and the pipe columns were also modeled using the properties from an internal database. The material model for the steel consisted of a modulus of elasticity of 200 GPa (29,000 ksi) and a yield stress of 345 MPa (50 ksi).

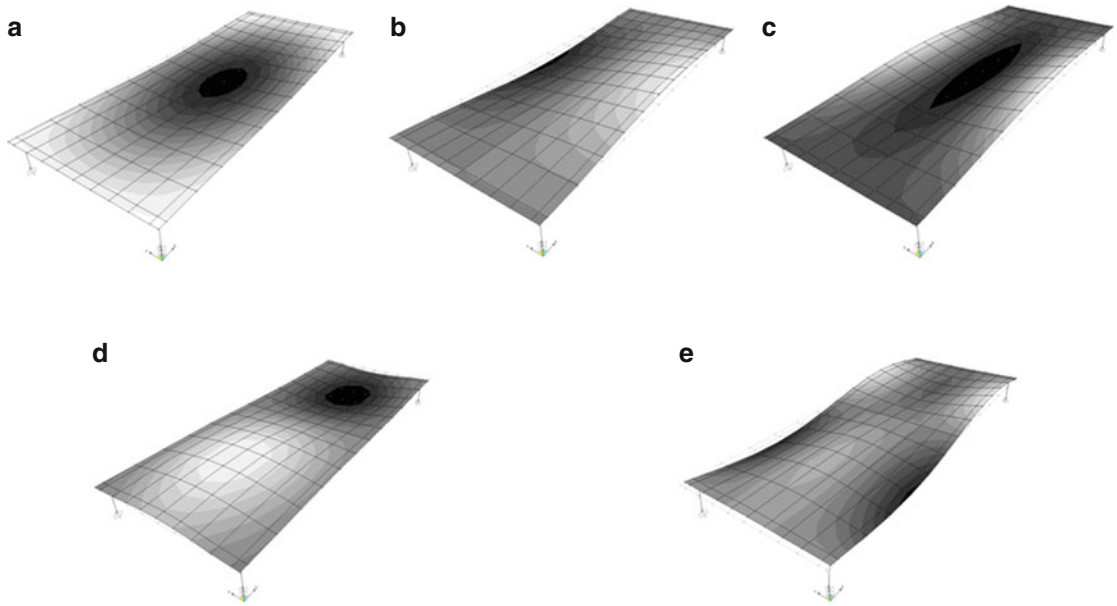

Fig. 6.4 Normalized mode shapes and frequencies for modes 1–5 (found numerically). (**a**) Mode 1 (7.12 Hz), (**b**) Mode 2 (11.13 Hz), (**c**) Mode 3 (16.47 Hz), (**d**) Mode 4 (19.54 Hz), (**e**) Mode 5 (27.85 Hz)

Figure 6.4 shows the mode shapes and frequencies for the first five vibration modes as calculated by SAP2000. These mode shapes do not include any effects due to the harvester.

The fundamental mode matches the experimental results very closely, with the numerical model being slightly stiffer than the experimental results. The second through fifth modes match closely, but the calculated frequencies have a greater percent difference from experimental than the fundamental frequency. However, the frequencies reasonably agree with the experimental results and the floor model is deemed acceptable for the parametric study.

It should be noted that the shapes for modes three and four switch between the numerical and experimental results. This is consistent with past analyses, where correlation between the modes was validated using modal assurance criterion. Full discussion can be found in reference [6].

The harvester was modeled simply as a spring-mass element placed at a point that was not on a nodal line for any mode. It was decided that the spring-mass element would be placed at the same point as the driving point from the experimental study [6, 7]. The stiffness of the spring and the magnitude of the mass were varied as part of the parametric study discussed in the next section.

6.6 Parametric Study of Energy Harvester Response

Having verified the numerical analysis via comparisons to the experimental floor data, the numerical results are presented for the device response to harmonic excitations imparted by the floor (i.e., results for device frequency, displacement and acceleration).

Due to the multiplicity of harvester types and designs, the relevant mechanical response data (acceleration, velocity and displacement) may vary depending on the specifics of the harvester design. In order to facilitate more specific device design from general dynamic behavior, the results of the current coupled system are presented in terms of scaled, non-dimensional terms of stiffness, mass and acceleration. The non-dimensionalized equivalent stiffness, κ, is defined as the ratio of the equivalent device stiffness, k_D, and the floor stiffness, k_F.

$$\kappa = \frac{k_D}{k_F} \tag{6.7}$$

The non-dimensionalized mass, μ, is defined as the ratio of the device mass, m_D, and the floor mass, m_F.

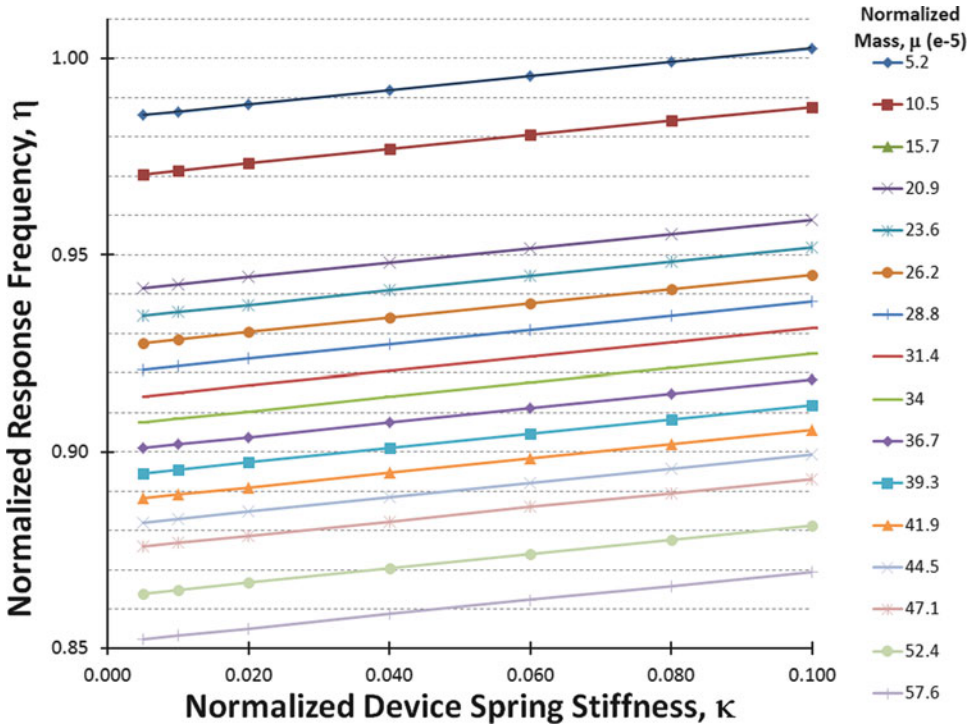

Fig. 6.5 Values for normalized device response frequency, η, for a range of normalized device spring stiffnesses, κ = (0.005, 0.10), and normalized mass, μ

$$\mu = \frac{m_D}{m_F} \tag{6.8}$$

The non-dimensionalized acceleration, α, is defined as the ratio of the device acceleration, $\ddot{y}_D$, and the acceleration due to gravity, g.

$$\alpha = \frac{\ddot{y}_D}{g} \tag{6.9}$$

Since one of the most meaningful physical constraints on the proposed device is the size of the floor plenum, the displacement magnitudes are not normalized in the plots to illustrate the scope of magnitude of the harvester's response.

The device acceleration, $\ddot{y}$, is often relevant for design of piezoelectric devices since the stress in the material can be related to the response of the proof-mass of the device through $F = m^*\ddot{y}^* \sin(\omega t)$. Moreover, device acceleration is important for harvesters with size constraints because increased acceleration permits the realization of higher velocities over shorter distances. Maximization of acceleration also allows for optimization of velocities which are often proportional to power generation (c.f. Faraday's law). The device displacements are also reported since changes in the displacements (and velocities) are relevant for magneto-style harvesters and are a common constraint for all devices operating within space restrictions.

The ranges of mass and stiffness considered are derived from practical ranges of harvester specifications and scaled by the results of the experimental floor modeled as described previously.

The harvester response frequencies are presented in Fig. 6.5 over a range of mass, μ = (5.2e-5, 5.8e-4) and stiffness, κ = (0.005, 0.10) values. As shown in Fig. 6.5, increasing spring stiffness results in a linear increase in response frequency. Conversely, increasing the mass tends to decrease the response frequency. These results follow the trends expected from the well-known undamped, SDOF relationship $\omega = \sqrt{k/m}$. The trends in Fig. 6.5 indicate that while frequency varies linearly with both mass and stiffness, the mass sensitivity of the frequency response are orders of magnitude greater than the stiffness sensitivity for the ranges of mass and stiffness considered.

Recalling the importance of the displacement constraint on device design, Figs. 6.6 and 6.7 show the relationship among the harvester displacement, mass and spring stiffness. As expected from a pseudo-linear elastic system, i.e., $\delta = \frac{\mu\alpha}{\kappa}$, increasing the proof-mass increases displacement by a ratio of 10:1, while increasing the equivalent spring stiffness decreases the displacement by a ratio of 1:1 as shown in Fig. 6.6. However, Fig. 6.7 shows that while the displacement varies linearly with spring stiffness for a given mass, the impact of mass on the displacement is non-linear. From Fig. 6.6, it is observed

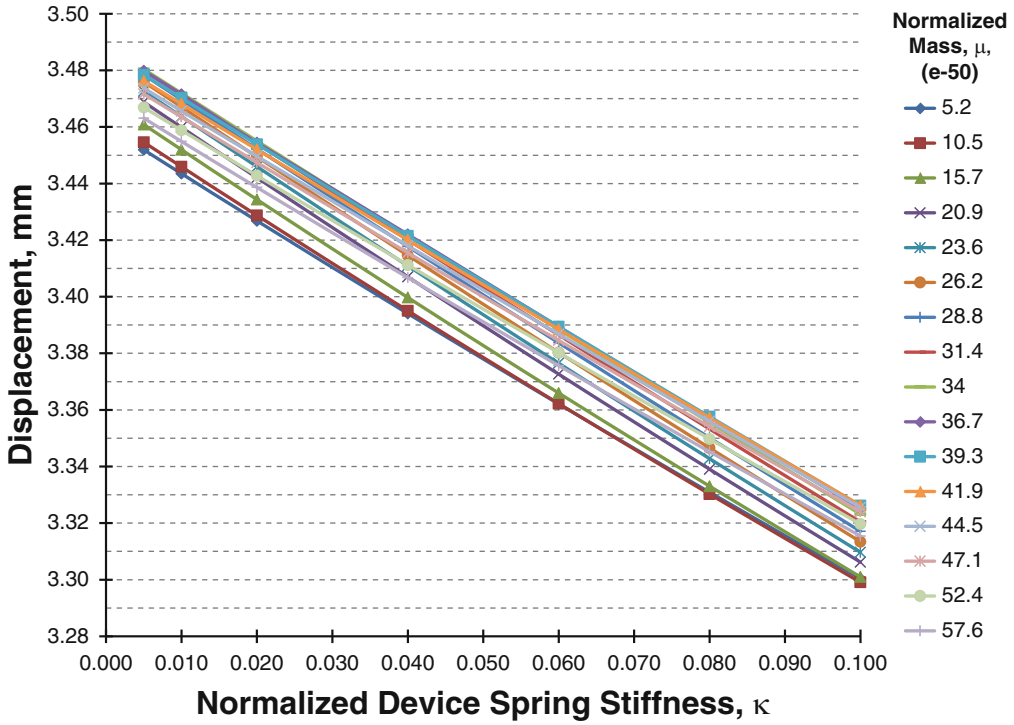

Fig. 6.6 Values for device displacement for a range of normalized device spring stiffnesses, $\kappa = (0.005, 0.10)$, and normalized mass, μ

that minimizing stiffness for a given mass results in largest displacements. Figure 6.7 shows that for a given spring stiffness, there is a critical mass value, [between $\mu = (0.00034, 0.00042)$ for the stiffness values considered in Fig. 6.7] that results in maximum results and the values above and below the critical mass represent the "over-forced" and "under-forced" regions, respectively. This trend is attributed to the inertial effects associated with changes in mass. Additionally, note that the decrease in displacement associated with increased stiffness exhibits effects that are analogous to the phase-shift associated with damping in frequency response spectra.

Plots of the device acceleration are shown in Fig. 6.8 for ranges of normalized mass and stiffness. The shape of the acceleration curves for the ranges of device mass considered are indicative of the harmonic support excitation due to the floor vibration. The first harmonic range for normalized mass values, $\mu = (0.0, 0.0008)$ is the focus of Fig. 6.7, but subsequent harmonics can be taken into account to achieve more detailed response characteristics. Considering the first harmonic, increasing the stiffness decreases accelerations monotonically over the range of mass values, $\mu = (0.00004, 0.0004)$ and then decreases the accelerations for $\mu = (0.0004, 0.00063)$. Similarly, increasing the device mass initially increases accelerations before reaching an inflection point where this trend is reversed. For both mass and stiffness, there is a series of inflection points. At these critical values, the governing influence alternates between that of the inertial effects (due to increases mass) and those associated with mass-spring behavior (associated with increase in stiffness). Figure 6.7 highlights the alternating behavior described for the first mass-harmonic occurring at the inflection points $\mu = 0.00004$, 0.0004, and 0.00063.

6.7 Conclusions

The generalized dynamic response of a coupled floor-harvester system is presented over a range of practical mass and stiffness values for current floor and harvester designs. The frequency response exhibits a linear dependence on the mass and stiffness. The maximum displacement and acceleration of the harvester is presented to identify ideal ranges of mass and stiffness ratios to guide harvester design. This research focuses on the interplay of the mechanical response of the system and highlights optimal mass-to-stiffness ratios for maximizing displacement and acceleration. Preliminary results indicate that minimizing spring stiffness under displacement constraints result in near maximization of the dynamic response of harvesters. However, it should be noted that maximum accelerations do not occur at the same mass-to-stiffness ratios

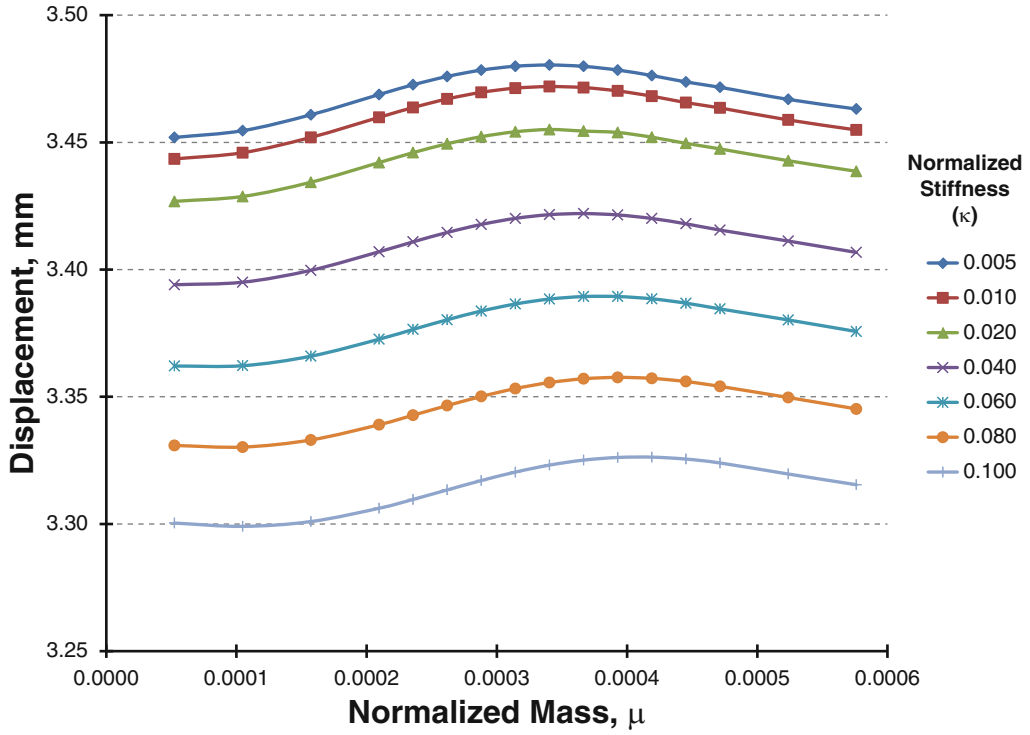

Fig. 6.7 Values for device displacement for a range of normalized mass, μ, and normalized device spring stiffnesses, κ = (0.005, 0.10)

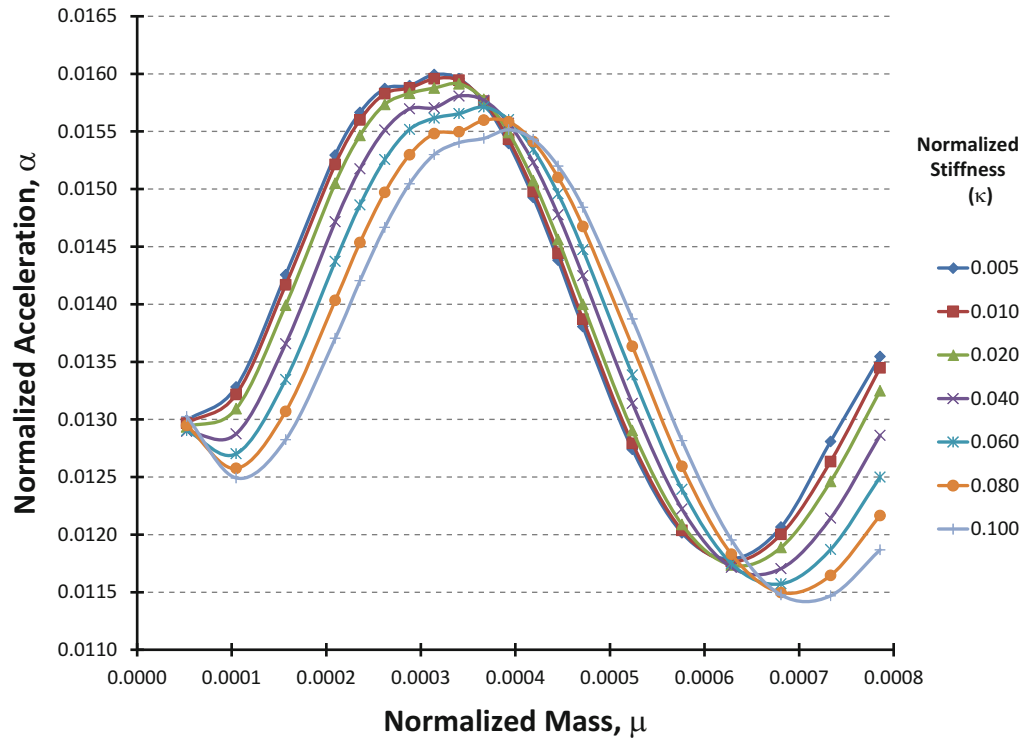

Fig. 6.8 Values for normalized device acceleration, α, for a range of normalized harvester mass, μ, and normalized spring stiffnesses, κ = (0.005, 0.10)

as maximum displacement. Accordingly, more refined initial designs may benefit from optimizing spring stiffness with constraints on displacement as well as acceleration.

Ongoing research includes consideration of damping in the harvester and system analysis for harmonic and time-history results. Subsequent work will include analytical description of the coupled system behavior. Computation of power and voltage outputs showing the proportionality of mechanical response to electrical is ongoing.

Acknowledgments The prior research performed on the experimental floor system was supported in part by National Science Foundation Grant No. CMS-9900099. The authors wish to acknowledge the work completed by the principal investigator of that research initiative, Dr. Linda Hanagan.

References

1. Murray TM, Allen DE, Ungar EE (1997) Floor vibrations due to human activity, AISC steel design guide #11. American Institute of Steel Construction, Chicago
2. Miller LM, Halverson E, Dong T, Wright PK (2011) Modeling and experimental verification of low-frequency MEMS energy harvesting from ambient vibrations. J Micromech Microeng 21(1):13 pp (IOP Publishing)
3. Galchev T, Kim H, Najafi K (2001) Micro power generator for harvesting low-frequency and nonperiodic vibrations. IEEE J Micromech Syst 24(4):852–866
4. Beeby SP, Torah RN, Tudor MJ, Glynne-Jones P, O'Donnell T, Saha CR, Roy S (2007) A micro electromagnetic generator for vibration energy harvesting. J Micromech Microeng 17(1):1257–1265
5. Gu L (2011) Low-frequency piezoelectric energy harvesting prototype suitable for the MEMS implementation. Microelectron J 42(2):277–282
6. Raebel CH (2000) Development of an experimental protocol for floor vibration assessment. Master's Thesis, The Pennsylvania State University, University Park
7. Raebel CH, Hanagan LM, Trethewey MW (2001) Development of an experimental protocol for floor vibration assessment. In: Proceedings of IMAC-XIX: a conference on structural dynamics. Society for experimental mechanics, Bethel, pp 1126–1132, 5–8 February 2001
8. Beker L, Ozguven HN, Kulah H (2013) Optimization of an energy harvester coupled to a vibrating membrane. In: Proceedings of IMAC-XXXI: a conference on structural dynamics. Society for experimental mechanics, Bethel
9. Schultz JA, Raebel CH (2013) Harvesting of ambient floor vibration energy utilizing micro-electrical mechanical devices. In: Proceedings of IMAC-XXXI: a conference on structural dynamics. Society for experimental mechanics, Bethel, 11–14 February 2013
10. Hanagan LM, Murray TM (1997) Active control approach for reducing floor vibrations. J Struct Eng ASCE 123(11):1497–1505
11. Computers and Structures, Inc. SAP2000 advanced v14.2.4 (2010)

Chapter 7
Identification of Tie-Rods Tensile Axial Force in Civil Structures

S. Manzoni, M. Scaccabarozzi, and M. Vanali

Abstract This paper is concerned with the problem of identifying the tensile axial force of metallic tie-rods used in civil structures. Tie-rods are generally used to transfer a tensile force between different structural elements. Specifically in civil structures, they are often used to unburden the lateral load exercised by the vaults and arcs on walls or columns, in ancient monumental masonry buildings as well as in modern concrete/iron constructions. A direct measure of this force is impossible and the tension is an unknown variable, as are the boundary conditions expressed by the constraints. Thus, in such a scenario, the characteristic equation has no analytical solutions. The paper proposes an experimental technique developed to identify, in situ, the tensile force on the rod. The identification method uses the first modal frequencies of the structure, identified by measuring the frequency response functions (FRFs) with instrumented hammer excitation. The frequencies are used to characterize some correlation indexes that change according to the variation in the tensile axial force of the rod. An FEM code numerical model allows to identify where the change in correlation indexes along the tie-rod could be greatest, in order to arrange a suitable measurement set up. Then the numerical model provides an evaluation of the tensile force corresponding to the set of correlation indexes identified. An estimation of the error in the identification of the force is given by a reasonable interval of stiffness of the constraints. The technique has been tested on laboratory system.

Keywords Tie-rod • Tensile axial load • Dynamic identification • COMAC • Structural health monitoring

7.1 Introduction

In many civil structures, both historical and modern kind, the tie-rods, or tie-beams, represent a useful and common tool to balance the lateral force at the base of arches and vaults. The possibility to measure the axial load acting on them is definitely a great help in order to monitor the overall health of the structure in which they are placed. Due to structural settlements, the tensile force in the tie-rods could change in time. An overload applied on one of them can cause the tie-rod to exceed the elastic range of the material which compounds the beam. This state could yield displacement larger than those bearable by the static balance of the structure. Moreover, the beam might not support any increase in load or, in a worst-case scenario, it could suffer a mechanical failure. This is particularly dangerous in the event of any environmental forcing such as earthquakes or wind action. Conversely, due to any constraint yielding, the work of a tie-rod may be ineffective in ensuring structural equilibrium. This would yield subsidence in the static attitude of the whole structure. Often, in ancient or historical buildings, chemical corrosion can play a role in decreasing the strength of tie-rods. In any case, monitoring change in time of a tie-rod's tensile force could provide timely warning of any change in the equilibrium of the structure.

The only way to have an accurate measure of the axial load may be to fix a strain gauge or a load cell on the beam before tensing it. Obviously, this requirement is impossible to have on the ancient tie-rods of a historical building. Without this condition, there is no non-destructive technique for direct in situ measurements of the tensile force on the beam. In order to

S. Manzoni (✉) • M. Scaccabarozzi
Dipartimento di Meccanica, Politecnico di Milano, Via La Masa 1, Milano 20156, Italy
e-mail: stefano.manzoni@polimi.it; matteo.scaccabarozzi@polimi.it

M. Vanali
Dipartimento di Ingegneria Industriale, Università di Parma, Parco Area delle Scienze, 181/A, 43124 Parma, Italy
e-mail: marcello.vanali@unipr.it

A. Wicks (ed.), *Structural Health Monitoring, Volume 5: Proceedings of the 32nd IMAC, A Conference and Exposition on Structural Dynamics, 2014*, Conference Proceedings of the Society for Experimental Mechanics Series, DOI 10.1007/978-3-319-04570-2_7,

get an indirect measurement of it, several techniques have been adopted in the recent past. Some of them are based on static measurements [1], others on dynamic type [2,3], still others use both kinds [4,5]. In any case the axial force is not the only one unknown variable. In real cases, also the parameters characterizing the constraints and the material specifications are unknown.

About static and hybrid technique, fitting out all the static measurements needed may be not so easy in a real case. Focusing on the fully dynamic techniques, until a few years ago, the axial stress was evaluated by considering the tie-rods as a vibrating wire and measuring its first natural frequency. The advantage in considering these methods is to have a closed-form expression to solve the problem. However, they generally underrate the tensile force not taking into account the bending stiffness of the beam and of the constraints. Currently many of the dynamic-based techniques use the natural frequency to identify the axial stress in ancient tie-rods but most of them are developed for beam of uniform-section, symmetrically hinged. In others cases there is not any experimental validation or methods need an accurate knowledge of rod's geometry or about the specifications of the material composing it.

The paper proposes an experimental technique developed to identify, experimentally, the tensile force on the rod. The identification method uses the first modal frequencies of the structure, identified by measuring the frequency response functions (FRFs) with instrumented hammer excitation. The modal shapes associated are identified in order to evaluate the correlation index CoMAC (Coordinate Modal Assurance Criterion) that changes according to the equivalent stiffness of the constraints, in relation with an ideal case. An FEM code numerical model allows to identify where the change in the correlation index along the tie-rod could be greatest, in order to arrange a suitable measurement set up, consisting only of three accelerometers placed in two different sections. Experimental identification of COMAC allows estimating an equivalent stiffness of the constraints, so that one of the unknown variables of the problem is set. The tensile axial force can be identified by a minimization algorithm working on the numerical model. An estimation of the error in the identification of the force is given by considering a reasonable interval of stiffness of the constraints. One of the advantages of the technique proposed is to be usable in any kind of rod's layout. Furthermore, the measurement method required to value the experimental data is easily realizable. The technique has been tested on laboratory system, one tie-rod instrumented with a force measurement system, in order to prove its effectiveness.

7.2 Methodology

In order to identify the axial tense force on a tie-rod, there are few unknown variables that must be taken into account: the behavior of the constraints at the ends; the presence and the effects of any concentrated mass or additional constraints; Young's modulus; the mass per unit length; the moment of inertia; the cross-section; the span. The last three are strictly geometrical values, they can be directly evaluated by measurements. However, the cross-section may change along the span, particularly for hand-made ancient tie-rods. The behavior of the constraints can result in a stiffness lower than that found with a fully restrained end and affect the length of the rod portion participating to the vibration modes, inside the wall. Young's modulus cannot be identified by means of a non-destructive test, so it has to be assumed.

The technique proposed here was developed starting from a numerical model of a tie-rods, solved by the ABAQUS code. The model has 100 nodes and 100 two-nodal 3D elements, using "Timoshenko-type" beams which take into account rotary inertia. The shape and dimension chosen are same as those of the rod where the measurements will be done. The system is modeled as a simply supported single-span beam of length L, subjected to a constant axial load N, with end elastic rotational constraints with flexural stiffness k. The layout is shown in Fig. 7.1.

The cross-section is assumed constant but any change in shape or dimension along the span could be modelled. Likewise the layout model can contemplate a screw shackle in the middle of the span, since this element can be found in many circular section tie-rods. Young's modulus and the mass per unit length chosen are the nominal values of the metal composing the rod. After fixing a set of material specifications and geometrical parameters, the axial tensile load N and the constraints stiffness k are the remaining unknown variables.

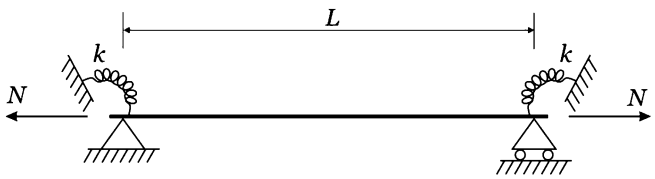

Fig. 7.1 Layout of the experimental tie-rod

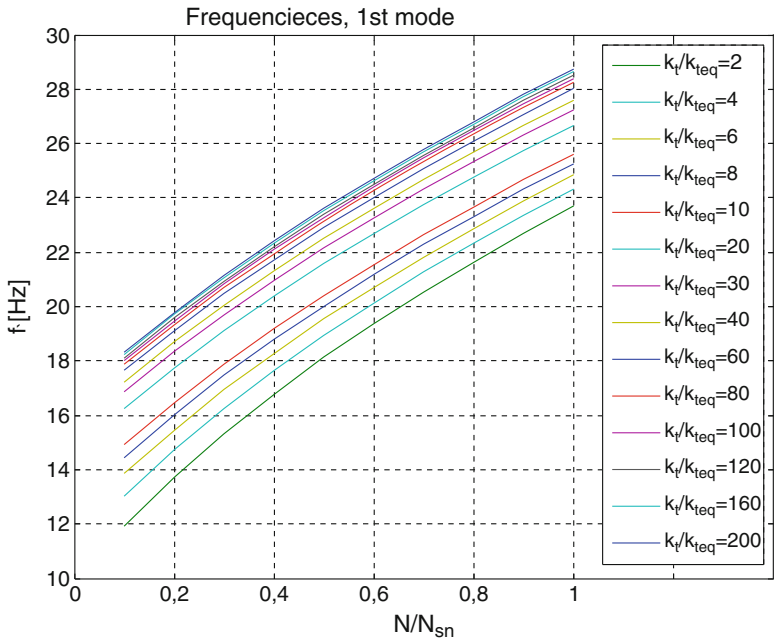

Fig. 7.2 Frequency f_1 vs. N, fixing k

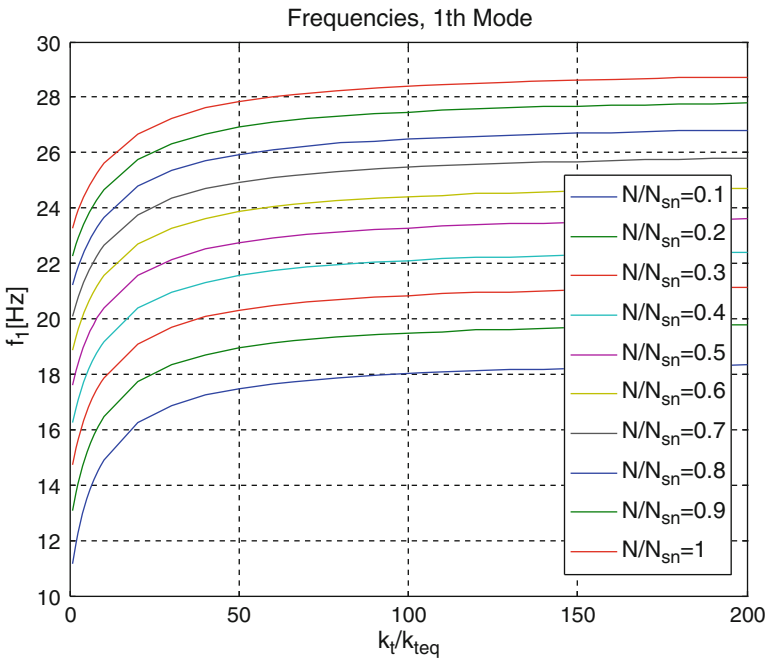

Fig. 7.3 Frequency f_1 vs. k, fixing N

The model is solved by the ABAQUS code in terms of non-dimensional axial load and stiffness. The former parameter is obtained as a ratio between the axial load acting on the model and the nominal yield tensile load (YL) of the material composing it. The latter is defined as the ratio between the stiffness of the constraint and an equivalent stiffness k_{eq}, consisting of the ratio between EJ and L of the tie-rod. The trend of the first natural frequency is shown in Figs. 7.2 and 7.3. The former shows the variation of frequency on the non-dimensional axial load, for different stiffness values. Vice versa, the latter shows the frequencies on the stiffness, for different axial load.

The trend shown in Fig. 7.3 points out that the values greater than a certain band of stiffness yield an asymptotic, nearly flat, increase in frequencies. This behaviour means that the constraints begin acting as a fully restrained ends after a k/k_e value of the magnitude of about 100. Large portion of the literature focused to this issue takes into account the natural frequencies to evaluate the axial load. These data are easily evaluable by measurements, with good accuracy. Combining frequency values, i.e. as a ratio between two of them, an evaluation of the axial load can be yielded with a reliability less affected by the uncertainty on k. Figures 7.4 and 7.5 show the trend of the functions $\frac{f_2}{f_1}\left(\overline{k}, N\right)$ and $\frac{f_2}{f_1}\left(k, \overline{N}\right)$.

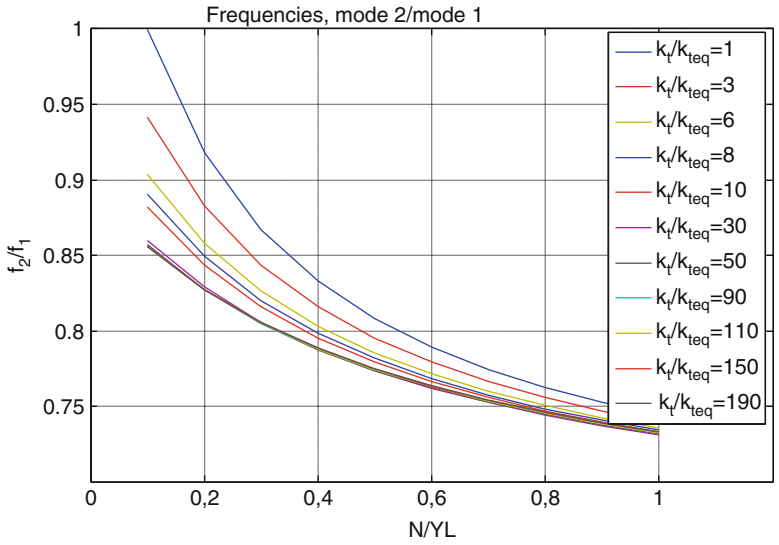

Fig. 7.4 Ratio f_2/f_1 vs. N, fixing k

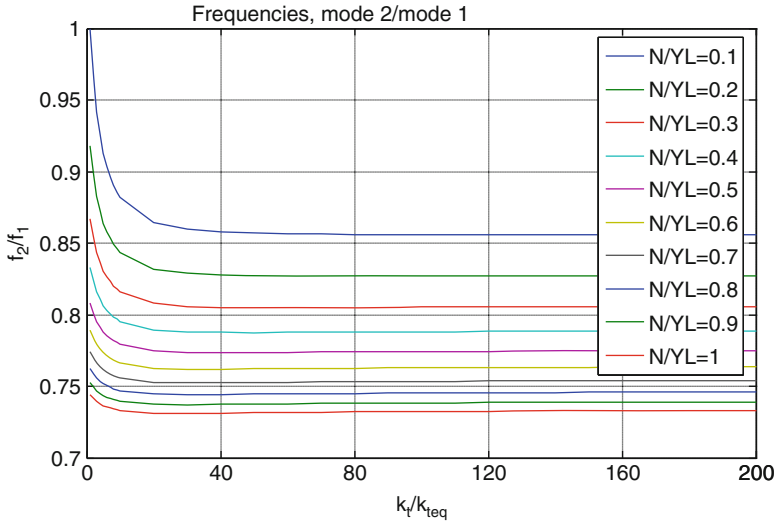

Fig. 7.5 Ratio f_2/f_1 vs. k, fixing N

The first diagram shows that the solutions for each stiffness parameters tend to get closer for increasing value of axial load. In the second it can be inferred that, except for of a narrow band of lower value of stiffness, the frequencies ratio is more affected by the axial load. A best-case scenario can be verified where a reliable evaluation of stiffness is not decisive to identify the axial load with accuracy. However, these remarks are discussed about a numerical model. Generally, a perfect matching between numerical and experimental models, which provides the frequency values, is unlikely.

To identify an accurate value of tensile axial load may be awkward to set without evaluating carefully the stiffness of the constraints. So, in order to seek a way to identify an accurate value of it, a correlation index has been challenged. The Coordinate Modal Assurance Criterion (CoMAC) is an expansion of the MAC, or Mode Shape Correlation Coefficient, in order to give an expression which takes into account a spatial dependence of the correlation parameter [6]. The CoMAC parameter includes the contribution of every correlation between any pair of mode vectors, respectively related to an analytic model and an experimental one. Suitably normalised to present a value between 0 and 1, the COMAC parameter for an individual degree of freedom (DOF), j, is expressed by (7.1):

$$CoMAC(j) = \frac{\left(\sum_{r=1}^{L} \left|(\phi_{ar})_j (\phi_{mr}{}^*)_j\right|\right)^2}{\sum_{r=1}^{L} (\phi_{ar})_j{}^2 \sum_{r=1}^{L} (\phi_{mr}{}^*)_j^2} \tag{7.1}$$

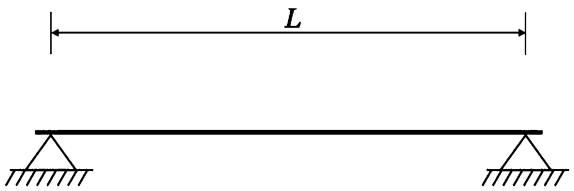

Fig. 7.6 A pinned–pinned beam

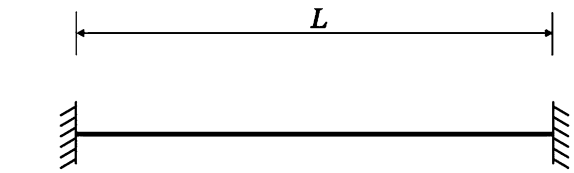

Fig. 7.7 A clamped–clamped beam

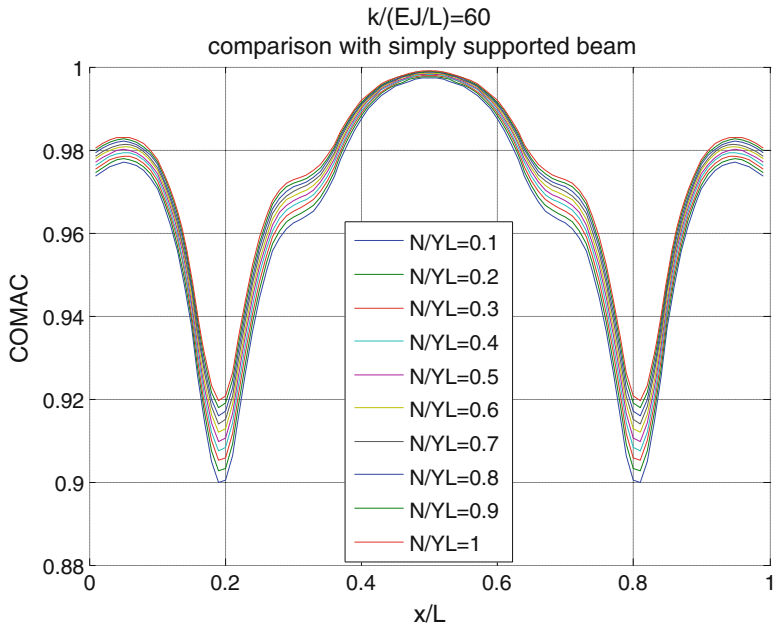

Fig. 7.8 CoMAC index with k fixed, related to "pinned–pinned beam"

Here, r represents an individual correlated mode pair, of which a total L is available; $(\phi_{ar})_j$ is the analytic r-mode shape valuated for the degree of freedom j and $(\phi_{mr})_j$ is the experimentally-measured one. The COMAC vector displaying against the DOF number shows any possible discrepancy between the two models.

The CoMAC could be a useful in order to value how specific parameters, such as axial load and stiffness of the constraints, can affect the vibrational modes. The correlation index has been evaluated comparing the assumed model of tie-rod with a couple of proper ideally constrained models, for different values of the parameters taken into account. The models assumed as references are: a pinned–pinned beam (Fig. 7.6) and a clamped–clamped beam (Fig. 7.7). The CoMAC index has been evaluated as the correlation between each reference model and the experimental model where N is fixed and k changes or, vice versa, k is fixed and N changes. The first six mode vectors of each model are taken into account.

Assuming a fixed value of k, the CoMAC solutions trend on the normalized rod's span are shown in Figs. 7.8 and 7.9, respectively, with reference to the "pinned–pinned beam" model and the "clamped–clamped beam" model. Trends are evaluated for several values of the axial tensile force N normalized by the yield load of the model taken into account. Vice versa, assuming a fixed value of N, the solutions of the same system are shown in Figs. 7.10 and 7.11, for several value of k.

Looking the diagrams above a couple of substantial evidences are inferable. First of all, there is a pair of absolute minima, placed in a symmetric position as much as the structure is symmetrically set. These minima are placed at above ¼ and ¾ of the span. Secondly, the CoMAC index is more sensitive to stiffness than to axial load.

These findings suggest to investigate the CoMAC index near the position where its minimum occurs and where, in the same time, there is a greater sensitivity to constraints stiffness. Identifying several mode shapes in only one point, in order to evaluate a CoMAC index, theoretically means that only one measuring position is required. Actually, another position is need in order to evaluate the acceleration in the co-locate point where the force in given by a hammer, as it will be discussed in the next section.

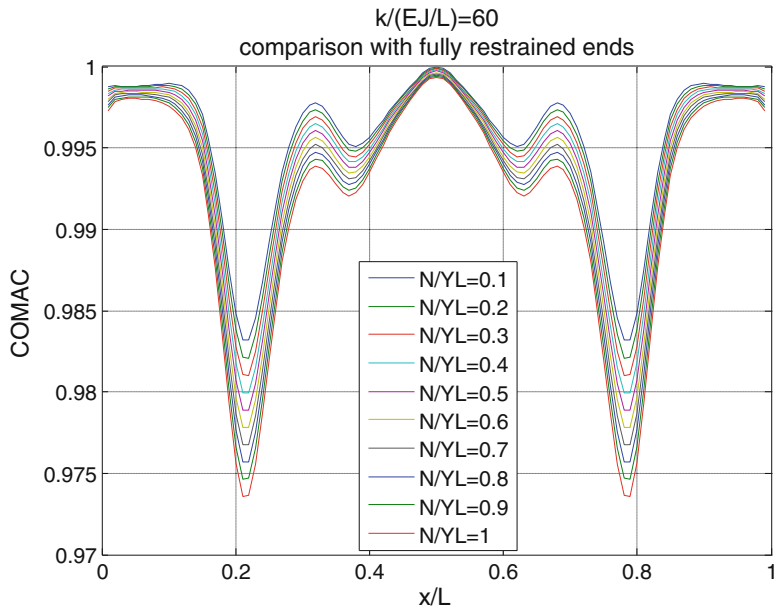

Fig. 7.9 CoMAC index with k fixed, related to "clamped–clamped beam"

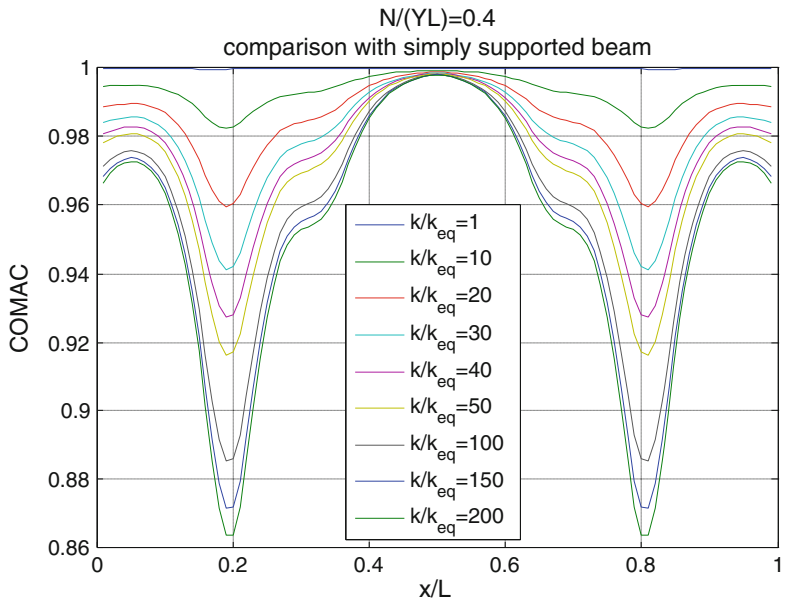

Fig. 7.10 CoMAC index with N fixed, related to "pinned–pinned beam"

In a three-axes diagram such as Figs. 7.12 and 7.13, where CoMAC is plotted versus the non-dimensional stiffness and load, the former affects index more strongly than the latter. Then the CoMAC index can represent an useful tool for evaluating a reliable value of constraints stiffness.

According to an experimental approach, measurements can provide a set of mode shapes in order to evaluate a couple of CoMAC indexes, one by the correlation with the numerical model of the simply supported beam and another referenced to the fully restrain ends beam model. The purely numerical solution provides each value of k corresponding to a unique couple of CoMAC indexes, for a specific axial load. In the real case, an experimental method, such as that proposed, for directly evaluating of the constraint stiffness cannot afford a single value of k for a couple of CoMAC indexes, because of a perfect matching between experimental and numerical models is unlikely. Generally, in this step, the technique provides two different values of k which are the extremes of an interval including all the possible stiffness of the system's constraints. This interval of stiffness allows identifying a range of solution for the tensile axial load. Obviously, the couple of CoMAC values also points out, in a qualitative way, what kind of constraint layout is closest to that of the tie-rod taken into account.

A practical way to evaluate an interval of faithful stiffness values, such as that outlined before, is a decisive contribution to estimate the axial load. However the uncertainties of other variables, such as Young's modulus and the mass per unit length

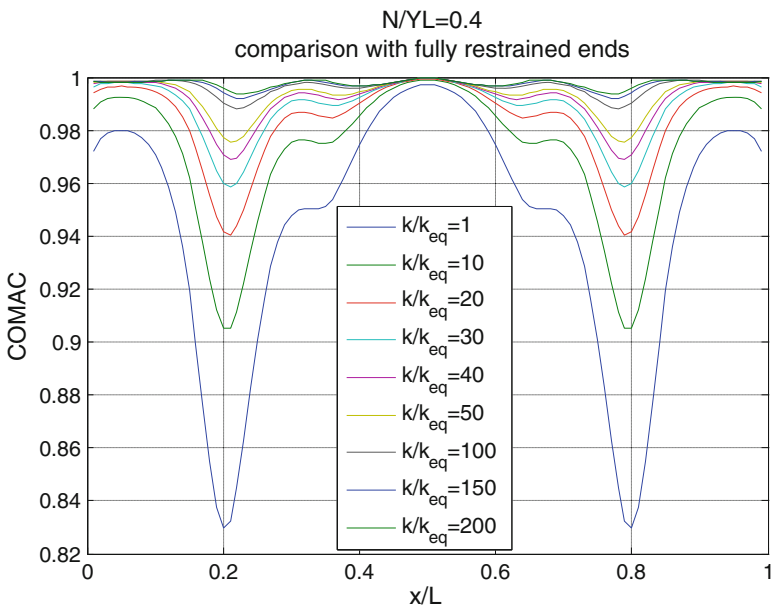

Fig. 7.11 CoMAC index with N fixed, related to "clamped–clamped beam"

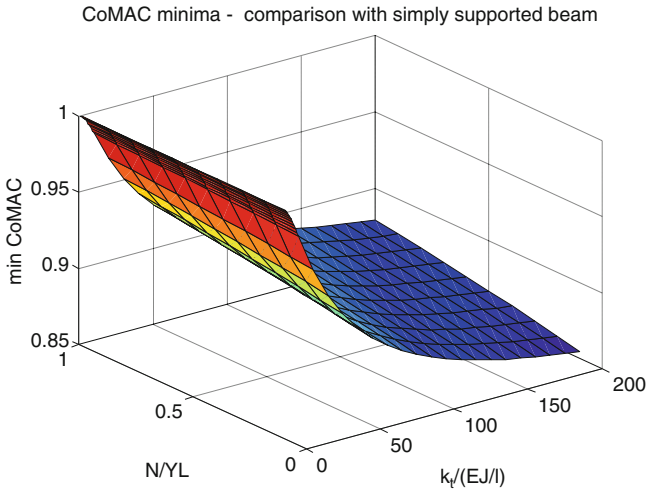

Fig. 7.12 CoMAC minima (N,k), related to "pinned–pinned beam"

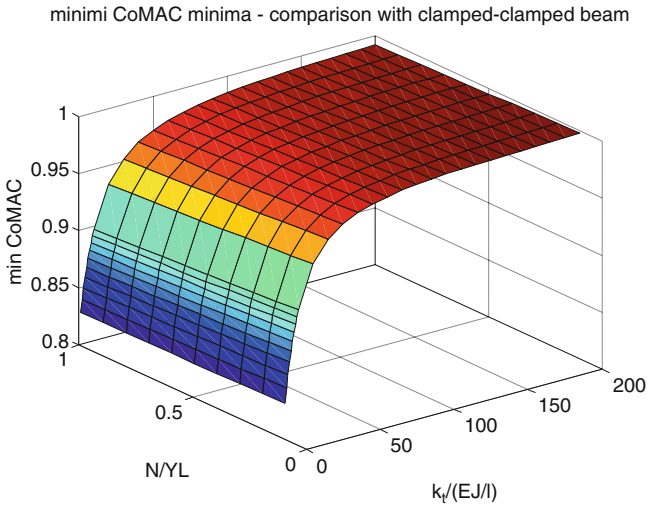

Fig. 7.13 CoMAC minima (N,k), related to "clamped–clamped beam"

of the rod's material, cannot be skipped. Moreover, the not perfect matching between FEM model and experimental model must be taken in account. A numerical model might not rightly include the effects on the dynamic behaviour of the tie-rod, due to the presence of a screw shackle in the middle.

The weight of the uncertainties due to all these variability can be reduced by means of a minimization process. The function chosen is based on the square deviation between the measured and the numerical values, such as (7.2):

$$f(\overline{p}) = \sum_{i=1}^{m} q_i (v_i - w_i)^2 \tag{7.2}$$

where $\overline{p}$ is a vector of input parameters, v_i and w_i are respectively the *i-th* numerical and measured value, q_i is the weight of each quantity. The function is processed in Matlab and minimized by means of one of the algorithm available in Toolbox Optimtool. In the method developed, the target value to be optimized is obviously the axial load. The parameters taken into account as variables of the process are Young's modulus and the mass per unit length, starting from the nominal values of the metal which the tie-rod is made, and a set of natural frequencies obtained respectively by means of numerical model and experimental measures.

7.3 Experimental Setup

A system strongly resembling with a common tie-rods was assembled in the Mechanical Department's laboratory. The model is a double connected beam with circular cross-section, joined by means of a screw shackle (Fig. 7.15). The constraints (Fig. 7.14) are composed of modular elements in order to give them a sort of yielding, by allowing a changing clamping along the grip span. Tie-rod and constraints are made in the same material, aluminium, in order to avoid differential thermal expansion which may change in time the behaviour of the clamping. Tensile axial load is changed by means of the screw shackle and is measured by strain gauges in full Wheatstone bridge configuration set for tensile strain sensitivity and for temperature compensation (Fig. 7.15).

The strain gauge was calibrated by a load cell mounted along the beam as shown in Fig. 7.16. Vibration measurements are made by three piezoelectric accelerometers PCB 333B30, which metrological specifications are shown in Table 7.1. One of

Fig. 7.14 The constraints on the ends of tie-rod

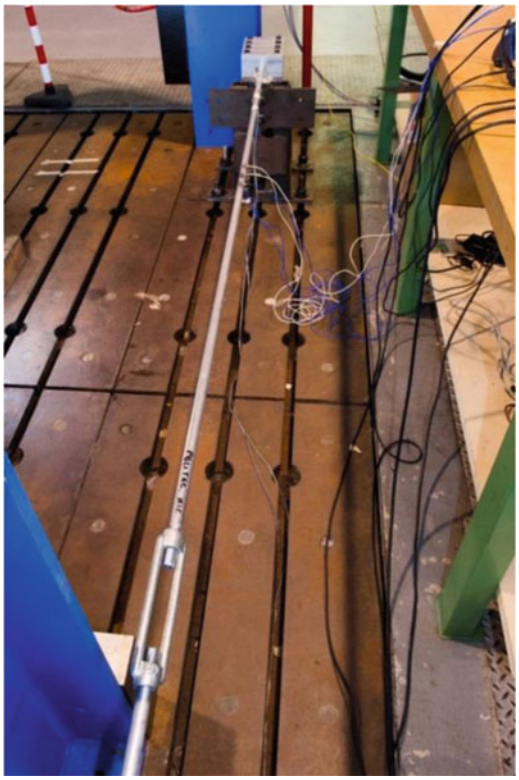

Fig. 7.15 The screw shackle used to change the axial load

Fig. 7.16 The gain strain and the cell load

Table 7.1 Product specifications of accelometers

Model	Sensitivity (±10 %)	Measurement range	Frequency range (±5 %)	Weight
PCB 333B30	10.2 mV/(m/s^2)	±490 m/s^2 pk	0.5–3,000 Hz	4.0 g

them is placed in the co-locate point where the hammer excitations in given and the other couple in a position symmetrically placed on the other beam composing the tie-rod. The former is set to measure in the excitation direction, the vertical one, and the last two set in orthogonal directions, vertical and horizontal (Fig. 7.17)

The analysis of the CoMAC minimum position, by means of the FEM model, allows identifying the best position where to place the accelerometers measuring the dynamic response. An example of measured FRF is shown in Fig. 7.18. FRF was estimated by averaging five impulses in order to reduce measurement noise.

Some double peaks are identifiable; they are due to the non-perfect axis-symmetry of the structure caused by the constraints and the presence of the screw shackle. By performing a modal identification of the natural frequencies and the associated mode shapes, it is possible to provide the results discussed in the next section.

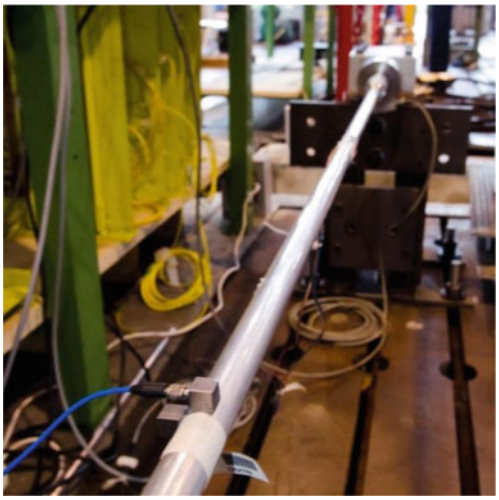

Fig. 7.17 A couple of accelerators used for response accelerometers

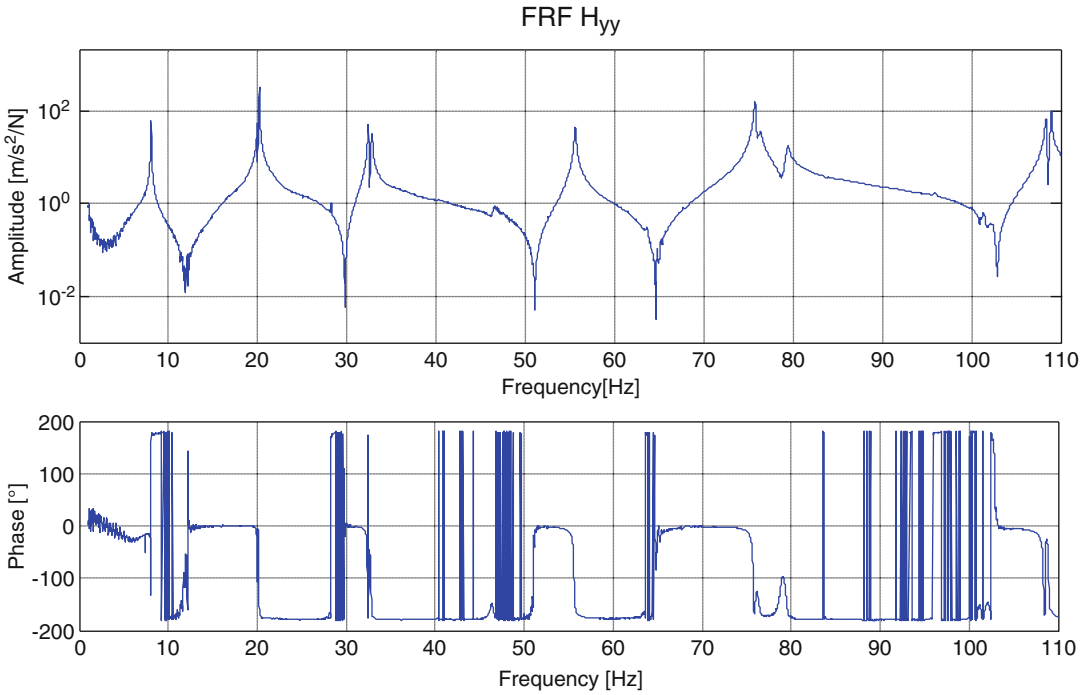

Fig. 7.18 Experimental measured FRF

7.4 Results

Diagram shown in Fig. 7.19 shows the results achieved by means to the technique earlier described, in terms of comparison between measured data and evaluated axial load, including a couple of band of relative error.

The results shown were obtained applying the various steps of the method suggested. Initially, the natural frequencies of the tie-rod were experimentally identified. Then the investigation of CoMAC index in the measuring point led to evaluate the constraints stiffness. Finally, minimization process was applied, yielding results close to the measured axial load values.

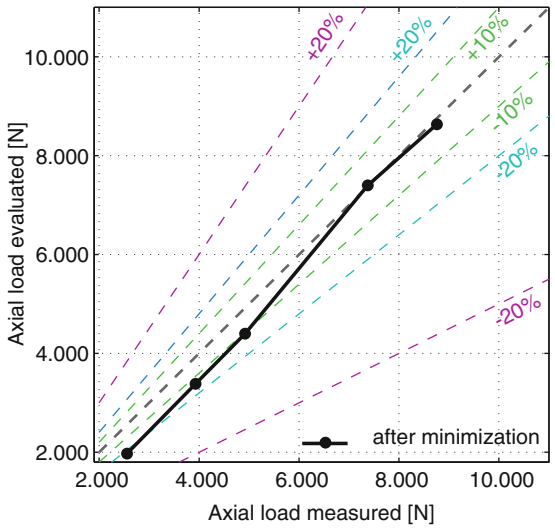

Fig. 7.19 Axial load estimated VS load measured

7.5 Conclusion

An analytical approach was presented to find a method for identifying the unknown tensile axial load in tie-rods. A numerical model aid allows to choose a suitable measurement set-up, in order to identify the natural frequencies of the first mode shapes and a correlation index (CoMAC) in proper position. This latter parameter allows reducing the uncertainty about the stiffness of the constraints. The uncertainties about some geometrical and mechanical parameters of the tie-rod, which are hard or impossible to measure, are redressed by a minimization process. Moreover, experimental tests were carried out to validate the method proposed.

References

1. Briccoli Bati S, Tonietti U (2001) Experimental method for estimating in situ tensile force in tie-rods. J Eng Mech 127:1275–1283
2. Tullini N, Laudiero F (2008) Dynamic identification of beam axial loads using one flexural mode shape. J Sound Vib 318:131–147
3. Lagomarsino S, Calderini C (2005) The dynamical identification of the tensile force in ancient tie-rods. Eng Struct 27:846–856
4. Blasi C, Sorace S (1994) Determining the axial force in mettallic rods. Struct Eng Int (IABSE) 4:241–246
5. Garziera R, Amabili M, Collini L (2011) A hybrid method for nonsestructive evaluation of the axial load in structural tie-rods. Nondestr Test Eval 26:197–208
6. Ewins DE (2000) Modal testing - theory, practice and application. Research Studies Press Ltd, Philadelphia

Chapter 8
A New Measure of Shape Difference

Shawn Richardson, Jason Tyler, Patrick McHargue, and Mark Richardson

Abstract The Modal Assurance Criterion (MAC) is currently the most popular method for measuring whether or not two mode shapes are strongly correlated. In fact, MAC can be applied to any two sets of data that can be defined as a shape, e.g. mode shapes, Operating Deflection Shapes (ODS's), or two time or frequency domain waveforms. When applied to two Frequency Response Functions (FRFs) MAC has been renamed FRAC (Allemang RJ, The modal assurance criterion (MAC): twenty years of use and abuse. In: Proceedings of the international modal analysis conference, 2002).

MAC values range between **0 and 1**. If **MAC = 1**, the two shapes are ***identical***. A "***rule of thumb***" is that two shapes are ***similar*** or ***strongly correlated*** if **MAC > 0.9**, and they are ***different*** or ***weakly correlated*** if **MAC < 0.9**.

MAC is a measure of the ***co-linearity*** of two shapes. That is, it measures whether or not two shapes lie together on the same straight line. MAC has two limitations however;

1. MAC does not measure the ***difference in values*** of two shapes.
2. MAC requires ***at least two*** shape components. The MAC value for two shapes with one component, i.e. two scalars, is ***always 1***.

In this paper, a new measure, called the **Shape Difference Indicator (SDI)**, is introduced which overcomes the two limitations of MAC. This new measure is more useful for machinery and structural health monitoring applications where, for instance, changes in vibration levels or temperatures are typically used to detect a fault.

An example is given showing how SDI indicates that shape pairs are different even when their MAC values indicate that they are the same, i.e. they are co-linear. A second example shows how SDI can be used not only to detect a fault, but also to correctly identify the fault by comparing its shape values with those in a database of known fault conditions.

Keywords Modal assurance criterion • Shape difference indicator • Operating deflection shape • Experimental modal analysis mode shape • Finite element analysis mode shape

8.1 Introduction

Figure 8.1 shows a photo model of the Jim Beam test article. This structure is made up of three aluminum plates fastened together with six Allen screws. Three screws attach the top plate to the vertical plate, and three screws attach the bottom plate to the vertical plate.

A set of 99 Frequency Response Functions (FRFs) was acquired during an impact test of the Jim Beam structure. An instrumented impact hammer was used to measure the impact force, and a tri-axial accelerometer was used to measure the structural responses to the impact force. The structure was impacted at a fixed DOF (15Z), and the accelerometer was attached to each of 33 different Points for each impact of the structure. During each impact, four signals (the force and three acceleration responses) were fed into a 4-channel FFT-based spectrum analyzer where three FRFs were calculated.

The imaginary parts of the 99 FRFs are overlaid in Fig. 8.2. They clearly show the presence of ten resonance peaks which indicate that at least ten modes were excited.

S. Richardson • J. Tyler • P. McHargue • M. Richardson (✉)
Vibrant Technology, Inc., Scotts Valley, CA 95066, USA
e-mail: shawn.richardson@vibetech.com; jason.tyler@vibetech.com; patrick.mchargue@vibetech.com; mark.richardson@vibetech.com

A. Wicks (ed.), *Structural Health Monitoring, Volume 5: Proceedings of the 32nd IMAC, A Conference and Exposition on Structural Dynamics, 2014*, Conference Proceedings of the Society for Experimental Mechanics Series, DOI 10.1007/978-3-319-04570-2_8,

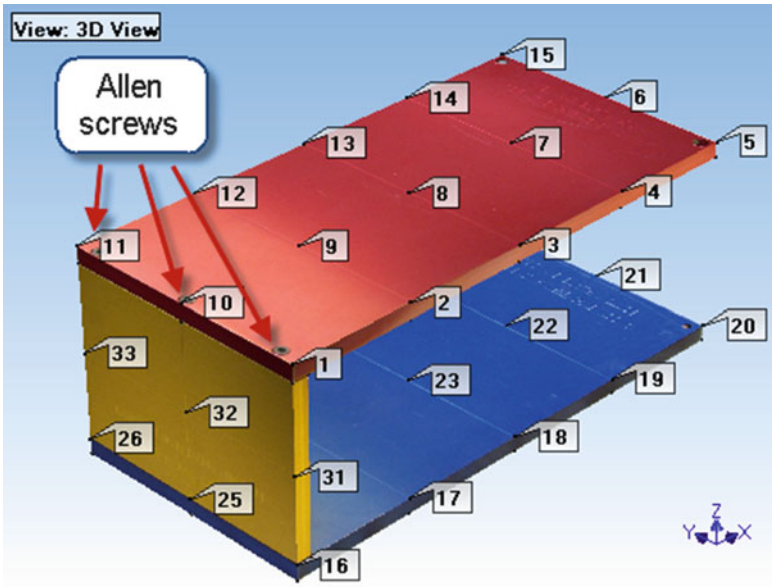

Fig. 8.1 Jim beam structure

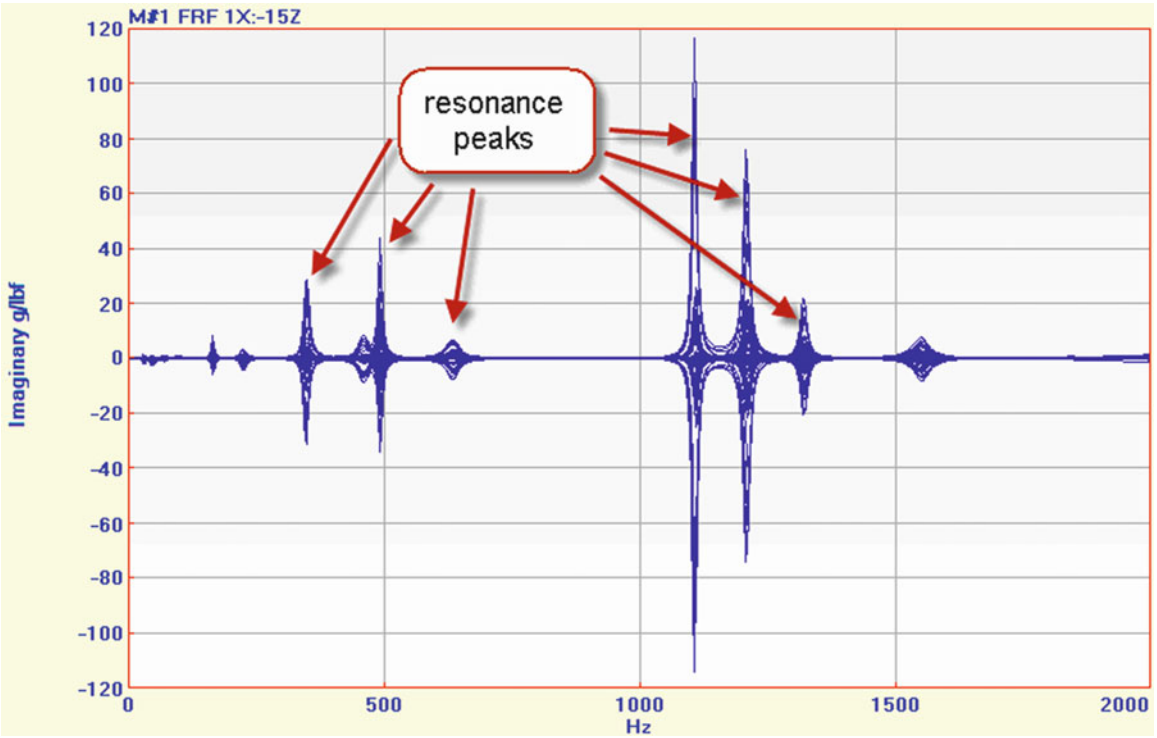

Fig. 8.2 Imaginary part of 99 FRFs overlaid

The FRFs were then curve fit using a least-squared-error curve fitting method to estimate the modal parameters for the ten modes. These parameters are listed in Fig. 8.3.

An FEA model was also created from the Jim Beam photo model [1], and it was solved for its FEA mode shapes, or ***eigenvalues and eigenvectors***. The FEA mode shapes are listed in Fig. 8.4.

The Jim Beam FEA model was meshed to provide more DOFs before solving for its FEA modes. Hence, the FEA mode shapes had 630 DOFs in them, but only 99 matched with the DOFs of the EMA mode shapes. By comparing the shape component values in Figs. 8.3 and 8.4, it is clear that the EMA shapes have ***different values*** in them than the FEA shapes.

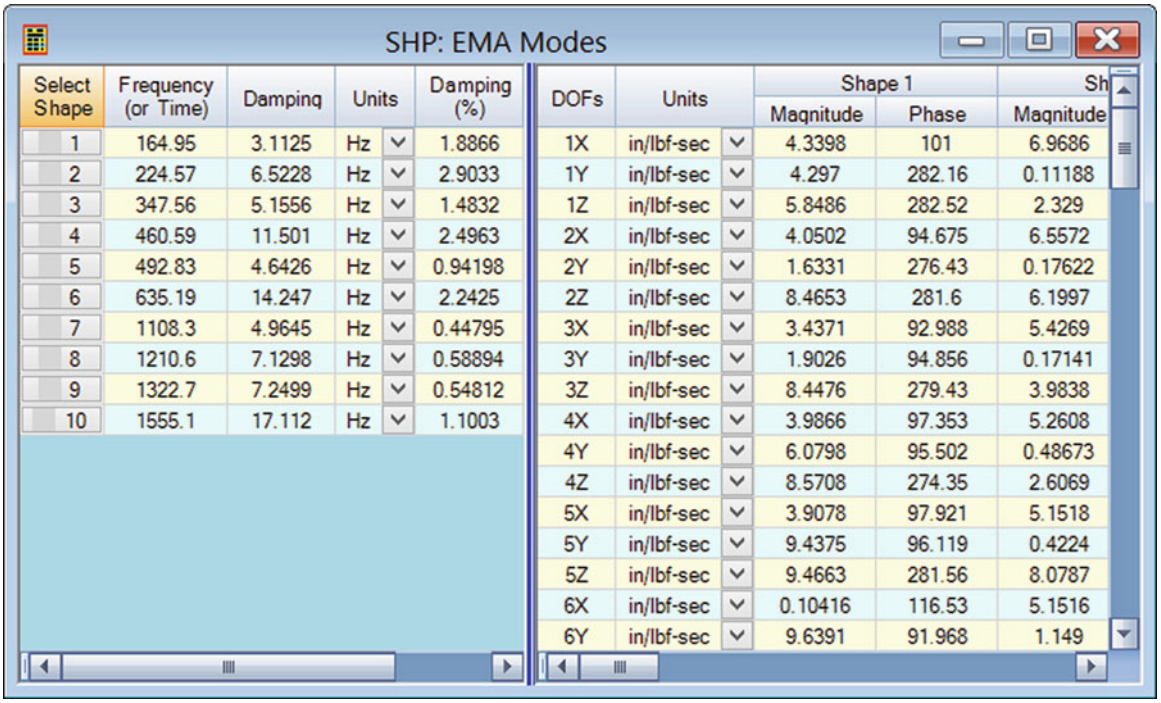

SHP: EMA Modes

Select Shape	Frequency (or Time)	Damping	Units	Damping (%)
1	164.95	3.1125	Hz	1.8866
2	224.57	6.5228	Hz	2.9033
3	347.56	5.1556	Hz	1.4832
4	460.59	11.501	Hz	2.4963
5	492.83	4.6426	Hz	0.94198
6	635.19	14.247	Hz	2.2425
7	1108.3	4.9645	Hz	0.44795
8	1210.6	7.1298	Hz	0.58894
9	1322.7	7.2499	Hz	0.54812
10	1555.1	17.112	Hz	1.1003

DOFs	Units	Shape 1		Sh
		Magnitude	Phase	Magnitude
1X	in/lbf-sec	4.3398	101	6.9686
1Y	in/lbf-sec	4.297	282.16	0.11188
1Z	in/lbf-sec	5.8486	282.52	2.329
2X	in/lbf-sec	4.0502	94.675	6.5572
2Y	in/lbf-sec	1.6331	276.43	0.17622
2Z	in/lbf-sec	8.4653	281.6	6.1997
3X	in/lbf-sec	3.4371	92.988	5.4269
3Y	in/lbf-sec	1.9026	94.856	0.17141
3Z	in/lbf-sec	8.4476	279.43	3.9838
4X	in/lbf-sec	3.9866	97.353	5.2608
4Y	in/lbf-sec	6.0798	95.502	0.48673
4Z	in/lbf-sec	8.5708	274.35	2.6069
5X	in/lbf-sec	3.9078	97.921	5.1518
5Y	in/lbf-sec	9.4375	96.119	0.4224
5Z	in/lbf-sec	9.4663	281.56	8.0787
6X	in/lbf-sec	0.10416	116.53	5.1516
6Y	in/lbf-sec	9.6391	91.968	1.149

Fig. 8.3 EMA mode shapes

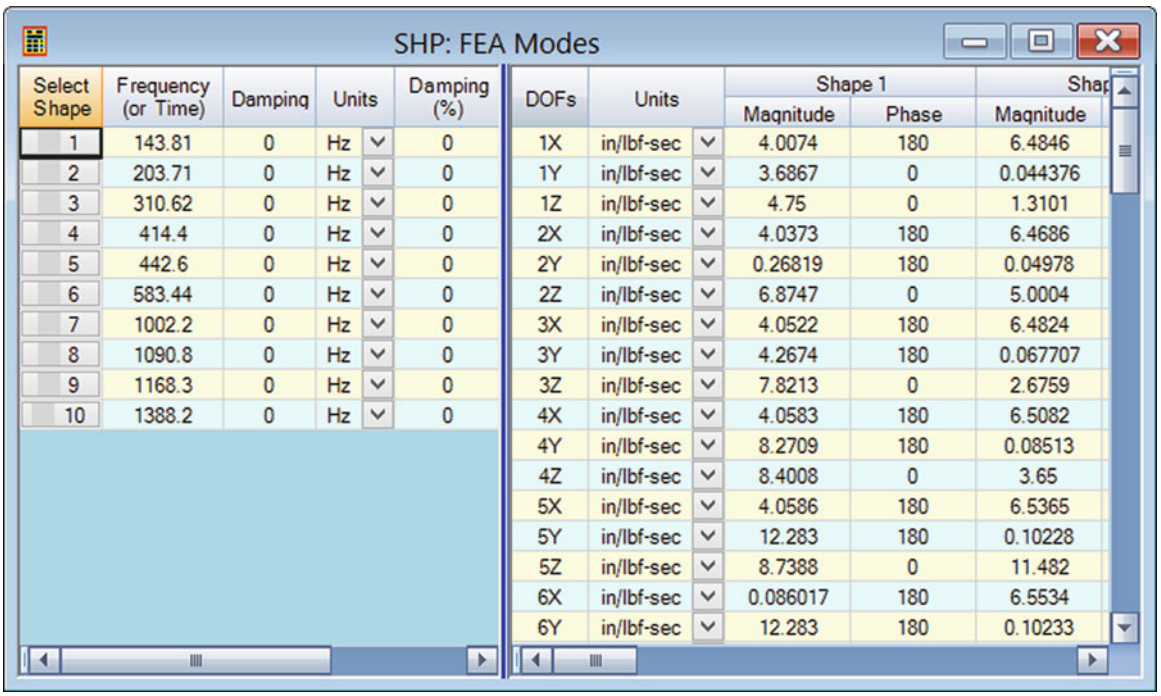

SHP: FEA Modes

Select Shape	Frequency (or Time)	Damping	Units	Damping (%)
1	143.81	0	Hz	0
2	203.71	0	Hz	0
3	310.62	0	Hz	0
4	414.4	0	Hz	0
5	442.6	0	Hz	0
6	583.44	0	Hz	0
7	1002.2	0	Hz	0
8	1090.8	0	Hz	0
9	1168.3	0	Hz	0
10	1388.2	0	Hz	0

DOFs	Units	Shape 1		Shap
		Magnitude	Phase	Magnitude
1X	in/lbf-sec	4.0074	180	6.4846
1Y	in/lbf-sec	3.6867	0	0.044376
1Z	in/lbf-sec	4.75	0	1.3101
2X	in/lbf-sec	4.0373	180	6.4686
2Y	in/lbf-sec	0.26819	180	0.04978
2Z	in/lbf-sec	6.8747	0	5.0004
3X	in/lbf-sec	4.0522	180	6.4824
3Y	in/lbf-sec	4.2674	180	0.067707
3Z	in/lbf-sec	7.8213	0	2.6759
4X	in/lbf-sec	4.0583	180	6.5082
4Y	in/lbf-sec	8.2709	180	0.08513
4Z	in/lbf-sec	8.4008	0	3.65
5X	in/lbf-sec	4.0586	180	6.5365
5Y	in/lbf-sec	12.283	180	0.10228
5Z	in/lbf-sec	8.7388	0	11.482
6X	in/lbf-sec	0.086017	180	6.5534
6Y	in/lbf-sec	12.283	180	0.10233

Fig. 8.4 FEA mode shapes

8.2 MAC Formula

For two shapes ({u},{v}), MAC is calculated with the formula, [2]

$$\mathrm{MAC} = \frac{\left\| \{u\}^h \{v\} \right\|^2}{\{u\}^h \{u\} \{v\}^h \{v\}} \tag{8.1}$$

{u} = complex shape (m-vector)
{v} = complex shape (m-vector)
m = number of *matching DOFs* between the shapes
h denotes the *transposed conjugate* vector

MAC is a measure of the ***co-linearity*** of two shapes. That is, if the two shapes lie together on the same straight line, **MAC = 1**. Equation (8.1) is the Dot Product of the two shapes ***normalized*** by each of their magnitudes squared. Therefore, MAC is not sensitive to the actual values of the shapes themselves, only their "***shapes***". If two shapes do not lie on the same line, then **MAC < 1**. If **MAC = 0**, then the two shapes are ***orthogonal*** to, or ***linearly independent*** of one another.

The MAC values between the EMA and FEA shapes of the Jim Beam are shown in Fig. 8.5. These values clearly indicate that ten pairs of EMA and FEA mode shapes are ***strongly correlated***. That is, each EMA shape is ***essentially the same*** as its corresponding FEA shape with a MAC value greater than 0.9.

Figure 8.6 is a bar chart of the ***scale factors*** that should be applied to the EMA shapes to make them equal to the FEA shapes, in a least-squared-error sense [3]. That is, if the EMA shapes are multiplied by the scale factors in Fig. 8.6, the EMA shape components will ***closely approximate*** the FEA shape component values, at least for the 99 matching DOFs.

The scaling matrix in Fig. 8.5 also contains some ***non-zero off-diagonal*** values, indicating that linear combinations of several EMA shapes are needed in order to more closely match the FEA shape values [3].

After the scale factors in Fig. 8.6 were applied to the EMA shapes, Fig. 8.7 shows the MAC values between the re-scaled EMA shapes and the FEA shapes. Clearly, there is an improvement in the correlation between shape pairs.

Figure 8.7 indicates that the rescaled EMA shapes are closer to being co-linear with the FEA shapes. But the question remains, "***How different are the EMA shape component values from the FEA shape component values*****?**" To answer that question, a new measure of the difference between two shapes will be introduced.

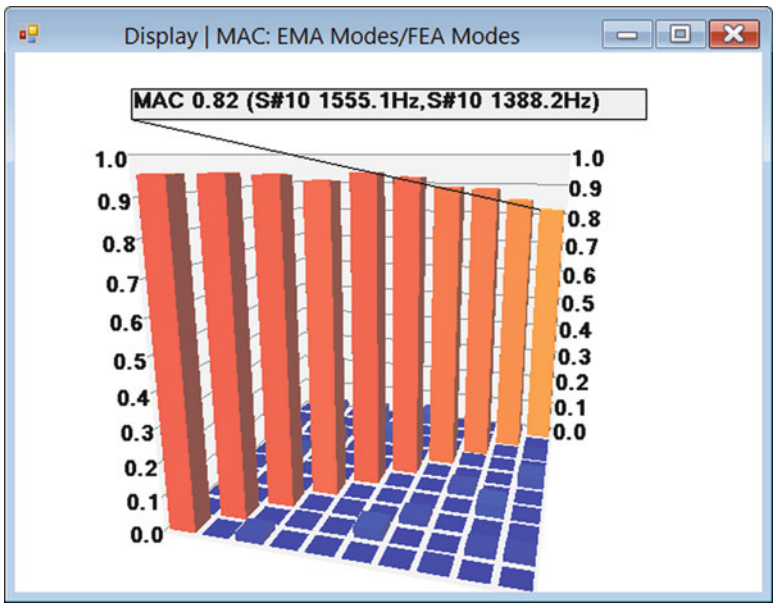

Fig. 8.5 MAC values between EMA and FEA shapes

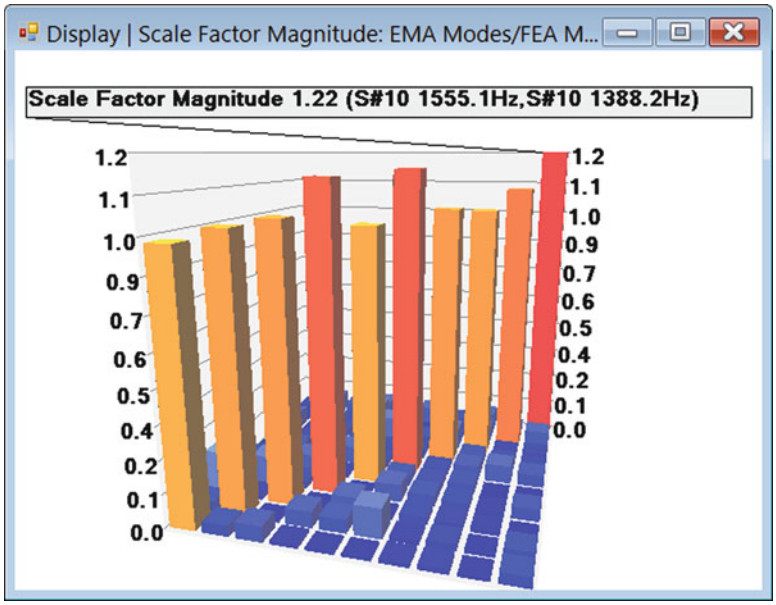

Fig. 8.6 EMA shape scale factors

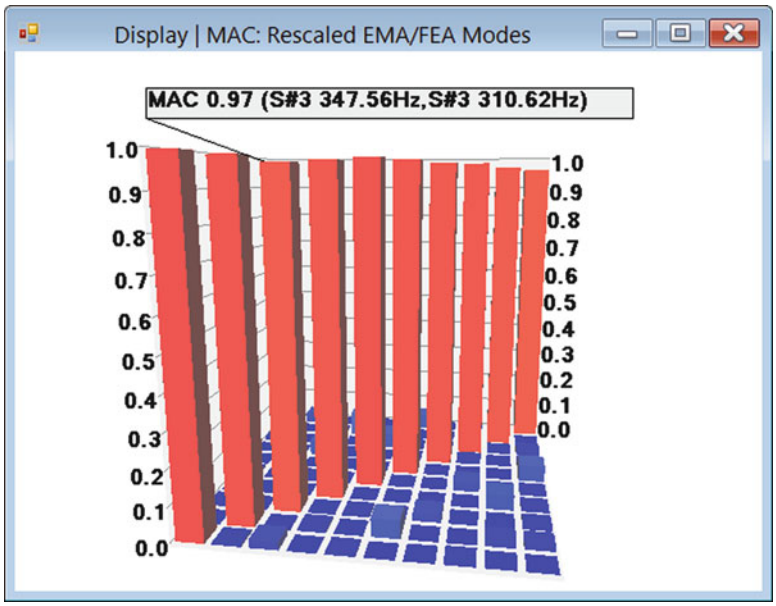

Fig. 8.7 MAC values between rescaled EMA and FEA shapes

8.3 Shape Difference Indicator (SDI)

For two shapes ({u},{v}), the Shape Difference Indicator is defined with the formula,

$$\mathrm{SDI} = \left(1 - \frac{\|\{v\} - \{u\}\|^2}{\{v\}^h \{v\} + \{u\}^h \{u\}}\right)^2 \tag{8.2}$$

or

$$\mathrm{SDI} = \left(\frac{2\ \mathrm{real}\left(\{v\}^h \{u\}\right)}{\{v\}^h \{v\} + \{u\}^h \{u\}}\right)^2 \tag{8.3}$$

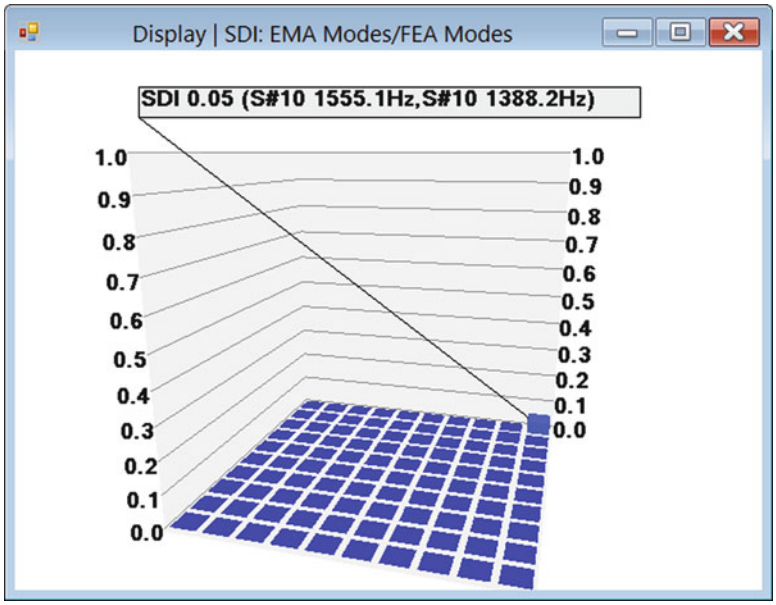

Fig. 8.8 SDI values for EMA and FEA shapes

real($\{v\}^h\{u\}$) = the real part of the vector dot product
$\{u\}$ = complex shape (m-vector)
$\{v\}$ = complex shape (m-vector)
m = number of *matching DOFs* between the shapes
h denotes the *transposed conjugate* vector

The SDI value is like the MAC value in that its values range between **0 and 1**. If **SDI = 1**, two shapes have ***identical values***. If **SDI < 1**, the two shapes have ***different values*** between their ***matching*** DOFs. Several examples illustrate the range of SDI values.

- If $\{v\} = \{u\}$, SDI = 1
- If $\{v\} = 0$ *or* $\{u\} = 0$, SDI = 0
- If $\{v\} = 2\{u\}$, SDI = 0.64
- If $\{v\} = 10\{u\}$, SDI = 0.04

The SDI values between the EMA and FEA shapes of the Jim Beam are shown in Fig. 8.8. The SDI values are ***nearly all zero***, indicating that the two sets of shapes have ***different component values***. Closer examination of the shape components in Figs. 8.3 and 8.4 reveals that the EMA shapes are ***mostly imaginary*** valued (with phases close to 90° and 270°) while the FEA shapes are ***real valued*** (with phases of 0° and 180°). Real valued shapes are also called ***normal*** shapes.

The SDI values between the rescaled EMA shapes and the FEA shapes are shown in Fig. 8.9. Clearly, the rescaled EMA shapes are ***nearly equal*** in value to the FEA shapes.

8.4 SDI and Cap Screw Torque

SDI can be used to detect differences between two shapes, no matter what type of data they contain. To illustrate this, different amounts of torque where applied to one of the Allen screws that attach the top plate to the back plate of the Jim Beam, as shown in Fig. 8.10.

For each of six different torque values; **30, 25, 20, 15, and 10 in-lbs**, the modal frequency and damping of six modes of the Jim Beam were stored as shape components. The modal frequency shapes are listed in Fig. 8.11, and the modal damping shapes in Fig. 8.12.

The SDI values between all frequency shape pairs are displayed in the bar chart in Fig. 8.13. The SDI values for all damping shape pairs are displayed in the bar chart in Fig. 8.13.

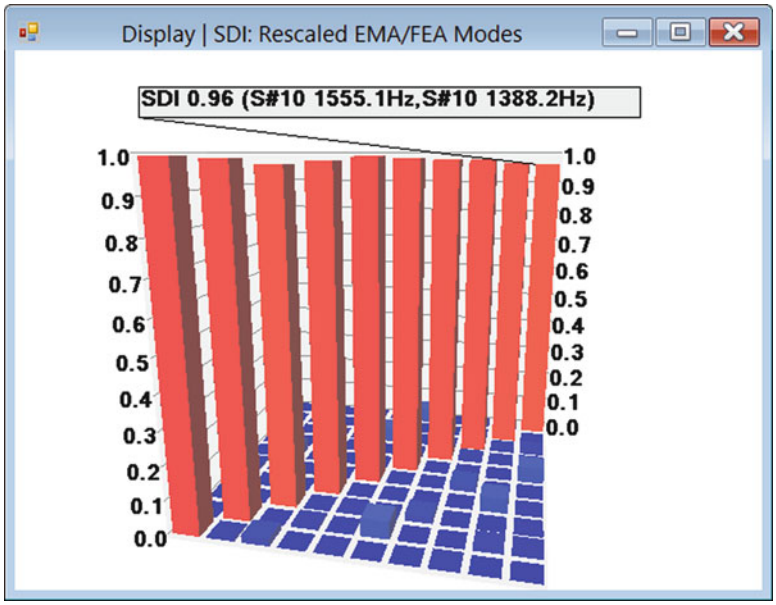

Fig. 8.9 SDI values for rescaled EMA and FEA shapes

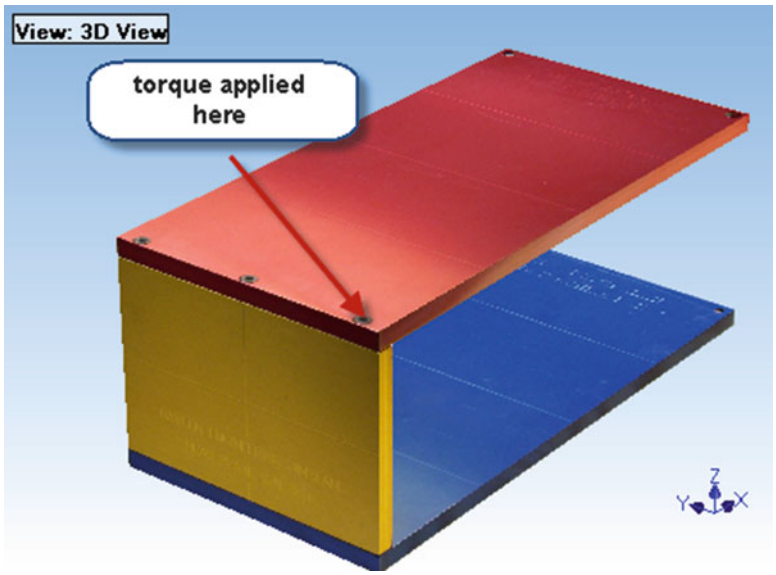

Fig. 8.10 Torque applied to Allen screw

All bars in Fig. 8.13 not only indicate a clear change in the modal frequencies for each torque value, but they also indicate that the SDI value ***dropped monotonically*** as the Allen screw was loosened from 30 to 10 in-lbs. In other words, the modal frequencies shifted more between cases, as the torque was reduced. On the other hand, the SDI bars in Fig. 8.14 indicate that there was ***no significant change*** in the modal damping due to loosening the Allen screw.

8.5 Conclusions

A new measure of the difference between two shapes, called the **Shape Difference Indicator** or **SDI**, was presented. Like MAC values, the SDI values range **between 0** and **1**. When $\mathbf{SDI = 1}$, the two shapes are ***identical***. When $\mathbf{SDI < 1}$, the two shapes have ***different*** values.

Unlike MAC though, SDI is sensitive to differences in the shape values, and also gives meaningful results even between ***two scalars***.

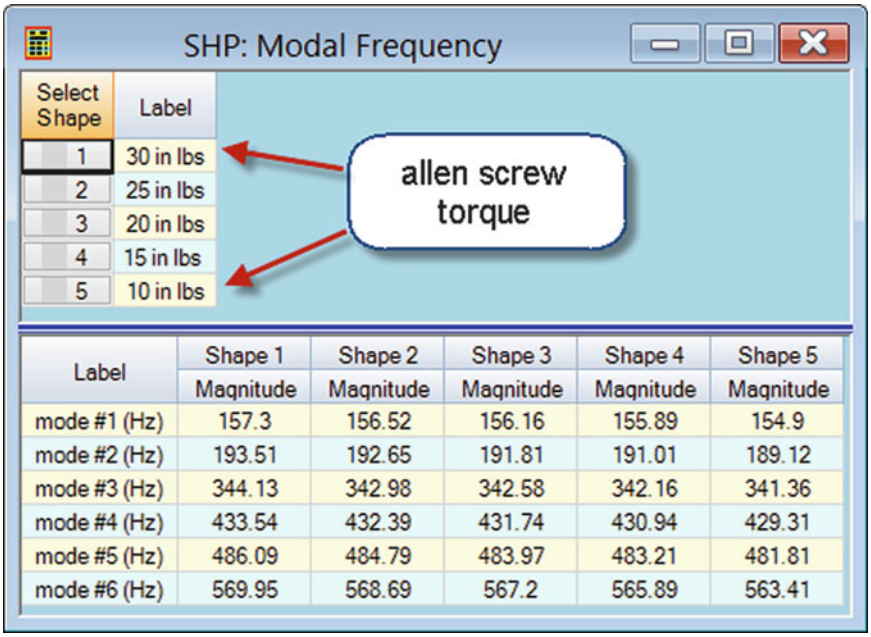

Label	Shape 1 Magnitude	Shape 2 Magnitude	Shape 3 Magnitude	Shape 4 Magnitude	Shape 5 Magnitude
mode #1 (Hz)	157.3	156.52	156.16	155.89	154.9
mode #2 (Hz)	193.51	192.65	191.81	191.01	189.12
mode #3 (Hz)	344.13	342.98	342.58	342.16	341.36
mode #4 (Hz)	433.54	432.39	431.74	430.94	429.31
mode #5 (Hz)	486.09	484.79	483.97	483.21	481.81
mode #6 (Hz)	569.95	568.69	567.2	565.89	563.41

Fig. 8.11 Modal frequency shapes

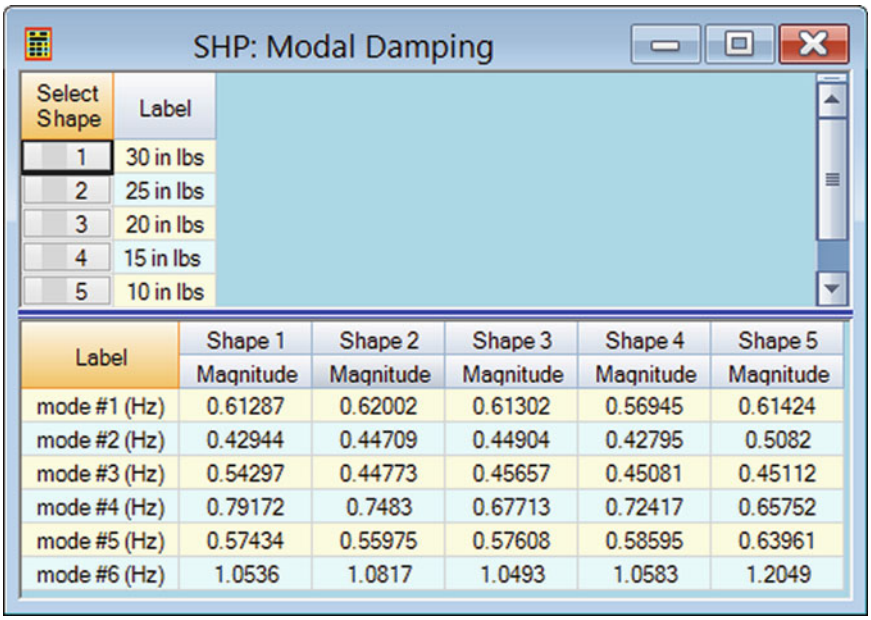

Label	Shape 1 Magnitude	Shape 2 Magnitude	Shape 3 Magnitude	Shape 4 Magnitude	Shape 5 Magnitude
mode #1 (Hz)	0.61287	0.62002	0.61302	0.56945	0.61424
mode #2 (Hz)	0.42944	0.44709	0.44904	0.42795	0.5082
mode #3 (Hz)	0.54297	0.44773	0.45657	0.45081	0.45112
mode #4 (Hz)	0.79172	0.7483	0.67713	0.72417	0.65752
mode #5 (Hz)	0.57434	0.55975	0.57608	0.58595	0.63961
mode #6 (Hz)	1.0536	1.0817	1.0493	1.0583	1.2049

Fig. 8.12 Modal damping shapes

Both MAC and SDI were calculated between the EMA and FEA mode shapes of the Jim Beam. The MAC values shown in Fig. 8.5 indicate an acceptable level of correlation between the EMA and FEA mode shapes.

The SDI values between the EMA and FEA shape pairs are shown in Fig. 8.8 and are all ***nearly zero***, indicating that the EMA shapes have different values than the FEA shapes. A cursory comparison of the shape values in Figs. 8.3 and 8.4 verifies that the phases of the EMA shape components are approximately 90° apart from the phases of the FEA shape components. MAC rightly indicates that the ***shapes are nearly the same***, but SDI indicates that their ***component values are different***.

After the EMA shapes were rescaled to more closely match the FEA shapes [3], the MAC values in Fig. 8.7 and the SDI values in Fig. 8.9 both indicate a ***strong correlation*** between the EMA and FEA shape pairs.

Next, the SDI calculation was used to classify the torque applied to one of the Allen screws used to hold the plates together on the Jim Beam. Five different torque values were applied to one Allen screw, as shown in Fig. 8.10. With each torque value applied to the screw, FRFs were acquired and curve fit to obtain the modal frequency and damping of the first six modes of the beam. Those values are listed as in Figs. 8.11 and 8.12.

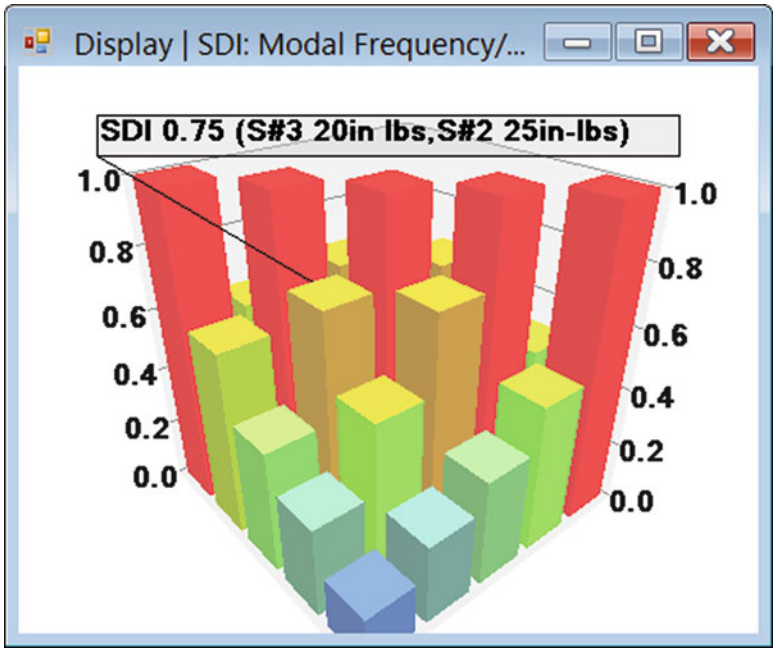

Fig. 8.13 SDI for modal frequency shapes

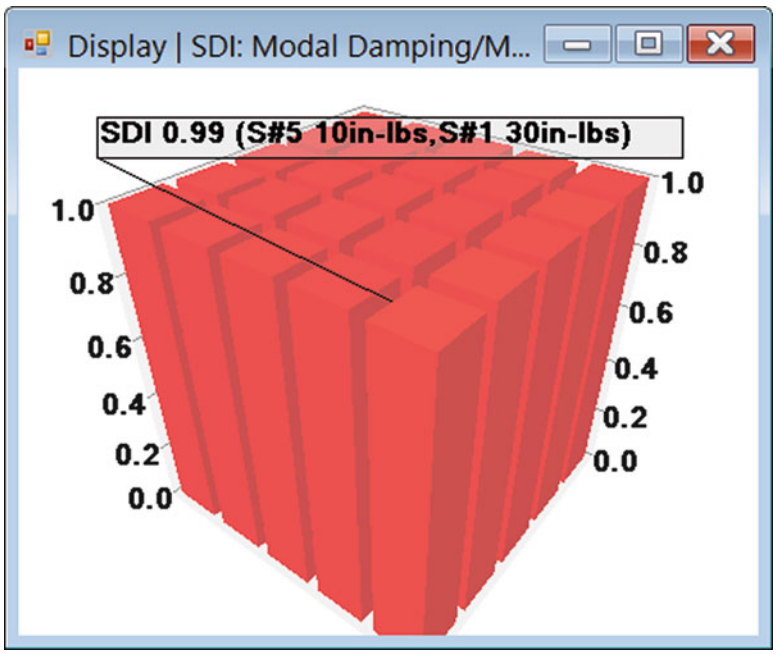

Fig. 8.14 SDI for modal damping shapes

Each table contains five shapes, one for each torque value. Each shape contains six components, each component containing either a modal frequency or damping value. The SDI bar chart values shown in Fig. 8.13 were calculated between all frequency shape pairs in Fig. 8.11. Likewise, the SDI bar chart values shown in Fig. 8.14 were calculated between all pairs of shapes in Fig. 8.12.

The SDI values in Fig. 8.13 indicate a ***significant difference*** in modal frequencies caused by the five different torque values. However, the SDI values in Fig. 8.14 indicate ***very little difference*** in modal damping values between the five different torque values.

8.6 Fault Correlation Tool (FaCTs™)

SDI has been implemented in the Vibrant Technology MechaniCom Machine Surveillance System™ and the MechaniCom Qualification Testing System™ as a tool for ***detecting and diagnosing faults*** in machinery and structures. This Fault Correlation Tool, called FaCTs™, uses an ***ordered table and bar chart*** for correlating shapes based on their SDI values.

To illustrate, suppose that multiple Jim Beam structures were being tested for proper assembly, and that 25 in-lbs was the correct torque value for tightening the Allen screw shown in Fig. 8.10. If shapes like those in Fig. 8.11 were stored in the MechaniCom database, then each time a Jim Beam was tested, the SDI values between its frequency shape and the stored shapes would be ordered in a FaCTs™ table, from the highest to lowest SDI value. The stored shape with the highest SDI value would then indicate whether the current torque used on the Allen screw was ***higher*** or ***lower*** than 25 in-lbs.

Any type of engineering data, including vibration, temperatures, pressures, flow rates, voltage, current, etc. can be used with SDI. A FaCTs™ table then, is not only useful for ***detecting*** a machine failure or improper structural assembly, but also for ***correlating*** it with a known machine failure or improper assembly.

References

1. Richardson SC, Richardson MH (2008) Using photo modeling to obtain the modes of a structure. In: Proceedings of the international modal analysis conference
2. Allemang RJ, Brown DL (1982) A correlation coefficient for modal vector analysis. In: Proceedings of the international modal analysis conference
3. Schwarz BJ, Richardson MH (2014) Linear superposition and modal participation. In: Proceedings of the 32nd international modal analysis conference, Orlando
4. Allemang RJ (2002) The modal assurance criterion (MAC): twenty years of use and abuse. In: Proceedings of the international modal analysis conference

Chapter 9
Non-destructive Examination of Multiphase Material Distribution in Uranium Hexafluoride Cylinders Using Steady-State Laser Doppler Vibrometery

David Goodman, Kelly Rowland, Sheriden Smith, Karen Miller, and Eric Flynn

Abstract The ability to detect the diversion of a significant quantity of nuclear material is the objective of international nuclear safeguards, and safeguarding uranium enrichment technology is especially important in preventing the spread of nuclear weapons. In gas centrifuge enrichment plants, the uranium is in the form of uranium hexafluoride (UF_6), which regularly transitions between phases during processing and storage due to its low triple point. The variation of material distribution in Uf_6 cylinders has a significant effect on enrichment measurement uncertainty, especially with increasing accuracy of passive neutron assay measurements, motivating interest in non-destructive methods of examining UF_6 cylinder fill distributions.

For this study, a novel steady-state scanning laser Doppler vibrometer (LDV) system is used to determine the material and phase distributions within small UF_6 cylinders. This technology induces steady-state ultrasonic waves throughout an object and then uses a scanning laser to measure vibrational wavenumber at pixilated points on the object. Different materials and phases are excited by the ultrasonic waves to different extents, changing the local measured wavenumbers and allowing fill distributions of the storage cylinders to be mapped. Through non-destructive examination of the variation in typical fill profiles of UF_6 cylinders, the uncertainty associated with neutron measurements of UF_6 cylinders may be better characterized.

Keywords Ultrasound • Non-destructive evaluation • Scanning laser Doppler vibrometer • Uranium hexafluoride • Nuclear safeguards

9.1 Introduction

The purpose of this study is to test whether a steady-state scanning laser Doppler vibrometer (LDV) system can be used to characterize the fill profile of uranium hexafluoride (UF_6) inside storage cylinders. The ability to detect the diversion of a significant quantity of nuclear material is the objective of international nuclear safeguards, and safeguarding uranium

D. Goodman
Department of Nuclear Engineering, University of Michigan, Ann Arbor, MI 48109, USA
e-mail: digoodma@umich.edu

K. Rowland
Department of Nuclear Engineering, University of California, Berkeley, CA 94704, USA
e-mail: rowlak@rpi.edu

S. Smith
Department of Mechanical Engineering, Colorado State University, Fort Collins, CO 80523, USA
e-mail: Sheriden@rams.colostate.edu

K. Miller
Safeguards Science & Technology Group, Los Alamos National Laboratory, Los Alamos, NM 87545, USA
e-mail: kamiller@lanl.gov

E. Flynn (✉)
Engineering Institute, Los Alamos National Laboratory, Los Alamos, NM 87545, USA
e-mail: eflynn@lanl.gov

A. Wicks (ed.), *Structural Health Monitoring, Volume 5: Proceedings of the 32nd IMAC, A Conference and Exposition on Structural Dynamics, 2014*, Conference Proceedings of the Society for Experimental Mechanics Series, DOI 10.1007/978-3-319-04570-2_9,

enrichment technology is especially important in preventing the spread of nuclear weapons. In gas centrifuge enrichment plants, the uranium is in the form of UF_6, which regularly transitions between phases during processing and storage due to its low triple point [1]. During this regular sublimation and deposition cycle, UF_6 crystallizes on container walls creating annular rings of varying thicknesses [2]. Vibrations and temperature gradients introduced by storage and handling conditions may loosen adhered UF_6 causing it to collect on cylinder bottoms. Alternatively, if the UF_6 is heated in the cylinder for sampling or homogenization, the material may also pool at the cylinder bottom. The toxicity and low vapor pressure of UF_6 as well as the small valves present on storage cylinders prevent the cylinders from being opened and visually inspected, requiring novel, fast, and inexpensive measurement techniques to ascertain fill profiles [3]. Recent advances in passive neutron assay of UF_6 storage cylinders and the potential extension to unattended systems [4], have motivated interest in examining the distribution of UF_6 within these cylinders due to the effect that variation in material distribution has on total measurement uncertainty in neutron assay techniques [2].

Earlier acoustical probes of sealed containers used acoustic resonant spectroscopy (ARS). ARS measures the resonant frequencies of a container induced by a piezoelectric transducer, revealing bulk container characteristics such as pressure [5]. However, the ARS method was designed for homogenous systems and fails to measure fine container features such as internal material distribution. The LDV system used in this project solves this issue by measuring a container's vibrational response to steady state waves at discrete points over the whole container, allowing for local measurement of container properties such as variations in wall thickness. It was hypothesized in this study that a steady-state LDV scanning system would be able to detect regions inside the storage cylinders with solid UF_6 affixed to the inside surface, and that these regions would be distinguishable from the regions of liquid or gaseous UF_6 or void space.

In the LDV system a piezoelectric transducer creates single tone, steady-state ultrasonic waves throughout the structure in question. A scanning laser then measures the induced vibrations at discrete points on the object in phase with the wave excitation cycle. An algorithm then uses each point velocity to generate a map of lamb wave propagation over the measured gridpoints [6]. Mapping wave propagation generates a full wavefield from which local wavenumbers, the spatial frequency at which waves propagate, are calculated. Lamb wave propagation is dependent on material geometry, stiffness, density, and Poisson's ratio. Variation in material geometries and properties cause different wavefield structures, altering local wavenumbers. Recent studies using LDV systems have successfully demonstrated defect detection based on wavenumber shifts by accurately locating areas of corrosion and wall thinning on metal plates by measuring increases in local wavenumber [6, 7]. These prior experiments highlight the ability of lamb waves to probe regions of decreased material thickness through wavenumber shifts. Alternatively, we propose that wavenumber can also be used to detect regions of increased material thickness. Coupling of excess material to objects changes the effective material stiffness, thickness, and mass, altering the measured wavenumbers. Regions of decreased wavenumber are then correlated to increased material thickness in a way similar to prior defect studies.

The LDV system used in this experiment, shown in Fig. 9.1, has been thoroughly described in previous papers [6, 7]. A piezoelectric transducer was affixed to the object that was to be investigated, which was vibrated at a steady-state, ultrasonic frequency, f. This was repeated for several different frequencies. Placed some distance d away, a 2D scanning LDV measured the surface velocity magnitude at pixelated points with spacing Δx on the object. This scan was done at rate s over a rectangular scan area A over some length of time t. The measured point velocities were then converted into vibrational wavenumber. For this project, the majority of the analysis consisted of attempts at correlating LDV scans with geometries of the corresponding physical systems. From each scan of an object, a number of different data sets were produced. These data sets consisted of raw velocity data converted into vibrational wavenumber.

9.2 Initial Tests

A variety of materials were scanned with the LDV system as proofs of concept prior to the scanning of an actual 5A UF_6 cylinder. For reference, the test scan parameters that were used for each of the specimens are listed in Table 9.1.

Due to the way this LDV system measures and calculates the values at each point [6], the discontinuities at the edges of the scan introduce significant distortion into the resulting images. For the scanning methods used in this study, each physical scan area was made larger than the area that was to be imaged so that 10 % of the scan could be cropped off the edges of each image to remove edge effects. This can be seen when comparing the scan areas listed in Table 1 and the dimensions of the following scan images.

The first materials tested were water and dry dirt, each of which were placed inside steel coffee cans, which served as mock UF_6 cylinders. Dry dirt was chosen as an example of a material that was very weakly coupled to the inside of the cylinder and water was chosen as a material with a somewhat stronger coupling to the inside of the cylinder. Another factor

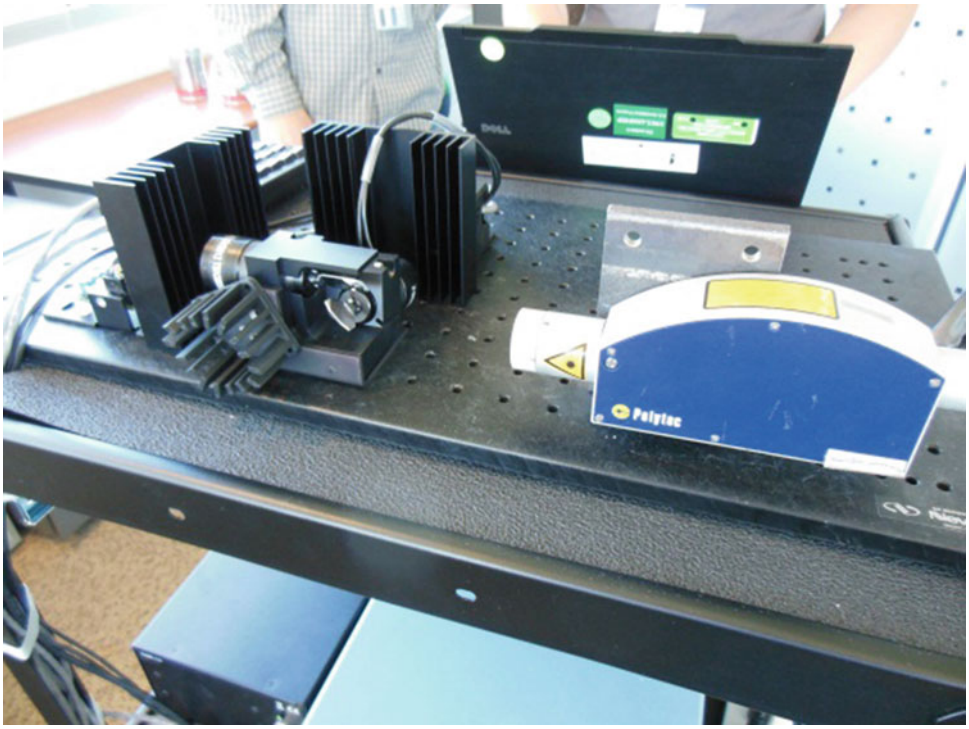

Fig. 9.1 LDV system used in this study

Table 9.1 LDV test scan parameters

Specimen	Distance from scanner, d (m)	Frequency, f (kHz)	Interval between scan points, Δx (mm)	Scan rate (points per second)	Scan rate, s (m/s)	Scan area, A (cm × cm)	Total scan time, t (s)
Steel can—water/dirt	1.5	125	0.50	2000	1	11 × 15	3.3
Steel can—epoxy	1.25	100	0.75	500	0.375	12 × 8	3.4
Thin aluminum plate	1.60	100	1.00	2000	2	54 × 20	5.4
Thick aluminum plate	1.55	150	1.00	2000	2	10 × 10	0.5

in choosing these two materials was the multiphase nature of UF_6, which prompted the investigation of a variety of phases of substances. Originally, the outside surfaces of the coffee cans were highly reflective for marketing purposes, so the outsides of the cans were abraded to decrease their reflectivity, making the can's surface roughness more similar to the surface of a UF_6 cylinder. Figure 9.2 shows the wavenumber maps of dry dirt and water inside of the mock cylinders. It can be seen that the system is not able to discern any level of dry dirt, while the height of water can be clearly distinguished as an increase in wavenumber.

With the relative success of water over dry dirt, a material with even greater coupling to the insides of cylinders was pursued as a candidate for LDV system testing. Epoxy was tested since it strongly bonded to the inside of the mock cylinder. For an initial LDV scan, epoxy was affixed to the inside of a coffee can in a similar manner to the way that UF_6 would hypothetically be crystallized on the inside wall of a 5A cylinder. Figure 9.3 shows the epoxy affixed to the inside wall of the mock cylinder as well as the corresponding wavenumber plot generated with the LDV system. Note that the projection of the 3D cylinder on to the 2D scan area causes vibrations along the scan curvature to be interpreted as closer together, increasing the apparent wavenumbers along the vertical edges.

After the results were obtained from the LDV scan of the epoxy affixed to the inside of the can, further tests with epoxy were pursued. Next, epoxy was applied to one side of an aluminum plate in a variety of widths and spacings, as seen in Fig. 9.4. Similar to the test cans, the side of the plate to be scanned was abraded to create a surface more representative of the actual storage cylinders. The plate was then scanned with the LDV system to determine whether or not the individual epoxy patterns could be distinguished from one another. All but the top two epoxy rectangles could be distinguished from one another, indicating a scan resolution of approximately 1.5 cm, corresponding to the distance between those two epoxy regions. This resolution would be more than sufficient for measuring the general fill profiles of large UF_6 cylinders.

Measurements were also conducted on a 3/8″ aluminum plate to quantify system effectiveness at detecting material coupling through thicker plates. The plate was prepared in an identical manner using epoxy to simulate crystallized UF_6. Epoxy coupled regions were easily visible by local wavenumber depression as measured earlier on thinner plates.

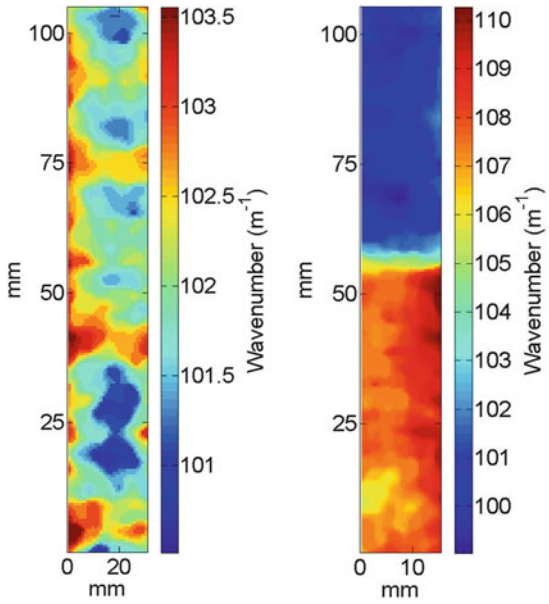

Fig. 9.2 Wavenumber plot of steel can partially filled with dry dirt (*left*), wavenumber plot of steel can partially filled with water (*right*)

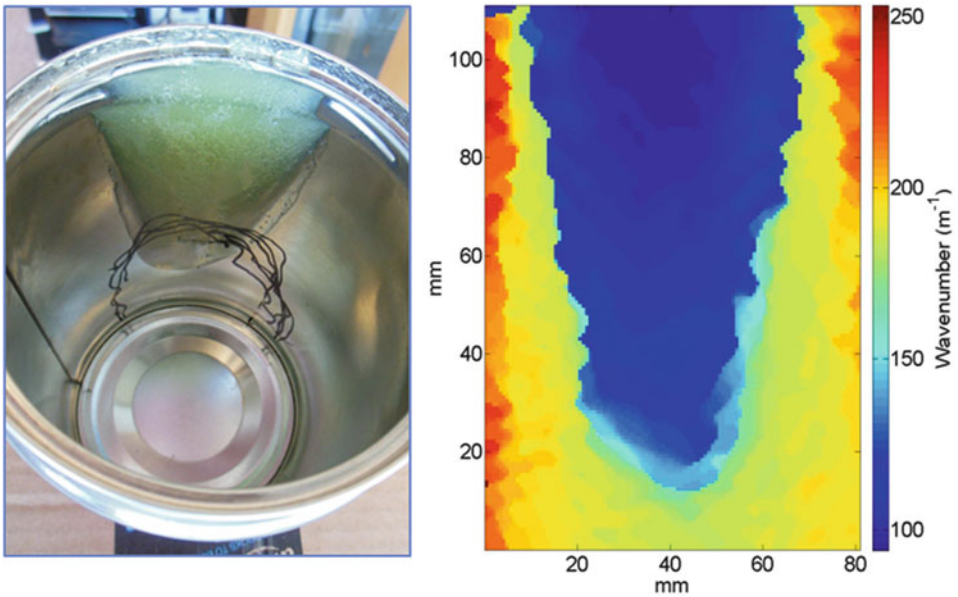

Fig. 9.3 Steel can with epoxy affixed to the inside wall of the can (*left*), corresponding wavenumber plot of the can (*right*)

Comparing measurements of 3/8″ and 1/16″ plates revealed that lamb wave wavenumber decreased with increasing plate thickness as well as with material thickness, corresponding to changes in the system stiffness. By comparing Figs. 9.4 and 9.5, it can also be seen that that thicker plates result in lower system resolution; the epoxy area in Fig. 9.5 is not as clearly distinguishable as the ones in Fig. 9.4.

9.3 UF_6 Cylinder Tests

Following the test scans, LDV scans were performed on an actual 5A UF_6 cylinder using methods similar to the ones described previously to determine if the LDV system could detect the fill profiles. A mechanical drawing of a 5A cylinder similar to the one scanned is shown in Fig. 9.6. From the cylinder dimensions and the approximate mass of the UF_6 in the cylinder (6 kg), the fill height was approximated to be 92 mm from the bottom of the cylinder, as shown in Fig. 9.7, assuming that the UF_6 was without voids and was not deposited on the walls of the cylinder. It was also hypothesized that in a resulting scan image the region below the very bottom weld would not indicate the presence of UF_6 because the outside surface would

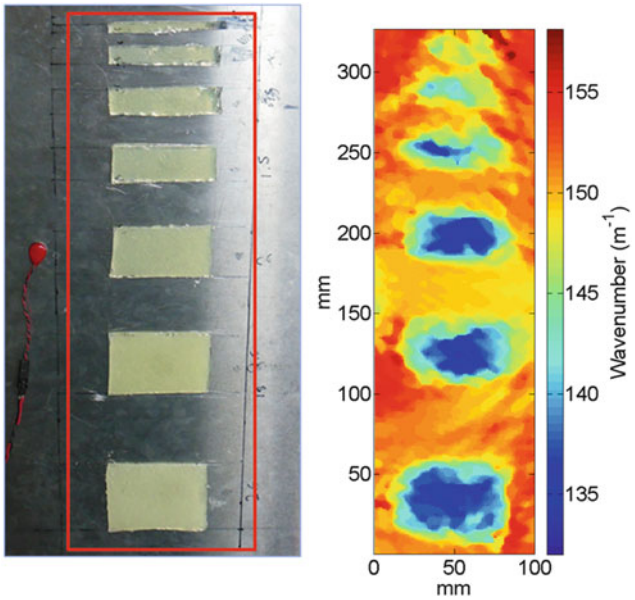

Fig. 9.4 Aluminum plate with epoxy pattern and highlighted scan area (*left*), corresponding wavenumber plot (*right*)

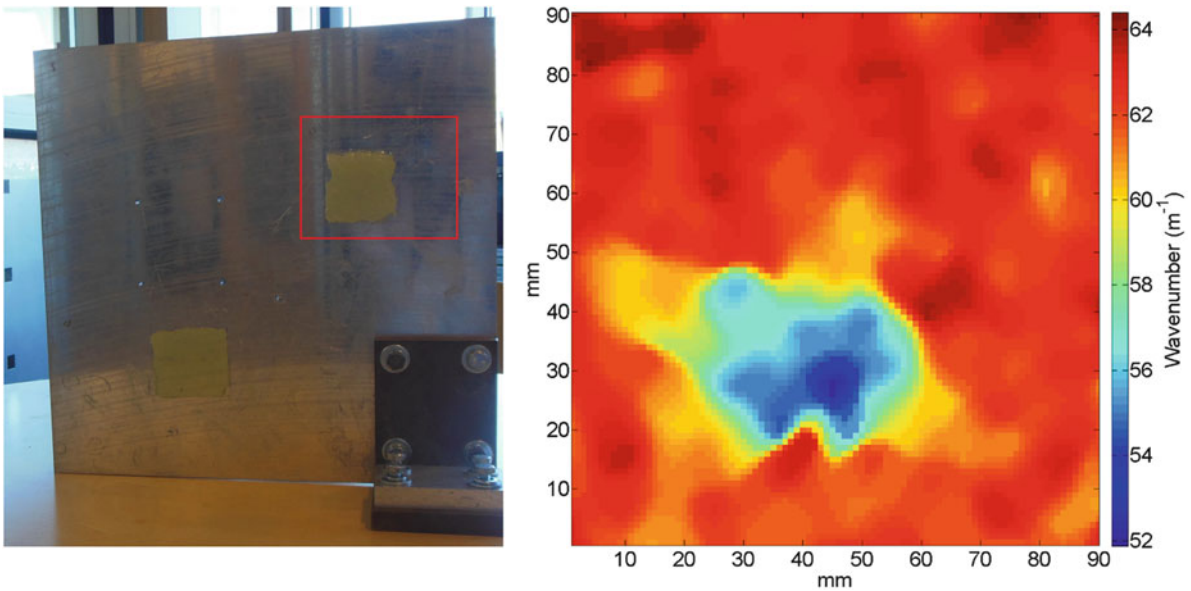

Fig. 9.5 3/8″ aluminum plate prepared with epoxy with scan area highlighted (*left*), and corresponding wavenumber plot of scan region (*right*)

not be coupled to the fill area in that region. In the cylinder tested, the UF_6 was expected to be a solid block at the bottom of the fill area based on its handling and storage records.

Many different scans were made of the available UF_6 storage cylinder at a variety of different scan parameters. A resultant wavenumber plot of one of these UF_6 scans can be seen in Fig. 9.7. In this figure, the processed image is shown on the left while the raw vibrational surface velocity image is shown on the right. A very clear low wavenumber region can be seen between the two welds, located mainly between 40 and 90 mm on the vertical axis. The difference in wavenumber between the low and high regions is relatively small compared to the difference measured in the can tests, likely due to the energy dissipation caused by the cylinder's larger size and wall thickness (1/4″). As expected, wavenumbers above and below the expected fill height were similar, and were higher than the suspected fill region, suggesting the presence of a gas behind the cylinder wall. This image reflects the expected results fairly well; the low wavenumber region begins at the lower weld and ends at approximately the hypothesized fill height. This region is very likely indicative of the presence of UF_6. However, the distance between the hypothesized fill height and the weld is within the resolution distance (about 1.5 cm) found in the previous test shown in Fig. 9.4. This means that the weld could be obscuring or distorting the actual UF_6 fill profile in the

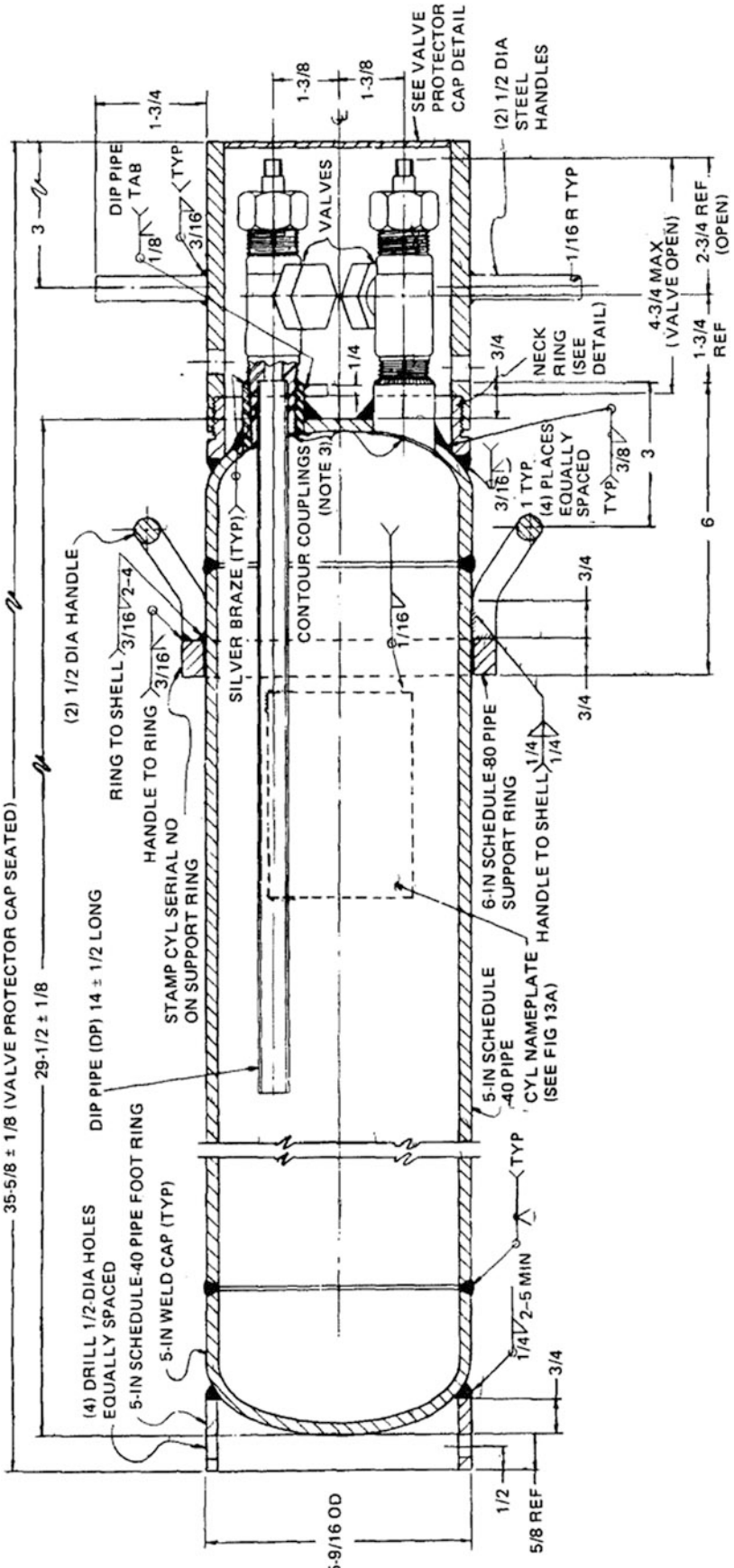

Fig. 9.6 United States department of energy mechanical diagram of a 5A UF_6 storage cylinder [8]

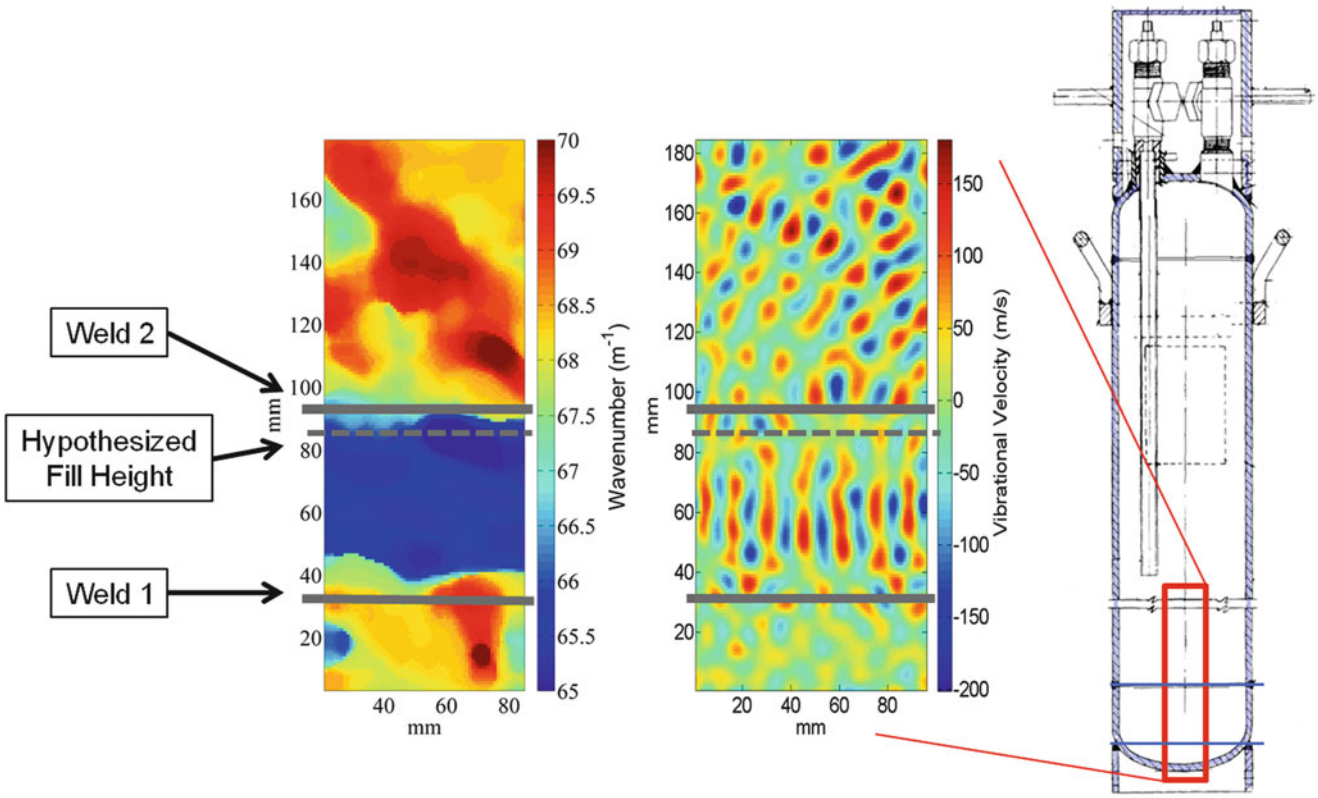

Fig. 9.7 Scan results from bottom section of a UF_6 5A cylinder excited at 175 kHz

scan results. In future investigations, effort should be made to verify the fill profile and determine the extent of the welds' effect on the scan results.

One source of uncertainty was inherent to the LDV system. The resolution of the scan was dependent on the wavelength of the excitation waves induced in the object scanned by the piezoelectric transducer; the shorter the wavelength, the higher the resolution. However, exciting the transducer at higher frequencies produces a smaller response in the object, consequently decreasing the anomaly detection ability of the LDV system. The resolution of the scan is also limited by the power of the transducer; the more energy that is put into the object by the transducer, the larger the vibrational response measured. For larger objects that dissipate more energy, such as a larger UF_6 cylinder, more powerful or a greater number of transducers may be needed to induce an adequate vibrational response for scanning.

9.4 Summary and Conclusions

The steady-state ultrasonic laser Doppler vibrometer is a promising method for scanning UF_6 cylinder profiles. The test scans were largely successful; as long as the material inside the cans or affixed to the back of the plates were well coupled to the outside surface, a satisfactory image could be obtained. The cylinder scans also showed positive results; they show a low wavenumber region in the area expected based on the hypothesized UF_6 fill height. However, the scan results from the UF_6 cylinders were made somewhat uncertain because the hypothesized fill height fell within the scan resolution of a weld on the cylinder. To conclusively identify the fill profile with this scanning system, the distance between the hypothesized fill height and the welds would need to be substantially larger. This study indicates that, given further investigation, this scanning system could be a useful tool for imaging UF_6 cylinder fill profiles.

Future experiments using laser Doppler vibrometer systems to measure UF6 distribution in cylinders should ensure that hypothesized fill heights are sufficiently distant from other distinguishable features given the known system resolution. On larger storage cylinders such as the 30B and the 48Y models typically found in enrichment plants, more scanning area is available that is free of complicating features such as welds. However, the thicker walls of these larger cylinders would likely dissipate more excitation energy, generating smaller wavenumber signal to noise ratios than thinner cylinders would.

One recommendation is to acquire more powerful and optimized transducers with which to excite the cylinders in order to increase the scans' signal to noise ratios. Averaging wavenumber scans conducted at similar excitation frequencies, assuming cylinder behavior is linear over a narrow frequency band, could also help improve signal to noise ratios.

Acknowledgements Some of the work presented herein was partially funded by Safeguards Science & Technology Group and the Engineering Institute at the Los Alamos National Laboratory. Any opinions, findings, and conclusions or recommendations expressed in this material are those of the authors and do not necessarily reflect the views of the particular funding agency. The authors are grateful for the support obtained.

References

1. United States Enrichment Corporation (1995) Uranium hexafluoride: a manual of good handling practices, 7th edn. United States Department of Energy, Bethesda
2. Miller KA, Menlove HO, Swinhoe MT, Marlow JB (2011) The passive neutron enrichment meter for uranium cylinder assay. In: ESARDA 2011, vol 46, Safeguards Science & Technology Group (N-1), Los Alamos National Laboratory, Los Alamos, pp 115–120
3. Morrow PE et al (1981) Metabolic fate and evaluation of injury in rats and dogs following exposure to hydrolysis products of uranium hexaflouride. Rep. CR-2268, University of Rochester, Rochester, October 1981
4. Goodman D, Rowland K, Smith S (2013) A multisensor unattended cylinder verification station for uranium enrichment plant safeguards using passive neutron enrichment. Los Alamos National Labs Engineering Institute, Los Alamos
5. Veirs DK, Heiple CR, Roesenblatt GM, Baiardo JP (1997) Measuring gas composition and pressure within sealed containers using acoustic resonance spectroscopy. Los Alamos National Laboratory, Los Alamos
6. Flynn EB, Jarmer GS (2013) High-speed, non-contact, baseline-free imaging of hidden defects using scanning laser measurements of steady-state ultrasonic vibration, 1 June 2013
7. Flynn EB, Chong SY, Jarmer GJ, Lee JR (2013) Structural imaging through local wavenumber estimation of guided waves. NDT&E Int vol 59 1–10
8. US Department of Energy Oakridge Operations (2011) Acquisition of services for depleted uranium hexafluoride (DUF6) conversion project request for proposal no. DE-RP05-01OR22717: cylinder and valve fabrication drawings. http://www.oro.doe.gov/duf6disposition/uf6_cylinder_Model_5-A.pdf

Chapter 10
Damage Detection Using Large-Scale Covariance Matrix

Luciana Balsamo, Raimondo Betti, and Homayoon Beigi

Abstract Statistical pattern recognition based structural damage detection is often developed exploiting the methods of outlier analysis. In this context, damage occurrence is assessed by analyzing whether a set of features extracted from the response of the system under unknown conditions departs from the population of features extracted from the response of the healthy system. The metric dominantly used for this purpose is the Mahalanobis Squared Distance (MSD). Evaluation of MSD of a point from a population requires the use of the inverse of the population's covariance matrix. It is known that when the feature dimensions are comparable or larger than the number of observations, the covariance matrix is ill-conditioned and numerically problematic to invert in the former case, while singular and not even invertible in the latter. To overcome this difficulty, three alternatives to the canonical damage detection procedure are investigated: data compression through Discrete Cosine Transform, use of pseudo-inverse of the covariance matrix, and use of shrinkage estimate of the covariance matrix. The performance of the three methods is compared using the experimental data recorded on a four story steel frame excited at the base by means of the shaking table available at the Carleton Laboratory at Columbia University.

Keywords Damage detection • Large-scale covariance matrix • Discrete cosine transform • Pseudo inverse • Shrinkage covariance matrix

10.1 Introduction

Statistical pattern recognition based structural damage detection is the task of assessing damage occurrence using information extracted from the structural response. It is developed by first learning the patterns drawn by such information when extracted from the system under healthy conditions, and by then comparing the learnt patterns with the patterns drawn by the same information extracted from the response of the system under unknown conditions: if the new patterns depart from the learnt ones more than a prescribed threshold, the structure is declared damaged. The information extracted from the structural response are known as *damage sensitive features* (dsf). Damage sensitive features need to be sensitive to structural changes due to damage, while remain insensitive to structural changes due to external effects, like environmental or operational conditions. The process of learning the patterns drawn by the damage sensitive features extracted from the response of the healthy system is known as *training*, while the process of comparing the trained features with those extracted from the structure under unknown conditions is named *testing*. One approach to measure the departure of the two populations of features is to evaluate the squared Mahalanobis distance of the testing features from the trained ones [1, 2].

Let us denote as $\mathbf{x}$ a p-dimensional point representing the testing feature vector, and by $\boldsymbol{\mu}$ and $\boldsymbol{\Sigma}$ the mean vector and covariance matrix of the trained feature population, the Mahalanobis squared distance of $\mathbf{x}$ from the trained model is defined as:

$$D(\mathbf{x}) = (\mathbf{x} - \boldsymbol{\mu})^T \boldsymbol{\Sigma}^{-1} (\mathbf{x} - \boldsymbol{\mu}). \tag{10.1}$$

L. Balsamo (✉) • R. Betti
Department of Civil Engineering and Engineering Mechanics, Columbia University, New York, NY 10027, USA
e-mail: lb2591@columbia.edu

H. Beigi
Recognition Technologies, Inc. White Plains, NY 10601, USA

A. Wicks (ed.), *Structural Health Monitoring, Volume 5: Proceedings of the 32nd IMAC, A Conference and Exposition on Structural Dynamics, 2014*, Conference Proceedings of the Society for Experimental Mechanics Series, DOI 10.1007/978-3-319-04570-2_10,

In the real applications, the values of $\boldsymbol{\mu}$ and $\boldsymbol{\Sigma}$ are unknown, so that an estimate of such statistics is required. Usually, the unbiased sample counterparts of such statistics are used. Let us assume that the population of training features is collected into a matrix $\mathbf{Y} = \{\mathbf{y}_1, \ldots, \mathbf{y}_n\} \in \mathbb{R}^{p \times n}$: each column of $\mathbf{Y}$ represents an observation of a p-dimensional feature vector. The sample mean of the training data set is given by:

$$\hat{\boldsymbol{\mu}} = \mathbf{m} = \frac{1}{n} \sum_{i=1}^{n} \mathbf{y}_i, \tag{10.2}$$

while the unbiased sample covariance matrix of the training set is evaluated according to

$$\hat{\boldsymbol{\Sigma}} = \mathbf{S} = \frac{1}{n-1} \sum_{i=1}^{n} (\mathbf{y}_i - \mathbf{m})(\mathbf{y}_i - \mathbf{m})^T. \tag{10.3}$$

As evidenced by Eq. (10.1), the evaluation of the Mahalanobis squared distance requires the computation of the inverse of the covariance matrix. Nonetheless, if one is presented with a data set of features of dimension p comparable or larger than the number of observations n, it is known that the estimate of the covariance matrix using its unbiased sample counterpart will not be neither accurate, nor reliable in the first case, and not even invertible in the second.

In this paper, three possible alternatives to the canonical damage detection approach are investigated. The first alternative focuses on decreasing the dimension of the feature vectors by employing a technique based on Discrete Cosine Transform (Sect. 10.2.1). The second approach overcomes the problem of covariance inversion by employing its pseudo-inverse (Sect. 10.2.2). The third option proposes the use of the shrinkage covariance matrix in place of the sample one (Sect. 10.2.3). In Sect. 10.3, the details of the feature extraction procedure and of the damage detection algorithm employed to obtain the results, presented in Sect. 10.4, are described. Damage detection is attempted using the acceleration time histories recorded on a four story steel frame excited by means of the shaking table available at the Carleton Laboratory of Columbia University. To mimic operational conditions variability, two undamaged conditions are considered. Damage is simulated by replacing some columns with elements of decreased cross section.

10.2 How to Handle Large-Scale Data Sets

10.2.1 Data Compression Using Discrete Cosine Transform

The objective of Principal Component Analysis (PCA) is that of projecting the original data set into a space whose basis are parallel to the principal components of the data set itself. A detailed treatment on the PCA technique is given in [3]. The principle behind PCA is that if one starts with a data set constituted of correlated features, it should be possible to decrease the dimensionality of such features by disregarding the dimensions associated with higher degree of correlation, and retaining only the ones associated with larger variance.

A popular approach to perform PCA is that of engaging into the Karhunen-Loève Transformation (KLT). Let us assume that a set of features is collected in a matrix $\mathbf{Y} = \{\mathbf{y}_1, \ldots, \mathbf{y}_n\} \in \mathbb{R}^{p \times n}$, whose i^{th} column represents the i^{th} observation of the p-dimensional feature vector $\mathbf{y}_i$. The first operation required to perform KLT is transforming the original data set $\mathbf{Y}$ into one of zero mean, $\hat{\mathbf{Y}}$. Subsequently, the covariance matrix of $\hat{\mathbf{Y}}$ may be estimated, typically through its unbiased sample estimate, $\hat{\mathbf{S}}$. The next operation requires the evaluation of the eigenvalues and eigenvectors of $\hat{\mathbf{S}}$, i.e. the definition of the matrix of eigenvectors, $\mathbf{V}$, and that of eigenvalues, $\boldsymbol{\Lambda}$, such that:

$$\mathbf{V}^{-1} \hat{\mathbf{S}} \mathbf{V} = \boldsymbol{\Lambda}, \tag{10.4}$$

where $\boldsymbol{\Lambda}$, is a diagonal matrix, whose main diagonal elements are the eigenvalues of $\hat{\mathbf{S}}$ sorted in descending order, $\mathbf{V}$ is the corresponding matrix of eigenvectors, whose columns are the eigenvectors of $\hat{\mathbf{S}}$ arranged such that the first column represents the eigenvector associated with the largest eigenvalue of $\hat{\mathbf{S}}$, while the last column is the eigenvector associated with the smallest eigenvalue of $\hat{\mathbf{S}}$. By pre-multiplying the data points in $\hat{\mathbf{Y}}$ by $\mathbf{V}^T$, the data set $\hat{\mathbf{Y}}$ is rotated into a space whose principal axes are aligned with the eigenvectors of $\hat{\mathbf{S}}$: the first axis is associated to the direction along which $\hat{\mathbf{Y}}$ has the largest variance, while the last dimension is associated with the direction along which $\hat{\mathbf{Y}}$ has the least variance. Then, by picking only the first d, $d \leq p$, elements of the rotated data set, it is possible to reduce the dimensions of the features in $\hat{\mathbf{Y}}$ to a smaller dimension, without losing much information.

KLT is optimal in decorrelating the features into the transformed domain, in compacting the most information using only few coefficients and in minimizing the mean-square error (MSE) between the reconstructed and original feature vector. An important drawback of KLT is that its basis vectors are data dependent, since the basis functions of KLT are the eigenvectors of the covariance matrix of the features population. However, the objective of this work is to investigate the case where the estimation of the covariance matrix is unreliable, due to scarcity of observations. To resolve this vicious cycle, the Discrete Cosine Transform comes into play [4]. The Discrete Cosine Transform of a data sequence $y[t]$,$t = 0, \ldots, N-1$, is given by:

$$g_y[k] = a_k \sum_{t=0}^{N-1} y[t] cos\left[\frac{(2t+1)k\pi}{2N}\right], \; k = 0, \ldots, N-1, \tag{10.5}$$

where a_k is equal to $\frac{\sqrt{2}}{N}$ for $k = 0$, and to $\frac{2}{N}$ otherwise, while $g_y(k)$ is the kth DCT coefficient. DCT shares with KLT the same characteristics of data decorrelation, energy compaction, and minimum MSE between reconstructed and original signal, but its basis vectors are data independent. In [4], it is shown how the basis vectors of the DCT provide a good approximation of the eigenvectors of a class of Toeplitz matrices, which are often used to model the data covariance matrix of some weakly stationary processes. For said reasons, one can avail of DCT to compact data dimensions. In this paper, after having evaluated the p-dimensional feature vectors, a d-point DCT is applied to each feature instance, where $d < p$.

10.2.2 Pseudo-Inverse of the Covariance Matrix

In this section, the details of the evaluation of the Monroe-Penrose pseudo-inverse , $\mathbf{S}^{\dagger}$, of a square matrix $\mathbf{S}$ of order p are briefly recalled. Pseudo-inverse computation starts by evaluating the singular value decomposition of the matrix to be inverted:

$$\mathbf{U}\mathbf{D}\mathbf{V}^T = \mathbf{S}, \tag{10.6}$$

where $\mathbf{U}, \mathbf{V} \in \mathbb{R}^{p \times p}$ are unitary matrices containing the left and right singular vectors of $\mathbf{S}$, respectively, while $\mathbf{D}$ is a diagonal matrix, whose main diagonal elements, $d_{ii}, i = 1, \ldots, p$, are the singular values associated with $\mathbf{S}$, sorted in descending order. The number of non-zero singular values is equal to the rank of the matrix. If $\mathbf{S}$ is ill-conditioned, some of its singular values are very close to zero. The rows and columns of $\mathbf{D}$ associated with the r singular values lower than a prescribed tolerance, τ, can be then deleted from $\mathbf{D}$, resulting in a new diagonal matrix $\hat{\mathbf{D}} \in \mathbb{R}^{(p-r)\times(p-r)}$ containing only non-zero singular values. In MatLab the tolerance value is set equal to $\epsilon \cdot p \cdot \max(d_{ii})$, where ϵ is the distance from 1 to the next largest double precision number, that is $\epsilon = 2^{(-52)}$ [5], and $\max(d_{ii})$ is the largest singular value. Subsequently, the last r columns of $\mathbf{V}$ and $\mathbf{U}$ are discarded, resulting in the matrices $\hat{\mathbf{V}}, \hat{\mathbf{U}} \in \mathbb{R}^{p\times(p-r)}$. Finally, the pseudo-inverse of $\mathbf{S}$ can be defined as

$$\mathbf{S}^{\dagger} = \hat{\mathbf{V}}\hat{\mathbf{D}}^{-1}\hat{\mathbf{U}}^T. \tag{10.7}$$

10.2.3 Shrinkage Covariance Matrix

Unbiased sample covariance matrix is the covariance matrix estimate most often employed for modeling the correlation properties of a features data set. However, as pointed out by Stein in [6], such estimate is reliable only as long as the number of observations is large enough, i.e. only as long as the number of observations, n, is at least one order of magnitude larger than the dimension of the single observation vector, p. If such condition is not satisfied, the sample estimate of the covariance matrix produces very poor results. In absence of enough observations, a popular approach is that of considering only the diagonal elements of the covariance matrix. As well described in [7], while the unbiased sample covariance matrix has zero bias, i.e. its expected value is prescribed to be equal to the value of the population covariance matrix, $\mathbf{\Sigma}$, the diagonal covariance matrix has minimum variance, but large bias. The shrinkage estimation of the covariance matrix allows for constructing a covariance matrix that shares the advantages of both models. Denoting as $\mathbf{S}$ the unbiased sample covariance matrix, and as $\mathbf{T}$ the diagonal covariance matrix, the shrinkage estimate of the covariance matrix is given by:

$$\mathbf{S}^{*} = \lambda\mathbf{T} + (1-\lambda)\mathbf{S}, \tag{10.8}$$

where λ is known as the *shrinkage coefficient*. Ledoit and Wolf [8] were the first to propose an analytical formula for the estimation of the shrinkage coefficient:

$$\lambda = \frac{\sum_{i=1}^{p}\sum_{j=1}^{p}\left[\mathrm{Var}(S_{ij}) - \mathrm{Cov}(S_{ij}, T_{ij})\right]}{\sum_{i=1}^{p}\sum_{j=1}^{p}(S_{ij} - T_{ij})^2}. \tag{10.9}$$

Adoption of Eq. (10.9) to estimate the shrinkage coefficient leads to the minimization of the mean square error between $\mathbf{S}^*$ and $\boldsymbol{\Sigma}$. Since $\mathbf{S}^*$ is given by the addition of an invertible matrix with a square matrix, the shrinkage estimate of the covariance matrix is invertible and can be then used in place of the unbiased sample estimate of $\boldsymbol{\Sigma}$.

10.3 Feature Extraction and Damage Detection Algorithm

In this section, the procedure to extract the damage sensitive feature, as well as the steps involved in the damage detection algorithm are described. For a more detailed treatment of the feature extraction procedure the reader is referred to [9].

The damage sensitive feature used in this work is a modified version of the Mel-Frequency Cepstral Coefficients. The use of such feature is novel in the field of civil engineering, but it is customary in the field of speaker and speech recognition [10]. The extraction of such features begins by segmenting the time history in pieces, called *frames*, short enough to be considered stationary. Non rectangular windows are then applied to each frame, in order to get rid of undesirable effects at the onset and offset of the frame spectra. The power spectrum of each frame is then evaluated and warped into a frequency scale given by:

$$f_{warping} = f_c \log_2\left(1 + \frac{f}{f_c}\right) \tag{10.10}$$

where $f_{warping}$ is the value of the frequency in the warped scale associated to the value f of the linear frequency scale, while f_c is a user-defined cutoff frequency representing the boundary of the major power content in the system spectrum. The relation between $f_{warping}$ and f is linear up to f_c, and becomes logarithmic after such value. Frequency warping is obtained by grouping together the spectrum values into M critical bands, and weighting each cluster by a triangular filter. The series of M triangular filters has centers equally spaced on the $f_{warping}$ scale. In this work, the value of M is set equal to the entire part of $3\log(f_s)$, as suggested in [11], where f_s is the value of the sampling rate in Hz. In particular, since all time histories used in this work are sampled at 400 Hz, 15 filters have been used to define the feature vectors. Figure 10.1 represents the spectrum obtained averaging all time histories recorded for the undamaged scenario 1 described in Sect. 10.4 from which the selection of f_c is made available, and the corresponding triangular filters. Finally, the logarithm of each warped spectrum is evaluated and the real part of an M-point inverse Fourier Transform is computed via inverse Discrete Cosine Transform. The first coefficient is then discarded, as it has been demonstrated that such coefficient is very sensitive to external factors effects, as well as input effects. Let us denote as ℓ the number of frames in which a time history is segmented, at the end of this process, ℓ $(M-1)$-dimensional vectors are extracted: the average of such vectors is evaluated leading to a single vector consisting of $(M-1)$ elements. Let us now assume that s sensors are available: in this work, a data set is defined as the ensemble of s time histories recorded from each available sensor during a single measurement campaign. From each of the s response time histories, an $(M-1)$-point long feature vector is extracted and stacked with the other $(s-1)$ vectors, so that each data set is represented by a feature vector $\mathbf{y} \in \mathbb{R}^{s\cdot(M-1)\times 1}$. From now on, for the sake of notation brevity and consistency with the previous treatments, the dimension of a feature vector extracted from a data set will be denoted as p, i.e. p is equal to $s \cdot (M-1)$.

Let us refer to n_{tr} as the number of data sets available for training. At the end of the feature extraction procedure, if the technique described in Sect. 10.2.1 is engaged, each of the n_{tr} feature vectors is transformed into a d elements vector by means of DCT, where d is either equal to $\frac{3p}{4}$ if $p \leq n_{tr}$, or to $\frac{3n_{tr}}{4}$ otherwise.

For the methods described in Sects. 10.2.1 and 10.2.2, the training model is constructed evaluating the sample mean $\mathbf{m}_{tr}$:

$$\mathbf{m}_{tr} = \frac{1}{n_{tr}}\sum_{i=1}^{n_{tr}}\mathbf{y}^{(i)} \tag{10.11}$$

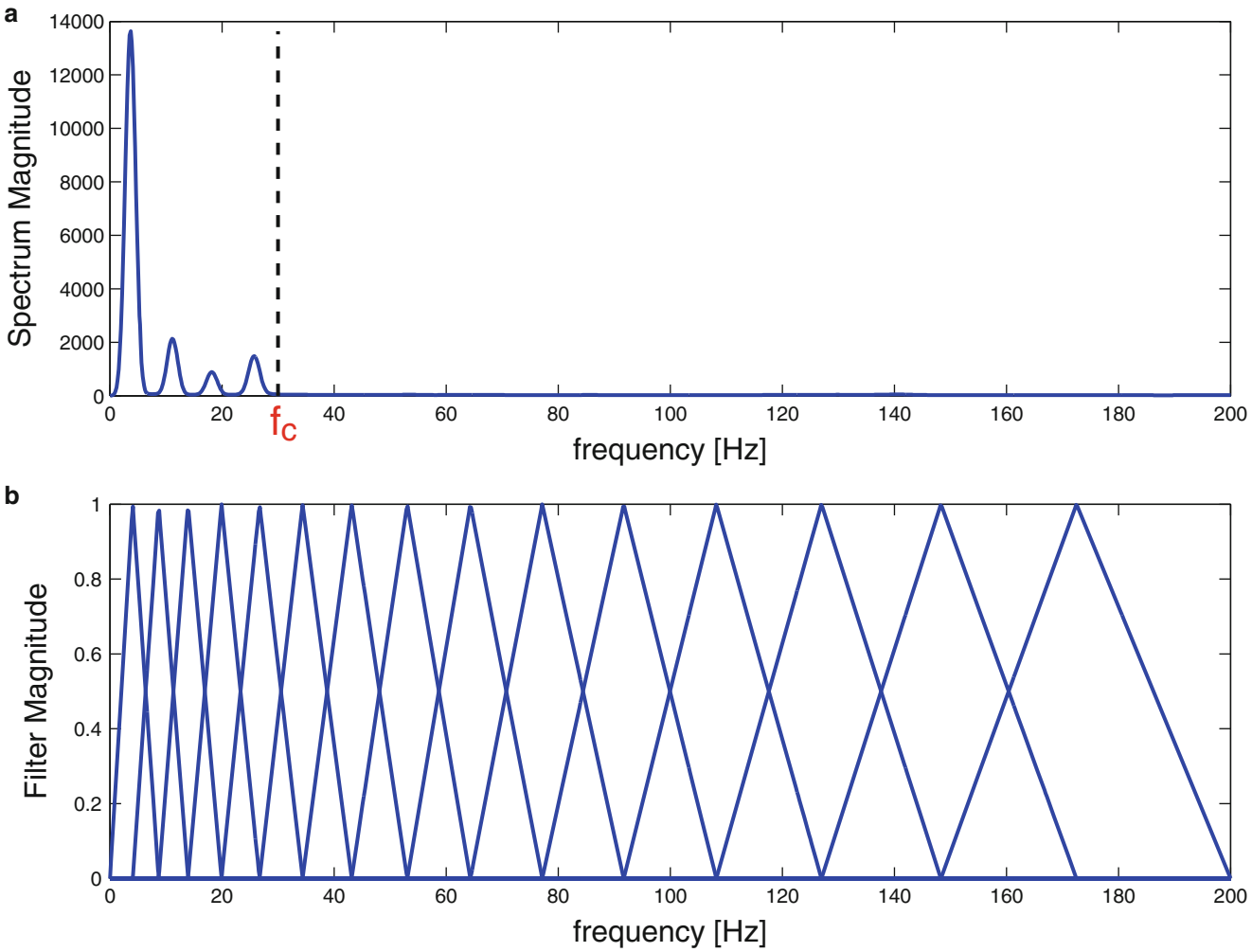

Fig. 10.1 Warping procedure: (**a**) cutoff frequency selection, (**b**) triangular filters

and the unbiased sample covariance matrix $\mathbf{S}_{tr}$:

$$\mathbf{S}_{tr} = \frac{1}{n_{tr}-1}\sum_{i=1}^{n_{tr}} \left(\mathbf{y}^{(i)} - \mathbf{m}_{tr}\right)\left(\mathbf{y}^{(i)} - \mathbf{m}_{tr}\right)^T \tag{10.12}$$

where $\mathbf{y}^{(i)}$ represents the realization of the feature vector extracted from the i^{th} training data set. If the technique described in Sect. 10.2.3 is engaged, the shrinkage estimate of the covariance matrix, $\mathbf{S}^*$, is evaluated in place of $\mathbf{S}$.

The threshold can then be defined. Since the paucity of observations makes the assumption of normally distributed features difficult to be satisfied, a resampling technique is employed to set the boundary between damaged and undamaged. As mentioned, the departure of the testing feature from the training model is analyzed by means of Mahalanobis Squared Distance. The MSD of the i^{th} training feature vector from a population, obtained from the training population from which the i^{th} realization is left out, is computed. The resulting n_{tr} values are sorted in ascending order, and the value exceeded by only the 5% of instances is picked as threshold value, γ.

Finally, let us denote as n_{te} the number of data sets available for testing. From each available data set, a p-dimensional feature vector is extracted. If feature dimension reduction is required, a d-point DCT of each testing feature vector realization is performed, where d has the same values considered for training. If more than one data set is available, the mean of the available testing vectors, $\mathbf{m}_{te}$, is computed. If n_{te} is equal to 1, as the case for short-time applications, and for the examples considered in this work, $\mathbf{m}_{te}$ is simply the single p-dimensional vector extracted from the only available data set. The structure can be then declared damaged if

$$D(\mathbf{m}_{te}) = (\mathbf{m}_{te} - \mathbf{m}_{tr})^T \mathbf{S}_{tr}^{-1} (\mathbf{m}_{te} - \mathbf{m}_{tr}) > \gamma. \tag{10.13}$$

where $\mathbf{S}_{tr}^{-1}$ is replaced either by the pseudo-inverse of $\mathbf{S}_{tr}$, $\mathbf{S}_{tr}^{\dagger}$, in case the second method is employed, or by the inverse of the shrinkage estimate of the covariance matrix, $(\mathbf{S}_{tr}^{*})^{-1}$, if the third approach is considered.

10.4 Results

The structure used to compare the performance of the three proposed approaches is a four-story A36 steel frame with an inter-story of 533 mm and floor plate dimensions of 610×457×12.7 mm. The floors are braced diagonally in only one direction, hereafter denoted as strong direction. The structure was excited along the weak direction of bending by means of a medium-scale uniaxial hydraulic shake table. All structural connections are bolted. In addition to said reference configuration, denoted as **U1** in the following, an additional undamaged scenario (**U2**) was considered in order to simulate operational variability. The second undamaged condition is simulated by adding two masses at the third floor between columns A and B, on both edges C and D. The first damage scenario (**D1**) was simulated by replacing the column elements on side A of the third inter-story with elements with a cross-section reduced to $\frac{3}{4}$ of the original, while the second damage scenario (**D2**) was modeled by replacing all the column elements of the third inter-story by elements of reduced cross-section.

The structure was instrumented with 8 piezo-electric accelerometers located as displayed in Fig. 10.2, measuring accelerations along the weak direction. The sensor setup is such that also torsional effects may be captured. In fact, preliminary studies have shown that the structure is not of ideal shear-type kind, but torsional modes in the strong direction of bending may be identified, even when the load is applied along the weak direction. Four ground acceleration time histories recorded during El Centro (1940), Hachinohe (1983), Northridge (1994) and Kobe (1995) earthquakes, in addition to the acceleration time history obtained from the design spectrum of EC8 were applied as inputs. To ensure that the structure was excited by the proper range of the time histories power spectra, a time scale of $\frac{1}{\sqrt{3}}$ was introduced and, to prevent yielding and additional unexpected damage, the input time histories were properly scaled in magnitude. Inputs and outputs were sampled at 400 Hz.

The training set is constituted by 50 data sets: for each of the two undamaged scenarios, 5 experiments for each of the five inputs are considered. The testing set is constituted by 40 data sets, 10 for the undamaged scenarios (5 for each condition), and 15 for each of the two damaged conditions. Each testing data set is used individually, so that 40 tests are performed. Five different sensor setups are simulated, using only the response of some instruments. In the following, the five sensor setups are denoted as **S1**, **S2**, etc.: **S1**) all sensors, **S2**) sensors 1, 2, 3, 4, **S3**) sensors 1, 3, 5, 7, **S4**) sensors 1, 4, 7, and **S5**) mid-span floor accelerations. The data set of the last sensor setup is obtained by adding the acceleration response time history recorded by the sensor on edge C with the one recorded by the sensor on edge D and dividing by 2, at each floor: for example, the first mid-span acceleration is evaluated by averaging the time histories recorded by sensors 1 and 8.

The results are presented in Table 10.1. In Table 10.1, the error for the individual condition identification, as well as the overall Type I and Type II errors, are shown. Type I error occurs when a healthy condition is labeled as damaged, while Type II error occurs when a damaged condition is classified as undamaged. The three approaches presented in Sects. 10.2.1, 10.2.2 and 10.2.3 are labeled as ***Method 1***, ***Method 2*** and ***Method 3***, respectively. In Table 10.1, under each sensor setup label, the reduced dimension d of the feature vector, its original dimension p and the value of the shrinkage coefficient λ are also presented.

While the first method results in better outcomes for what concerns Type I error, methods 2 and 3 perform generally better than the first in detecting damage. Firstly, the high Type I error rate observed for some sensor setups for Method 2 is worth of a comment. For each undamaged scenario, only 5 tests are performed: it is sufficient that only one instance be incorrectly classified as damaged, for that state to be characterized by 20% error. Therefore, even though Method 2 gives certainly the worst results in terms of Type I error, probably the error rate would decrease if more test data sets were available. On the other hand, the high Type II error rate observed for the first method for the first three sensor setups is due to a too high threshold value, as shown from Fig. 10.3. The explanation of this behavior is clarified analyzing the results of Method 4, where, in an attempt to combine the advantages of the three approaches, the three techniques are used together. This combination is pursued by extracting the damage sensitive features as described in Sect. 10.3, applying the DCT-based feature dimension reduction, by then modeling the training covariance matrix via shrinkage estimation, and, finally, by evaluating the squared Mahalanobis distance using the pseudo-inverse of the shrunk covariance matrix. As expected, the results improve dramatically and clarify that the model of the covariance matrix used in the first method is not reliable enough to be inverted and delivering accurate squared Mahalanobis distance. In fact, the inaccuracy of the sample covariance matrix estimate of the features used in the first method is directly related to the value of the threshold, as its inverse is evaluated to define such value. Indeed, that a well conditioned covariance matrix estimate can deliver accurate results is confirmed

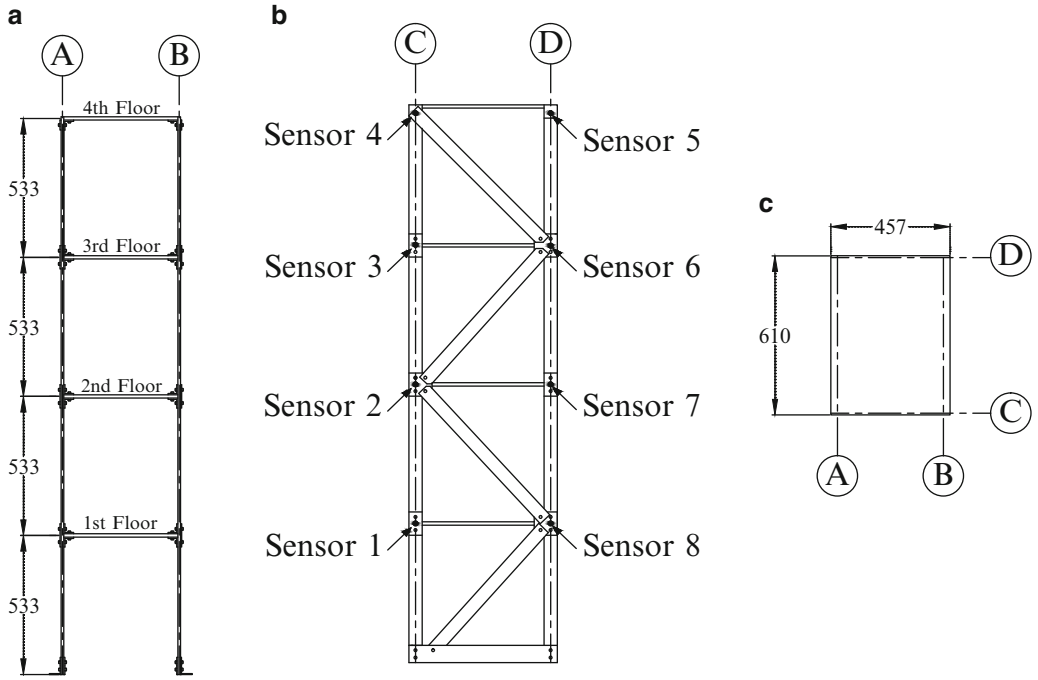

Fig. 10.2 Sensors location

Table 10.1 Results

Sensor Setup	State	*Method 1*	*Method 2*	*Method 3*	*Method 4*
S1:	**U1**	0.00%	0.00%	0.00%	0.00%
$d = 40$	**U2**	0.00%	0.00%	0.00%	0.00%
$p = 120$	**Type 1**	**0.00%**	**0.00%**	**0.00%**	**0.00%**
$\lambda = 0.0164$	**D1**	40.00%	0.00%	0.00%	0.00%
	D2	0.00%	0.00%	0.00%	0.00%
	Type II	**20.00%**	**0.00%**	**0.00%**	**0.00%**
S2:	**U1**	0.00%	0.00%	0.00%	0.00%
$d = 40$	**U2**	0.00%	0.00%	0.00%	0.00%
$p = 60$	**Type 1**	**0.00%**	**0.00%**	**0.00%**	**0.00%**
$\lambda = 0.0163$	**D1**	40.00%	0.00%	0.00%	0.00%
	D2	0.00%	0.00%	0.00%	0.00%
	Type II	**20.00%**	**0.00%**	**0.00%**	**0.00%**
S3:	**U1**	0.00%	20.00%	0.00%	0.00%
$d = 40$	**U2**	0.00%	20.00%	0.00%	0.00%
$p = 60$	**Type 1**	**0.00%**	**20.00%**	**0.00%**	**0.00%**
$\lambda = 0.0165$	**D1**	13.33%	0.00%	0.00%	0.00%
	D2	0.00%	0.00%	0.00%	0.00%
	Type II	**6.67%**	**0.00%**	**0.00%**	**0.00%**
S4:	**U1**	0.00%	0.00%	0.00%	0.00%
$d = 45$	**U2**	0.00%	20.00%	0.00%	0.00%
$p = 36$	**Type 1**	**0.00%**	**10.00%**	**0.00%**	**0.00%**
$\lambda = 0.0169$	**D1**	0.00%	0.00%	0.00%	0.00%
	D2	0.00%	0.00%	0.00%	0.00%
	Type II	**0.00%**	**0.00%**	**0.00%**	**0.00%**
S5:	**U1**	0.00%	0.00%	20.00%	0.00%
$d = 40$	**U2**	0.00%	20.00%	0.00%	0.00%
$p = 60$	**Type 1**	**0.00%**	**10.00%**	**10.00%**	**0.00%**
$\lambda = 0.0168$	**D1**	0.00%	0.00%	0.00%	0.00%
	D2	0.00%	0.00%	0.00%	0.00%
	Type II	**0.00%**	**0.00%**	**0.00%**	**0.00%**

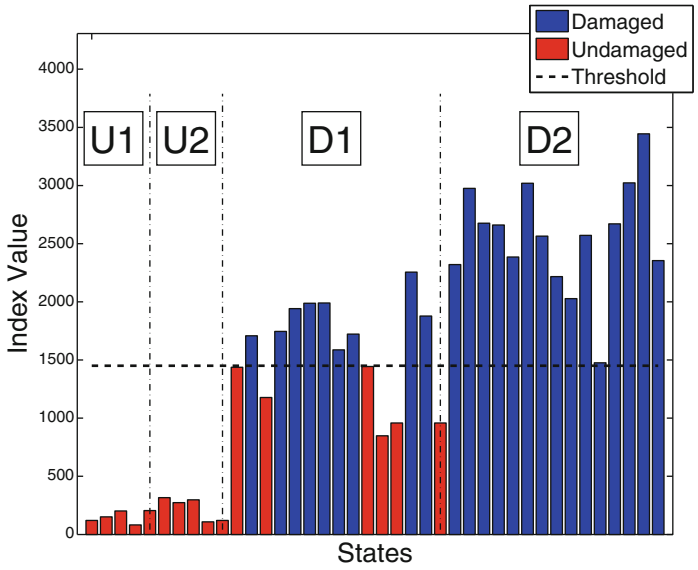

Fig. 10.3 Results for Method 1, Sensor Setup 1

also by analyzing the results of Method 3, where the feature dimensions are not reduced, but the shrinkage estimate of the covariance matrix is used. It is also noteworthy that the shrinkage coefficient is very small (the values of λ oscillate between 0.0163 and 0.0169), so that the correction imposed to the sample covariance matrix is minimal.

10.5 Conclusions

Three alternatives have been proposed to deal with the problem of paucity of data to solve the structural damage detection assignment, namely reduction of feature dimensionality via discrete cosine transform, inversion of the unbiased sample covariance matrix via pseudo-inverse, and use of the shrinkage estimate in place of the more common sample estimate of the covariance matrix. Used by itself, each approach has its own advantages and disadvantages. Mainly, it has been observed that while reducing the feature dimension to the principal components allows to decrease the Type I error rate, to the detriment of Type II error, operating on the stability of the inverse of the covariance matrix estimate aids decreasing false acceptance error, leading, however, to an increase of false alarm error rate. Nonetheless, it has been shown that the advantages of all methods may be combined by using all alternatives together.

Acknowledgements The authors would like to acknowledge the other members of the Shake Table Facility Group, namely, the manager of the Carleton Laboratory Adrian Brügger, Prof. Andrew Smyth, Dr. Manolis Chatzis and Suparno Mukhopadhyay, for the collaboration during the experimental phase of the work. The authors would also like to acknowledge the support from the Center for Advanced Infrastructure and Transportation (CAIT), Rutgers, the State University of New Jersey, Award No. Rutgers S1760924.

References

1. Worden K, Manson G, Fieller NRJ (2000) Damage detection using outlier analysis. J Sound Vib 229(3):647–667
2. Cross EJ, Manson G, Worden K, Pierce SG (2012) Features for damage detection with insensitivity to environmental and operational variations. Proc Roy Soc A Math Phys Eng Sci 468(2148):4098–4122
3. Joliffe I (2002) Principal component analysis, 2nd edn. Springer, New York
4. Ahmed N, Natarajan T, Rao KR (1974) Discrete cosine transform. IEEE Trans Comput 23:P90–93
5. MATLAB 7.9 (R2009b) The MathWorks, Inc., Natick, MA, United States, 2009
6. Stein C (1956) Inadmissibility of the usual estimator for the mean of a multivariate distribution. Proceedings of the third Berkeley symposium on mathematics, statistics and probability, vol 1. University of California Press, Berkeley, p 197–206
7. Schäfer J, Strimmer K (2005) A shrinkage approach to large-scale covariance matrix estimatimation and implications for functional genomics. Stat Appl Genet Mol Biol 4(1):1–30
8. Ledoit O, Wolf M (2003) Improved estimation of the covariance matrix of stock returns with an application to portfolio selection. J Empir Finance 10:603–621

9. Balsamo L, Betti R, Beigi H (2013) Structural damage detection using speaker recognition techniques. In: Proceedings of the 11th international conference on structural safety and reliability (ICOSSAR), Columbia University, New York, NY, USA, June 16–20, 2013
10. Beigi H (2011) Fundamentals of speaker recognition. Springer, New York
11. Fraile R, Sáenz-Lechón N, Godino-Llorente J, Osma-Ruiz V, Gómez-Vilda P (2008) Use of mel-frequency cepstral coefficients for automatic pathology detection on sustained vowel phonations: mathematical and statistical justification. In: Proc. 4th international symposium on image/video communications over fixed and mobile networks, Bilbao, Brazil, July, 2008

Chapter 11
Load Identification of Offshore Platform for Fatigue Life Estimation

Nevena Perišić, Poul Henning Kirkegaard, and Ulf T. Tygesen

Abstract The lifetime of an offshore platform is typically governed by accumulated fatigue damage. Thus, the load time history is an essential parameter for prediction of the lifetime of the structure and its components. Consequently, monitoring of structural loads is of special importance in relation to re-assessment of offshore platforms. Structural monitoring systems (SMS's) on offshore structures typically consist of a set of sensors such as strain gauges, accelerometers, wave radars and GPS's, however direct measuring of the actual loading is usually not feasible. One approach is to measure the loads indirectly by monitoring of the available dynamic responses of the structure. This work investigates the possibility for using an economically beneficial, model-based load estimation algorithm for indirect measuring of the loading forces acting on the offshore structure. The algorithm is based on the reduced order model of the structure and the discrete Kalman filter which recursively estimates unknown states of the system in real time. As a test-case, the algorithm is designed to estimate the equivalent total loading forces of the structure. The loads are estimated from noised displacement measurements of a single location on the topside of the offshore structure. The method is validated using simulated data for two wave loading cases: regular and irregular wave loadings.

Keywords Load identification • Kalman filter • Offshore oil platforms • State-space model • Structural monitoring systems

11.1 Introduction

Structural monitoring systems (SMS's) of offshore structures usually consist of a set of sensors, such as strain gauges, accelerometers, wave radars and GPS's. However direct measuring of the actual loading is usually not feasible as it would require a high number of sensors, if possible at all. Consequently the loading forces need to be extracted indirectly. Knowledge of the actual loading on the structure is crucial for: prediction of the remaining lifetime and lifetime extension [1], component design validation and application of the advanced control algorithms in case of the need for accumulated fatigue monitoring. The fatigue loads have direct influence on the lifetime of the structure, where as extreme loads can cause instantaneous failures. Sometimes, monitoring of response characteristics can also be used as part of a warning system to provide alerts even before damages are developed which is very important for improving structure performance and increasing reliability.

Dynamic load estimation is a well-known problem, which represents a specific type of an inverse identification problem. The main challenge with the inverse problem is that it is "ill-posed" [2] in mathematical sense thus existence, stability and uniqueness of its solution are violated. Methods that are solving the problem of load estimation are based on the idea to transfer the ill-posed problem into a well-posed one. Based on the type of the system model, they can be divided in three main categories [3]:

N. Perišić (✉) • U.T. Tygesen
Ramboll Oil & Gas, Willemoesgade 2, Esbjerg 6700, Denmark
e-mail: nepe@ramboll.com; utt@ramboll.com

P.H. Kirkegaard
Department of Civil Engineering, Aalborg University, Sohngaardsholsvej 57, Aalborg, 9000, Denmark
e-mail: phk@civil.aau.dk

A. Wicks (ed.), *Structural Health Monitoring, Volume 5: Proceedings of the 32nd IMAC, A Conference and Exposition on Structural Dynamics, 2014*, Conference Proceedings of the Society for Experimental Mechanics Series, DOI 10.1007/978-3-319-04570-2_11,

1. **Deterministic methods**: Majority of the available load estimation algorithms belong to this group [4]. These methods are based on the deterministic dependencies between data, and their results depend strongly on the accuracy of the identified inverse model. The solutions can be find in the time [5, 6] or frequency domains [7–12].
2. **Stochastic methods**: This group of methods is based on statistical, i.e. stochastic models between the input and the output data [13–15]. Thus, these methods require the measurements of the input and the output data from the real, operational systems in order to identify stochastic models of the systems. However, for some systems is not possible to measure input at all.
3. **Artificial intelligence methods**: This group of methods includes use of the artificial neural networks [16], the evolutionary algorithms [17] and the fuzzy logic's [18] for load identification. The artificial intelligence methods are used when there is not enough physical knowledge about the structure or when the model is very complex so it cannot be processed in the real time. These methods assume that the model of the system is a black-box, so they require a learning process in order to determine the relations between the inputs and the outputs.

Lately, the focus of the research has been shifted towards combined deterministic-stochastic methods. These methods are based on the Kalman filter [19] and their origins are in the control theory. They are spread from the completely deterministic to those where the stochastic noise is assumed to be present in all measurements and states of the system. The Kalman filter is an optimal, recursive, computationally efficient, state-estimation algorithm. It requires storing only the previous estimation and it is very efficient in handling the measurement and process noise in real time. One of the first applications of the Kalman filters to the problem of the input-estimation are presented in [20–23]. The method consists of two stages. In the first stage, the Kalman filter estimates states of the system assuming that the input force is not available. In the next stage, a recursive least-square estimator provides estimation of the unknown loading force. In [24] an improved and changed method for the load reconstruction is presented. The new algorithm is simplified and it is based on estimation of all unknown signals using only the first stage of the previously described method, i.e. the Kalman filter.

In a recent work [25], an augmented Kalman filter was used for direct estimation of the unknown loading force. The state of the system is augmented with the unknown load, and its dynamic evolution is assumed known, i.e. as a tuning factor. The augmented Kalman filter is tested on simulated data, and in a laboratory experiment on an instrumented steel beam. The augmented Kalman filter was also used for the wind turbine load estimation in [26, 27] for the online estimation of the drive-train shaft torque and the tower root bending moment from the standard turbine measurements. The limitation of the augmented Kalman filter approach is that it is suitable for load identification in static environment, i.e. where the structure operates in one operating regime. In [27] the method is expanded to allow for more dynamic environment and changes of the operating points by applying the multi-model estimation algorithm.

Problem statement and the scope of the work: This work investigates a possibility of using the augmented Kalman filter for the load estimation on offshore platform structure. The presented method is model-based and it transforms a FE model of the structure into the state-space form, where all unknown signals are collected in the state vector and further estimated recursively using the Kalman filter. How well the distribution of the structural loads acting on the structure can be estimated depends on the complexity of the used model, and its observability. The Kalman filter approach assumes that stochastic noise is present in all measurements of the system and it accounts for model uncertainties.

A test-case for estimation of the total equivalent loading force on the platform from f displacement measurements for a single node and simple two-degree-of-freedom (2DOF) model of the structure is presented. The total equivalent loading force is for simplicity in the present study defined as the point force acting on the topside of the offshore oil and gas platform, which results in the measured displacements, i.e. the estimated loading force is equivalent to the effect from the wave loading. As a consequence of trying to represent all of the frequencies observed in the simulated displacement signal by a 2DOF system, the estimated equivalent loading force also includes some unwanted higher structural modes. From the estimated equivalent loading force, it is straightforward to calculate e.g. the total overturning moment acting on the structure at the soil level. Additionally, the estimated signals will be post-processed by using low-pass filter, in order to validate their accuracy in the wave loading frequency range. All data used in this work are simulated data and the measurement noise is artificially added in order to account for measurement uncertainties.

11.2 Load Identification Algorithm

The proposed load identification algorithm consists of the following steps that should be iterated until sufficient accuracy of the estimated signal is reached:

1. **System modeling:** Specify and identify a state-space model of the system that includes all relevant dynamics. Start with the simplest possible, and if necessary increase complexity.
2. **Design of the load model observer:** Design a linear or nonlinear of the model state estimator for recursive estimation of the state vector of the model identified in the previous step.
3. **Parameter tuning and algorithm validation:** Tune the parameters of the estimator by using simulated or measured data. Compare the estimated signal with the referent signal if available.

11.2.1 State-Space Model of the Reduced Order System

Usually, the responses of structures exposed to wind or wave dynamic loading are driven by the first few fundamental modes so reduced order, linear models can be used. For the estimation of the total equivalent loading forces acting on the offshore platform, the simplest possible model consists of the first north-south (N-S) and the first east-west (E-W) fundamental modes, thus it can be represented by a linear two degrees-of-freedom model (2DOF). In this way, only translation is considered where it is assumed that rotational motion is not present. Also, in this work it is assumed that elevation is negligible and that motions in N-S and E-W directions are independent and uncoupled, thus they can be approached independently. These assumptions are valid for the simulated data, where in practice potential coupling need to be checked. 2DOF model is given by:

$$\ddot{\mathbf{q}}(t) + 2\xi_n \mathbf{w}_n \dot{\mathbf{q}}(t) + \mathbf{w}_n^2 \mathbf{q}(t) = \mathbf{F}(t)\mathbf{m}^{-1} \tag{11.1}$$

where $\mathbf{m}$ is the equivalent mass matrix and $\mathbf{F}(t)$ corresponds to the total equivalent loading force applied to the top point of the structure, which would have the equivalent effect on the platform as wind and wave loading forces acting on the whole structure. The displacement vector $\mathbf{q}(t)$, the natural frequencies vector $\mathbf{w}_n(t)$, the damping ratio vector $\xi(t)$ and driving force vector $\mathbf{F}(t)$ are given by:

$$\mathbf{q}(t) = \begin{bmatrix} x(t) \\ y(t) \end{bmatrix}, \mathbf{w}_n = \begin{bmatrix} w_{n,x} & 0 \\ 0 & w_{n,y} \end{bmatrix}, \xi_n = \begin{bmatrix} \xi_x & 0 \\ 0 & \xi_y \end{bmatrix}, \mathbf{F}(t) = \begin{bmatrix} F_x(t) \\ F_y(t) \end{bmatrix}, \mathbf{m} = \begin{bmatrix} m_x & 0 \\ 0 & m_y \end{bmatrix} \tag{11.2}$$

By defining the displacement and the velocity of the platform tower top as states of the system, Eq. (11.1) can be represented in a state-space form as follows:

$$\underbrace{\begin{bmatrix} \dot{x}(t) \\ \dot{y}(t) \\ \ddot{x}(t) \\ \ddot{y}(t) \end{bmatrix}}_{\dot{\mathbf{X}}(t)} = \underbrace{\begin{bmatrix} 0 & 0 & 1 & 0 \\ 0 & 0 & 0 & 1 \\ -w_{n,x}^2 & 0 & -2\xi_x w_{n,x} & 0 \\ 0 & -w_{n,y}^2 & 0 & -2\xi_y w_{n,y} \end{bmatrix}}_{\mathbf{A}_c} \underbrace{\begin{bmatrix} x(t) \\ y(t) \\ \dot{x}(t) \\ \dot{y}(t) \end{bmatrix}}_{\mathbf{X}(t)} + \underbrace{\begin{bmatrix} 0 & 0 \\ 0 & 0 \\ m_x^{-1} & 0 \\ 0 & m_y^{-1} \end{bmatrix}}_{\mathbf{B}_c} \underbrace{\begin{bmatrix} F_x(t) \\ F_y(t) \end{bmatrix}}_{\mathbf{U}(t)} \tag{11.3}$$

The measurements assumed available are positions, thus the measurement equation is specified by:

$$\underbrace{\begin{bmatrix} Y_1(t) \\ Y_2(t) \end{bmatrix}}_{\mathbf{Y}(t)} = \underbrace{\begin{bmatrix} 1 & 0 & 0 & 0 \\ 0 & 1 & 0 & 0 \end{bmatrix}}_{\mathbf{C}_c} \underbrace{\begin{bmatrix} x(t) \\ y(t) \\ \dot{x}(t) \\ \dot{y}(t) \end{bmatrix}}_{\mathbf{X}(t)} \tag{11.4}$$

In practice, the measurements of the system are obtained at discrete time intervals. Thus, it is more feasible to use a model of the system that directly maps discrete input to discrete output data sets. Such a discrete-time model can be obtained from the continuous-time model by performing discretisation and it is determined by the sampling time T_s. The discrete-time model has the following form:

$$\mathbf{X}_k = \mathbf{A}_d \mathbf{X}_{k-1} + \mathbf{B}_d \mathbf{U}_{k-1} \tag{11.5}$$

$$\mathbf{Y}_k = \mathbf{C}_d \mathbf{X}_{k-1} \tag{11.6}$$

The system matrices in the discrete time are defined by:

$$\mathbf{A}_d = e^{\mathbf{A}_c T_s}, \mathbf{B}_d = \mathbf{A}\left[\mathbf{I} - e^{-\mathbf{A}_c T_s}\right]\mathbf{A}_c^{-1}\mathbf{B}_c, \mathbf{C}_d = \mathbf{C}_c \tag{11.7}$$

The state-space model in a discrete-time defined by Eqs. (11.5) and (11.6) represents deterministic model of the system. In order to account for uncertainties, unknown process and measurement noises are included in the model:

$$\mathbf{X}_k = \mathbf{A}_d\mathbf{X}_{k-1} + \mathbf{B}_d\mathbf{U}_{k-1} + \mathbf{W}_{k-1} \tag{11.8}$$

$$\mathbf{Y}_k = \mathbf{C}_d\mathbf{X}_{k-1} + \mathbf{V}_{k-1} \tag{11.9}$$

where $\mathbf{W}_k$ and $\mathbf{V}_k$ are the stationary, stochastic system and measurement noise vectors with appropriate dimensions. For the sake of clarity, it is assumed that they are zero mean with covariance matrices $\mathbf{Q}$ and $\mathbf{R}$ respectively. In the case that noise is not zero mean, it is possible to transform the colored noise to the white noise [28], hence use the same approach as described in the following. In order later to allow the state estimator to identify the unknown input signals, the state vector is augmented as follows:

$$\mathbf{X}_k^A = \begin{bmatrix} \mathbf{X}_k \\ F_{x,k} \\ F_{y,k} \end{bmatrix} \tag{11.10}$$

It is assumed that the unknown input vectors can be represented as the outputs of the first order dynamic systems in discrete time:

$$F_{x,k} = \alpha_x F_{x,k-1} + \Psi_{x,k-1} \tag{11.11}$$

$$F_{y,k} = \alpha_y F_{y,k-1} + \Psi_{y,k-1} \tag{11.12}$$

The covariances of the Ψ_x and Ψ_y are S_x and S_y. S_x, S_y, α_x and α_y represent tuning parameters that should be experimentally determined for a specific problem and they are part of the augmenter process noise covariance matrix:

$$\mathbf{Q}^A = \begin{bmatrix} \mathbf{Q} & \mathbf{0} \\ \mathbf{0} & \mathbf{S} \end{bmatrix}, \mathbf{S} = \begin{bmatrix} S_x & 0 \\ 0 & S_y \end{bmatrix} \tag{11.13}$$

The augmented system matrices are consequently:

$$\mathbf{A} = \begin{bmatrix} \mathbf{A}_d & \mathbf{B}_d \\ \mathbf{0} & \mathbf{D} \end{bmatrix}, \mathbf{C} = \begin{bmatrix} \mathbf{C}_d & \mathbf{0} \end{bmatrix} \tag{11.14}$$

where $\mathbf{0}$ is (2 x 2) zero matrix and $\mathbf{D}$ is (2 x 2) diagonal matrix where elements on diagonal are α_x and α_y, selected to be 1 in this work. The system matrices $\mathbf{A}_d$, $\mathbf{B}_d$ and $\mathbf{C}_d$ are defined by the first natural frequencies, the damping ratios and the sampling time. Modal parameters are identified from the dynamic responses of the structure and the sampling ratio corresponds to the measurement sampling ratio, thus completely defining the grey-box reduced order model of the system. Thus, the augmented state-space model in discrete-time is:

$$\mathbf{X}_k^A = \mathbf{A}\mathbf{X}_{k-1}^A + \mathbf{W}_{k-1}^A \tag{11.15}$$

$$\mathbf{Y}_k = \mathbf{C}\mathbf{X}_{k-1}^A + \mathbf{V}_{k-1} \tag{11.16}$$

11.2.2 Load Estimation Algorithm

In order to estimate unknown values of the augmented vector, Eqs. (11.15) and (11.16), the Kalman filter [19] is used as an optimal, linear state estimator. The idea is to estimate states of the system by using recursive algorithm. The structure of the Kalman filter is given in Fig. 11.1, [29], where K_k represents the Kalman gain calculated at time instant k. One way to describe the Kalman filter is as a filter that whitens the measurements and extract the maximal information from them. The Kalman filter is the optimal filtering solution for the discrete-time filtering model, when the dynamic and measurements

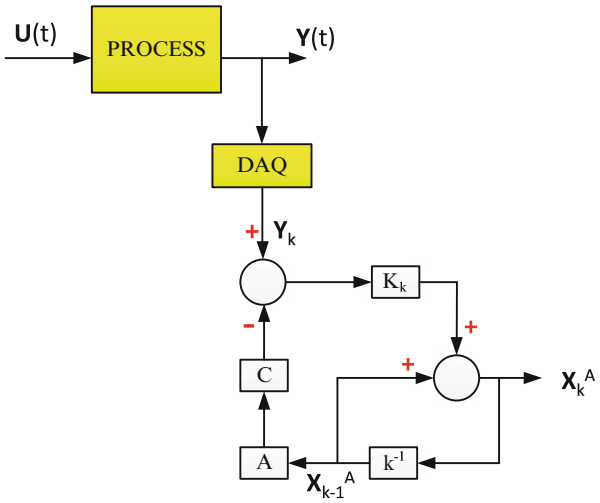

Fig. 11.1 Structure of the Kalman filter in parallel with the real process

models are linear Gaussian, uncorrelated, unbiased and independent white noises. If they are uncorrelated, unbiased and independent white noises but not Gaussian, the Kalman filter represents the best linear filter. The filter is optimal in a sense that the Kalman gain K_k is calculated so that it minimizes a weighted 2-norm of the expected value of the estimation error $\mathbf{e} = \mathbf{Y} - \hat{\mathbf{Y}} = \mathbf{Y} - \mathbf{CX}$.

The complete procedure for deriving the Kalman filter equations can be found in [29]. The tuning parameters of the Kalman filter are covariance matrices of the measurement and process noises. By increasing the covariance of the process noise, more emphasis is given to the measurements where by increasing the covariance of the measurement noise, more confidence is placed on the model than on the measurements.

11.3 Results

11.3.1 Simulation Setup

In order to generate simulated data for testing of the load estimation algorithm, the RAMBOLL Offshore Structure Analysis Program package, ROSAP is used. The ROSAP package is a finite element program for static, dynamic and non-linear analysis of frame and truss structures for wind and wave load conditions. The Valdemar offshore platform is a tripod platform, installed in 2006 in the Danish North Sea 250 km west of Denmark. The platform is designed as a Not-Normally-Manned Platform (NNMP). The operator of the platform is Maersk Oil. Ramboll Oil & Gas (ROG) is the engineering consultant preparing technical specification for the SMS, data post-processing, analysis and documentation. The FE model of the Valdemar platform installed with the sensor set-up is shown in Fig. 11.2.

Simulations are performed for both regular and irregular wave loading. Regular waves are characterized by single harmonic sinus with wave height, frequency, phase and direction. Irregular waves are characterized by a sum of harmonic sinus with different wave heights, frequencies, phases and directions. Figure 11.3 shows simulated time series of the normalized total wave loading forces acting on the structure for the case of regular and irregular waves. The total loading force is calculated as a sum of all the forces acting on each of the elements in the FE model of the structure.

In order to compare the quality of the estimations, the normalized mean square error (NMSE) function is calculated for the estimated equivalent loading force time-series, see Eq. (11.17). The NMSE compares the simulated total loading force time series $\tilde{\mathbf{F}}$ with the estimated $\hat{\mathbf{F}}$ signal, where σ_F^2 is the variance of the simulated force. Generally, a NMSE of under 5% indicates good estimations, where the values under 1% correspond to perfect estimations.

$$NMSE[\%] = \frac{100}{N\sigma_{\mathbf{F}}^2} \sum_{i=1}^{N} \left(\mathbf{F} - \hat{\mathbf{F}}\right)^2 \tag{11.17}$$

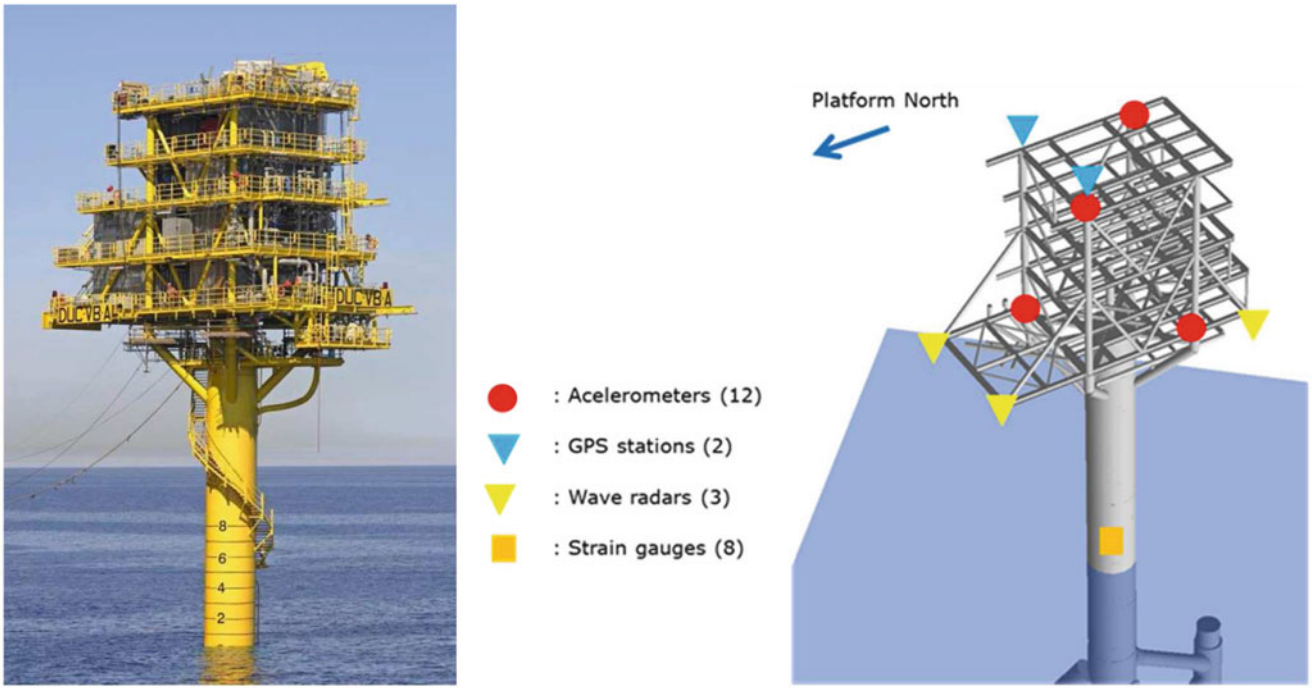

Fig. 11.2 Valdemar offshore platform (*left*) and FE model (*right*). In the FE model, the installed sensors for the SMS are also shown

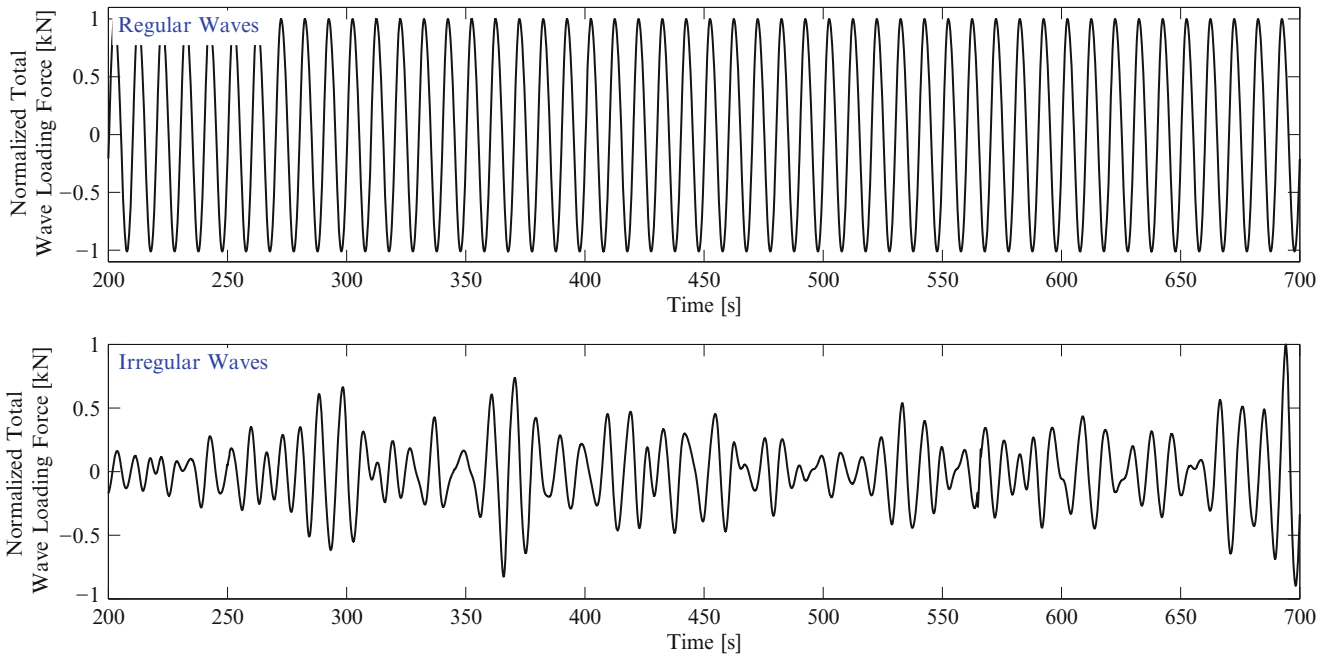

Fig. 11.3 Total normalized loading force of the regular and irregular waves acting on the structure, time domain

The location on the platform where the displacement is assumed to be measured corresponds to the location of one of the GPS sensors installed on the Valdemar offshore platform. Thus, in the following simulations, it is also tested if this single point sensor location is sufficient for reconstruction of the total equivalent loading force on the structure.

Table 11.1 NMSE for the total equivalent loading force estimations for different signal to noise ratios, for the case of regular waves

SNR	Direction	$NMSE[\%]$
Inf	N-S	1.002
1000	N-S	1.941
500	N-S	2.572
200	N-S	3.974
100	N-S	4.632
20	N-S	5.194
10	N-S	5.783
Inf	E-W	0.588
1000	E-W	0.842
500	E-W	1.491
200	E-W	3.013
100	E-W	4.633
20	E-W	4.998
10	E-W	5.525

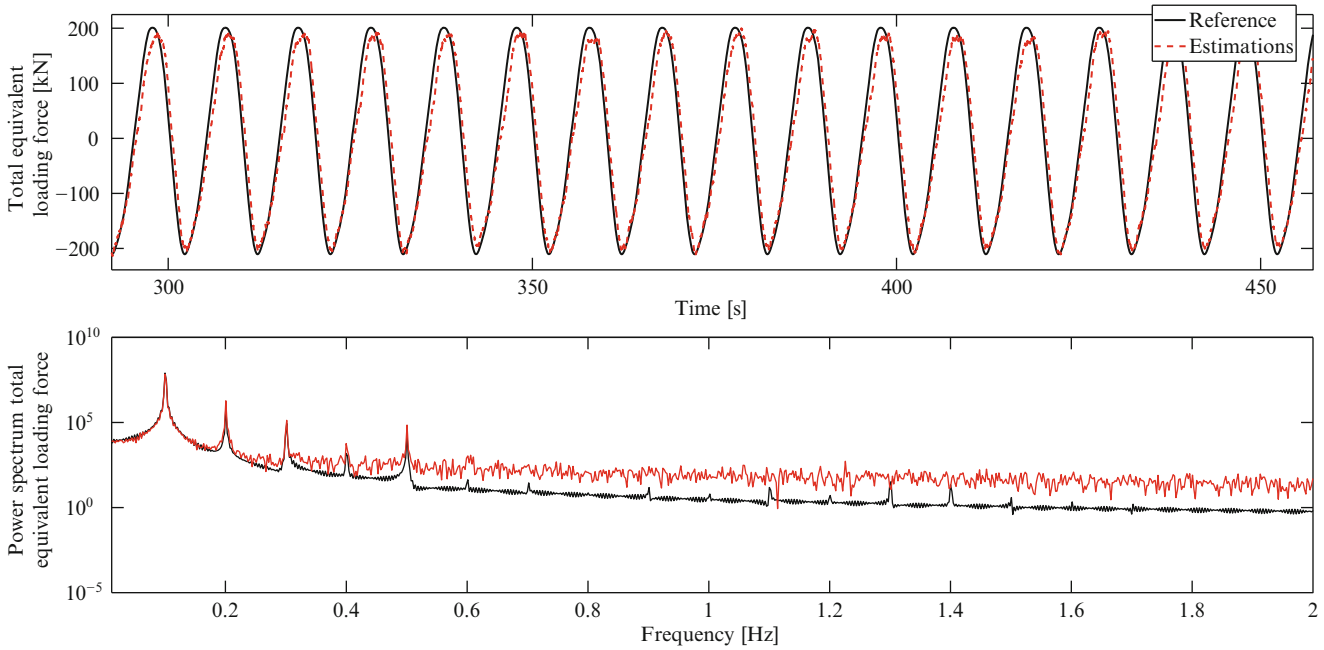

Fig. 11.4 Estimated vs. simulated total equivalent loading force for the case of very high measurement noise (SNR=20) and N-S motion of the platform

11.3.2 Load Estimation Results: Regular Waves

Table 11.1 presents the NMSE values calculated for the estimated total equivalent loading force, in N-S and E-W directions. Estimations are obtained for different measurement noise levels. Noise is characterized by signal-to-noise ratio (SNR) meaning the ratio between the simulated signal and noise powers. In the case where no measurement noise is present, SNR tends to infinity. High noise level is characterized by a low SNR value.

As it can be seen from the Table 11.1, very good estimations are achieved even in the presence of high measurement noise. Taking in consideration that only the 2DOF model of the platform was used, it is observed that the selected simulated measurement of the displacement placed at the top side of the oil platform contains sufficient information for estimation of the total platform reaction forces/ moments when the structure is exposed to regular wave loading. Thus, the Kalman filter can extract this information from the measurement signal and estimate the unknown loading even in the presence of high noise (Fig. 11.4).

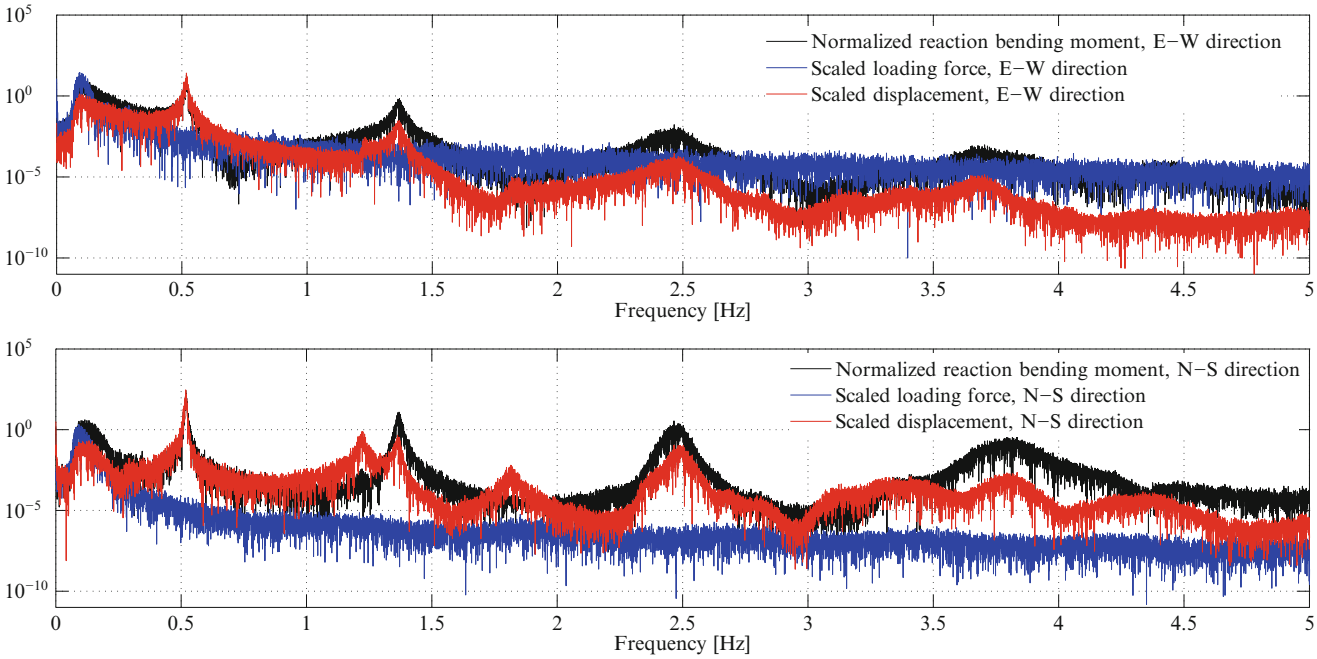

Fig. 11.5 Comparison of the power spectrums of the normalized displacement measurement, the total wave loading force and the total reaction moment

Table 11.2 NMSE values of the total equivalent loading force estimations (NMSE1) and total wave force estimations (NMSE2) for different signal to noise ratios, for the case of irregular waves

SNR	Direction	$NMSE1[\%]$	$NMSE2[\%]$
Inf	E-W	28.50	5.50
1000	E-W	28.58	5.51
500	E-W	28.37	5.48
200	E-W	28.59	5.55
100	E-W	29.23	5.65
20	E-W	31.64	5.83
10	E-W	35.31	6.92
Inf	N-S	41.56	10.59
1000	N-S	42.27	10.80
500	N-S	41.45	10.48
200	N-S	43.57	10.65
100	N-S	41.58	10.79
20	N-S	42.55	15.31
10	N-S	46.15	21.15

11.3.3 Load Estimation: Irregular Waves

In the case when the structure is exposed to irregular waves, the power spectrum of the waves contains more frequencies as can be seen from the wider spectrum compared to the spectrum for the regular waves. By comparing the normalized power spectrums for the simulated displacement, the wave loading and the overtuning moment at sea bed level, see Fig. 11.5, it can be seen that the irregular waves excite more modes of the structure than the linear waves, as expected. However, the wave loading at high frequencies does not cause large displacements of the platform.

Also, in the simulated displacement in the N-S direction, see Fig. 11.5, lower plot, torsional modes of the structure are present at 1.219 Hz and 1.816 Hz. However, torsional modes do not affect the overturning moments of the structure at sea bed level. As these peaks will also be present in the estimated equivalent loading force, the estimation in the N-S direction will be of lower quality than in the E-W direction.

The NMSEs of the total equivalent loading force estimations for different measurement noise levels, for the case of irregular waves are presented in Table 11.2, NMSE1 values. As it can be seen from the results, estimations are of lower quality than for regular waves. The NMSE values are around 30% for the E-W case, and around 42% for the N-S case. In order to understand the observed higher NMSE's, the reference signal (the original simulated data) and the estimations for

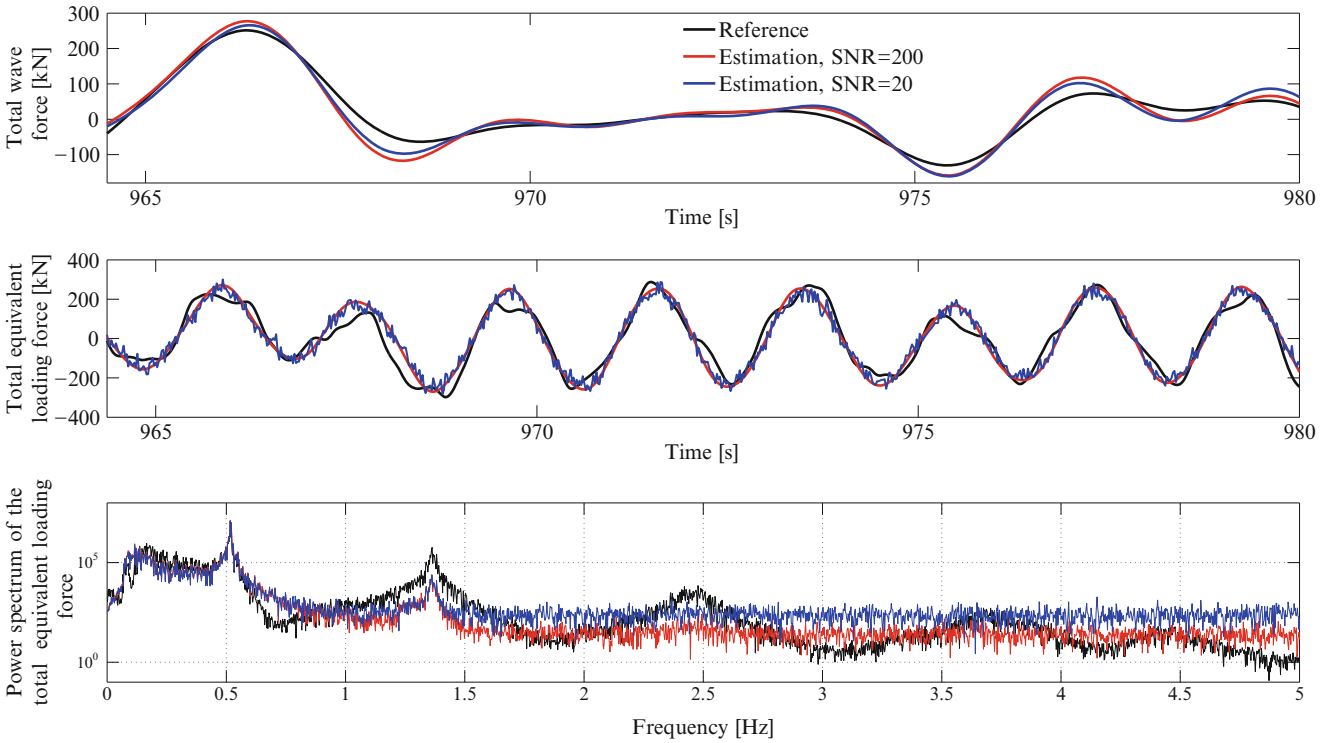

Fig. 11.6 Estimated vs. simulated wave loading force and total equivalent loading force in time and frequency domains, for the case of low (SNR=200) and high measurement noise (SNR=20) and E-W motion of the platform

medium and high measurement noise levels, in both time and frequency domain, are presented in Figs. 11.6 and 11.7. It is seen that the wave loading and motion of the structure is dominant in the E-W direction (wave load amplitude range is approx. [0–300kN]), where only very little motion is present in the N-S direction (wave load amplitude range is approx. [0–5kN]). This explains much higher values of the NMSE in N-S direction. For determination of the resulting loading force, estimation of the force in E-W direction is more relevant. Figure 11.6 corresponds to displacement in the E-W direction and from this plot it can be seen that the estimation error is a result of considering a high frequency range from 0Hz and up to 5Hz. When estimating the quasi-static wave loading only the frequency range from 0Hz to say 0.4Hz is of interest. Figure 11.7 corresponds to N-S motion and one can conclude that the wave and the structural frequencies except the first mode (around 0.5Hz) are slightly underestimated, but this is probably due to very low wave loading, i.e. almost no wave loading in this direction, hence more noise content. Also, the torsion frequency content around 1.2Hz is present in the estimations, but of cause not present in the reference signal (overtuning moment at sea bed level). This explains for the higher NMSE levels.

In order to see how well the estimations perform in the lower frequency range that corresponds to the quasi-static wave loading force, estimated and reference signals are post-processed using low-pass filter. The NMSE values are calculated again, see NMSE2 in Table 11.2, and top plots in Figs. 11.6 and 11.7. As it can be seen from the results, much better NMSE values are achieved when the contribution of the fictive structural frequencies to the response is filtered. In the main wave direction, E-W, the NMSE of the filtered estimations are around 5% which is very good, especially taking in consideration the simplicity of the used model and the assumptions that were made in the work. It is important to highlight that filtering is allowed as the first structural mode is around 0.5Hz whereas the dominating wave loading frequencies are in the range of 0Hz and up to around 0.4 Hz.

11.4 Conclusions and Future Work

This paper has tested a model-based, load estimation algorithm on the problem of online estimation of the total equivalent loading force on an oil and gas platform based on simulated displacement measurement from a single location on the top side of the platform. The algorithm is using the augmented Kalman filter as a recursive state estimator and a simple, 2DOF model

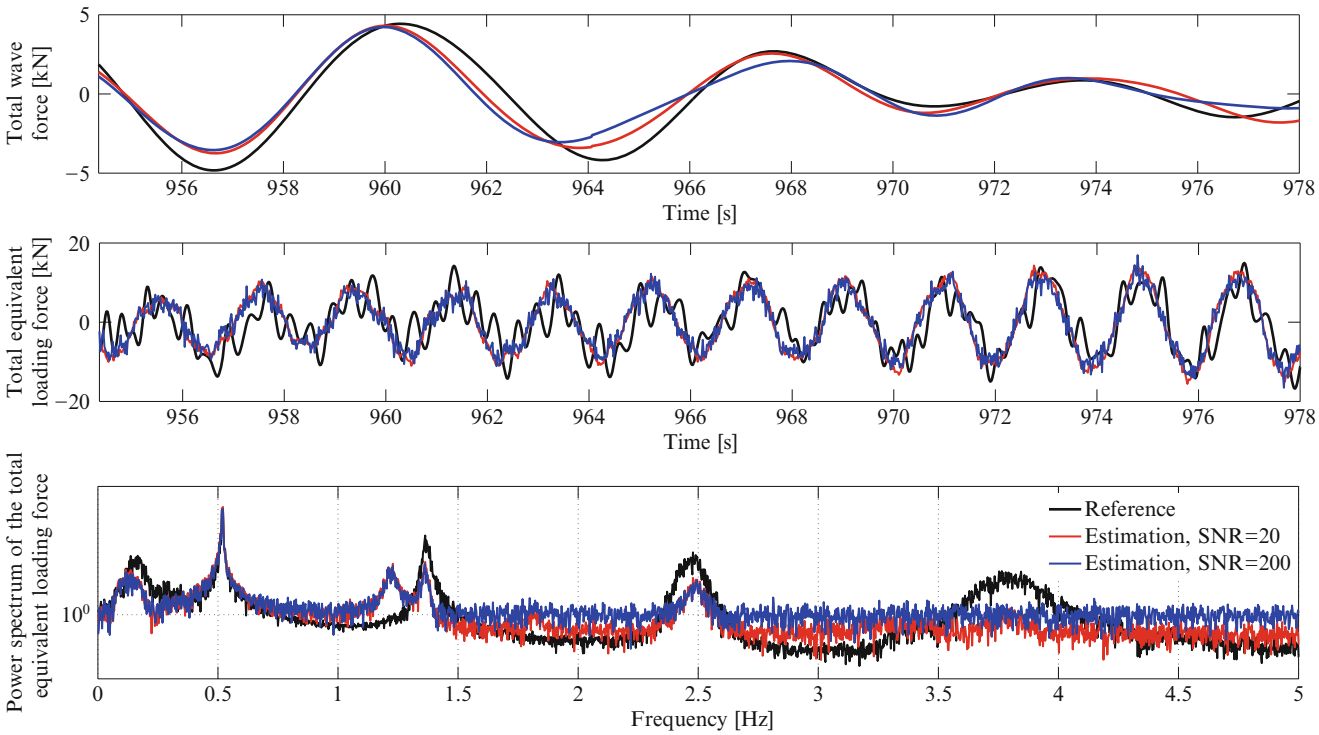

Fig. 11.7 Estimated vs. simulated wave loading force and total equivalent loading force in time and frequency domains, for the case of low (SNR=200) and high measurement noise (SNR=20) and N-S motion of the platform

of the platform. The method is tested on simulated data, assuming two loading scenarios: regular and irregular wave loading. In order to test robustness of the algorithm on the measurement noise, white noise is artificially added to the displacement data. In the case of irregular waves, estimated forces are post processed using a low-pass filter in order to validate their goodness in the wave loading frequency range. Conclusions from this work are given in the following:

Regular waves: For the case of regular wave loadings, the estimations of the equivalent loading force are almost perfect for low values of the SNR (NMSE values are under 1%). For very high SNR, estimation results are still very good both for low and high frequencies with the NMSE values around 5% for the highest simulated measurement noise level. As the estimation of the equivalent loading force is very good, the estimation of the quasi-static wave load is also very good.

Irregular waves: In the case of irregular waves, the equivalent loading estimation degrades significantly. The simulated wave loading power spectrum is wider than in the case of the regular waves. As a consequence, more structural modes of the structure are excited at higher frequencies. However, the high frequency content present in the simulated displacement measurement corresponds to very small displacement amplitudes with no structural impact. Also, some fictive structural frequencies are present in the estimated total equivalent loading, which is not represented in the reference overtuning moment (torsion cannot be detected in the overturning moment), hence contributing to the higher NMSE values. When estimating only the quasi-static wave loading forces by filtering processes and comparing to the reference wave loading very good results are obtained. In the main wave direction (E-W), NMSE values in the range of 5% is achieved.

Overall results are very good and promising, especially taking in consideration the model simplicity. In the future work more complex models of the platform will be considered so that the estimation of the total equivalent loading force could be further improved. The future work will consider use of multi DOF systems, instead of the presented simple 2DOF model of the structure in order to estimate and represent the distribution of the wave loading forces on the offshore structure.

Acknowledgements Cooperation of Maersk Oil in preparing this paper and providing data is gratefully acknowledged.

References

1. Johannesson P (1999) Rainflow analysis of switching Markov loads. PhD thesis, Lund Inst. of Technology, Lund University, Sweden
2. Hadamard J (1923) Lectures on coughy's problem in linear partial differential equations. Yale University Press, New Haven
3. Uhl T (2007) The inverse identification problem and its technical application. Arch Appl Mech 77:325–337. Springer
4. Gladwell GML (1986) Inverse problems in vibration. Kluwer Academic, Dordrecht
5. Klinkov M, Fritzen CP (2007) An updated comparison of the force reconstruction methods. Key Eng Mater 347:461–466
6. Nordstroem LJL, Nordberg TP (2002) A critical comparison of time domain load identification methods. In: Proceedings of the sixth international conference on motion and vibration control, Saitama, Japan, 2002, p 1151–1156
7. Fabunmi JA (1986) Effects of structural modes on vibratory force determination by the pseudoinverse technique. AIAA J 24(3):504–509
8. Hillary B, Ewins DJ (1984) The use of strain gauges in force determination and frequency response function measurements. In: Proceedings of IMAC II international modal analysis conference, Orlando, 1984, p 627–634
9. Stevens KK (1987) Force identification problems: an overview. In: Proceedings of SEM Spring meeting, Houston, Texas, 1987, p 838–844
10. Parloo E, Verboven P, Guillaume P, Van Overmeire M (2003) Force identification by means of in-operational modal models. J Sound Vib 262 (1):161–173
11. Vanlanduit S, Guillaume P, Cauberghe B, Parloo E, De Sitter G, Verboven P (2005) On-line identification of operational loads using exogenous inputs. J Sound Vib 285:267–279
12. Nordström LJL (2006) A dynamic programming algorithm for input estimation on linear time-variant systems. Comput Meth Appl Mech Eng 195:6407–6427
13. Zion L (1994) Predicting fatigue loads using regression diagnostics. In: Proceedings of the American Helicopter Society Annual Forum, Washington, DC, May 11–13, p 1337–1358
14. Trujillo DM, Busby HR (1997) Practical inverse engineering. CRC Press, London
15. Stelzner DA, Krammer DC (1999) Input force estimation using an inverse structural filter. In: Proceedings of 17th IMAC, Orlando, FL, February 8–11
16. Uhl T (2002) Identification of loads in mechanical structures-helicopter case study. Comput Assist Mech Eng Sci 9:151–160
17. Uhl T, Pieczara J (2003) Identification of operational loading forces for mechanical structures. Arch Transp 16(2):109–126
18. Goral G, Zbydón K, Uhl T (2002) Intelligent transducers of in-operational loads in construction fatigue monitoring. Mach Dyn Probl 2–3:73–78
19. Kalman RE (1960) A new approach to linear filtering and prediction problems. J Basic Eng 82(1):35–45. Retrieved 2008-05-03
20. Chan YT, Hu AGC, Plant JB (1979) A Kalman filter based tracking scheme with input estimation. IEEE Trans Aero Electron Syst AES-15(2) 237–244
21. Bogler PL (1987) Tracking a maneuvering target using input estimation. IEEE Trans Aero Electron Syst AES-23:298–310
22. Hou M, Xian S (1989) Comments on "tracking a maneuvering target using input estimation" . IEEE Trans Aero Electron Syst 25(2) pp. 280–281
23. Tuana PC, Jia CC, Fonga LW, Huanga WT (1996) An input estimation approach to on-line two-dimensional inverse heat conduction problems. Numer Heat Tran B Fund Int J Comput Meth 29(3) p. 345–363
24. Hwang JS, Kareem A, Kim WJ (2009) Estimation of modal loads using structural response. J Sound Vib 326:522–539
25. Lourens E, Reynders E, De Roeck G, Degrande G, Lombaert G (2012) An augmented Kalman filter for force identification in structural dynamics. Mech Syst Signal Process 27:446–460
26. Perisic N, Pedersen BJ, Kirkegaard PH (2012) Gearbox fatigue load estimation for condition monitoring of wind turbines. In: Proceedings of international conference on noise and vibration engineering ISMA2012: International conference on uncertainty in structural dynamics. KU Leuven, Department Werktuigkunde, p 4381–4392
27. Perisic N, Kirkegaard PH (2013) Low-cost tower root fatigue load estimation for structural health monitoring of grouted connections in offshore wind turbines. In: Damage Assesment of Strucure X: 10th International Conference on Damage Assessment of Structures (DAMAS 2013), July 8–10, 2013, Dublin, Ireland. Schweiz: Trans Tech Publications Ltd., p 676. (Key Engineering Materials, vol 569)
28. Simon D, (2006) *Optimal State Estimation: Kalman, H Infinity, and Nonlinear Approaches*, by John Wiley & Sons Interscience, Hoboken, New Jersey
29. Perisic N, (2013) *System Identification of Wind Turbines for Structural Health Monitoring*, PhD Thesis, Aalborg University

Chapter 12
Monitoring Proximity Tunneling Effects Using Blind Source Separation Technique

Soroush Mokhtari, Nader Mehdawi, Si-Hyun Park, Amr M. Sallam, Manoj Chopra, Lakshmi N. Reddi, and Hae-Bum Yun

Abstract The recent advances in sensing methods and data acquisition technologies have facilitated the collection of instrumentation data for continuous structural health monitoring (SHM). However, interpretation of raw sensor data, affected by various known and unknown environmental factors in field conditions is a challenging task. Structural systems are usually undetermined due to limited sensor data that are not sufficient for finding explicit relations between system inputs and outputs. This study aims to introduce a data-driven methodology using response-only data for underdetermined structural systems. The Principle Component Analysis (PCA) as a Blind Source Separation (BSS) method has been used to decompose the mixed raw response data into a linear combination of statistically uncorrelated mode shapes of input data. Being a data-driven method, the proposed framework is not limited in application to a specific sensor type. To evaluate the efficiency of the method in practice, the close proximity excavation effects of a new tunnel on an existing tunnel has been considered. The analysis results show that the method is not only able to decompose measurements into excavation-induced and the environment-induced deformations but also the calculated eigen-parameters can be used as excellent indicators of structural behaviors during excavation by visualizing the tunnel lining deformations.

Keywords Close proximity tunnelling • Structural health monitoring • Blind source separation • Principal component analysis • Underdetermined system

12.1 Introduction

One main objective of monitoring the tunnelling effects on neighboring structures is to identify the signs of failure or damage from structural behavior. Monitoring structural behaviour has been facilitated by recent advances in sensing methods and data acquisition technologies. But in sensor based monitoring methods, the analysis of raw sensor data can be a challenging task. Recorded data are mixed signals which are produced by various known and unknown structural and environmental sources; Therefore, the input and output data that should be collected, are numerous. In practice, however, such data collection is costly and unjustifiable. Consequently, available input and output data are insufficient to identify system parameters and the system remains underdetermined in terms of the input–output relationships [1].

S. Mokhtari • N. Mehdawi • M. Chopra • H.-B. Yun (✉)
Department of Civil, Environmental and Construction Engineering, University of Central Florida, Orlando, FL, USA
e-mail: smokhtari@knights.ucf.edu; nader@mehdawi.com; Manoj.Chopra@ucf.edu; Hae-Bum.Yun@ucf.edu

S.-H. Park
Korea Infrastructure Safety Technology Corporation, GoYang-Si, GyeongGi-Do, South Korea
e-mail: parksh@kistec.or.kr

A.M. Sallam
Terracon, Winter Park, FL, USA
e-mail: Amsallam@terracpn.com

L.N. Reddi
Dean of University Graduate School, Florida International University, Miami, FL, USA
e-mail: lreddi@fiu.edu

A. Wicks (ed.), *Structural Health Monitoring, Volume 5: Proceedings of the 32nd IMAC, A Conference and Exposition on Structural Dynamics, 2014*, Conference Proceedings of the Society for Experimental Mechanics Series, DOI 10.1007/978-3-319-04570-2_12,

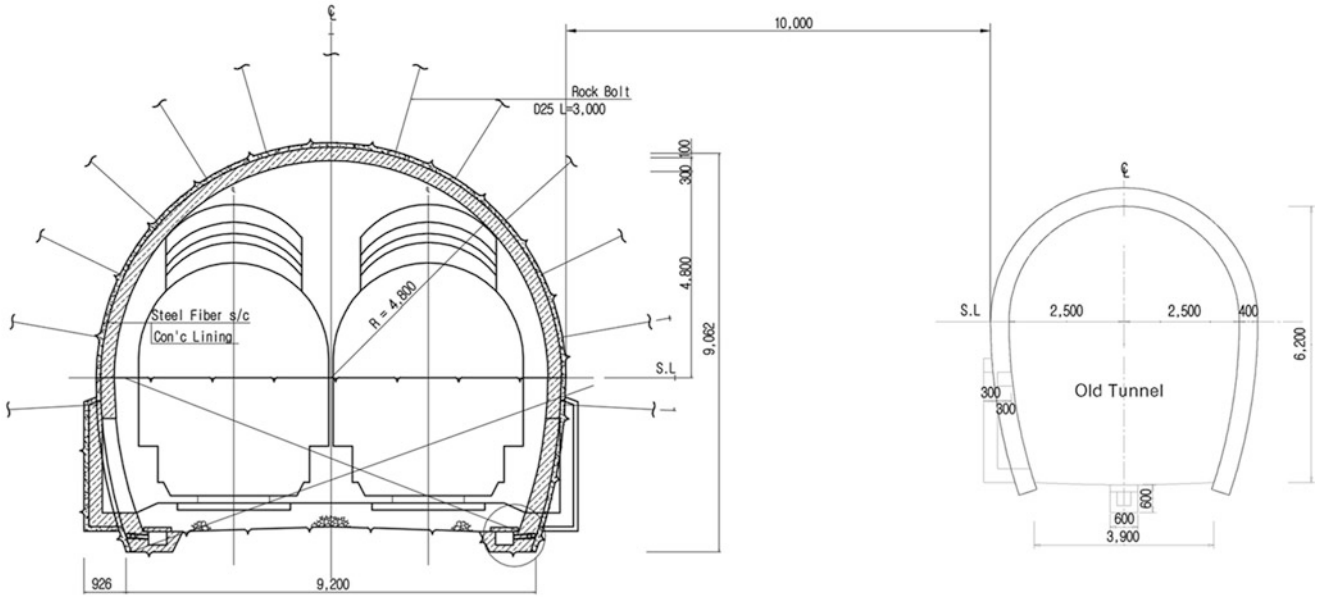

Fig. 12.1 Cross sections of the tunnels (the dimensions are shown in millimeter)

In this study, a Blind Source Separation (BSS) technique namely, Principle Component Analysis (PCA) has been applied to response-only sensor data. Decomposing mixed output signals into a set of source signals can separate the effect of structurally induced responses from environmental factors. Being a data-driven method, PCA does not rely on explicit input–output relationships and can be applied to underdetermined structural systems. The PCA is validated using the data from a tunnelling project in Korea.

12.2 Site Description

In 2008, a new tunnel (NT) was excavated between the Ajoong and Sinri Stations on the Jeolla Line in Korea [2]. The ground pillar between the new tunnel (NT) and the old tunnel (OT) of this line was only about 10 m wide; therefore monitoring the behavior of the OT was critical to ensure that it can endure the excavation effects of the NT. The cross section of the tunnels is presented in Fig. 12.1.

The NT was constructed using the top-heading and bench method. The timeline of top-heading and bench excavation advances were recorded during construction (Table 12.1). To monitor the behavior of the OT during construction of the NT, four extensometers and four tilt gages were installed at Sta. 30k475, 190 m from the starting point of the project (Sta. 30k285). Using the timeline of excavations, the distances between the top-heading and bench fronts and the sensor location (d_t and d_b, respectively), were calculated.

12.3 Continuous Monitoring for Tunnel Deformation

Elongation and slope on the OT lining were recorded at four locations (Fig. 12.2) using extensometers and tilt gauges. Sample time-history datasets for extension and tilt measurements are presented in Fig. 12.3 (Sampling frequency is 1 per 30 min for all channels).

Technical challenges of analyzing the sensor data include,

1. The mechanical characteristics of the soil would change due to excavation loads but, such changes cannot be quantified using response-only data.
2. The OT was constructed using American Steel Support Method (ASSM). In this method the interface of surrounding soil and the tunnel lining is not uniform. Consequently, the distribution of load on OT lining cannot be determined.

Table 12.1 Advances of the new tunnel excavation of top-heading and bench tunnelling

Dates	Top-heading excavation location (m)[a]	Bench excavation location (m)[a]	Distance b/w top-heading and bench fronts	Note
2008/05/27	0 (−190)	0 (−190)	0	Excavation begun
2008/08/21	85 (−105)	75 (−115)	10	–
2008/09/12	147 (−43)	110 (−80)	37	9/12–9/16 holidays
2008/09/17	147 (−43)	110 (−80)	37	–
2008/09/30	188 (−2)	110 (−80)	78	–
2008/10/02	199 (+9)	110 (−80)	89	The top-heading front passed the sensor location
2008/10/15	224 (+34)	152 (−38)	72	–
2008/10/23	252 (+62)	152 (−38)	100	–
2008/10/28	256 (+66)	180 (−10)	76	–
2008/10/30	260 (+70)	190 (0)	70	The bench front reached the sensor location

[a]The positive or negative values indicate that the excavation front locates before or after the sensor location in the direction of excavation

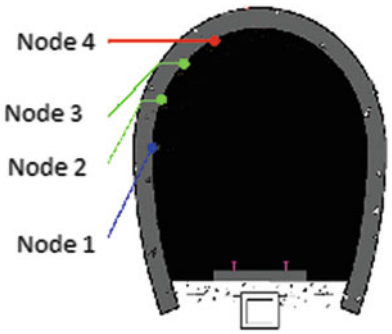

Fig. 12.2 Sensor locations on OT lining. Each sensor node consists of one extensometer and one tilt gauge (figure is not in scale)

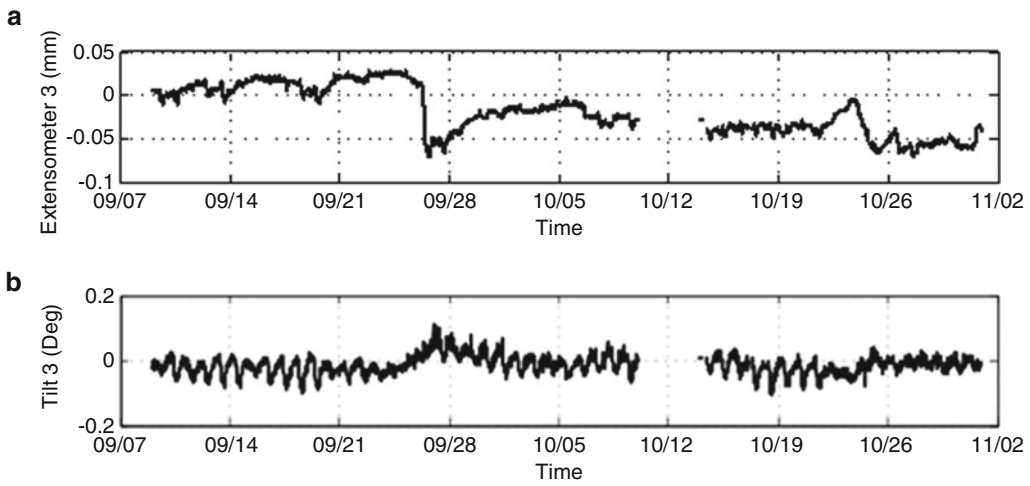

Fig. 12.3 Sample elongation and tilt time-histories at Node 3. (**a**) Extensometer at Node 3, (**b**) Tilt gauge at Node 3

3. Several environmental factors such as temperature and humidity can affect the recorded datasets and cause daily trends and fluctuations. However, the available sensor data is not sufficient to separate environmentally induced deformations from excavation effects.

12.4 Data-Driven Analysis Using Limited Sensor Data

Principle Component Analysis (PCA) has been used as a BSS method in this study to separate environmentally induced responses from excavation effects. A brief description of this method is presented here.

The matrix of observations can be described as a (m × n) matrix, where each column is associated with the recordings of a sensor (m is the number of sensors). Each row, then, is associated with a set of samples each sensor (n is the number of samples).

$$X = [x_1; x_2; \ldots; x_m] \tag{12.1}$$

where x_i is an (n × 1) vector associated with sensor i. The goal of the algebraic solution is to find the orthogonal matrix of the principal components (P), where

$$Y = PX \tag{12.2}$$

which renders the correlation matrix R_Y diagonal. The correlation matrix can be determined from Eq. (12.3).

$$R_Y = \frac{1}{n-1} YY^T = \frac{1}{n-1} PAP^T \tag{12.3}$$

such that

$$A = XX^T = V\lambda V^T \tag{12.4}$$

where A is an (m × m) symmetric matrix, V is the (m × m) matrix of eigenvectors arranged as column, λ is the (m × m) diagonal matrix of the eigenvalues. It should be emphasized that PCA removes linear correlations based on the second-order statistics of the data; therefore is limited by its global linearity. A detailed description of the method can be found at [3, 4].

12.4.1 PCA Results

A 3-day moving window with 30-min time increments was selected to apply PCA to the elongation datasets. The size of the moving window has been selected based on the stability of Modal Assurance Criterion (for detailed description of Modal Assurance Criterion, please see [5]). The application of PCA to four elongation time-history datasets resulted in four eigenvalues (λ) and four eigenvectors (V). Considering that eigenvectors (V) of each time window are statistically uncorrelated, they can be used to visualize the mode shapes of elongation deformations. In other words, relative elongation at the sensor locations can be illustrated using eigenvectors (V) but the magnitudes are normalized to 1. Correspondingly, the eigenvalue (λ) can be used to visualize the magnitude of the corresponding mode shape.

The results indicate that Mode 1 (λ_1) is the dominant mode. The fluctuations of eigenvalues can be compared with the distance between of top-heading front and sensor location (d_t) and the distance from bench front to the sensor location (d_b). It should be noted that no daily fluctuation was observed in the PCA results as opposed to the raw data in which, daily trends were significant.

According to the results (Fig. 12.4), from September 11 to September 28 a significant increase in elongation of Node 1 was observed since $\frac{(\lambda_1)_B}{(\lambda_1)_A} = 115.5$ (A and B represent the time windows on September 11 and September 28, respectively). This increasing trend happened during the period in which the top-heading excavation was getting closer to the sensor location. The eigenvalue decreased after this period which can be interpreted as the effect of soil stabilization after the top-heading front passed the sensor location. On October 30, when the bench front reached the sensor location, the elongation of Mode 1 increased again and $\frac{(\lambda_1)_D}{(\lambda_1)_C} = 1.583$ and $\frac{(\lambda_1)_D}{(\lambda_1)_A} = 164.8$ (C and D represent the time windows on October 9 and October 31, respectively). Similar results were observed with the tilt dataset.

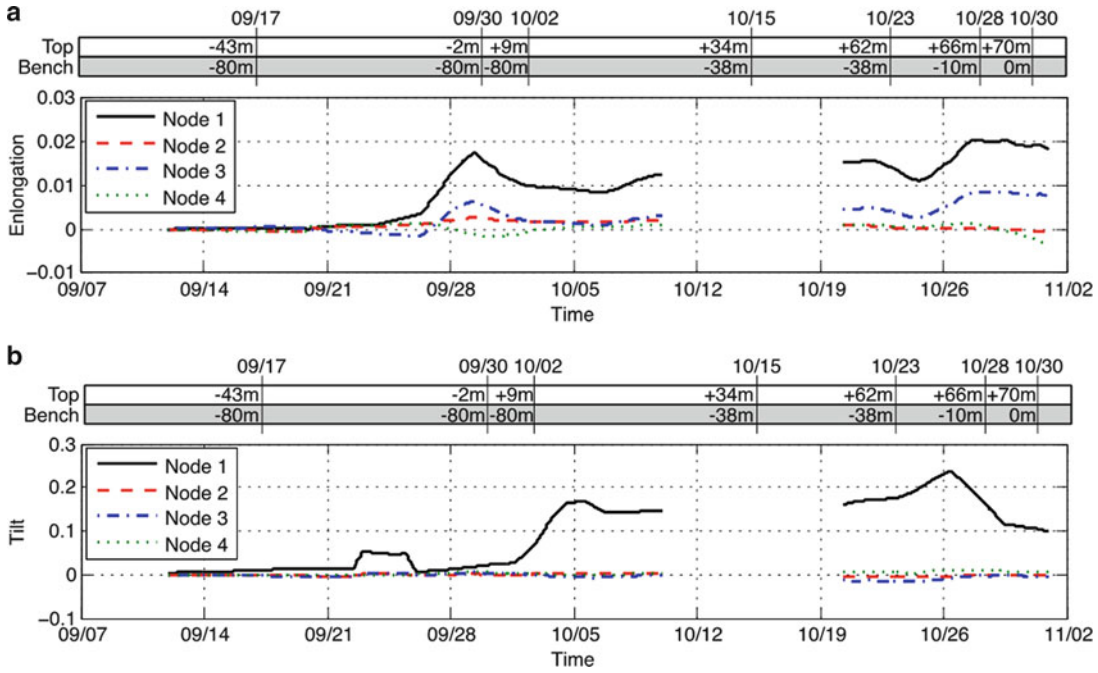

Fig. 12.4 Nodal deformation in dominant mode shape. (**a**) Elongation, (**b**) Tilt

12.5 Conclusions

In this paper, Principle Component Analysis (PCA) as a Blind Source Separation (BSS) technique was used to draw a framework for analyzing response-only sensor data. This method is not limited in application to a certain type of sensor and can be used in different sensor-based monitoring applications. Being a data-driven method, PCA is suitable for analyzing underdetermined systems where available sensor data is not sufficient for defining the exact input–output relations; therefore, the proposed framework can be used in monitoring applications where the structural damage and behavior of the system should be monitored using a limited number of sensors. The capabilities of the method were evaluated using the sensor data from a tunnelling project in proximity of an old tunnel. The mixed raw sensor data was decomposed into statistically uncorrelated mode shapes of source data using the PCA and eigen parameters were used to visualize the deformations of the structure. Further analysis of the results, presented the correlation between the structural deformations and excavation procedure. Moreover, no daily fluctuation was observed in the PCA results. It shows that the presented method is capable of separating the environmentally-induced deformation from excavation effects.

References

1. Yun HB, Reddi LN (2011) Nonparametric monitoring for geotechnical structures subject to long-term environmental change. Adv Civil Eng 3:1–17
2. Lee I, Han M, Lee JS (2006) Major tunnelling projects in Korea. In: Proceeding of international symposium on underground excavation and tunnelling, Bangkok, pp 75–84
3. Yan A, Kerschen G, Deboe P, Golinval J (2005) Structural damage diagnosis under varying environmental conditions—part I: a linear analysis. Mech Syst Signal Process 19(4):847–864
4. Yan A, Kerschen G, Deboe P, Golinval J (2005) Structural damage diagnosis under varying environmental conditions—part II: local PCA for non-linear cases. Mech Syst Signal Process 19(4):865–880
5. Maia NMM (1997) Theoretical and experimental modal analysis. Taylor & Francis, London, Research Studies Press Limited, Baldock, UK

Chapter 13
Endowing Structures with a Nociceptive Sense Enabled by a Graphene-Oxide Sensing Skin

Alan Kuntz, Cole Brubaker, Stephanie Amos, Nathan Sharp, Wei Gao, Gautam Gupta, Aditya Mohite, Charles Farrar, and David Mascarenas

Abstract In this work we use bio-inspired strategies to move towards a low bandwidth, robust, asynchronous structural health monitoring approach which mimics biological nociceptive sense. A novel sensing skin is developed with graphene-oxide capacitive sensors which act as structural damage receptors.

Contemporary structural health monitoring paradigms require numerous sensor nodes distributed spatially across a structure. Data collected synchronously from all sensor nodes must undergo analog to digital conversion and aggregation at a centralized processor to determine state of health. Order n interconnects must be established between nodes and the processor for a system of n sensors, leading to challenges in wiring and robustness. The large amounts of data collected by each sensor can lead to difficulty in data storage and analysis.

We take inspiration from biological nervous systems to develop an efficient structural health monitoring system featuring large sensor arrays in which data is only transmitted when a change indicative of damage occurs. This is made possible with graphene-oxide supercapacitors and resistors that can be integrated into structural systems as well as robust data transmission buses. Our system requires an asymptotically smaller than order n number of interconnects. This technique may introduce a new paradigm for approaching the structural health monitoring paradigm.

Keywords Structural health monitoring • Nocioception • Graphene-oxide • Sensing skin • Asynchronous

13.1 Introduction

Structural health monitoring (SHM) has applications in a broad range of engineering fields including civil, mechanical and aerospace. When applied to structural elements, SHM is an effective way to ensure the safety of structural elements, while providing financial benefits for the owner or operator. SHM systems enable engineers to more easily detect damage in a structural element before it reaches a point of impending critical failure. The graphene-oxide based sensing skin has been designed to detect cracks or damage in locations that may not be easily observed during a traditional inspection on a given structure.

Drawbacks with current SHM systems is that they often require the collection and evaluation of large amounts of data, and consequently require high power consumption rates to continuously monitor the integrity of the structural elements in question. These drawbacks can be linked to the fact that numerous sensors are frequently required for precise monitoring over

A. Kuntz
University of New Mexico, Albuquerque, NM, USA

C. Brubaker
Colorado State University, Fort Collins, CO, USA

S. Amos
Georgia Tech, Atlanta, GA, USA

N. Sharp
Purdue University, West Lafayette, IN, USA

W. Gao • G. Gupta • A. Mohite • C. Farrar • D. Mascarenas (✉)
Los Alamos National Laboratory, Los Alamos, NM, USA
e-mail: dmascarenas@lanl.gov

A. Wicks (ed.), *Structural Health Monitoring, Volume 5: Proceedings of the 32nd IMAC, A Conference and Exposition on Structural Dynamics, 2014*, Conference Proceedings of the Society for Experimental Mechanics Series, DOI 10.1007/978-3-319-04570-2_13,

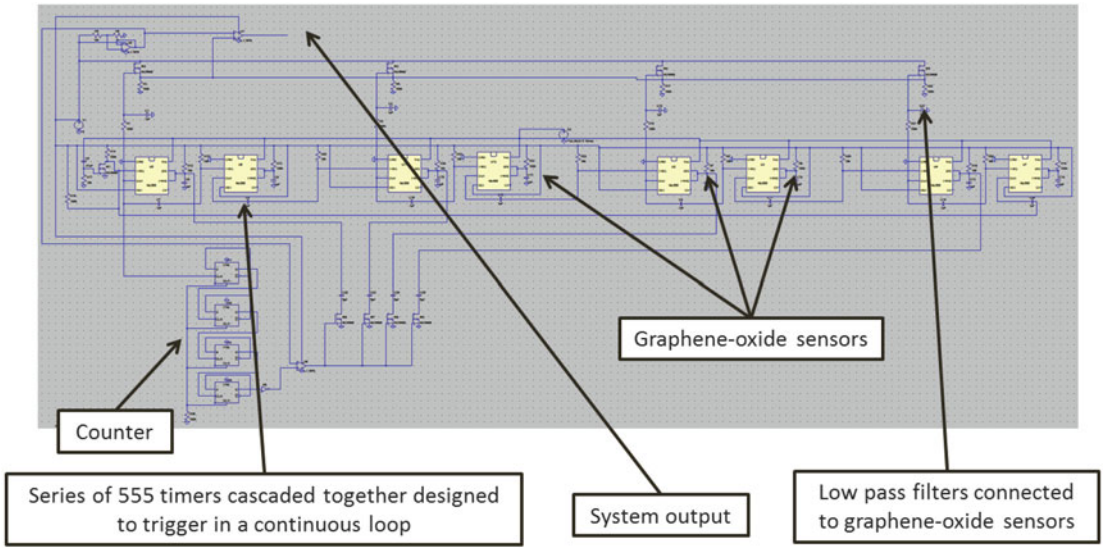

Fig. 13.1 Spice model of the asynchronous circuit

a large area. A system which can minimize data processing requirements while concurrently reducing power consumption would prove to be a breakthrough in structural health monitoring; conserving both time and economic resources. To accomplish this goal, our design is heavily focused on implementing asynchronous computing methods within our system to minimize data processing, as well as analyzing solutions to reduce the overall power consumption for the graphene-oxide based sensing skin.

Taking inspiration from the biological nervous system, asynchronous computing methods are designed such that a system will only output data and send a signal when a change, or stimulus, has occurred [1]. For the purposes of SHM, this stimulus in our system is triggered when the structural element in question experiences damage. Our graphene-oxide based sensing skin effectively functions as a structure's sensory nodes, communicating with a central processing unit, relaying information about the current state of a structural element in question. Utilizing the concept of asynchronous computing techniques, the computational power and overall amount of data required to continuously monitor the state of a system drastically decreases. Further building upon the concept of asynchronous computing, large sensor arrays can be efficiently analyzed without a drastic increase in data or power consumption. A multitude of sensors can be 'bussed', or linked, together and designed to only send information when damage to our system has occurred.

For the purposes of this research, the sensing skin implementation is created with an array of capacitive sensors produced from reduced graphene-oxide. Graphene-oxide is a material with unique and interesting behavior. In its unreduced form, graphene-oxide acts as an insulator, but when reduced, functions as a conductor. Due to this distinctive material property, electrical components such as resistors and capacitors can be produced in a single plane of reduced graphene-oxide. To create these resistors and capacitors, the graphene-oxide is reduced using a heat source and the desired design, shape and placement of electrical components can be specified.

There are numerous methods available for reducing graphene-oxide. One method involves the use of the laser in a generic light scribe printer [2]. Using the laser as the heat source, it is possible to reduce and print identical shapes for electrical components with relatively high levels of accuracy and precision; depending on the printer being used. Large scale lasers and laser printing devices are also used to create extremely accurate and consistent shapes on the graphene-oxide skin.

13.2 Experimental Methods

13.2.1 Asynchronous System

The asynchronous circuit is comprised of various low power components and chips. A spice model representation of the circuit can be seen below in Fig. 13.1 and a breadboard prototype of the circuit in Fig. 13.2. The circuit design implements common electrical components such as resistors and capacitors, MOSFET transistors, op-amps (one serving as a buffer

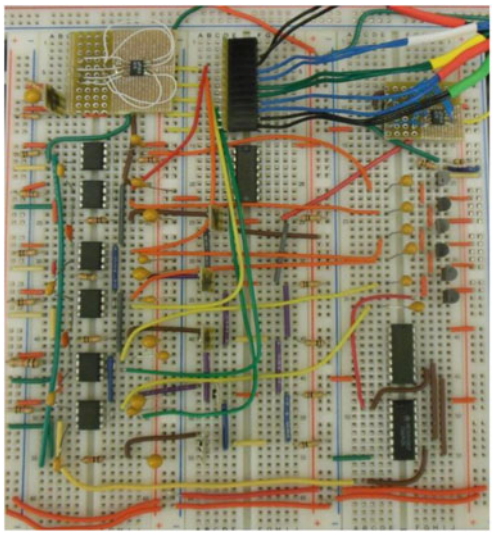

Fig. 13.2 Breadboard prototype the asynchronous circuit

and the other as a comparator), low pass filters, a low power counter, low power 555 timers as well as the graphene-oxide sensors. These components have been labeled on the figure below for reference. To increase the robustness and efficiency of the design, similar components are cascaded and bussed together within the circuit.

The core of our asynchronous circuit design is based on the implementation of multiple 555 timers which are cascaded together to continuously trigger in a loop. 555 timers are common electrical chips frequently used for basic timing and pulse wave generation applications. These chips can be configured to either send single pulses, referred to as the monostable configuration, or send a continuous stream of rectangular square wave pulses in the astable configuration. Our asynchronous circuit design utilizes a series of 555 timers in a monostable configuration. Each 555 timer in this system is connected to and paired with an individual graphene-oxide senor, and the associated pulse width of the timer is a function of the capacitance of its graphene-oxide sensor.

In an undamaged case, the asynchronous circuit does not output any information to the processing unit. This is accomplished by passing the output from each 555 timer and its associated graphene-oxide sensor through a low pass filter prior to the interface of the circuit and the processor. The output from each low pass filter is then fed directly into a MOSFET transistor which ultimately generates the output signal for each graphene-oxide sensor. The low pass filter in our circuit is designed such that it filters out the square wave pulses generated by each 555 timer in the cases where the graphene-oxide sensors are undamaged. These square wave pulses have small enough widths, and high enough frequencies, such that they are well above the cut off frequency of the low pass filter, and their signals are completely filtered out. As a result, in the undamaged case there is no output from the low pass filter. Since the original signal generated by the 555 timer is completely filtered out and there is no input signal generated for the MOSFET, the circuit does not send an output signal to the processing unit.

In the case of damage to a graphene-oxide sensor, though, output signals are generated by the circuit and relevant information is transmitted to the processing unit. When a graphene-oxide sensor is damaged, its corresponding capacitance value is altered. This deviation in capacitance causes the width of the 555 timer pulse to increase. When this lower frequency signal from a damaged sensor is fed through the low pass filter, its output is no longer completely filtered out as in the undamaged scenario. This is because the 555 timer signal with an increased pulse width contains lower frequency components. It follows that the MOSFET transistor receives an input that is above its threshold value, causing it to trigger an output signal. This signal is then sent through a comparator op-amp to convert the triangular wave created by the MOSFET to a square wave signal that can easily be interpreted by the microcontroller interfacing with the processing unit.

Since this circuit is designed to only send output signals when damage has occurred, it would be nearly impossible to distinguish between a completely undamaged state as opposed to one in which the entire system has failed and is no longer generating any output signals. To compensate for this issue, a heartbeat signal was created to send pulses at regular intervals, indicating that the system and sensors are still functioning correctly. The output of this heartbeat signal, displayed on an oscilloscope, can be seen below in Fig. 13.3. Having this heartbeat signal adds a level of safety to the circuitry design, ensuring that the circuitry is functioning correctly even when outputs are not seen due to the asynchronous nature of the design.

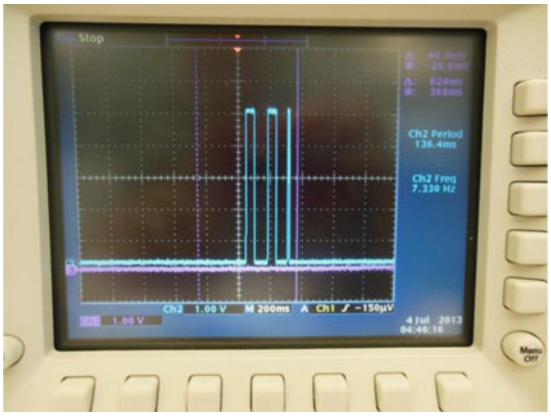

Fig. 13.3 Heartbeat signal

Fig. 13.4 Graphene-oxide capacitors

13.2.2 Graphene-Oxide Resistor and Capacitor

Both resistors and capacitors were created using the graphene-oxide material. These resistive and capacitive components were implemented into the electrical circuitry design as sensors with varying rates of success. Graphene-oxide resistors were created using a single sheet of graphene-oxide, reduced via the branding method previously mentioned. Metal brands were heated to approximately 500°C on a traditional hot plate and immediately placed on the skin until the graphene-oxide was sufficiently reduced. After reduction, resistance values ranged from 10 up to 100 kΩ, depending on the overall level of reduction. Unreduced, graphene-oxide behaves as an insulator with resistance values well above 500 MΩ. As such, when the graphene-oxide skin was well reduced, lower resistance values were recorded. The overall values of resistance were dependent on several factors including, but not limited to, the length of exposure time to the metal brand and the pressure with which the brand was applied to the graphene-oxide skin. Similar in behavior to traditional resistors, the shape and size of the graphene-oxide resistors influenced the overall resistance capacities. However, it was determined that the graphene-oxide resistors are much more dependent on temperature and humidity conditions compared to traditional resistors.

An array of graphene-oxide capacitors was created using a high precision laser as the reduction source. Similar to the graphene-oxide resistors created, these capacitors were variable. Capacitance depended on the individual sensor being measured, and external conditions such as temperature and humidity played large roles in the overall level of capacitance.

Values for the graphene-oxide capacitors ranged from a few nanofarads to a maximum of three millifarads during testing. Figure 13.4 below shows the array of capacitor sensors used in our research.

13.3 Sensor Skin Results

An array of sensorsmade of conductive ink was successfully implemented as a sensor in the RC circuit. The sensor array is shown in Fig. 13.5. Each sensor was created so that there are four possible paths for current to travel. In this way one sensor can increase the knowledge about crack size. Figure 13.6 shows that there is no output signal when all four paths remain intact but that the output pulse gets longer as the crack propagates through one, two, and then three of the four possible paths.

An array of graphene-oxide capacitors was also created, and implemented into the asynchronous circuit to detect damage. Originally we had planned to replace the capacitors making up the low pass filter in the circuit described above with the graphene-oxide sensors, which would allow the signal through when a cut develops and the capacitors decreased in

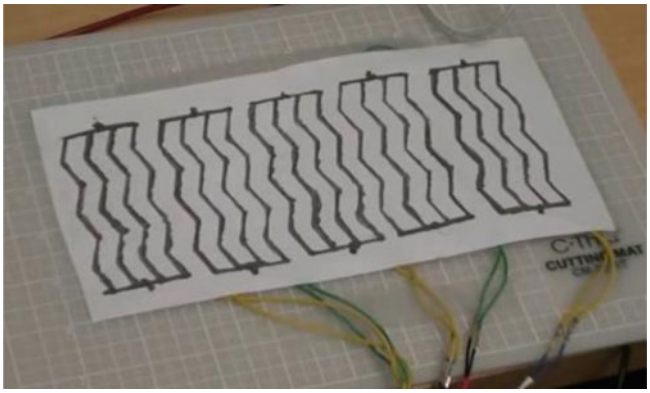

Fig. 13.5 Resistive ink sensor array

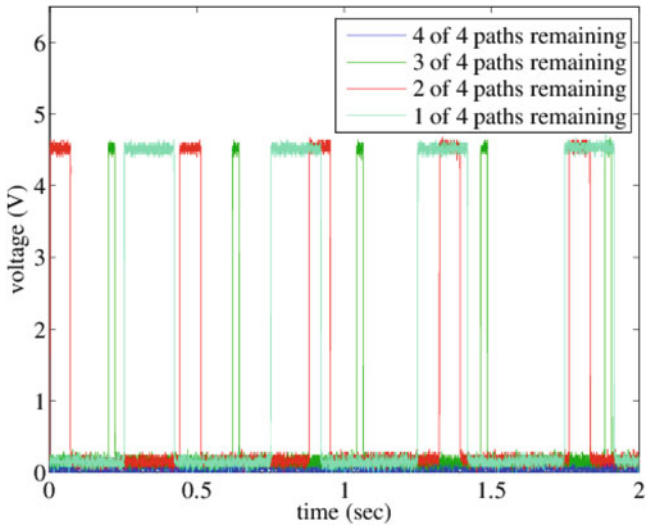

Fig. 13.6 Output pulse width increases with increased sensor resistance

capacitance. However, this did not work because all electrochemical capacitors are frequency dependent, with the capacitance dropping at higher frequencies [3]. Because of this phenomenon, GO capacitors are limited in their ability to act as low pass filters since the capacitance is itself a function of frequency. Therefore, the original design was slightly changed so that the GO sensors would be input into the capacitor associated with the monostable 555 timers. When a sensor is cut the capacitance drops, decreasing the pulse width. In order to make a pulse width drop trigger the output instead of a pulse width increase, the inputs to the comparator were simply switched so that the circuit triggers on low bus voltage instead of high bus voltage and the filter parameters were chosen such that the voltage remained above the threshold unless the pulse width dropped. The GO capacitors were input into the circuit and damage was simulated by cutting the capacitors with a razor blade. Figure 13.7 shows the bus and output signals before damage and after two sensors were cut.

13.4 Sensor Shape Considerations

Beyond creating an asynchronous sensing skin, our research focused on analyzing sensor shapes that would most efficiently and effectively detect cracks within our sensing skin. As such, multiple shapes were considered for the sensor layout in the array. In order to obtain maximum sensing capacity with the fewest number of sensors, the optimal sensor configuration is one which maximizes the area covered per sensor, while minimizing the length of cracks that could go undetected within the system. This means that the optimal sensor layout and shape can be represented by the following relationship:

$$\max\left[\frac{A}{d}\right] \tag{13.1}$$

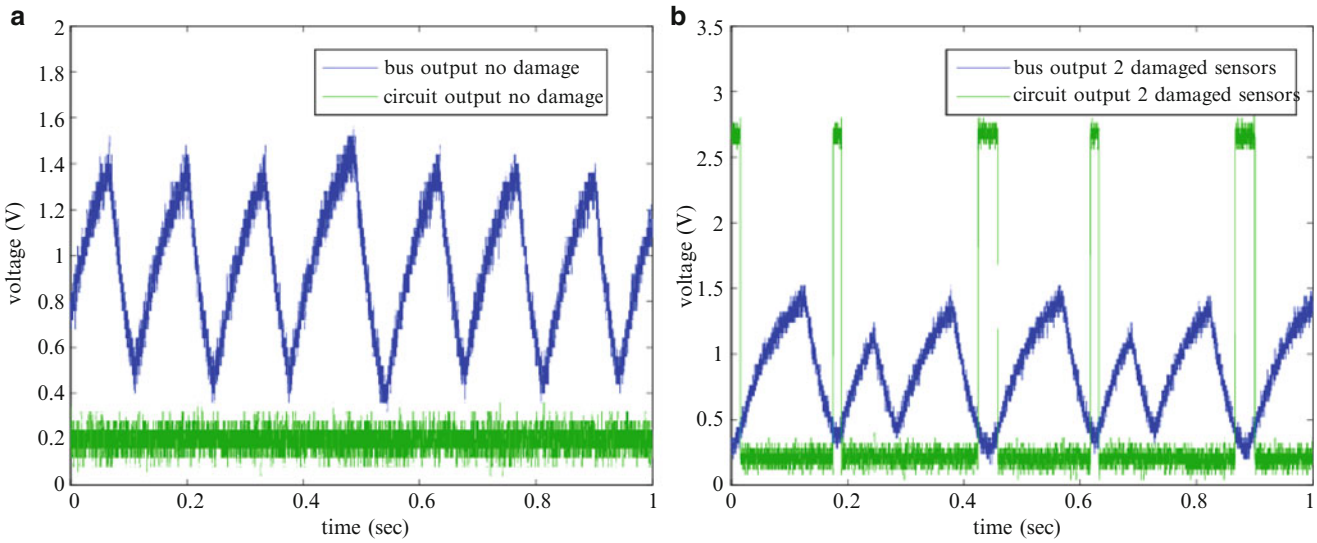

Fig. 13.7 Oscilloscope signals of (**a**) healthy and (**b**) damaged skin

Fig. 13.8 Sensor shapes

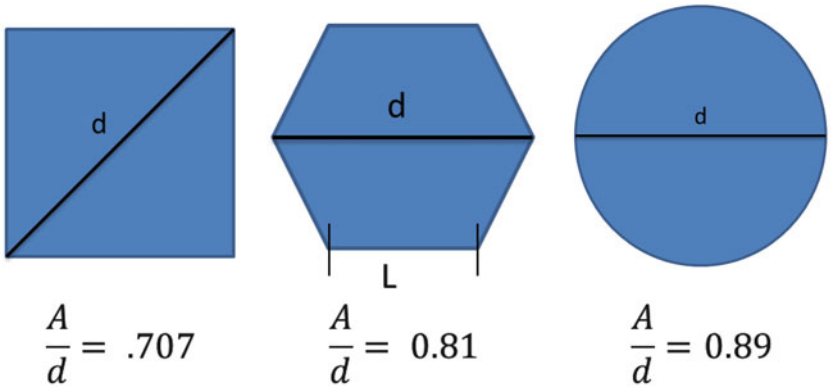

This relationship between sensor area, A, and the maximum distance a crack can travel without being detected, d, was defined as the means for which the effectiveness of sensors would be evaluated. The values for common sensor shapes can be found in Fig. 13.8. Again, the goal of this calculation is to maximize the ratio of area to crack length, ensuring that the largest number of cracks can be detected with the fewest number of sensors.

In total three shapes were tested against our measure of efficiency: squares, hexagons and circles. From our calculations, the hexagon and circle produce the most preferable results, so arrays consisting of these two shapes were evaluated using a computer generated crack simulation. This simulation indicated that the array which most efficiently detected the shortest cracks over the largest areas was composed of hexagons. Although the circular sensors have a larger maximum area to crack length, the probability for creating the maximum crack length for the circle is very high, while the probability for creating the maximum crack length for the hexagon is smaller in comparison. For this reason, the average maximum area to crack length for the hexagon array is smaller than that for the circular sensor arrays. The results for the simulation are shown in Fig. 13.9 below, where a single nested hexagonal sensor outperformed a circular sensor shape for a majority of crack length simulations.

13.5 Conclusions

Biological health monitoring devices provide a good blueprint for creating a monitoring system which is large, accurate, and robust without consuming large amounts of power. We created a design and prototype that mimics some of the strategies employed by biological systems by making the information delivery asynchronous and by bussing sensors together. These

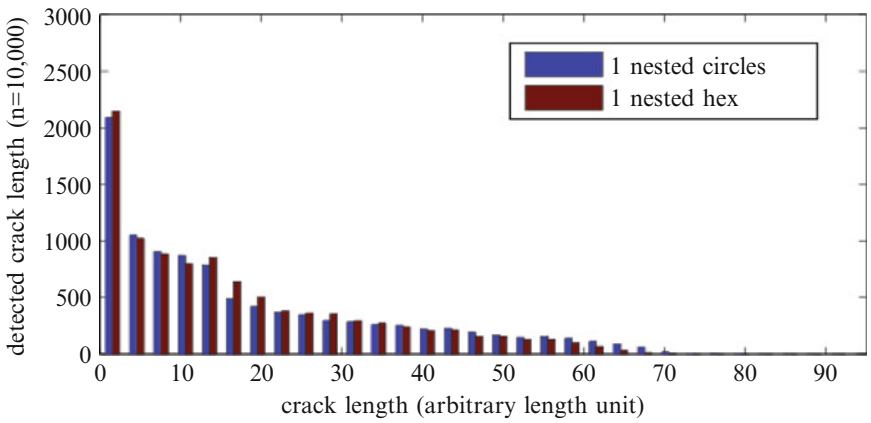

Fig. 13.9 Crack length detected for circles and hexagons

strategies have shown to be an effective way to deal with large sensor arrays. We have also analyzed the effects different sensor shapes have on its crack detection performance and found hexagons to perform better than squares or circles.

Acknowledgements This work is supported by the Los Alamos National Laboratory Laboratory-Directed Research and Development Program.

References

1. Dafny N (1997) Neuroscience online. UTHealth 1997. http://neuroscience.uth.tmc.edu/s2/chapter06.html
2. Malasarn D (2013) UCLA researchers develop new technique to scale up production of graphene micro-supercapacitors. UCLA Newsroom 2013. http://newsroom.ucla.edu/portal/ucla/ucla-researchers-develop-new-technique-243553.aspx
3. Sarangapani S, Tilak BV, Chen C-P (1996) Materials for electrochemical capacitors: theoretical and experimental constraints. J Electrochem Soc 143(11) 3791–3799

Chapter 14
Modal Strain Energy Based Damage Detection Using Multi-Objective Optimization

Young-Jin Cha and Oral Buyukozturk

Abstract Modal strain energy has been reported by researchers as one of the sensitive physical measures that can be used as a damage index in structural health monitoring. Inverse problem-solving based approaches using single-objective optimization algorithms are also one of the promising damage identification methods. However, integration of these potential methods is currently limited with partial success in the detection of structural damages due to errors and noises. In this study, a novel damage detection approach using hybrid multi-objective optimization algorithms is proposed to detect multiple damages in a 3-dimensional steel structure. This study developed an approach to overcome the shortcomings of the single-objective genetic algorithm based approaches using multi-objective formulations for minimizing errors of damage indices between actual damaged structures and simulated damages. The performance of the proposed hybrid multi-objective genetic algorithm is compared to that of traditional single-objective optimizations based approaches. This study accurately detects the location and extent of induced multiple minor damages of the laboratory 3-dimensional steel structure.

Keywords Damage detection • Modal strain energy • Inverse problem solving • Multi-objective • Genetic algorithm • Structural health monitoring

14.1 Introduction

Modal strain energy has been considered in research as a damage index because it is sensitive to damages in structures and used in assessing the extent and location of the structural damages in 2-dimmensional structures [1–3]. Petro et al. [1] showed that modal strain energy based damage detection may be more sensitive than other mode shaped based approaches. The strain energy method was applied to a space truss model to detect multiple damages [2]. The method detected severe damages, while some of the less severe damages went undetected. A damage quantification method using changes in the modal strain energy (MSE) was applied to a simple 2-story plain structure [3]. The damage quantification method proved partially successful in quantification of the structural damage in a multiple damage case with noises. An efficient algebraic algorithm of element MSE sensitivity was proposed to detect location and severity of damages [4]. However, all these studies had limitations in localizing and identifying the extent of multiple damages with low accuracy and high noise, and some of the predicted damages were localized in undamaged structural elements.

In order to detect structural damages, inverse problem solving methods have also been used. As one of the inverse problem solving methods, genetic algorithms (GA) have been widely used to detect damages as a concept of model updating. GA was used to detect damages in a simple cantilever beam using modal assurance criterion of frequencies and mode shapes [5]. A two level micro GA was applied to detect multiple damages in a simply supported single span beam and a continuous three-span beam [6]. An implicit redundant representation (IRR) GA was also applied to detect damages using a frequency response function-based damage index for simple 2-dimensinal (2-D) structures. The performances of the IRR GA and those of the simple GA were compared to detect damages using the same damage index [7]. This study showed that the performance of the IRR GA based approach was superior to those of other simple genetic algorithm based approaches. Correlation-based methods were proposed to facilitate damage determination for 3-D truss bridge using multi-layer GA [8].

Y.-J. Cha • O. Buyukozturk (✉)
Department of Civil and Environmental Engineering, Massachusetts Institute of Technology, Cambridge, MA 02139, USA
e-mail: yjcha@mit.edu; obuyuk@mit.edu

A. Wicks (ed.), *Structural Health Monitoring, Volume 5: Proceedings of the 32nd IMAC, A Conference and Exposition on Structural Dynamics, 2014*, Conference Proceedings of the Society for Experimental Mechanics Series, DOI 10.1007/978-3-319-04570-2_14,

From the first GA layer, damage-suspicious elements were divided into several groups and the groups were combined to larger groups and optimization process started over at the normalized point of the result of the first layer. This multi-layer GA based approach assumed that user knew approximate locations of the damage in the first-layer. This means that if the user chooses an incorrect location of the damage-suspicious elements, the damages may be assigned the wrong locations. Most studies cited above used single-objective GAs to detect damages in simple cantilever beams or idealized 2-D structures. Moreover, these simple GA based damage detection methods showed limitations to finding multiple damages in cases of 3-D structures. In addition, many trials were necessary to find proper parameters of the genetic algorithms in order to get satisfying results. The parameters include population size, crossover and mutation rates, and type of selection method.

In an effort to overcome these limitations, the present study proposes a multi-objective formulation based damage detection method by integrating modified modal strain energy as a damage index and multi-objective genetic algorithms as an inverse problem solving method to explore damages in 3-D structures. In this study, two objective functions are formulated using modified modal strain energy for the multi-objective formulation. To demonstrate the effectiveness of the proposed approach, a 3-D structure has been developed. Minor damages such as a 5 % reduction of stiffness of the structural elements have little effect to change of the modal properties of the structure. Consequently, these minor damages with multiple locations in a structure are difficult to detect using traditional damage detection methods based on modal properties. Thus, multiple minor damage scenarios are created to evaluate the proposed damage detection method. The results of the proposed method are compared to those of the methods based on traditional single-objective genetic algorithms.

14.2 Damage Detection Method Based on Inverse Problem Solving

In order to detect structural damages, inverse solving concept is adopted using heuristic genetic algorithms. The overall procedures for the damage detection using proposed multi-objective GA and traditional single-objective GA are described in a flowchart shown in Fig. 14.1. A baseline structural model is developed using finite element method (FEM) as a first step. A damage-induced structural model is also developed from the baseline structure by reducing Young's modulus of the structural members. The damage-induced model is that damages are artificially created in the baseline structure as possible damage scenarios. Mass and stiffness matrices of the both damage-induced and damage-simulated models are obtained. From the obtained matrices, mode shapes of the damage-induced and the damage-simulated structures from genetic algorithms

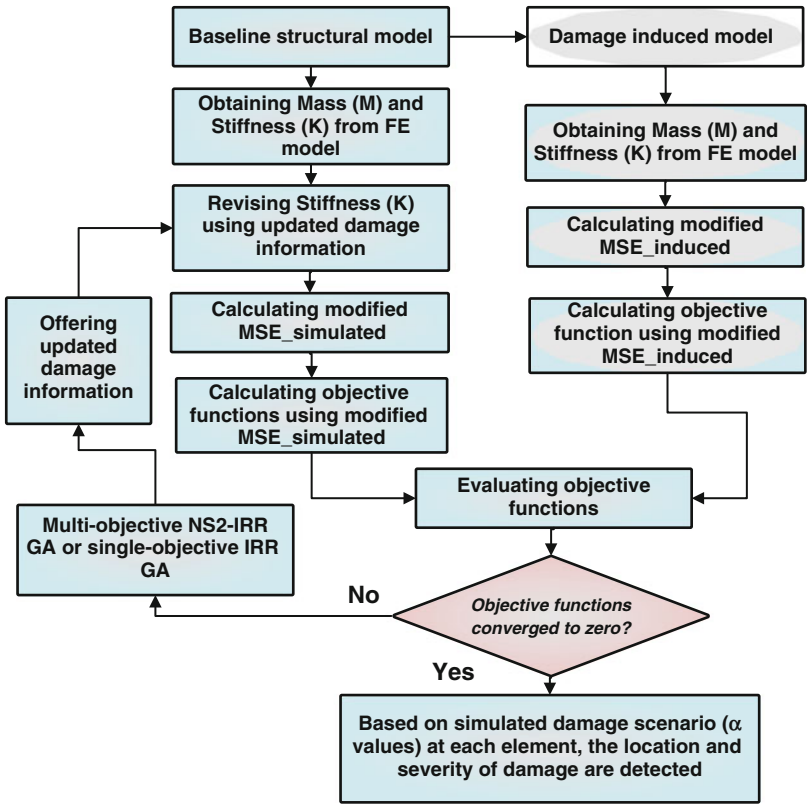

Fig. 14.1 Overall procedure for the damage detection using multi-objective NS2-IRR GA and single-objective GA

are calculated. Modified modal strain energy is calculated using those calculated mode shapes. The modified modal strain energy uses absolute values of mode shapes. Thus, it is more convenient to compare the modal strain energy between damage-induced model and damage-simulated model because the global direction of the mode shapes is highly dependent on location of damages. In this study, objective functions are defined as the discrepancy of the modified modal strain energy between the induced damages and the simulated damages using GAs. If the discrepancy of the two modified modal strain energy is zero, then the simulated damages are the same as the induced damages. The simulated damage scenarios are the detected damages of the structure. Thus, in order to minimize the objective functions, the stiffness matrix of the damage simulated structure is dynamically changed based on fitness of the objective functions using the two types of genetic algorithms. The optimization process is stopped when the objective functions converge to zero value, otherwise it is continued to the next generation until the objective functions are converged to zero values or required criteria are met, such as the predefined maximum number of generations.

14.2.1 Strain Energy Based Damage Index

The modal strain energy is more effective for detecting damage than using modal properties as a damage index [3, 8, 9]. Thus, modified modal strain energy as a damage index is proposed to detect multiple minor damages for 3-D structures. The modal strain energy (MSE) is calculated as the product of the elemental stiffness matrix and the second power of the mode shape component. For the *j*th element and the *i*th mode, the MSE before and after occurrence of damage is given as

$$MSE_{ij}^{s} = \boldsymbol{\Phi}_i^{sT} \mathbf{K}_j \boldsymbol{\Phi}_i^{s} \tag{14.1}$$

$$MSE_{ij}^{d} = \boldsymbol{\Phi}_i^{d^T} \mathbf{K}_j \boldsymbol{\Phi}_i^{d} \tag{14.2}$$

where MSE_{ij}^{s} is the MSE of the *j*th element for the *i*th mode shape of the damage simulated and MSE_{ij}^{d} is those of the damage-induced structural element, respectively, and $\boldsymbol{\Phi}_i^{d}$ and $\boldsymbol{\Phi}_i^{s}$ are *i*th mode shapes of the damage-simulated and damage-induced structures, respectively. In order to approximate MSE_{ij}^{d}, the undamaged elemental stiffness matrix $\mathbf{K}_j$, for which the global coordinate is used for each elemental stiffness matrix, is used instead of the damaged one since the damage elements are not known. In order to calculate the change in the MSE, modified MSE is suggested as,

$$mMSE_{ij}^{s} = \left|\boldsymbol{\Phi}_i^{d^T}\right| \mathbf{K}_j \left|\boldsymbol{\Phi}_i^{d}\right| \tag{14.3}$$

$$mMSE_{ij}^{d} = \left|\boldsymbol{\Phi}_i^{sT}\right| \mathbf{K}_j \left|\boldsymbol{\Phi}_i^{s}\right| \tag{14.4}$$

Using the modified MSE, the change of modal strain energy (MSEC) of the *i*th element for the *j*th mode is obtained as

$$MSEC_{ij} = \left|\boldsymbol{\Phi}_i^{d^T}\right| \mathbf{K}_j \left|\boldsymbol{\Phi}_i^{d}\right| - \left|\boldsymbol{\Phi}_i^{sT}\right| \mathbf{K}_j \left|\boldsymbol{\Phi}_i^{s}\right| \tag{14.5}$$

where *j* and *i* denote the element number and mode number, respectively. Thus, the total energy difference of the modal strain energy between induced damaged structure and simulated structure is expressed as

$$\text{Total change of MSE} = \sum_{i=1}^{ms} \sum_{j=1}^{el} \left| \left|\boldsymbol{\Phi}_i^{d^T}\right| \mathbf{K}_j \left|\boldsymbol{\Phi}_i^{d}\right| - \left|\boldsymbol{\Phi}_i^{s}\right| \mathbf{K}_j \left|\boldsymbol{\Phi}_i^{s}\right| \right| \tag{14.6}$$

where *ms* and *el* denote the total number of elements of a structure and total number of the mode shapes considered, respectively. Structural damages are eventually expressed as reduction of the structural stiffness. Thus, in order to simulate damages to any extent and at any element of the structure, Young's modulus of each structural element is reduced from the original value using the following formulation

$$E_j^{s} = \left(1 - \alpha_j\right) E_o \tag{14.7}$$

where E_o is the intact Young's modulus of elasticity, E_j^s is the damage-simulated Young's modulus of elasticity of jth element, and α_j is a percentage of the reduction of the Young's modulus at jth element of the structure. Consequently, reduction in the Young's modulus in the entire structure is expressed as

$$\boldsymbol{\alpha} = \left(\alpha_1\ \alpha_1\ \ldots\ \alpha_{el}\right) \tag{14.8}$$

Therefore, any extent and any location of the damages in structures can be generated based on these randomly simulated $\boldsymbol{\alpha}$ by this proposed multi-objective or single-objective genetic algorithms.

14.2.2 Single-Objective Genetic Algorithms

Implicit redundant representation genetic algorithms (IRR GA) as a single-objective GA has been shown to perform well for detection of damages in steel structures [7]. For this reason we choose IRR GA as single-objective GA. The IRR GA was first proposed by Raich and Ghaboussi [10]. The IRR GA uses gene locator indicating starting point of a gene instance containing encoded Young's modulus information (i.e., $\boldsymbol{\alpha}$), and redundant segments containing currently non-encoded segments that can become part of the encoded gene instances in later generations. These features of the IRR GA make it dynamic changes of the optimization variables, in which the dynamic changes can prevent early converges to local optimal solutions. In order to compare the performance of the proposed hybrid multi-objective genetic algorithms with traditional single-objective GA, the objective function of the single-objective GA process is also defined as a composite type of objective function:

$$\min(Objective) \tag{14.9}$$

$$Objective = \sum_{i=1}^{ms}\sum_{j=1}^{el}\left|\left|\Phi_i^{d^T}\right| K_j \left|\Phi_i^d\right| - \left|\Phi_i^T\right| K_j \left|\Phi_i\right|\right| \tag{14.10}$$

14.2.3 Hybrid Multi-Objective Genetic Algorithms

Detection of structural damages is a complex nonlinear problem. In order to localize and quantify structural damages, hybrid multi-objective NS2-IRR GA which is the integration of best features of the implicit redundant representation (IRR) GA as encoding policy and non-dominated sorting genetic algorithm-II (NSGA-II) as a selection method, is proposed. This multi-objective NS2-IRR GA was proposed to find optimal layouts of the control devices and sensors for 3-D high-rise buildings [11–13]. The IRR encoding allows the percentage reduction of the Young's modulus to dynamically change by the actions of crossover and mutation among individuals in the same population and in future generations during the search process. The NSGA-II is used as a selection method to keep competitive candidate solutions and transfer those to next generation of the genetic iterations [14]. NS2-IRR GA uses crowding distances to calculate a fitness value of each individual to consider density of solutions and then to remove conversing to local optimal solutions. The crowding distance estimating the density of individuals surrounding a particular individual in the phenotype non-dominated Pareto front, is calculated as an average distance of the two individuals on either side of this point along each of the objectives based on following equation

$$I[i]_{\text{distance}} = I[i]_{\text{distance}} + \left(I\left[i+1\right].m - I\left[i-1\right].m\right) \tag{14.11}$$

where m is the number of objectives and $I[i]_{\text{distance}}$ is the mth objective function value of the ith individual in the set I. Thus, current population is sorted according to a crowded comparison operator. Thereafter, only N number (i.e., population size) of individuals will be selected for the next population. The crowded comparison operator is presented as following equation,

$$i \geq_n j \ \text{ if } \left(i_{rank} < j_{rank}\right) \text{ or } \left(\left(i_{rank} = j_{rank}\right) \text{ and } \left(i_{\text{distance}} > j_{\text{distance}}\right)\right) \tag{14.12}$$

where i_{rank} and j_{rank} are non-dominated rank of the i and jth individuals, respectively, and i_{distance} and j_{distance} are local crowding distance of the i and jth individuals, respectively. The selection, crossover, and mutation operator are carried out to create a new child population from the current population. The binary tournament selection is carried out to create the child population, with predefined size N. These steps are continued until the defined criteria or generation is satisfied.

The hybrid multi-objective NS2-IRR GA is used in this study to detect structural damages for a 3-D structure. The change of the modified MSE between the damage induced structure and the damage simulated structure by GA process is expressed as objective functions of the NS2-IRR GA. The proposed GA minimizes the objective functions expressed as Eq. (14.6). To calculate objective functions from modified MSEs, incomplete mode shapes are used after removing rotational components which are difficult to measure. Therefore, to detect induced damage scenarios, the objective functions as a manner of multi-objective optimization are defined as follows:

$$\min\left(Objective1,\ Objective2\right) \tag{14.13}$$

where *Objective*1 and *Objective2* are

$$Objective1 = \sum_{i}^{ms/2} \sum_{j=1}^{el} \left| \left| \Phi_i^{d^T} \right| K_j \left| \Phi_i^d \right| - \left| \Phi_i^T \right| K_j \left| \Phi_i \right| \right| \tag{14.14}$$

$$Objective2 = \sum_{ms/2+1=1}^{ms} \sum_{j=1}^{el} \left| \left| \Phi_i^{d^T} \right| K_j \left| \Phi_i^d \right| - \left| \Phi_i^T \right| K_j \left| \Phi_i \right| \right| \tag{14.15}$$

where *ms* is the selected number of incomplete mode shapes. The rotational components of the mode shapes are difficult to measure, thus, in this study, the translational components of the mode shapes are only used to calculate change of the modal strain energy.

14.3 Application to Modular Steel Structures

The proposed algorithm is evaluated on synthetic data from a FEM model. To ensure that the dynamics represented by this model are realistic, the FEM model is based on a physical lab structure. The properties of this structure are as follows: The detailed material properties are given in Table 14.1. The column section is 0.25 in. (0.00635 m) × 2 in. (0.0508 m) with a length of 24 in. (0.6096 m), and the frame section is 0.00635 m × 0.0508 m with a length of 0.6096 m in each bay.

As a prototype structure model, a numerical 4-story 2-bay by 1-bay scale-model steel frame building structure with dimensions 0.6096 m × 1.2192 m wide and 2.4384 m high is used. The structure model is developed using FEM with 12 × 12 stiffness matrix and consistent mass matrix. The first ten natural frequencies for the designed structures are calculated using SAP2000 (2.2022, 4.2186, 5.5575, 6.9149, 12. 078, 16. 422 and 27.038 Hz) and using MATLAB (2.2086, 4.5295, 5.6076, 7.0849, 12.8728, 18.5872, and 27.8020 Hz). Those separately calculated natural frequencies showed good-agreement with each other.

14.3.1 Multiple Minor Damage Scenario Case 1

In order to compare the performance of the single-objective GA and multi-objective GA approaches, a damage scenario having multiple damages in multiple locations is generated. A minor damage, which causes only small effects of change to the global mode shapes of the structure, is hard to detect using traditional modal property based damage detection methods. Five percent of the stiffness reduction of the structural elements 1 and 10 and structural elements 1, 10, 17, 33, and 52 is generated by reducing Young's modulus using Eq. (14.8) in the prototype 4-story structure as shown in Fig. 14.2a, b, respectively. The italic and non-italic numbers are the node numbers and element numbers of the structure, respectively. Induced damages in structural elements are expressed as thick dashed red lines. In order to calculate modified MSE, and to eventually calculate predefined objective functions [i.e., Eqs. (14.10, 14.14, and 14.15)], first two mode shapes with

Table 14.1 Member material properties

Structural element	Young's modulus (N/m^2)	Density (kgf/m^3)	Volume (cm^3)	Mass (kg)
Frame for 2-bay	1.96E11	7,800.00	1, 327.00	10.35
Column	1.96E11	7,800.00	217.57	1.70

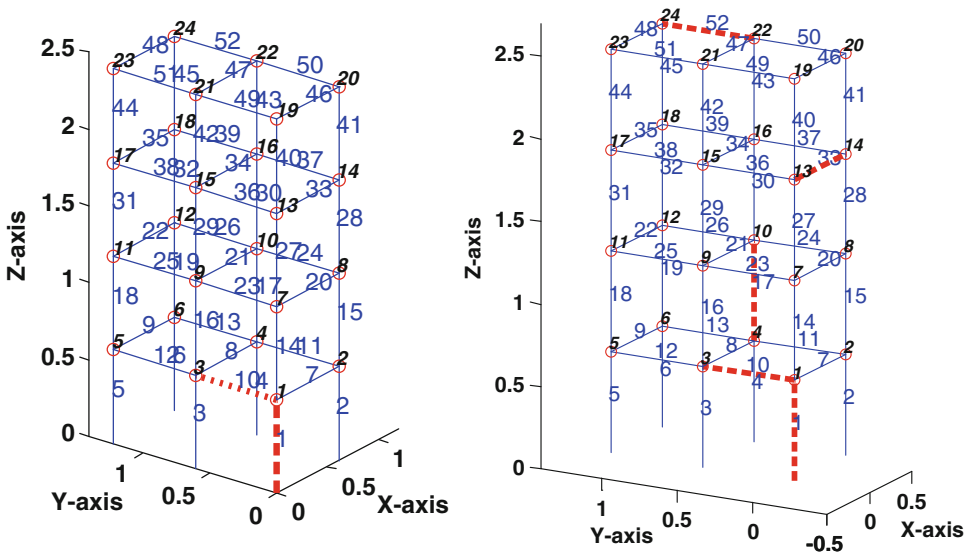

Fig. 14.2 Structural element numbering of 4-story 2-bay prototype structure (structural dimensions in meter). (**a**) Two minor damages, (**b**) Five minor damages (color figures online)

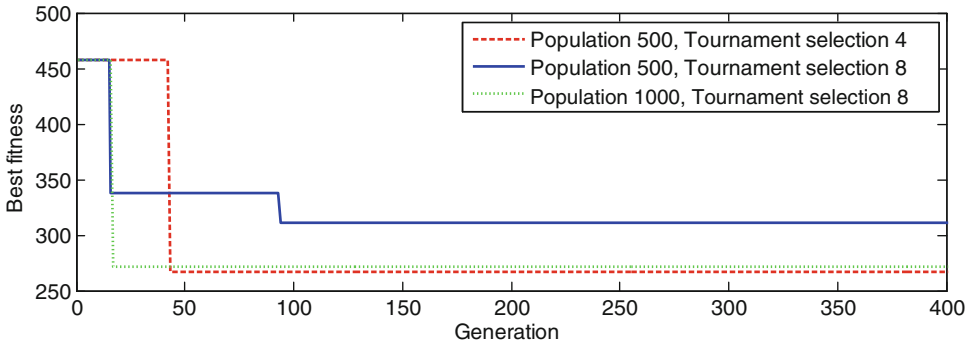

Fig. 14.3 Single-objective IRR GA approach

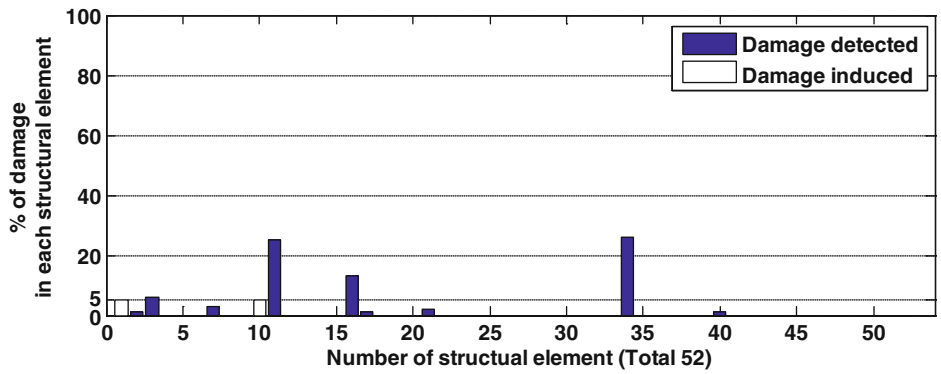

Fig. 14.4 Damages detected by single-objective IRR GA approach

only global X and Y translational components of the mode shapes are used. For the single-objective GA, IRR GA is chosen because of its effective performance in detection of various damages in 2-D plain steel structures and its superiority compared to other simple GAs [7].

The IRR GA does not give exact locations and extent of the induced damages from several trials by changing GA properties such as population size and tournament selection sizes. Figure 14.3 shows the trials of the single-objective IRR GA and its best fit solutions during generations are plotted. Even though the IRR GA continued to more than 400 generations with a population size of 500, it does not give optimal solutions as shown in Fig. 14.4. In order to obtain an optimal solution from single-objective IRR GA, the best fitness of the objective function, expressed as Eq. (14.10), should be zero value which means that the simulated damages using GA are the same as the induced damages. The final damages detected from the IRR GA using 500 for the population size and 2 for the size of the tournament selection are plotted in Fig. 14.4. Even though the locations of the induced damages are at structural element 1 and 10 with each 5 % reductions of the member stiffness, the single-objective GA failed to detect locations and extent of those induced damages with large errors and noises.

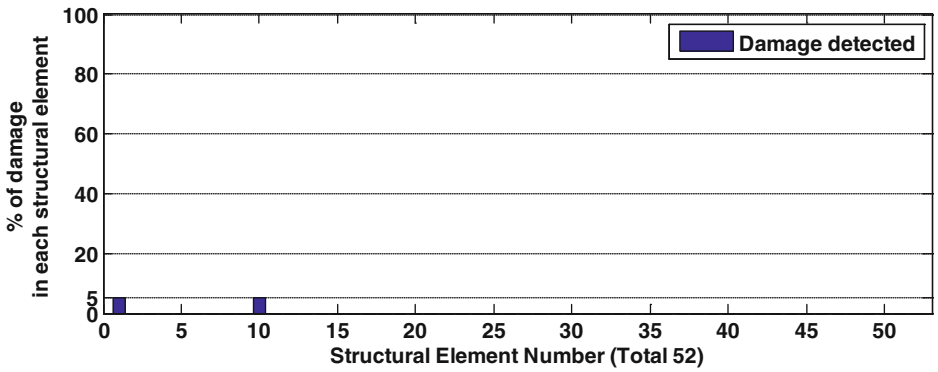

Fig. 14.5 Damages detected by multi-objective NS2-IRR GA approach

However, using a multi-objective NS2-IRR GA approach, all the induced damages are detected with correct locations and extent of the damages as shown in Fig. 14.5. The multi-objective NS2-IRR GA used 500 for population size, which is the same as that of single-objective IRR GA. It used a total of 130 generations to detect all induced structural damages. It should be noted that the trials of the single-objective IRR GA are $500 \times 400 = 200{,}000$, and the trials of the multi-objective NS2-IRR GA are $500 \times 130 = 65{,}000$. The total possible number of damage scenarios of the optimization domain is 101^{52} because each structural element has 101 cases of the damage scenarios from 0 to 100 % damage scenarios with 1 % discrete unit, and the 4-story prototype structure has 52 structural elements, expressed as non-italic numbers in Fig. 14.2. Thus, it should be noted that the multi-objective NS2-IRR GA uses a much smaller number of trials and offers exact solutions. Multi-objective NS2-IRR GA tried only $65{,}000/101^{52}$ cases (i.e., 3.8744e-098 % of the total possible damage scenarios). It is worth mentioning that the suggested multi-objective NS2-IRR GA has significant performance in solving this nonlinear optimization problem. The multi-objective NS2-IRR GA uses a crowding distance schema [i.e., Eq. (14.11)] and crowded operation selection method [i.e., Eq. (14.12)] in the step of assigning fitness values for the next generation of the GA to each individual and selection step to keep well fit individuals (i.e., solutions). These advanced fitness assigning methods and selection schema may prevent individuals of the population in the multi-objective NS2-IRR GA from premature convergence to local optimal solutions by keeping various individuals which have competitive design variables of the optimization [i.e., $\alpha_1\ \alpha_1\ \ldots\ \alpha_{el}$ from Eq. (14.8)].

14.3.2 Multiple Minor Damage Scenario Case 2

In order to do extensive investigations of the suggested methodologies of the structural damage detection, multiple minor damage scenario having damages in five different locations is examined as shown in Fig. 14.2b. All damages are expressed as thick dashed red lines in the structure. To investigate the robustness of the suggested damage detection methodology, damage locations are well scattered in the entire structures.

For the 4-story prototype structure, multi-objective NS2-IRR GA is applied with a population size of 1,000, where tournament selection size is 2, crossover rate is 0.9, and mutation rate is 0.01. In order to calculate two objectives of the hybrid multi-objective NS2-IRR GA, the first eight mode shapes are used with only global translational X and Y components of the mode shapes. For the *Objective*1, the first, third, fifth and seventh mode shapes are used, and for the *Objective*2 the second, fourth, sixth, and eighth mode shapes are used. Figure 14.6 shows near optimized population in the 1,000th generation. The near optimized individuals are well converged to zero values of the both objectives. Then, the $\boldsymbol{\alpha}$ of the individual, which has minimum summation values of the both objectives, is plotted as locations and extent of the detected damages. Even though 1 % errors in structural elements 1, 10, and 17 are found and three 1 % noises are also found as shown in Fig. 14.7, the overall induced damages are well detected. In order to remove these negligible minor errors and noises, the optimization problem domain is reduced to maximum 10 % possible damages based on currently detected damage information. With this reduced optimization domain, the population is fast converged to zero values of the both objectives, and one of the individuals is converged to zero values of the both objectives as shown in Fig. 14.8. The $\boldsymbol{\alpha}$ of the fully converged individual to zero values for the both objectives is plotted in Fig. 14.9. The hybrid multi-objective NS2-IRR GA with same GA properties, which are used in previous full damage domain, detected all the induced multiple minor damages, as shown in Fig. 14.9.

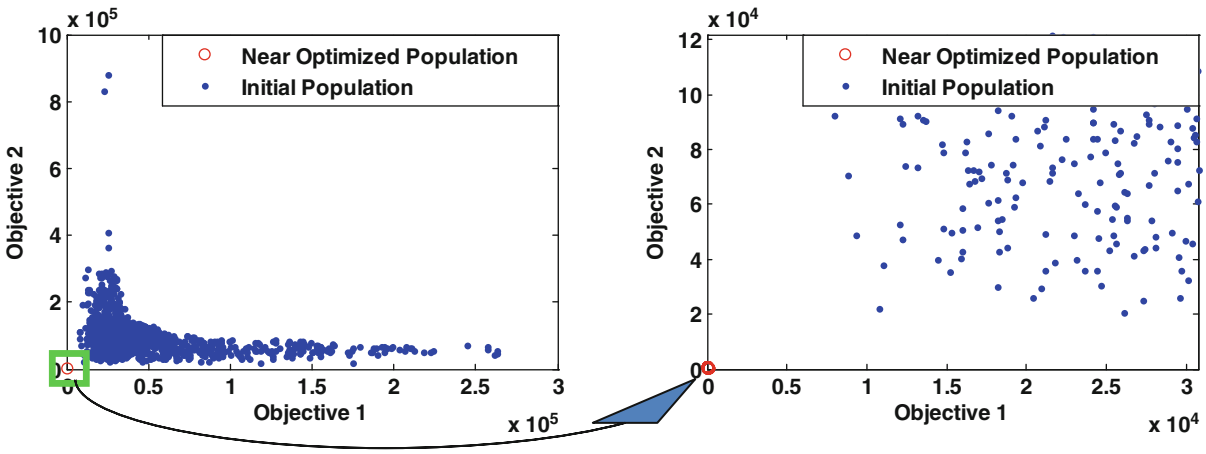

Fig. 14.6 Nearly converged population of multi-objective NS2-IRRGA in entire prototype structure

Fig. 14.7 Damages detected in entire prototype structure

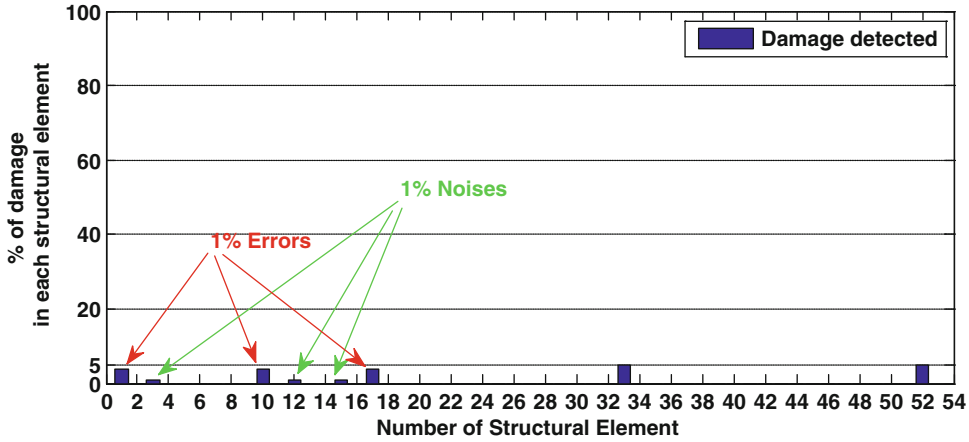

Fig. 14.8 Fully converged population of multi-objective NS2-IRRGA in entire prototype structure

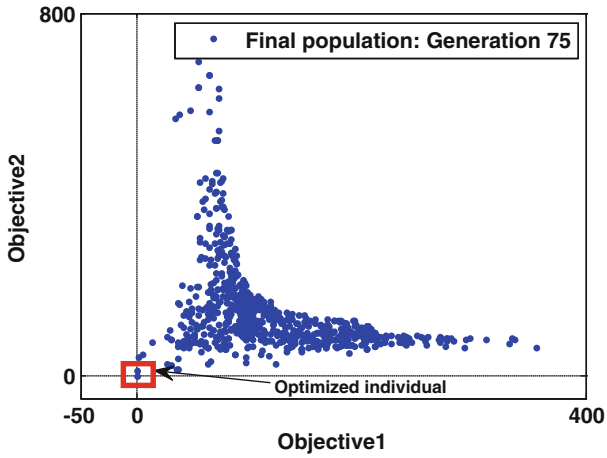

14.4 Conclusion

Modal strain energy as a damage index is widely used to detect structural damages. To localize and quantify damages, single-objective genetic algorithms have been used as a method of inverse problem solving. However, these approaches have provided less satisfying results to detect damages in 3-dimmentional structures. In this paper hybrid multi-objective genetic algorithms are proposed as a damage detection method by solving inverse problem to minimize change of the modified modal strain energy in each structural element. In order to investigate the performance of the proposed method, 3-dimensional 2-bay

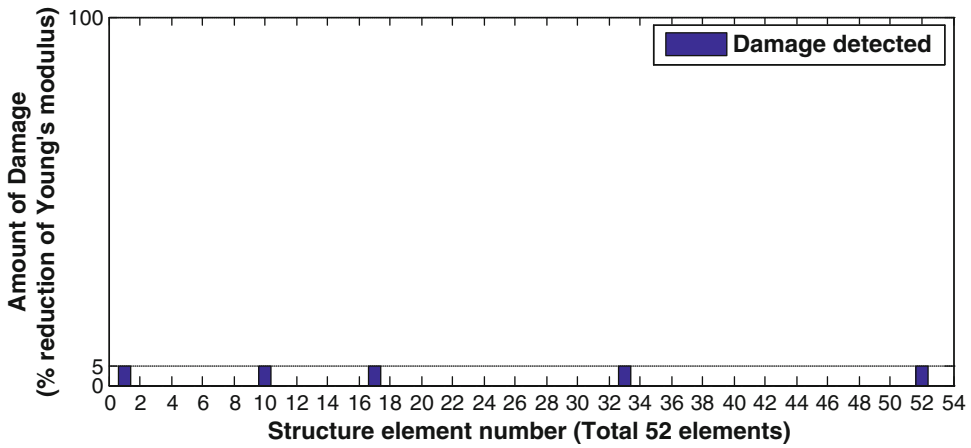

Fig. 14.9 Damages detected in entire prototype structure

4-story modular steel structures are designed and numerically modeled using finite element methods. The performance of the proposed approach is compared to those of the traditional approach using single-objective genetic algorithm. The newly proposed approach showed significantly better performance in detecting multiple minor damages, which have little effect to change of the modal properties of the structure. The newly proposed approach used incomplete mode shapes containing only global translational components to remove difficulties of measuring rotational components of the mode shapes. For the future study, physical laboratory experimental model will be used to validate proposed damage detection method using various damage scenarios.

Acknowledgement The authors acknowledge the support provided by Royal Dutch Shell through the MIT Energy Initiative, and thank chief scientists Dr. Dirk Smit, Dr. Sergio Kapusta, project manager Dr. Yile Li, and Shell-MIT liaison Dr. Jonathan Kane for their oversight of this work. Thanks are also due to James Long for his help with finalizing this paper.

References

1. Petro SH, Chen SE, GangaRao HVS, Venkatappa S (1997) Damage detection using vibration measurements. In: IMAC XV – 15th international modal analysis conference 1997
2. Carrasco CJ, Osegueda RA, Ferregut CM, Grygier M (1997) Damage localization in a space truss model using modal strain energy. In: Proceedings-SPIE the international society for optical engineering, pp 1786–1792
3. Shi ZY, Law SS, Zhang LM (2000) Structural damage detection from modal strain energy change. J Eng Mech 126(12):1216–1223
4. Yan WJ, Huang TL, Ren WX (2010) Damage detection method based on element modal strain energy sensitivity. Adv Struct Eng 13(6):1075–1088
5. Friswell MI, Penny JET, Garvey SD (1998) A combined genetic and eigensensitivity algorithm for the location of damage in structures. Comput Struct 69(5):547–556
6. Au FTK, Cheng YS, Tham LG, Bai ZZ (2003) Structural damage detection based on a micro-genetic algorithm using incomplete and noisy modal test data. J Sound Vib 259(5):1081–1094
7. Raich AM, Liszkai TR (2007) Improving the performance of structural damage detection methods using advanced genetic algorithms. J Struct Eng 133(3):449–461
8. Wang FL, Chan TH, Thambiratnam DP, Tan AC, Cowled CJ (2012) Correlation-based damage detection for complicated truss bridges using multi-layer genetic algorithm. Adv Struct Eng 15(5):693–706
9. Sazonov E, Klinkhachorn P (2005) Optimal spatial sampling interval for damage detection by curvature or strain energy mode shapes. J Sound Vib 285(4):783–801
10. Raich AM, Ghaboussi J (2000) Evolving structural design solutions using an implicit redundant genetic algorithm. Struct Multidiscip Optim 20(3):222–231
11. Cha Y-J, Agrawal AK, Kim Y, Raich AM (2012) Multi-objective genetic algorithms for cost-effective distributions of actuators and sensors in large structures. Expert Syst Appl 39(9):7822–7833
12. Cha Y-J, Raich AM, Barroso LR, Agrawal AK (2013) Optimal placement of active control devices and sensors in frame structures using multi-objective genetic algorithms. Struct Control Health Monit 20(1):16–44
13. Cha Y-J, Kim Y, Raich AM, Agrawal AK (2013) Multi-objective formulation for actuator and sensor layouts of actively controlled 3-D buildings. J Vib Control 19(6):942–960
14. Deb K, Pratap A, Agarwal S, Meyarivan TAMT (2002) A fast and elitist multiobjective genetic algorithm: NSGA-II. IEEE Trans Evol Comput 6(2):182–197

Chapter 15
Development of Vibration Damper for Energy Harvesting

Nobuyuki Okubo, Taiju Kunisaki, and Takeshi Toi

Abstract In vibration engineering, unnecessary vibration energy can be dissipated by a damper into not only heat energy but also electric energy for energy harvesting. But a common damper for energy harvesting has to be tuned into a resonance in order to reserve large vibration and therefore for frequency varying case, the efficiency is very low and the application is limited. In this study a special damper system is so designed as to generate sufficient electric power even for frequency varying case based on two approaches: the resonance of the damper can be adjusted corresponding to the input frequency and the fixture of the damper has multiple resonances which coincide the structural resonances. The damper system consisted of permanent magnet and coil is verified to have variable resonance and the resonances of the damper fixture are found to have coincident resonances. Finally the damper system is applied to a motor bike where sufficient power is generated in case of varying engine rotation.

Keywords Vibration damper • Energy harvesting • Magnet • Resonance frequency • Input frequency varying

15.1 Introduction

Currently, energy saving and replacement from oil resources is widespread in various fields for global warming prevention such as emissions of carbon dioxide. In the field of vibration many studies are carried out upon attenuate unwanted vibration, instead of dissipating into thermal energy, converted to the effective electric energy by a damper.

However, since it is necessary to cause resonates with the vibration of the input, when the frequency of the vibration is varied, the efficiency is lowered and consequently the application is limited. Therefore in this study a special damper system is so designed as to generate sufficient electric power even for frequency varying case based on two approaches: the resonance of the damper can be adjusted corresponding to the input frequency and the fixture of the damper has multiple resonances which coincide the object structural resonances.

First the mechanism to vary the resonance frequency of the damper is described and the developed damper is tested and evaluated its performance. Then the fixture is designed to coincide the resonances of the object structure and tested. Finally the damper with the fixture is installed on a motor bike and when the input frequency is varied due to engine rotation, it is verified whether there is effective in damping of vibration and power generation.

15.2 Variable Resonance Frequency and Power Generation

The mechanism to vary the resonance frequency of the damper is described and the possible frequency range and generated power are measured.

N. Okubo (✉) • T. Kunisaki • T. Toi
CAMAL, Chuo University, 1-13-27 Kasuga, Bunkyo-ku, Tokyo 112-8551, Japan
e-mail: okubo@mech.chuo-u.ac.jp

A. Wicks (ed.), *Structural Health Monitoring, Volume 5: Proceedings of the 32nd IMAC, A Conference and Exposition on Structural Dynamics, 2014*, Conference Proceedings of the Society for Experimental Mechanics Series, DOI 10.1007/978-3-319-04570-2_15,

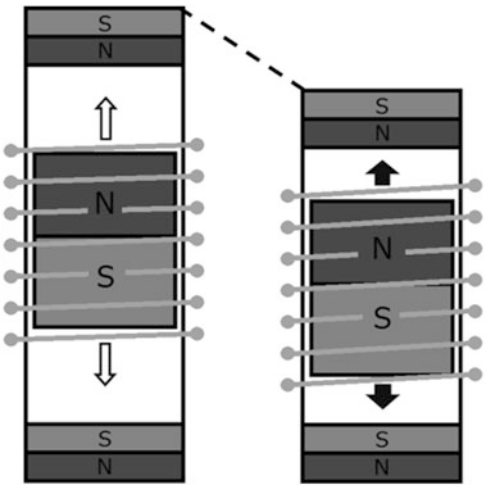

Fig. 15.1 Principle of damper

Fig. 15.2 Developed damper

15.2.1 Overview of the Damper Development

The principle of the damper is shown in Fig. 15.1 which consists of three permanent magnets; two fixed magnets at the top and bottom and one moving center magnet in a pipe, where the poles of two magnets face each other is the same to hold the reaction force. The coil is wound outside the pipe and generates current due to magnetic induction during the center magnet is moving. This mechanism provides the attenuation of the vibration and power generation at the same time. Also when the distance between the top and bottom magnet is decreased, the reaction force is increased and consequently the stiffness is increased namely the resonance frequency is shifted higher. Figure 15.2 shows the photo of the developed damper. Three cylindrical neodymium magnets of height 20, 30 and 8 mm with 20 mm diameter each are placed in acrylic pipe of outer diameter 22 mm, inner diameter 20 mm and height 130 mm. The coil of 0.2 mm enameled wire is wrapped outside of the pipe at the center height whose width is 40 mm approximately 200 laps with 4 layers that is 800 laps. At both ends of the coil a carbon film resister is connected to measure the generated electric power.

To adjust the distance between the magnets, a bolt and nut with M12 and pitch 1.5 mm is installed at the top and by turning the bolt the distance can be changed to vary the resonance frequency of the damper.

15.2.2 Evaluation on the Performance of the Damper Alone

For evaluation on the performance, the damper alone is excited by an electromagnetic shaker with chirp sine signal of linear sweep rate 1 Hz/s. The power generated in the resistance by the vibration of the center magnet is measured and transformed

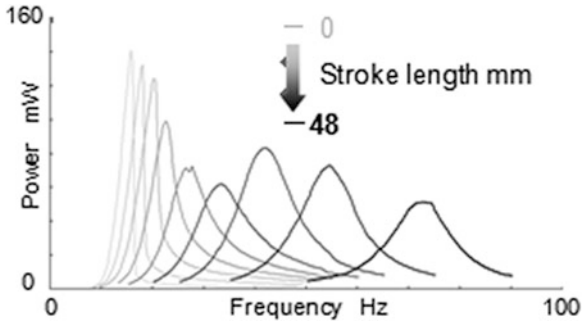

Fig. 15.3 Generated electric power in each amount of strokes

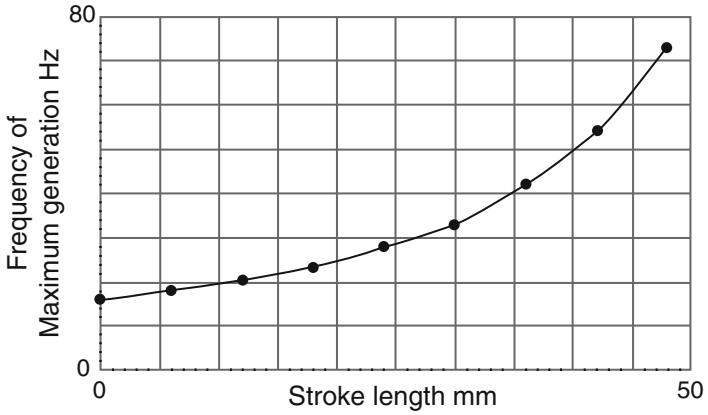

Fig. 15.4 Relations of amount of stroke and frequency of maximum generation

by FFT once per 0.5 s. Nine stroke length (the bolt sink, 6 mm each for 0–48 mm range) are taken into account. In spite of that the excitation force is varied with respect to the input frequency, the output of the amplifier for the exciter is adjusted to gain about 10 N at the frequency with maximum generation.

Figure 15.3 shows the effective electric power with respect to each stroke (darker the stroke larger). It is observed that the maximum generation frequency is shifted higher when the stroke is larger. Also the maximum power is decreased in function of frequency because the amplitude of vibration is decreased. The reason why the generated maximum power is especially decreased for 20 to 30 Hz range is that the center magnet is moved at the middle of the pipe and stayed within the width of the coil. Nevertheless it is verified that by adjusting the stroke namely the distance between the top and bottom magnet, the resonance frequency can be appropriately adjusted as shown in Fig. 15.4.

15.3 Fixture with Two Coincide Resonance Frequencies

In order to generate the power for wider frequency range, the fixture of the damper is so designed as to have two resonance frequencies coincided with two those of object structure. Thus the damper can work to attenuate the vibration and at the same time to reserve enough movement of the center magnet of the damper to generate the power. The basic configuration of the fixture is two legs: one leg is allocated at the maximum amplitude point of the one resonance mode shape of the object structure and the other leg at the other resonance mode. A simple box structure is used to verify this idea.

15.3.1 Fixture Design

A simple aluminum box shown in Fig. 15.5 with side wall partly cuts is used (height 110 mm, width 110 mm, length 800 mm, thickness 2 mm) excited at the end plate in transverse direction. Based on modal testing, the box has two resonance mode shapes shown in Fig. 15.6 at 26 and 63 Hz. The maximum amplitude point of these two mode shapes marked in circle in the figure respectively is apart 200 mm.

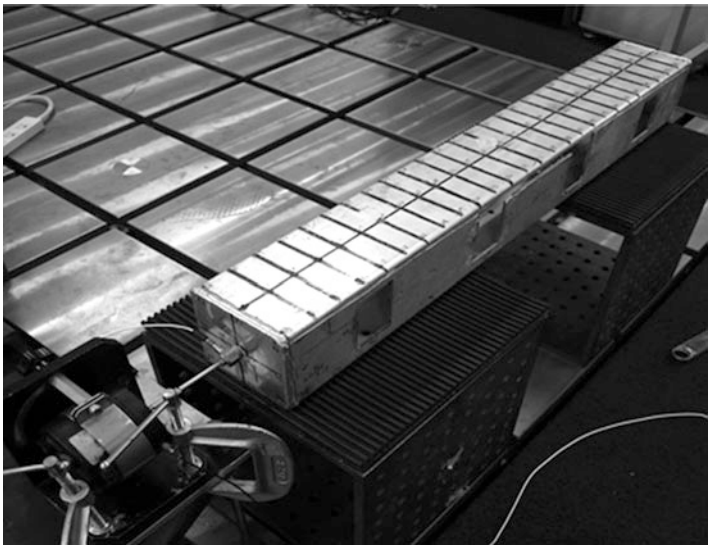

Fig. 15.5 Test object: 1 (box structure)

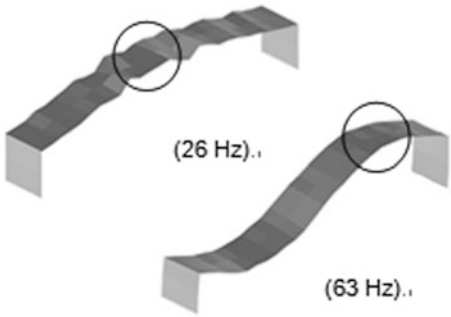

Fig. 15.6 Mode shapes (Test object: 1)

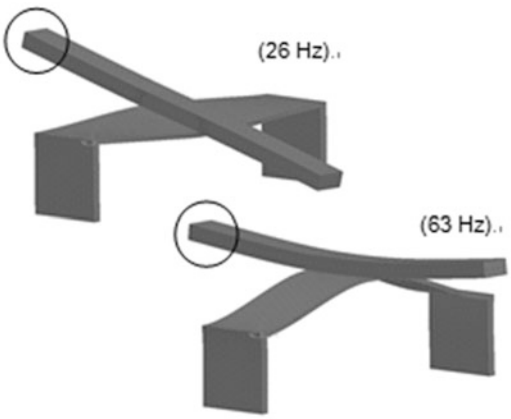

Fig. 15.7 Mode shapes of fixture

According to the concept of dynamic damper, the mass and stiffness of the damper is tuned to have approximately the same resonance frequency of the object structure. Therefore the fixture should be considered the following two targets:

1. To have two resonance frequencies, 26 and 63 Hz besides the damper installed point to have the maximum amplitude at both resonances.
2. The distance between two legs is 200 mm.

Thanks to CAE simulation, a fixture shown in Fig. 15.7 is found to have two resonances at 26 Hz (bridge torsion mode) and 63 Hz (bridge bending mode) and the same maximum amplitude point at left end of bestride beam marked in circle.

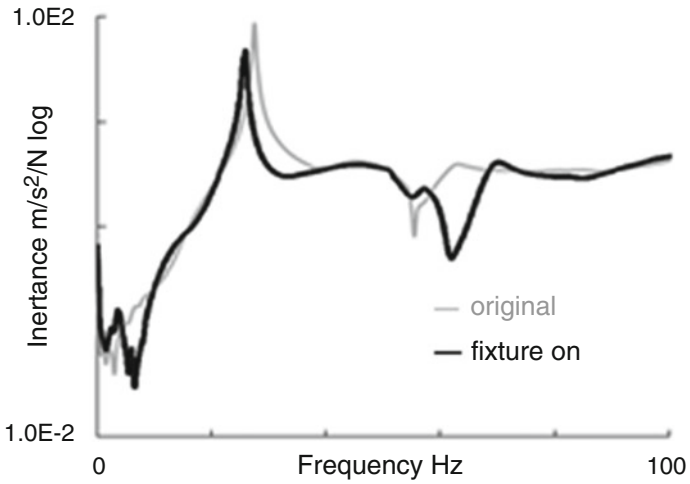

Fig. 15.8 FRF at the point of maximum amplitude of first mode

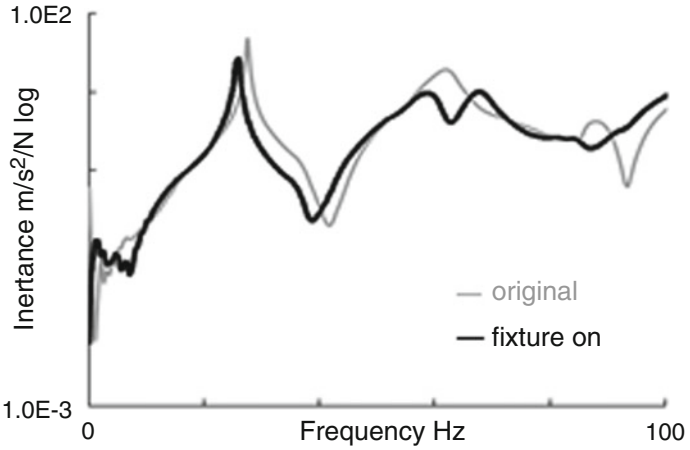

Fig. 15.9 FRF at the point of maximum amplitude of second mode

15.3.2 Verification of the Fixture as Damper

The fixture under consideration is tested whether it meets the requirement. Figures 15.8 and 15.9 show the FRF of the maximum amplitude point of 26 Hz mode and that of 63 Hz mode respectively, where the dark line shows the original without the fixture and the light with the fixture. Both 26 and 63 Hz peak can be suppressed by the fixture that confirms the dynamic damper work.

15.3.3 Verification of Fixture as Power Generation

For efficient energy harvesting, the damper is always activated for wider frequency range and therefore Fig. 15.10 shows the comparison of FRF at the maximum amplitude point of the fixture namely the left end of bestride beam in dark line against FRF of 26 Hz maximum amplitude point without the fixture in light bold line and that of 63 Hz in light line. It can be seen that the damper installed point is vibrated large at not only 26 Hz but also 63 Hz which guarantees efficient power generation.

15.4 Application to Motor Bike

The proposed approach on variable resonance of the damper and the fixture coincided with two resonances of the object structure is applied to a motor bike.

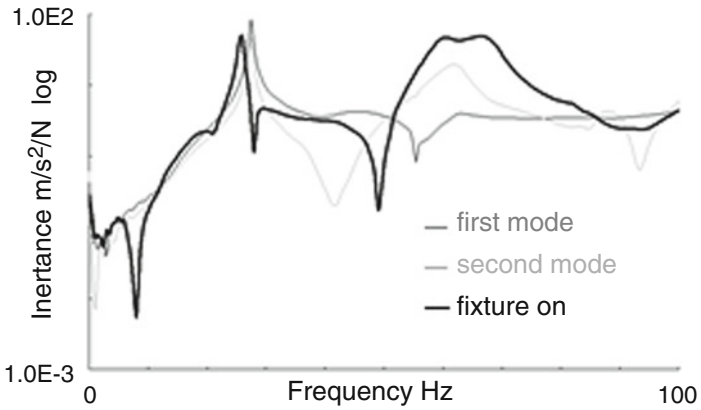

Fig. 15.10 Comparison of FRF for power generation

Fig. 15.11 Test object: 2 (motor bike)

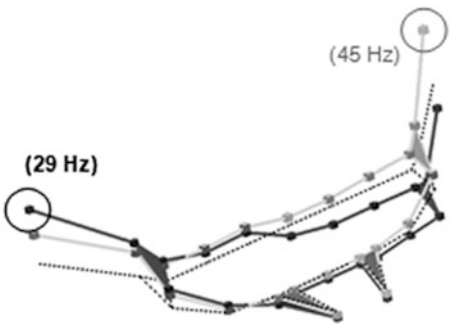

Fig. 15.12 Mode shapes (Test object: 2)

15.4.1 Target Mode and Fixture Design

Figure 15.11 shows the motor bike especially focused on the handle vibration. Taking into account the variable range of damper resonance and the engine rotation, two mode shapes at 29 and 45 Hz shown in Fig. 15.12 are on target. The maximum amplitude point of two mode shapes are marked in the figure whose distance is 400 mm.

Therefore the requirements for damper design are;

1. To have two resonance frequencies 29 and 45 Hz and besides the damper installed point to have the maximum amplitude at both resonances
2. The distance of two legs is 400 mm.

By good use of CAE simulation, a damper system shown in Fig. 15.13 is proposed where the fixture behaves as the same as the previous one that is torsion mode at 29 Hz and bending mode at 45 Hz.

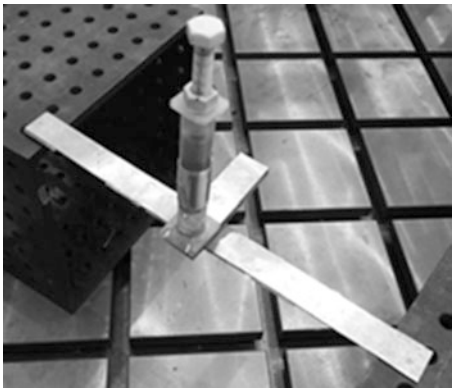

Fig. 15.13 Damper system developed

Fig. 15.14 Setup

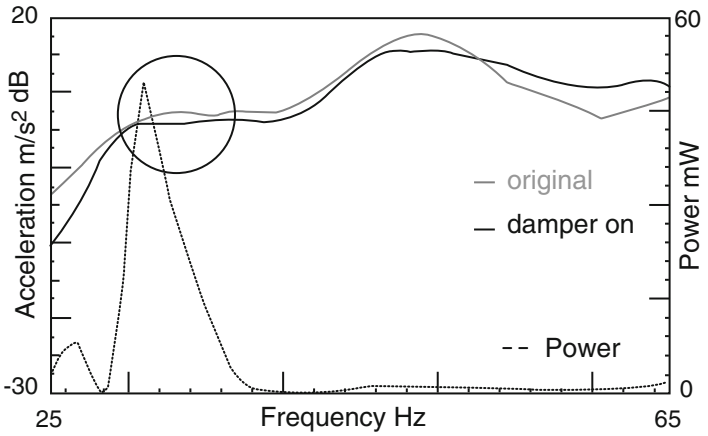

Fig. 15.15 Comparison of response (29 Hz) and generated electric power

15.4.2 Verification of Vibration Reduction and Power Generation

The damper system developed is installed on the motor bike as shown in Fig. 15.14. When the engine rotates from 1,000 to 4,500 rpm during idling, the vibration and generated power are measured at 60 rpm interval and transformed by FFT into frequency domain. The damper stroke is set by the bolt to coincide 29 Hz and the vibration and generated power are monitored at the frequency of the first order of engine rotation (for example 600 rpm = 10 Hz) while engine running up.

Figure 15.15 shows the comparison of vibration in acceleration at the maximum amplitude point of 29 Hz mode without the damper system in light line and with in dark line together with the generated power in dot line. Around 29 Hz range marked in the circle, the vibration can be suppressed and at the same time the maximum power is generated.

Also in Fig. 15.16 in case of the stroke set 45 Hz the vibration can be efficiently suppressed and the power is harvested. Although the stroke is manually adjusted, it is possible to turn the bolt to track the first order of engine rotation automatically and as a result efficient power generation can be expected at every engine rotation.

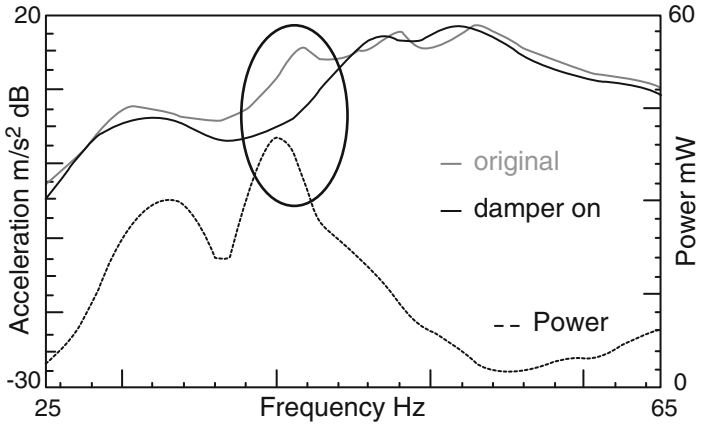

Fig. 15.16 Comparison of response (45 Hz) and generated electric power

15.5 Conclusions

1. A vibration damper can be designed to vary its resonance frequency to coincide the input frequency.
2. A fixture can be design to coincide its resonance frequencies with those of the object structure as dynamic damper and besides the damper installed point is always the maximum amplitude.
3. The damper system is applied to a motor bike and it is confirmed that the vibration can be suppressed as dynamic damper and at the same time enough power can be generated even when the input frequency varying case.

References

1. Okubo N (1982) Modal analysis of mechanical structure. Chuo University Press
2. Seto K (2010) Application of dynamic damper. Korona Shuppan
3. Mapelli F, Sabbioni E, Tarsitano D (2010) Energy recovering from vibrations in road vehicle. IMAC-XXVIII, pp 223–231
4. Torincass S, Bonisoli E, DiMonaco F, Moos S, Repetto M, Freschi F (2011) Nonlinear dynamics of an electro-mechanical energy scavenger. IMAC-XXXIX, pp 171–181
5. Green P, Worden K, Atallah K (2010) Performance of linear and nonlinear resonance frequency energy harvesters under uncertain loading conditions. ISMA-2010, pp 4775–4790

Chapter 16
Structural Damage Detection Using Soft Computing Method

S.J.S. Hakim, H. Abdul Razak, S.A. Ravanfar, and M. Mohammadhassani

Abstract Damage in structures can negatively affect their functionality and safety and leads to failure. Thus it is very important to monitor structures for occurrence, location and severity of damage. Structural health monitoring techniques provide information on the life expectancy of structures simultaneously detects and locates structural damage. Damage identification of structures based on vibration has always been important subjects and are being rapidly used to damage and location of structures. Artificial Neural Networks (ANNs) as a soft computing method using dynamic parameters of structures have been utilized increasingly for structural damage detection due to their excellent pattern recognition capability. Dynamic parameters of structure are easy to implement for damage identification and can directly linked to the topology of structure. This study presents the application of ANN for damage identification in steel beams using dynamic parameters. For identification of severity and location of damage, at first, five individual neural networks corresponding to mode 1 to mode 5 are considered. At the second step, a method based on neural network ensemble is proposed to combine the outcomes of the individual neural networks to a single network. Ensemble results were evaluated and discussed according to the differences between predicted output by ANN and desire data (target data) obtained from experimental modal analysis of structure.

Keywords Artificial neural networks • Mean square error • Modal analysis • Damage detection • Neural network ensemble

16.1 Introduction

Reduction in the structural stiffness produces changes in the dynamics characteristics, such as the natural frequencies and mode shapes. The fact that changes in structural properties cause shifts in natural frequencies, warrant the use for structural health monitoring and damage detection. Dynamic characteristics have been applied increasingly for damage detection using artificial neural networks (ANNs) as an artificial intelligence technique.

For example, Guo and Wei [1] proposed a method to detect damages of different locations and severity on a simply supported rectangular beam using ANN based on the frequency change parameters. This method had strong robustness that was not impacted by small model errors and the detection accuracy was not influenced by incomplete measurement information. Kanwar et al. [2] developed a correlation between the damage in the 2D rigid frame of the RC three-storey building with dynamic parameters using an ANN model. In this study, the dynamic characteristics were obtained analytically under different levels of damage using modal analysis of the frame by changing the rigidity of the structure. In this work, authors showed that an increasing of the damage index in each storey with reducing in the frequency during the damage. It was noted by the authors that the trained neural network could predict the damage index values in the RC frame building based on their approach with maximum error of 6 % which indicates high accuracy for the prediction of damage.

S.J.S. Hakim (✉) • S.A. Ravanfar • M. Mohammadhassani
StrucHMRS Group, Department of Civil Engineering, University of Malaya, Kuala Lumpur, Malaysia
e-mail: jamalhakim@siswa.um.edu.my; r.ravanfar@gmail.com; mmh356@yahoo.com

H.A. Razak
Department of Civil Engineering, University of Malaya, Kuala Lumpur, Malaysia
e-mail: hashim@um.edu.my

A. Wicks (ed.), *Structural Health Monitoring, Volume 5: Proceedings of the 32nd IMAC, A Conference and Exposition on Structural Dynamics, 2014*, Conference Proceedings of the Society for Experimental Mechanics Series, DOI 10.1007/978-3-319-04570-2_16,

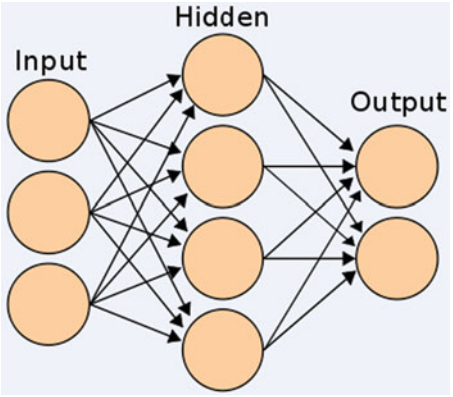

Fig. 16.1 Architecture of a typical multilayer feedforward neural network

The technical literature for past two decades on structural damage identification using ANNs with modal parameters were presented and reviewed by Hakim and Abdul Razak [3]. Also many other research efforts were attempting to apply ANNs to identify damage in structural engineering [4–7].

The main focus of this research is to investigate the applicability of using ANNs trained with natural frequencies and mode shapes data to identify the damage in I-beam structures. In this study, the inputs to the network for predicting the severity and location of damage were include the first five flexural modes and all corresponding mode shape values at the points on the centerline of beams (except the points at supports, as give 0 values in all modes). For identification of severity and location of damage, at first, five individual neural networks corresponding to mode 1 to mode 5 are considered. At the second step, a method based on neural network ensemble (NNE) is proposed to combine the outcomes of the individual neural networks to a single network. In the NNE, five individual networks are trained, and then the outputs of these individual neural networks are combined in an ensemble network. Ensemble network has advantages of all individual networks from different vibrational modes. The required data for the ANNs are obtained from experimental modal analysis.

16.2 Artificial Neural Networks (ANNs)

ANNs are simplified models of the human brain and evolved as one of the most useful mathematical concepts used in almost all branches of science and engineering. They have the ability to learn from experience in order to improve their performance and to adapt themselves to changes in the environment [8–10]. ANNs can provide meaningful answers even when the data to be processed include errors or are incomplete and can process information extremely rapidly when applied to solve real problems.

A typical neural network has three layers namely the input layer, the hidden layer and the output layer. Signals are received at the input layer, pass through the hidden layer, and reach the output layer. Each layer can have a different number of neurons and activation functions such as sigmoid and linear functions. All neurons are interconnected to the neurons in the next layer through their weights. Architecture of an ANN with three neurons in input layer, four neurons in hidden layer and two neurons in output layer is demonstrated in Fig. 16.1. Backpropagation algorithm in multi-layer feed-forward supervised networks is considered to be the most applicable due to the mathematical design of the learning complex nonlinear relationships [11]. This algorithm has a performance index, which is the least Mean Square Error (MSE) [12–15]. In MSE algorithm, the error is calculated as the difference between the target output and the network output. Among various neural networks, Multi-Layer Perceptron (MLP) is most commonly used in structural identification problems. Their applications to engineering problems have been summarized and reported in literature [16, 17].

16.3 Damage Identification Strategy and Experimental Modal Analysis

In this study, steel I-Beam structure is investigated experimentally. Four identical healthy steel beams with length of 3,200 mm including a 100 mm overhang at both support ends were considered. The dimensions of the beams were 75 mm flanges width, section depth of 150 mm and thickness of 7 and 5 mm for flange and web, respectively. The modulus of elasticity of steel was 2.1×10^{11} kg/m^2, the Poisson's ratio was 0.2 and the density was 7,850 kg/m^3. To identify the modal

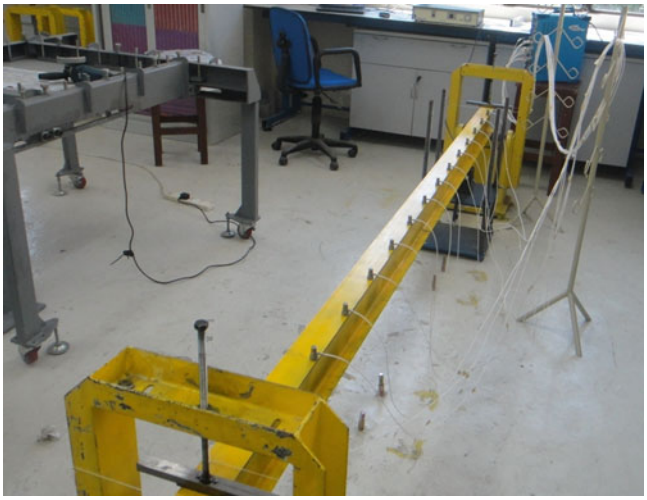

Fig. 16.2 Experimental set up

Table 16.1 First five natural frequencies for the undamaged I-Beams

	F1	F2	F3	F4	F5
B1	56.21	202.01	440.95	709.42	951.21
B2	55.88	198.56	439.47	713.31	947.11
B3	55.74	206.16	440.26	716.21	967.21
B4	54.55	202.47	440.58	715.95	963.94

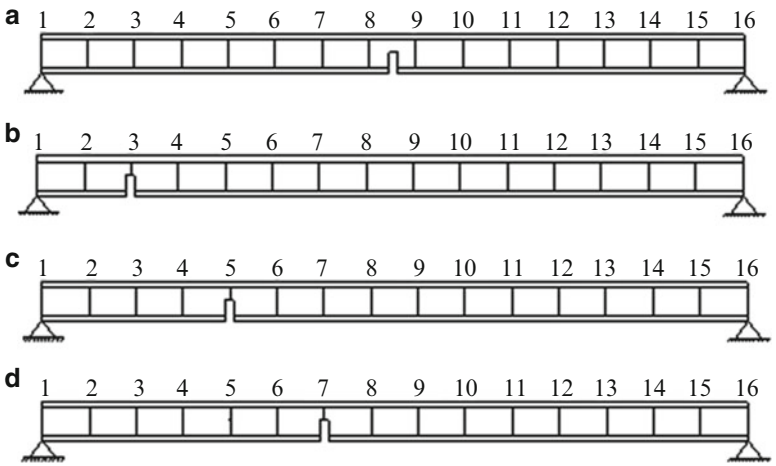

Fig. 16.3 Location of single damages. (**a**) Beam B1 (**b**) Beam B2 (**c**) Beam B3 (**d**) Beam B4

parameters of the structure, experimental modal analysis and modal testing with different damage scenarios was performed. Experimental modal analysis is the process of experimentally identifying the modal parameters (natural frequencies, mode shapes and damping ratio) of a structure from the acquired data. A photo of the experimental test set up of beam is illustrated in Fig. 16.2.

The four I-Beam structures were tested in its undamaged state and under different damaged states to determine the first five natural frequencies and mode shapes. Table 16.1 lists the first five natural frequencies for the undamaged I-Beams.

In the experimental study various damage scenarios were given to the test structures. These scenarios consisted of 8 locations with 25 severities for each location. The eight damage locations were at L/15, 2 L/15, 3 L/15, 4 L/15, 5 L/15, 6 L/15, 7 L/15 and L/2 away from the left support of beams. The 25 damage severities with 5 mm width and depth of 3–75 mm with the increment of 3 mm were gradually induced for each severity. Four identical steel beams were investigated in this research. These beams including B1–B4 were considered to single damaged at above locations. Locations of damage in beams B1–B4 are depicted in Fig. 16.3.

The same experimental procedure as described in the undamaged cases repeated for damaged states. Any reduction in stiffness of a structure can lead to a change in the dynamic parameters such as natural frequencies and mode shapes. A change in these parameters from the datum state indicates a possible defect in the structure. The results of the extracted first five natural frequencies of the undamaged and all damaged states for beam B1 are demonstrated in Fig. 16.4.

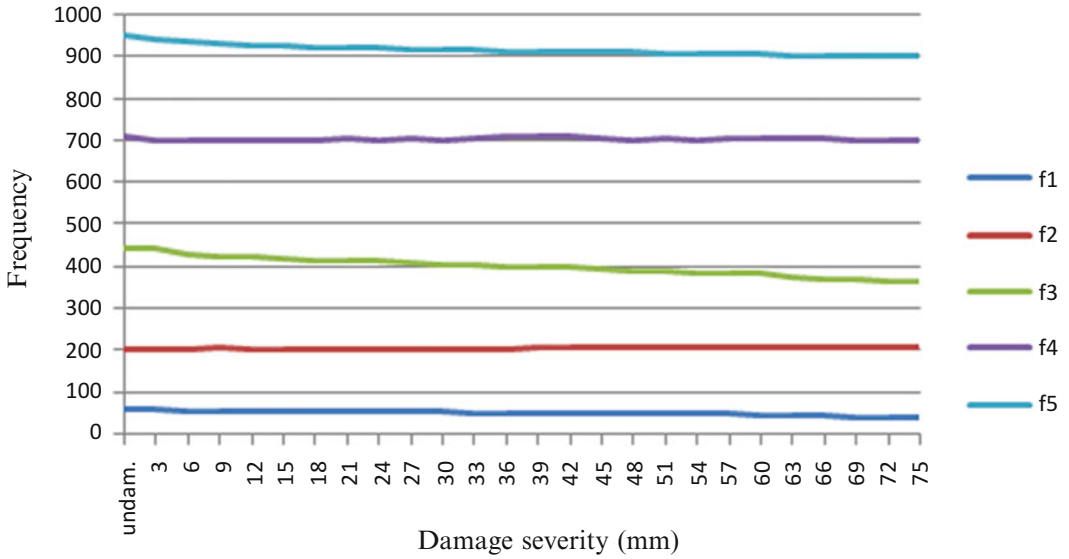

Fig. 16.4 Influence of damage severities on natural frequencies of first five mode shapes in B1

Figure 16.4 specify that the natural frequencies of a structure drop when damage is induced. According to this figure natural frequencies decreases with the increase of damage extent. For this reason natural frequency can be applied as an indicator to damage identification in the beam structure. A mode shape that is an indication of the shape of vibrational deformation of the system can give more information about local damage than natural frequencies and are much more sensitive to damage location of a structure. However in this study, mode shape variations of first five modes between undamaged and different damage severities of 3–75 mm for all beams were extracted. According to mode shape results, changes in mode shapes can be happened with different severities of damage. Also it can be concluded that when the severity of damage is high, the mode shape changes will larger. Mode shapes show high sensitivity of mode shapes to local damage.

16.4 Damage Detection of I-Beam Structures Using ANNs

Development and application of ANNs for damage identification using modal parameters of I-beam structures are investigated in this section. In this study, the inputs to the network for predicting the severity and location of damage are including the first five flexural modes and all corresponding mode shape values at the points on the centerline of beams.

As mentioned earlier, for identification of severity and location of damage, at first, five individual neural networks corresponding to mode 1 to mode 5 are considered. At the second step, a method based on neural network ensemble (NNE) is proposed to combine the outcomes of the individual neural networks to a single network.

Several numbers of multilayer feedforward neural networks using first natural frequency and all mode shape values of mode 1 at the points on the centerline of beam to predict damage characteristics of I-beams, which are damage severities and locations, are constructed and designed. Therefore the input layer of ANN has 15 neurons comprising of the one input that is first natural frequency and fourteen inputs corresponding to all mode shape values of mode 1 at the points on the centerline of beam (except the points at supports). Output layer of ANN has two neurons consists of severity and location of damage. The ratio of damage depth to height of beam (d_d/h) and the ratio of damage location from support to length of beam (l_d/L), were considered as damage severity and damage location indices. Therefore, the inputs and outputs of ANN for mode 1 is an array as:

$$\{f_1, \phi_{1,2}, \phi_{1,3}, \phi_{1,4}, \phi_{1,5}, \phi_{1,6}, \phi_{1,7}, \phi_{1,8}, \phi_{1,9}, \phi_{1,10}, \phi_{1,11}, \phi_{1,12}, \phi_{1,13}, , \phi_{1,14}, \phi_{1,15}, d_d/h, l_d/L\}$$

In this array, f and ϕ are representing natural frequency and mode shape values. The number of "1" stands for first mode shape. Also, numbers 2–15 stand for mode shapes values at the points 2–15 in the centerline of beam. Mode shape values for points 1 and 16 which are in the supports provide the value of 0 and have not considered. For example, $\phi_{1,2}$ represents the value of first mode shape at node 2 in test specimen.

In this section 208 different sets of data from undamaged and damaged I-beams with single location of damage were considered to ANN. These data were collected from experimental research work carried out at light structure laboratory of University of Malaya (UM). In this research, divisions of the datasets were carried out into training, validation and testing datasets. Out of the 208 datasets, 146 (70 %) were used as training datasets, while the remaining data (30 %) are used for validation and testing phase.

In this study, feedforward backpropagation algorithm is applied for ANN training. At first an input vector as mentioned earlier was fed to the input layer. These input vectors produce a set of output. The difference between the given output and the target output is error, which will propagate through the network in backward step.

The process of training is successfully completed, when the iterative process has converged. During this process, the mean square error (MSE) will be minimized, and consequently the output of ANN will be closed to the target output. An accurate trained ANN gives successful damage identification when a new sample is given as input.

Alyuda Neuro Intelligence software, version 2.2 [18] is used for the purpose of training. Once the network is trained using training datasets, it is ready for predicting the severity and location of damage in the beam structure. The datasets were normalized between −1 and 1 and fed to the input neurons. The training process continues to update and adjust the weights of the ANN until the network can produce satisfactory outputs compared to target values. The training process was stopped when any of the following conditions were satisfied:

1. The maximum number of iterations reached 50,000.
2. The mean square error (MSE) of the network for the training set reached 0.00001.

Many architecture networks having different conditions such as, connectivity weights, the numbers of hidden layers and the numbers of neurons in each layer, type of activation function in hidden and output layers, were conducted, trained and tested using available datasets in this work.

According to results, the network architecture decided was 15-7-4-2. In this network absolute errors for testing and validation datasets are lower than other networks. Consequently, the correlation of this network is higher than other networks. However this network is selected as the best possible architecture for predicting severity and location of damage in I-beam structures with single damage and good convergence has been achieved.

This architecture comprises of 15 neurons in the input layer corresponding to the first natural frequency and 14 inputs corresponding to all mode shape values of mode 1 at the points on the centerline of beam, two hidden layer with 7 and 4 neurons and 2 neurons in the output layer corresponds to severity and location of damage in the structure. The final architecture for this network is depicted in Fig. 16.5.

The network is then trained until the training error reach minimum and the network is stable. The MSE and absolute training error for this network reach to 0.001878 and 0.82 %, respectively. After that, the network was saved and the corresponding connectivity weights were kept. Comparison of predicted damage severity and location by ANN and actual value from experimental testing (target value) for training datasets are depicted in Figs. 16.6 and 16.7.

As can be seen in Figs. 16.6 and 16.7, the selected network was capable in providing good correlation between the modal parameters information and extent and location of damage. This network has minimum error and maximum correlation as compared to other networks. The value of correlation was 0.9984 for damage severity and 0.9579 for damage location. According to results, the outcomes for damage severities were better than the results for damage locations. The low errors and high correlation values for damage severity obtained from the architecture of 15-7-4-2 show that, this network was quite accurate in predicting damage severity for single damage cases, but was less accurate in locating the damage.

Same architecture as explained in previous section is applied for predicting damage severity and damage location of I-beams with single location of damage using second, third, fourth and fifth natural frequency and mode shapes values. From the performance of individual networks it was apparent that the severity prediction of modes 1, 3 are more accurate for all single damage cases. Networks of modes 1 and 3 could predict the severity of damage with the maximum absolute error of 0.92 and 1.25 % for testing datasets, respectively. Also the correlation of all datasets for these networks was 0.9914 and 0.9954, respectively. One of the main reasons of the larger errors in the neural networks trained with datasets of mode 2 and mode 4, is the existence of node points in some beams for these modes in single damage locations. Therefore, for damage severity prediction the individual networks of modes 2 and 4 provided larger errors than other networks, because damage index values (d_d/h) did not provide any information data for damages located at the node points of modes 2 and 4.

An ensemble neural network then combines the outputs of five individual networks and give merge the output results. In ensemble network the damage severities and damage locations predicted by ANN for all five individual networks were chosen as inputs, while the final damage severity and damage location were the required outputs of ensemble neural network. Therefore the initial architecture of ensemble network has ten neurons in input layer and two neurons in output layer, as shown in following array:

$$\{SM_1, LM_1, SM_2, LM_2, SM_3, LM_3, SM_4, LM_4, SM_5, LM_5, d_d/h, l_d/L\}$$

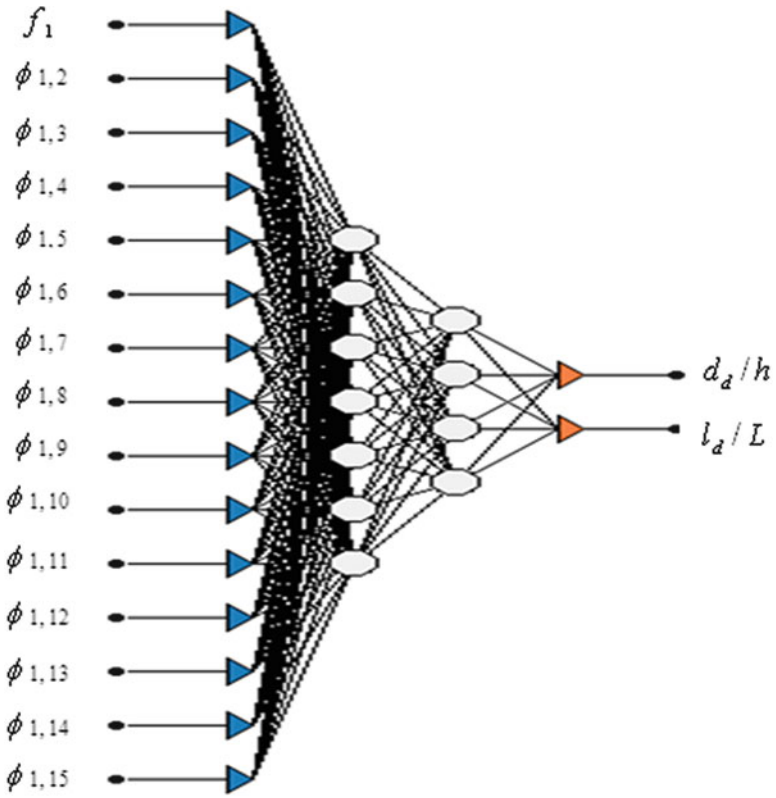

Fig. 16.5 Final architecture

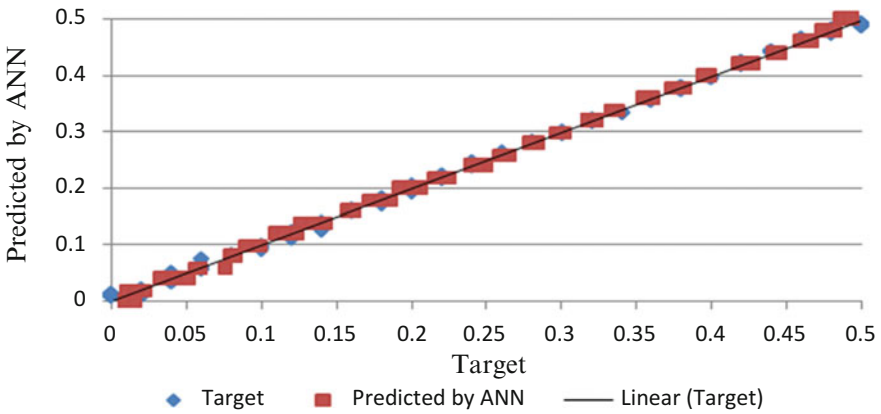

Fig. 16.6 Comparison of damage severity predicted by ANN and actual values of mode 1 (training)

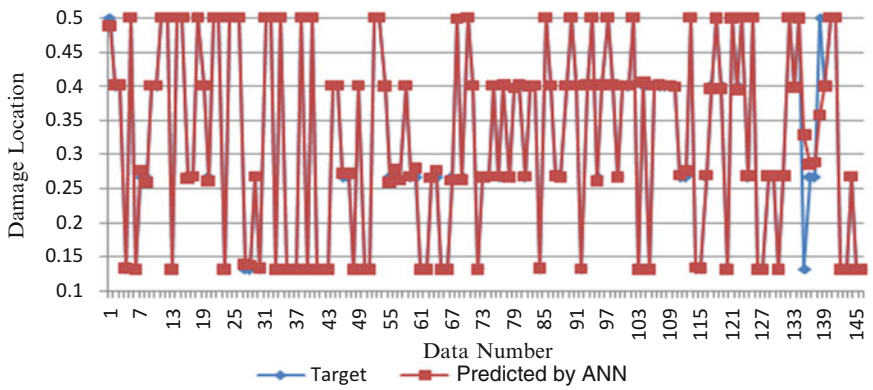

Fig. 16.7 Comparison of damage location predicted by ANN and actual values of mode 1 (training)

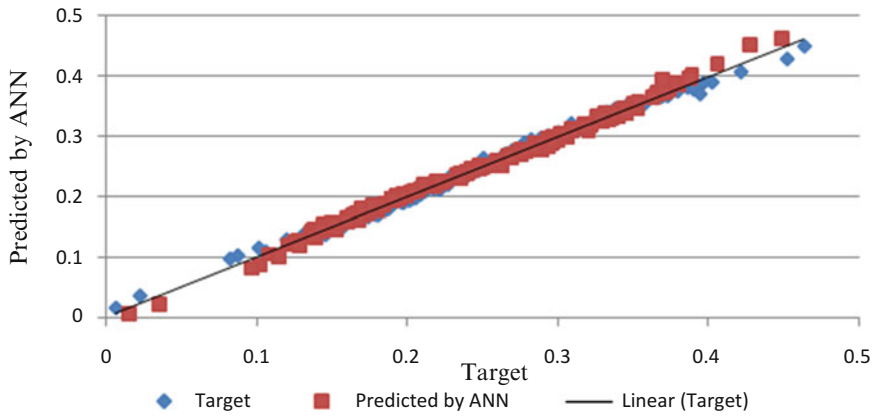

Fig. 16.8 Damage severity predicted by ANN and actual values of ensemble network (all datasets)

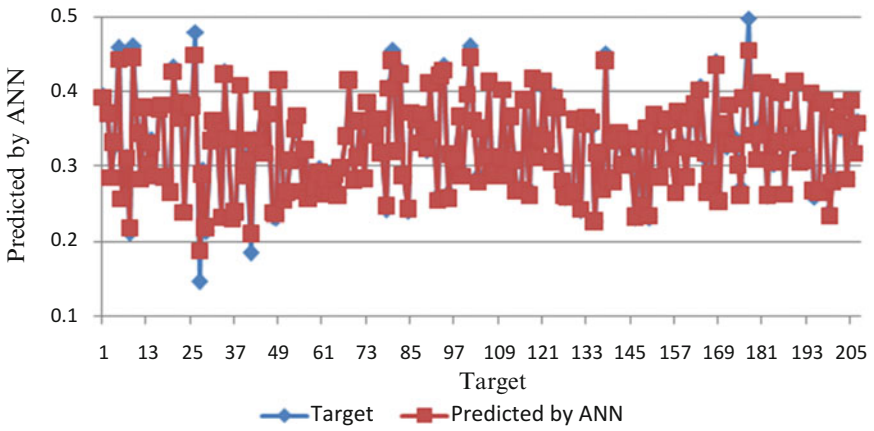

Fig. 16.9 Damage location predicted by ANN and actual values of ensemble network (all datasets)

In this array, "S" represents severity which is d_d/h and "L" represents location of damage which is l_d/L. For example, S_M1 and L_M1 are corresponding to damage severity and damage location in mode 1.

Several numbers of multilayer feedforward neural networks using above inputs–outputs were trained to find the optimal architecture of ensemble network. From training, testing and validation process, the optimal structure was obtained with two hidden layers with six and three hidden neurons in first and second hidden layers, respectively at 16,627 iterations. The minimum MSE was found to be 0.000396 and the maximum value of correlation obtained. Correlation of all datasets reached to 0.9946 and 0.9873 for severity and location of damage, respectively.

The ensemble network reached a maximum absolute error of 0.91, 1.22, 1.15 %, for training, validation and testing datasets, respectively, for damage severity predictions. This error for damage location prediction for training, validation and testing datasets was 0.90, 1.29, and 1.18 %, respectively. The performance of the ensemble network provides very good results. Comparison of the predicted damage severity and location from the neural network to target values for all datasets are depicted in Figs. 16.8 and 16.9, respectively.

According to Figs. 16.8 and 16.9, the calculation of absolute of all datasets showed that ANN predicted damage severity and location with percentage error of 0.946 and 0.954 %, which indicate the performance of ensemble network has been reached to a very low error after 16,627 iterations. Results of ensemble network accurately located damage cases except some incorrect results for damage severity of extra-light cases. Also, the outcomes of ensemble network showed that using the proposed architecture for neural network ensemble, the damages were identified with high accuracy, as compared to individual networks.

The final architecture of ensemble neural network is depicted in Fig. 16.10.

As discussed earlier, more of the individual networks provided good damage severities but were less accurate in predicting the location of damage. The ensemble network provides the best network outcomes with precise damage location. Correlation of all datasets for ensemble network to predict the location of damage was 0.9873, while this value for the best individual network (network for mode 3) was 0.9751. Therefore the damage location prediction results generated by ensemble neural network improved compared to individual network results.

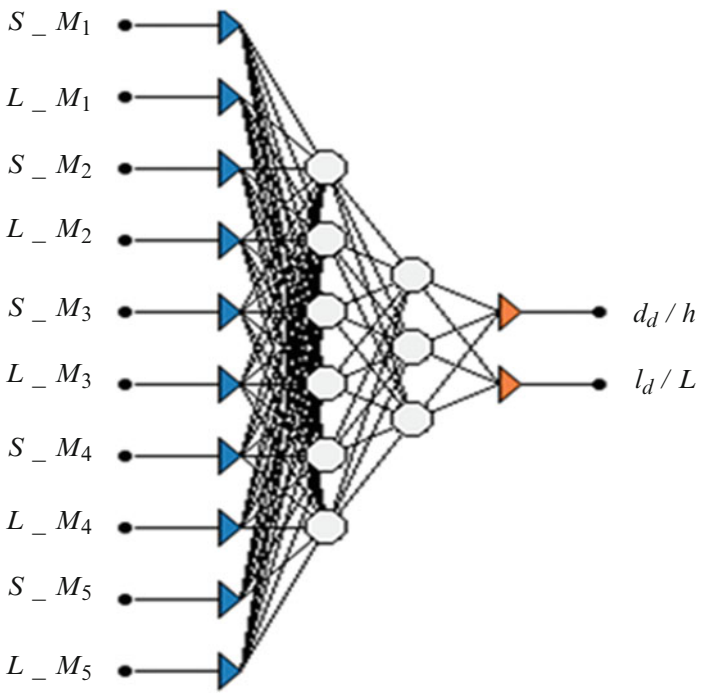

Fig. 16.10 Architecture of ensemble NN for damage identification in single damage location

Also the results of ensemble network for damage severity predictions were more accurate and robust predictions compared to results of all individual networks except mode 3. However, the performance of ensemble network was slightly less accurate than individual network of modes 3, which is insignificant.

16.5 Conclusions

This work has been devoted to the development and application of artificial neural network models using modal parameters data from experimental modal analysis which can predict the damage severity and location of I-beam structures. A combination of natural frequencies and mode shapes for detecting damage using ANNs shows more accurate and reliable results and has been used in this research.

For identification of severity and location of damage, five individual neural networks corresponding to mode 1 to mode 5 are considered. To take advantage of individual networks of different modes, a method based on neural network ensemble is proposed to combine the outcomes of the individual neural networks to a single network. In the ensemble network, five individual networks are trained, and then the outputs of these individual neural networks are combined in an ensemble network.

According to this study, the artificial neural networks were able to detect single damage cases accurately. The combination of natural frequency and mode shapes gives better identifications of faults than the individual using of them.

Large errors for outcomes of some individual networks in damage predictions in I-beams are caused by node points, as produces the great effect of noise on damage values in structure, which resulting faulty damage predictions. The performance of ensemble network shows high accuracy of predictions even when data applied to train is polluted with noise. Therefore the ensemble network gives better damage identification outcomes than the individual networks and the results show the ability of ANN to predict the damage severity of the structure with high accuracy.

References

1. Guo L, Wei J (2010) Structural damage detection based on backpropagation neural network technique. In: 2010 International conference on intelligent computation technology and automation (ICICTA), IEEE conference publications, vol 3, Changsha, 11–12 May 2010, pp 398–401
2. Kanwar V, Kwatra N, Aggarwal P (2007) Damage detection for framed RCC buildings using ANN modeling. Int J Damage Mech 16:457–472
3. Hakim SJS, Abdul Razak H (2014) Modal parameters based structural damage detection using artificial neural networks – a review. Smart Struct Syst (In Print)

4. Rosales MB, Filipich CP, Buezas FS (2009) Crack detection in beam-like structures. J Eng Struct 31:2257–2264
5. Ramadas C, Balasubramaniam K, Joshi M, Krishnamurthy CV (2008) Detection of transverse cracks in a composite beam using combined features of lamb wave and vibration techniques in ANN environment. Int J Smart Sens Intell Syst 1(10):970–984
6. Lam HF, Ng CT (2008) The selection of pattern features for structural damage detection using an extended Bayesian ANN algorithm. J Eng Struct 30:2762–2770
7. Gonzalez MP, Zapico JL (2008) Seismic damage identification in buildings using neural networks and modal data. J Comput Struct 86(3): 416–426
8. Hakim SJS, Noorzaei J, Jaafar MS, Jameel M, Mohammadhassani M (2011) Application of artificial neural networks to predict compressive strength of high strength concrete. Int J Phys Sci 6(5):975–981
9. Hola J, Schabowicz K (2005) Application of artificial neural networks to determine concrete compressive strength based on non-destructive tests. J Civ Eng Manag 11(1):23–32
10. Mansour MY, Dicleli M, Lee YL, Zhang J (2004) Predicting the shear strength of reinforced concrete beams using artificial neural networks. J Eng Struct 26:781–799
11. Hakim SJS, Abdul Razak H (2013) Adaptive Neuro Fuzzy Inference System (ANFIS) and Artificial Neural Networks (ANNs) for structural damage identification. Struct Eng Mech 45(6):779–802
12. Hakim SJS, Abdul Razak H (2013) Structural damage detection of steel bridge girder using artificial neural networks and finite element models. Steel Compos Struct 4(14):367–377
13. Fonseca ET, Vellasco PCG, Vellasco MMBR, Andrade SAL (2008) A neuro-fuzzy evaluation of steel beams patch load behavior. Adv Eng Softw 39:558–572
14. Ince R (2004) Prediction of fracture parameters of concrete by artificial neural networks. J Eng Fract Mech 71:2143–2159
15. Lee SC (2003) Prediction of concrete strength using artificial neural networks. J Eng Struct 25:849–857
16. Chen HM, Tsai KH, Qi GZ, Yang JCS, Amini F (1995) Neural network for structure control. J Comput Civ Eng 9(2):168–175
17. Wu ZS, Xu B, Yokoyama K (2002) Decentralized parametric damage based on neural networks. J Comput Aided Civ Infrastruct Eng 17: 175–184
18. http://www.alyuda.com/index.html

Chapter 17
Multiple Crack Detection in Structures Using Residual Operational Deflection Shape

Erfan Asnaashari and Jyoti K. Sinha

Abstract Fatigue cracks are one of the common defects in structures which are vital to be detected as a part of structural health monitoring systems. It has recently been shown that a simplified method called the residual operational deflection shape (R-ODS) is capable of detecting single fatigue crack in beam-like structures. The method is based on the ODSs at exciting frequency and its higher harmonic components which consider both amplitude and phase information of responses to map the deflection pattern of structures. In this paper, the R-ODS method is extended further to beams with multiple cracks. Details of the method and its application for detection of multiple cracks through numerical and experimental examples are presented.

Keywords Crack detection • Crack breathing • Dynamic characterisation • Frequency spectrum • Operational deflection shape

17.1 Introduction

Detection of cracks at an early stage of their development is an important part of any structural health monitoring system to prevent failures. Over the past few decades, vibration-based methods have widely been used in identifying and locating cracks in different types of structures. These methods are mainly based on variations in local flexibility of the structure due to the presence of crack. A comprehensive overview of various vibration based methods for damage detection in structures can be found in [1].

Fatigue cracks are one of the common defects in structures which cause failures. They may initiate when the structure is subjected to cyclic stresses mostly below the ultimate tensile stress. Surace et al. [2] identified the fatigue crack in a cantilever beam by using higher order frequency response functions based on Volterra series. Yan et al. [3] used the difference between natural frequencies of stiffness regions of beams to detect breathing fatigue cracks. Sinha [4] employed bi- and tri-higher order coherence to detect fatigue cracks in a cantilever beam. The presence of fatigue crack in a structure can also be recognised by the frequency spectrum of vibration responses obtained from external excitation of the structure. Whether the responses are in displacement, velocity or acceleration, the frequency spectrum shows higher harmonic components in addition to the exciting frequency. This is due to the breathing of the fatigue crack which means the crack opens and closes repeatedly during every cycle of loading and produces non-linear behaviour. The higher harmonic components of external excitation were used by Tsyfansky and Beresnevich [5] and Semperlotti et al. [6] to identify fatigue cracks in flexible geometrically bars and an isotropic rod respectively. Ullah and Sinha [7] stated that amplitude of deflection (AOD) at higher harmonics of exciting frequency can be used to locate centre and off-centre delamination in composite plates. However, the AOD method lacks phase information to construct the true deflection pattern of structures [8].

E. Asnaashari (✉) • J.K. Sinha
School of Mechanical, Aerospace and Civil Engineering, University of Manchester, Sackville Street, Manchester M13 9PL, UK
e-mail: erfan.asnaashari@postgrad.manchester.ac.uk

A. Wicks (ed.), *Structural Health Monitoring, Volume 5: Proceedings of the 32nd IMAC, A Conference and Exposition on Structural Dynamics, 2014*, Conference Proceedings of the Society for Experimental Mechanics Series, DOI 10.1007/978-3-319-04570-2_17,

The operational deflection shape takes advantage of both amplitude and phase of vibration responses to construct the deflection patterns of structures. This requires taking measurements at a number of locations along the structure. Different damage detection methods based on the ODS are presented in [9, 10]. However, Asnaashari and Sinha [8] have shown that it is not always possible to locate cracks in structures by using only the ODS. Therefore, they proposed a new term called residual operational deflection shape (R-ODS) for single crack detection in beam-like structures and verified it both numerically and experimentally [8]. This paper presents the results for the application of the R-ODS method to beams with multiple cracks. Details of the numerical simulations and experimental examples with single crack are included.

17.2 R-ODS Method

As a result of fatigue crack breathing, when the cracked structure is excited at a frequency, higher harmonic components of that exciting frequency are generated in the frequency spectrum. Figure 17.1 shows a typical spectrum for the cracked beam where the exciting frequency (1×) as well as its higher harmonics (2×, 3×, 4× ...) can be seen. The R-ODS method is based on constructing the ODS at the frequency of excitation and its higher harmonics to map deflection pattern of the cracked structure. Since the exciting frequency affects the ODSs at higher harmonics to a great extent, the ODSs at 2× and other higher harmonics contain the effect of first harmonic component in addition to nonlinearity due to the crack breathing. Before using the R-ODS method, all the ODSs at 1× and higher harmonics are normalised using Eq. (17.1):

$$(NODS)_{i,m} = \frac{(ODS_k)_{i,m}}{(MODS)_{i,m}}. \qquad i = 1, 2, 3, 4, \ldots \tag{17.1}$$

where $(NODS)_{i,m}$ is the normalised ODS at i-th harmonic for mode m. The subscript k refers to the node number, and $(MODS)_{i,m}$ is the maximum value of ODS data at i-th harmonic for mode m.

The residual operational deflection shape ($R-ODS$) is then defined as the $NODS$ at the p-th harmonic with respect to the first harmonic as expressed in Eq. (17.2). It removes the effect of the first harmonic from the ODS at p-th harmonic so that only the non-linear effect remains which is useful for the purpose of crack detection.

$$(R-ODS)_{p,m} = (NODS)_{p,m} - (NODS)_{1,m}. \qquad p = 2, 3, 4, \ldots \tag{17.2}$$

Therefore, when a cracked beam is excited at its first natural frequency and the R-ODS is calculated for 2× data, p and m are equal to 2 and 1 respectively. In this paper acceleration responses are used to construct the ODSs; however, either of displacement, velocity or acceleration responses could be utilised.

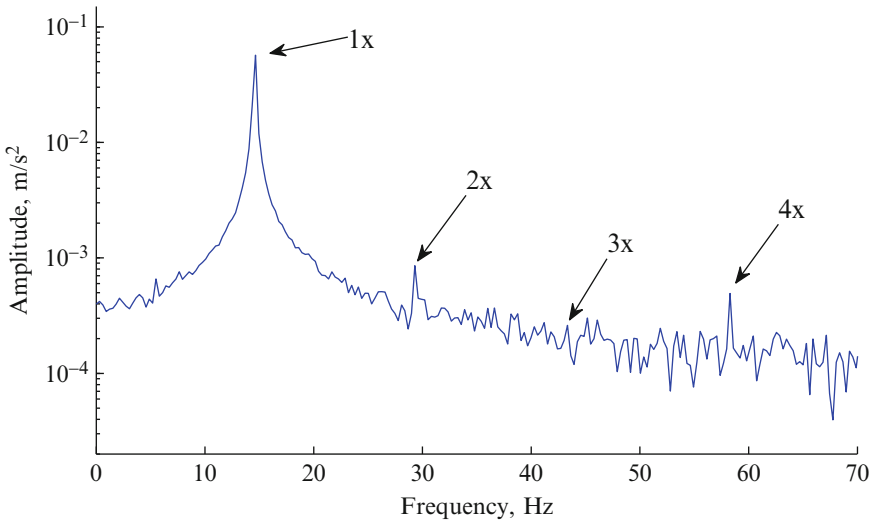

Fig. 17.1 A typical frequency spectrum for the cracked beam

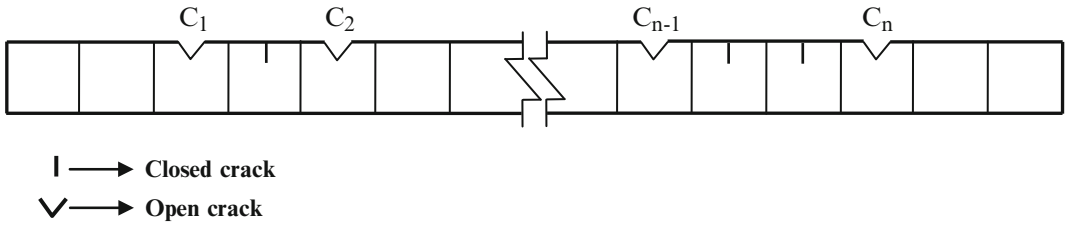

Fig. 17.2 Schematic view of a beam with multiple open and closed cracks

17.3 Finite Element Modelling

Euler–Bernoulli beam elements are employed to model the beam. Each element has two nodes and each node has two degrees of freedom; translational displacement and bending rotation. Proportional damping is obtained using the constructed mass and stiffness matrices.

Among different approaches available to model cracks in beam-like structures, the one proposed in [11] is used here to introduce cracks to the finite element model of the beams. This approach uses the concept of Christides and Barr [12] to modify the local flexibility in the vicinity of the crack within Euler–Bernoulli beam elements. It assumes that the flexibility from uncracked to cracked section of the beam varies linearly and considers triangular reduction in the stiffness of cracked element. If this reduction happens over more than one element, the nodes of the model will be moved so that the crack effect remains within a single element.

Nodal displacements of cracked element are considered to model the opening and closing of the breathing crack. When the displacement of nodes of the cracked element is greater than zero then the crack is open. Otherwise, the crack is assumed to be closed. The equation of motion for the cracked beam under external excitation is:

$$M\ddot{x}(t) + C\dot{x}(t) + K(t)x(t) = F(t) \tag{17.3}$$

where M, C and K are the mass, damping and stiffness matrices for the beam respectively and F is the external force.

In Eq. (17.3), stiffness matrix is time dependant because it changes with opening and closing of the crack(s) during the external excitation. When the crack is closed, no change happens in the stiffness; therefore, healthy (global) stiffness matrix can be used in Eq. (17.3). However, open crack reduces the stiffness of the cracked element and this reduction needs to be taken into consideration in the stiffness matrix in Eq. (17.3). In the case where multiple cracks exist in the beam, the number and location of all open cracks at every time step should be determined so that the stiffness reduction corresponding to each open crack can be considered in the global stiffness matrix. Figure 17.2 depicts a beam with a number of open and closed cracks.

The stiffness matrix in presence of open cracks can be obtained as:

$$K_c = K - \sum_{p=1}^{n} \Delta K_{c,p} \tag{17.4}$$

where K_c is the stiffness matrix for the cracked beam, K is the stiffness matrix for the healthy beam (global), n is the number of open cracks and $\Delta K_{c,p}$ is the reduction in the stiffness due to p-th open crack. This reduction depends on the location and depth of the crack.

The Newmark-β method is used to solve Eq. (17.3) with time steps of 200 μs assuming that the initial displacement and velocity is zero.

17.4 Numerical Validation

An aluminium beam with cross-section of 25×100 mm and length of 3 m has been considered. The density and Young's modulus of the beam are 2,700 kg/m^3 and 74 GPa respectively. Multiple cracks at different locations with depth of 5 mm are introduced to cantilever aluminium beams. Table 17.1 shows the details of all the investigated beams.

Table 17.1 Number and locations of cracks used in the beams for numerical simulations

	Boundary condition	No. of cracks	Crack location (m)
Beam 1	Cantilever	2	0.8, 1.6
Beam 2	Cantilever	2	1.0, 2.2
Beam 3	Cantilever	3	0.5, 1.2, 2.0

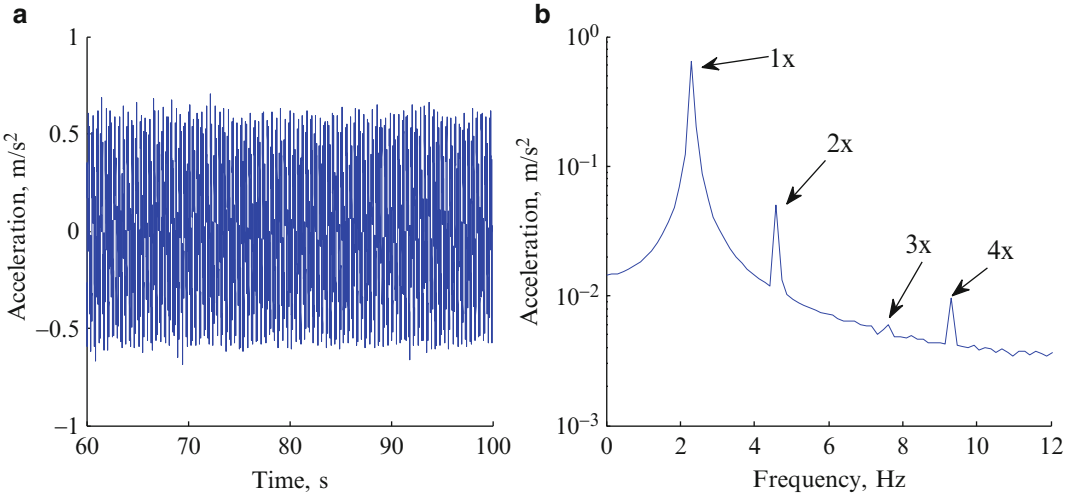

Fig. 17.3 Calculated acceleration response with noise in (**a**) time domain and (**b**) frequency domain for the cantilever beam at mode 1

Modal analysis is carried out to compute the natural frequencies of the beams assuming all the cracks are open. The first natural frequency of Beams 1–3 are 2.314, 2.322 and 2.300 Hz respectively. Beams are then excited by a sinusoidal input at their first natural frequency. In order to simulate experimental condition, signal to-noise ratio (SNR) of 20 dB is used to pollute the calculated acceleration responses with normalised random noise.

Fast Fourier transform (FFT) was used to convert the time-domain signals into frequency-domain with sampling frequency of 5 KHz. Figure 17.3 shows a typical noisy acceleration response in time domain and its frequency spectrum from a specific node for Beam 1 at mode 1 where the higher harmonics of the exciting frequency can be observed clearly.

Figure 17.4 depicts the numerical R-ODSs obtained for the cantilever beams at the first resonant frequency. Figure 17.4a,b shows the results for two cracks and Fig. 17.4c illustrates the R-ODS when three cracks exist in the cantilever beam. The location of cracks can be seen as positive discontinuities. The reason is that maximum difference between the ODSs at 2× and those of 1× happens at the location of cracks. The numerical results prove that the R-ODS method is able to identify the location of multiple cracks in beam-like structures.

17.5 Experimental Example [13]

The result of an experimental test on a single cracked solid aluminium beam [13] having dimensions of $25 \times 100 \times 3{,}000\ \text{mm}^3$ is presented here to show the effectiveness of the proposed R-ODS method. The crack was created in the form of small slot at the middle of the beam (1.5 m) using laser cutting method. The depth and width of the crack are 6 and 0.2 mm respectively.

The cracked beam was tested under free–free boundary condition and then excited at its first resonant frequency. In order to suspend the beams freely, two clamps were placed at the nodal points of the first mode where there are no vibrations during external excitation. Other details of the test setup as well as instrumentation used in the experiment can be found in [13]. Figure 17.5 shows the picture of the experiment. Same as in the numerical examples, continuous sinusoidal waves at natural frequency of the beam, 14.95 Hz, were used as the external excitation.

A set of accelerometers were employed to acquire the vibration responses simultaneously so that valid ODSs with correct magnitudes and phases can be guaranteed. Again, sampling frequency of 5 KHz was used to convert time domain responses into frequency domain.

The R-ODS method is applied to frequency-domain responses of the cracked aluminium beam and the result is shown in Fig. 17.6. As it can be observed, positive peak is appeared after removing the effect of mode 1 from the ODSs at second higher harmonics. This peak shows the location of the sensor which had the closest distance to the crack location. Therefore, the method can be employed as a trustworthy tool for crack detection in beam-like structures.

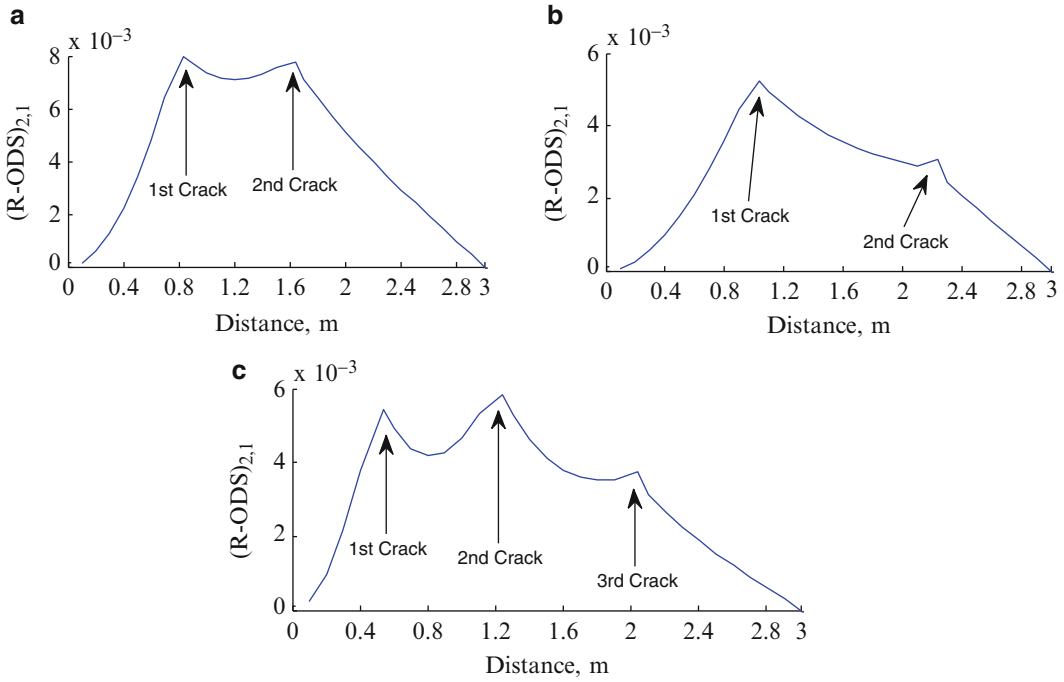

Fig. 17.4 The $(\text{R-ODS})_{2,1}$ results for (**a**) Beam 1, (**b**) Beam 2 and (**c**) Beam 3

Fig. 17.5 Test setup [13]

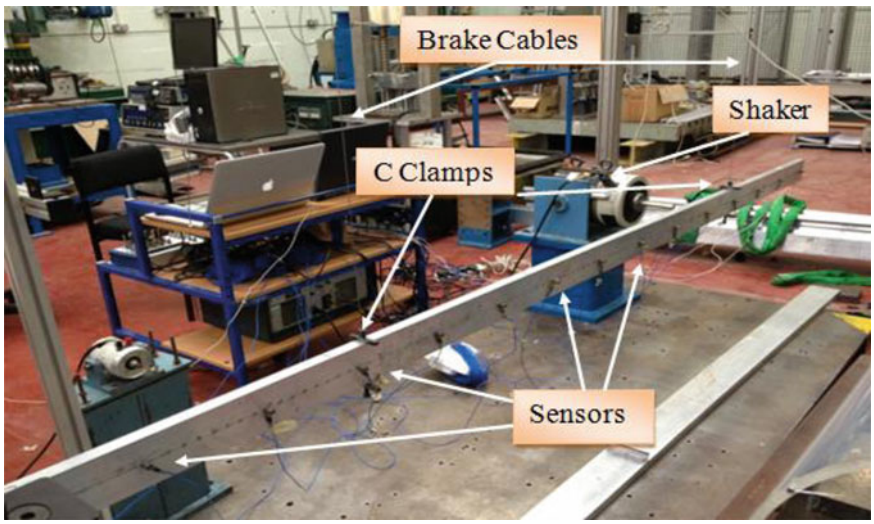

17.6 Concluding Remarks

It is known that the breathing of crack in a structure which is excited at a frequency generates vibration responses at the frequency of excitation and its higher harmonics in the frequency domain. The R-ODS method utilises the difference between the ODSs at the exciting frequency and its higher harmonics to identify the location of the crack. The method is extended to investigate its ability to detect multiple cracks in beam-like structures. The obtained results indicate that the R-ODS method has been successful in localising multiple cracks at different locations along the cantilever beam. The method is also verified experimentally for the beam with single crack. The future work will involve the application of the R-ODS method to experimental beams with multiple cracks as well as plate-like structures.

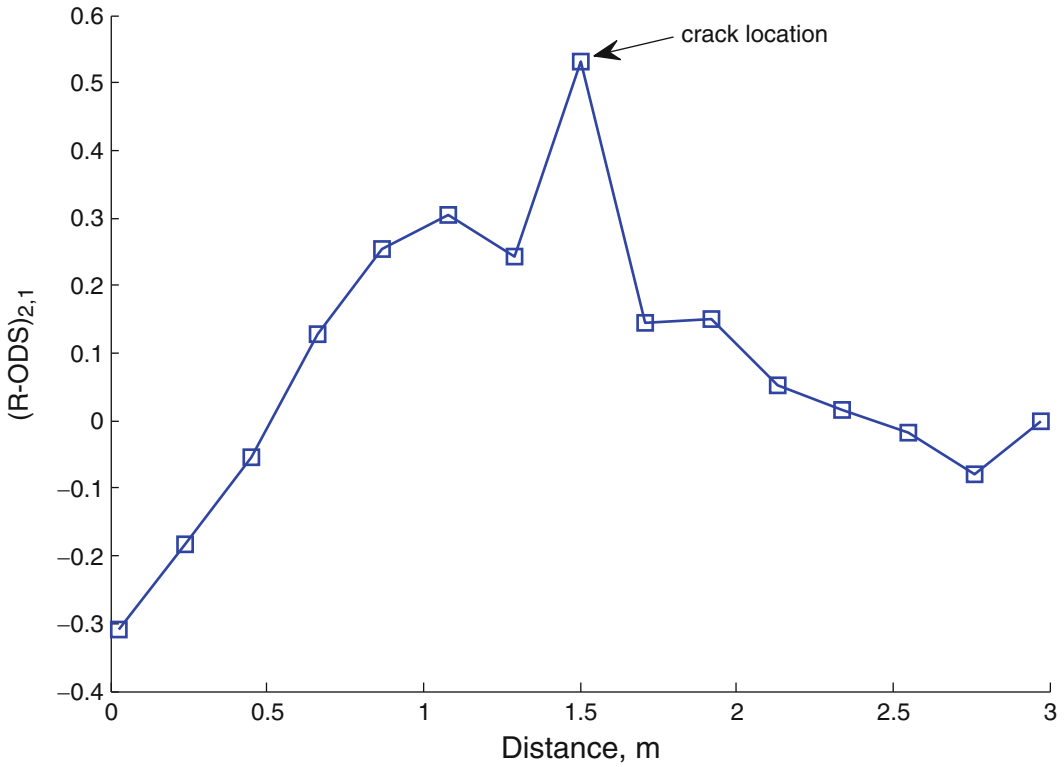

Fig. 17.6 The experimental $(\text{R-ODS})_{2,1}$ for the free–free aluminum beam

References

1. Wei F, Pizhong Q (2011) Vibration-based damage identification methods: a review and comparative study. Struct Health Monit 10:83–111
2. Surace C, Ruotolo R, Storer D (2011) Detecting nonlinear behaviour using the Volterra series to assess damage in Beam-like structures. J Theor Appl Mech 49:905–926
3. Yan G, De Stefano A, Matta E, Feng R (2013) A novel approach to detecting breathing-fatigue cracks based on dynamic characteristics. J Sound Vib 332:407–422
4. Sinha JK (2009) Higher order coherences for fatigue crack detection. Eng Struct 31:534–538
5. Tsyfansky SL, Beresnevich VI (1998) Detection of fatigue cracks in flexible geometrically non-linear bars by vibration monitoring. J Sound Vib 213:159–168
6. Semperlotti F, Wang KW, Smith EC (2009) Localization of a breathing crack using super-harmonic signals due to system nonlinearity. Am Inst Aeronaut Astronaut 47:2076–2086
7. Ullah I, Sinha JK (2011) Experimental vibration study on the healthy and delaminated composite plates. J Phys Conf Ser 305:012048
8. Asnaashari E, Sinha JK (2013) Operational deflection shape for crack detection in structures. Presented at the 10th international conference on damage assessment of structures, Dublin, 2013 (Key Eng Mat 570:8)
9. Sundaresan MJ, Schulz MJ, Hill J, Wheater EA, Ferguson F (1999) Damage detection on a wind turbine blade section. Presented at the IMAC XVII conference, Orlando 1999
10. Zhang Y, Lie ST, Xiang Z (2013) Damage detection method based on operating deflection shape curvature extracted from dynamic response of a passing vehicle. Mech Syst Signal Process 35:238–254
11. Sinha JK, Friswell MI, Edwards S (2002) Simplified models for the location of cracks in beam structures using measured vibration data. J Sound Vib 251:13–38
12. Christides S, Barr ADS (1984) One-dimensional theory of cracked Bernoulli–Euler beams. Int J Mech Sci 26:639–648
13. Asnaashari E, Sinha JK (2014) Development of residual operational deflection shape for crack detection in structures. Mech Syst Signal Process, Vol. 43(1-2):113–123

Chapter 18
Numerical Enhancement of NMT for Predicting Fatigue Failure

Timothy A. Doughty, Matthew R. Dally, and Mikah R. Bacon

Abstract Nonlinear Model Tracking (NMT) has been shown to be a robust method for predicting failure through nondestructive health monitoring. The method has been applied to slender cantilever beams of varying geometry subjected to harmonic nonstationary base excitation around the beams second natural frequency. Working with a nonlinear differential equation model, model parameters are mapped as the system health degrades. Continuous Time System Identification is populated with healthy system stimulus and response data and updated with aging real time response data. While the NMT method indicates with repeatability the onset of plasticity, crack initiation and growth well in advance of system failure, a phenomenon associated with specific geometries known as early onset drift can incorrectly flag system failure. Through numerical methods this phenomenon is explored. Additionally, two investigative numerical techniques are developed to give greater understanding and utility to the NMT method.

Keywords Nonlinear • Fatigue • Health Monitoring • Failure • Numerical Enhancement

18.1 Introduction

Fatigue is the primary failure mechanism in oscillating systems. Plasticity, crack initiation, and crack growth ultimately lead to failure. Developing a method to detect pending failure early in the life of the system is of great interest because a failure that is detected early can be avoided. In recent decades, the area of Nondestructive evaluation (NDE) has greatly advanced; see Doebling et al. [1] for a comprehensive view. The most common NDE procedures use linear approximations despite the widespread recognition of the nonlinear behavior in all physical systems [2–6] and despite the nonlinear nature of crack dynamics in vibrating structures [7]. New methods are still appearing for crack detection in vibrating systems as the field of NDE advances [8–11].

Here, Nonlinear Model Tracking (NMT), previously proven to be successful under various conditions [12–14], is enhanced in an attempt to more accurately track the nonlinear behavior of the beams being tested. System identification is performed on a slender cantilever beam excited near its second natural frequency. The Cantilever beam is understood to be the building block for more complex systems. The slenderness of the beam allows for more pronounced nonlinear behavior. The second natural frequency is chosen due to the dynamic characteristics in shaker performance. Stimulus and response data are fed into Continuous Time System Identification yielding parameter estimates allowing for the mapping of the nonlinear parameter over time [15]. A large change in the nonlinear term has been shown to effectively predict catastrophic failure well in advance of the failure of the beam.

T.A. Doughty (✉) • M.R. Dally • M.R. Bacon
University of Portland, 5000 N Willamette Blvd, Portland, OR 97203, USA
e-mail: doughty@up.edu; dally14@up.edu; bacon14@up.edu

A. Wicks (ed.), *Structural Health Monitoring, Volume 5: Proceedings of the 32nd IMAC, A Conference and Exposition on Structural Dynamics, 2014*, Conference Proceedings of the Society for Experimental Mechanics Series, DOI 10.1007/978-3-319-04570-2_18, © The Society for Experimental Mechanics, Inc. 2014

18.2 Background

Linear models have obvious advantages over nonlinear models, but the simplifications associated with linearization can prevent accurate modeling. In cases where nonlinearities are present, linear models fail to properly track the system health accurately. For example, a change in forcing amplitude can cause an apparent change in the system's natural frequency, which linear model analysis would misidentify as a sign of pending failure. Nonlinear models can accurately describe the healthy, complex behavior of systems as well as the linear behavior. The nonlinear model will change only when the nonlinearity of the system changes. This is associated with failing systems and serves as the early indicator of the onset of failure.

Through ongoing study, the NMT has shown to successfully detect damage significantly prior to catastrophic failure without much effort to identify an accurate nonlinear model. Additionally, it has been shown that the amount of data required to identify the system parameters is minimal, and that a generic set of data could be used to track the health of similar type beams. Users can therefore identify a healthy system beforehand and perform health monitoring in situ. The method requires a simple nonlinear model to be developed to be used for the system studied. The simplest nonlinear model considered for the NMT was determined to be the best, which included a cubic stiffness term [14].

18.3 Theoretical Model Development

This study uses vertically excited, horizontally mounted cantilever beam. The beam is excited near its second natural frequency, allowing spatial dependence of the model to be assumed. A theoretical configuration is shown in Fig. 18.1.

In this configuration, v is the vertical displacement, s is a reference variable defined by the distance from the point of excitation, t is time, m is the beam's mass per unit length, v is the vertical displacement of the base, Ω is the excitation frequency, D_ξ is the bending stiffness and L is the length of the beam.

The model for the transverse displacement of a cantilevered beam with nonlinear bending stiffness developed in [16] is given with the following partial differential equation and associated boundary conditions:

$$m\ddot{v} + c\dot{v} + D_\xi \left\{ v^{iv} + \left[v' \left(v' v'' \right)' \right]' \right\} = -mA\Omega^2 \cos\left(\Omega t\right), \tag{18.1}$$

$$v\left(0,t\right) = v'\left(0,t\right) = v''\left(L,t\right) = v'''\left(L,t\right) = 0. \tag{18.2}$$

Allowing $\phi(s)$ to be the orthonormalized mode shape which satisfies the boundary conditions we obtain:

$$\Phi(s) = C\left[\sin\left(\beta s\right) - \sinh\left(\beta s\right) - \Psi\left(\cos\left(\beta s\right) - \cosh\left(\beta s\right)\right)\right] \tag{18.3}$$

Where:

$$\Psi = \frac{\sin\left(L\beta\right) + \sinh\left(L\beta\right)}{\cos\left(L\beta\right) + \cosh\left(L\beta\right)} \tag{18.4}$$

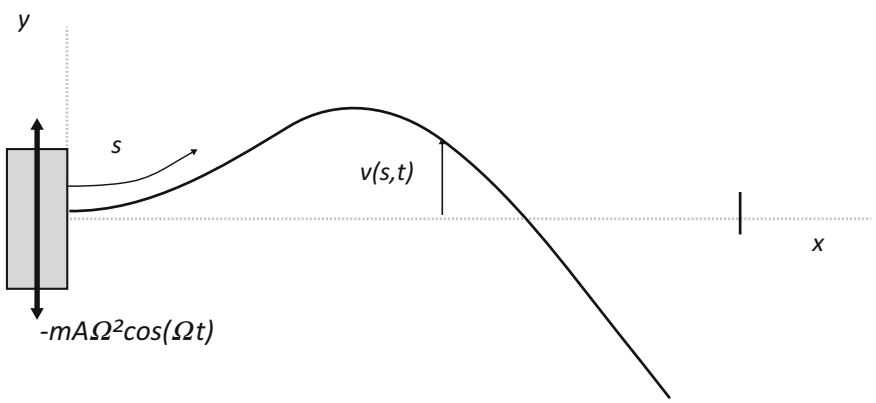

Fig. 18.1 Theoretical configuration for base-excited cantilever beam demonstrating the second mode

and:

$$\beta L = 4.694. \tag{18.5}$$

Separating with $v(s,t) = a(t) \bullet \phi(s)$, the nonlinear partial differential equation can be reduced to the form:

$$m\ddot{a} + c\dot{a} + ka + \alpha a^3 = F(t), \tag{18.6}$$

where:

$$k = \left\{ D_\xi \int_0^L \phi\phi^{iv} ds \right\}, \tag{18.7}$$

$$\alpha = \left\{ D_\xi \int_0^L \phi\phi'' 3 + 4\phi\phi'\phi''\phi''' + \phi\phi' 2\phi^{iv} ds \right\}, \tag{18.8}$$

and:

$$F(t) = \int_0^L \phi ds \left(-mA\Omega^2\right) \cos(\Omega t). \tag{18.9}$$

Using a combination of forcing, $F(t)$, and response, $a(t)$, we can estimate the system parameters. It should be noted that in cases where α is zero the model becomes the standard model for forced mass-spring-damping system. A previous study [14] showed the cubic nonlinearity term outperformed quadratic and combination nonlinearities. The cubic nonlinearity term is understood to be the most significant nonlinearity in base excited cantilever beam systems.

18.4 System Identification

In application of the Continuous Time Method forcing and response accelerations are collected, scaled with respect to mode and sensor placement, and integrated to give velocity and position. The position vector is then cubed and the linear vectors are collected in a matrix relation. The matrix relation can then be solved using a least squares method. Arranging Eq. (18.6) yields:

$$\left[\ddot{a}(t) \quad \dot{a}(t) \quad a(t) \quad a(t)^3\right] [m \quad c \quad k \quad \alpha]^T = F(t), \tag{18.10}$$

and:

$$\left\{ a(t)^3 \right\} [\alpha] = \left\{ F(t) - m\ddot{a}(t) - c\dot{a}(t) - ka(t) \right\}. \tag{18.11}$$

Equation (18.10) allows for direct estimation for the parameter vector. Equation (18.11) is derived because of this and isolates α as the only unknown in the matrix relation. α is approximated by solving Eq. (18.8) in a least squares sense where state vectors are concatenated steady state time responses form selected excitation frequencies.

While traditional methods allow for linear parameters to be estimated, this approach is not used in this study. Previous work [14] indicated that physically accurate linear parameters were detrimental to the success of the NMT Method. Resulting values are believed to differ from actually values because they absorb some inaccuracies in the system model. Linear parameters are instead estimated with Eq. (18.10) for the healthy system and then fixed in Eq. (18.11) for the duration of the fatigue test.

Nonlinear model parameters are inherently more difficult to estimate because the system must be excited in a way that pronounces nonlinear behavior. Nonlinear differential equations have no analytical solution, so the formulation of the algorithms is dependent on the method of approximating the solution to the governing model. While the methods of Multiple Time Scales and Harmonic Balance have both proven to be effective in identifying nonlinear model parameters [17], Continuous Time Method was chosen due to ease of use and acceptance of non-harmonic data.

Though it is not the case, the method can be appreciated if one considers the estimation to be a parametric curve fit to the nonlinear frequency response for the system. The analytic form of the frequency response model is not known, so

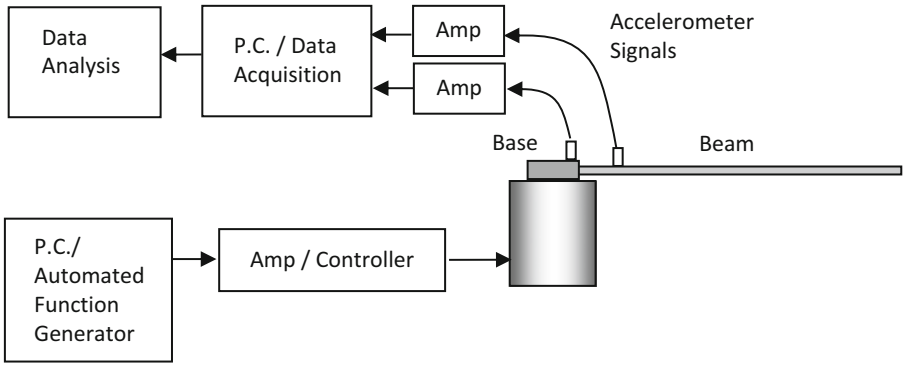

Fig. 18.2 Experimental configuration for Fatigue testing

experimental data must be complied as described above to find the best fit for the time based model. Considering the system in the frequency domain does emphasize the need to collect steady state data for more than one forcing frequency, as one frequency point does not yield an exclusive set of model parameters. Thus, steady state data is collected over a range of frequencies around the system's second natural frequency. Steady state data points were chosen at frequencies near resonance because it has been experimentally shown to accurately identify similar nonlinear models [11, 18].

18.5 Experiment and Analysis

The testing schematic is shown in Fig. 18.2. A long slender beam of 6061 aluminum was excited using a 45 N shaker over a range of frequencies near the second natural frequency for each beam. National Instrument's LabVIEW and accelerometers were used to record accelerations at the beam's base and 4.5 cm down from the base. These accelerations are called the stimulus acceleration and the response acceleration respectively. The response acceleration is differenced from the stimulus acceleration according to the accelerometer's calibration and scaled for the location of the response accelerometer on the beam. The base acceleration was multiplied by the system mass to give the forcing, and then scaled based on the mode shape given in Eq. (18.9). These new data sets were then treated as the system's input and output.

Noise was addressed by fitting the harmonic stimulus and response data with an 11 term Fourier Series approximations based on the forcing frequency. The fit functions were then integrated analytically to yield approximate velocity and position functions for use in the parameter identification matrices.

Sweep tests were performed to identify the resonant frequency and steady state data was then collected at nearby frequencies. The linear parameters, *m, c,* and *k,* were then identified using Eq. (18.10) and fixed for the remainder of the experiment. The solved linear parameters do not need to match actual linear parameters found in traditional linear estimates, the solved linear parameters help absorb inaccuracies in the model [15]. With these fixed for the healthy beam, the nonlinear cubic stiffness value is the only parameter left to compensate for changes in the beam's behavior.

In the final fatigue test, the beam was excited near the beam's resonance and allowed to shake until catastrophic failure. Data collected during this portion is split up into 2 s intervals with acceleration data collected at 1 kHz. Data is collected for the life of the beam, which in some cases is several days. The accelerometer signals are once again filtered, amplified, and fit with a Fourier Series to yield an acceleration approximation and then integrated to give velocity and position. These approximations are fed into Eq. (18.11) along with the set linear parameters, *m, c,* and *k*. α is then solved for using a least squares method.

18.6 Results and Discussion

The focus of this study is to address the early onset drift phenomenon. In practice, the NMT method produces time plots of the estimate of α and significant changes in this estimate indicate a loss of system health. Early onset drift is the name given to apparent changes in alpha associated with healthy systems at the start of testing. Three tools were developed to address this issue. They include healthy steady state data selection, excitation frequency identification, and visual mapping of identified models to data.

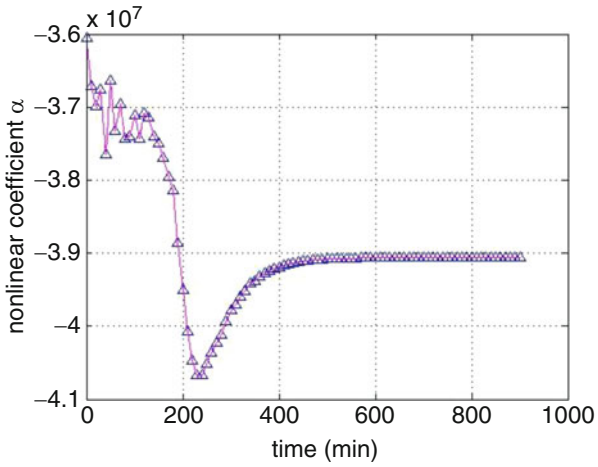

Fig. 18.3 Alpha plot vs. time using close steady state data points

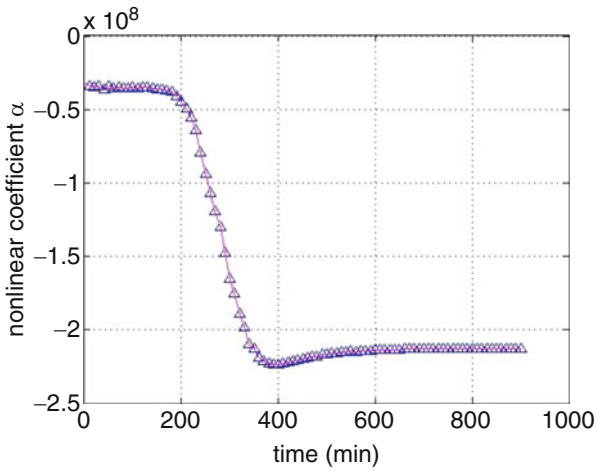

Fig. 18.4 Alpha plot vs. time using spread steady state data points

18.7 Healthy Steady State Data Selection

Two sets of six steady state data records for each beam were collected for analysis: a close set at ±0.2, ±0.4, and ±0.6 Hz from resonance, and a spread set at ±0.75, ±1.25, and ±2 Hz from resonance. As before, data was recorded at 1 kHz for 2 s. This corresponds to approximately 60 cycles of steady state response at each frequency. Figures 18.3 and 18.4 show α plots of the same beam where Fig. 18.3 used the close steady state set and Fig. 18.4 used the spread steady state points.

Figure 18.3 does not appear to have a steady initial estimation for the nonlinear term α so it is not clear where the warning sign for impending failure occurs. In contrast the plot using the spread steady state data successfully shows an initial steady estimation for α, indicating a healthy beam, and then shows a large change in α that corresponds accurately to visual cues as the beam was shaking in the final fatigue test. Figure 18.4 gives a warning time of impending catastrophic failure of approximately 83 % of the life time of the beam. Worth noting, despite the early wavering Fig. 18.3 predicts the same onset of failure near the 200 min mark. Also, in the systems studied where close data sets did not generate early changes in α's estimate, the spread steady state data had little effect.

18.8 Excitation Frequency Identification

The biggest contribution to early onset drift was the result of assuming the forcing and response frequencies were known. Function generators are known to drift, and even a little drift was paramount to large errors in the Fourier Series fit of both forcing and response data over the 2 s data duration. To remedy this, a fitting code was generated that would find the best fit frequency for a given forcing data record. A simple sweep and least squares error approach yielded results, which were then implemented in the Fourier fitting for both the stimulus and response data sets.

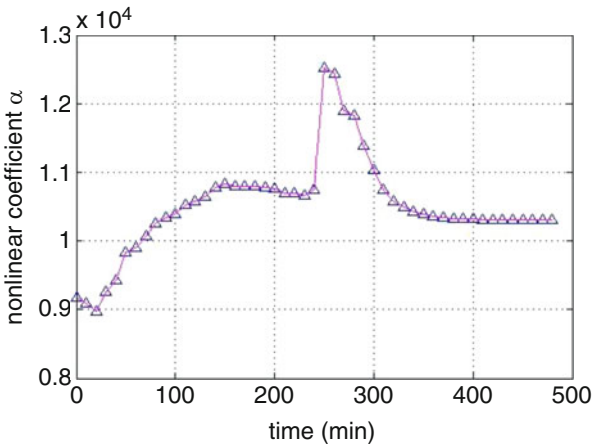

Fig. 18.5 Alpha plot vs. time using manual inputs for frequency

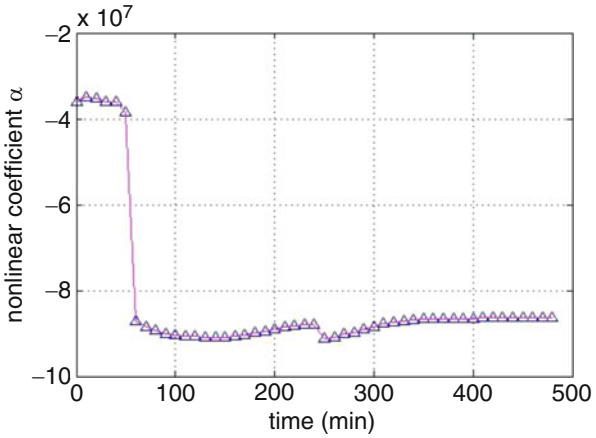

Fig. 18.6 Alpha plot vs. time using frequency chase

Correctly identifying the forcing frequency provided many improvements to the signaling of the beam's pending failure as seen in Figs. 18.5 and 18.6. There, the same beam data is analyzed, where the only change in the analysis is the use of the identified stimulus frequency for the plot in Fig. 18.6.

Not only is there a lack of onset drift, but the qualitative behavior of the plot and the associated premonition of failure are quite different. It can be seen in Fig. 18.5 that the apparent warning sign that the beam has begun to crack is around minute 240. It is true that there was a visually small change in the behavior of the beam at this time but a much more apparent change was seen at minute 50. This larger behavior change is captured much better in Fig. 18.6, where a warning time of impending catastrophic failure is approximately 88 % of the lifetime of the beam.

18.9 Visual Mapping of Identified Models

Early onset drift is prevalent in cases presented in [12]. The differing geometries presented there displayed early onset drift. Figure 18.7 uses a data set borrowed from those tests. New processing techniques generated a new plot of α vs. time, but early onset drift is still present. Figure 18.7 shows an early change in theestimation of α and then a steady period until minute 370 where a large change in α correctly indicates the premonition of failure of the beam.

Visual mapping of identified models provides the user with another lens with which to see the changes in α. We simply use the estimates of the system parameters to numerically generate a frequency response curve and superimpose this result on the plot of the steady state data records. Here we performed this at minutes 0, 10, 210, and 600. Results are shown in Fig. 18.8.

These times were chosen in order to compare the difference of the response of the beam before, during, and after early onset drift and after the signal of pending failure. The curves associated with the varying α estimates are the direct result of the changing data sets collected at the forcing frequency of 26.77 Hz, and as the response data amplitude varied, so changed the mapping. In cases where the amplitude of the response is high, as in the early onset drift, the identified α attempts to compensate as evidenced by the lifted model curve.

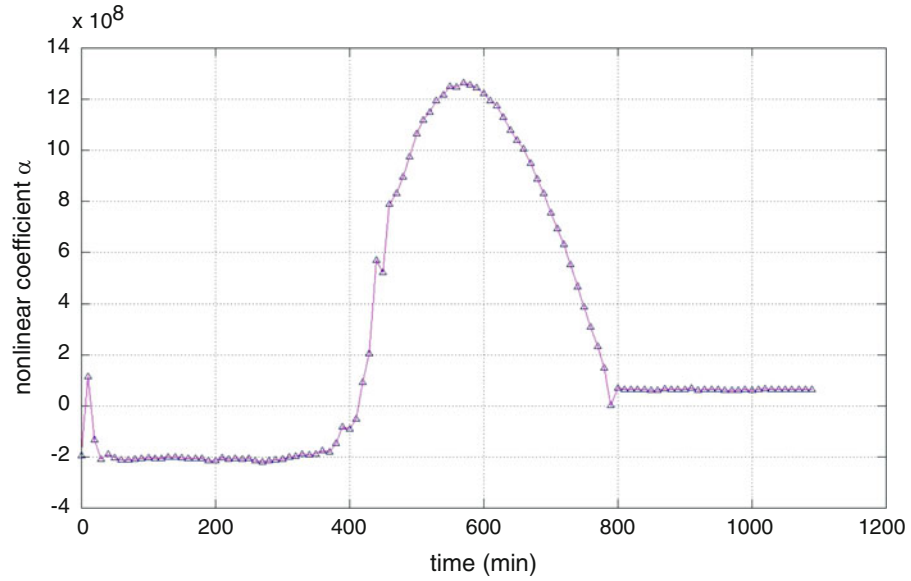

Fig. 18.7 Alpha plot vs. time displaying early onset drift

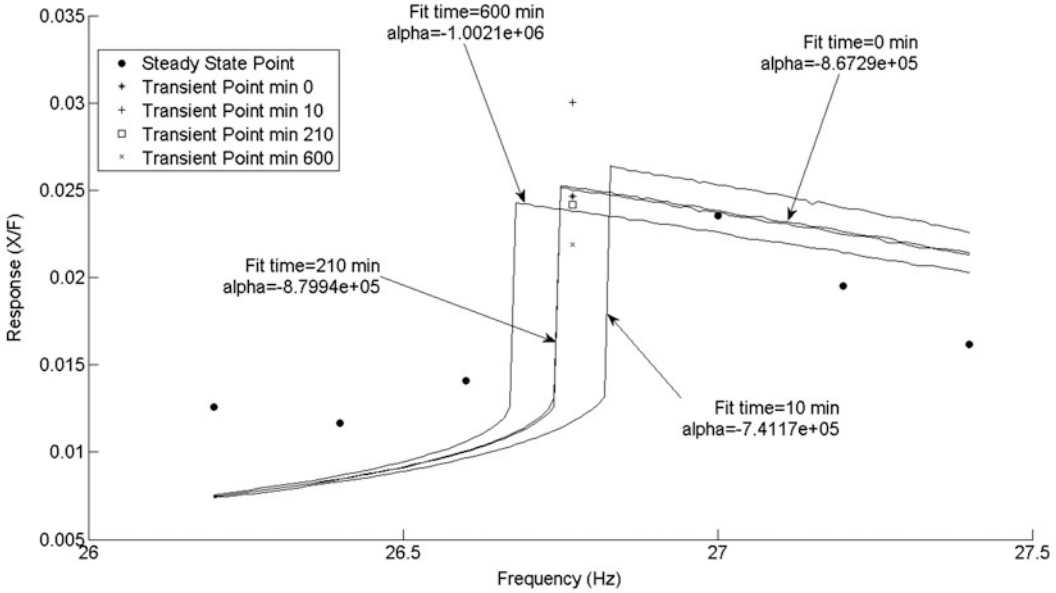

Fig. 18.8 Time step analysis of a beam displaying early onset drift

18.10 Conclusions

The alterations to the analysis methods of the NMT have proven to improve the precision and effectiveness of the prediction of the pending failure of the beam in many cases. More importantly the modifications did not negatively affect the signal of premonition of failure in any case tested. Both identifying the stimulus frequency and choosing a spread of healthy steady state data will help eliminate early onset drift. This adds to the robustness of the method and its ability to accurately signal failure in cantilever beams.

Currently, cases still demonstrating early onset drift are indicative of systems that are actually failing at the onset of the failure testing. Further examination of early onset drift will verify that the early changes are not an indication of model sensitivity or equipment limitations..

References

1. Doebling SW, Farrar CR, Prime MB (1998) A summary of vibration-based damage identification methods. Shock Vib Digest 30:91–105
2. Khiem NT, Lien TV (2004) Multi-crack detection for beam by the natural frequencies. J Sound Vib 273:175–185
3. Loutridis S, Douka E, Hadjileontiadis LJ (2005) Forced vibration behavior and crack detection of cracked beams using instantaneous frequency. NDT E Int 38:411–419
4. Lee YY, Liew KM (2001) Detection of damage locations in a beam using the wavelet analysis. Int J Struct Stab Dyn 1:455–465
5. Gudmundson P (1984) Changes in modal parameters resulting from small cracks. Proc Int Modal Anal Conf Exhibit 2:690–697
6. Kim J-T, Ryu Y-S, Cho H-M, Stubbs N (2003) Damage identification in beam-type structures: frequency-based method vs. mode-shape based method. Eng Struct 25:57–67
7. Ding JL, Pazhouh J, Lin SB, Burton TD (1994) Damage characterization by vibration test. Scripta Metall Mater 30:839–844
8. Sih GC, Tzou DY (1984) Mechanics of nonlinear crack growth: effects of specimen size and loading step. Martinus Nijhoff, Boston, pp 155–169
9. Bovsunovsky A, Bovsunovsky O (2007) Crack detection in beams by means of the driving force parameters variation at non-linear resonance vibrations. Key Eng Mater 347:413–420 (Damage assessment of structures VII)
10. Andreaus U, Casini P, Vestroni F (2005) Nonlinear features in the dynamic response of a cracked beam under harmonic forcing. In: Proceedings of the ASME international design engineering technical conferences and computers and information in engineering conference-DETC2005, 5th international conference on multibody systems, nonlinear dynamics, and control, vol 6C, Long Beach, pp 2083–2089
11. Doughty TA, Leineweber MJ (2009) Investigating nonlinear models for health monitoring in vibrating structures. In: ASME International Mechanical Engineering Congress and Exposition, Lake Buena Vista, November 2009
12. Doughty TA, Dally MR, Bacon MR (2013) Nonlinear model tracking for varying system geometries. In: International modal analysis conference, Garden Grove, 2013
13. Doughty TA, Higgins NS, Etzel N (2011) Nonlinear model tracking in application to non destructive evaluations. In: ASME International Mechanical Engineering Congress and Exposition, Denver, November 2011
14. Doughty TA, Higgins NS (2010) Effect of nonlinear parametric model accuracy in crack prediction and detection. In: SEM annual conference & exposition on experimental and applied mechanics, Indianapolis, 2010
15. Wowk V (1991) Machinery vibration measurement and analysis. McGraw Hill, New York
16. da Crespo Silva MRM, Glynn CC (1978) Nonlinear flexural-flexural-torsional dynamics of in extensional beams: II forced motions. Int J Solids Struct 6:449–461
17. Doughty TA, Davies P, Bajaj AK (2002) A comparison of three techniques using steady-state data to identify nonlinear modal behavior of an externally excited cantilever beam. J Sound Vib 249(4):785–813
18. Doughty TA (2002) System identification of modes in nonlinear structures. PhD Thesis, Ray W. Herrick Laboratories, School of Mechanical Engineering, Purdue University, Purdue

Chapter 19
Subspace-Based Damage Detection on Steel Frame Structure Under Changing Excitation

M. Döhler and F. Hille

Abstract Damage detection can be performed by detecting changes in the modal parameters between a reference state and the current (possibly damaged) state of a structure from measured output-only vibration data. Alternatively, a subspace-based damage detection test has been proposed and applied successfully, where changes in the modal parameters are detected, but the estimation of the modal parameters themselves is avoided. Like this, the test can run in an automated way directly on the vibration measurements. However, it was assumed that the unmeasured ambient excitation properties during measurements of the structure in the reference and possibly damaged condition stay constant, which is hardly satisfied by any application. A new version of the test has been derived recently that is robust to such changes in the ambient excitation. In this paper, the robust test is recalled and its performance is evaluated both on numerical simulations and a real application, where a steel frame structure is artificially damaged in the lab.

Keywords Damage detection • Ambient vibration • Changing excitation • Subspace methods • Robust tests

19.1 Introduction

In the last 20 years, monitoring the integrity of the civil infrastructure has been an active research topic, including in connected areas such as automatic control, for mastering the aging of bridges, or the resistance to seismic events and the protection of the cultural heritage. The structural response to unknown ambient excitation is measured, and vibration-based monitoring can be performed under the premise that changes in the structural properties due to damage lead to changes in the eigenstructure of a system. Since the ambient excitation is unknown, it can change during the monitoring of a structure, e.g. in changing wind or traffic conditions. The focus of this paper is damage detection under possible changes in the ambient excitation.

A standard approach for damage detection is modal parameter identification and their comparison to a reference state of the monitored structure, e.g. as in [8, 11]. The modal parameters are not afflicted by different ambient excitations, but their automatic estimation and matching from measurements of different states of the structure might require an extensive preprocessing step.

In this paper we consider the subspace-based damage detection approach developed in [2, 3, 5, 6]. With this approach, a data-driven model obtained in the reference state is compared to data from the possibly damaged state using a subspace-based residual function and a χ^2-test built on it for a hypothesis test, without actually estimating the modal parameters in the tested, possibly damaged states. This has the advantage that the computations in the tested (possibly damaged) state are fully automated. The computed χ^2-value is compared to a threshold to decide if damage occurred or not.

M. Döhler (✉)
BAM Federal Institute for Materials Research and Testing, Safety of Structures Department, 12200 Berlin, Germany

Inria, Campus de Beaulieu, 35042 Rennes, France
e-mail: michael.doehler@inria.fr

F. Hille
BAM Federal Institute for Materials Research and Testing, Safety of Structures Department, 12200 Berlin, Germany
e-mail: falk.hille@bam.de

A. Wicks (ed.), *Structural Health Monitoring, Volume 5: Proceedings of the 32nd IMAC, A Conference and Exposition on Structural Dynamics, 2014*, Conference Proceedings of the Society for Experimental Mechanics Series, DOI 10.1007/978-3-319-04570-2_19,

Since this kind of methods process the measurement data in a much more direct way, the original algorithms from [2, 3] have the drawback of being influenced by changes in the unknown ambient excitation, which may lead to false alarms. Recently, the original algorithms have been extended and modified to be robust under such changes in the excitation in [6]. This approach has been shown to be promising under changing excitation in numerical simulations [6,7,12]. It is the purpose of this paper to validate the new approach on a case study in the lab under different excitation levels.

This paper is organized as follows. In Sect. 19.2, the basics of the considered damage detection approach are presented and in Sect. 19.3 the extension from [6] that is robust to changing ambient excitation. In Sect. 19.4, a numerical application is presented on a simulated truss, as well as a case study on a steel frame structure in the lab that was artificially damaged. Finally, concluding remarks are given in Sect. 19.5.

19.2 Subspace-Based Damage Detection

19.2.1 Models and Parameters

The behavior of a structure is assumed to be described by a linear time-invariant (LTI) dynamical system

$$\mathcal{M}\ddot{X}(t) + \mathcal{C}\dot{X}(t) + \mathcal{K}X(t) = \upsilon(t) \tag{19.1}$$

where t denotes continuous time, $\mathcal{M}, \mathcal{C}, \mathcal{K} \in \mathbb{R}^{d\times d}$ are the mass, damping and stiffness matrices respectively and $X \in \mathbb{R}^d$ collects the displacements of the d degrees of freedom (DOF) of the structure. The external and non-measured force $\upsilon(t)$ is modeled as white noise.

Let the system (19.1) be observed at r coordinates, e.g. with accelerometers. Discretizing system (19.1) in time and transformation to a first order system leads to the discrete time state-space model

$$\begin{cases} x_{k+1} = Ax_k + v_k \\ y_k = Cx_k + w_k \end{cases} \tag{19.2}$$

with the states $x_k \in \mathbb{R}^n$, the outputs $y_k \in \mathbb{R}^r$, the state transition matrix $A \in \mathbb{R}^{n\times n}$ and the observation matrix $C \in \mathbb{R}^{r\times n}$, where r is the number of sensors and n is the system order. The excitation v_k is an unmeasured Gaussian white noise sequence with zero mean and (during a measurement) constant covariance matrix Q: $\mathbf{E}(v_k v_{k'}^T) \stackrel{\text{def}}{=} Q\,\delta(k-k')$, where $\mathbf{E}(\cdot)$ denotes the expectation operator, and w_k is the measurement noise.

19.2.2 Properties from Subspace-Based System Identification

For the damage detection method in [2, 3] a residual function is constructed based on properties from covariance-driven output-only subspace-based system identification [10, 13].

Let $G = \mathbf{E}(x_{k+1}y_k^T)$ be the cross-covariance between the states and the outputs, let $R_i = \mathbf{E}(y_k y_{k-i}^T) = CA^{i-1}G$ be the theoretic output covariances and

$$\mathcal{H}_{p+1,q} \stackrel{\text{def}}{=} \begin{bmatrix} R_1 & R_2 & \dots & R_q \\ R_2 & R_3 & \dots & R_{q+1} \\ \vdots & \vdots & \ddots & \vdots \\ R_{p+1} & R_{p+2} & \dots & R_{p+q} \end{bmatrix} \stackrel{\text{def}}{=} \text{Hank}\,(R_i) \tag{19.3}$$

be the theoretic block Hankel matrix of size $(p+1)r \times qr$, where parameters p and q are chosen such that $\min\{pr, qr\} \geq n$ with often $p+1 = q$. Matrix $\mathcal{H}_{p+1,q}$ possesses the well-known factorization property

$$\mathcal{H}_{p+1,q} = \mathcal{O}_{p+1}\mathcal{C}_q \tag{19.4}$$

into the matrices of observability and controllability

$$O_{p+1} = \begin{bmatrix} C \\ CA \\ \vdots \\ CA^p \end{bmatrix}, \quad C_q = \begin{bmatrix} G & AG & \dots & A^{q-1}G \end{bmatrix}. \tag{19.5}$$

From the observability matrix O_{p+1}, the matrices C and A could be recovered [10, 13] and subsequently the modal parameters. However, the fact is used that damages lead to changes in A and C and subsequently in $\mathcal{H}_{p+1,q}$ through properties (19.4) and (19.5), which will be directly checked in a statistical test, instead of doing system identification.

19.2.3 The Damage Detection Test

In the following, the non-parametric damage detection test [1] based on [2,3] is described. Using measured data $(y_k)_{k=1,\dots,N}$, a consistent estimate $\hat{\mathcal{H}}_{p+1,q}$ of the Hankel matrix is obtained from the empirical output covariances

$$\hat{R}_i = \frac{1}{N} \sum_{k=1}^{N} y_k y_{k-i}^T, \quad \hat{\mathcal{H}}_{p+1,q} = \text{Hank}\left(\hat{R}_i\right). \tag{19.6}$$

Let $\hat{\mathcal{H}}^{\text{ref}}_{p+1,q}$ be the Hankel matrix in the reference state. Compute its left null space S from the singular value decomposition (SVD)

$$\hat{\mathcal{H}}^{\text{ref}}_{p+1,q} = \begin{bmatrix} \hat{U}_1 & \hat{U}_0 \end{bmatrix} \begin{bmatrix} \hat{\Delta}_1 & 0 \\ 0 & \hat{\Delta}_0 \end{bmatrix} \begin{bmatrix} \hat{V}_1^T \\ \hat{V}_0^T \end{bmatrix} \tag{19.7}$$

as $S = \hat{U}_0$, where $\hat{\Delta}_1$ is of size $n \times n$ and where $\hat{\Delta}_0 \approx 0$.

The characteristic property of the reference state then writes as

$$S^T \hat{\mathcal{H}}_{p+1,q} \approx 0, \tag{19.8}$$

while the product deviates from 0 in the damaged state. To decide whether measured data corresponds to the reference state or not, the residual vector ζ with

$$\zeta = \sqrt{N}\, \text{vec}\left(S^T \hat{\mathcal{H}}_{p+1,q}\right) \tag{19.9}$$

is defined [2, 3]. It is tested if this residual is significantly different from zero or not, using the χ^2 test

$$\chi^2_\zeta = \zeta^T \Sigma_\zeta^{-1} \zeta, \tag{19.10}$$

where the empirical residual covariance $\Sigma_\zeta = \text{cov}(\zeta)$ is computed on several datasets from the reference state. To decide if damage occurred or not, the test value χ^2 is compared to a threshold, which can also obtained from χ^2 test values on several datasets from the reference state.

19.3 Robust Damage Detection Test Under Changing Excitation

A change in the covariance Q of the unmeasured ambient excitation v_k of system (19.2) provokes a change in the cross-covariance G between the states and the outputs and thus in the Hankel matrix estimate $\hat{\mathcal{H}}_{p+1,q}$ (see (19.3)), even if no structural change occurs. Hence, the residual ζ and the corresponding test value χ^2 are influenced by changes in the ambient excitation, which may lead to false alarms.

Due to these reasons, a robust variant of the presented damage detection test was derived in [6]. It is based on the property that the Hankel matrix $\hat{\mathcal{H}}_{p+1,q}$ and the matrix of its principal left singular vectors $\hat{U}_1$ (see SVD in (19.7)) share the same left null space S—another characteristic property of the reference state can be written as

$$S^T \hat{U}_1 \approx 0,$$

analogous to (19.8). While the Hankel matrix $\hat{\mathcal{H}}_{p+1,q}$ is dependent on the ambient excitation properties, matrix $\hat{U}_1$ is a matrix with orthonormal columns and thus can be regarded as independent of the excitation properties. Note that matrix $\hat{U}_1$ is defined by a unique SVD (e.g. by forcing the first entry in each column to be positive) to ensure no changing modal basis.

Since $\hat{U}_1$ is independent of the excitation, a robust residual vector is defined as

$$\xi = \sqrt{N}\,\mathrm{vec}\left(S^T \hat{U}_1\right) \tag{19.11}$$

is defined [6]. It is tested if this residual is significantly different from zero or not, using the χ^2 test

$$\chi^2_\xi = \xi^T \Sigma_\xi^{-1} \xi, \tag{19.12}$$

where the empirical residual covariance $\Sigma_\xi = \mathrm{cov}(\xi)$ is computed on several datasets from the reference state as detailed in [6].

19.4 Applications

19.4.1 Numerical Application: Simulated Truss Structure

A truss model with 25 DOF (see Fig. 19.1) was considered in a first numerical application as in [6]. The output data was generated at six sensor positions in vertical direction at the lower chord by exciting the structure at the same positions with white noise. The excitation noise at these six positions was generated with a diagonal covariance matrix Q, whose diagonal entries were randomly chosen from a uniform distribution in the interval $[1, 36]$. Five percent white noise were added on the generated outputs.

Damage was simulated by decreasing the stiffness of element 16 in a first step by 10% and in a second step by 20%, leading to a decrease of the structure's natural frequencies of up to 1.0% and 2.2% compared to the reference state, respectively. In the reference state, the null space S and the residual covariance Σ_ζ (for the conventional test (19.10)) and Σ_ξ (for the robust test (19.12)) were computed on 10 data sets to set up the parameters of the damage detection tests.

In each structural state, data sets of length $N = 25{,}000$ at a sampling frequency of 50 Hz were generated. To compare both damage detection tests under changing excitation, 100 new data samples were generated with random excitation covariance in the reference and both damaged states, on which the χ^2-tests were computed in Fig. 19.2. For each of the compared tests, an empirical threshold was computed from the χ^2-values of the reference state allowing a 5% type I error (horizontal dashed line).

As can be seen in Fig. 19.2a, the damage detection fails with the conventional test under changing excitation properties, while the new robust damage detection test in Fig. 19.2b manages to separate the reference state from the damaged states very well.

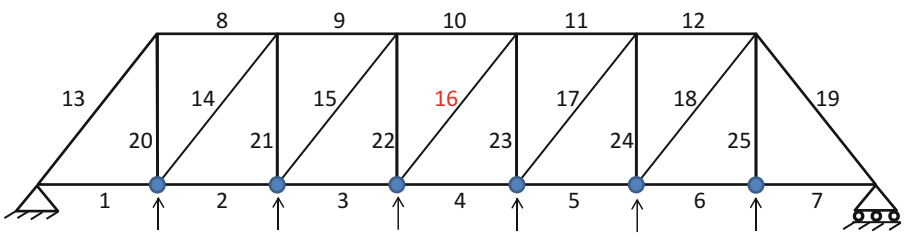

Fig. 19.1 Truss structure with six sensors

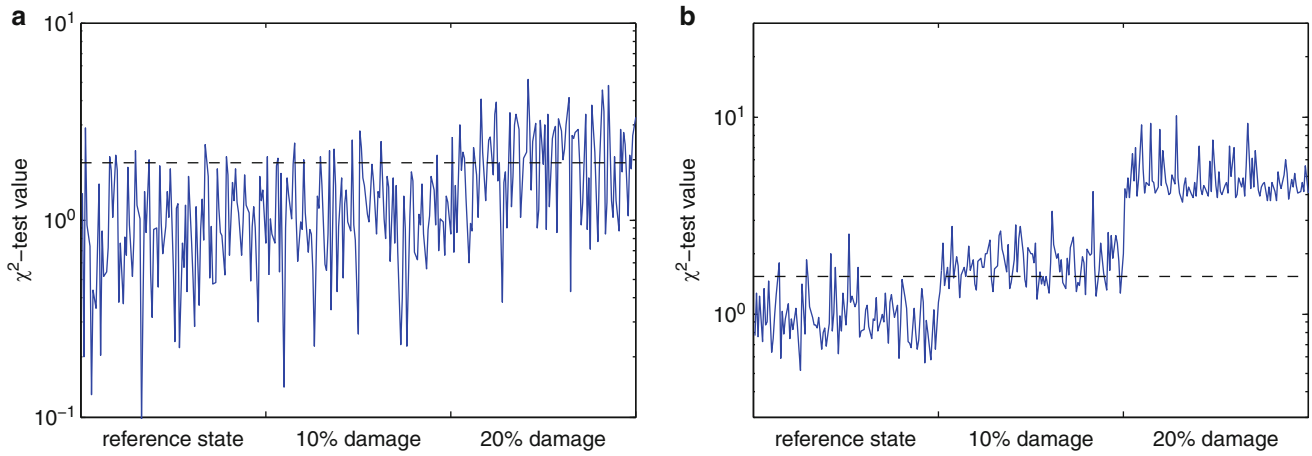

Fig. 19.2 Comparison of damage detection tests on simulated truss structure (log-scale). (**a**) Conventional test (19.10). (**b**) New robust test (19.12)

19.4.2 Laboratory Application: Steel Frame Structure

A test series has been performed at a jacket-like steel structures within the lab facilities of BAM to verify the usability, reliability and robustness of the introduced damage detection algorithm under changing excitation properties. The test structure provides the ability to gradually and reversibly increase artificially induced structural damage. The test stand can be used to analyze vibration based damage identification methods or just the sensitivity of single parameters influencing the identification of structural damage.

19.4.2.1 The Lab Structure and Damage Modeling

For the lack of options to test damage identification methods on real size civil engineering structures it is common to experimentally analyze newly developed procedures on scaled medium size laboratory structures. This is especially true for new structural types as e.g. offshore wind energy converters. As part of the research work on subspace-based damage detection on offshore structures at BAM a particular steel frame structure has been constructed and is provided as laboratory model.

The model structure is made of steel pipe components representing a scaled two-dimensional section of a jacket-type support structure for an offshore wind energy converter. For this purpose one and a half diagonal bracings are designed between the two legs. The upper completion is formed by an I-sectional steel beam. At the lower end the legs end in steel foot plates. With exception of the damage sections all structural parts of the model are welded. The foot plates are screwed via a transition piece to the floor. In the z-direction the structure is held on its head girder by a complex construction, whose two fork-like support poles allow a movement of the structure in the x-direction (Fig. 19.3).

The lab structure is constructed such that a defined local loss of stiffness can be modeled, which complies with the requirements of a realistic projection of an individual fatigue crack as a damage, and the reversibility of the induced damages is assured for the repeatability of test series. Though, cracks as damage can be induced artificially at one K-type gusset of the model structure by loosening bolts of a flange connection. Four of such flange connections were designed, each at the four ends of the K-type gusset. The progress of a crack-like damage is then simulated by the number of bolts that are loosened. Each flange joint was equipped with a maximal possible number of bolts to provide a high resolution of the induced stiffness loss.

19.4.2.2 Measurement Setup

The excitation for the tests was provided by an electrodynamic shaker. A broadband random acceleration signal with a frequency content between 10 and 1,000 Hz was produced by a shaker control unit and was induced via the shaker at the top of the structure after amplification. The shaker was equipped with a 5 kg excitation mass and the excitation direction was horizontal and approximately 30° rotated out of the in-plane-direction.

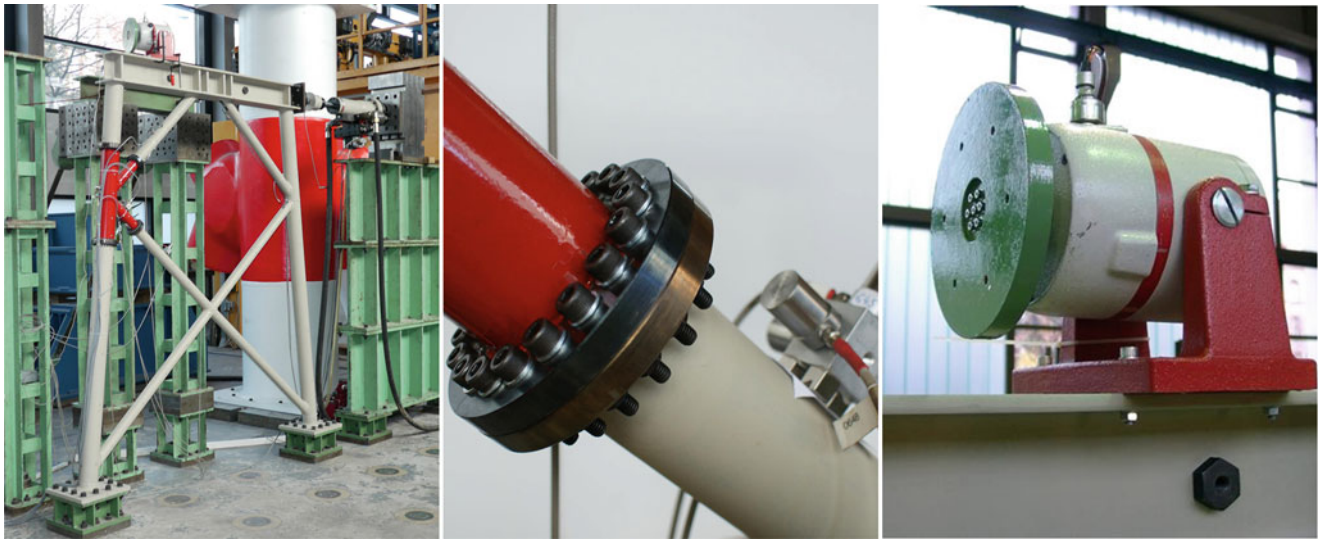

Fig. 19.3 Test stand for proof testing of damage identification algorithms; *left*: laboratory structure, *middle*: flange connection for damage modeling, *right*: electrodynamic shaker for excitation

Nine piezoelectric accelerometers were applied at the structure for the vibration measurements. The sensors were connected with the structure by permanent magnets and measured in the direction perpendicular to the surface they were applied to. The signals were amplified, recorded and stored with a 20 channel DIFA measurement unit.

19.4.2.3 Damage Detection Test

A test series was conducted to validate the reliability and sensitivity of the described robust damage detection procedure under changing excitation. In the tests, the time signals were measured for 16.4 s with a sampling rate of 2,500 Hz, which results in 40,960 data points per signal.

The damage location was chosen at the lower brace of the flange. In the reference state all bolts were screwed tight. For inducing damage, successively 1, 2, 3, 5 or 7 adjacent bolts were unscrewed, each representing a fatigue crack of increasing length. Thereby, the loosening of 3 bolts is comparable with a reduction of the moment of inertia by 3%, whereas the unscrewing of 7 bolts means a loss of already 30% of the bending stiffness.

To validate the damage detection algorithm under changing excitation, three excitation (power) levels were used for each damage state. Besides the full scale level, a reduction of 5 dB and a reduction of 10 dB with respect to the full scale level were performed and are denoted as "Excitation 1", "Excitation 2" and "Excitation 3" in the tests, respectively. A reduction of 5 dB accounts for a power ratio of $\approx$0.31 and an amplitude ratio of $\approx$0.56 and a reduction of 10 dB for a power ratio of 0.1 and an amplitude ratio of $\approx$0.31. The full scale excitation power level was chosen preliminary in dependence of the shaker performance. For each damage level and each excitation level, four signals of 16.4 s length was measured.

19.4.2.4 Results

Both the conventional damage detection test presented in Sect. 19.2.3 and the robust damage detection test under changing excitation in Sect. 19.3 are applied to the measured data with exactly the same parameters.

Two data sets from Excitation 1 and two data sets from Excitation 3 in the reference state are used to compute the null space S and the covariance Σ for both test variants. The tests were set up with the parameters of the block Hankel matrix $p+1 = q = 15$ and model order $n = 120$, resulting in the dimension of the null space S of $qr-n = 15$. The mentioned data sets were separated into altogether 1,000 pieces for the computation of the covariance matrix. See also [6] for the numerical details and an efficient implementation of these computations.

Then, both tests (see Eqs. (19.10) and (19.12), respectively) are applied to all the measured data sets in the reference and damaged states at the three different excitation levels. The computed χ^2 test values are presented in Fig. 19.4a,b for both tests, respectively, together with an empirical threshold that was set up using the χ^2 test values of the reference state.

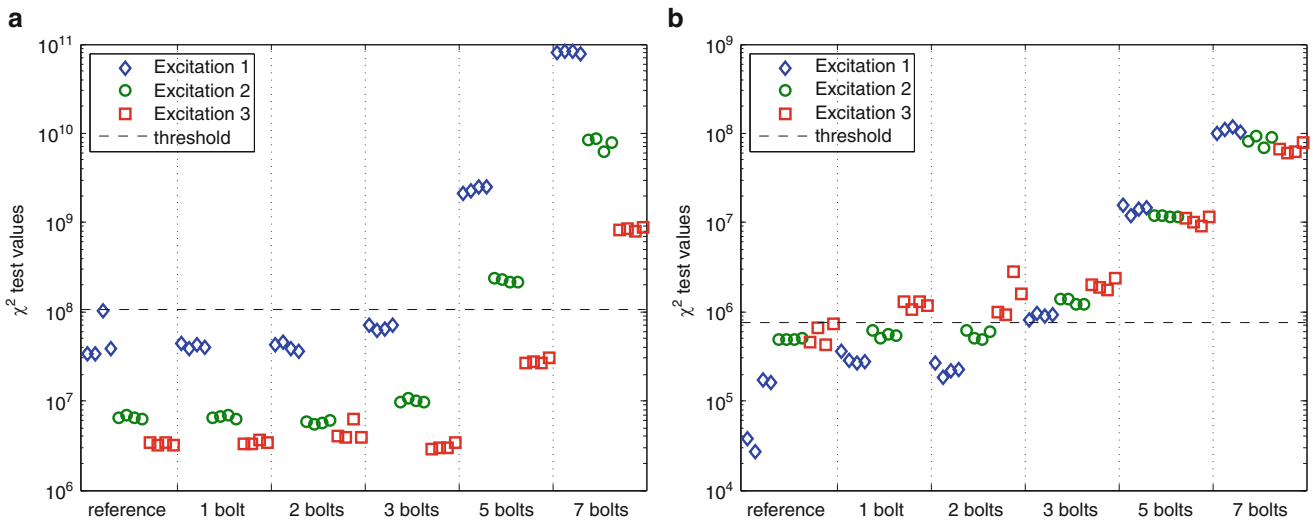

Fig. 19.4 Comparison of damage detection tests on steel frame structure in a lab experiment (log-scale). (**a**) Conventional test (19.10). (**b**) New robust test (19.12)

In Fig. 19.4a it can be seen that the conventional test reacts strongly to different excitation levels. A decrease in the excitation level results also in a decrease in the χ^2 test value, independently of the damage. While the χ^2 test values increase with the damage size for each excitation level, this increase is not distinguishable for the different excitation levels. Only the χ^2 test values of a significant damage (7 loosened bolts) all lie over the threshold that was established in the reference state. Thus, only damages can be clearly detected with the conventional test, whose influence on the χ^2 test is stronger than the changes in excitation.

On the other side, the results of the new test in Fig. 19.4b clearly show a stronger robustness to changing excitation properties. While there are still small fluctuations of the test values in the reference state and in the states with small damage, these fluctuations are less significant. For the damages from 3 loosened bolts on, these variations seem to be independent from the excitation level, which validates the robustness of the new test to changing excitation. Furthermore, the relatively small damage of only 3 loosened bolts can be clearly detected under changing excitation with the new test thanks to its robustness.

19.5 Conclusions

In this paper, the recently developed statistical subspace-based damage detection test from [6] that is robust to changing ambient excitation properties was successfully tested on real data from a lab experiment for the first time. In this experiment a steel frame structure was artificially damaged by loosening bolts of a flange connection and output-only data was recorded under different excitation levels. The new test that was designed to be robust to changing excitation properties showed much better damage detection results in this setting with an earlier detection of damage than a previous conventional damage detection test. Since the applied damage detection framework already proved to be feasible for real civil structures in the field (see e.g. case studies [4, 9, 14]), the presented test robust to excitation changes should be of value for such applications, where the excitation is ambient and uncontrolled, and where the new test is thus expected to detect damage earlier and more reliably. The application of the new test to structures in the field is part of future work.

Acknowledgements The partial support from the European project FP7-PEOPLE-2009-IAPP 251515 ISMS is gratefully acknowledged.

References

1. Balmès E, Basseville M, Bourquin F, Mevel L, Nasser H, Treyssède F (2008) Merging sensor data from multiple temperature scenarios for vibration-based monitoring of civil structures. Struct Health Monit 7(2):129–142
2. Basseville M, Abdelghani M, Benveniste A (2000) Subspace-based fault detection algorithms for vibration monitoring. Automatica 36(1): 101–109
3. Basseville M, Mevel L, Goursat M (2004) Statistical model-based damage detection and localization: subspace-based residuals and damage-to-noise sensitivity ratios. J Sound Vib 275(3):769–794
4. Döhler M, Hille F, Mevel L, Rücker W (2014) Structural health monitoring with statistical methods during progressive damage test of S101 Bridge. Eng Struct. Under revision
5. Döhler M, Mevel L (2013) Subspace-based fault detection robust to changes in the noise covariances. Automatica 49(9):2734–2743
6. Döhler M, Mevel L, Hille F (2014) Subspace-based damage detection under changes in the ambient excitation statistics. Mech Syst Signal Process. 45(1):207–224, 2014
7. Döhler M, Mevel L, Siegert D (2012) Statistical subspace-based damage detection under changing ambient excitation. In: Proc. 5th european conference on structural control, Genoa, Italy, 2012
8. Magalhães F, Cunha A, Caetano E (2008) Dynamic monitoring of a long span arch bridge. Eng Struct 30(11):3034–3044
9. Mevel L, Goursat M, Basseville M (2003) Stochastic subspace-based structural identification and damage detection and localization - Application to the Z24 Bridge benchmark. Mech Syst Signal Process 17(1):143–151
10. Peeters B, De Roeck G (1999) Reference-based stochastic subspace identification for output-only modal analysis. Mech Syst Signal Process 13(6):855–878
11. Ramos L, Marques L, Lourenço P, De Roeck G, Campos-Costa A, Roque J (2010) Monitoring historical masonry structures with operational modal analysis: Two case studies. Mech Syst Signal Process 24(5):1291–1305. Special Issue: Operational Modal Analysis
12. Strout J, Döhler M, Bernal D, Mevel L (2012) Changes in the statistics of ambient excitations in the performance of two damage detection schemes. In: Proc. 30th international modal analysis conference, Jacksonville, FL, USA, 2012
13. Van Overschee P, De Moor B (1996) Subspace identification for linear systems: theory, implementation, applications. Kluwer Academic, Dordrecht
14. Zhou W, Wu Z, Mevel L (2010). Vibration-based damage detection to the composite tank filled with fluid. Struct Health Monit 9(5):433–445

Chapter 20
Real-Time Structural Damage Identification of Time-Varying Systems

Jiann-Shiun Lew

Abstract This paper presents an investigation of real-time structural damage identification for time-varying systems, such as aircraft with changing flight condition. The on-line damage detection is implemented by comparing the changes of the identified model, which is updated by synthesizing time-domain input/output data, with the changes of the analytical model due to damage. The study is based on the identified models with various model structures, state space model, transfer function, and Auto-Regressive eXogenous (ARX) model. Some identified parameters are much more sensitive to noise, and the inclusion of these parameters in damage identification may significantly reduce the reliability of damage detection with false indications of damage. A technique is presented for the selection of the identified parameters for damage identification. The investigation is demonstrated by application to the Benchmark Active Controls Technology (BACT) wind-tunnel model with time-varying dynamic pressure and Mach number.

Keywords System identification • Damage identification • Time varying system • Model uncertainty • Model structure

20.1 Introduction

Real-time structural damage identification, based on the measured input/output data, of a time-varying system can be a challenging task because of system variation, disturbance, and environmental uncertainty. This brings a challenging problem to vibration-based structural health monitoring (SHM) methods [1, 2] for time-varying systems, which compare the change of the identified modal parameters and the change of the analytical model due to damage. Real-time damage identification of time-varying systems requires that the identified model be updated effectively and accurately to get reliable damage detection results.

The study in this paper is based on the simulation of the Benchmark Active Controls Technology (BACT) wind-tunnel model [3], which was developed by researchers at the NASA Langley research center to address the flutter problem. Aircraft structural damage and component damage can cause unwanted aerodynamic effects and may lead to a catastrophic structural failure of the flight vehicle [4]. If these anomalies can be identified, they can be used as input to an adaptive control system to properly adjust to accommodate these conditions. The real-time structural damage identification of aircraft is a challenging task due to the flight condition variation and flight environmental uncertainty.

This paper presents an investigation of real-time structural damage identification for time-varying systems. The proposed technique integrates real-time system identification and damage identification. First, time-domain system identification techniques, such as OKID [5] and subspace system identification techniques [6], are applied to synthesize the collected time-domain input/output data to get the identified models in various conditions. The study in this paper is based on the identified models of different model structures: state space model; transfer function; and Auto-Regressive eXogenous (ARX) model. The residual errors between the identified parameters of the tested system and the estimated parameters of the health

J.-S. Lew (✉)
Center of Excellence in Information Systems, Tennessee State University, Nashville, TN 37209, USA
e-mail: lew@coe.tsuniv.edu

A. Wicks (ed.), *Structural Health Monitoring, Volume 5: Proceedings of the 32nd IMAC, A Conference and Exposition on Structural Dynamics, 2014*, Conference Proceedings of the Society for Experimental Mechanics Series, DOI 10.1007/978-3-319-04570-2_20,

structure are used for damage identification. Some identified parameters are much more sensitive to noise and have significant errors due to noise and environmental uncertainty. The inclusion of these identified parameters, which are sensitive to noise, in damage identification may significantly reduce the reliability of damage identification with false indications of damage. This paper presents a technique for the selection of the identified elements for damage identification. A correlation approach [2, 7], which is based on the comparison of the change of the identified model with the change of the analytical model due to damage, is used to identify the damage type and intensity. The proposed approach is demonstrated by application to the BACT wind-tunnel model with changing flight conditions. The results of the examples based on the BACT model with various flight conditions show that the proposed damage identification technique can effectively identify damage status, damage type, and precisely estimate the intensity of damage.

20.2 System Identification

The investigation in this paper is based on the identified models of three different model structures, state space model, transfer function, and ARX model. System identification is done on-line to generate a real-time updated model for the time-varying system for damage identification.

20.2.1 State Space Model

The identified state space model is expressed as the companion canonical form [8] to insure a small number of parameters. The state space model of an m-output and n-input system with l-state can be expressed as

$$A = \begin{bmatrix} 0 & \cdots & 0 & a_1 \\ 1 & \cdots & 0 & a_2 \\ \vdots & \ddots & \vdots & \vdots \\ 0 & \cdots & 1 & a_l \end{bmatrix}, \quad B = \begin{bmatrix} 1 & b_{12} & \cdots & b_{1n} \\ 0 & b_{22} & \cdots & b_{2n} \\ \vdots & \vdots & \ddots & \vdots \\ 0 & b_{l2} & \cdots & b_{ln} \end{bmatrix},$$
$$C = \begin{bmatrix} c_{11} & \cdots & c_{1l} \\ \vdots & \ddots & \vdots \\ c_{m1} & \cdots & c_{ml} \end{bmatrix}, \quad D = \begin{bmatrix} d_{11} & \cdots & d_{1n} \\ \vdots & \ddots & \vdots \\ d_{m1} & \cdots & d_{mn} \end{bmatrix}. \tag{20.1}$$

The number of parameters of this state space model is $nl + m(l + n)$. The identified parameter vector of this state space model can be expressed as

$$\theta = \begin{bmatrix} a_1 \cdots a_l & b_{12} \cdots b_{ln} & c_{11} \cdots c_{ml} & d_{11} \cdots d_{mn} \end{bmatrix}. \tag{20.2}$$

Time-domain system identification techniques, such as OKID [5] and subspace system identification techniques [6], can be applied to synthesize the collected time-domain input/and output data to get the identified state space model. Then the identified space model can be transferred as the companion canonical form.

20.2.2 Transfer Function

The transfer function of the ith output from the jth input of an m-output and n-input system can be expressed as

$$f_{ij}(s) = \frac{f_{ij}^{l+1} s^l + f_{ij}^l s^{l-1} + \cdots + f_{ij}^1}{s^l + f^l s^{l-1} + \cdots + f^1}, \quad i = 1, \cdots m, \; j = 1, \cdots, n, \tag{20.3}$$

where l is the order of the transfer function. The number of the transfer function coefficients of this system is $l + mn(l + 1)$. The identified parameter vector of this transfer function can be expressed as

$$\theta = \left[f^1 \cdots f^l \quad f_{11}^1 \cdots f_{11}^{l+1} \cdots f_{mn}^1 \cdots f_{mn}^{l+1} \right]. \tag{20.4}$$

System identification techniques can be applied to synthesize the collected input/and output data to update the identified transfer function.

20.2.3 ARX Model

The relationship between the input and output time histories of a linear system is described by the time-domain ARX finite-difference model as follows

$$\begin{aligned} &y(k) + \alpha_1 y\,(k-1) + \alpha_2 y\,(k-2) + \cdots + \alpha_p y\,(k-p) \\ &= \beta_0 u(k) + \beta_1 u\,(k-1) + \cdots + \beta_p u\,(k-p)\,. \end{aligned} \tag{20.5}$$

This equation states that the current output $y(k)$ at time step k may be estimated by using p sets of the previous output and input measurements and the current input measurement. The integer p is called the order of the ARX model. The coefficient matrices α_i and β_i in this equation are referred to as observer Markov parameters (OMP) or ARX parameters and are the quantities to be determined by the identification algorithm. The goal of system identification is to determine the OMP, based on input and output data. The OMP may be determined by any identification techniques that return an ARX model of the system [9].

20.3 Damage Identification

The on-line damage identification is implemented by comparing the changes of the elements of the identified parameter vector with the changes of the analytical model due to damage. The identified model includes structural modes, disturbance modes, and computational modes due to higher model order. Some identified parameters are sensitive to the change of the flight condition and structural damage. Some identified parameters are much more sensitive to noise and have significant errors due to noise and environmental uncertainty. The inclusion of the identified parameters, which are sensitive to noise, in damage identification may significantly reduce the reliability of damage identification with false indications of damage. A technique is presented for the selection of the identified elements for damage identification.

The variance of the *j*th identified parameter under various flight conditions (n_e experimental tests or different time periods of data) is computed as

$$\sigma_j^2 = \frac{1}{n_e - 1} \sum_{i=1}^{n_e} \left[\theta_j\,(t_i) - \frac{1}{n_e} \sum_{k=1}^{n_e} \theta_j\,(t_k) \right]^2, \tag{20.6}$$

where $\theta_j(t_i)$ is the *j*th element of the identified parameter vector at time t_i based on the collected data in the *i*th time period ended at time t_i. The change of each identified element due to noise can be estimated as

$$\Delta\theta_j\,(t_i) = \tilde{\theta}_j\,(t_i) - \theta_j\,(t_i)\,, \tag{20.7}$$

where $\tilde{\theta}_j\,(t_i)$ is the *j*th element of the identified parameter vector for the output with the added noise as

$$\tilde{y}(k) = y(k) + \nu, \tag{20.8}$$

where ν is the added normally distributed white noise with zero mean and the specified standard deviation. The variance of the *j*th identified parameter due to noise is estimated as

$$\tilde{\sigma}_j^2 = \frac{1}{n_e - 1} \sum_{i=1}^{n_e} \left[\Delta\theta_j\,(t_i) - -\frac{1}{n_e} \sum_{k=1}^{n_e} \Delta\theta_j\,(t_k) \right]^2. \tag{20.9}$$

The ratio between the change due to flight condition variation and the change due to noise is defined as

$$\lambda_j = \frac{\sigma_j}{\tilde{\sigma}_j}. \tag{20.10}$$

If this ratio λ_j is larger than the specified threshold value λ, then the jth element is chosen for damage identification.

The deviation between the identified parameter vector of the tested system and the estimated parameter vector of the healthy structure can be computed as

$$\Delta\hat{\theta}\left(t_i\right) = \hat{\theta}\left(t_i\right) - \hat{\theta}_h\left(t_i\right), \tag{20.11}$$

where $\hat{\theta}\left(t_i\right)$ is the identified parameter vector of the selected elements at time t_i, and $\hat{\theta}_h\left(t_i\right)$ is the estimated parameter vector of the healthy structure based on the tests without damage. To identify the damage, the change of the parameter vector of the analytical model due to a referred damage is computed as

$$\Delta\theta_d = \theta_d - \theta_h, \tag{20.12}$$

where θ_d is the parameter vector of the damage case, and θ_h is the parameter vector of the healthy structure. The correlation between the weighted parameter vector change of the tested system and the weighted change vector of the analytical model caused by the referred damage is defined as [2]

$$C\left(t_i\right) = \frac{\left(\Delta\hat{\theta}^W\left(t_i\right)\right)^T\left(\Delta\theta_d^W\right)}{\left|\Delta\hat{\theta}^W\left(t_i\right)\right|\left|\left|\Delta\theta_d^W\right|\right|}, \tag{20.13}$$

where the weight of each element is the standard deviation of this identified element of various tests. The correlation $C(t_i)$ represents the cosine between two vectors. The value of the correlation $C(t_i)$ is between -1 and 1. When the absolute value of $C(t_i)$ is close to 1, it indicates that the damage [7] occurs before time t_i. The magnitude ratio between the weighted change vector of the tested system and the weighted change vector of the analytical model caused by the referred damage is defined as

$$G\left(t_i\right) = \frac{\left|\Delta\hat{\theta}^W\left(t_i\right)\right|}{\left|\Delta\theta_d^W\right|}. \tag{20.14}$$

The magnitude ratio can be used to identify the type and intensity of damage [7].

20.4 Results and Discussions

The Benchmark Active Controls Technology system consists of a rigid wing section and a flexible mounting system as shown in Fig. 20.1. The accelerometers are the primary sensors for feedback control and are located at each corner of the wing [3].

A simplified state-space model was generated for the dynamics of the BACT wind-tunnel model [3]. The open-loop BACT model has two modes, where the second mode (flutter mode) becomes unstable when the dynamic pressure is above 150.8 psf at a Mach number of 0.77. In this study, the model has two inputs, the trailing edge deflection control surface

Fig. 20.1 Photograph of BACT wing section and flexible mount

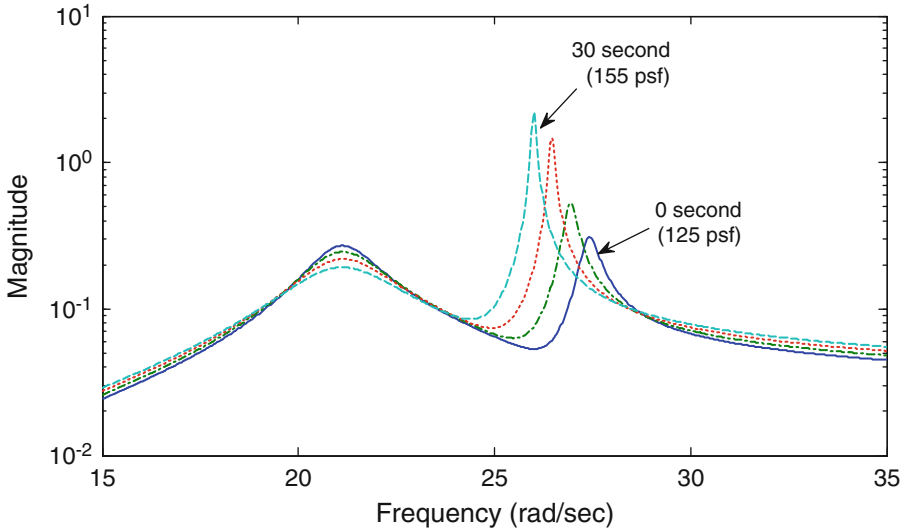

Fig. 20.2 Transfer function at various times

and the upper spoiler deflection control surface, and two outputs, the trailing edge inboard acceleration and the leading edge inboard acceleration. The real-time random input response data are generated from this BACT model with one added sine-wave disturbance input at a frequency of 6 Hz plus the added measurement noise, normally distributed white noise with zero mean. The dynamic pressure of the simulated BACT model increases with time, starting from 125 psf with an increment rate of 60 psf/min, while the Mach number decreases with time, starting from 0.85 with a reduction rate of 0.18/min. Figure 20.2 shows the magnitude of a transfer function, corresponding to the leading edge inboard acceleration measurement with trailing edge deflection control surface, at four different times: 0th second, 10th second, 20th second, and 30th second. Structural dynamics change significantly over time with flight condition variation. In particular, the natural frequency and damping ratio of the second mode change dramatically with time.

The input/output data are generated with a sampling rate of 80 samples/s. System identification techniques are applied to synthesize the input/output data within every two seconds, where 160 data points are used, to get each identified model. The identified model is updated every second based on the data in 2 s with 160 data points. In this example, the considered damage is the reduction of the plunge stiffness. The plunge stiffness of the healthy structure is 2,686 lb/ft. The structural damage happens at the 13th second with a dynamic pressure of 145 psf and a Mach number of 0.79, where the plunge stiffness reduces 6.92 % to 2,500 lb/ft.

20.4.1 State Space Model

The investigation is based on three cases with different noise levels: noise free; low noise; and high noise. The added sine-wave disturbance and the added measurement noise of the high noise case are ten times those of the low noise case. The subspace system identification (SSID) technique [6] is applied to synthesize the input/output data within every 2 s, where 160 data points are used, to update each identified model. The damage identification is based on the preceding technique. In this example, the model order of the identified state space model is chosen as 4, and the identified state space model in the companion canonical form in Eq. (20.1) has 20 parameters. Figure 20.3 shows two identified parameters of the eight identified models in the first 9 s for the low noise case, where the dynamic pressure and the Mach number change linearly within 7 s. The identified element in Fig. 20.3a, which has the largest ratio λ_j, varies linearly with time due to the linear flight condition variation. The identified element in Fig. 20.3b, which has the smallest ratio λ_j, has significant uncertainty, which is mainly due to the identified model error from the changing flight condition. This parameter in Fig. 20.3b should be excluded in damage identification for the low noise case.

Figure 20.4 shows the ratios for element selection of three cases, where the ratios are plotted from the largest to the smallest. The ratios of the low noise case are very close to the ratios of the noise free case, and the ratios have a significant drop from the third one to the fourth one. The added noise and disturbance of the low noise case increases the ratios a little, and the first ten ratios are larger than 1. For the high noise case, the added noise and disturbance significantly affects and increases the ratios, and there is no clear drop between the third and the fourth. The ratios from the fourth to the twentieth are dominated by the added noise and disturbance, and they decreases slowly.

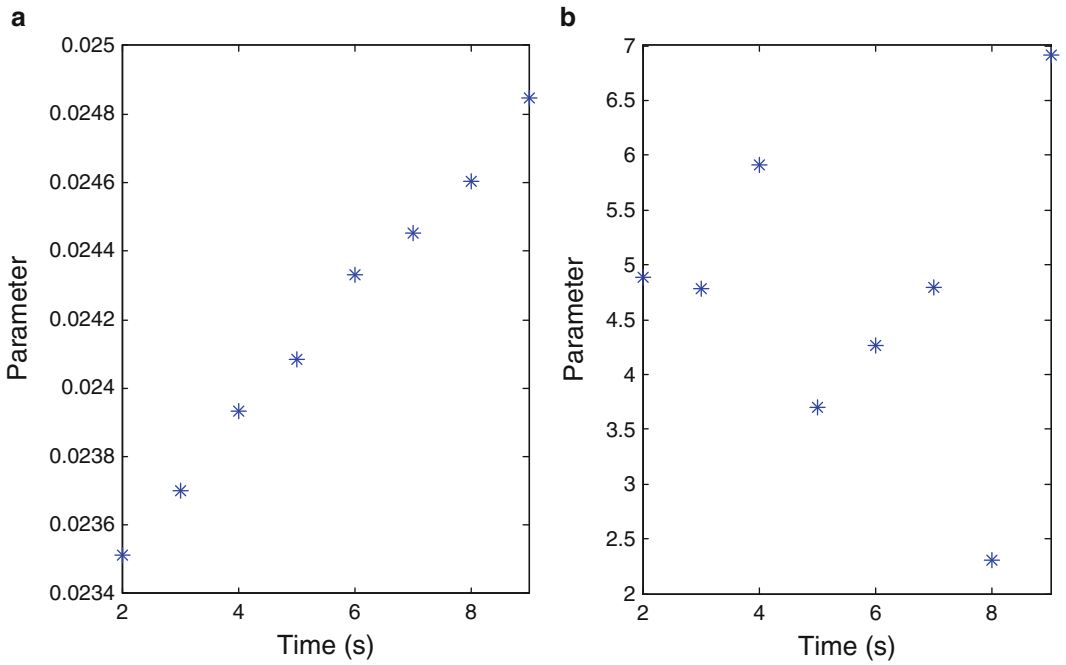

Fig. 20.3 Variation of two identified elements from 2 to 9 s: (**a**) with largest ratio λ_j; (**b**) with smallest ratio λ_j

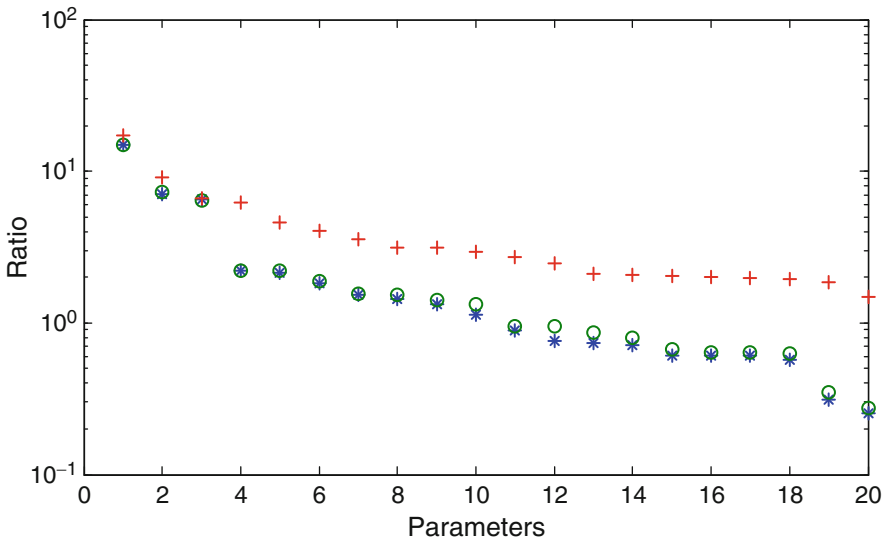

Fig. 20.4 Ratios λ_j of the identified parameters of state space model: (*asterisk*) noise free; (*open circle*) low noise; (*plus*) high noise

The first referred damage case for damage identification in Eq. (20.13) has a plunge stiffness reduction of 10 lb/ft, and the second referred damage case has a pitch stiffness reduction of 10 lb/ft. In the damage identification, the identified model is updated every half a second after 10 s. Figure 20.5 shows the correlations defined in Eq. (20.13) between the deviations of the identified elements for the referred damage case with plunge stiffness loss for the noise free case when the threshold value λ for the element selection is chosen as 1, where 10 elements are chosen for damage identification. The correlation is close to 1 after the 15th second, whereas the identified model at the 15th second is based on the data from the 13th second to the 15th second after damage occurs. Figure 20.6 shows the correlations for the referred damage case with pitch stiffness loss. The correlation is not close to 1 after 15 s, and it clearly indicates that the damage type is not the pitch stiffness loss. Figure 20.7 shows the magnitude ratios defined in Eq. (20.14) for the referred damage case with plunge stiffness loss. The estimated magnitude ratio increases after 13 s and it is close to 20 after 15 s. The magnitude ratio at the 15th second is 20.1, and the magnitude ratio for the analytical model with the plunge stiffness reduction to 2,500 lb/ft is 19.9. The intensity of damage is well estimated.

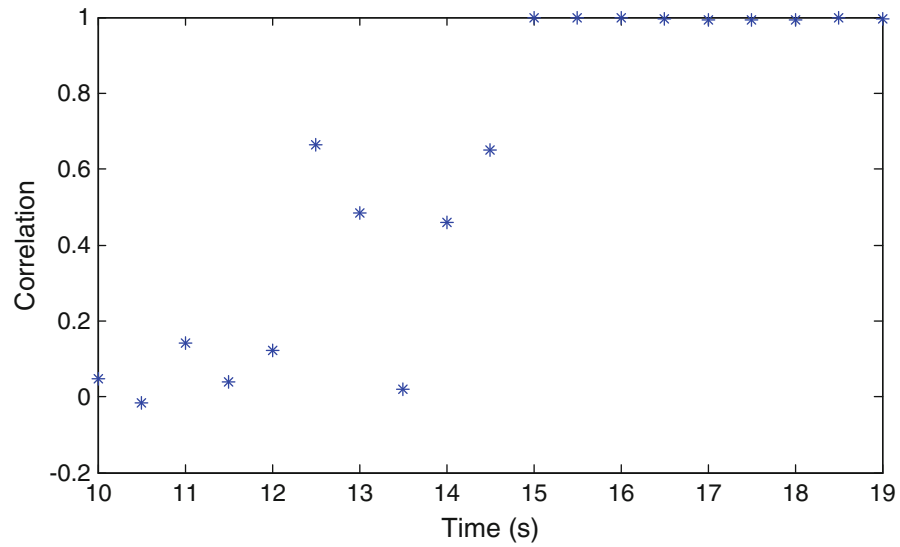

Fig. 20.5 Correlation as a function of time for the referred damage case with plunge stiffness loss of noise free case for $\lambda = 1$

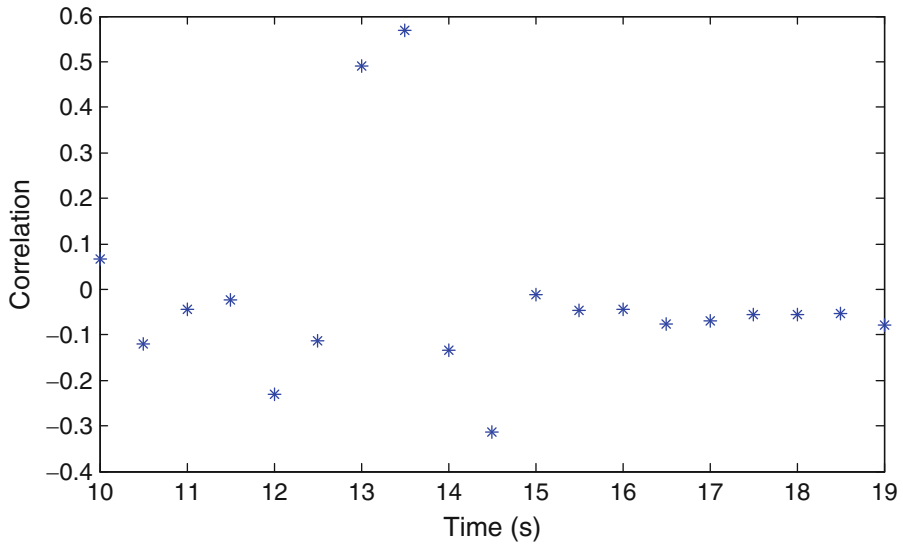

Fig. 20.6 Correlation as a function of time for the referred damage case with pitch stiffness loss of noise free case for $\lambda = 1$

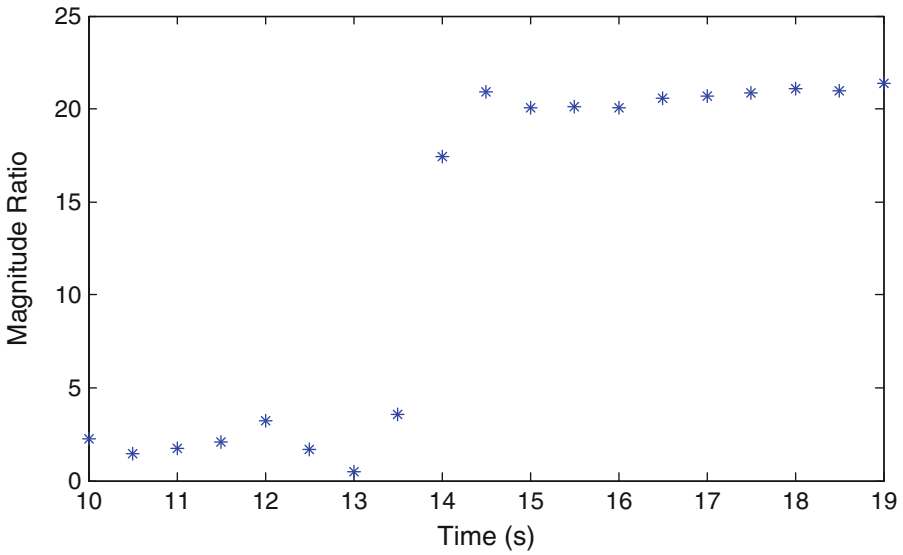

Fig. 20.7 Magnitude ratio as a function of time for the referred damage case with plunge stiffness loss of noise free case for $\lambda = 1$

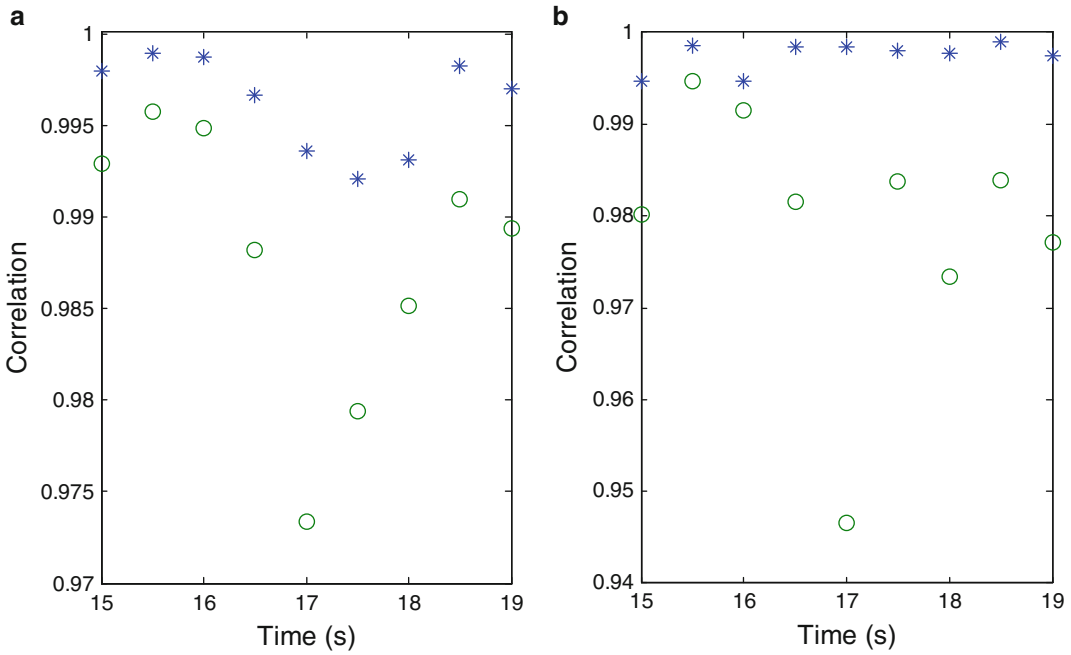

Fig. 20.8 Correlation as a function of time for the referred damage case with plunge stiffness loss: (*asterisk*) $\lambda = 1$; (*open circle*) $\lambda = 0.1$. (**a**) Noise free; (**b**) low noise

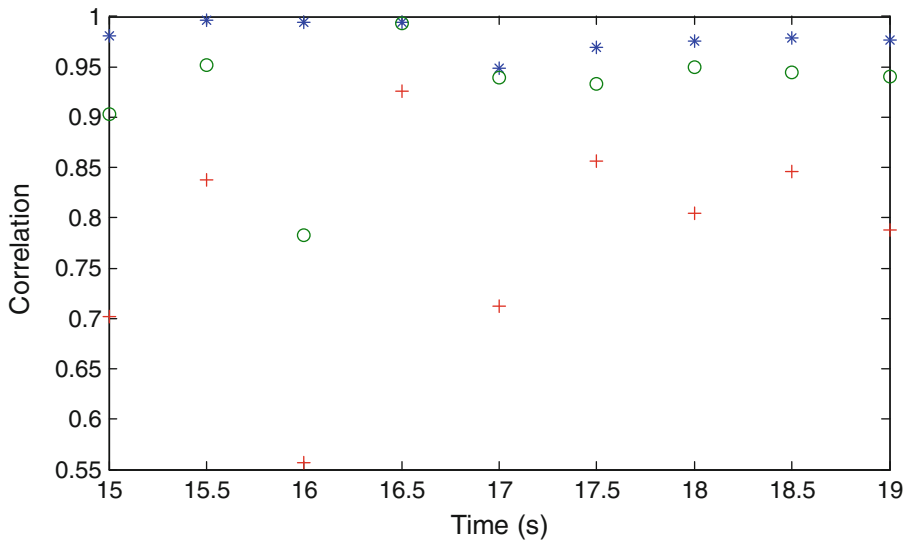

Fig. 20.9 Correlation as a function of time for the referred damage case with plunge stiffness loss of high noise case: (*asterisk*) $\lambda = 5$; (*open circle*) $\lambda = 4$; (*plus*) $\lambda = 1$

Figure 20.8 shows the correlations for the noise free and low noise cases when the threshold value λ for the element selection is 1 or 0.1, where 10 elements or 20 elements are used for damage identification. For the noise free case, the use of the 10 identified elements with the ratios larger than 1 can well identify the damage as the plunge stiffness loss, and the use of all the identified elements can still identify the damage. For the low noise case, the use of the 10 identified elements can well identify the damage, and the use of all the identified elements can still indicate the damage type except that the correlation at the 17th second is lower than 0.95, which doesn't clearly identify the damage.

Figure 20.9 shows the correlations for the high noise case when the threshold value λ for the element selection is 5, 4, or 1, where 4, 6, or 20 elements are used for damage identification. The use of 4 elements with the ratios larger than 5 can identify the damage, the use of 6 elements with the ratios larger than 4 cannot clearly identify the damage, and the use of 16 elements cannot identify the damage. Figure 20.10 shows the magnitude ratios for the high noise case when the threshold value λ is 5. The magnitude ratio is around 18 at the 15th second and it is 10 % lower than the true one due to the effect of the added disturbance and noise.

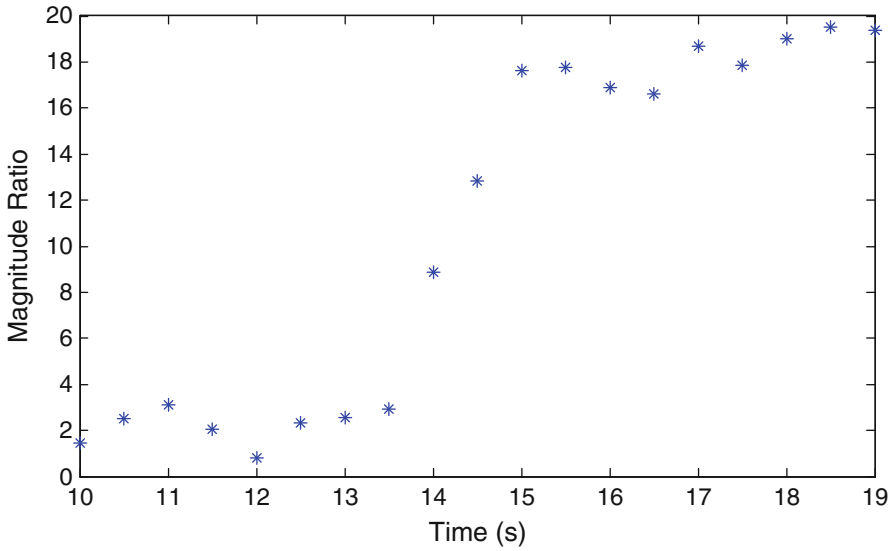

Fig. 20.10 Magnitude ratio as a function of time for the referred damage case with plunge stiffness loss of high noise case for $\lambda = 5$

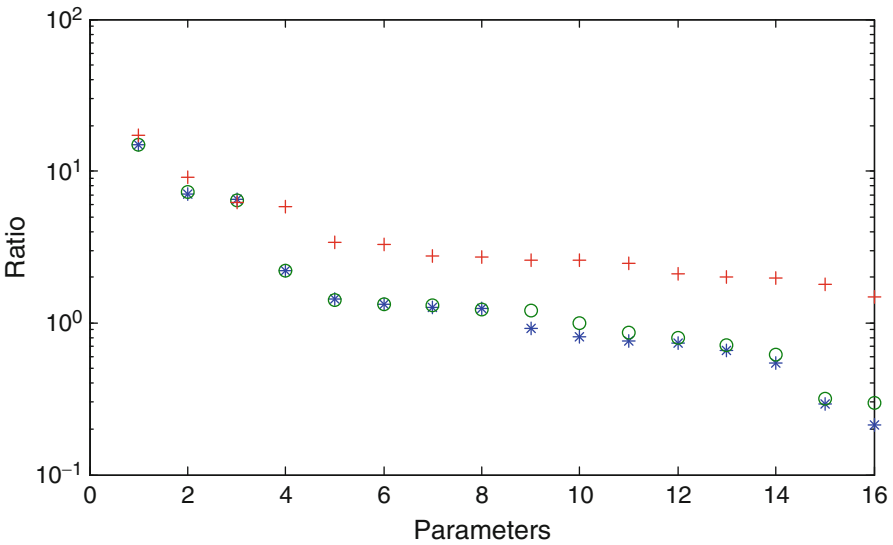

Fig. 20.11 Ratios λ_j of the identified parameters of transfer function: (*asterisk*) noise free; (*open circle*) low noise; (*plus*) high noise

20.4.2 Transfer Function

In this example, the model order of the identified transfer function is chosen as 4, and there are two inputs and two acceleration outputs. The identified transfer function has 16 parameters. The subspace system identification (SSID) technique [6] is applied to synthesize the input/output data within every 2 s, where 160 data points are used to update each identified model. Figure 20.11 shows the ratios for element selection for three cases: noise free; low noise; and high noise. The results in Fig. 20.11 are similar to the results in Fig. 20.4. Figure 20.12 shows the correlations for the noise free case when the threshold value λ for the element selection is 1 or 0.1, where 8 elements or 16 elements are used for damage identification. The use of the 8 identified elements with the ratios larger than 1 can well identify the damage, but the use of all the identified elements cannot clearly identify the damage. Figure 20.13 shows the correlations for the high noise case when the threshold value λ for the element selection is 5, 3, or 1, where 4, 6, or 16 elements are used for damage identification. The use of 4 elements with the ratios larger than 5 can still identify the damage except at the 17th second, the use of 6 elements cannot clearly identify the damage, and the use of 20 elements cannot identify the damage.

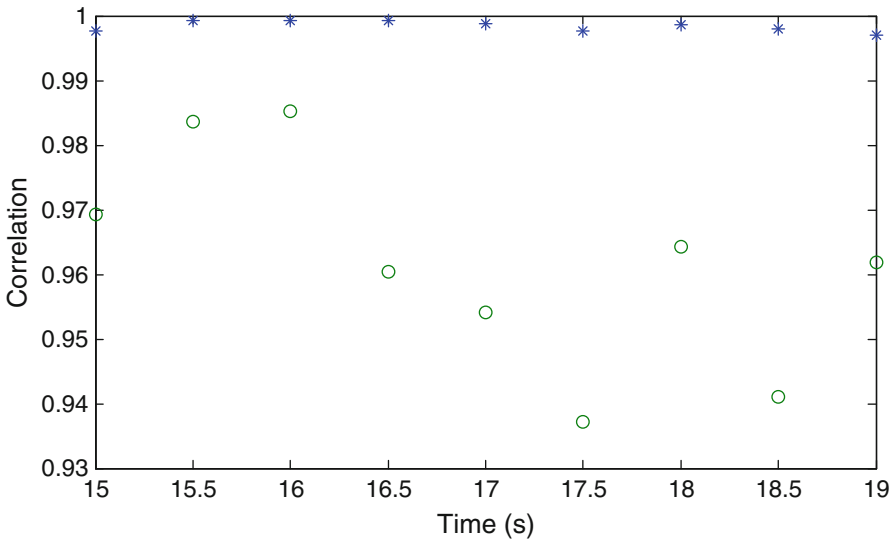

Fig. 20.12 Correlation as a function of time for the referred damage case with plunge stiffness loss of noise free case: (*asterisk*) $\lambda = 1$; (*open circle*) $\lambda = 0.1$

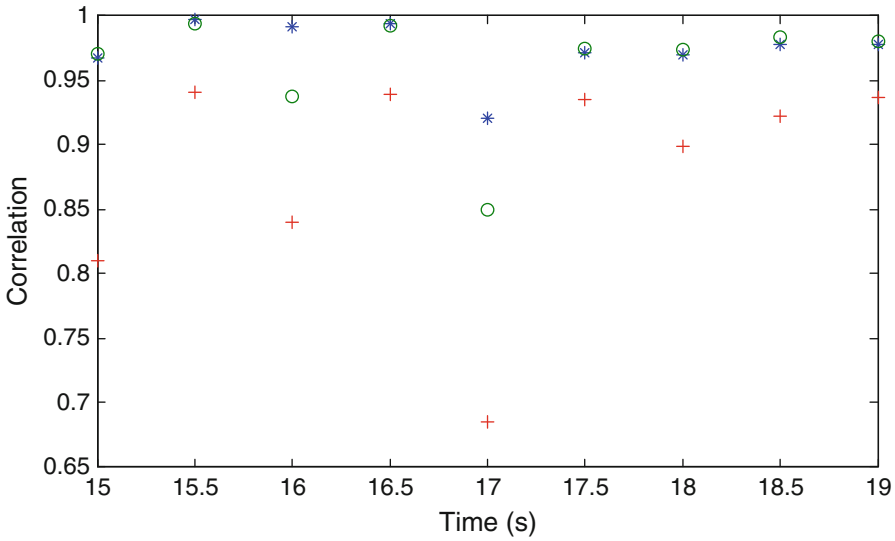

Fig. 20.13 Correlation as a function of time for the referred damage case with plunge stiffness loss of high noise case: (*asterisk*) $\lambda = 5$; (*open circle*) $\lambda = 3$; (*plus*) $\lambda = 1$

20.4.3 ARX Model

In this example, the order of the ARX model is chosen as 2. The identified ARX model has 20 parameters. A least-squares technique [9] is applied to synthesize the input/output data within every 2 s, where 160 data points are used, to update each identified model. Figure 20.14 shows the ratios for element selection for three cases: noise free; low noise; and high noise. For the low noise case, the added disturbance and noise has little effect on the ratios. The high noise has significant effects on the ratios. Figure 20.15 shows the correlations for the noise free case when the threshold value λ for the element selection is 3 or 0.2, where 10 elements or 20 elements are used for damage identification. The use of the 10 identified elements with the ratios larger than 3 can well identify the damage as the plunge stiffness loss, but the use of all the identified elements cannot identify the damage. Figure 20.16 shows the correlations for the high noise case when the threshold value λ for the element selection is 7.5, 6, or 1, where 5, 7, or 20 elements are used for damage identification. The use of 5 elements cannot clearly identify the damage, and the use of 7 elements or 20 elements cannot identify the damage.

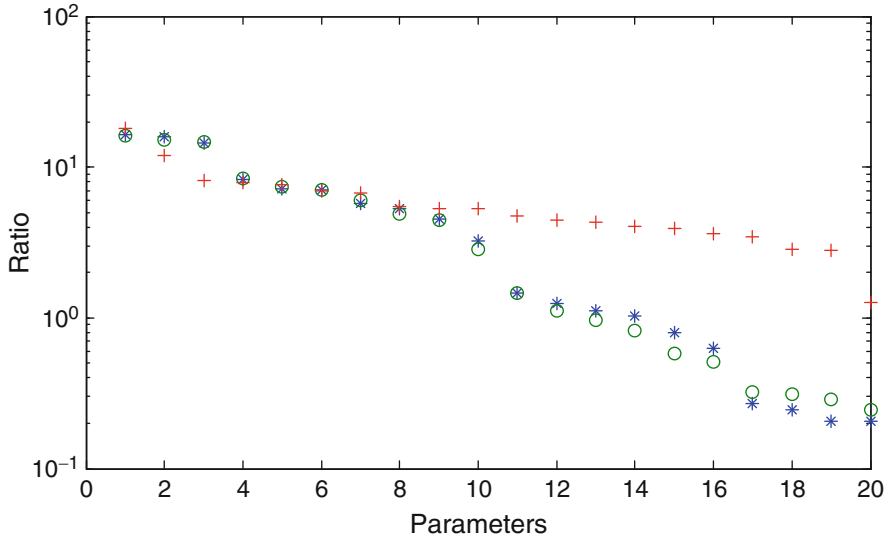

Fig. 20.14 Ratios λ_j of the identified parameters of ARX model: (*asterisk*) noise free; (*open circle*) low noise; (*plus*) high noise

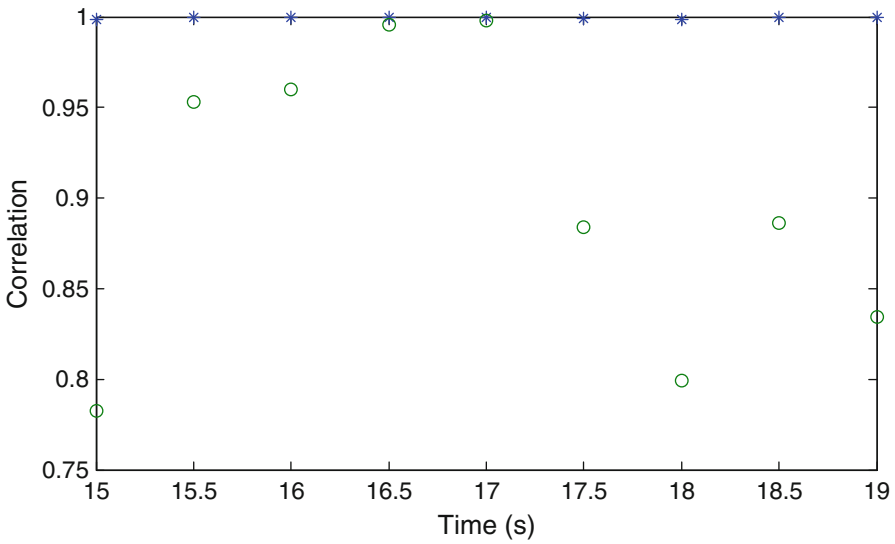

Fig. 20.15 Correlation as a function of time for the referred damage case with plunge stiffness loss of noise free case: (*asterisk*) $\lambda = 3$; (*open circle*) $\lambda = 0.2$

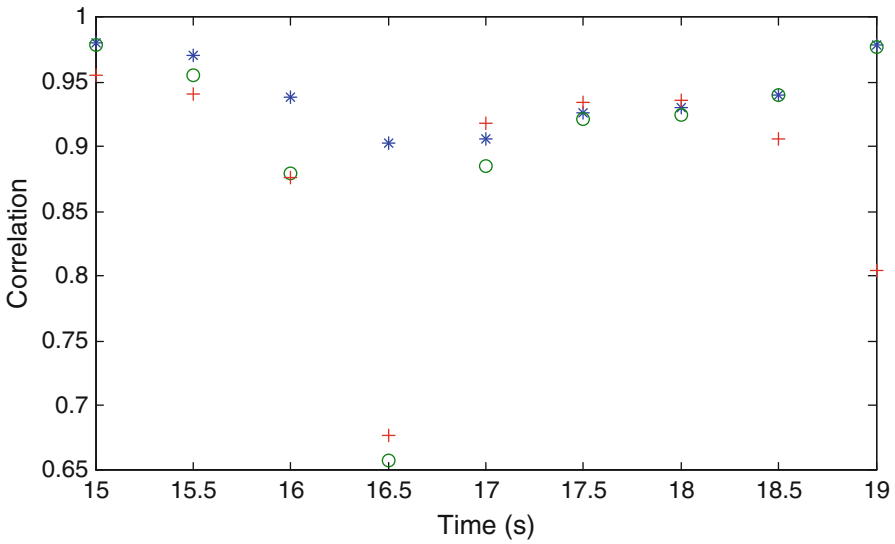

Fig. 20.16 Correlation as a function of time for the referred damage case with plunge stiffness loss of high noise case: (*asterisk*) $\lambda = 7.5$; (*open circle*) $\lambda = 6$; (*plus*) $\lambda = 1$

20.5 Conclusions

This paper presents an investigation of real-time structural damage identification of aircraft with changing flight condition. The study is based on the identified models of three different model structures: state space model; transfer function; and ARX model. For the time-varying system, a linear-time invariant model is identified to represent the system, so a short length of data is required to effectively and accurately update the identified model. The results show that the use of all the parameters of the identified state space model can identify the damage type and intensity when the added noise and the added disturbance are insignificant. But the use of all the elements of the identified ARX model cannot identify the damage for the low noise situation, and it requires using the selected elements with the relatively large ratios to successfully identify the damage. When the added noise and disturbance becomes significant and dominates the variations of most of the identified parameters, the inclusion of the elements dominated by noise may significantly reduce the reliability of damage identification with false indications of damage. The proposed method with element selection can significantly improve the performance of damage identification. The results show that the damage identification based on the identified SSI state space model is more reliable that the damage identification based on the identified ARX model.

References

1. Sohn H, Farrar CR, Hemez FM, Czarneki JJ, Shunk DD, Stinemates DW, Nadler BR (2002) A review of structural health monitoring literature: 1996–2001. LA-13976-MS, Los Alamos National Laboratory Report
2. Lew J-S (1995) Using transfer function parameter changes for damage detection of structures. AIAA J 33:2189–2193
3. Waszak MR (1998) Modeling the benchmark active control technology wind-tunnel model for active control design application. NASA/TP-1998-206270
4. Reveley MS, Briggs JL, Leone KM, Kurtoglu T, Withrow CA (2010) Assessment of the state of the art of flight control technologies as application to adverse conditions. NASA/TM-2010-216226
5. Juang J-N (1994) Applied system identification. Prentice-Hall, Englewood Cliffs
6. Mevel L, Benveniste A, Basseville M, Goursat M, Peeters B, Van der Auweraer H, Vecchio A (2006) Input/output versus output-only data processing for structural identification-application to in-flight data analysis. J Sound Vib 295:531–552
7. Lew J-S (2005) Optimal controller design for structural damage detection. J Sound Vib 281:799–813
8. Kailath T (1980) Linear systems. Prentice-Hall, Englewood Cliffs
9. Juang J-N, Phan MQ (2001) Identification and control of mechanical systems. Cambridge University Press, New York

Chapter 21
Wavelet Transformation for Damage Identification in Wind Turbine Blades

M.D. Ulriksen, J.F. Skov, P.H. Kirkegaard, and L. Damkilde

Abstract The present paper documents a proposed modal and wavelet analysis-based structural health monitoring (SHM) method for damage identification in wind turbine blades. A finite element (FE) model of a full-scale wind turbine blade is developed and introduced to a transverse surface crack. Hereby, post-damage mode shapes are derived through modal analysis and subsequently analyzed with continuous two-dimensional wavelet transformation for damage identification, namely detection, localization and assessment. It is found that valid damage identification is obtained even when utilizing the mode shape of the first structural blade mode. However, due to the nature of the proposed method, it is also found that the accuracy of the damage assessment highly depends on the number of employed measurement points.

Keywords Wind turbine blades • Structural health monitoring • Damage identification • Finite element modal analysis • Wavelet transformation

21.1 Introduction

Current maintenance costs of new turbines are very high and can easily make up to 20–25 % of the total cost of produced energy, and sometimes even more [1]. Consequently, the development of structural health monitoring (SHM) techniques has been of great interest in the last decade. For wind turbines, many studies have been conducted aiming to implement SHM techniques for warning of failures in, e.g., gearboxes, generator bearings and blades. In order to ensure consistency in evaluation of the study findings, a damage identification classification defining four levels, namely damage (1) detection, (2) localization, (3) assessment and (4) consequence [2], is often utilized.

While failure can occur in any structural component of the wind turbine, one of the most common and critical components to fail is the blade [3]. Here, several different damage types can be introduced [4], and in an extreme, complete failure can occur. Since the blades account for 15–20 % of the total wind turbine costs [5], great focus has been dedicated to monitoring of this particular structural component to reduce the amount of costly repairs and replacements, see e.g. [6]. The different proposed blade monitoring methods utilize a wide range of quantities like temperature, noise and vibration for damage identification. As concluded in [6], especially the noise- and vibration-based approaches show great promise for future employment in operating wind turbine blades.

The present paper documents a proposed vibration-based SHM method employing continuous wavelet transformation of spatial mode shape signals for level 1, 2 and 3 damage identification in a finite element (FE) model of a blade from a 1,500 kW onshore wind turbine, namely the GE 1.5 XLE [7]. The blade model is introduced to a transverse crack, and hereby post-damage mode shapes are extracted through linear free-vibration FE modal analysis and subsequently analyzed with continuous two-dimensional wavelet transformation for combined detection, localization and assessment of the crack. The use of two-dimensional wavelet transformation for damage identification has, to the authors knowledge, only been treated for rectangular plates, see e.g. [8]. In [9], one-dimensional wavelet transformations are used for damage detection and localization of a transverse crack in a residential-sized wind turbine blade. The present paper therefore serves to expand this approach to two-dimensional wavelet transformation such direct three-level damage identification analysis can be conducted

M.D. Ulriksen (✉) • J.F. Skov • P.H. Kirkegaard • L. Damkilde
Department of Civil Engineering, Aalborg University, Sohngaardsholmsvej 57, DK-Aalborg, Denmark
e-mail: mdu@civil.aau.dk; jskov08@student.aau.dk; phk@civil.aau.dk; lda@civil.aau.dk

A. Wicks (ed.), *Structural Health Monitoring, Volume 5: Proceedings of the 32nd IMAC, A Conference and Exposition on Structural Dynamics, 2014*, Conference Proceedings of the Society for Experimental Mechanics Series, DOI 10.1007/978-3-319-04570-2_21, © The Society for Experimental Mechanics, Inc. 2014

for the blade surfaces. An important aspect of the proposed method, and vibration-based damage identification methods in general, is the amount and placement of measurement points. Several studies, see e.g. [10, 11], have treated this aspect and clearly emphasized the importance of it. Despite this, the present paper does not treat measurement point amount and placement because the predominant scope here is to examine the general potential of the proposed method.

21.2 Theoretical Background

The theory behind modal analysis is well-documented in numerous publications, see e.g. [12], and will therefore not be treated here. Instead, focus will be on describing the basics of continuous wavelet transformation and its applicability in damage identification, including mode shape signal inter- and extrapolation procedures employed for improving the wavelet transform as damage indicator.

21.2.1 Basics of Continuous Wavelet Transformation

Originally, the continuous wavelet transformation was developed as an alternative to the short-time Fourier transformation in order to overcome typical resolution problems [13]. In analogy to the well-known Fourier transformation, the one-dimensional wavelet transformation uses inner products to measure the similarity between, e.g., a spatial signal in Hilbert space of a square-integrable one-dimensional function, $f(x) \in \mathbf{L}^2(\mathbb{R})$, and an analyzing function. In Fourier transformation, the analyzing function is complex exponentials, i.e. regular waves, whereas wavelet transformation employs a so-called wavelet, $\psi(x) \in \mathbf{L}^2(\mathbb{R})$. A wavelet is a zero-mean function with a wave-like oscillation over, typically, a small interval of, e.g., space. In Fig. 21.1, the analyzing functions for the Fourier transformation and wavelet transformation, respectively, are illustrated. The plotted wavelet is a specific Gaussian wavelet.

By comparing the spatial signal, $f(x)$, to the wavelet function, $\psi(x)$, at various wavelet scales, $a_i \in \mathbb{R}\backslash\{0\}$, and positions, $b_i \in \mathbb{R}$, the continuous wavelet transform

$$\mathrm{CWT}(a, b; f(x), \psi(x)) = \frac{1}{\sqrt{|a|}} \int_{-\infty}^{\infty} f(x)\psi^* \left(\frac{x-b}{a} \right) \mathrm{d}x \tag{21.1}$$

is obtained as the inner product of $f(x)$ and the complex conjugated, indicated with the superscript *, of the so-called wavelet family. The wavelet family consists of functions constructed from dilations and translations of ψ, i.e.

$$\psi_{a,b}(x) = \frac{1}{\sqrt{|a|}} \psi \left(\frac{x-b}{a} \right), \tag{21.2}$$

thus large values of a correspond to big wavelets, i.e. low spatial frequencies, and consequently coarse features of $f(x)$, while low values of a correspond to small wavelets, i.e. high spatial frequencies, and fine details of $f(x)$. In Eq. (21.2), the factor $1/\sqrt{|a|}$ is applied as a normalization operator such $||\psi_{a,b}(x)|| = ||\psi(x)||$.

Due to the effectively limited duration of the waveform, signals with abrupt changes can be better analyzed with a wavelet than with a smooth sinusoid. This is exploited in the proposed modal and wavelet analysis-based damage identification method, where the spatial mode shapes are transformed by use of Eq. (21.1). The idea is that a structural damage in the blade will introduce local mode shape irregularities which are then captured in the continuous wavelet transformation by

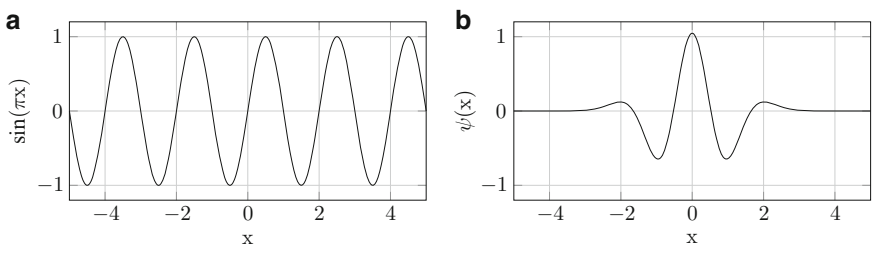

Fig. 21.1 Analyzing functions for different transformation types. (**a**) Sinusoidal wave (Fourier transformation). (**b**) Gaussian wavelet (wavelet transformation)

significantly magnified CWT coefficients, thus providing both damage detection, localization and assessment. Studies in e.g. [14], however, suggest that the effectiveness of wavelet transformation for damage identification is typically increased when the derivatives of the mode shapes are examined. This can easily be exploited since the studies in [15] prove that

$$\exists \theta(x): \quad \psi(x) = \frac{\mathrm{d}^n \theta(x)}{\mathrm{d}x^n} \;\Rightarrow\; \int_{-\infty}^{\infty} \theta(x)\mathrm{d}x \neq 0 \tag{21.3}$$

for wavelets with a fast decay and n vanishing moments, i.e.

$$\int_{-\infty}^{\infty} x^k \psi(x)\mathrm{d}x = 0, \qquad k = 0, 1, \ldots, n-1. \tag{21.4}$$

In Eq. (21.3), it is stated how a wavelet has n vanishing moments when $k = n - 1$. This means that a wavelet with n vanishing moments is orthogonal to polynomials up to degree $n - 1$, thus resulting in zero-valued wavelet coefficients for these polynomials. When expressing the wavelet with n vanishing moments as the nth order derivative of $\theta(x)$, which is referred to as the smoothing function, the wavelet transformation can be written as the convolution integral

$$\mathrm{CWT}(a, b; f(x), \theta(x)) = a^n \frac{\mathrm{d}^n}{\mathrm{d}b^n} \left(f * \theta_a^*\right)(b), \qquad \theta_a^*(x) = \frac{1}{\sqrt{|a|}} \theta\left(\frac{-x}{a}\right), \tag{21.5}$$

from which it is seen that the CWT of the nth derivative of the mode shape is found as the original mode shape convolved with a wavelet with n vanishing moments.

21.2.2 Two-Dimensional Wavelet Transformation

The one-dimensional wavelet transformation formulated in Eq. (21.5) can be directly expanded to two dimensions, i.e. $f(x, y) \in \mathbf{L}^2(\mathbb{R}^2)$, such

$$\exists \theta(x, y): \quad \psi^1(x, y) = \frac{\partial^n \theta(x, y)}{\partial x^n} \quad \wedge \quad \psi^2(x, y) = \frac{\partial^n \theta(x, y)}{\partial y^n}, \tag{21.6}$$

where $\psi^1(x, y)$ and $\psi^2(x, y)$ are the x- and y-directional wavelets, respectively, and $\theta(x, y)$ is the unscaled smoothing function whose scaled counterpart is defined by

$$\theta_{a,b,c} = \frac{1}{a} \theta\left(\frac{x - b}{a}, \frac{y - c}{a}\right). \tag{21.7}$$

By employing the convolution approach, the CWT coefficients are, in analogy to Eq. (21.5), derived through

$$\begin{pmatrix} \mathrm{CWT}^1(a, b, c; f(x, y), \theta(x, y)) \\ \mathrm{CWT}^2(a, b, c; f(x, y), \theta(x, y)) \end{pmatrix} = a^n \begin{pmatrix} \frac{\partial^n}{\partial b^n}\left(f * \theta_a^{1*}\right)(b, c) \\ \frac{\partial^n}{\partial c^n}\left(f * \theta_a^{2*}\right)(b, c) \end{pmatrix} = a^n \nabla \left(f * \theta_a^*\right)(b, c), \tag{21.8}$$

with ∇ being the gradient operator. Thus, the absolute CWT coefficient in an arbitrary coordinate point (i, j) in the measurement grid can simply be found as the resultant, i.e.

$$\mathrm{CWT}_{ij} = \sqrt{\left\{\mathrm{CWT}_{ij}^1\right\}^2 + \left\{\mathrm{CWT}_{ij}^2\right\}^2} \tag{21.9}$$

in which the function variables are omitted in the notation for the sake of clarity.

In the present study, several wavelets were tested. It was found that the isotropic Morlet wavelet yields the best results and therefore this was chosen in the analysis. In spatial frequency domain, the aforementioned wavelet is defined as [16]

$$\Psi(\mathbf{k}) = -e^{\frac{-(|\mathbf{k}| - k_0)^2}{2}}, \tag{21.10}$$

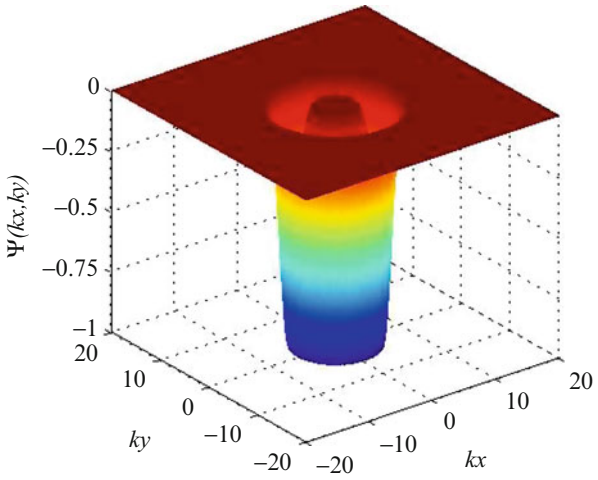

Fig. 21.2 Isotropic Morlet wavelet in spatial frequency domain with $k_0 = 6$

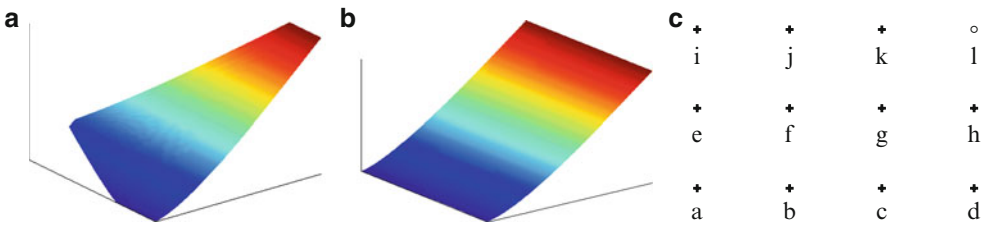

Fig. 21.3 Spatial extrapolation for generation of regular grid. (**a**) Original plate mode shape. (**b**) Expanded plate mode shape. (**c**) Grid for description of extrapolation scheme

where Ψ is the Fourier transform of the wavelet ψ, $\mathbf{k}$ is the spatial frequency vector and k_0 is a parameter which must be greater than 5.5 to ensure that $\Psi(\mathbf{0}) = 0$ is satisfied numerically. In Fig. 21.2, the isotropic Morlet wavelet with $k_0 = 6$ is plotted in spatial frequency domain.

21.2.3 Spatial Extrapolation for Grid Generation

Calculation of the two-dimensional CWT requires a regular measurement grid. In the present study, this was obtained by extrapolating the mode shapes such these were expanded to corresponding deformation patterns of a rectangular surface. The principle is shown in Fig. 21.3a, b where an original mode shape and an expanded counterpart are plotted for a simple plate. The plate was plotted instead of the actual blade since the former facilitates better illustrative description. The extrapolation was conducted in simple linear fashion, i.e. $l = k + h - g$ when referring to Fig. 21.3c. This extrapolation scheme ensures that no discontinuities are introduced in the transition between the actual blade surface and the non-physical, extrapolated areas.

21.2.4 Spatial Interpolation for Removal of Artificial Irregularities

When conducting modal analysis to derive spatial mode shapes, a finite, and often sparse, number of measurement points is employed, hence resulting in introduction of discontinuities in the CWT due to low resolution. In order to overcome this issue, a smoothing scheme was applied in the form of bicubic spline interpolation such the original mode shape signals were oversampled.

21.2.5 Additional Spatial Extrapolation for Removal of Boundary Distortions

Since the CWT is an infinite integral transformation, adverse boundary effects will be introduced when employing the finite mode shape signal and wavelet function. These boundary effects will yield significant increases in the CWT coefficients at the boundaries which may conceal actual damage-induced CWT coefficient maxima. Therefore, a bivariate extrapolation

scheme was included for removal of these boundary effects by shifting them to outside the signal interval. Several studies, see e.g. [8], suggest using cubic spline extrapolation for one-dimensional signals, but in the present study, it was found that bilinear extrapolation utilizing the two outermost points in each end of the longitudinal and transverse smoothed signal line sequences yields the most effective removal of adverse boundary effects in the two-dimensional signals. It is important to notice that this approach of course depends on the spatial resolution in the smoothed signals.

21.3 FE Modal Analysis

The FE analysis in this study was conducted in the commercial FE program ANSYS Workbench 14.5. The analysis was carried out as a free-vibration analysis of the blade model in a fixed-free configuration, i.e. the blade was clamped at the root. Damping was omitted since several studies, see e.g. [17], suggest that the impact of structural damping is small on the vibration modes of wind turbine blades.

21.3.1 Blade Modeling

The 41.2 m long GE 1.5 XLE blade consists of a shell surface and a shear web, both constructed in glass fibre reinforced plastic [7]. In the lack of specific material data for the GE 1.5 XLE blade, both the outer surface and the shear web were assigned a one-layer glass fibre reinforced plastic (GFRP) material with an orthotropic material model. In Table 21.1, the material properties of GFRP are presented. It is noticed that x, y and z refer to the axes of the local element coordinate system shown in Fig. 21.4b.

The initial blade geometry was obtained from [19]. Subsequently, the model was globally meshed with 0.15 m 8-node hexahedral shell elements (SHELL281), as shown in Fig. 21.4a. The element size was chosen on the basis of a convergence study of the low-frequency modes of the blade model. In the damaged areas, local mesh refinements with 0.01 m SHELL281 elements were employed.

21.3.2 Damage Introduction

In [4], 15 blades of 300 kW wind turbines and 81 blades of 100 kW wind turbines, all with a life time ranging between 16 and 19 years, were inspected. Based on these inspections, it was concluded that the most frequently occurring structural damages in wind turbine blades are debondings plus longitudinal and transverse cracks. Additionally, the aforementioned damage types were found to be the most severe, and therefore it was chosen to treat one of these, in the form of a transverse crack, in the present study. The crack was introduced with a length and width of 0.05 and 0.01 m, respectively, by simply removing this in the FE blade model. The damage size was chosen on the basis of damage findings in several 100 kW wind turbine blades [4] which were then scaled proportionally to the GE 1.5 XLE blade.

Table 21.1 Material parameters for GFRP material [18]

E_x	E_y	E_z	ν_{xy}	ν_{yz}	ν_{xz}	G_{xy}	G_{yz}	G_{xz}	ρ
11.511	11.511	4.552	0.204	0.305	0.305	2.922	1.406	1.406	1400

The unit of the Young's and shear moduli, E and G, is GPa and the unit of the density, ρ, is kg/m^3

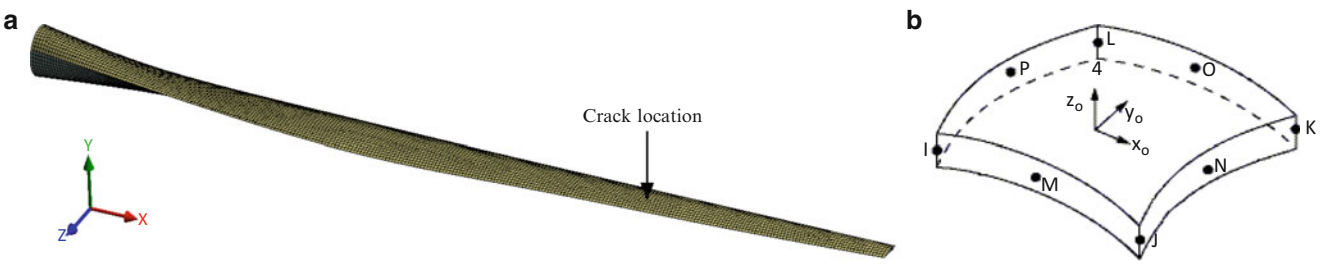

Fig. 21.4 Discretization of GE 1.5 XLE blade model. (**a**) Meshed model with indication of crack location and presentation of global coordinate system. (**b**) SHELL281 element with presentation of local element coordinate system [20]

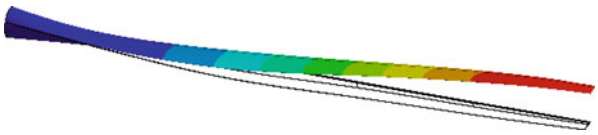

Fig. 21.5 First flapwise bending mode shape of undamaged GE 1.5 XLE blade model, with the wireframe being the undeformed state

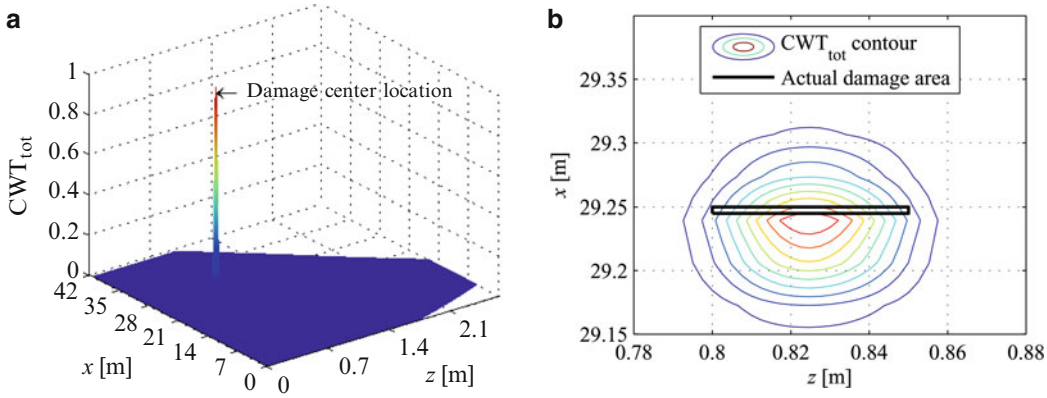

Fig. 21.6 CWT_{tot} of first mode shape of GE 1.5 XLE blade model with transverse crack. (**a**) Surface plot with indication of damage location. (**b**) Zoomed contour plot with indication of damage location

21.3.3 Modal Results

By introducing the transverse crack, post-damage mode shapes were derived. In the damage identification analysis, only the first flapwise bending mode, see Fig. 21.5, was utilized. The measurement points, which capture the modal displacements composing the mode shapes, were spaced 0.15 m in longitudinal (x-) direction and 0.05 m in transverse (z-) direction such a regular measurement grid was established.

21.4 Damage Identification

The chosen spatial mode shape was signal processed as described in Sects. 21.2.3–21.2.5 so that additional measurement points with 0.01 m spacing in both directions were introduced along with extrapolated, non-physical areas. Subsequently, the processed mode shape signal was transformed by use of Eq. (21.8) with $k_0 = 6$ in the isotropic Morlet wavelet defined in Eq. (21.10). It was chosen to conduct a wavelet transformation for each integer in the scale interval $a \in [6; 12]$ and subsequently multiply these to a total CWT product, CWT_{tot}, such damage-induced wavelet peaks were magnified in proportion to the ones in the undamaged areas. Finally, CWT_{tot} was normalized for the sake of clarity.

The obtained CWT_{tot} coefficients are presented in Fig. 21.6a for the actual blade surface area, i.e. the established non-physical areas have been omitted. Evidently, the transverse crack is detected and unambiguously localized. Regarding the assessment, it is seen in Fig. 21.6b that the CWT_{tot} yields a damage length and width of 0.065 and 0.15 m, respectively. The substantial width overestimation is a direct consequence of the longitudinal sampling distance since damage indications can only be obtained in the actual measurement points, recall $\Delta x = 0.15$ m, hence emphasizing the importance of the measurement grid spacing.

21.5 Conclusion

The present paper deals with modal and wavelet analysis-based damage identification in wind turbine blades. The proposed damage identification method is based on modal analysis for derivation of post-damage mode shapes which are subsequently signal-processed in spatial domain and analyzed by means of two-dimensional continuous wavelet transformation for combined detection, localization and assessment of structural damages. In the study conducted in this paper, the applicability

of the method has been examined by introducing a transverse surface crack in a FE model of a full-scale wind turbine blade. It is found that the crack can be detected, unambiguously localized and acceptably length assessed, but for an accurate width assessment, the sampling distance must be smaller or equal to the actual damage size since damage indications can only be obtained in the measurement points.

21.5.1 Future Work

Subsequent to the studies documented in the present paper, the general applicability of the proposed method will be examined by introducing the blade to other structural damage types alternately and simultaneously, thus simulating both single- and multi-damage scenarios. Furthermore, the robustness of the method will be challenged by adding Gaussian noise to the spatial mode shape signals in order to simulate typical experimental findings. In this way, the significance of the adverse shear web effects in the CWT will also be investigated.

Acknowledgements The research documented in the present paper was conducted in cooperation with the EUDP-LEX project.

References

1. Wind Energy (2013) The facts, operation and maintenance costs of wind generated power. http://www.wind-energy-the-facts.org/en/part-3-economics-of-wind-power/chapter-1-cost-of-on-land-wind-power/operation-and-maintenance-costs-of-wind-generated-power.html. Accessed 30 July 2013
2. Rytter A (1993) Vibration based inspection of civil engineering structures. Ph.D. Thesis, Aalborg University, Denmark
3. Khan MM, Iqbal MT, Khan F (2005) Reliability and condition monitoring of a wind turbine. In: Proceedings, 18th Annual Canadian conference on electrical and computer engineering
4. Ataya S, Ahmed MMZ (2011) Forms of discontinuities in 100 KW and 300 KW Wind Turbine Blades. In: Proceedings, 10th World wind energy conference & renewable energy exhibition
5. Larsen FM, Sorensen T (2003) New lightning qualification test procedure for large wind turbine blades. In: Proceedings, international conference on lightning and static electricity
6. Skov JF, Ulriksen MD, Dickow KA, Kirkegaard PH, Damkilde L (2013) On structural health monitoring of wind turbine blades. In: Proceedings, 10th international conference on damage assessment of structures
7. The Windpower (2013) Wind turbines and farms database, GE Energy 1.5xle. http://www.thewindpower.net/turbine_en_58_ge-energy_1.5xle.php. Accessed 21 Aug 2013
8. Rucka M, Wilde K (2006) Application of continuous wavelet transform in vibration based damage detection method for beams and plates. J Sound Vib 297(3–5) pp. 536–550
9. Doliński L, Krawczuk M (2009) Damage detection in turbine wind blades by vibration based methods. J Phys: Conf Ser 181(1)
10. Kirkegaard PH, Brincker R (1994) On the optimal location of sensors for parametric identification of linear structural systems. J Mech Syst Signal Process 8(6) pp. 639–647
11. Furukawa A, Kiyono J (2004) Identification of structural damage based on vibration responses. In: Proceedings, 13th world conference on earthquake engineering
12. Inman DJ (2009) Engineering vibrations, 3rd edn. Prentice Hall, Englewood
13. Gao RX, Yan R (2011) Wavelets - theory and applications for manufacturing. Springer Science+Business Media, Berlin
14. Fan W, Qiao P (2011) Vibration-based damage identification methods: a review and comparative study. J Struct Health Monit 10(1) pp. 83–111
15. Mallat S, Zhong S (1992) Characterization of signals from multiscale edges. J IEEE Trans Pattern Anal Mach Intell 14(7) pp. 710–732
16. Dallard T, Spedding GR (1993) 2-D wavelet transforms: generalisation of the Hardy space and application to experimental studies. Eur J Mech B Fluids 12(1) pp. 107–134
17. Yanbin C, Lei S, Feng Z (2010) Modal analysis of wind turbine blade made of composite laminated parts. In: Power and energy engineering conference, 2010 Asia-Pacific
18. Vasileios K, Strengthening of steel bridges by GFRP plates. Master's thesis, Faculty of Civil Engineering & Geosciences, Delft University of Technology
19. Mullen BJ (2013) ANSYS WB - wind turbine blade - problem specification. https://confluence.cornell.edu/display/SIMULATION/ANSYS+WB+-+Wind+Turbine+Blade+-+Problem+Specification. Accessed 10 May 2013
20. Release 11.0 Documentation for ANSYS, Shell281. http://www.kxcad.net/ansys/ansys/ansyshelp/hlp_e_shell281.html, Accessed7February2014

Chapter 22
Vision Device Applied to Damage Identification in Civil Engineer Structures

Giorgio Busca, Alfredo Cigada, and Emanuele Zappa

Abstract The challenge of identifying structural damage has gained a lot of attention among the research community during the last decades. Many damage identification algorithms are available in literature and most of them are based on vibration measurements. The accuracy of these methods depends on the measurement quality and especially on the number of sensors used to perform the monitoring activity. The need for a large number of devices does not comply with the economic advantage of an efficient structural maintenance based on remote monitoring. The purpose of this work is to explore the application of cameras to damage identification. The main advantage in using a camera is that every row or column in the pixel matrix can be considered a sensor on its own. This characteristic makes a camera an interesting device for damage detection, since it possible to estimate the structural dynamic behaviour on a continuous field by one single device at a reasonable price. In this work a camera will be used for the mode shape curvatures estimation of a cantilever beam with the final goal to identify damages in the structure. The results will show the efficacy of vision-based measurements for the monitoring purpose.

Keywords Damage detection • Structural health monitoring • Curvature • Mode shapes • Vision

22.1 Introduction

The task of identifying structural damage before it gets irreversible or dangerous has gained a lot of attention among the research community in the last decades. Structural health monitoring by means of reliable and effective non-destructive damage identification techniques will be essential in the next years to extend the life of civil or mechanical structures and guarantee their safety, deciding for refurbishment rather than demolition.

The damage identification process is based onto four main issues: the damage presence identification; the damage localisation; the damage type qualification and the damage severity quantification [1, 2]. When all these four goals are reached, the damage identification process can be considered complete. The damage identification procedures described in literature are simple to be described in terms of steps to be implemented, but the task is difficult to achieve by an automatic process, since structural damage can appear under many different configurations. The damage configurations could depend upon several elements, such as the number of damage locations and their severity, but also the structure material, the structure architecture and the environment conditions.

Many damage identification algorithms are available in literature and most of them are based on the measurement of the structural vibrations coupled to a proper mechanical modelling. Linear methods are very popular because they are based on simple assumptions: damage is a stiffness reduction, which modifies the structural dynamic parameters such as vibration frequencies [3–5], mode shapes and their curvatures [6–9], flexibility matrix [10–12], modal strain energy [13–15] and so on. The aim of these methods is the identification of one or more features, based on the dynamic parameters listed above, in order to define the presence of damage, its localization and its severity. Usually, damage is recognized by the comparison of these features between undamaged and damage scenarios. Some reviews compare many of these algorithms and outline their performances, when they are applied to the same damage conditions in terms of damage type, localizations and severity [1, 16, 17]. What appears almost clearly is that all these methods depend on the measurement quality and in particular on

G. Busca (✉) • A. Cigada • E. Zappa
Dipartimento di Meccanica, Politecnico di Milano, via La Masa 1, Milan, Italy
e-mail: giorgio.busca@mail.polimi.it; alfredo.cigada@polimi.it; emanuele.zappa@polimi.it

A. Wicks (ed.), *Structural Health Monitoring, Volume 5: Proceedings of the 32nd IMAC, A Conference and Exposition on Structural Dynamics, 2014*, Conference Proceedings of the Society for Experimental Mechanics Series, DOI 10.1007/978-3-319-04570-2_22,

the number of devices used to perform monitoring. The performances indeed improve as the sensors number increase, since the damage features used by the algorithms are often based on the estimation of dynamic parameters along the monitored structure, for example, the mode shapes. However, the requirement of a large number of devices does not comply with the economic advantage of a remote and continuous structural monitoring and, in particular in the very common case of contact measurements, it might pose severe loading effect (i.e. modification in the structure behaviour due to the presence of transducers). Consequently, the need of a complete but cheap measurement setup is a prerogative.

This paper will be focused on linear methods and the application of cameras to damage identification purposes. In recent years, many applications for civil structure monitoring by means of such devices have been proposed [18–21]. However, most of them deal with structural monitoring, but they do not apply any damage identification method. The main advantages of camera-based measurement devices, that makes them attractive for the application of structural monitoring, are: remote contactless monitoring, possibility to perform a multipoint measurement by a single camera, quick and simple measurement device set-up (no transducers nor cables on the structure but only some targets placed on it). An additional advantage in using a camera for structural health monitoring is that every row or column in the pixel matrix can be considered a sensor on its own. Due to this reason, cameras are usually referred to as "dense" sensors. This last specification makes a camera an interesting device for damage identification, since it is possible to estimate the structural dynamic behaviour on a continuous field grabbed by a camera at a reasonable price. These properties are especially useful for curvature-based methods, where damage is linked to the localization of discontinuities in the modal shape curvature, which is more accurate as several measurement points are available on the structure [22].

In this work camera-based measurements will be tested for the mode shape curvatures estimation of a simple cantilever beam. There are two reasons for focusing on a simple structure: first, most structures or their main components in civil and mechanical engineering can be simplified as a beam; second, the problem of identifying a specific damage in a beam provides an evident benchmark for effectiveness and accuracy of damage identification by means of vision devices. The beam will be damaged in specific locations and with controlled severity and then a camera will be used to estimate the mode shape curvatures by means of image elaboration techniques.

22.2 Mode Shape Curvature Methods

A method based on mode shape curvature (MSC) was proposed for the first time by Pandey et al. [6], who stated that the damage location can be identified by the difference between the mode shape curvatures of the damage and undamaged structure, respectively $\{\Phi_d''\}$ and $\{\Phi''\}$:

$$\{\Delta\Phi''\} = \{\Delta\Phi_d''\} - \{\Phi''\}. \tag{22.1}$$

Once the mode shapes Φ (undamaged) and Φ_d (damaged) are identified, the generic mode shape curvature at each location i on the structure can be estimated as:

$$\Phi_i'' = (\Phi_{i+1} - 2\Phi_i + \Phi_{i-1}) / h^2, \tag{22.2}$$

where h is the distance between the measurement points $i+1$ and $i-1$. If it is possible to have more than one mode, a *curvature damage factor* (CDF) can be proposed, as shown in the following equation [23]:

$$CDF_i = \frac{1}{N}\sum_{n=1}^{N} \Delta\Phi_{i,n}'', \tag{22.3}$$

where N is the total number of modes to be considered and $\Delta\Phi_{i,n}''$ is the difference of the mode shape curvatures (damaged and undamaged condition) estimated for the n mode at point i. However, since the mode curvature estimation depends upon the sensor number, higher modes can be involved in the damage localization only if many sensors are available to describe the mode shapes with a good spatial resolution. Then, in order to reduce a false damage warning, only few low curvature mode shapes should be used [6].

Curvature-based methods have been shown to be very promising techniques and for this reason they are deeply studied in literature. Salawu and Williams compared the performance of both curvature and displacement mode shapes for locating damage and stated MSC as a sensitive indicator [24]. Abdel Wahab and De Roeck investigated the accuracy of using the central difference approximation to compute the MSC and they found that a fine mesh is required to correctly estimate the

nodal curvature for higher modes [23]. Because the curvature estimation by means of finite difference computation may leads to considerable errors, the direct measurement by getting the strain mode shape was proposed in several works [25, 26]. Moreover, Ratcliffe developed a method based on fitting MSC by a localized cubic polynomial curve, called GSM, which is similar to Pandley's original method, but it does not require the baseline mode shape of the undamaged structure and for this reason, it was developed in many works [27]. All these solutions aim to cut down the uncertainty of the curvature estimation in order to increase the damage detection efficiency, but the problem about the spatial resolution is still present, because it depends on the number of sensors attached to the structure.

In this paper MSC method proposed by Pandey will be used as reference to evaluate the performance of a vision-based curvature estimation system. In the next section, the measurement setup will be shown and the signal analysis procedures used to estimate the mode shape curvatures will be explained.

22.3 Measurement Setup

This section describes the experimental setup used to test the performances of a camera as suitable instrument for damage detection. The device was tested onto three cantilever beams with the same dimensions. Normally, modal analysis on a simple structure like a beam should be performed in free–free boundary conditions, because it is difficult to guarantee the theoretical behaviour of the joints; also, their behaviour might be affected by a number of factors, making it difficult to have reproducible measurements. However structural health monitoring is usually applied to structures under working conditions, where joints cannot be neglected. For this reason, a cantilever beam was chosen as the test structure and the joint was properly designed to guarantee the needed boundary condition. The beams and the joint are shown in Fig. 22.1a, b. Every beam was 750 mm long, it had a rectangular cross-section of 30×10 mm and it was made of aluminium. All these characteristics were chosen in order to have bending modes at relatively low vibration frequencies, at least for the first mode, which allowed the camera to correctly grab the images, as it will be explained in the next section. Defects were simulated in terms of cross section reduction, obtained by means of a thin blade saw, as shown in Fig. 22.1c, where a 2 mm slot is visible on the 10 mm beam side.

The measurement setup involved an Allied Prosilica GX 3300 camera with a $3{,}296 \times 2{,}472$ pixels resolution, mounting a Zeiss Makro-Planar 2/100 mm focal lens and 17 fps max frame rate at full resolution. The camera was placed in front of the beam side, in order to view the bending motions projected on the sensor plane, as shown in Fig. 22.2. The lighting conditions were controlled by two led lamps, white painting on the beam surface and a black curtain in the background. As it will be explained in the next section, the tests also required an impact hammer: in this case a PCB model 086C03 with a 2.25 mV/N sensitivity, a 0–8 kHz frequency range and a 2,200 N pk measurement range was used.

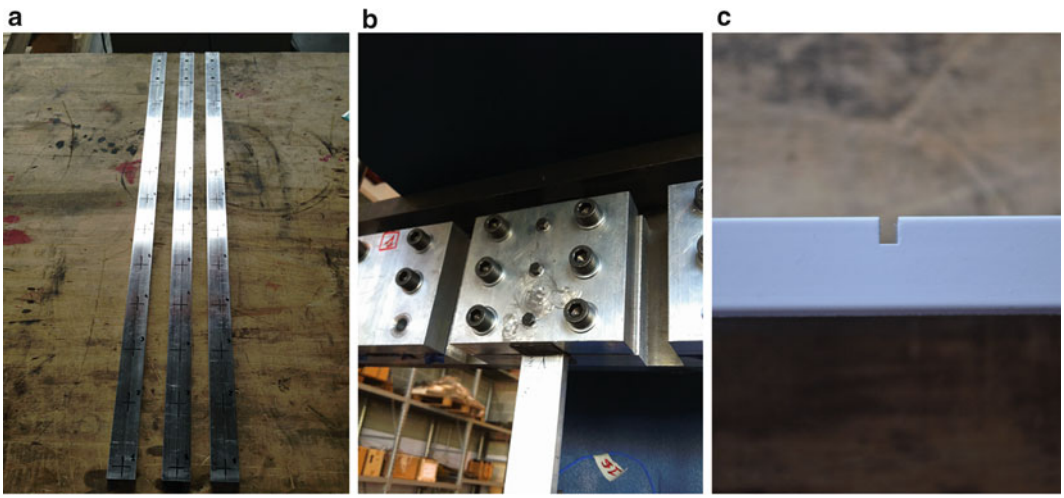

Fig. 22.1 (**a**) Beams; (**b**) joint design; (**c**) damage example

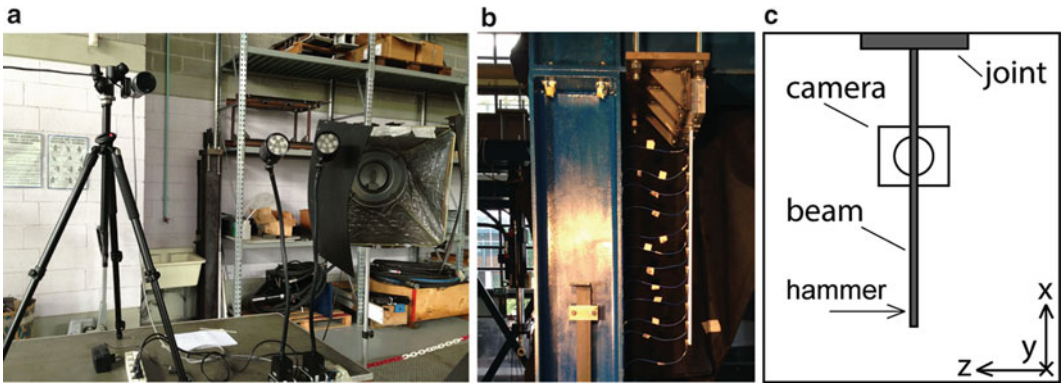

Fig. 22.2 Measurement setup

22.4 Experimental Tests and Data Processing

The tests have been scheduled as described in the following. Each beam under undamaged conditions was excited along the z direction by one impulse provided by the hammer (see Fig. 22.2). In the meantime, the camera acquired the video of the beam transverse vibrations with a custom image resolution of $3{,}296 \times 120$ pixels; this reduced resolution allowed to increase the sampling frequency up to 50 fps. The clip acquisition and the signal of the impact hammer were synchronized by means of a trigger signal.

Once the video was acquired at a fixed grabbing frequency, each frame was considered the instantaneous status of the vibrating beam. Since the first bending frequency was between 10 and 15 Hz, the sampling theorem, fixing a sampling frequency at least double with respect to the highest frequency in the signal (in this case the mode frequency), was respected with the adopted sampling frequency of 50 Hz (higher modes have motion amplitudes in the order of the camera resolution threshold—the camera does not have anti-aliasing filters). Moreover, a short exposure time of 5 ms was fixed in order to avoid motion blurring and its negative effect on dynamic measurements by cameras [28]. Then, an edge detection algorithm (implemented in Labview®) analysed every frame in order to estimate the vibrating beam shape at each time stamp. As shown in Fig. 22.3, the x-axes defined the pixel position along the beam length, whereas the y-axes corresponded to the thickness direction, which is the bending motion direction too. The edge detection was performed along the y-axis from the bottom to the top in correspondence of every pixel along the x direction. For each frame, the result of the analysis was the function of the position of the inferior beam outline along the y coordinate as a function of the x coordinate, both in terms of pixels:

$$y = f\,(x,t) \quad [px] \tag{22.4}$$

where t was the time corresponding to the analysed frame. Once all the frames were processed, it was possible to reconstruct the time histories of the y value at a fixed value $\tilde{x}$, assuming the starting position of the first frame to be the zero and estimating the positions in the next frames as the difference with respect to this one, as explained by the following equation:

$$y = f\,(\tilde{x},t) - f\,(\tilde{x},t_0) \quad [px]\,, \tag{22.5}$$

where $\tilde{x}$ was the fixed value on the x axis and t_0 was the time corresponding to the first frame. Figure 22.3 shows an example of the transient response obtained for pixel 1 on the x-axis. As a final step, the signals were calibrated knowing the image mm/px ratio, obtained by means of a traditional calibration procedure [29].

The previously described test was repeated twenty times for each beam, under undamaged conditions, in order to have twenty experimental transient responses, each providing a single measurement for each pixel along the x-axes. Once the transient responses were available for every pixel along the beam length, it was possible to estimate a frequency response function (FRF) between the force applied by the dynamometric hammer and the beam response detected by means of the image processing approach. The function used to evaluate the FRF was the well-known H_1 estimator with a 0.1 Hz frequency resolution [30]. Because the image size used for these tests was $3{,}296 \times 120$ pixels, the number of estimated FRFs along the beam was 3,296, which clearly emphasises the advantage of using a camera as a displacement transducer.

The FRFs were analysed by means of a modal identification algorithm known as Least squares complex exponential (LSCE) in order to estimate the normalized mode shapes, excited by the hammer [31]. As it will be shown in the results

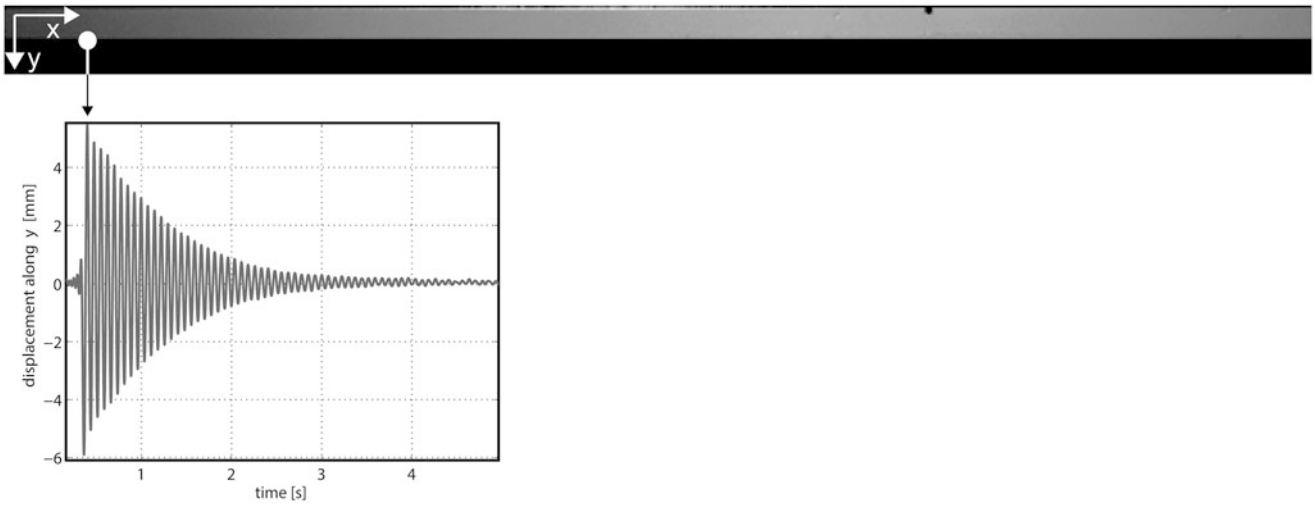

Fig. 22.3 Edge detection processing and transient response example

Table 22.1 Damage configurations

Beam	Damage location	Damage level
1	1/2 L = 350 mm (pixel 1,770–1,783)	10 % = 1 mm slot depth
		20 % = 2 mm slot depth
		30 % = 3 mm slot depth
2	1/3 L = 250 mm (pixel 2,513–2,526)	10 % = 1 mm slot depth
		20 % = 2 mm slot depth
		30 % = 3 mm slot depth
3	2/3 L = 500 mm (pixel 1,033–1,047)	10 % = 1 mm slot depth
		20 % = 2 mm slot depth
		30 % = 3 mm slot depth

paragraph and as stated at the beginning of this section, in the actual situation the camera allows to analyse only the beam first mode because higher modes are characterised by vibration amplitudes too small to be correctly measured by the camera. In order to measure higher frequency modes it would be necessary to increase the image resolution (in terms of mm/px) and this could be obtained reducing the field of view (i.e. increasing the zoom) but in this case only a portion of the beam could be framed. Moreover, to acquire high frequency modes it would also be necessary to increase the sampling frequency, which could be done changing the camera or further reducing the acquired portion of the camera sensor (and therefore further reducing the field of view). This is probably the main drawback of using of cameras. In fact they exhibit poor resolution for measurements at higher frequencies; in addition cameras are relative sensors, so the tripod supporting them must guarantee stability for proper absolute displacement measurements.

After the dynamic characterization of the three cantilevers beams under undamaged conditions, a single progressive damage was imposed to each beam at three difference positions along z direction, one position for each beam (1/3 L, 1/2 L and 2/3 L where L is the beam length). The damage was produced by a transversal slot with a rectangular section 2 mm width and three different depth levels, in order to simulate different damage severities, as shown in Fig. 22.1c. Table 22.1 sums up the damage configurations of the three beams for an amount of nine damage combinations.

The first damage level imposed to the three beams was about 10 % of the cross-section. Then, the tests necessary to evaluate the modal displacement shapes were performed in the same way of the undamaged case. The procedure was repeated for all the three beams and the other two damage levels, 20 and 30 %. In the next section, the results of the damage detection algorithm based on mode shape curvatures will be shown.

22.5 Results

This section will show the results obtained by the image processing in terms of frequency response function (FRF), mode shape estimation and damage detection by means of curvature difference.

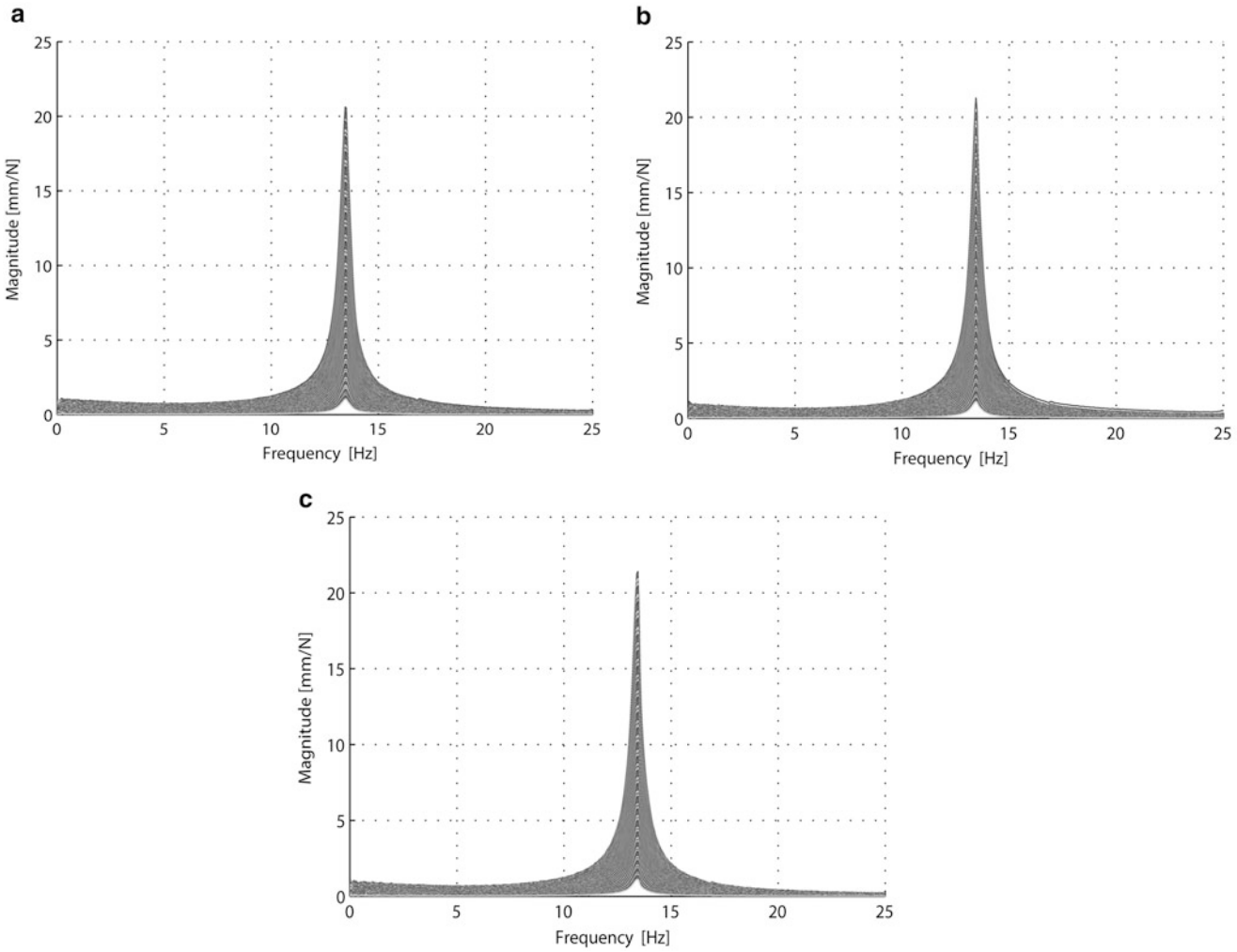

Fig. 22.4 Superimposed FRF amplitudes of the three cantilever beams: (**a**) beam 1; (**b**) beam 2; (**c**) beam 3

22.6 FRF

Figure 22.4 shows the superimposition of the FRF amplitudes obtained by the three cantilever beams under undamaged conditions. The graphs show 155 FRF, one every 20, pixels corresponding to an interval of 3.4 mm, since the mm/px ratio was 0.17. Because the amount of data is huge to be managed even by a personal computer with a 8 GB RAM, it has been decided to reduce the density of the measurement points, since the effectiveness of the measurement method and the considerations about its performances would not be affected by this choice.

The FRFs are shown in the range between 0 and 25 Hz, since the grabbing frequency was 50 fps. In this range the camera was able to detect only the first mode, as previously discussed. The FRF amplitudes identify the same natural frequency at 13.45 Hz for all the beams under undamaged conditions; moreover, the values are congruent with the decreasing trend of the first bending vibrating mode from the free-end (FRF number 1) to the fixed joint (FRF number 155).

22.7 Mode Shapes

Figure 22.5 shows the first bending mode identified from the FRFs of Fig. 22.4 by a LSCE identification algorithm, for the case of undamaged beam. As it can be seen, the three beams show quite similar mode shapes, as expected, since the three beams had the same characteristics.

Figure 22.6 shows the difference between the undamaged mode and the damaged mode shapes for each beam. The evaluation is proposed for each of the three damage levels. The black dotted line points the damage position out. As shown in

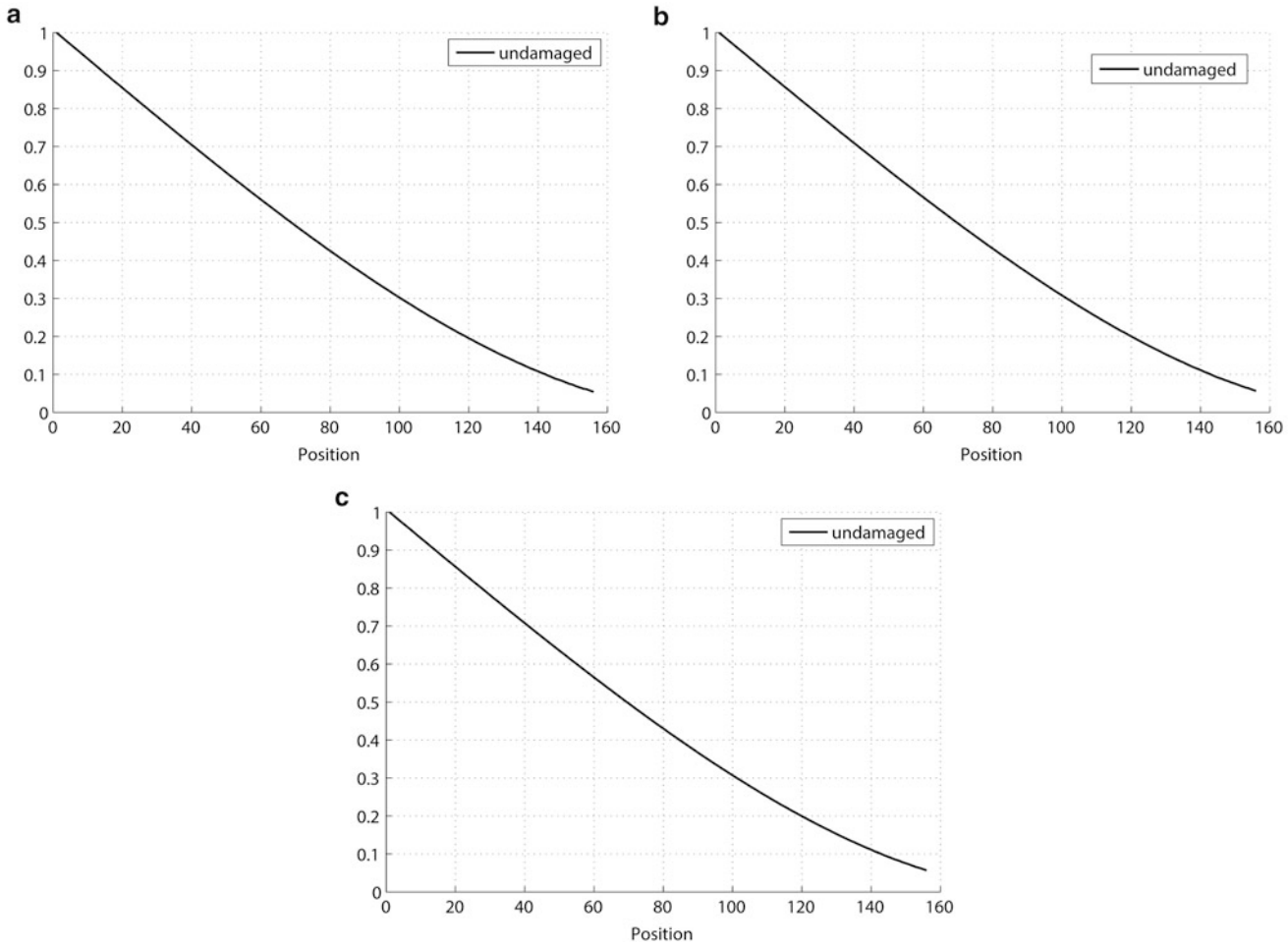

Fig. 22.5 First bending mode in the undamaged case: (**a**) beam 1; (**b**) beam 2; (**c**) beam 3

Fig. 22.7, the first mode shape seems to be not so sensitive to the imposed damage; the bending modes do not show evident trends from undamaged to damaged scenarios, even for the worse case of the 3 mm notch. The differences are all below 7×10^{-3} and their shapes are not easily readable in terms of damage location identification: the modes show a change due to damage, but the link between this behavior and the damage position is not clear without an a priori knowledge of where the damage is.

It is true that mode shapes are less sensitive to damage than the mode shape curvatures, as stated by several papers [1, 2]; however, for the proposed method, also the measurement uncertainty of the image-processing algorithm should be taken into account. Indeed, the mode shape is obtained by an identification algorithm, whose uncertainty depends on the measurement quality in terms of signal to noise ratio. In this application, the displacement measurement is estimated by an edge detection algorithm, which is affected by its own uncertainty. Consequently, the displacement estimation is affected by measurement noise of the image sensor, but also by the image-processing algorithm uncertainty. These considerations will be useful to understand the result of curvature differences reported in the next section.

22.8 Damage Detection by Curvature Mode Shapes

The identification of the mode shapes is the first step also in case of damage detection, based on the difference between the curvature mode shapes. As the number of measurement points increase, the mode shape is better defined, and this specially applies to higher modes, though, as stated, they are hardly measured. Once the modes are identified, the next step, as shown in Eq. (22.2), is the computation of mode shape curvatures by a finite difference. However, a high spatial resolution (number of sampling points) cannot be a real advantage.

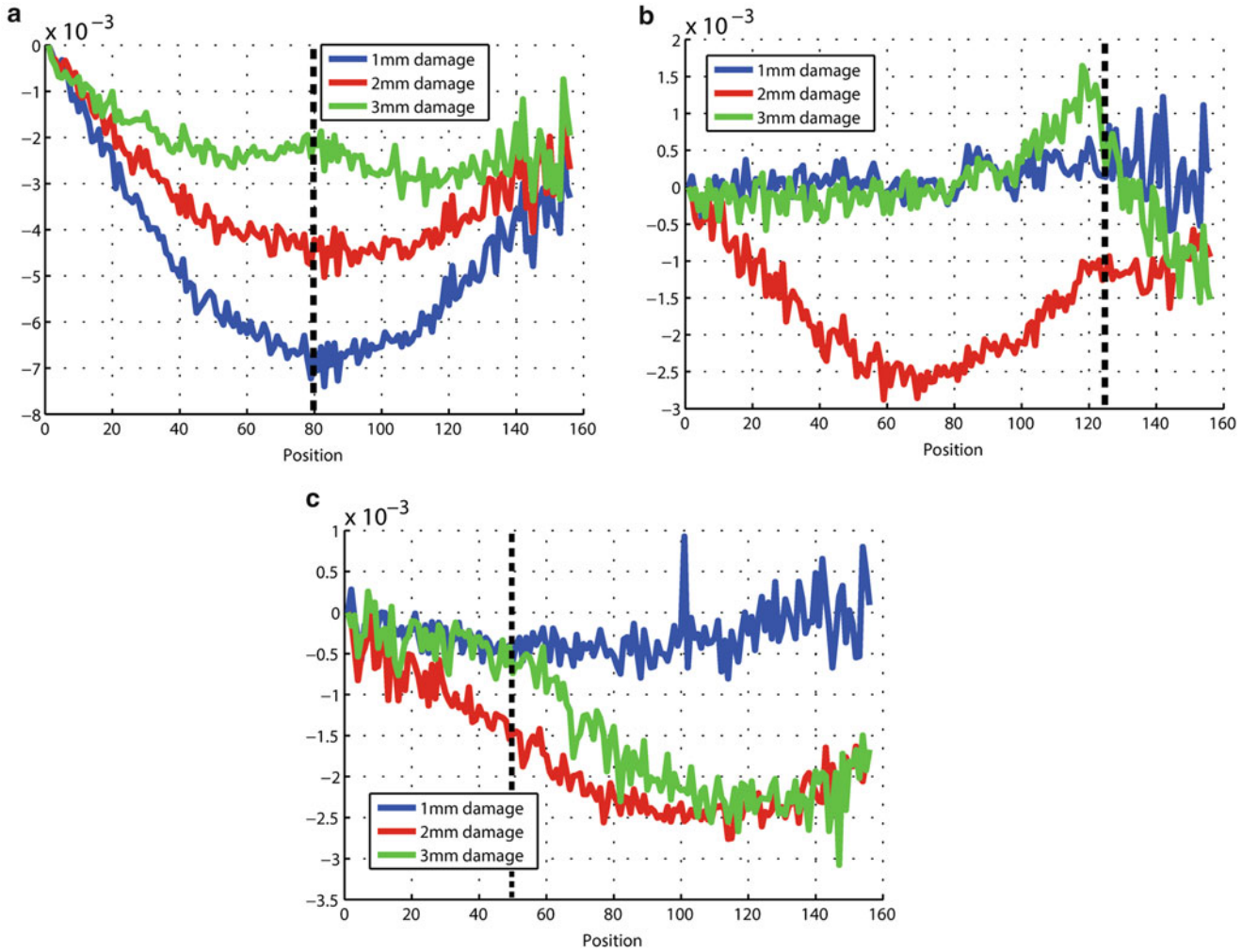

Fig. 22.6 Difference between undamaged and damage mode: (**a**) beam 1; (**b**) beam 2; (**c**) beam 3

Fig. 22.7 Curvature estimation among 165 consecutive points

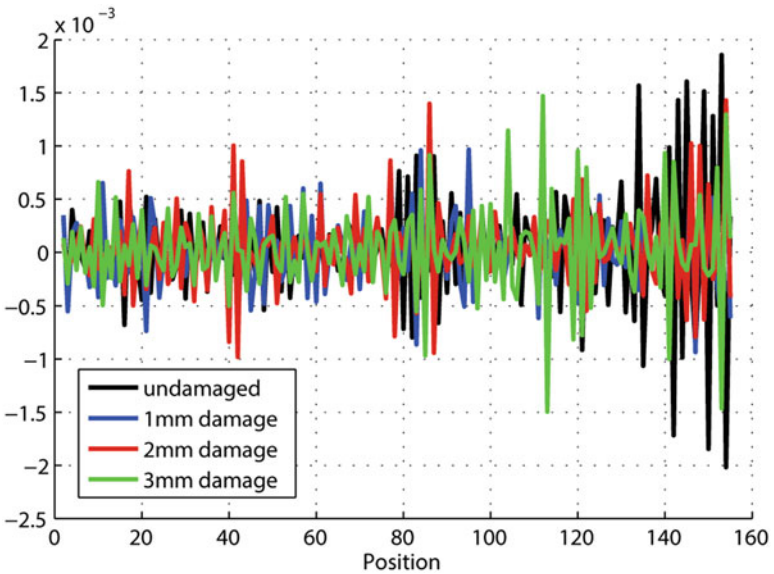

A lower sampling interval should be helpful to localize the damage with higher precision, but the curvature estimation could be affected by significant errors. Many authors verified that measurement noise could corrupt the quality of the curvature estimation [22]. Because the curvature is a discrete difference among consecutive points, if their spacing is too low, measurement noise has a really bad effect on the second order slope estimation. This problem is well known in damage detection methods based on measurements by laser Doppler vibrometers [32]. The damage detection method proposed in this work faces the same difficulty, since the displacement along the y direction is estimated for each pixel along the x axes (Fig. 22.3). Figure 22.7 shows how the curvature estimated on 165 consecutive points is useless when the discrete derivatives are calculated on a short sampling interval (in this case only 3.4 mm over a 750 mm length). The diagram is about the first beam in all the four possible configuration: undamaged, 1 mm damage, 2 mm damage and 3 mm damage.

The solution could be the decimating of the measurement points, but this choice will be in contradiction with the advantage of having a dense measurement useful for the damage localization. Many works propose to overcome the problem by a spline o polynomial fitting of the mode shapes in order to reduce noise, but when the spatial resolution is too high, this is not enough. The solution we propose is the curvature computation by the following equation applied to modes preprocessed by a cubic-spline fitting:

$$\Phi_i'' = \left(\Phi_{i+k} - 2\Phi_i + \Phi_{i+k}\right) / h^2 \text{ with } i = 1+k, 2+k, 3+k, \ldots . N-k \tag{22.6}$$

where i is the measurement point where the curvature is being calculated, k is the spatial interval chosen to estimate the curvature, N is the number of measurement points and h is the distance between the points $i+k$ and $i-k$. When $k=1$, Eq. (22.6) becomes equal to Eq. (22.2), whereas the curvature estimation interval increases for larger values of k. This formula shows how it is possible to correctly estimate the curvature avoiding the noise, since it is evaluated among a higher sampling interval when k is bigger than 1. Moreover, the curvature is calculated for all the measurement points, since the index i takes values between $1+k$ and $N-k$, and the advantage of having a dense measurement is preserved. The last task is the definition of the correct value for the parameter k. The correct span of the sampling interval was demonstrated to be linked to the shape of the mode curvature by Sazonov et al. [22], who showed how to calculate the optimum sampling interval to correctly estimate the mode shape curvature by means of discrete differences, when the mode shape is known. Looking at the modes shapes shown in Fig. 22.5 (defined over 165 measurement points), the value k was fixed to 30, corresponding to a span of about 100 mm.

The mode shape curvatures obtained with Eq. (22.6) are shown in Fig. 22.8. As statedbefore, the curvatures are calculated on all the measurement points used to estimate the mode shapes, except for the first k points and the last k points, in this case $k=30$.

Then, the results of the damage detection based on this vision-based measurement method are proposed in Fig. 22.9.

Since the measurements points are reduced by a factor of 20 with respect to the video pixels along the x axes (but the number of "virtual sensors" still remains much higher than that offered by more "traditional" sensors), the new estimated damage positions are: between 89 and 90 for the first beam, 125–126 for the second one and 51–52 for the third one. The results show that the damage is correctly located (peak of $\triangle_{\text{curvature}}$) for all the three beams only in the worst case (damage 30 %). The plots of Fig. 22.9 show areas of higher values around the damage locations (Table 22.1) and the maximum is found at the damage location. The second damage severity (20 %) is correctly individuated for the second beam, whereas the third beam shows a region of higher values near the damage location but the maximum peak is not centered on this position. The curvature difference of the first beam instead is not able to detect the damage; it is possible to observe a change of the curvature difference close to the damage, but all the values remain below zero. At the end, the method is not able to detect the lower damage severity (10 %) for all the three beams. As for the 20 % damage, the curve difference of the first beam shows a slope change in correspondence of the damage position, but the values are all negative.

The results demonstrate that damage detection is possible with only one device, contactless and at a reasonable price. Moreover, the structural health monitoring is performed by a dense measurement, which allows one detecting the position of damage with lower uncertainty with respect to traditional methods, using accelerometers or displacement transducers. The critical aspect in these tests is the measurement uncertainty. If the camera has to frame a wide portion of the structure, the scaling factor gets obviously worse. Under these conditions, the measurement uncertainty is combined with the image-processing error, which could be high in the case of damage detection applied to a moving object. The behavior of the curvature difference values of the first beam are a proof of the high uncertainty of the data obtained by image processing. An improvement of the method could be the application of more accurate image-processing algorithm, such as digital image correlation, in order to reduce the uncertainty on the data obtained by the image elaboration.

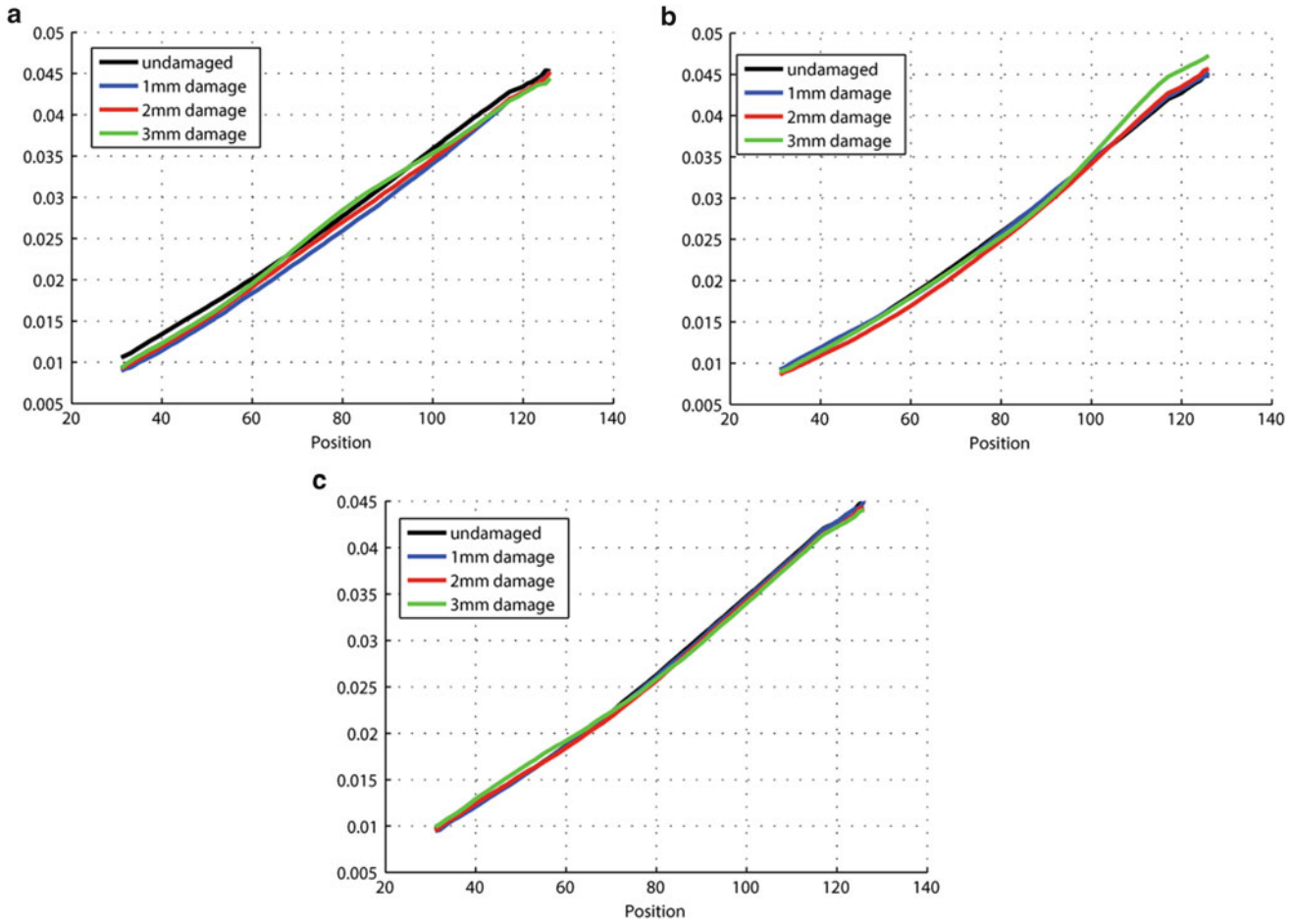

Fig. 22.8 Curvature estimation using Eq. (22.6): (**a**) beam 1; (**b**) beam 2; (**c**) beam 3

22.9 Conclusions

In this work the possible application of cameras to damage identification has been explored. The main advantages of cameras is that it is possible to estimate the structural dynamic behavior on a continuous field by one single device at a reasonable price and without any contact with the structure. The contactless characteristic is relevant, particularly for slender structures, where the mass and the damping added to the system by traditional accelerometers may dramatically change the structure behavior. In the actual paper, mode shapes are identified by analyzing the acquired images and then damage detection estimation is being performed relying on the difference between the curvature mode shapes of not damaged and damaged beams. Results show that the damage is correctly located (peak of $\triangle_{\text{curvature}}$) for all the three beams only in the case of severe damage (i.e. slot deep equal to 30 % of the width). To further develop the proposed technique in order to obtain more reliable and effective damage detection, developments on both hardware for image acquisition (mainly in terms of resolution and acquisition frequency) and image processing are needed. As for the image processing, it is expected that the use of digital image correlation can reduce the motion detection uncertainty; however this requires a beam surface preparation in order to produce a very fine surface pattern.

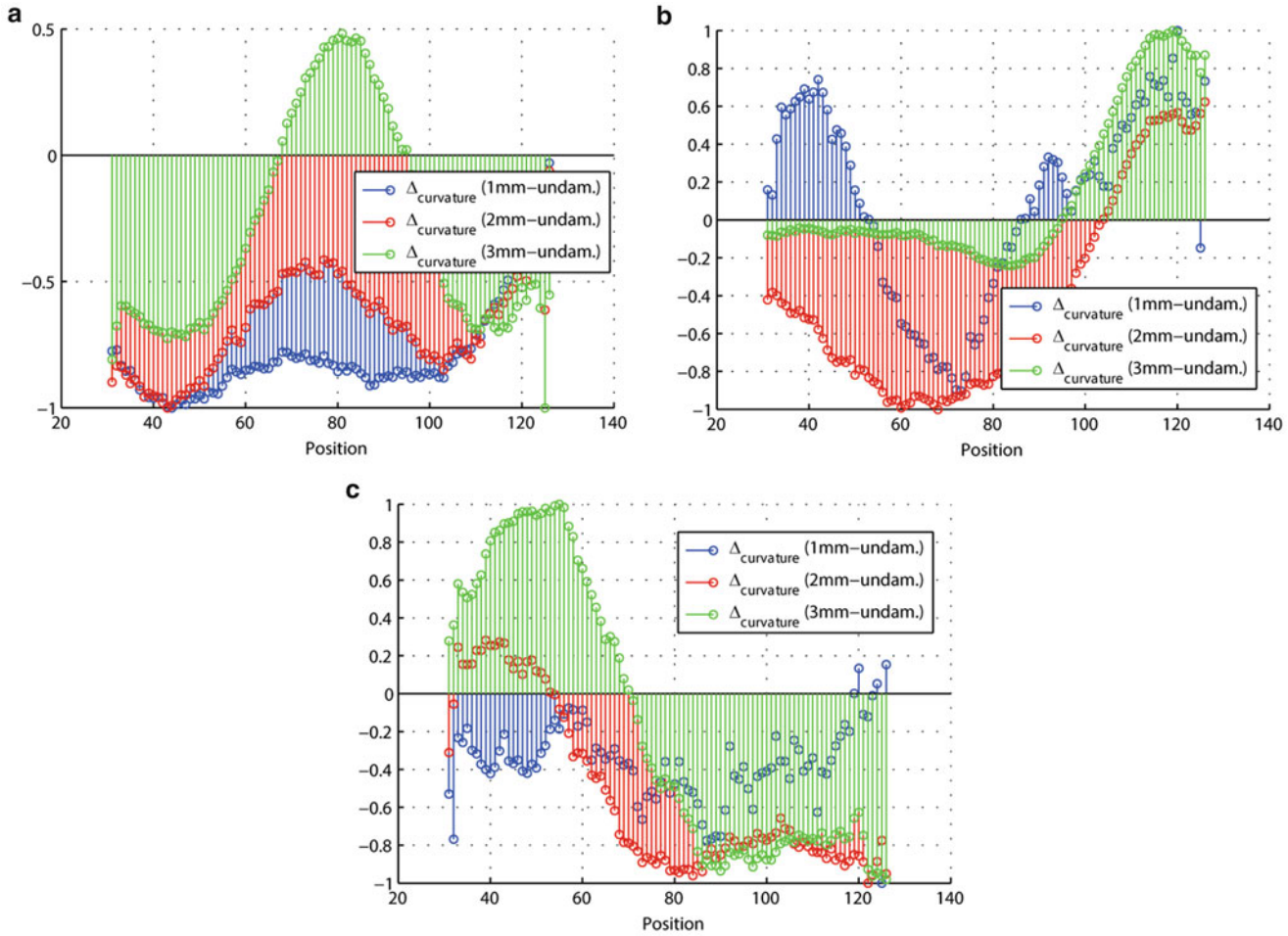

Fig. 22.9 Curvature differences: (**a**) beam 1; (**b**) beam 2; (**c**) beam 3

References

1. Carden EP (2004) Vibration based condition monitoring: a review. Struct Heal Monit 3(4):355–377
2. Farrar CR, Jauregui DA (1999) Comparative study of damage identification algorithms applied to a bridge: I. Experiment. Smart Mater Struct 7(5):704–719
3. Salawu OS (1997) Detection of structural damage through changes in frequency: a review. Eng Struct 19(9):718–723
4. Patil DP, Maiti SK (2003) Detection of multiple cracks using frequency measurements. Eng Fract Mech 70(12):1553–1572
5. Yang Z, Wang L (2009) Structural damage detection by changes in natural frequencies. J Intell Mater Syst Struct 21(3):309–319
6. Pandey A, Biswas M, Samman M (1991) Damage detection from changes in curvature mode shapes. J Sound Vib 145:321–332
7. Ratcliffe C (2000) A frequency and curvature based experimental method for locating damage in structures. J Vib Acoust 122:324–329
8. Hamey CS (2004) Experimental damage identification of Carbon/Epoxy composite Beams using curvature mode shapes. Struct Heal Monit 3(4):333–353
9. Yoon M-K, Heider D, Gillespie JW, Ratcliffe CP, Crane RM (2009) Local damage detection with the global fitting method using mode shape data in notched beams. J Nondestruct Eval 28(2):63–74
10. Li GQ, Hao KC, Lu Y, Chen SW (1999) A flexibility approach for damage identification of cantilever-type structures with bending and shear deformation. Comput Struct 73(6):565–572
11. Zhou Z, Wegner LD, Sparling BF (2007) Vibration-based detection of small-scale damage on a bridge deck. J Struct Eng 133(9):1257–1267
12. Li J, Wu B, Zeng QC, Lim CW (2010) A generalized flexibility matrix based approach for structural damage detection. J Sound Vib 329(22):4583–4587
13. Shi Z, Law S, Zhang L (1998) Structural damage localization from modal strain energy change. J Sound Vib 218:825–844
14. Kim J-T, Stubbs N (2002) Improved damage identification method based on modal information. J Sound Vib 252(2):223–238
15. Choi S, Park S, Park N-H, Stubbs N (2006) Improved fault quantification for a plate structure. J Sound Vib 297(3–5):865–879
16. Fan W, Qiao P (2010) Vibration-based damage identification methods: a review and comparative study. Struct Heal Monit 10(1):83–111
17. Alvandi A, Cremona C (2006) Assessment of vibration-based damage identification techniques. J Sound Vib 292(1):179–202

18. Olaszek P (1999) Investigation of the dynamic characteristic of bridge structures using a computer vision method. Meas J Int Meas Confed 25(3):227–236
19. Wahbeh A, Caffrey J, Masri S (2003) A vision-based approach for the direct measurement of displacements in vibrating systems. Smart Mater Struct 12(5):785–794
20. Lee J, Shinozuka M (2006) A vision-based system for remote sensing of bridge displacement. NDT E Int 39(5):425–431
21. Lee J, Fukuda Y, Shinozuka M, Cho S, Yun C (2007) Development and application of a vision-based displacement measurement system for structural health monitoring of civil structures. Smart Struct Syst 3(3):373–384
22. Sazonov E, Klinkhachorn P (2005) Optimal spatial sampling interval for damage detection by curvature or strain energy mode shapes. J Sound Vib 285(4):783–801
23. Wahab MA, De Roeck G (1999) Damage detection in bridges using modal curvatures: application to a real damage scenario. J Sound Vib 226:217–235
24. Salawu OS, Williams C (1995) Review of full-scale dynamic testing of bridge structures. Eng Struct 17(2):113–121
25. Reynders E, De Roeck G, Gundes Bakir P, Sauvage C (2007) Damage identification on the Tilff bridge by vibration monitoring using optical fiber strain sensors. J Eng Mech 133(2):185–193
26. Unger JF, Teughels A, De Roeck G (2005) Damage detection of a prestressed concrete beam using modal strains. J Struct Eng 131(9): 1456–1463
27. Ratcliffe CP (1997) Damage detection using a modified Laplacian operator on mode shape data. J Sound Vib 204(3):505–517
28. Busca G, Cigada A, Zappa E (2012) Dynamic characterization of flexible structures through vision-based vibration measurements. Conf Proc Soc Exp Mech Ser 1:189–196
29. Hornberg A (ed) (2007) Handbook of machine vision. Wiley, Weinheim, Germany
30. Ewins DJ. Modal testing: theory, practice and application. Mechanical engineering research studies: engineering dynamics series. Wiley, Weinheim, Germany
31. Peeters LB, Van der Auweraer H, Guillaume P, Leuridan J (2004) The PolyMAX frequency-domain method: a new standard for modal parameter estimation? Shock Vib 11(3–4):395–409
32. Qiao P, Lestari W, Shah MG, Wang J (2007) Dynamics-based damage detection of composite laminated beams using contact and noncontact measurement systems. J Compos Mater 41(10):1217–1252

Chapter 23
Damage Detection and Quantification Using Thin Film of ITO Nanocomposites

Breno Ebinuma Takiuti, Vicente Lopes Júnior, Michael J. Brennan, Elen Poliani S. Arlindo, and Marcelo Ornaghi Orlandi

Abstract Many techniques for structural health monitoring (SHM) have been studied with the objective of ensuring the structural integrity of aeronautical structures. One of the most recent solutions for this problem is the use of continuous sensors, constituted by thin films made of nanocomposites. Since the nanocomposites, as any other composite material, can be tailored according to the application needs, there is a vast range of material that has the properties needed to detect damage. The work in this paper proposes the use of a new kind of sensor with nanowires or nanobelts of ITO (indium tin oxide) inserted in a polymeric matrix, such as PMMA (poly(methyl methacrylate) or acrylic). PMMA is transparent and it gives a very nice appearance to the monitored surface. In order to evaluate the effectiveness of this method, several tests are proposed. These tests consist of monitoring the behavior of the nanocomposites when affected by some kind of damage, which can be a mass addition, excessive strains or a crack. The resistivity of the nanocomposite was measured using a two point conventional conductivity test and showed promising results, where the sensors form a net, similar to a neural network capable of sensing structural variations.

Keywords Structural health monitoring • Nanocomposite • Continuous sensors • Neural network • ITO

23.1 Introduction

The objective of structural health monitoring (SHM) is to ensure structural integrity, maintaining its functionality without risking the user's safety. For this reason, SHM is widely applied in aerospace systems in order to try to predict when the monitored structure is going to fail and thus avoid catastrophic failures [4].

Among the most commonly used structural damage detection methods are the electromechanical impedance and Lamb waves methods. In both cases the types of surfaces which can be monitored are limited. In order to monitor a larger area, a larger number of sensors are needed, which means a larger number of wires and a bigger acquisition system, making these methods limited in terms of geometry and range. Another limitation for these methods is the difficulty to bond the sensors on irregular surfaces or in elements with complex geometry such as joints, ribs, fasteners, hybrid materials, and highly damped devices, such as honeycomb sandwich structures [12].

One way to solve this problem is suggested by Lee et al. [7]. To cover a larger area, long piezoelectric sensors (PZT) were used, resulting in a greater range compared to conventional sensors. By using several ribbon-like sensors positioned perpendicularly forming a net of sensors, which they called a "neural network", they were able to detect and localize damage by mapping all the sensors simultaneously. One problem with this method is the use of long PZTs, which are very fragile, making them very difficult to handle, and sometimes impossible to attach to surfaces with small irregularities. To overcome this problem, the authors proposed the use of nanocomposite sensors made of PMMA and CNTs (carbon nanotubes).

B.E. Takiuti (✉) • V.L. Júnior • M.J. Brennan
Department of Mechanical Engineering, Univ Estadual Paulista – UNESP, CEP 15385-000 Ilha Solteira, SP, Brazil
e-mail: takiuti.breno@gmail.com

E.P.S. Arlindo • M.O. Orlandi
Department of Physical Chemistry, Univ Estadual Paulista – UNESP, CEP 14801-970 Araraquara, SP, Brazil

A. Wicks (ed.), *Structural Health Monitoring, Volume 5: Proceedings of the 32nd IMAC, A Conference and Exposition on Structural Dynamics, 2014*, Conference Proceedings of the Society for Experimental Mechanics Series, DOI 10.1007/978-3-319-04570-2_23,

CNTs are long carbon chains, made of tubular sheets of graphite. They present high electric conductivity, and depending on the chirality they can be metallic or semiconductors, have high mechanical resistance and have piezoelectric properties. The greatest advantage of CNTs is that they can be used to produce composite materials with polymers, in which they enhance the composite material's properties with the addition of very little mass. By using this advantage, one can create several types of materials with properties such as piezoelectricity, piezoresistivity, electrochemical actuation, higher mechanical resistance, higher electric or thermal conductivity, etc.

There are several ways to apply CNTs as SHM sensors. In general they are applied as coatings or inserted in the material itself. The advantage in the first case is that the use of continuous polymeric sensors (since the most of the composite material is a polymer) makes it easier to attach them to large areas, or in irregular or complex surfaces. The advantage of the second case, is the structure itself already has the sensor inside, which can be a good option for polymeric or composite structures.

Rainieri et al. [10] studied the use of SWNT (single-wall carbon nanotube) in the shape of films, commonly called "buckypaper", inserted in a cement matrix for civil structure applications. Their studies show that pure CNT films are fragile because of their intermolecular forces (Van de Waals forces), therefore it is necessary to put the CNTs into a polymeric matrix in order to avoid sliding between the NTs (nanotubes). It permits the insertion of the sensors in the monitored structure without the risk of breaking them.

Kang et al. [6] proposed the use of a PMMA/MWNT (multi-wall carbon nanotube) nanocomposite, applied by aerosol spray onto the monitored surface, forming a conductive composite with an easy application process. After coating the surface, they monitor the electric resistance of the film that rises with the appearance of cracks. This process continues until the crack is large enough to cut the film completely and with this the conductibility becomes null, indicating that there is a crack in the surface and there is a need for maintenance.

Liu et al. [8] suggested the use of the MWNTs inserted in to an epoxy matrix, with the objective of monitoring glued joints of two CFRP (carbon-fiber-reinforce polymer) slabs. Abot et al. [1] proposed the use of strings made from CNT coated with epoxy or polyurethane sewn between the fibers of a polymeric laminate, with the objective of detecting the delamination process. In both cases the sensors were put inside the material, trying to detect specific internal failures.

Ashrafi et al. [3] used two types of SWNT thin films using epoxy as matrices. These films were glued at the start and at the end of a crack. Both films had a different composition, isolation and setup, and both of them were able to monitor the growth of the crack efficiently.

Zhou et al. [13] studied the use of a thin film similar to the SWNT film, but instead of using SWNTs they used magnetic strings. Although in this case no nanocomposites were used. The film sensor used by was similar to the one proposed by Kang et al. [6] and it was equally effective in monitoring the crack's growth.

The conclusion that can be reached by evaluating the state of the art methods for SHM using CNTs is that the key properties to effectively use nanocomposites as damage sensors are the electrical conductivity and the piezoelectric effect. With this in mind, a partnership between the Department of Mechanical Engineering, UNESP – Ilha Solteira and the Department of Physical Chemistry, UNESP – Araraquara was formed with the objective of seeking alternative nanocomposite materials that have these properties and can be used for development of new methods for damage detection, based on CNTs.

The goal of this work is to study several alternatives to the CNT nanocomposites applied in the form of thin films coating an aluminum surface. The intention is to be able to detect and localize cracks by monitoring the conductibility and the piezoelectric effect.

23.2 Basic Concepts for SHM

23.2.1 Structural Health Monitoring in Aerospace Applications

Statistical studies show that around 20 % of aircraft accidents between 1918 and 2009 were caused by technical failures, while 31 % of the failures on metallic structures in planes were caused by the development of a crack generated by fatigue, as shown in Tables 23.1 and 23.2. With the objective of enhancing the reliability of aircrafts and therefore reducing the number of accidents caused by structural damage, many studies are being carried out to improve advanced damage detection methods for metallic structures. It is hoped that the SHM method presented here can be used to detect impact damage, which are responsible for 7 % of the aircraft structural failures.

Table 23.1 Accidents causes around the world

Accident cause	Percentage of responsibility
Human error	67.57 %
Technical failure	20.72 %
Bad weather	5.95 %
Sabotage	3.25 %
Other causes	2.51 %

Source: Bureau of Aircraft Accidents Archieves [5]

Table 23.2 Failure causes in aeronautic metallic structures

Failure type	Percentage of failures
Fatigue crack	30.96 %
Corrosion	25.39 %
Joints attachment/detachment	21.67 %
Corrosion cracks by tension	14.55 %
Impact damage	7.43 %

Source: Boller et al. [4]

Generally most metallic structures in aircrafts are made from aluminum plates, which corresponds to 60–80 % of the global mass of the aircraft [11]. Taking this in account, the base material used for damage monitoring in this work is an aluminum plate.

Nowadays, there is a tendency to use composite material in the primary aircraft structure, as in Boeing 787, which is the first plane with more than 50 % of composite material present in its structure. The greatest problem with this is that it is are difficult to monitor the structural integrity of composite materials by conventional methods because of high damping rates. A secondary objective for the work presented in this paper is to solve this problem by using continuous nanocomposite sensors, which do not require the propagation of any kind of wave through the structure.

23.2.2 Nanomaterials and Nanocomposites

It is well known that the mechanical, thermal and electrical properties of polymeric materials can be manipulated through the fabrication of composite materials, which are made of the union of one or more different types of reinforcement phases. Usually polymeric materials are reinforced with carbon fiber or glass microfiber to enhance its mechanical properties and several metals and/or organic materials are inserted into the mixture into obtain better electric and/or thermal properties. Recently, much research has been done to obtain even better properties without losing the good properties of the matrix. This research has focused on producing composites using nanometric fillers, which have better properties and can enhance the properties of the composites without interfering with the already existing good properties of the matrix material. This can be achieved because of the extremely small size of the filler, resulting in a larger specific surface and interface area. With this, the mass percentage of the fillers can be greatly reduced. While the normal composites have about 40 % of their mass of fillers, the nanocomposites are around 10 %. This difference reflects on how much of the matrix properties will remain in the composite. In this work, it is aimed to maintain the transparency and flexibility of the PMMA.

23.2.2.1 Indium Tin Oxide (ITO)

One of the alternative fillers proposed here are ITO nanowires. These nanowires are highly transparent and highly conductive ceramic materials and can be added as fillers to give conductivity to the PMMA matrix, attaining percolation with about 5 % of filler without interfering significantly in the optical properties of the composite [2]. Figure 23.1 shows FEG-SEM (Field Emission Guns-Scanning Electron Microscope) images of typical ITO nanowires.

ITO nanowires are a one-dimensional nano-structured material, which means they have only one significant dimension (length) compared to the other two (width and thickness), and that dimension is nanometric. Furthermore, they have different properties from their non nanometric counterpart. The reason for using ITO for this application is the fact that they have low electrical resistivity and good transparency when used as fillers for thin film nanocomposites. The ITO are synthesized by a carbothermal reduction method using coevaporation of oxides proposed by Orlandi et al. [9].

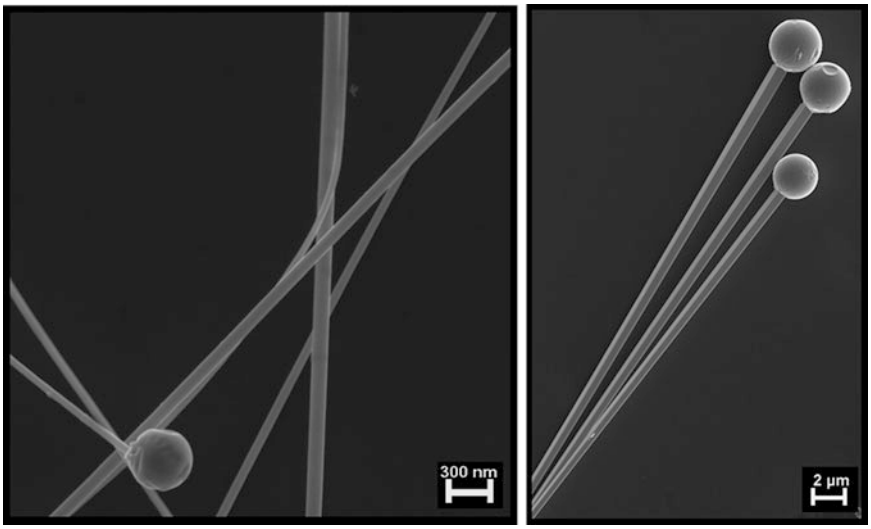

Fig. 23.1 FEG-SEM images of IndiumTin Oxide. *Source*: Arlindo et al. [2]

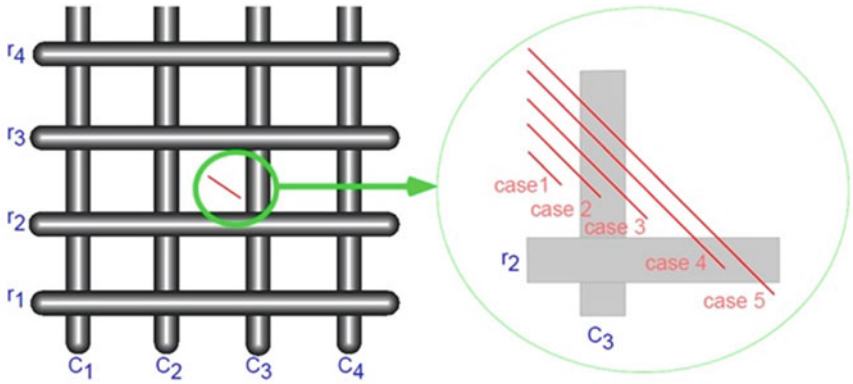

Fig. 23.2 Neural network proposed by Yun et al. [12]

23.3 Experimental Setup

The idea is to use the "neural network" concept proposed by Yun et al. [12] to form a net of conducting nanofillers. In case of the appearance of a crack one of the "wires" of this network would have its conductibility reduced or even nulled, which would indicate that a crack has appeared in the monitored system. One advantage of this method is that since there is a net of wires covering the system, it is possible to detect not only if there is a crack, but to locate it by mapping all of the wire's conductibility. The monitored "ways", or the "wires", are the ITO nanowires and one of the challenges is the fact that the position of all of the nanowires is not known. Figure 23.2 shows the neural network proposed by Yun et al. [12], where the "r's" and "C's" represents the ways (wires) and the red lines represents different crack cases.

The first step for the development of the sensor is the synthesis of the ITO. After synthetizing the fillers, several tests were performed regarding the casting method using different weight percentage addition of fillers.

The method tested for coating consisted of just pouring the dissolved nanocomposite over the base material. This method ensured that the fillers were uniformly distributed in the entire composite. Since the structural material monitored in this case was already conductive (aluminum) it was necessary to ensure that the nanowires did not touch the aluminum. One of the proposed solutions for this is the use of a pure PMMA layer under the nanocomposite layer, providing insulation between the aluminum structure and the nanowires. This method proved to be ineffective since the addition of the pure PMMA layer interfered with the nanocomposite composition and made it difficult to achieve the percolation even using high values of weight percentage. An effective solution was the use of a pure PMMA layer over the aluminum and then the nanowires were mixed with a solvent and poured over the PMMA layer, resulting in the mixture of ITO only at the surface of the PMMA layer. By doing this, it was possible to achieve percolation in the most of the area of the aluminum plate. Figure 23.3 shows the resulting coatings using different coating methods.

After the coating process, ten golden points were deposited on the nanocomposite surface, as seen in Fig. 23.3b. These golden points were used as electrodes, in which copper wires were glued with a conductive liquid solder MY203,

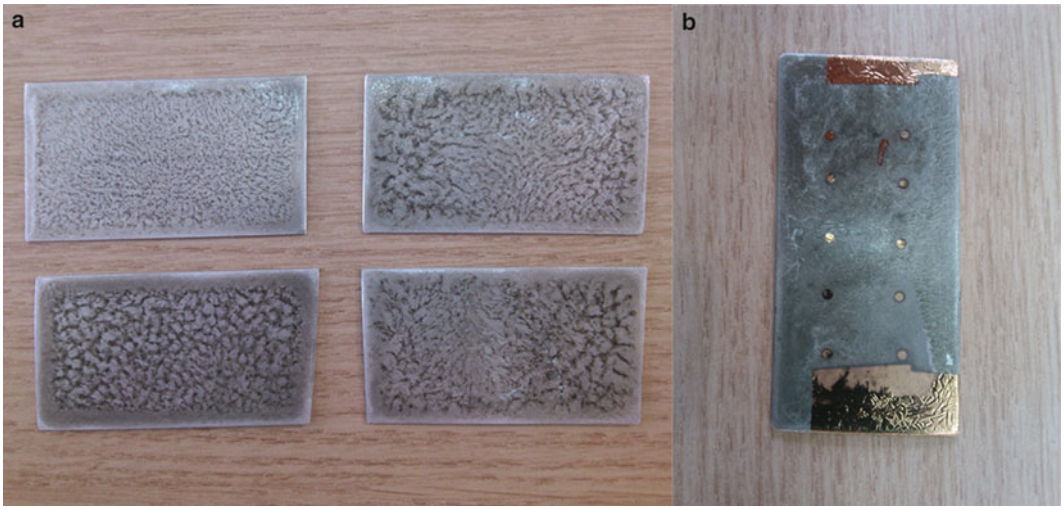

Fig. 23.3 Examples of coated aluminum plates. (**a**) Coated by pouring dissolved nanocomposite. (**b**) Coated by pouring ITO mixed with a solvent over a PMMA layer

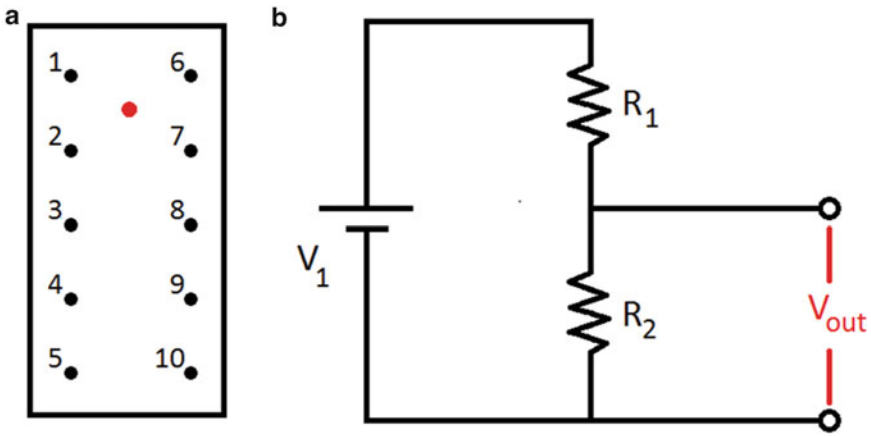

Fig. 23.4 Measurement details. (**a**) Electrodes disposition. (**b**) Voltage divider

from Mhnano. Each of these electrodes was identified with a number, as seen in Fig. 23.4a. In order to measure the resistance between these electrodes, the two point method was used and the data acquisition instrument used was a National Instruments USB-6251 with a voltage divider circuit, as seen in Fig. 23.4b, where a known resistance (R_1) and voltage (V_1) are used to determine an unknown resistance (R_2) by measuring the voltage (V_{out}).

The measured value is converted to resistance by.

$$R = \frac{R_1 V_{out}}{(V_1 - V_{out})} \tag{23.1}$$

The resistances were measured without damage at first and them with damage in the form of a hole of 1 mm diameter, shown as a red dot shown in Fig. 23.4a.

23.4 Results and Discussions

Using 5 V for V_1 and 1 kΩ for R_1 some preliminary results are shown in Table 23.3.

As it can be observed in Table 23.3, the results diverge from those expected. It was expected that the resistances between 1_7 and 2_6 would greatly rise, but that between 1_7 practically did not change, and 2_6 increased very little. Although most of the values rose, the resistances 1_2 and 2_7 suffered resistance reduction. This was not expected and the reason for this effect is yet to be investigated. The other problem is the lack of uniformity in the measurements in the different positions,

Table 23.3 Experimental tests on the aluminum plate

Measured position	Resistance without damage (Ω)	Resistance with damage (Ω)
1_2	522.17	269.74
6_7	951.00	1,017.70
1_6	1,058.30	1,080.80
2_7	88.53	76.95
2_6	1,030.80	1,097.70
1_7	97.47	97.48

Fig. 23.5 Test sample

varying from 88 Ω to 1,058 Ω, which is a too large a range. Figure 23.5 shows the test sample. By observing one reason for the non-uniformity of the results can be seen, which is due to the non-uniformity of the test sample. However, this was the first sample produced, and the process is yet to be fine-tuned, for better nanocomposites with more uniform resistance.

23.5 Conclusions

This paper has presented some preliminary results of work on ITO/PMMA thin film damage detection sensors. The initial nanocomposites produced, however, had low uniformity and some unexpected response to damage. Further research will be carried out to create better nanocomposites, with uniform resistivity through all the coated area. To achieve these characteristics, the nanocomposite creation process would need fine tuning to establish the relationship of the film matrix volume (PMMA volume) with the coated volume, as well as to the mass of ITO, so that the best concentration of ITO per volume of PMMA is found. For this, several tests will be required in which different composites, with different concentrations of ITO per PMMA will be produced and have their resistances measured and tested in the presence of different sizes and damage positions. The initial value of 10 % of filler was just a start, based on previous studies but as expected, several samples with different filler percentage will be required to be tested in order to find the best concentration, which would provide the best sensitivity to damage, therefore creating the ideal thin film damage sensor.

One of the main problems found during the development of the nanocomposite was the limitation of the size of the coated area. The next step in this research will be the development of a production process that can overcome this limitation, while creating an uniform sensor with good sensitivity. Another step will be the development of a data acquisition system, to monitor the damage so that it can be not just identified, but its location and size can be determined.

Acknowledgments The authors would like to thank the FAPESP (Process number: 2012/25153-1) for its financial support and CNPq and FAPEMIG for partially funding the present work through the INCT-EIE.

References

1. Abot JL, Song Y, Vatsavaya MS, Medikonda S, Kier Z, Jayasinghe C, Rooy N, Shanov VN, Schulz MJ (2010) Delamination detection with carbon nanotube thread in self-sensing composite materials. Compos Sci Technol 70(7):1113–1119
2. Arlindo EPS, Lucindo JA, Bastos CMO, Emmel PD, Orlandi MO (2012) Electrical and optical properties of conductive and transparent ITO@PMMA nanocomposites. J Phys Chem C 116(23):12946–12952
3. Ashrafi B, Johnson L, Martinez-Rubi Y, Martinez M, Mrad N (2012) Single-walled carbon nanotube-modified epoxy thin films for continuous crack monitoring of metallic structures. Struct Health Monit 11(5):589–601
4. Boller C, Staszewski WJ (2004) Aircraft structural health and usage monitoring. In: Health monitoring of aerospace structures. Wiley, London
5. Bureau of Aircraft Accidents Archieves (2012) http://www.baaa-acro.com/. Accessed 13 Nov 2012
6. Kang I, Schulz MJ, Kim JH, Shanov V, Shi D (2006) A carbon nanotube strain sensor for structural health monitoring. Smart Mater Struct 15(3):737
7. Lee JW, Kirikera GR, Kang I, Schulz MJ, Shanov VN (2006) Health monitoring method for plate structures using continuous sensors and neural network analysis, pp 61741R–61741R
8. Liu Y, Yekani Fard M, Rajadas A, Chattopadhyay A (2012) Autonomous sensing of composites with carbon nanotubes for structural health monitoring, pp 83421H–83421H
9. Orlandi MO, Aguiar R, Lanfredi AJC, Longo E, Varela JA, Leite ER (2005) Tin-doped indium oxide nanobelts grown by carbothermal reduction method. Appl Phys A 80(1):23–25
10. Rainieri C, Fabbrociono G, Song Y, Shanov V (2011) CNT composites for SHM: a literature review. In: International workshop: smart materials, structures & NDT in aerospace, 2–4 November 2011.
11. Rezende MC (2007) Fractografia de Compósitos Estruturais. Polímeros 17:E4–E11
12. Yun Y-H, Kang I, Gollapudi R, Lee JW, Hurd D, Shanov VN, Schulz MJ, Kim J, Shi D, Boerio JF, Subramaniam S (2005) Multifunctional carbon nanofiber/nanotube smart materials, pp 184–195
13. Zhou J, Gu Y, Fei P, Mai W, Gao Y, Yang R, Bao G, Wang ZL (2008) Flexible piezotronic strain sensor. Nano Lett 8(9):3035–3040

Chapter 24
The Use of Orbitals and Full Spectra to Identify Misalignment

Michael Monte, Florian Verbelen, and Bram Vervisch

Abstract In this paper a "SpectraQuest" demonstrator is used to introduce misalignment in a rotating set-up. The vibrations caused by misalignment are measured by two accelerometers on the bearings and two eddy-current probes on the shaft itself. A comparison is made between the classical spectral analysis, orbitals and full spectra. Orbitals are used to explain the physical interpretation of the vibration caused by misalignment. Full spectra allow to distinguish imbalance from misalignment by looking at the forward and reversed phenomena. This analysis is done for different kinds of misalignment, couplings and combined machinery faults.

Keywords Machinery fault • Diagnostics • Misalignment • Full spectrum • Orbital

24.1 Introduction

In industry misalignment is one of the main causes of excessive vibrations leading to wear or even premature failure. The higher the speed, the bigger the impact of a small misalignment will be. The sooner misalignment is detected, the better for the condition of the machinery, energy consumption, and the costs of the maintenance of the set-up.

Several techniques, such as vibration monitoring, thermal imaging and oil particle analysis are used to detect and analyze machinery faults. Techniques to analyze the collected data is still an ongoing research topic. The most widespread method is the use of vibration spectra and that method will be used in this paper. The problem with the spectra is that it is not always obvious to distinguish between different types of faults such as misalignment or other machinery faults. To analyze the data, the time-based signal is measured by an accelerometer or eddy-current probe. From this signal the (half) spectrum is calculated in order to facilitate the analysis.

Modeling and analyzing simultaneous occurring faults in rotating machinery, is an ongoing research topic [1, 2]. New models and methods are still being developed and applied on test set-ups to find the best technique for every single fault and a combination of faults [3].

The type of misalignment has an impact on the spectrum. From the conducted measurements it is clear that the spectrum not only depends on parallel or angular misalignment, but also on the coupling, the excitation force and the rotating speed. Moreover, misalignment occurs generally in combination with other faults. Analysis of spectra when faults occur simultaneously demands experience and a thorough knowledge of the machinery.

Full spectra and orbitals need data from two orthogonal signals and are still being studied by different researchers [4–7]. The vibration data can provide information about movement of the shaft and the direction of the vibration. The orbital has an elliptical shape due to the superposition of two circular movements. This forward and reverse movements are also shown in the frequency domain in a full spectrum and are a useful tool for analyzing machinery faults.

M. Monte (✉) • F. Verbelen
Department of Industrial Systems and Product Design, University of Ghent, Graaf Karel de, Goedelaan 5, 8500 Kortrijk, Belgium
e-mail: michael.monte@ugent.be; florian.verbelen@UGent.be

B. Vervisch
Department of Industrial Systems and Product Design, University of Ghent, Graaf Karel de, Goedelaan 5, 8500 Kortrijk, Belgium

Department of Electrical Engineering, Systems and Automation, University of Ghent, Technologiepark 914, 9052 Zwijnaarde, Belgium
e-mail: BramF.Vervisch@UGent.be

A. Wicks (ed.), *Structural Health Monitoring, Volume 5: Proceedings of the 32nd IMAC, A Conference and Exposition on Structural Dynamics, 2014*, Conference Proceedings of the Society for Experimental Mechanics Series, DOI 10.1007/978-3-319-04570-2_24, © The Society for Experimental Mechanics, Inc. 2014

24.2 Misalignment

Misalignment is a well-known phenomenon and a lot of research is done in order to understand and detect this machinery fault. Several techniques exist to eliminate the different kinds of misalignment [8]. Alignment errors can be divided into four categories: horizontal offset, vertical offset, horizontal angle and vertical angle error. In reality misalignment consists of combinations of the above. A parallel misalignment occurs when the alignment error is limited to pure offset (horizontal or vertical).

Parallel misalignment causes a shearing force and a bending moment at the end of the coupled shaft. This leads to a large radial reaction force in the bearings which is measured as vibration. This radial vibration is situated at the 1×, 2× and 3× order peaks in the spectrum. When the misalignment is very serious, the higher orders will also be excited. The peak at 2× can be partly explained as follows. When the shaft rotates there will be two excitations every rotation.

Angular misalignment will provide a bending moment resulting in a large axial vibration which can be measured at 1×, 2× and 3× order peaks. Unlike parallel misalignment the 1× component will be more pronounced, which makes it difficult to distinguish this error from imbalance.

24.3 Experimental Results

The set-up used for the experiments is the Machinery Fault Simulator from SpectraQuest. Besides using the simulator as an educational tool it can also be used for research [9]. For the measurements two sensors are needed. For these measurements accelerometers or eddy-current probes were used. Before discussing the different faults, reference measurements had to be made in order to see the difference between a good aligned set-up and a misaligned set-up. Figure 24.1 shows the spectrum of data from an accelerometer. Peaks are expected at 1× (35 Hz) (little imbalance) and 2× (70 Hz) (small misalignment). The presence of a peak at 3× (105 Hz) is due to the flexible coupling. This coupling makes the 2× peak more pronounced. The peaks 1× and 2× at the second lager are also bigger compared to the first lager (closer to the coupling). The displacement at the lager will become bigger the further it is from the coupling.

First measurements on parallel misalignment are treated, then angular misalignment is discussed. The measurements on parallel and angular misalignment have been carried out at different rotational speeds. For parallel misalignment a flexible coupling had to be used. The rigid coupling does not allow parallel misalignment. For the angular misalignment both the flexible and the rigid coupling are used to show the difference between the two couplings. The sample frequency was 2,048 Hz and the measuring time was 10 s for all measurements.

24.3.1 Measurements on Parallel Misalignment

With parallel misalignment a peak is expected at 2× the rotational speed in the spectrum of the signal. This peak has a greater amplitude compared to the 1× peak. This is according to the characteristics of parallel misalignment. This peak is shown in the horizontal (Fig. 24.2) and vertical (Fig. 24.3) (half) spectrum. The large peak at 3× the rotational speed (3× 35 Hz) comes from the flexible coupling used in the set-up.

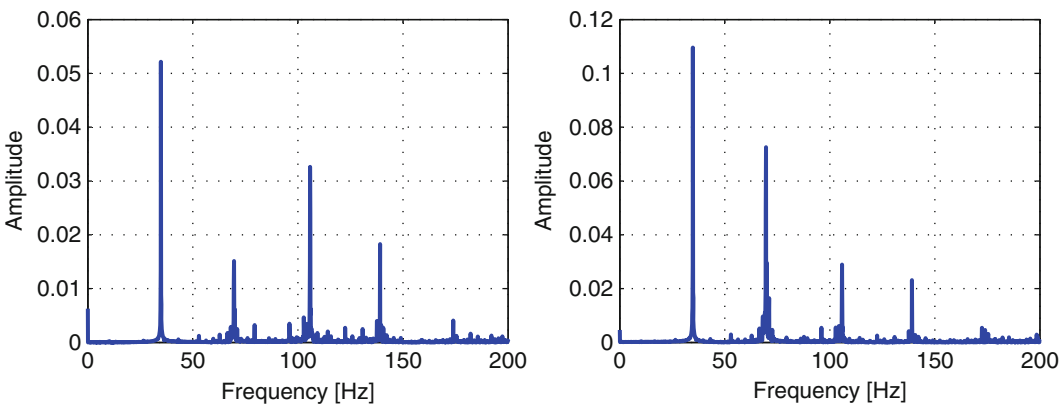

Fig. 24.1 Horizontal measurement without imbalance

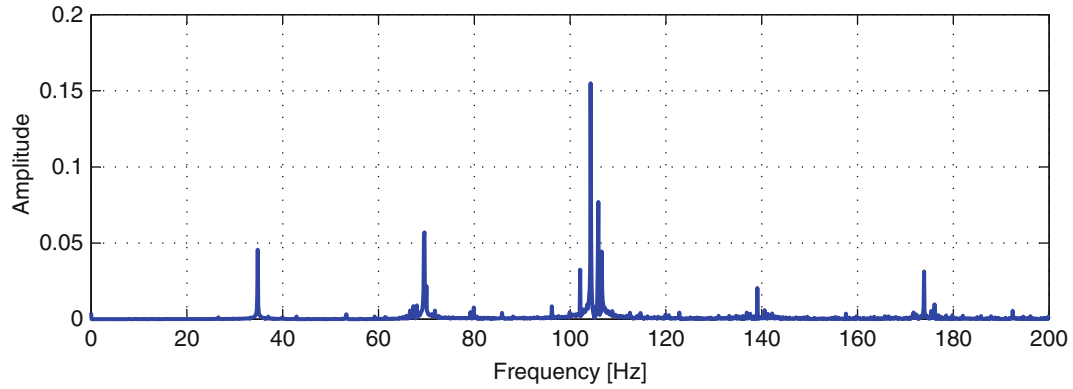

Fig. 24.2 Horizontal measurement on parallel misalignment

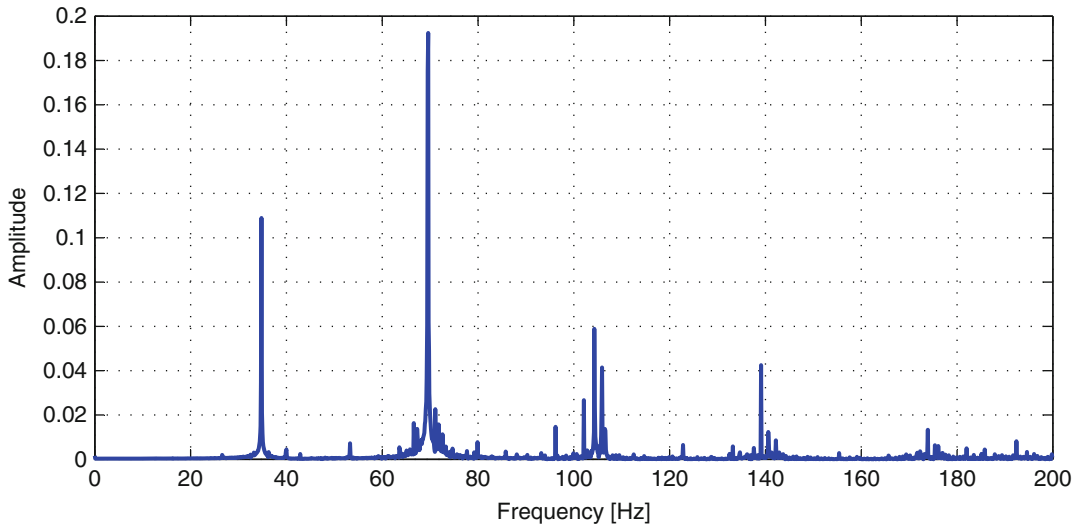

Fig. 24.3 Vertical measurement on parallel misalignment

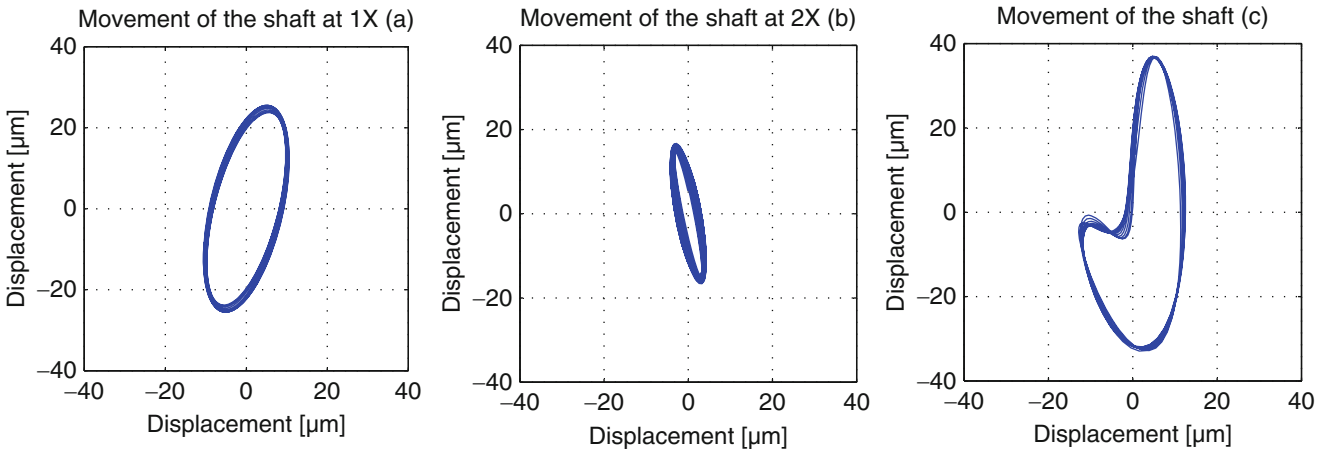

Fig. 24.4 Movement of the rotor as a result of parallel misalignment (accelerometer)

The movement of the shaft under the influence of parallel misalignment is now studied with orbitals. In Fig. 24.4 measurements with an accelerometer are shown and the movement of the 1× vibration is plotted together with the 2× vibration. These plots are ellipses and they do not show any distortion. The third plot is the movement of the 1× and 2× vibration together. This figure shows that the movement of the shaft is disturbed. This is clearly a sign of parallel misalignment. The same results are obtained when measuring with an eddy-current probe (Fig. 24.5).

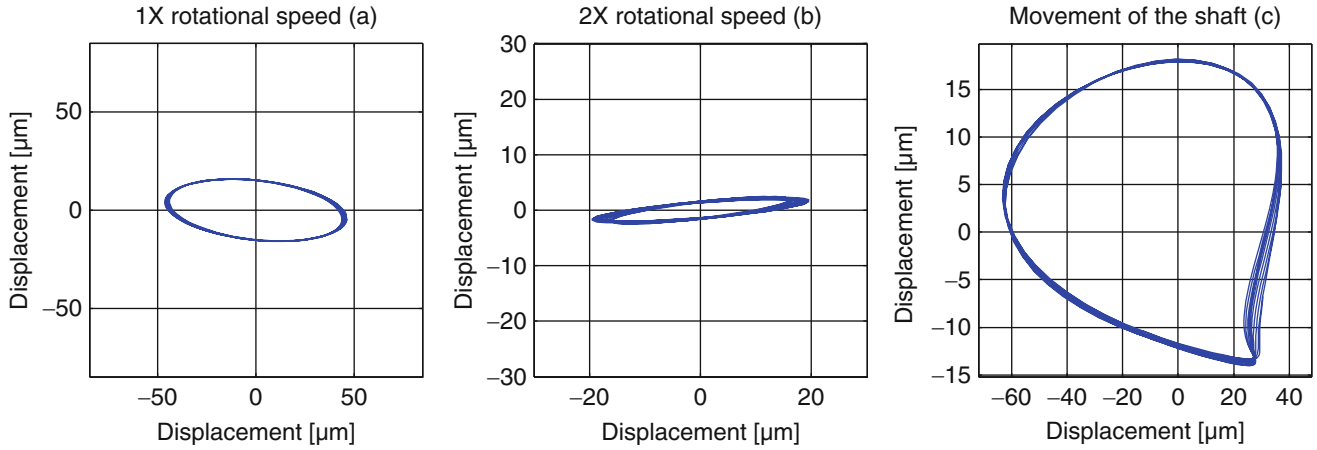

Fig. 24.5 Movement of the rotor as a result of parallel misalignment (eddy-current probe)

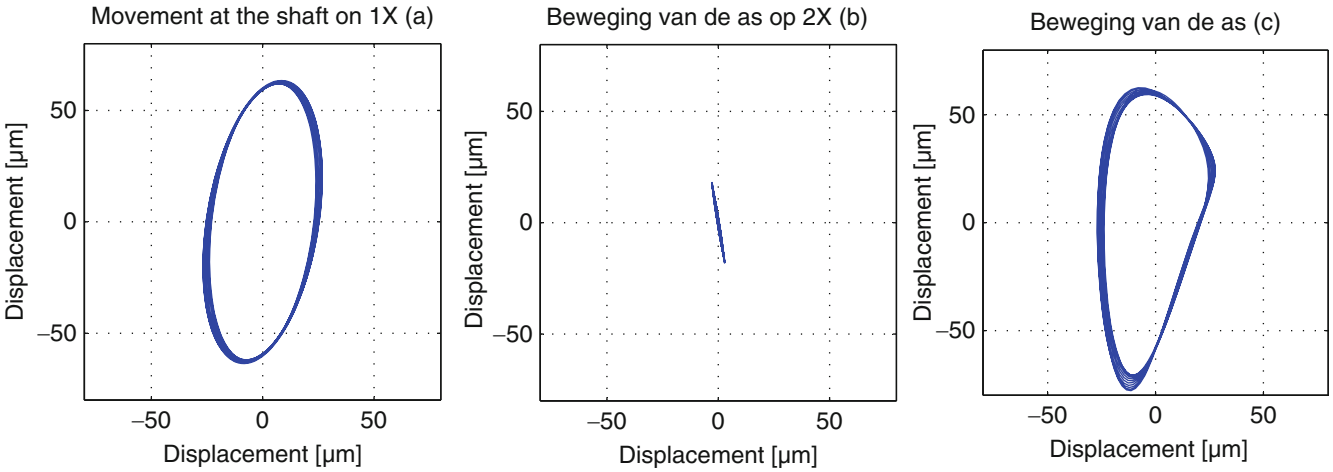

Fig. 24.6 Movement of the rotor as a result of parallel misalignment and imbalance

To study the influence of imbalance the measurements are done again with static imbalance added to the setup. The influence of the imbalance is shown by the enlargement of the orbital at 1× the rotational speed while the shape remains the same. The influence of the 2× vibration is decreased and shown in the orbital at 2× which indicates parallel misalignment (Fig. 24.6).

24.3.2 Measurements on Angular Misalignment

For angular misalignment a big 1× component is expected (Figs. 24.7 and 24.8). The problem with these spectra is that they resemble imbalance problems. Wrong conclusions can be drawn very easily.

Orbitals offer an excellent solution because the movement of the shaft when it is in imbalance is different compared to angular misalignment. Figure 24.9 shows the orbitals of the 1×, 2× and a total image of the shaft movement measured by an accelerometer. From the 1× component no conclusion can be drawn. This again is an ellipse. On the other hand, the 2× component exhibits a very special form. Whereas the 2× component in an imbalance problem leads to an ellipse, the figure is distorted. This image is typical for angular misalignment with a flexible coupling. The figure shows the difference with imbalance problems. The same image is seen when looking at the orbitals from measurements by eddy-current probes (Fig. 24.10). However, the preliminary alignment was not perfect. A combination of a parallel and angular misalignment is present.

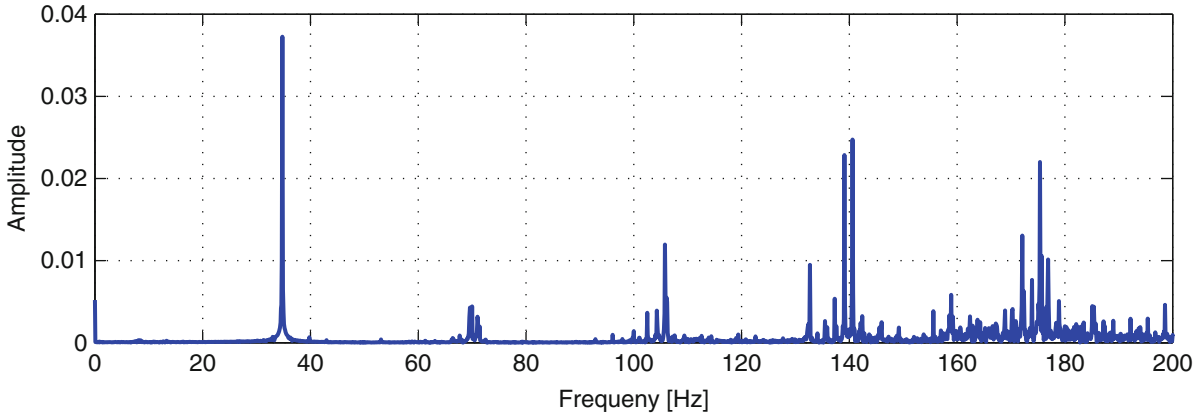

Fig. 24.7 Horizontal measurement on angular misalignment

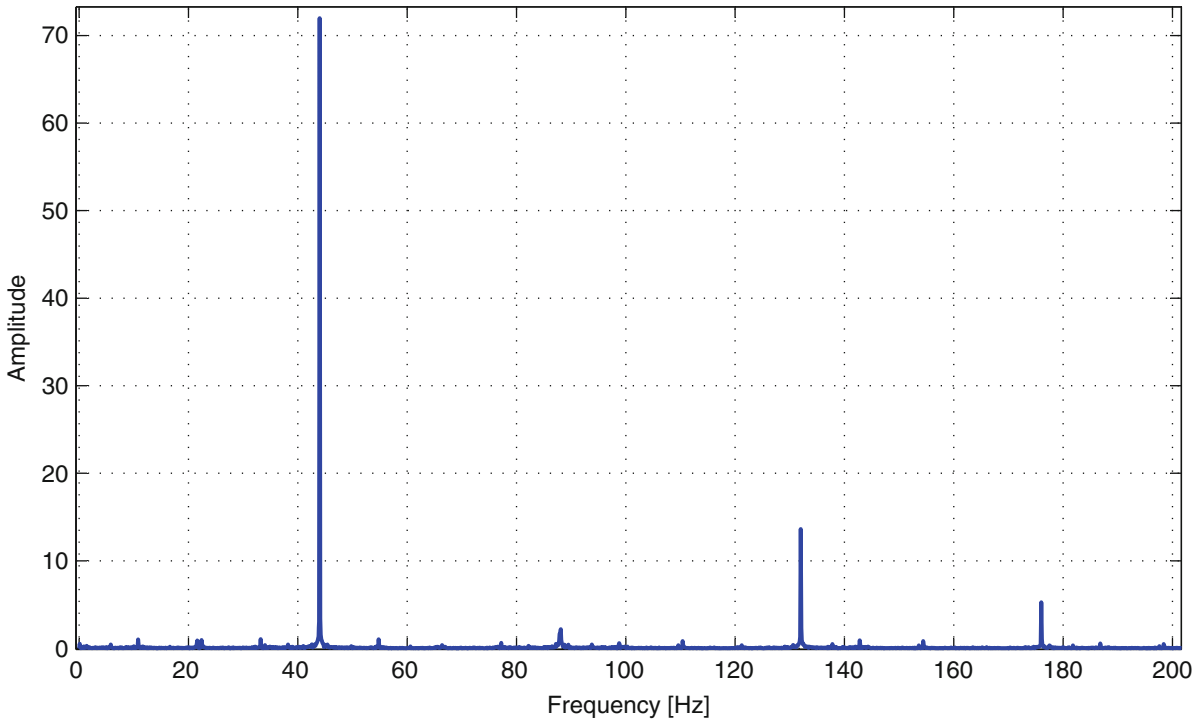

Fig. 24.8 Horizontal measurement on angular misalignment (45 Hz)

In Fig. 24.11 the orbital of angular misalignment with a rigid coupling is shown. Note that the 2× image again is an ellipse in contrast to the flexible coupling. The rigid coupling does not allow the same movement as a flexible coupling.

24.3.3 Measurements on Combined Faults

Many combined faults can lead to misinterpretation. In the spectrum of Fig. 24.12 a fault is shown that can be interpreted as an imbalance problem, an angular misalignment or a parallel misalignment with imbalance. Just as in the previous cases an orbital can give clarification. An alternative tool to detect the difference between imbalance and misalignment is the full spectrum (Fig. 24.13). The difference between the positive and negative frequencies gives a clarification.

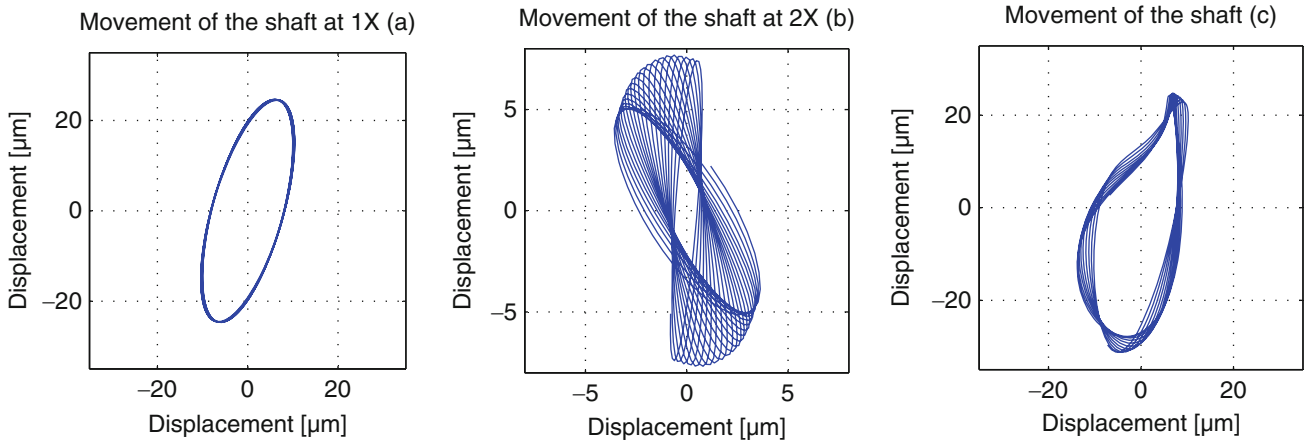

Fig. 24.9 Movement of the rotor as a result of angular misalignment with a flexible coupling

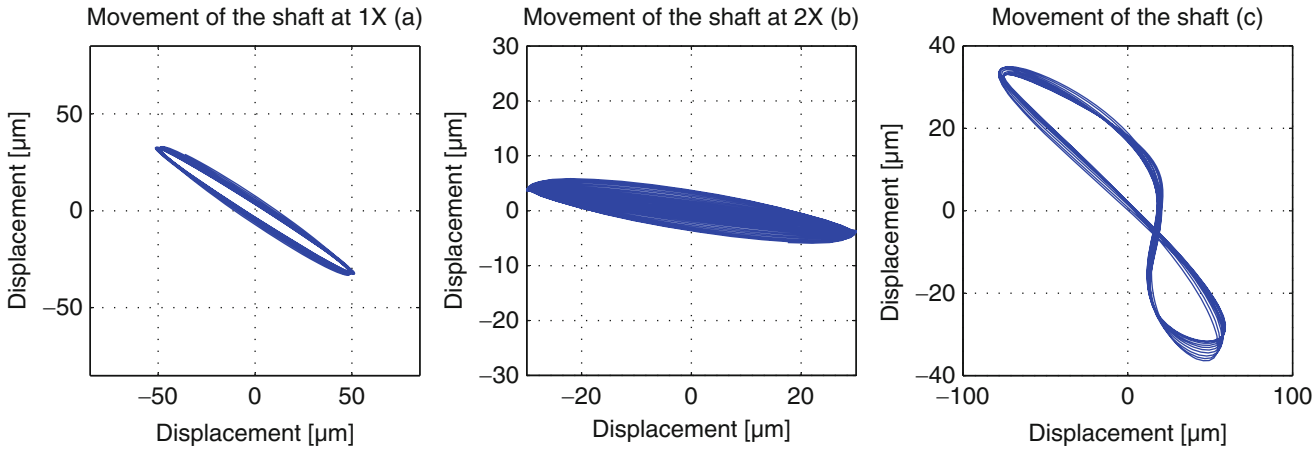

Fig. 24.10 Movement of the rotor as a result of angular misalignment with a flexible coupling (eddy-current probe)

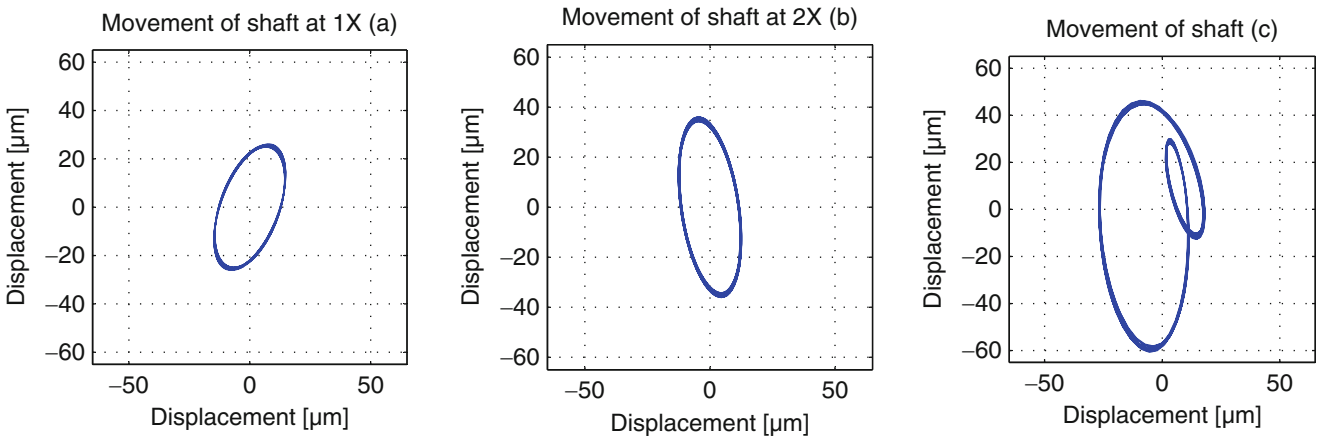

Fig. 24.11 Movement of the rotor as a result of angular misalignment with a rigid coupling

Figure 24.13 shows the full spectrum of Fig. 24.12. The peak at 1× is clearly larger than the −1× peak which indicates imbalance. There is also a clear peak on both 2× as −2× which indicates parallel misalignment. The problem shown is parallel misalignment with imbalance. From the original spectrum it is difficult to come to the same conclusion. The full spectrum, on the other hand, makes it fairly easy to draw a conclusion. A similar result is shown in Fig. 24.14 with measurements with an eddy-current probe.

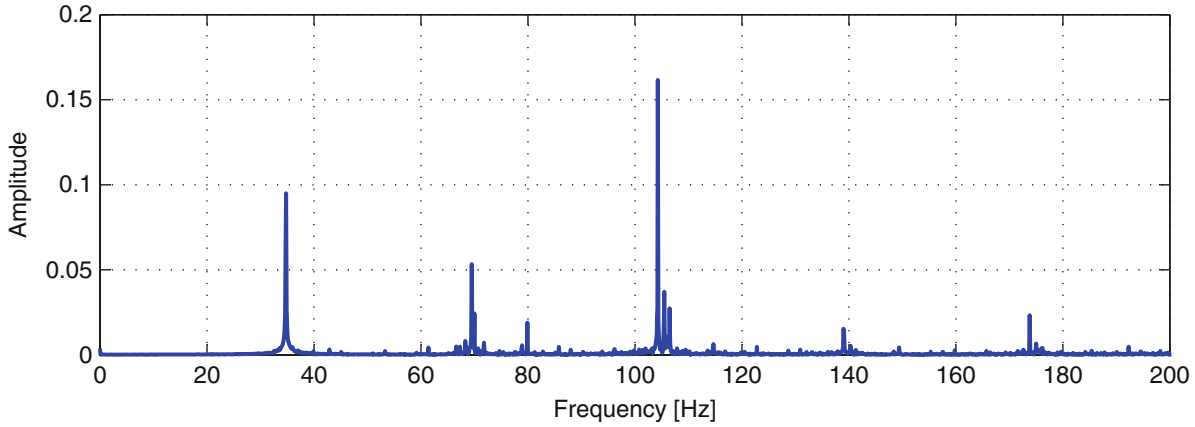

Fig. 24.12 (Half) spectrum of parallel misalignment with imbalance

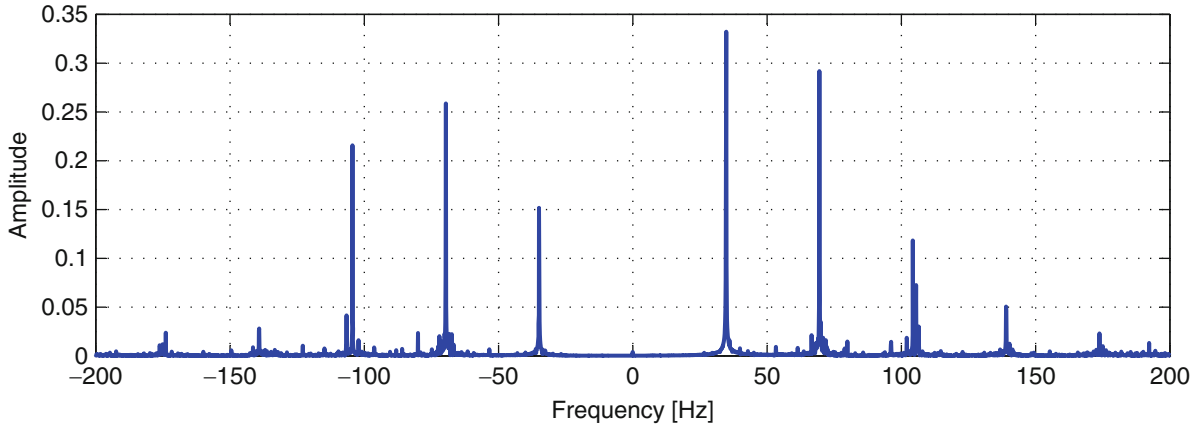

Fig. 24.13 Full spectrum of parallel misalignment with imbalance

24.4 Conclusions

Orbitals and full spectra have proven their usefulness in detecting machinery faults from vibration measurements. Misalignment is not always as clear to detect compared to imbalance in a (half) spectrum. For misalignment orbitals and full spectra can be used to make a proper analysis of the problem. An important finding from the many measurements is that the difference between parallel and angular misalignment can be seen in orbitals by the presence or absence of a twist in the contour. The presence of the twist indicates angular misalignment.

Imbalance mainly generates a forward vibration meaning that imbalance influences only the positive frequency range. Misalignment is evenly represented in the positive and negative frequency range. Summarized combined fault leads to the following in full spectra. For imbalance a large $1\times$ peak and a small $-1\times$ peak is expected while for angular misalignment an equally large $1\times$ and $-1\times$ peak is expected. For parallel misalignment combined with imbalance is a combination expected.

The coupling also plays an important role in the measured spectrum and the shape of the resulting orbitals. Besides the large $1\times$ and $2\times$ vibration peaks the $3\times$ component is also used.

Additional research is absolutely needed in order to confirm these findings. Furthermore, the different faults in a system and their influence on each other needs to be studied. Also the conclusion about the coupling is an interesting research topic. Nevertheless, at present the orbitals and full spectrum can be used as an additional tool when vibrational data are studied.

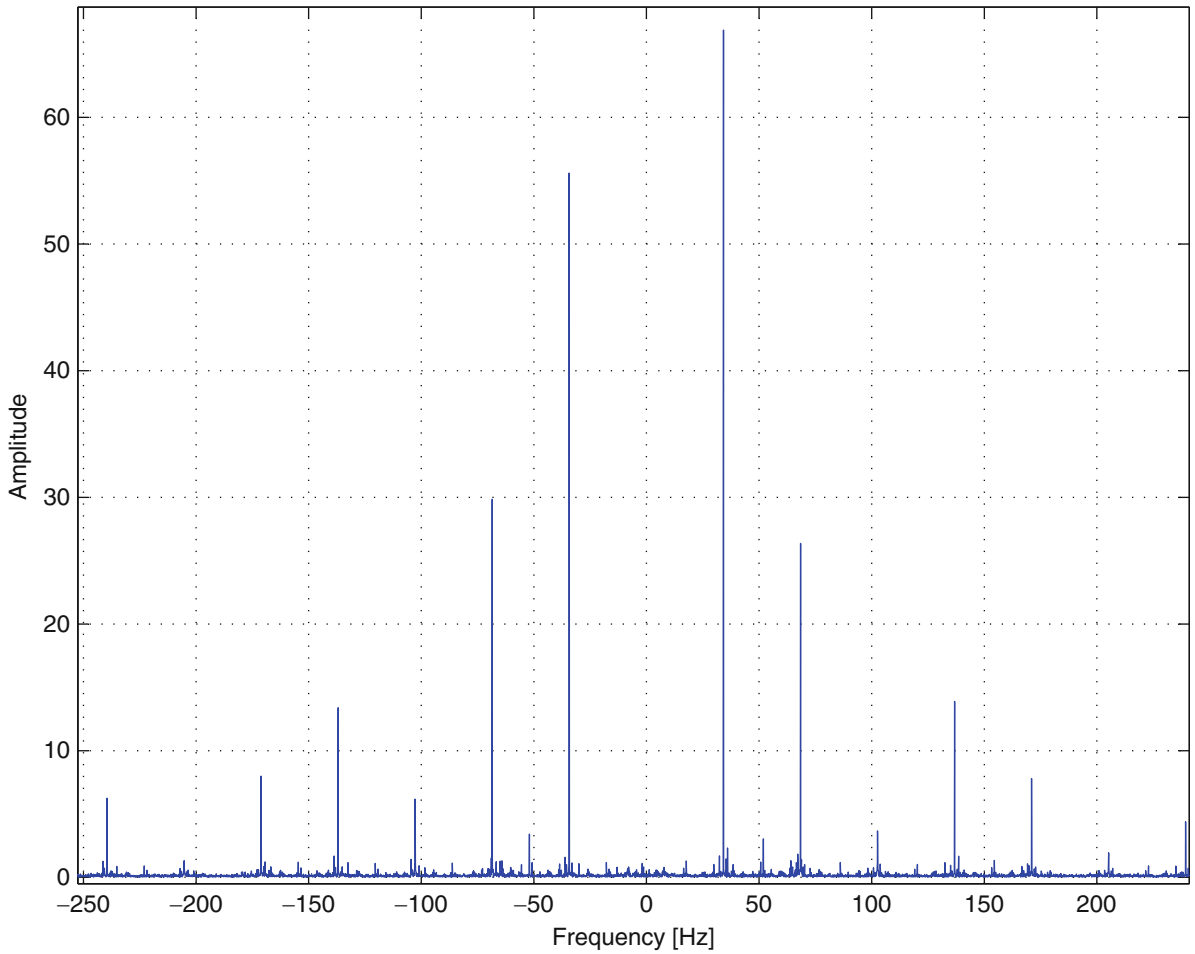

Fig. 24.14 Full spectrum of parallel misalignment with imbalance (eddy-current probe)

References

1. Bachschmid N, Pennacchi P, Vania A (2002) Identification of multiple faults in rotor systems. J Sound Vib 254:327–366
2. Lal M, Tiwari R (2012) Multi-fault identification in simple rotor-bearing-coupling systems based on forced response measurements. Mech Mach Theory 51:87–109
3. Sinha JK, Elbhbah K (2013) A future possibility of vibration based condition monitoring of rotating machines. Mech Syst Signal Process 34(1–2):231–240
4. Goldman P, Muszynska A (1999) Application of full spectrum to rotating machinery diagnostics. Orbit 20(1):17–21
5. Balitsky F, Sokolova A (2010) Application of full spectrums and other vibration two-dimensional characteristics for gas transportation units condition monitoring. In: 10th European conference on, non-destructive testing, no. 1, pp 2–6
6. Southwick D (1994) Using full spectrum plots. Orbit 15(2):11–15
7. Tůma J, Biloš J (2007) Fluid induced instability of rotor systems with journal bearings. Eng Mech 14(1):69–80
8. Piotrowski J (2010) Shaft alignment handbook. CRC, Boca Raton
9. Ganeriwala S, Patel S, Hartung HA (1999) The truth behind misalignment vibration spectra of rotating machinery. In: Proceedings of the international modal analysis conference, pp 2078–2085

Chapter 25
Damage Detection Based on Wavelet Packet Transform and Information Entropy

S.A. Ravanfar, H. Abdul Razak, Z. Ismail, and S.J.S. Hakim

Abstract In this study, a new approach for damage detection in beam-like structures is presented. Damage feature such as relative wavelet packet entropy (RWPE) based on the decomposed component is used to identify the damage location and evaluate the damage severity. RWPE describes present information of relative wavelet energies correlated with different frequency ranges. It is should be noted that the acceleration measured in the all three directions should be used in computation of RWPE. Numerical and experimental results are used to verify the practicality of this method. Results show that the damage index technique has great potential in detection of location and depth of cut in a steel beam. The procedure can be applied for health monitoring of other complex structures.

Keywords Damage detection • Wavelet packet transform • Information entropy • Wavelet packet entropy • Beams

25.1 Introduction

To ensure structural integrity, safety and minimal maintenance, structural health monitoring (SHM) is a powerful tool to assess performance, by identifying and quantifying damage based on measurement by sensors and data analysis [1–4]. Vibration-based analysis has been reported as a promising method for SHM [5]. The premise of vibration-based SHM is that dynamic characteristics of a structure are a function of its physical properties. Therefore, changes in these physical properties, such as reduction in stiffness resulting from the localized structural damage will cause observable changes in the dynamic characteristics of the structure. The vibration-based damage detection methods have received great consideration in the past few decades, and several approaches have been suggested [6].

One subject matter of vibration-based damage detection techniques is to seek some damage features that are sensitive to damage of structure [7, 8]. The damage features that have been indicted with various degrees of achievement include mode shapes, natural frequencies, modal flexibility, mode shape curvatures, modal strain energy, etc. Doebling et al. [9] summarized the extensive development of damage evaluation methodologies based on these features as well as indicating their applicability and limitations. Most vibration-based structural damage detection techniques require the modal properties that are extracted from measured signals through system identification techniques. It is realistic to extract structural damage features directly from the measured vibration signals.

Recently, wavelet analysis has become a promising damage detection tool in the area of structural and machine health monitoring because of its shows potential features such as singularity detection, good handling of noisy data and being very informative about damage location/time and extent. For this reason, many damage detection studies focused on the wavelet transform (WT) scheme. Wavelet functions are included in the family of basis functions that are capable of depicting a

S.A. Ravanfar (✉) • H.A. Razak • S.J.S. Hakim
Department of Civil Engineering, StrucHMRS Group, University of Malaya, Kuala Lumpur, Malaysia
e-mail: r.ravanfar@gmail.com; hashim@um.edu.my; jamalhakim@siswa.um.edu.my

Z. Ismail
Faculty of Engineering, Department of Civil Engineering, University of Malaya, Kuala Lumpur, Malaysia
e-mail: zu_ismail@um.edu.my

A. Wicks (ed.), *Structural Health Monitoring, Volume 5: Proceedings of the 32nd IMAC, A Conference and Exposition on Structural Dynamics, 2014*, Conference Proceedings of the Society for Experimental Mechanics Series, DOI 10.1007/978-3-319-04570-2_25,

signal in a localized frequency (or scale) and time (or space) domain. The main advantage obtained by using wavelets is the capability to execute local analysis of a signal, i.e. zooming on any interval of space or time. Wavelet analysis is capable of demonstrating some hidden features of the data that conventional Fourier analysis fails to detect. This characteristic is especially important for damage identification applications. An extensive literature survey on the subject is presented in the work of Kim and Melhem [10], with particular applications including damage detection of beam and mechanical gear and roller damage detection.

The wavelet packet transform (WPT) is a development of the WT, for recording the characteristic under every frequency band. In WT, a signal is split into an approximation and a detail. The approximation is then split into a second-level approximation and detail, and the process is repeated. In WPT, the details as well as the approximations are split, which provide complete decomposition of a signal. The WPT creates the same frequency bandwidths in every resolution. The wavelet packets are other bases formed by linear combinations of the common wavelet functions [11]. Sun and Chang [12] and Han et al. [13] have improved WPT-based component energy as damage sensitivity index for diagnosis of structural damage in a beam structure.

Damage will give arise to irregularity in the structural response signal. The entropy is a quantitative measure of the degree of disorder in measured signals. The wavelet entropy, which is a combination of entropy and wavelet, could take advantage of both methods to explain the characteristics of a signal, which are not directly visible in original space. In particular, Ren and Sun [14] proposed a damage-sensitive feature with the combination of discrete wavelet transform and information entropy to characterize the level of disorder in the measured signals to identify the occurrence and location of damage in beam structures.

This present study combines multi-resolution wavelet packet transform with information entropy to achieve higher as well as lower frequency signal components accuracy. Damage feature such as RWPE based on the decomposed component are used to identify the damage location and evaluate the damage severity through the vibration signals. RWPE is described to present information of relative wavelet energies correlated with different frequency ranges. Both numerically simulated and experimental data with different damage scenarios show that the proposed method has great potential in the field of damage detection of beam-like structures.

25.2 Damage Feature Extraction from Wavelet Packet Entropy

Wavelet packet transform (WPT) could be considered as an extension of the WT which provide a complete level-by-level time-frequency decomposition. In addition, it can give a rich structure to adapt a particular signal. WPT also enables multi resolution damage detection since it can localize multi-frequency bands in time domain. The wavelet packet function is defined as

$$\psi_{\mathrm{j,k}}^{\mathrm{i}}(\mathrm{t}) = 2^{j/2}\psi^{i}\left(2^{j}t-k\right) \quad i = 0,1,2,\ldots,2^{j}-1 \tag{25.1}$$

where a wavelet packet $\psi^{i}_{j,k}(\mathrm{t})$ is a function of three indices which integers i, j and k are the modulation, the scale and the translation parameter respectively. Moreover, $\psi^{0}(t) = \varphi(t)$ for $i = 0$ and $\psi^{1}(t) = \psi(t)$ for $i = 1$. The wavelet $\varphi(t)$ is called the scaling function and $\psi^{1}(t)$ called the mother wavelet function.

In this study, the measured structural dynamic response is decomposed into wavelet component functions. When the decomposition level is j, 2^{j} wavelet packet decomposed (WPD) components can be obtained. Figure 25.1 shows the decomposition process of a time-domain signal $f(\mathrm{t})$ up to the 3rd level. The original signal can be expressed as a summation of WPD components as,

$$f(t) = \sum_{i=1}^{2^{j}} f_{j}^{i}(t) \tag{25.2}$$

where t is time lag; $f_{j}^{i}(t)$ is the WPD component signal that can be represented by a linear combination of wavelet packet functions as follows:

$$f_{j}^{i}(t) = \sum_{k=-\infty}^{\infty} C_{j,k}^{i}\psi_{j,k}^{i}(t) \tag{25.3}$$

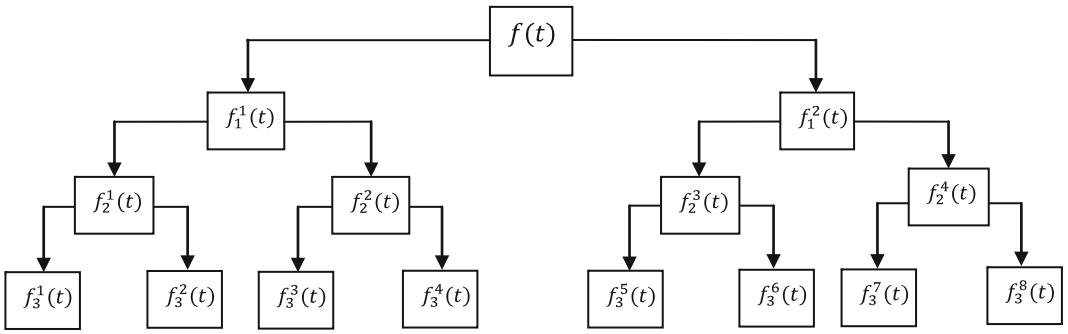

Fig. 25.1 Wavelet packet decomposition process

where $C_{j,k}^i$ are wavelet packet coefficient and can be calculated from

$$C_{j,k}^i = \int_{-\infty}^{\infty} f(t)\psi_{j,k}^i(t)dt \tag{25.4}$$

For WPT offers good time resolution in the high-frequency range of a signal and good frequency resolution in the low-frequency range of the signal. For application of WPT in SHM, there is no specific recommendation about the decomposition level. The level of wavelet packet decomposition is generally determined by trial and error sensitivity analysis, through which the decomposition level 6 is used in this study.

25.2.1 Wavelet Energy and Entropy

The wavelet packet component energy is a suitable tool to identify and characterize a specific phenomenon of signal in time-frequency domain. It has been shown in Yen and Lin's [11] study that the energy stored in a specific frequency band at a certain level of wavelet packet decomposition provides a more potential for signal feature than the coefficients alone. Sun and Chang [15] compared the sensitivity of four damage indices based on frequency change, mode shape change, flexibility change and wavelet packet energy change, and concluded that wavelet packet energy based index has the best ability to capture structural stiffness reduction. Ren et al. [16] has explored the practical application of wavelet packet energy change based damage detection method to the bridge shear connector monitoring. The wavelet packet energy E_f of a signal is defined as

$$E_f = \int_{-\infty}^{\infty} f^2(t)dt = \sum_{m=1}^{2^j}\sum_{n=1}^{2^j}\int_{-\infty}^{\infty} f_j^m(t)f_j^n(t)dt \tag{25.5}$$

where f_j^m and f_j^n are decomposed wavelet components. The total energy of signal can be extracted as the sum of wavelet packet components energies:

$$E_f = \sum_i^{2^j} E_{f_j^i} = \sum_{i=1}^{2^j}\int_{-\infty}^{\infty} f_j^i(t)^2 dt \tag{25.6}$$

Then, the normalized values for the j-th scale, which represents the relative wavelet packet energy is

$$p_{ij} = \frac{E_{f_j^i}}{E_f} \tag{25.7}$$

The p_{ij} values correspond to a ratio of the energy of a particular coefficient $E_{f_j^i}$ to the total energy. The p_{ij} value acts like a probability distribution of the energy. Therefore, the p_{ij} values sum to one.

The entropy of relative wavelet packet energy can characterize the level of order and disorder of a vibration signal, therefore it can supply valuable information about the dynamic process correlated with measured vibration signals. Ren and Sun [14] applied the concept of the wavelet entropy to structural damage detection problems. According to the Shannon entropy theory and wavelet energy ratio defined above, wavelet packet entropy is defined as

$$S_{WPE} = S_{WPE}(p) = -\sum_j \sum_i p_{ij}.lnp_{ij} \tag{25.8}$$

Damage to a structure causes a change in the entropy of wavelet. The damage detection problem can be formulated through the changes in the wavelet packet entropy before and after damage to characterize the location and quantification of damage. To identify the change in wavelet packet entropy of vibration signals from a structure, relative wavelet packet entropy (RWPE) is introduced as follows:

$$S^k_{RWPE}\left(p^k \middle| q^k\right) = \sum_j \sum_i \left| p^k_{ij} \ln\left(\frac{p^k_{ij}}{q^k_{ij}}\right)\right| \quad k = x, y, z \tag{25.9}$$

The RWPE value will be zero while the relative wavelet energy ratios p_{ij} and q_{ij} are identical. It is important that the measured accelerations in the same direction must be used in computations of RWPE. However, when the structure is damaged the values of p_{ij} and q_{ij} will become different, and as a consequence an increase in RWPE value.

25.3 Numerical Simulation

To verify the suitability of proposed damage identification method, numerical simulations were considered on the three I-section steel beams with a span length of 3 m and with several assumed damage elements, as shown in Fig. 25.2. A commercial finite element analysis package is employed to perform a modal dynamic analysis to provide the time history response of the beams.

Beam 0 is considered as the reference beam without damage while Beam 1 is the single damage scenario at the middle of the beam. Beam 2 is the single damage scenario with damage located at point 5. Dimension of all damages is 3 mm width with 3 mm depth. There was a total of 25 damages, and there was gradual increase of the damage depth of 3 mm for all beams at each step up to 75 mm.

A three dimensional solid element was used in the finite element modeling of beam geometry having Young's modulus of 210 G Pa and density of 7,850 kg/m^3 for the material properties. The analysis was carried out for different levels of damage severity as depicted in Fig. 25.2. The node acceleration responses of the beams under vibration test were obtained on sixteen locations on the top flange at the sampling frequency of 2,000 Hz and to find out the characteristics of the notch.

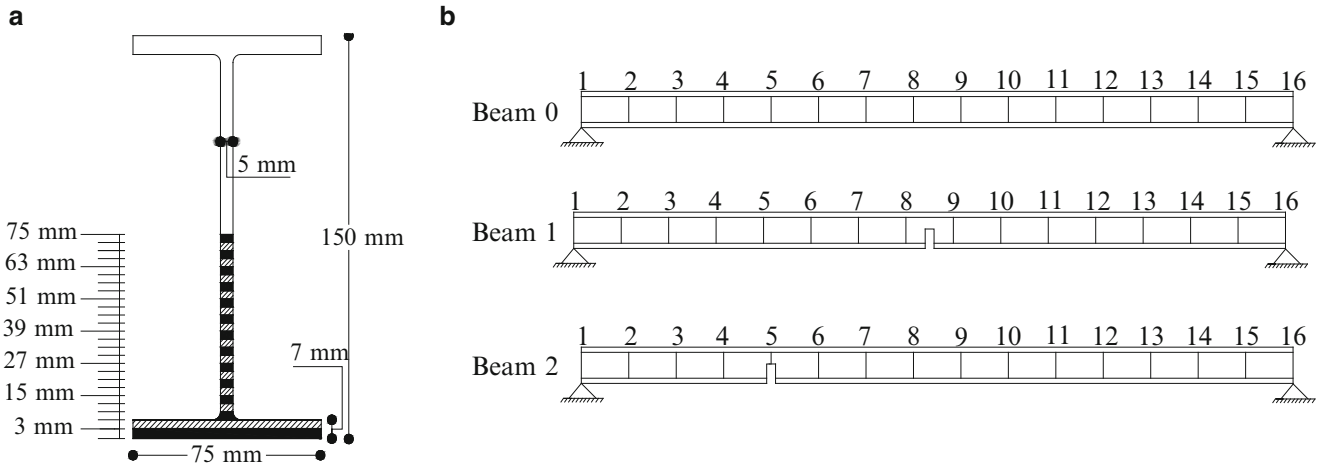

Fig. 25.2 I-beam damage scenario: (**a**) dimension and damage depth of beams; (**b**) damage location of beams

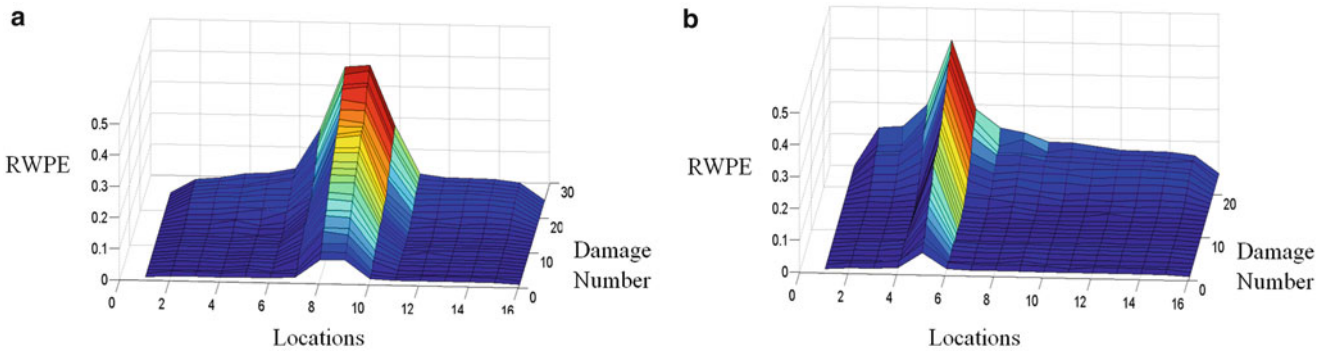

Fig. 25.3 Finite element model of the beams: (**a**) RWPE for damaged beam 1; (**b**) RWPE for damaged beam 2

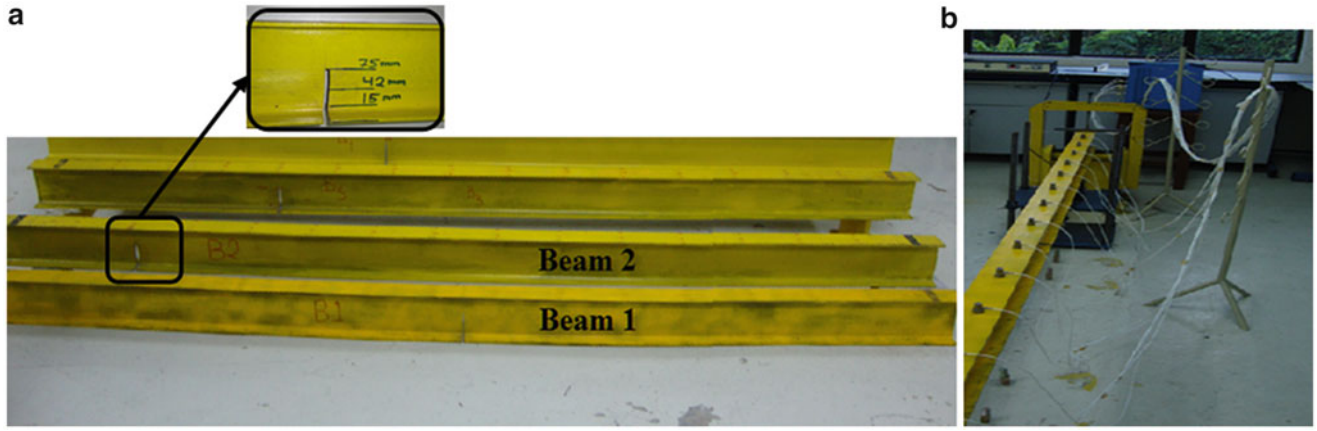

Fig. 25.4 Dynamic test in laboratory: (**a**) beams tested; (**b**) data acquisition

25.3.1 Damage Identification

Decomposition of wavelet packet resulted in 128 components by setting the decomposition level to 7 for the measured data obtained from the vibration tests. The RWPE at 16 locations calculated for each damaged scenario based on Eq. (25.9) gave the corresponding 3D contour plots of the RWPE of the single and multiple damage scenarios as shown in Fig. 25.3. According to these figures the value and distribution of RWPEs changed considerably after damage, which can be used as damage indicators.

Single damage scenarios indicate that the peak value of the RWPE in beam 1 occurred at the middle of the beam which is marginally greater than beam 2, which occurred at point 5. From the above observation, it may be construed that increase of damage depth in beams will influence the vibration response signal and subsequently RWPE values.

25.4 Experimental Verification

An experimental study on a test beam was conducted to validate the proposed procedure. The proposed damage identification technique has to be validated using real measurement data from vibration tests in the presence of measurement errors and noise. Vibration tests were carried out the noise and measurement error are present, as depicted in Fig. 25.4, under undamaged and several damage states.

Excitation is provided by a shaker at location 13. Sixteen accelerometers are placed along the beam to measure the time acceleration responses with a sampling frequency of 2,000 Hz. Figure 25.4 shows a typical acceleration response under white noise excitation. The level of decomposition is selected to be 7 resulting in a total of 128 component signals.

RWPE of acceleration responses of beam 1 and beam 2 are depicted in Fig. 25.5 demonstrates that the energy of structural vibration is increased with the depth of damage. Accordingly, the RWPE of every damage scenario indicates significant

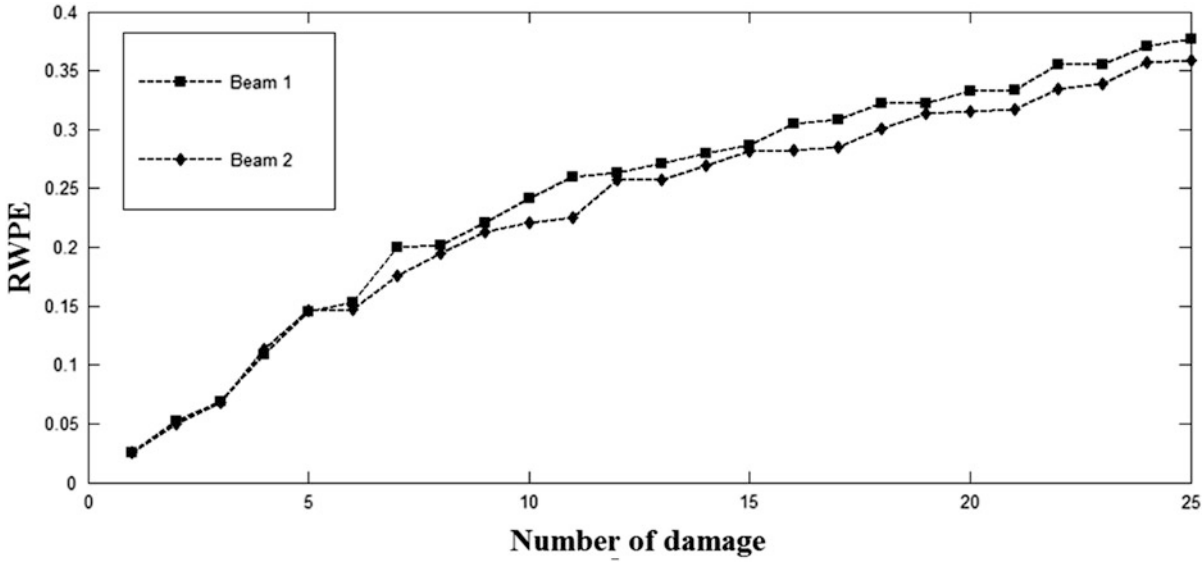

Fig. 25.5 RWPE for different damage depths in beam 1 and beam 2

difference of the signal distribution energy. Consequently, it is possible to identify the occurrence of structural damage based on the variation of RWPEs calculated from vibration signals of various damage scenarios. However, the extent of damage are recognized using RWPE.

All results demonstrated that the locations for all damage scenario as well as quantification of the extent of the damage can be successfully identified from the dynamic measurements.

25.5 Conclusion

In this paper, a new index RWPE based on the information entropy and wavelet packet energy through the vibration responses are proposed to identify the existence and quantify the extent of structural damage. To verify the viability and efficiency of the suggested method, both numerical simulation and experimental tests were carried out. It was shown that the proposed methods are sensitive to identify and also to quantify the damage using the vibration signals. The verification utilizes real measurement data when the signals are affected by experimental noise and measurement errors. Therefore, it can be deduced that the proposed indices are partially insensitive to noise of data collected.

References

1. Nomura Y, Furuta H, Hirokane M (2007) An integrated fuzzy control system for structural vibration. Comput-Aided Civ Inf Eng 22:306–316
2. Park H, Lee H, Adeli H, Lee I (2006) A new approach for health monitoring of structures: terrestrial laser scanning. Comput-Aided Civ Inf Eng 22:19–30
3. Kim JH, Kwak HG (2008) Nondestructive evaluation of elastic properties of concrete using simulation of surface waves. Comput-Aided Civ Inf Eng 23:611–624
4. Belli K, Wadia-Fascetti S, Rappaport C (2008) Model based evaluation of bridge decks using ground penetrating radar. Comput-Aided Civ Inf Eng 23:3–16
5. Farrar CR, Doebling SW, Nix DA (2001) Vibration-based structural damage identification. Philos Trans R Soc A 359:131–149
6. Carden EP, Fanning P (2004) Vibration based condition monitoring: a review. Struct Health Monit 3:355–377
7. Ren WX, De Roeck G (2002) Structural damage identification using modal data I: simulation verification. J Struct Eng 128:87–95
8. Ren WX, De Roeck G (2002) Structural damage identification using modal data. II: test verification. J Struct Eng 128:96–104
9. Doebling SW, Farrar CR, Prime MB (1998) A summary review of vibration-based damage identification methods. Shock Vib Digest 30: 91–105
10. Kim H, Melhem H (2004) Damage detection of structures by wavelet analysis. Eng Struct 26:347–362
11. Yen GG, Lin KC (2000) Wavelet packet feature extraction for vibration monitoring. IEEE T Ind Electron 47:650–667
12. Sun Z, Chang C (2004) Statistical wavelet-based method for structural health monitoring. J Struct Eng 130:1055–1062

13. Han JG, Ren WX, Sun ZS (2005) Wavelet packet based damage identification of beam structures. Int J Solids Struct 42:6610–6627
14. Ren WX, Sun ZS (2008) Structural damage identification by using wavelet entropy. Eng Struct 30:2840–2849
15. Sun Z, Chang C (2007) Vibration based structural health monitoring: wavelet packet transform based solution. Struct Inf Eng 3:313–323
16. Ren WX, Sun ZS, Xia Y, Hao H, Deeks AJ (2008) Damage identification of shear connectors with wavelet packet energy: laboratory test study. J Struct Eng 134:832–841

Chapter 26
Identification of Localized Damage in Structures Using Highly Incomplete Modal Information

Eric M. Hernandez

Abstract The objective of this paper is to provide a new theoretical basis to localize and quantify sparse damage in a structure based on highly incomplete modal information. Although a large number of papers have been written on the subject, this paper offers a new perspective on the problem by proposing the L-1 norm minimization criteria, in contrast to the more traditional L-2 (Euclidean) norm minimization criterion. The proposed L-1 norm approach enables accurate and robust examination of a number of potential damage locations much larger than the number of frequencies used in the formulation of the modal sensitivity matrix. In addition, it is shown that L-1 minimization leads to sparse solutions, this is in contrast with the L-2 criteria, which leads to disperse solutions. The computational effort necessary to solve the L-1 optimization is significantly larger than in the traditional Euclidean norm and requires the use of convex optimization algorithms. However, given the results that can be obtained, the computational effort is justified. The efficacy of the proposed framework is demonstrated in detecting sparse damage in a simulated 21 degree of freedom shear building structure.

Keywords Damage detection • l_1 norm • Sparsity • Modal analysis

26.1 Introduction

The use of vibration measurements, and more specifically, identified modal information to detect damage (stiffness reductions) in structures can be traced back almost to the dawn of microcomputers in the late 1970s and early 1980s [1, 2]. The realization that changes in structural properties induce changes in vibration frequencies was the primary impetus for developing vibration-based damage identification technology. Since then, numerous analytical methods and experimental techniques have been developed in order to expand the limits of what can be detected by processing limited vibration measurements [3–5].

Modal information for damage detection includes changes in modal frequencies, modal shapes and(or) modal damping between the assumed healthy state and the potentially damaged state. It has been shown theoretically and verified experimentally that the uncertainty and difficulty to identify modal shapes and damping ratios increases significantly in comparison with that associated with identification of modal frequencies [6, 7]. Therefore, it is highly desirable to develop computational methods that operate solely based on changes of identified modal frequencies as a criterion for damage detection.

While the amount of literature that proposes the use of modal frequency shifts as a feature for damage detection is extense [8, 9], it has not been yet possible to generalize their use in damage detection. Some authors have claimed that the use of modal information, specially modal frequencies is not sufficient to locate damage and that in general, changes in frequencies cannot provide spatial information about structural changes [10].

The main difficulty in localizing damage using modal information, such as changes in mode shapes and frequencies, resides in that the number of potential damage locations is by far larger than the number of identified modal parameters. If a sensitivity method is used, the result is an underdetermined system of linear equations with infinite number of possible solutions. If one decides to use exclusively modal frequencies, the problem is exacerbated even further.

E.M. Hernandez (✉)
University of Vermont, 301 Votey Hall, 33 Colchester Ave., Burlington, VT 05405, USA
e-mail: eric.hernandez@uvm.edu

A. Wicks (ed.), *Structural Health Monitoring, Volume 5: Proceedings of the 32nd IMAC, A Conference and Exposition on Structural Dynamics, 2014*, Conference Proceedings of the Society for Experimental Mechanics Series, DOI 10.1007/978-3-319-04570-2_26,

The first objective of this paper is to clarify the mathematical nature of the underdetermined system of equations that arise from the application of the sensitivity method and to show that among the infinite number of possible solutions; in general, there are only a handful of sparse solutions. A sparse solution of degree s is one that only has at most s number of non-zero entries. Since structures are typically damaged in a small number of locations in comparison with the complete domain, we are interested in sparse solutions with low value of s, i.e. solutions with very few and sometimes only one non-zero component. Even though the concept of sparsity has been exploited to solve inverse problems in other disciplines [11, 12], only until very recently it has begun to attract some attention in structural health monitoring applications [13].

The second objective of this paper is to propose a method to find sparse solutions of the underdetermined system of equations that result from formulating the sensitivity method in structural dynamics. The proposed method relies on the use of the l_1 norm as opposed to the traditional l_2 norm. Previous results show that the l_1 minimum solution to a system of under determined system of linear equations is sparse [14]. The computational effort necessary to solve the l_1 optimization is larger than the traditional l_2 optimization and requires the use of convex optimization algorithms [15].

The paper begins with a brief review of the sensitivity method for finite element model updating. This is followed by a section on Banach vector spaces (complete normed vector spaces), with special emphasis on the contrast between l_1 and the l_2 normed spaces. The paper continues with a section describing one possible algorithm to solve the l_1 minimization problem, namely the primal-dual interior point method. We conclude with a section illustrating the proposed methodology in a non-uniform shear beam. In all cases, it is shown that changes in a small subset of the spectrum are sufficient to accurately locate small and localized stiffness reductions at arbitrary locations in the presence of moderate measurement noise.

26.2 Sensitivity-Based Model Updating

The sensitivity approach is one of the most popular and practical frameworks for finite element model updating in structural dynamics [16]. The basic idea is to relate small variations in the stiffness and mass of a finite element model (FEM) to the corresponding variations in the eigenvectors and eigenvalues. In this paper, we seek a relationship between small changes in eigenvalues to small changes in the parameters that define the stiffness matrix, that is

$$\Delta\lambda = \mathbf{S}\Delta\theta \tag{26.1}$$

where $\Delta\theta \in \mathbb{R}^{p\times 1}$ is a vector of changes in the parameters that define the stiffness matrix of the structure, $\mathbf{S} \in \mathbb{R}^{n\times p}$ is the sensitivity matrix, and the $\Delta\lambda \in \mathbb{R}^{n\times 1}$ is the corresponding change in the model's eigenvalues due to $\Delta\theta$.

In particular, we restrict our attention to the cases where the stiffness matrix $\mathbf{K} \in \mathbb{R}^{n\times n}$ can be expressed as

$$\mathbf{K} = \sum_{i=1}^{p} \mathbf{E}_i f_i(\theta_i) \tag{26.2}$$

where $\mathbf{E}_i$ is an elementary influence matrix corresponding to the ith parameter, $f_i(\cdot)$ is a differentiable function and p is the total number of independent parameters that define $\mathbf{K}$. Consequently

$$\frac{\partial \mathbf{K}}{\partial\theta} = \sum_{i=1}^{p} \mathbf{E}_i \frac{\partial}{\partial\theta} f_i(\theta_i) \tag{26.3}$$

By taking the first term of the Taylor series expansion around the current parameter value, the partial derivative of the stiffness matrix with respect to any particular parameter θ_k can be approximated as

$$\frac{\partial \mathbf{K}}{\partial\theta_k} \approx \frac{\Delta\mathbf{K}}{\Delta\theta_k} = \mathbf{E}_k \frac{\Delta f}{\Delta\theta_k} \tag{26.4}$$

It has been previously shown [16] that

$$\mathbf{S}_{j,k} = \frac{\partial\lambda_j}{\partial\theta_k} = \phi_j^T \frac{\partial \mathbf{K}}{\partial\theta_k}\phi_j \approx \phi_j^T \left(\mathbf{E}_k \frac{\Delta f}{\Delta\theta_k}\right)\phi_j \tag{26.5}$$

where λ_j and ϕ_j satisfy

$$\mathbf{K}\phi_j = \mathbf{M}\phi_j\lambda_j \tag{26.6}$$

and

$$\phi_j^T\mathbf{M}\phi_j = 1 \tag{26.7}$$

where $\mathbf{M} = \mathbf{M}^T \in \mathbb{R}^{n\times n}$ is the mass matrix of the model, ϕ_j is the mass normalized eigenvector corresponding to the eigenvalue λ_j.

If only a subset of $q < p < n$ frequencies is identified from vibration data, then only the corresponding q rows of $\mathbf{S}$ can be used in the inversion. Furthermore, since errors in system identification are inevitable and damage produces finite changes in the model parameters, the following approximate underdetermined system of equations results

$$\Delta\lambda_q = \mathbf{S}_q\Delta\theta + \epsilon \tag{26.8}$$

where $\Delta\lambda_q \in \mathbb{R}^{q\times 1}$ is the difference between the q eigenvalues of the damaged and undamaged structures, $\Delta\theta \in \mathbb{R}^{p\times 1}$ is the change in the stiffness parameters and the components of $\mathbf{S}_q \in \mathbb{R}^{q\times p}$ are given by Eq. (26.5). The vector $\epsilon \in \mathbb{R}^{q\times 1}$ represents the error in the vector $\Delta\lambda_q$ and it is the byproduct of the combined effect of numerical errors in the system identification algorithms, modeling errors and measurement noise, among others.

In general Eq. (26.8) has infinite number of solutions. In order to obtain a unique solution (or a few feasible solutions) we propose exploiting the fact that damage typically occurs at a very small number of sparse, yet unknown points r within the domain of the structure such that $r < q$. Traditionally, sparsity has not been exploited in damage identification.

26.3 The l_p Norm

A norm is a mapping $\|\cdot\|$ from a vector space X into $\mathbb{R}$ which satisfies the following properties for every $x \in X$ and $y \in X$ and every $\alpha \in \mathbb{C}$:

1. $\|x\| \geq 0$
2. $\|\alpha x\| = |\alpha|\,\|x\|$
3. $\|x + y\| \leq \|x\| + \|y\|$

A norm generalizes the concept of distance that we inherit from Euclidean geometry. One of the most commonly used norms are the l_p norms, which for a vector space $X \in \mathbb{C}^n$ and $1 \leq p \leq \infty$ is defined as

$$\|x\|_p = \left(\sum_{i=1}^{n} |x_i|^p\right)^{1/p} \tag{26.9}$$

In the case of $p = 2$ we obtain the usual l_2 norm or Euclidean distance. For $p = 1$ we obtain the l_1 norm or the Manhattan distance, which corresponds to the sum of the absolute value of the components. For $p = 0$, although not a proper norm, since it does not meet requirements (26.2) and (26.3), we obtain the l_0 norm which corresponds to the number of components with non-zero elements (provided one accepts $0^0 = 0$). The l_0 norm defines the sparsity of $x \in X$. A vector $x \in \mathbb{R}^n$ is said to be s-sparse, for $s < n$ if it contains s non-zero components and we represent it as $\|x\|_0 = s$.

We define an l_p-ball B_r^p as the closed set whose elements satisfy

$$x \in B_r^p \text{ if } \|x\|_p = r \tag{26.10}$$

To develop some intuition regarding the effect of using different norms as criteria to select solutions to underdetermined system of linear equations consider Fig. 26.1. The line representing all the possible solutions to the generic underdetermined linear equation $ax_1 + bx_2 = c$ is shown (a, b, c are constants). Figure 26.1a depicts the solution that minimizes the l_2 norm. This is obtained by determining the smallest l_2-ball that contains an element that satisfies the equation $ax_1 + bx_2 = c$. By definition, every point in the depicted circle has the same l_2 norm and only one point satisfies the equation. Figure 26.1b depicts the solution that minimizes the l_1 norm. Similarly, in Fig. 26.1b the minimum l_1 solution is obtained by finding the

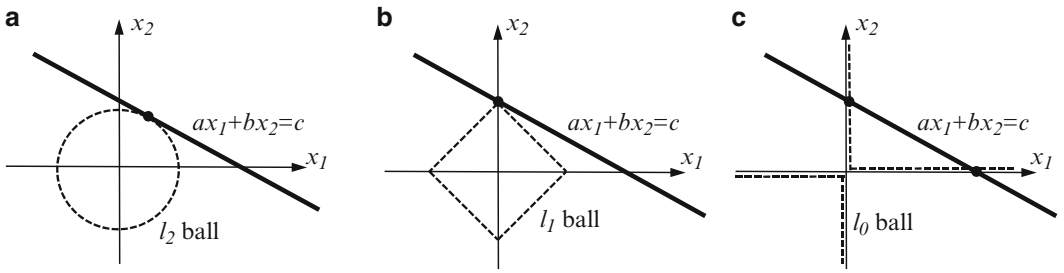

Fig. 26.1 (**a**) l_2 solution to an underdetermined linear equation. (**b**) l_1 solution to an underdetermined linear equation. l_1 solutions will provide the sparsest solution possible, while l_2 solution will provide the least sparse solution possible. (**c**) Depicts the solutions obtained by minimizing the l_0 norm

smallest l_1-ball that contains an element that satisfies $ax_1 + bx_2 = c$. As can be seen, the shape of the l_1 ball is very different from its l_2 counterpart. Moreover, except for the trivial cases of lines with slope of $\pm\pi/4$ radians, the l_1 solution will always be sparse, i.e., only one component will be non-zero. On the other hand, the l_2 solution, except for trivial cases of vertical and horizontal lines, will always have a non-sparse solution,i.e. all non-zero components. Finally, Fig. 26.1c shows the solutions obtained by minimizing the l_0 norm, as expected two solutions are obtained, one of them is the same that was obtained by minimizing the l_1 norm. Finally, note that proper l_p norms are convex, which make them very suitable for solutions using convex optimization algorithms, while the l_0 norm is of combinatorial nature and non-convex.

26.4 Numerical Methods for l_1 Minimization of Linear System of Equations

In contrast with l_2 minimization, which can be readily solved using well known algorithms such as singular value decomposition, the l_1 minimization requires significantly greater computational effort and no closed form solution exist. There are at least five family of computational methods for obtaining sparse solutions to underdetermined linear set of equations. These are:

- Greedy pursuit: Iteratively refines a sparse solution by successively identifying one or more components that yield the greatest improvement in quality.
- Convex relaxation: Replaces the combinatorial l_o norm problem with a convex l_1 optimization problem. Solves the convex optimization problem using algorithms that exploit the structure of the problem.
- Non-convex optimization: relaxes the l_0 problem to a related nonconvex problem and finds an stationary point.
- Bayesian framework: Assumes a prior distribution for the unknown coefficients that favors sparsity. Develops a posteriori estimates that incorporate observations. After computing the posterior, identifies maximum a posteriori estimate or region with large probability mass.
- Brute force: Searches through all possible sets. Clearly unfeasible for moderate and large scale problems.

In this paper we concentrate on convex relaxation methods, specifically the primal-dual interior point algorithm [15]. We replace the combinatorial l_0 by the l_1 norm, yielding a convex optimization problem with tractable solution. Intuitively, this makes sense, since the l_1 norm is the closest convex norm to the l_0 norm (see Fig. 26.1).

26.5 Numerical Verification

In this section we show numerical results to illustrate the applicability of the proposed methodology and some of the challenges that can be expected. We will simulate a 21 degree of freedom (DoF) shear beam with variable stiffness and mass. The main objectives are: (a) to detect a 1 % stiffness reduction in any single element given a limited number of system frequencies (no noise), (b) to detect multiple damaged elements selected at random given a limited number of identified frequencies of the system in the ideal noiseless case, and finally (c) to detect a 10 % reduction in stiffness in any single element in the presence of noise in the identified frequencies. For all cases the log-barrier interior-point optimization method was implemented using the `l1-magic` optimization package in `MATLAB` [17].

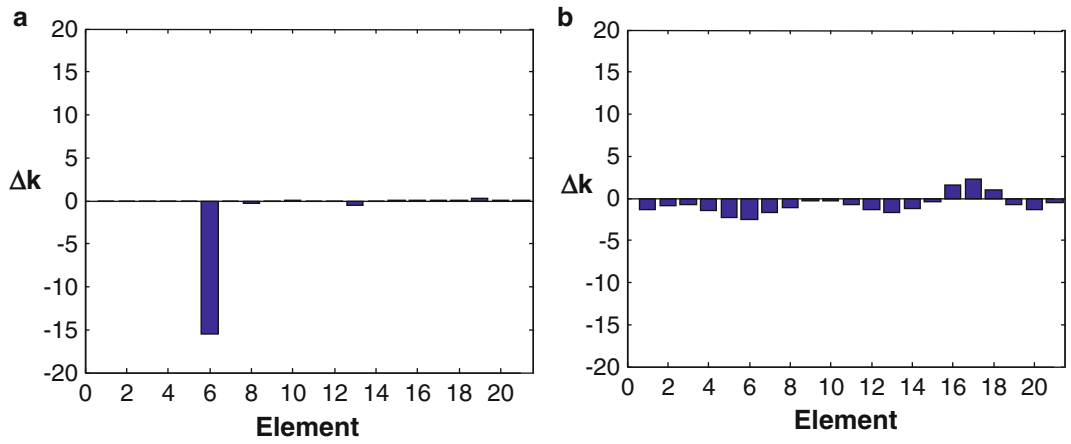

Fig. 26.2 Estimated stiffness reduction for every element. In this case only element No. 6 was damaged with a reduction in stiffness of 10. (**a**) Depicts the l_1 solution and (**b**) depicts the l_2 solution

The degrees of freedom of the model are numbered from 1 in the first mass closest to the support, to 21 at the free end. The stiffness of the springs varies as follows $k_1 = \ldots = k_7 = 1{,}000$, $k_8 = \ldots = k_{14} = 750$ and $k_{15} = \ldots = k_{21} = 500$ and masses vary as follows $m_1 = \ldots = m_7 = 1$, $m_8 = \ldots = m_{14} = 0.75$ and $m_{15} = \ldots = m_{21} = 0.50$. All expressed in consistent units. The resulting fundamental frequency of the structure is 0.436 Hz.

The damage sensitive features are a subset of the differences between the frequencies of the original system and the damaged system. We selected the lower frequencies as these are typically the ones that can be identified from measured vibration data in structures. The objectives here are: (1) to show the number of frequencies required in order to accurately identify the location and intensity of sparse damage, (2) to illustrate the difference between using an l_2 norm minimization criteria versus the proposed l_1 norm criteria for damage detection and (3) to show the effect of identification errors (noise) on the probability of detection (POD) of the proposed method.

To begin consider Fig. 26.2. Here we present the results of one particular ideal case (no noise) in which the damage (1 % stiffness reduction) was present in element No. 6 and the lowest 4 frequencies were selected as damage sensitive features. Thus, the sensitivity matrix $\mathbf{S}_q \in \mathbb{R}^{4\times 21}$. In Fig. 26.2a the l_1 norm minimization solution is presented and in Fig. 26.2b the solution obtained using l_2 minimization. As stated previously, the proposed l_1 methodology finds the correct sparse solution, while the l_2 minimization generates an incorrect non-sparse solution.

The damage was identified as 15 units of stiffness reduction, this in contrast with the actual damage of 10 units. This result can be further refined if needed by simply fixing the damage location (found using the proposed algorithm) and optimizing the intensity to match the observed changes in frequency. At this point it is essential to emphasize that no prior information was given to the algorithm as to the potential number or locations of the damage. The method correctly identifies that there is a single element damaged (No. 6) and simultaneously estimates its intensity using changes in the lowest four eigenvalues.

We now proceed to examine the performance of the algorithm in detecting 1 % damage in any single element (taken separately, one at a time). Figure 26.3a presents a plot depicting in the ordinate the required number of frequencies in order to properly identify damage in each element considered (abscissa). In all cases, frequencies were selected starting from the lowest in increments of one until adequate identification was obtained. As can be seen, the number ranges from 2 in order to identify damage in element 15 up to 9 in order to identify damage in element 11. In average the number of frequencies required is close to 4.

Figure 26.3b displays the level of damage quantification accuracy obtained with the proposed method. As can be seen, the actual simulated stiffness reduction was 1 % for each member (considered separately), the proposed algorithm is typically within 0.5 % of the actual value.

Next we investigate the scenario where multiple elements are damaged. Consider first the specific example where element No. 6 is affected by 1 % stiffness reduction (10 units) and element No. 15 by 5 % stiffness reduction (25 units). A comparison of the results using the l_1 minimization versus the l_2 minimization are shown in Fig. 26.4. For this case the lower 6 frequencies were used as damage sensitive features. As can be seen, the algorithm correctly identifies the locations of damage. The stiffness reduction identified by the algorithm was 1.6 % (16.33 units) for element No. 6, and 7.7 % (38.82 units) for element No. 15. We can also see from Fig. 26.4 that one could potentially assign some small damage (< 1 %) to element No. 3 which was not damaged.

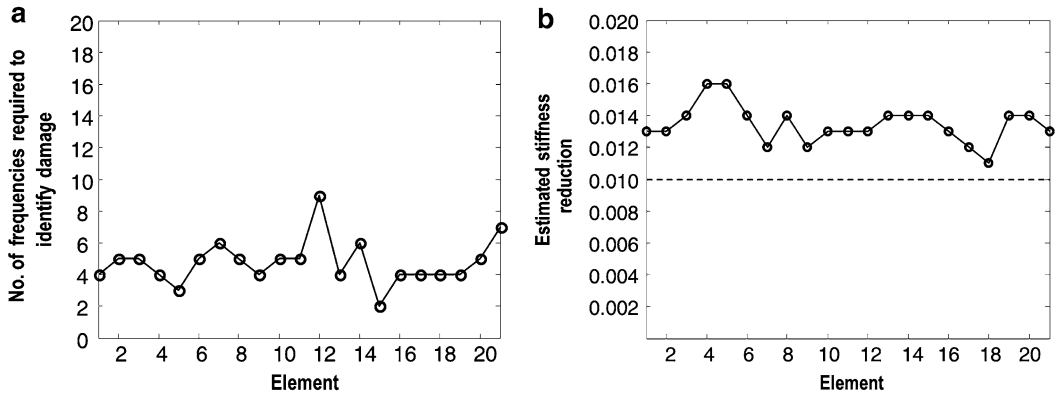

Fig. 26.3 (**a**) Number of frequencies required in order to properly identify the damaged element indicated in the abscissa. The frequencies are selected sequentially from the lowest in increments of one until a proper detection is obtained. (**b**) Estimated stiffness reduction for every element

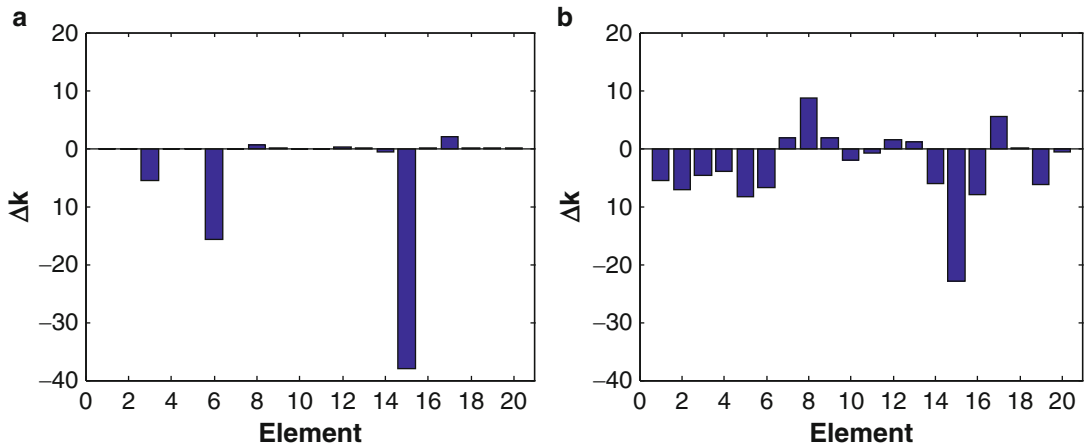

Fig. 26.4 Estimated stiffness reduction for every element. In this case elements No. 6 and 15 were damaged with a reduction in stiffness of 10 and 25 units respectively. (**a**) Depicts the l_1 solution and (**b**) depicts the l_2 solution

To investigate the effect of errors ϵ in Eq. (26.8) we simulate ϵ as a realization of an n-dimensional Gaussian random vector with zero mean and standard deviation of each component ϵ_i proportional to the value of the corresponding λ_i where n is the number of "identified" frequencies included in the inversion. We varied the number of "identified" frequencies, starting from 2 up to 10. In each case 1,000 simulations were performed to obtain the corresponding probability of detection (POD). The criteria for detection were: (1) The method correctly identifies the element as damaged (reduced stiffness) and (2) it does not assign any other element a stiffness reduction greater than 20 % of the stiffness reduction assigned to the element with the highest reduction. This last condition assures that the identified damage is indeed sparse. A summary of the results for four selected elements are shown in Fig. 26.5.

By examining Fig. 26.5 in conjunction with Fig. 26.3a one can see that independently of the noise level, if not enough frequencies are included in the analysis, it will not be possible to achieve an accurate damage identification. In general the plots show the expected trend, i.e. the POD increases as the coefficient of variation of the noise decreases and as the number of frequencies included increases beyond those needed in the ideal case. It can also be observed that the POD curves tend to converge and that beyond a certain number of frequencies the increase in accuracy is minimal. An interesting case occurs with spring 2, in this case, when less than the minimal number of frequencies are used, the presence of noise improves the POD up to a certain point. This should be seen as an exception and not as a rule, as can be observed from the other cases. The range of values selected for the coefficient of variation of the "identified" frequencies was taken from uncertainty quantification studies on system identification results of real structures [6].

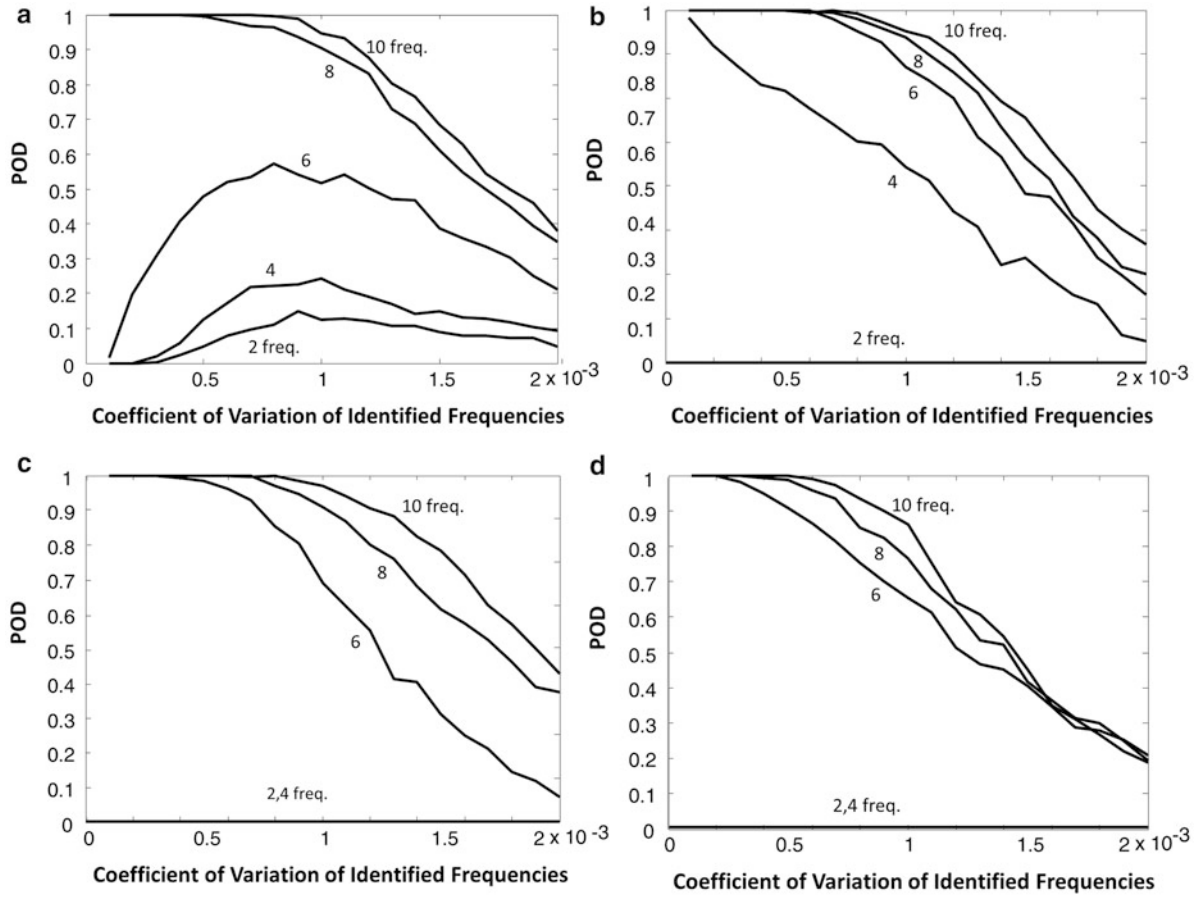

Fig. 26.5 Probability of detection (POD) as a function of the coefficient of variation of the selected frequencies. (**a**) Corresponds to spring 2, (**b**) to spring 6, (**c**) to spring 14 and (**d**) to spring 20

Finally we proceed to examine the efficacy of the proposed l_1 minimization algorithm as a function of the damage size for a fixed level of noise. Figure 26.6 depicts the POD for 1,000 independent simulations for each fraction of damage (stiffness reduction) between 0 and 0.20 in increments of 0.02. In all cases a fixed coefficient of variation of 0.001 was used for each frequency considered. As expected, the POD increases with the number of frequencies included and with the damage size. In majority of cases one can verify that for a damage severity corresponding to a 0.10 stiffness reduction a POD$>$ 0.75 can be obtained with eight frequencies (or less in some cases), which is less than half the minimal number of frequencies required for a unique inversion of the sensitivity matrix.

26.6 Conclusions

This paper presents a new framework based on l_1-norm minimization to localize and quantify isolated structural damage in the form of stiffness reduction. The damage sensitive feature is the change in a subset of the eigenvalues of the system. The main contribution of the paper is to show that the l_1 based sensitivity approach is capable of accurately identifying damage using a noise contaminated subset of the spectrum which has significantly fewer elements (sometimes an order of magnitude less) than the set of potentially damaged elements. Furthermore, since the proposed algorithm does not rely on mode shapes, the number of sensors needed to perform the estimation can be relatively small, in many cases a single sensor could suffice.

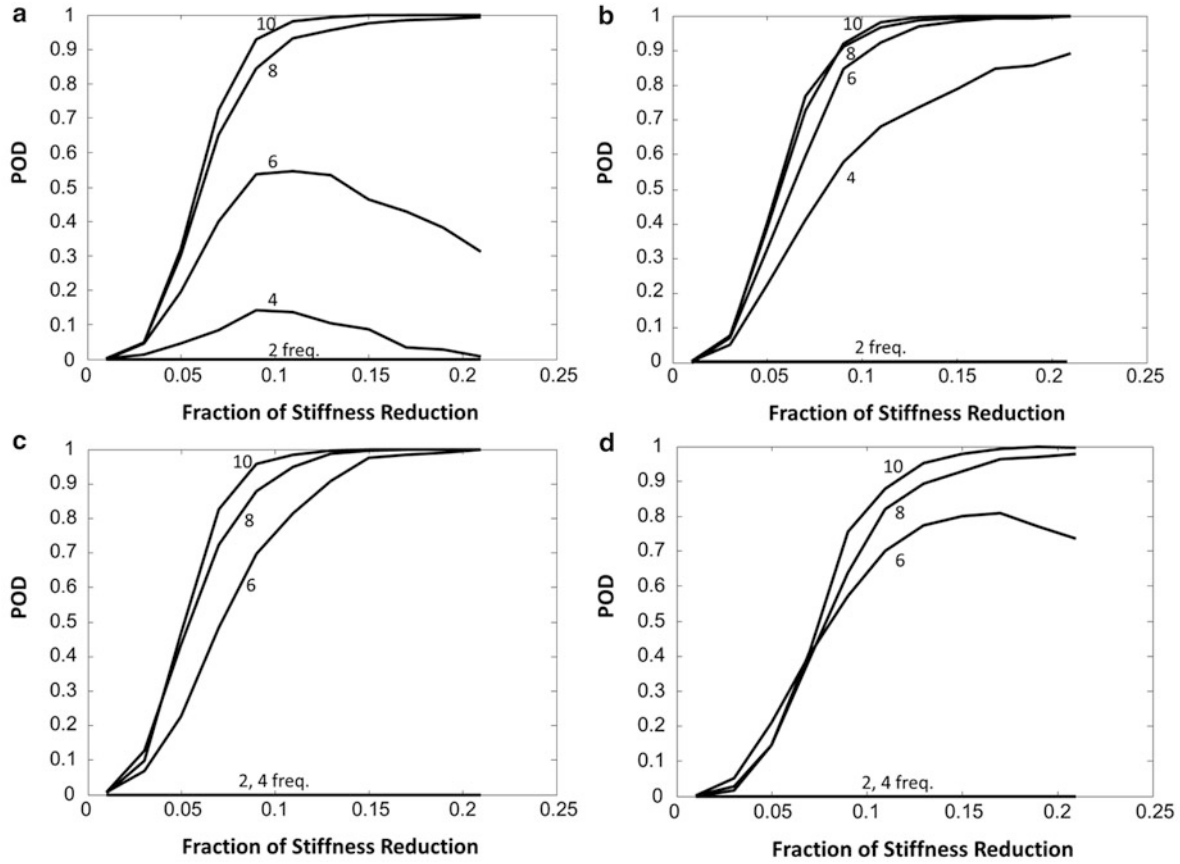

Fig. 26.6 Probability of detection (POD) as a function of the damage size. (**a**) Corresponds to spring 2, (**b**) to spring 6, (**c**) to spring 14 and (**d**) to spring 20

References

1. Richardson MH (1980) Detection of damage in structures from changes in their dynamic(modal) properties- a survey. NUREG/CR-1431, U.S. Nuclear Regulatory Commission, Washington, DC
2. Potter R, Richardson MH (1974) Identification of the modal properties of an elastic structure from measured transfer function data. In: 20th International instrumentation symposium, Albuquerque
3. Doebling SW, Farrar CR, Prime MB, Shevitz DW (1996) Damage identification and health monitoring of structural and mechanical systems from changes in their vibration characteristics: a literature review. Los Alamos National Laboratory Report, LA-13070-MS
4. Sohn H, Farrar CR, Hemez F, Shunk DD (2003) A review of structural health monitoring literature: 1996–2001. Los Alamos National Laboratory Report, LA-13976-MS
5. Yuen K-V (2012) Updating large models for mechanical systems using incomplete modal measurement. Mech Syst Signal Process 28:297–308
6. Reynders E, Pintelon R, De Roeck G (2008) Uncertainty bounds on modal parameters obtained from stochastic subspace identification. Mech Syst Signal Process 22:948–969
7. Moser P, Moaveni B (2011) Environmental effects on the identified natural frequencies of the Dowling Hall Footbridge. Mech Syst Signal Process 25(7):2336–2357
8. Slawu OS (1997) Detection of structural damage through changes in frequency: a review. Eng Struct 19(9):718–723
9. Wang X, Yang C, Wang L, Yang H, Qiu Z (2013) Membership-set identification method for structural damage based on measured natural frequencies and static displacements. Struct Health Monit 12(1):23–34
10. Farrar CR, Doebling SW, Nix DA (2001). Vibration-based structural damage detection. Philos Trans R Soc Lond A 359(1778):131–149
11. Ghosh S, Rudyi Y (2009) Application of L1-norm regularization to epicardial potential solution of the inverse electrocardiography problem. Ann Biomed Eng 37(5):902–912
12. Candes E, Romberg J (2007) Sparsity and incoherence in compressive sampling. Inverse Probl 23:969–985
13. Zhou S, Bao Y, Li H (2013) Structural damage identification based on substructure sensitivity and l_1 sparse regularization. In: Proceedings of SPIE 8692 sensors and smart structures technologies for civil, mechanical and aerospace systems
14. Donoho DL, Elad M (2003) Optimally sparse representation in general (nonorthogonal) dictionaries via l_1 minimization. Proc Natl Acad Sci 100:2197–2202

15. Boyd S, Vandanberghe L (2004) Convex optimization. Cambridge University Press, New York
16. Mottershead JE, Link M, Friswell M (2011) The sensitivity method in finite element model updating. A tutorial. Mech Syst Signal Process 25(7):2275–2296
17. Candes E, Romberg J (2006) l_1-magic: a collection of MATLAB routines for solving the convex optimization programs central to compressive sampling. www.acm.cal-tech.edu/l1magic/

Chapter 27
Damage Detection Using Derringer's Function based Weighted Model Updating Method

Shankar Sehgal and Harmesh Kumar

Abstract Aim of this research paper is to present the application of Derringer's function based weighted model updating method for damage detection in a cantilever beam structure installed near an electric motor. Individual desirability functions have been used to provide scale-free representations of ten sub-objectives of model updating based multi-objective optimization problem. First five vibration modes of beam structure are considered for model updating purpose and hence ten individual desirability functions (sub-objectives) are formulated. Maximization of an individual desirability function leads to minimization of error in corresponding finite element response to which the individual desirability function is attached. Since there are more chances of excitation of those vibration-modes which lie close to the operational frequency of the electric motor; more relative importance is given to such modes by increasing the relative importance index of their individual desirability function. Such kind of relative importance selection is not possible in widely used model updating methods such as response function method. Comparative study is performed for Derringer's function based non-weighted and weighted model updating methods. Results show that weighted model updating method performs better than its non-weighted counterpart.

Keywords Structural dynamics • Damage detection • Derringer's function based model updating • Weighted sub-objectives

Abbreviations

ANOVA	Analysis of variance
FE	Finite element
FEMU	Finite element model updating
MAC	Modal assurance criterion
RS	Response surface
RSM	Response surface method
SE	Simulated experimental

S. Sehgal (✉) • H. Kumar
Mechanical Engineering, University Institute of Engineering and Technology, Panjab University, Chandigarh 160014, India
e-mail: sehgals@pu.ac.in; harmesh@pu.ac.in

A. Wicks (ed.), *Structural Health Monitoring, Volume 5: Proceedings of the 32nd IMAC, A Conference and Exposition on Structural Dynamics, 2014*, Conference Proceedings of the Society for Experimental Mechanics Series, DOI 10.1007/978-3-319-04570-2_27, © The Society for Experimental Mechanics, Inc. 2014

Nomenclature

A	Coded parameter related to elastic modulus of first finite element
B	Coded parameter related to elastic modulus of fifth finite element
C	Coded parameter related to elastic modulus of ninth finite element
C_i	Coefficient of ith linear term of polynomial model
D	Coded parameter related to elastic modulus of 13^{th} finite element
D_i	Coefficient of ith quadratic term of polynomial model
D_o	Overall desirability function
E	Coded parameter related to elastic modulus of 17^{th} finite element
E_i	Elastic modulus of ith finite element
F	Coded parameter related to elastic modulus of 24^{th} finite element
MAC_{ii}	Modal assurance criterion value for ith finite element mode with ith simulated experimental mode
$\widehat{MAC}_{ii}$	Response surface predicted modal assurance criterion value for ith finite element mode with ith simulated experimental mode
$\mathbf{V}$	Variance-covariance matrix
$\mathbf{X}$	Design matrix as being a set of value combinations of coded parameters
X_i	ith independent parameter
Y	Response predicted by response surface method
d_i	ith individual desirability function
f	Response function
i	Integer
j	Integer
m	Number of independent parameters
n	Number of individual desirability functions/natural frequencies/modes
r_i	Relative importance index of the ith individual desirability function
ε	Experimental error
σ	Standard deviation
ω_i	Finite element predicted ith natural frequency
$\widehat{\omega}_i$	Response surface predicted natural frequency of ith mode

27.1 Introduction

Use of thin parts made up of low density materials in latest machines and structures is increasing day by day. Thin and light weight products have lot more tendencies to vibrate than their thick and heavy weight counterparts. Excessive vibrations may even cause pre-mature failure of products. Therefore prediction of accurate dynamic behavior is a major step in design of machines and structures. Dynamic behavior can be represented by natural frequencies, mode-shapes, damping ratios, frequency response functions etc. Further, to analyze the dynamic behavior of structures, either experimental route or theoretical approach [1, 2] can be followed. Theoretical route involves the formation of an analytical model of the system either using a classical method [3] or through Finite Element (FE) method [4]. Application of classical method is generally limited to simple systems only, while FE method is preferred for real life complex systems. However, FE method is not able to predict dynamic responses of structures with complete accuracy due to presence of certain errors in FE model. Thus there is a need to correct an FE model so that its vibration behavior matches with the actual dynamic response obtained experimentally. The procedure used to update the FE model is called Finite Element Model Updating (FEMU) [5–7].

FEMU methods can be broadly classified into direct and iterative methods. Direct (non-iterative) methods are essentially the one step methods such as those proposed by Baruch and Bar-Itzhack [8], Baruch [9], Berman [10], Berman and Nagy [11]. Updated FE models produced by such methods may not be symmetric and positive definite, hence such methods are not much useful in industry. Industrial applications generally rely upon the use of iterative methods such as those proposed by Collins et al. [12], Lin and Ewins [13], Atalla and Inman [14], Li [15], Lin and Zhu [16], Arora et al. [17, 18] and Silva [19].

This paper makes use of Derringer's function based iterative FEMU method developed by Sehgal and Kumar [20]. In this method, FEMU is treated as multi-objective optimization problem; where number of objectives need to be defined in such a way as to reduce errors in responses predicted by FE model. In this paper, it is shown that by using Derringer's function based FEMU one can attach relative importance indices with sub-objectives of different modes of vibration. This

is particularly helpful when one particular mode of vibration is quite more important than rest of the modes of vibration. In this paper, fourth mode of vibration is considered to be more important than others and this aspect is very well formulated and handled in Derringer's function based FEMU.

Basic theory of Derringer's function based FEMU technique used in this research paper is discussed in Sect. 27.2. In order to apply Derringer's function based FEMU technique, FE, Simulated Experimental (SE) results and Response Surface (RS) models are required as explained in Sect. 27.3. Section 27.4 presents the current research work related to damage detection using weighted model updating method. Section 27.5 discusses the conclusions drawn out of the present research work.

27.2 Theory

Derringer' function based FEMU technique [20] is based upon the use of D-optimal design, Response Surface Method (RSM) and desirability function; basic theory of which is presented in Sects. 27.2.1, 27.2.2 and 27.2.3 respectively. Section 27.2.4 presents the details about Derringer's function based weighted FEMU method.

27.2.1 D-Optimal Design

There are several design optimality criterion available in literature such as D-optimality, A-optimality, G-optimality. Among all, D-optimality is the most popular one [21]. It is a type of computer-generated designs, which are an outgrowth of the original work by Kiefer [22, 23] and Kiefer and Wolfowitz [24]. In general, modeling accuracy, namely, goodness-of-fit, can be measured by a variance-covariance matrix $\mathbf{V}$ given by (27.1).

$$\mathbf{V} = \sigma^2 \left(\mathbf{X}'\mathbf{X}\right)^{-1} \tag{27.1}$$

where σ is the standard deviation and $\mathbf{X}$ is the design matrix being a set of value combinations of coded parameters. Naturally, it is expected to minimize $(\mathbf{X}'\mathbf{X})^{-1}$ in order to obtain an accurate RS model. In statistics, minimizing $(\mathbf{X}'\mathbf{X})^{-1}$ is equivalent to maximizing the determinant of $\mathbf{X}'\mathbf{X}$. Therefore, the criteria for constructing the design matrix with a maximized $|\mathbf{X}'\mathbf{X}|$ from a set of candidate samples can be defined as the D-optimality. The initial "D" stands for "determinant". By using D-optimal designs, the generalized variance of a predefined model is minimized, which means the "optimality" of a specific D-optimal design is model dependent. Unlike standard designs, D-optimal designs are straight optimization and their matrices are generally not orthogonal with the effect estimates correlated.

27.2.2 Response Surface Method

RSM is a collection of mathematical and statistical techniques that are useful for modeling and analysis of problems in which a response of interest is influenced by several input variables and the objective is to optimize this response [25–27].

By conducting experiments and applying regression analysis, a model of the response to some independent input variables can be obtained. Based on the model of the response, a near optimal point can then be deduced. RSM is often applied in the characterization and optimization of processes. In RSM, it is possible to represent independent process parameters in quantitative form as written in (27.2).

$$Y = f\left(X_1, X_2, X_3, \ldots X_m\right) \pm \varepsilon \tag{27.2}$$

where Y is the response, f is the response function, ε is the experimental error, and $X_1, X_2, X_3, \ldots X_m$ are independent parameters. By plotting the expected response of Y, a surface, known as RS is obtained. The form of f is unknown and may be very complicated. Thus, RSM aims at approximating f by a suitable lower ordered polynomial in some region of the independent process variables. If the response can be well modeled by a linear function of the m independent variables, the function Y can be written as:

$$Y = C_0 + C_1 X_1 + C_2 X_2 + \cdots + C_m X_m \pm \varepsilon \tag{27.3}$$

However, if a curvature appears in the system, then a higher order polynomial such as the quadratic model as shown in (27.4) may be used.

$$Y = C_0 + \sum_{i-1}^{m} C_i X_i + \sum_{i-1}^{m} D_i X_i^2 \pm \varepsilon \tag{27.4}$$

Objective of using RSM is not only to investigate the response over entire factor space, but also to locate the region of interest where the response reaches its optimum or near optimal value. By studying carefully the RS model, the combination of factors, which gives the best response, can then be established.

27.2.3 Desirability Function

Derringer and Suich [28] describe a multiple response method called desirability. The method makes use of an objective function, D_o, called overall desirability function and transforms an estimated response into a scale free value (d_i) called *i*th individual desirability function. The desirable ranges are from zero to one (least to most desirable, respectively). The factor settings with maximum D_o value are considered to be the optimal parameter conditions. The simultaneous objective function is a geometric mean of all transformed responses as sown in (27.5).

$$D_o = \left(d_1^{r_1} \times d_2^{r_2} \times d_3^{r_3} \times d_4^{r_4} \times \cdots \times d_i^{r_i}\right)^{1 \Big/ \sum r_i} \tag{27.5}$$

where r_i represents the relative importance index of *i*th individual desirability function. If any of the responses falls outside the desirability range, the overall desirability function becomes zero. Desirability is an objective function that ranges from zero outside of the limits to one at the goal. The numerical optimization finds a point that maximizes the desirability function. For several responses, all goals get combined into one desirability function. For simultaneous optimization, each response must have a lower and upper limit assigned to each goal. The "Goal" field for responses must be one of five choices: "none", "maximum", "minimum", "target", or "in range". Factors will always be included in the optimization at their design range by default, or as a maximum, minimum of target goal. The meanings of the goal parameters are:

- Maximum:
  - $d_i = 0$ if response < lower limit
  - $0 \le d_i \le 1$ as response varies from lower to upper limit
  - $d_i = 1$ if response > upper limit
- Minimum:
  - $d_i = 1$ if response < lower limit
  - $1 \le d_i \le 1$ as response varies from lower to upper limit
  - $d_i = 0$ if response > upper limit
- Target:
  - $d_i = 0$ if response < lower limit
  - $0 \le d_i \le 1$ as response varies from lower limit to target
  - $1 \ge d_i \ge 0$ as response varies from target to upper limit
  - $d_i = 0$ if response > upper limit
- Range:
  - $d_i = 0$ if response < lower limit
  - $d_i = 1$ as response varies from lower to upper limit
  - $d_i = 0$ if response > upper limit

The d_i for "in range" are included in the product of the overall desirability function "D_o", but are not counted in determining "n": $D = \left(\prod d_i\right)^{1/n}$. If the goal is none, the response will not be used for the optimization.

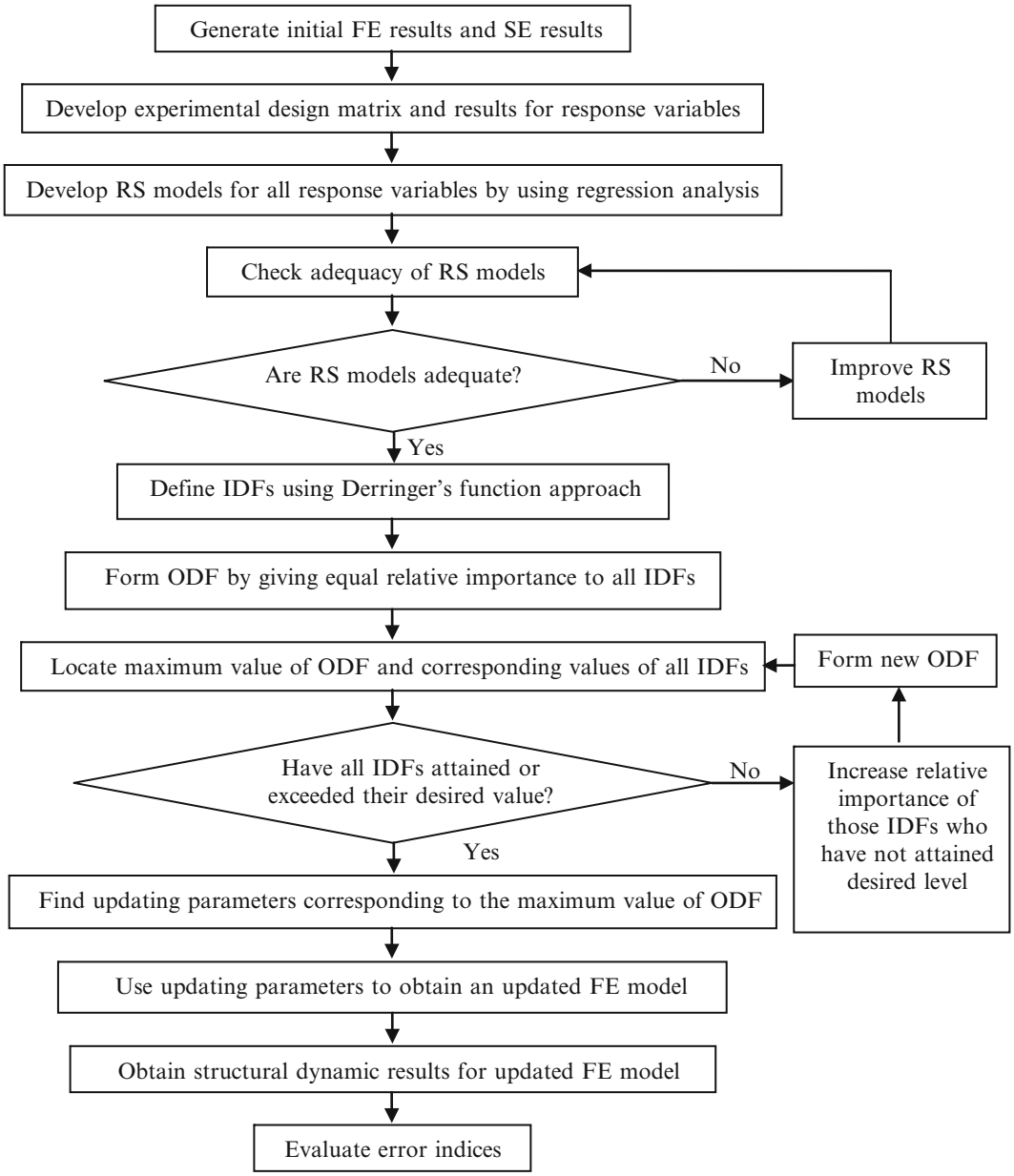

Fig. 27.1 Algorithm for Derringer's function based weighted FEMU method

27.2.4 Weighted Model Updating using Derringer's Function based Updating Method

In this paper model updating method of Sehgal and Kumar [20] is used in a damage detection application where all modes of vibration are not equally important. Figure 27.1 shows the algorithm of Derringer's function based weighted FEMU method. First step in the proposed model updating technique is to generate initial FE and SE results. If experimental set-up is available then SE results can be better replaced by actual experimental results. After that experimental design matrix is formed as per central composite design method. Experimental design matrix is then used to produce corresponding data set for response variables. This data set is then used for developing response surfaces for all response variables such as natural frequencies and Modal Assurance Criterion (MAC) values by regression analysis. Response surface models are then checked for their accuracy and significance by using ANalysis Of VAriance (ANOVA) method. If RS models are not good enough then these are to be modified and checked again for their adequacy. After achieving adequate RS models for all response variables, individual desirability functions are formulated using Derringer's function approach. Individual desirability functions for natural frequencies and MAC values are of the type "Target" and "Maximum" respectively due to their different nature.

All individual desirability functions are then combined to produce D_o as per (27.5); thereby transforming the complex multi-objective type FEMU problem to a rather simpler single-objective type. Maximum value of D_o is then searched out using an optimization algorithm. Corresponding to the maximum value of D_o, the values of all individual desirability functions are found out and are then checked for attaining or exceeding their desired values. If any individual desirability function does not attain its desired value then the relative importance index of that individual desirability function is increased. This leads to the formation of new overall desirability function, which is then again maximized. This process of increasing the relative importance indices is continued till all the individual desirability functions achieve their desired level. After that updating parameters are found corresponding to maximum value of overall desirability function and are then used for forming an updated FE model which is then simulated to produce updated structural dynamic results and error indices.

27.3 Development of RS Models

A cantilever beam structure as drawn in Fig. 27.2 is considered in present study. This beam structure is taken because of its resemblance with many real life products such as blade of rotor of a turbine, wing of an airplane, wing of a ceiling fan, an integrated chip of a mechatronic product etc. Cantilever beam is having the dimensions $910 \times 49 \times 7$ mm^3, density 6,728 kg/m^3 and Young' modulus of elasticity as 200 GPa. Initial FE model of undamaged beam is constructed using 30 beam elements each having two nodes.

The FE model developed in Matlab [29] is then used for producing initial FE natural frequencies and mode-shapes for first five modes of undamaged beam. After that, perturbation is introduced into the FE model of beam structure by reducing the value of modulus of elasticity of six finite elements as per the data provided in Table 27.1. Six damage locations have been selected in such a way so as to distribute these over entire length of beam. FE model of damaged beam is then processed in Matlab to produce SE natural frequencies and mode-shapes, which are later treated as target results. SE results have been used earlier also by many researchers as target results for model updating related research work [30–33]. In this paper, responses such as natural frequencies of first five modes (ω_1 to ω_5) and first five diagonal elements of MAC matrix (MAC_{11} to MAC_{55}) are used during formulation of objective functions of FEMU problem.

RS models are a basic requirement for Derringer's function based FEMU. In order to develop RS models, firstly an experimental design matrix is generated by using D-optimal design in Design-Expert software [34]. Range of each input physical parameter (E_1, E_5, E_9, E_{13}, E_{17} and E_{24}) is decided. Lower and upper limits for all the input parameters are taken as 20 and 60 % of their corresponding initial FE values respectively. Thus lower limit for each input parameter is taken as 40 GPa and the upper limit of the input parameter is taken as 120 GPa. Six coded parameters (A, B, C, D, E and F) are defined in such a way that each coded parameter varies linearly between -1 and $+1$ over complete range of its corresponding physical parameters (E_1, E_5, E_9, E_{13}, E_{17} and E_{24}). Coordinate exchange method [35] is used for candidate selection, because it does not require a candidate list, which if unchecked grows exponentially as the size of the problem increases [36]. D-optimality criterion is used to develop the design matrix of actual physical variables. Design matrix is consisting of a total of 33 test runs and contains the information about various combinations of different levels of input physical parameters at which different SE runs need to be performed. Design matrix is then imported in Matlab and used as input to FE model. FE model is then used to produce response variables matrices as its output. The matrices of response variables are then supplemented to the experimental design matrix available in Design-Expert. Relationship between the set of input parameters (E_1, E_5, E_9, E_{13}, E_{17} and E_{24}) and corresponding set of response variables ($\omega_1, \omega_2, \omega_3, \omega_4, \omega_5, MAC_{11}, MAC_{22}, MAC_{33}, MAC_{44}$ and MAC_{55}) is

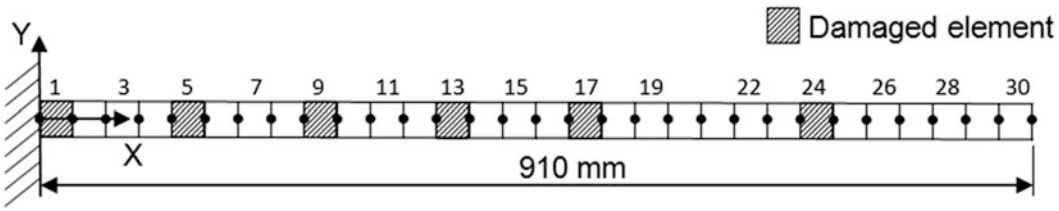

Fig. 27.2 FE model of a damaged cantilever beam structure

Table 27.1 Physical parameters of undamaged and damaged beams

Physical input parameter (stiffness)	E_1	E_5	E_9	E_{13}	E_{17}	E_{24}
Stiffness in FE model of undamaged beam (GPa)	200	200	200	200	200	200
Stiffness in FE model of damaged beam (GPa)	60	80	100	60	80	100

assumed to be quadratic. A quadratic fit is assumed because it is giving better results than a linear or a cubic model. In order to check adequacy of the RS model, ANOVA is performed [37]. F-test method is used to carry out the hypothesis testing to check significance of different parameters. Regression analysis is used in developing the RS model for first natural frequency, as given by the polynomial equation in (27.6).

$$\begin{aligned}\widehat{\omega}_1 =& 6.18 + 0.37A + 0.25B + 0.15C + 0.08D + 0.03E + 0.04AB + 0.03AC + 0.02AD + 0.02BC \\ & - 0.17A^2 - 0.13B^2 - 0.05C^2 - 0.04D^2 - 0.03E^2 + 0.02F^2 \end{aligned} \tag{27.6}$$

Similar analysis is also performed for next nine RS predicted response variables viz. $\widehat{\omega}_2, \widehat{\omega}_3, \widehat{\omega}_4, \widehat{\omega}_5$, $\widehat{MAC}_{11}, \widehat{MAC}_{22}, \widehat{MAC}_{33}, \widehat{MAC}_{44}$, and $\widehat{MAC}_{55}$. After fitting RS models to actually observed results, the RS models for next nine responses (in coded terms) are given by the regression equations (27.7)–(27.15).

$$\begin{aligned}\widehat{\omega}_2 =& 39.40 + 1.94A + 0.20B + 0.27C + 1.17D + 1.42E + 0.30F + 0.11AB - 0.09AC + 0.14AE \\ & - 0.05BD + 0.09CD + 0.09CE + 0.19DE + 0.05EF - 0.63A^2 - 0.12B^2 - 0.18C^2 \\ & - 0.57D^2 - 0.68E^2 \end{aligned} \tag{27.7}$$

$$\begin{aligned}\widehat{\omega}_3 =& 112.08 + 4.15A + 0.43B + 3.24C + 0.89D + 1.28E + 3.68F - 0.41AB + 0.26AD - 0.23AE \\ & + 0.30AF + 0.36CD + 0.29CF + 0.41EF - 1.10A^2 - 1.39C^2 - 0.44D^2 - 0.59E^2 - 1.88F^2 \end{aligned} \tag{27.8}$$

$$\begin{aligned}\widehat{\omega}_4 =& 214.34 + 6.12A + 3.79B + 2.56C + 3.58D + 4.15E + 9.25F - 0.87AB + 0.59AC - 0.55AD \\ & + 0.70AE + 0.73BC - 0.28BD + 0.46BE - 0.47CD + 0.95DE + 0.75DF - 0.94EF - 1.20A^2 \\ & - 2.03B^2 - 1.08C^2 - 1.58D^2 - 1.48E^2 - \end{aligned} \tag{27.9}$$

$$\begin{aligned}\widehat{\omega}_5 =& 358.61 + 8.18A + 11.60B + 1.95C + 9.33D + 8.85E + 7.32F - 0.57AB - 0.55AC + 1.42AD \\ & - 1.28BC + 2.10BD + 0.68CD - 1.83DE - 0.66DF + 0.64EF - 1.06A^2 - 4.22B^2 - 3.64D^2 \\ & - 3.26E^2 - 2.12F^2 \end{aligned}$$

$$\widehat{MAC_{11}} = 10^{-4} \times \begin{pmatrix} 9998.94 - 2.57A - 0.96B + 0.49C + 1.07D + 0.50E \\ - 1.33AB + 1.70AC + 2.40AD + 1.58AE + 0.66BD - 0.79 \\ CD - 0.72DE - 2.37A^2 - 1.87D^2 \end{pmatrix} \tag{27.11}$$

$$\widehat{MAC_{22}} = 10^{-4} \times \begin{pmatrix} 9991.36 - 14.19A + 1.29B - 2.85C - 4.65D + 5.51E + 6.69F \\ - 5.83AC - 1.78AD + 16.12AE + 7.13AF - 2.24CD + 4.50CE + 3.45CF \\ + 3.20DF - 12.30A^2 + 3.95C^2 - 11.13E^2 - 5.60F^2 \end{pmatrix} \tag{27.12}$$

$$\widehat{MAC_{33}} = 10^{-4} \times \begin{pmatrix} 9986.63 - 33.57A - 11.77C + 38.82F - 15.94AB - 19.63AC + 8.83AD \\ + 55.40AF + 16.58BF + 32.80CF + 8.34DE - 10.18DF + 26.83EF \\ -34.20A^2 - 70.70F^2 \end{pmatrix} \tag{27.13}$$

$$\widehat{MAC_{44}} = 10^{-4} \times \begin{pmatrix} 9925.18 - 69.34A - 40.64B - 30.36D + 40.53E \\ + 104.23F - 56.69AB + 29.06AE + 88.89AF \\ - 21.35BD + 22.89BE + 52.74BF + 26.02CF + 35.00DE + 20.52DF \\ - 51.93E^2 - 122.71F^2 \end{pmatrix} \tag{27.14}$$

$$\widehat{MAC_{55}} = 10^{-4} \times \begin{pmatrix} 9931.21 - 32.15A + 45.96C - 62.02D + 69.05E + 80.61F - 84.45AB - 19.27AC \\ + 59.11AE + 53.46AF - 40.75BC + 30.14BD + 44.71BE + 58.88BF + 35.52CD \\ + 24.57DF - 46.67EF - 43.15A^2 - 57.74C^2 - 58.64E^2 - 76.35F^2 \end{pmatrix} \tag{27.15}$$

After having generated RS models for all response variables, next major step is the objective-function-formulation for Derringer's function based FEMU problem and its use in damage detection.

27.4 Damage Detection using Weighted Model Updating

All modes of vibration may not be equally important. In this study it is assumed that that there is an electric motor (or any other exciter) situated near to the beam and operating at a rotational speed of 213 Hz. Because of presence of an external exciter the main excitation frequency is 213 Hz. Therefore that mode of vibration of beam has more chances of getting excited easily which lies closest to the main excitation frequency of 213 Hz rather than other modes of vibration. Hence fourth mode with a natural frequency of 213.02 Hz should be given more importance over other modes. Such method of assigning the relative importance is not possible with response function method [13], but can be easily implemented using Derringer's function based model updating method. Considering fourth mode as the most important mode of vibration, the minimum acceptable desirability value for d_4 and d_9 are taken as 1 and 0.35 respectively. On the other hand the minimum acceptable desirability values for all other d_i's are taken as 0.35. To start with, relative importance indices are set to unity. Corresponding updating results related to individual desirability functions are drawn in Fig. 27.3.

Figure 27.3 shows that d_4 and d_9 have attained only 0.76355 and 0.263511 respectively. These results do not seem to be quite satisfying considering the importance of fourth mode. Therefore in order to obtain better updating results for fourth mode, the relative importance indices for d_4 and d_9 are to be increased. Figure 27.4 shows the results obtained by setting the relative importance indices of d_4 and d_9 to 2. It is seen that as the relative importance indices for d_4 and d_9 are increased,

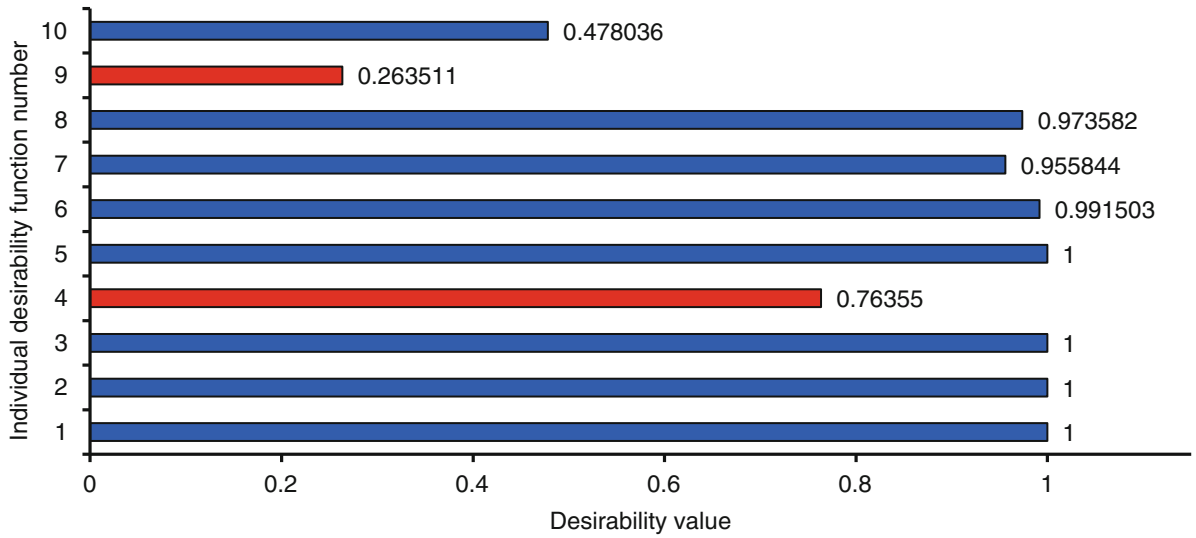

Fig. 27.3 Desirability graph (taking relative importance index of both d_4 and d_9 as one)

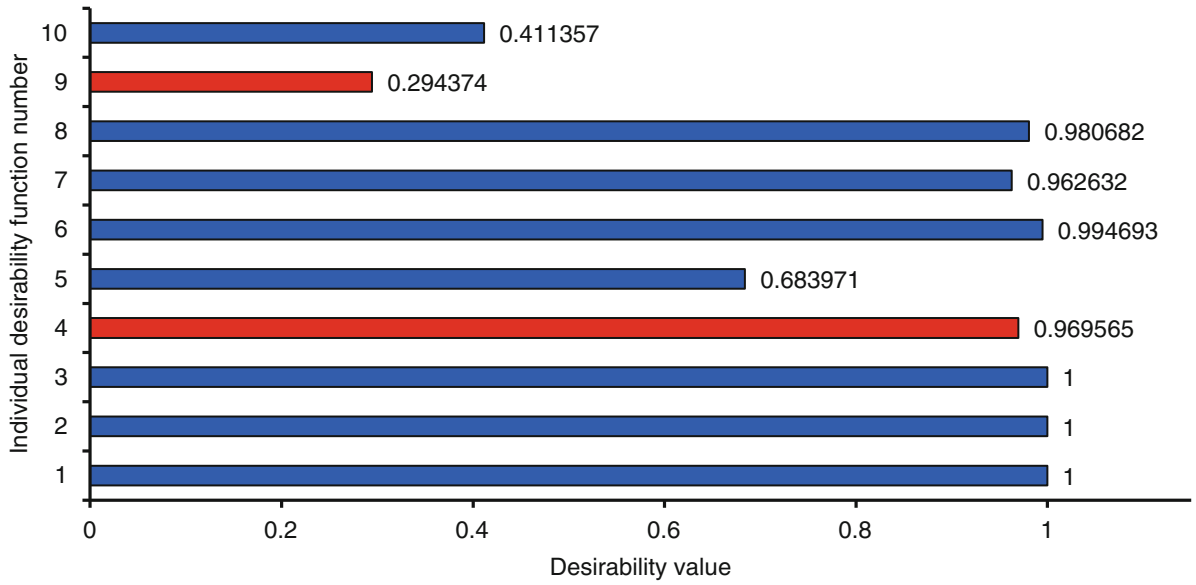

Fig. 27.4 Desirability graph (taking relative importance index of both d_4 and d_9 as two)

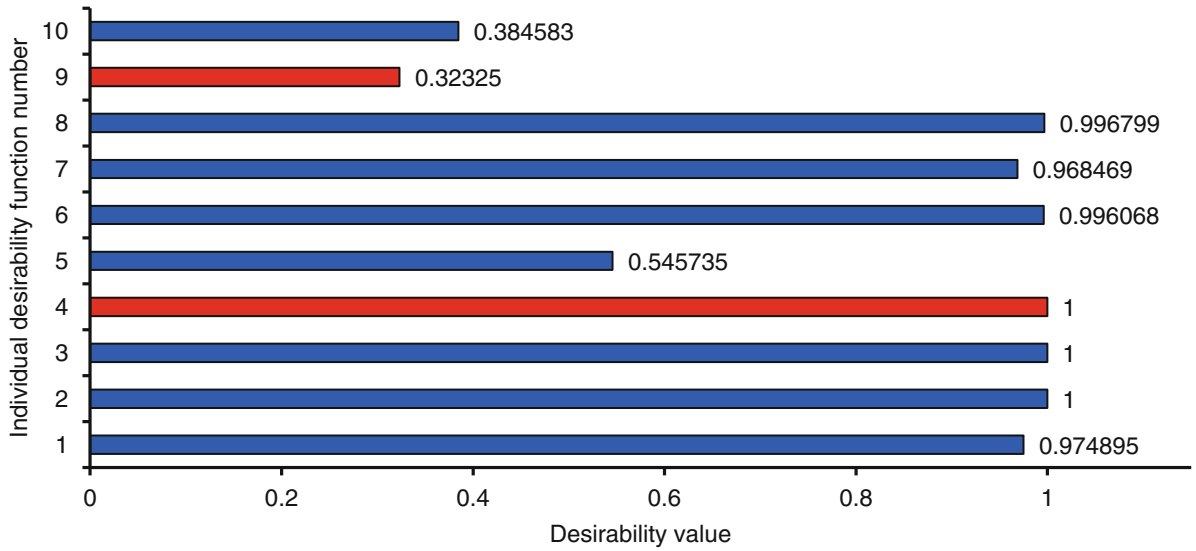

Fig. 27.5 Desirability graph (taking relative importance index of both d_4 and d_9 as three)

values attained by them during FEMU get increased, thereby depicting that better updating results related to fourth mode of vibration are obtained. But still the values of d_i's related to fourth mode of vibration are lesser than their desired values, so the relative importance indices of d_4 and d_9 are successively increased to 3, 4 and 5 in three stages. Results of these three stages are presented in Figs. 27.5, 27.6, and 27.7. Finally desired values of d_4 and d_9 are attained when relative importance indices of d_4 and d_9 are set to 5 as shown in Fig. 27.7.

Figures 27.8 and 27.9 show the improvement trend in the values of d_4 and d_9 respectively. It is seen that d_4 gets stagnant at relative importance index 3 after achieving its highest possible value of unity. However d_9 keeps on increasing almost linearly and steadily with increase in value of relative importance index. Table 27.2 presents the FEMU results when relative importance indices of d_4 and d_9 are set to 5. Updating results show that final average error in damage detection is only 3.06 %, which is far below its initial level of 161.11 %. Natural frequencies and MAC values are also predicted sufficiently accurately

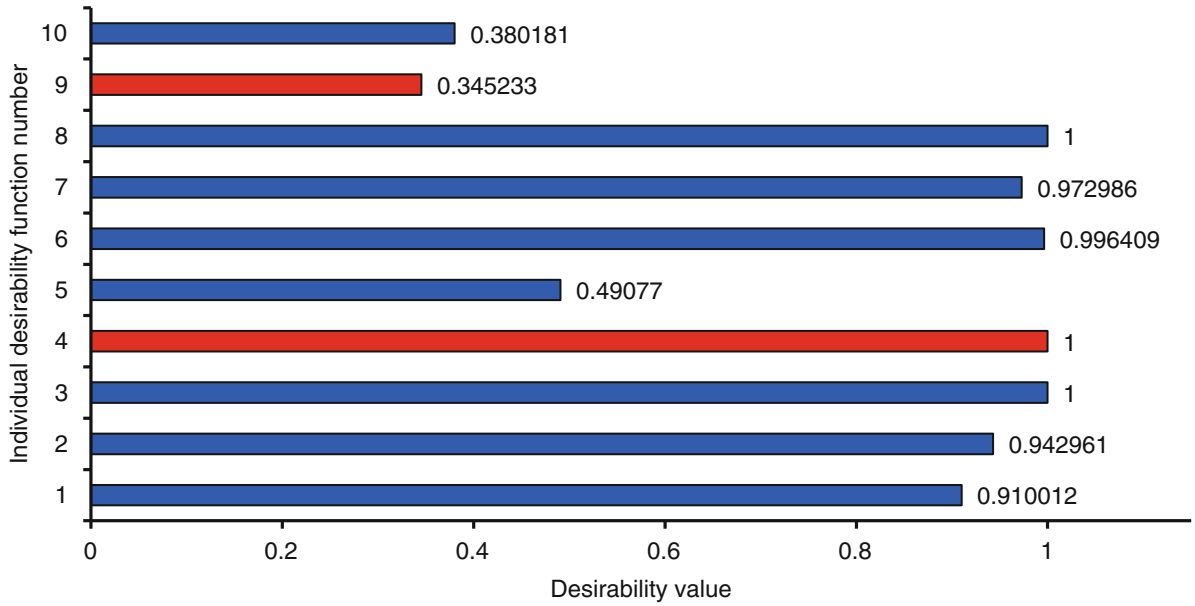

Fig. 27.6 Desirability graph (taking relative importance index of both d_4 and d_9 as four)

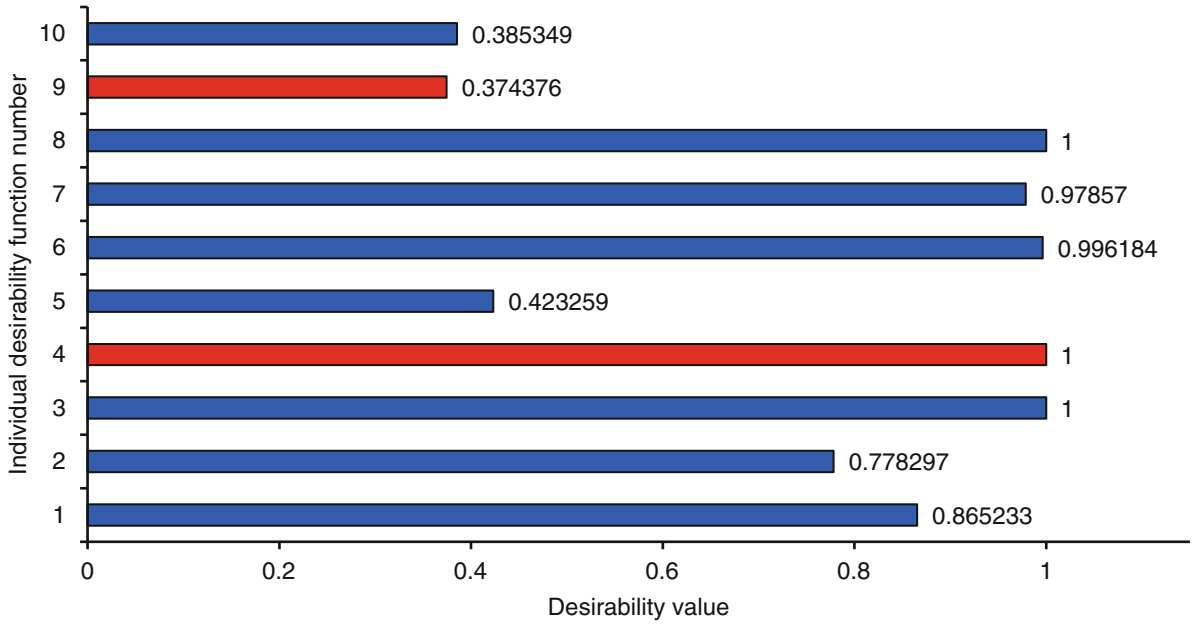

Fig. 27.7 Desirability graph (taking relative importance index of both d_4 and d_9 as five)

with an error of just 0.15 and 0.01 % respectively. Further it is observed that during weighted model updating (when relative importance indices are set to 5), d_4 and d_9 attain a value of 1 and 0.374376 respectively. While during non-weighted model updating (when all relative importance indices are set to 1) d_4 and d_9 attain a value of only 0.76355 and 0.263511 respectively. This shows that weighted model updating performs better than it non-weighted counterpart by 30.97 % considering the value of d_4. Performance of weighted model updating method is again superior to its non-weighted counterpart by 42.07 % when value of d_9 is considered.

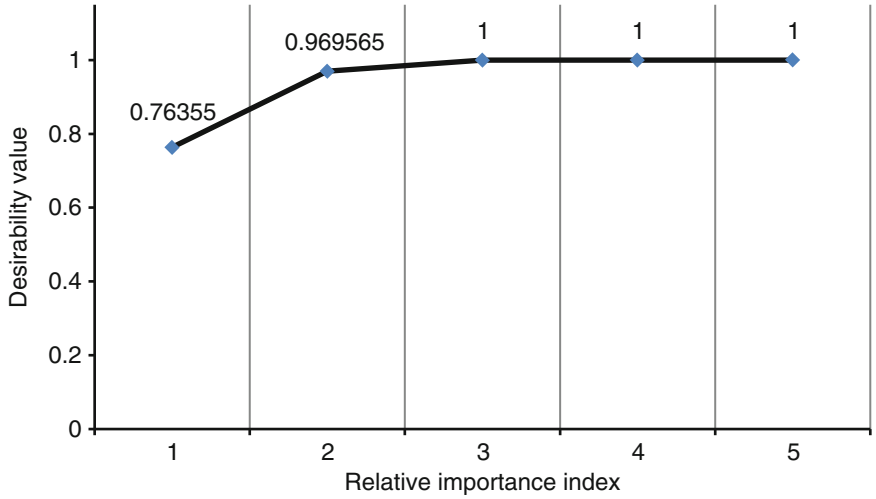

Fig. 27.8 Improvement trend in the value of d_4

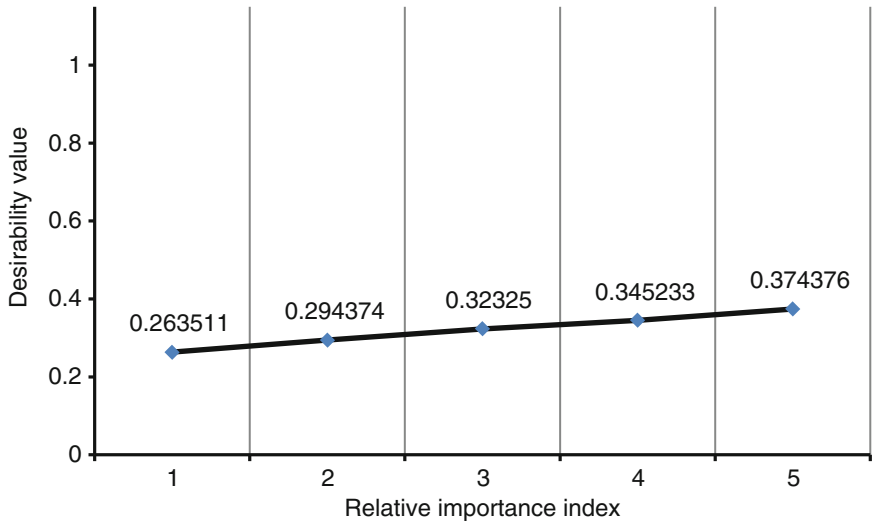

Fig. 27.9 Improvement trend in the value of d_9

27.5 Conclusion

In this paper, weightedmodel updating has been performed for damage detection of a beam. Fourth mode of vibration is considered more important than others in the numerical example considered in this paper. Effect of increasing the relative importance index of individual desirability functions related to fourth mode of vibration is studied. It is seen that as the relative importance index increases, corresponding individual desirability function value also increases thereby leading to better updating results for fourth mode of vibration. Moreover weighted model updating performs better than its non-weighted counterpart. In this paper importance of only one mode has been studied and presented but the method can be easily extended to more number of modes and individual desirability functions.

Table 27.2 Updating results (taking relative importance index of both d_4 and d_9 as five)

	Comparison of physical parameters based results						Comparison of natural frequencies based results						Comparison of MAC values based results					
Sr. no.	Physical parameter	SE value (GPa)	FE results before FEMU (GPa)	Initial error (%)	FE results after FEMU (GPa)	Final error (%)	Natural frequency	SE results (Hz)	FE results before FEMU (Hz)	Initial error (%)	First case study FE results after FEMU (Hz)	Final error (%)	MAC value	Desired value	FE results before FEMU	Initial error (%)	FE results after FEMU	Final error (%)
1	E_1	60	200	233.33	60.23	0.38	ω_1	5.98	7.45	24.6	5.99	0.23	MAC_{11}	1	0.9996	0.04	1	0.00
2	E_5	80	200	150.00	81.99	2.49	ω_2	37.91	46.66	23.1	38.00	0.25	MAC_{22}	1	0.9949	0.51	1	0.00
3	E_9	100	200	100.00	100.92	0.92	ω_3	111.82	130.64	16.8	111.80	0.02	MAC_{33}	1	0.9873	1.27	0.9999	0.01
4	E_{13}	60	200	233.33	58.44	2.60	ω_4	213.02	256.01	20.2	212.88	0.07	MAC_{44}	1	0.9769	2.31	0.9999	0.01
5	E_{17}	80	200	150.00	85.91	7.39	ω_5	353.51	423.21	19.7	354.13	0.18	MAC_{55}	1	0.9544	4.56	0.9999	0.01
6	E_{24}	100	200	100.00	95.42	4.58	–	–	–	–	–	–	–	–	–	–	–	–
Average error (%)				161.11		3.06				20.9		0.15				1.74		0.01

References

1. Maia NMM, Silva JMM (1997) Theoretical and experimental modal analysis. Research Studies Press Limited, Baldock
2. Ewins DJ (2000) Modal testing: theory, practice and application. Research Studies Press Limited, Baldock
3. Den Hartog JP (1934) Mechanical vibrations. McGraw-Hill Book Company, Inc., New York
4. Petyt M (1998) Introduction to finite element vibration analysis. Cambridge University Press, New York
5. Friswell MI, Mottershead JE (1995) Finite element model updating in structural dynamics. Kluwer Academic, Dordrecht
6. Imregun M, Visser WJ (1991) A review of model updating techniques. Shock Vib Dig 23:141–162
7. Mottershead JE, Friswell MI (1993) Model updating in structural dynamics: a survey. J Sound Vib 167(2):347–375
8. Baruch M, Bar-Itzhack IY (1978) Optimal weighted orthogonalization of measured modes. AIAA J 16(4):346–351
9. Baruch M (1978) Optimization procedure to correct stiffness and flexibility matrices using vibration tests. AIAA J 16(11):1208–1210
10. Berman A (1979) Mass matrix correction using an incomplete set of measured modes. AIAA J 17:1147–1148
11. Berman A, Nagy EJ (1983) Improvement of a large analytical model using test data. AIAA J 21(8):1168–1173
12. Collins JD, Hart GC, Hasselman TK, Kennedy B (1974) Statistical identification of structures. AIAA J 12(2):185–190
13. Lin RM, Ewins DJ (1990) Model updating using FRF data. In: 15th international seminar on modal analysis, pp 141–163
14. Atalla MJ, Inman DJ (1998) On model updating using neural networks. Mech Syst Signal Process 12(1):135–161
15. Li WL (2002) A new method for structural model updating and joint stiffness identification. Mech Syst Signal Process 16(1):155–167
16. Lin RM, Zhu J (2007) Finite element model updating using vibration test data under base excitation. J Sound Vib 303:596–613
17. Arora V, Singh SP, Kundra TK (2009) Finite element model updating with damping identification. J Sound Vib 324:1111–1123
18. Arora V, Singh SP, Kundra TK (2009) Damped model updating using complex updating parameters. J Sound Vib 320:438–451
19. da Silva S (2011) Non-linear model updating of a three-dimensional portal frame based on Wiener series. Int J Non Linear Mech 46:312–320
20. Sehgal S, Kumar H (2014) Structural dynamic finite element model updating using Derringer's function: a novel technique. WSEAS Trans Appl Theor Mech 9:11–26
21. Myers RH, Montgomery DC ((1995)) Response surface methodology: process and product optimization using designed experiments. John Wiley and Sons, New York
22. Kiefer J (1959) Optimum experimental designs. J R Stat Soc Ser B Stat Methodol 21:272–304
23. Kiefer J (1961) Optimum designs in regression problems. Ann Math Stat 32:298–325
24. Kiefer J, Wolfowitz J (1959) Optimum designs in regression problems. Ann Math Stat 30:271–294
25. Montgomery DC ((2004)) Design and analysis of experiments. John Wiley and Sons, New York
26. Cochran G, Cox GM (1962) Experimental design. Asia Publishing House, New Delhi
27. Kansal HK, Singh S, Kumar P (2005) Parametric optimization of powder mixed electrical discharge machining by response surface methodology. J Mater Process Technol 169:427–436
28. Derringer G, Suich R (1980) Simultaneous optimization of several response variables. J Qual Technol 12(4):214–219
29. Matlab (2004) User's guide of Matlab v7. The Mathworks Incorporation
30. Dhandole SD, Modak SV (2010) A comparative study of methodologies for vibro-acoustic FE model updating of cavities using simulated data. Int J Mech Mater Des 6:27–43
31. Dhandole SD, Modak SV (2009) Simulated studies in FE model updating with application to vibro-acoustic analysis of the cavities. In: Third international conference on integrity, reliability and failure, 1–11 July 2009
32. Modak SV, Kundra TK, Nakra BC (2002) Comparative study of model updating methods using simulated experimental data. Comput Struct 80:437–447
33. Mares C, Mottershead JE, Friswell MI (2006) Stochastic model updating: part 1—theory and simulated example. Mech Syst Signal Process 20:1674–1695
34. Design-Expert (2004) User's guide for version 8 of Design-Expert. Stat-Ease Incorporation
35. Meyer RK, Nachtsheim CJ (1995) The coordinate-exchange algorithm for constructing exact optimal experimental designs. Technometrics 37(1):60–69
36. Smucker BJ, del Castillo E, Rosenberger JL (2012) Model-Robust two-level designs using coordinate exchange algorithms and a maximin criterion. Technometrics 54(4):367–375
37. Montgomery DC, Peck EA, Vining GG ((2003)) Introduction to linear regression analysis. John Wiley and Sons, New York

Chapter 28
Energy Harvesting in a Coupled System Using Nonlinear Impact

K. Vijayan, M.I. Friswell, H.H. Khodaparast, and S. Adhikari

Abstract Energy harvesting from broadband excitation, such as aircraft noise, and low frequency excitation, such as human motion, has gained significant interest recently. Vibro-impact is one of the methods used to improve capability of the harvester by low to high frequency conversion. The present paper analyses the effect of vibro-impact within a coupled beam system. The system is base excited and a localised non-linearity is induced at the point of impact. Modal reduction techniques are applied to reduce the computational time. The localisation effect on the coupled beam system is performed by varying the system parameters, for example the amplitude of excitation, the clearance and stiffness between the beams.

Keywords Vibro-impact • Energy harvesting • Frequency-conversion • Piezoelectric • Modal reduction

28.1 Introduction

Harvesting vibration energy for low-powered devices has received significant attention in recent years. In early studies harvesting was carried out using stationary and linear assumptions. Recently vibration-based MEMS energy harvesters have received increased attention as a potential power source for microelectronics and wireless sensor nodes. The principal challenge associated with the system is to extend their useful range beyond a narrowband near the resonance and stationary excitation near their natural frequency. The effectiveness of linear oscillators reduces when the excitation from ambient vibration is distributed over a wide range of frequencies, the spectrum is non-stationary or very low frequencies dominate [1, 2].

MEMS based harvesters based on piezoelectric, electromagnetic and electrostatic transduction mechanism operates at frequencies more than 100 Hz [3–5]. Achieving small size and low resonant frequency is a major design challenge. The limitations are due to the micro fabrication process and brittle properties of silicon material. The generated power from the harvester is proportional to the cube of the excitation frequency and drops dramatically at low frequencies [6]. However there are a wide range of applications where the energy could be harvested from low frequency vibration. The application areas range from human motion (<10 Hz), vehicle (<20 Hz) and machine vibrations (50 Hz) [1, 7, 8]. Harvesters could be used in implantable electronic devices and wireless sensor nodes. The need for an effective harvester for low frequency and broadband excitation environment provided an impetus to exploit the effects of non-linearity. Various techniques were explored to exploit the non-linearity namely Duffing [9–11], impact [12–14] and bistable oscillator designs [15]. Babitsky [16] analysed a vibro-impacting oscillator with symmetry stops and the effect of random vibration on the system. It was observed that the frequency of oscillation is high, when the clearance is less than the standard deviation of the seismic mass displacement in the absence of stops. This finding has important implications from a design perspective to restrict the clearance. The present paper focusses on frequency up-conversion utilising non-linearity induced from impact in an otherwise linear structure. A multi degree freedom system is considered for the analysis.

K. Vijayan (✉) • M.I. Friswell • H.H. Khodaparast • S. Adhikari
College of Engineering, Swansea University, Singleton Park, Swansea SA2 8PP, UK
e-mail: k.vijayan@swansea.ac.uk; m.i.friswell@swansea.ac.uk; H.HaddadKhodaparast@swansea.ac.uk; S.Adhikari@swansea.ac.uk

A. Wicks (ed.), *Structural Health Monitoring, Volume 5: Proceedings of the 32nd IMAC, A Conference and Exposition on Structural Dynamics, 2014*, Conference Proceedings of the Society for Experimental Mechanics Series, DOI 10.1007/978-3-319-04570-2_28, © The Society for Experimental Mechanics, Inc. 2014

28.2 Theoretical Model: Coupled Beams

A system consisting of two beams is proposed to explore the effect of frequency up conversion. The beams are clamped at the end and the whole system is base excited. A schematic of the system is shown in Fig. 28.1 and the dimensions of the system are given in Table 28.1. The dimensions of the system were chosen such that the base excitation forces are within controllable limits and within the constraints of the available shaker. The two beams were chosen of different thickness in order to gain insight into the influence of asymmetry on the non-linearity [17]. The two beams behave as independent cantilevers without impact. The displacements of the thick and the thin beams, at the free ends, are y_1 and y_2 respectively. The clearance between the beams is denoted by δ. During contact the thicker beam is excited both by base excitation and from the non-linear contact element.

The coupled system is modelled by finite element analysis using 30 Euler-Bernoulli elements for each beam. The impact force is given by

$$\begin{aligned} F_{imp} &= K_{cont}((y_2 - y_1) - \delta) \qquad if \quad y_2 - y_1 < \delta \\ &= 0 \qquad\qquad\qquad\qquad\quad \text{Otherwise} \end{aligned} \tag{28.1}$$

The contact element is active only when $y_2 - y_1$ is less than clearance (δ) between the beams. The non-linearity is induced by the intermittent contact occurring between the systems.

The equation of motion of the system is given by

$$[\mathrm{M}]\left\{\ddot{\mathrm{Y}}\right\} + [\mathrm{C}]\left\{\dot{\mathrm{Y}}\right\} + [\mathrm{K}]\{\mathrm{Y}\} + \left\{F_{imp}\right\} = \alpha[\mathrm{M}]\{\mathrm{Y_{adof}}\}\omega_e^2 \sin(\omega_e t) \tag{28.2}$$

where [M] is the mass matrix, [C] is the damping matrix, [K] is the stiffness matrix, {Y} is the displacement vector, $\{\mathrm{Y_{adof}}\}$ is a vector with unit entries corresponding to the translational d.o.f for the base excitation, $\left\{F_{imp}\right\}$ is the impact force vector having non zero entries with opposite sign corresponding to the d.o.f where impact occurs, α is the base excitation amplitude and ω_e is the base excitation frequency. Model reduction was applied to reduce the computational cost. The reduced model included the first 12 modes under the presumption that these modes will be influenced by non-linear impact. The system was integrated in the time domain using the 4th order Runge-Kutta method with variable time step. Proportional modal damping was included in the coupled system beams and the damping coefficient (ζ) was assumed to be 0.1 %. The natural frequencies of the uncoupled system are given in Table 28.2. The mode shapes and natural frequencies of a linear system with a coupling spring of 10^3 N/m are shown in Fig. 28.2. The base excitation frequency was varied up to 35 Hz.

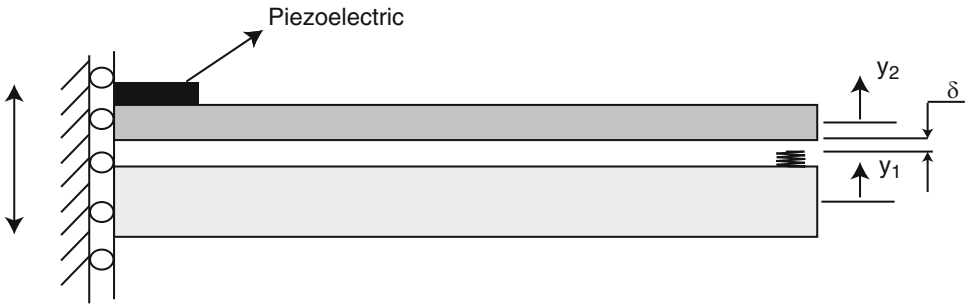

Fig. 28.1 Schematic of the energy harvester

Table 28.1 Dimensions of the coupled beam system

Length of the beam	305 mm
Thickness of the beam1	0.5 mm
Thickness of the beam2	0.25 mm
Width of the beam	16 mm
Young's modulus	210 GPa
Mass of beam 1	140 g
Mass of beam 2	70 g
Density of beams	7,000 kg/m^3

Table 28.2 Natural frequencies of the individual beams

ω_{thin} (Hz)	ω_{thick} (Hz)
2.32	4.64
14.54	29.09
40.72	81.44
79.80	159.59

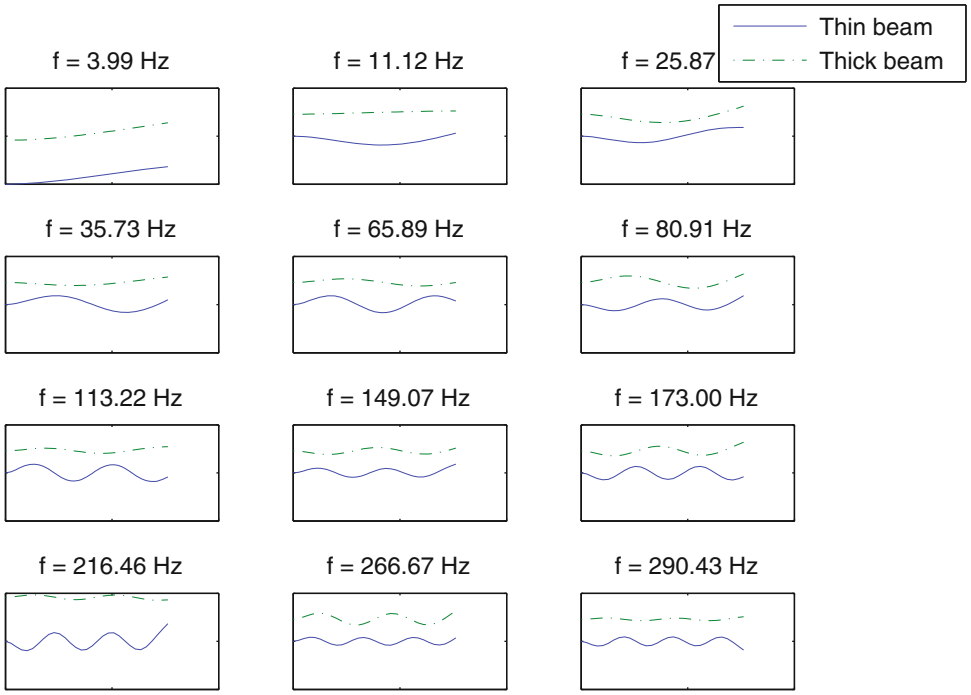

Fig. 28.2 Mode shapes of the system with a fixed coupling spring

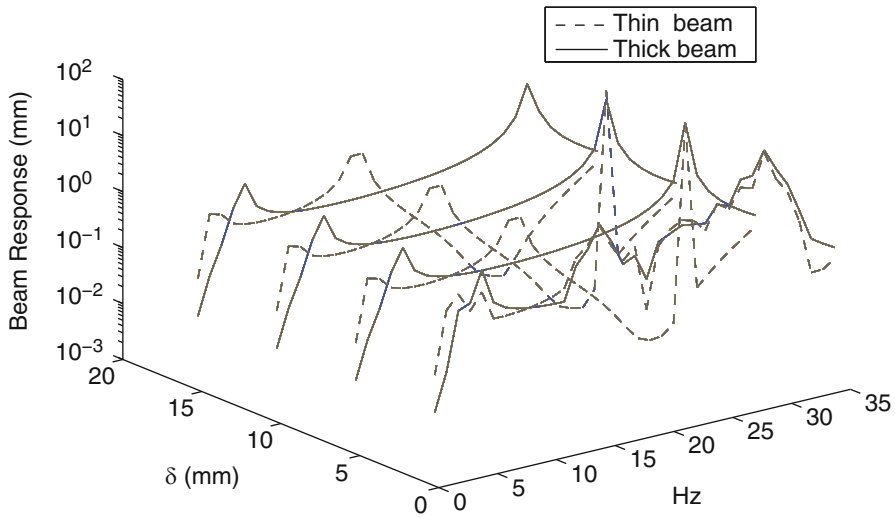

Fig. 28.3 Stepped sine beam response for four equally spaced clearances between 4 and 20 mm

28.2.1 Parametric Study

The magnitude of base excitation and the coupling spring constant was fixed at 0.03 m and 10^3 N/m respectively. The clearances between the two beams were varied from 4 to 20 mm. Typical for a high clearance between the two beams the response would be linear as expected. However with reduced clearance the system response becomes non-linear with induced non-linearity from the contact. The response of the system is given as a three dimensional plot with frequency, clearance and beam response forming the x, y and z axes respectively. A sine sweep in frequency was carried out from 0 to 35 Hz with a step size of 0.5 Hz for each of the clearance cases. Figure 28.3 depicts the variation in response for different

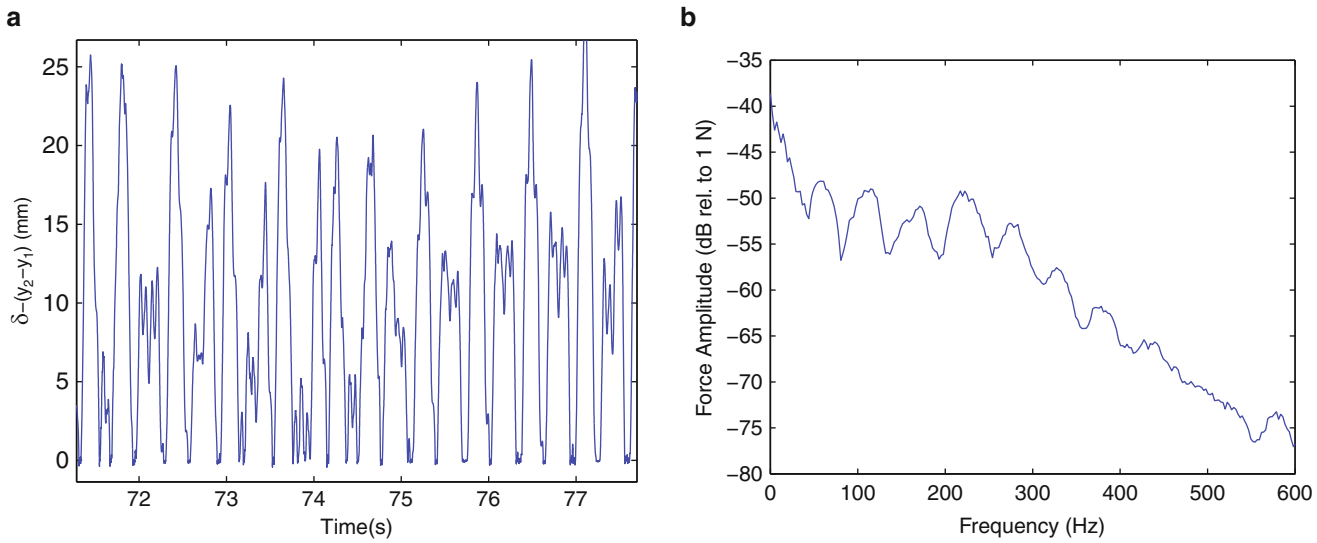

Fig. 28.4 Variation in the displacement of beams and the force spectrum. (**a**) Variation in clearance between the beams for excitation at 14.45 Hz. (**b**) Force spectrum at 14.45 Hz

clearances between the beams. It can be observed that for a clearance of 4 mm the response of the system at the resonance peaks are less sharp. However as the clearance increases the resonance peaks becomes more distinct and typical of a linear system behaviour. The system response for 4 mm clearance however does indicate an increase in response near 14 and 30 Hz, which are close to the second natural frequencies of the thin and thick beam respectively.

In order to understand the effect on the system response better a simulation was performed by base exciting the system at 14.45 Hz. Variations in the clearance between the beams were analysed. The variation in the time response of the clearance between the beams is shown in Fig. 28.4a. A negative value indicates $\delta < (y_2 - y_1)$ and the beams are in contact. Figure 28.4b shows the spectrum of impact force. The spectrum is obtained by carrying out block averaging of the Fourier transform of response from 40 to 100 s using 146 sections. The block averaging was carried out to smooth the response spectrum. The general stochastic nature of the response could be due to the fact that the system contains both steady and transient responses since the impact can be considered as repeated impacts with an impulse hammer.

28.2.2 Excitation Bandwidth

The advantage of using an energy harvester using impact is that the higher modes are excited and this feature is explored by exciting the system at 14.45 Hz, which corresponds to a maximum response. The response of the thick beam at the point of impact is analysed. Two cases with different excitation force and clearance are analysed. The response spectrum of the system obtained corresponding to two different clearances of 4 and 10 mm between the beams are shown in Fig. 28.5a. The spectrum is block averaged to smooth the response. It can be observed from the figure that for the high clearance case the response is linear with the peak amplitude occurring near the resonance. However for the system with reduced clearance more modes are excited as observed in the response spectrum. A similar observation can be made with the variation in base excitation amplitude. Figure 28.5b shows the frequency response function for a fixed δ of 10 mm corresponding to two different base excitation amplitudes of 0.03 and 0.09 m. The spectrum is block averaged to smooth the response. It can be observed that for lower base excitation amplitude the response of the system is linear with a single peak, however for the higher base excitation amplitude multiple peaks can be observed indicating the excitation of higher modes.

28.2.3 Power Generation

The next stage is to analyse the effectiveness of the power generation. Piezoelectric material can be added to a beam in either unimorph or bimorph configurations [18]. The mechanical deformation produces an electric current from the strain in the piezoelectric material. The model includes only the direct piezoelectric effect and the converse effect is not considered in

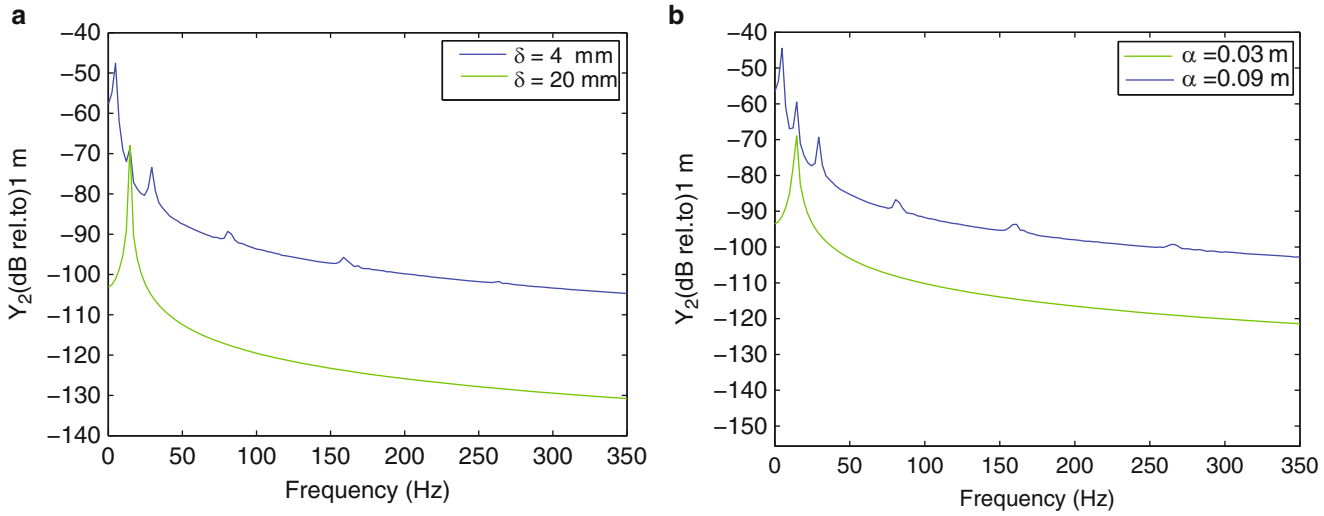

Fig. 28.5 Frequency response variation with system parameters. (**a**) Frequency response corresponding to excitation of the system at 14.45 Hz for two different clearances between the coupled beams for a fixed base excitation amplitude α of 0.03 m. (**b**) Frequency response corresponding to the excitation of the system at 14.45 Hz for two different base excitation amplitudes for a fixed clearance δ of 10 mm

Table 28.3 Parameters of the Piezopatch

Length of the piezo	28 mm
Thickness of the piezo	0.254 mm
Width of piezo	7 mm
Capacitance, C_p	51.4 nF
Resistance, R	$10^5\,\Omega$
γ_c	-4×10^{-5} Nm/V

the present model. The voltage produced is proportional to the strain in the PZT which is proportional to y'' where y is the deformation of the beam. For the present study a unimorph is considered and the parameters are given in Table 28.3.

The piezoelectric patch can be considered as a capacitor and the charge produced is assumed proportional to the slope of the modes at the extremes of the piezoelectric patch. Thus the work done is

$$W \approx \theta_1 V \tag{28.3}$$

where

$$\theta_1 = \gamma_c \int_0^{L_c} y''(s)\, ds = \gamma_c y'(L_c) \tag{28.4}$$

and V is the voltage and L_c is the length of the PZT patch. The piezoelectric patch is attached to the root of the clamped thin beam as shown in Fig. 28.1. This position was chosen to be the optimum on the presumption that a high curvature is expected at the root compared to other locations for the mode considered. The piezoelectric equation of motion given by

$$C_p \dot{V} + \frac{V}{R} + \theta_1 \dot{v} = 0 \tag{28.5}$$

The average power scavenged between time t_1 and t_2 is calculated by integrating the temporal response as

$$P_{avg} = \frac{1}{T_2 - T_1} \int_{T_1}^{T_2} \frac{V(t)^2}{R} dt \tag{28.6}$$

A parametric study on the influence of different system parameters, namely the contact stiffness, damping and the clearance, on the power generated was carried out as shown in Fig. 28.6. A frequency sweep from 0 to 35 Hz with a finer step size near the resonance of the uncoupled natural frequencies of the individual beams was performed and the average power generated

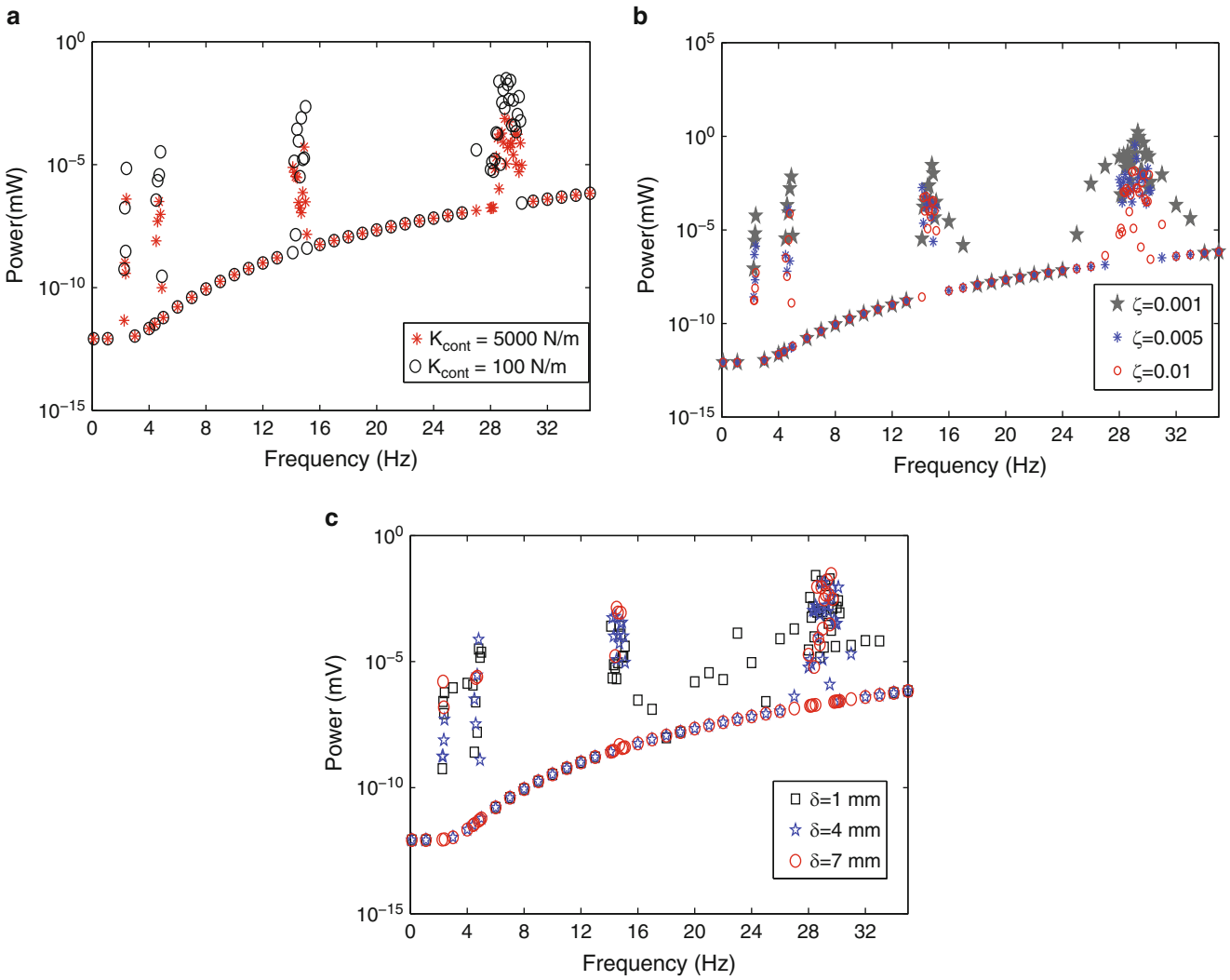

Fig. 28.6 Parametric study on the variation of power generated with system parameters. (**a**) Variation in the power produced by the system with excitation frequency for two different contact stiffnesses for a fixed damping factor of 0.01 % and clearance of 4 mm. (**b**) Variation in the power produced by the system with excitation frequency for three different damping ratios for a fixed contact stiffness of 500 N/m and clearance of 4 mm. (**c**) Variation in the power produced by the system with excitation frequency for three different clearances for a fixed contact stiffness of 500 N/m and a damping factor of 0.01 %

was estimated. Figure 28.6a shows the variation in the average power generated across the frequencies for different contact stiffnesses. It can be observed that the power generated shows a sensitivity to the contact stiffness since it influences the number of modes excited. The power generated is significantly higher at the resonance frequencies of the individual beams. Figure 28.6b shows the variation in the average power generated across the frequencies corresponding to different damping ratios, and shows that with an increase in mechanical damping the effectiveness of the harvester reduces. The influence of clearance on the power generated is shown in Fig. 28.6c. With the reduced clearance the possibility of impact between the beams increases even in the frequency regions slightly away from the resonant peaks, where response amplitudes are generally lower. This has a positive influence on the power generated.

28.3 Conclusion

The results from the study indicated that energy harvesting using impact is a viable option to improve the operational bandwidth of the harvester. Contrary to the linear system where only one mode is excited, with non-linear impact a larger number of modes are excited for the same excitation frequency. The key mechanical parameters of the system which can be

used to control the performance are the clearance, the base excitation amplitude and the contact stiffness. Further study will explore the sensitivity of the system parameters for the electrical and mechanical domains, their interactions and optimisation of the energy harvested. Future work will also include validation using an experimental test rig.

Acknowledgements The authors acknowledge the support of the Engineering and Physical Sciences Research Council through grant number EP/K003836.

References

1. Roundy S, Wright PK, Rabaey J (2003) A study of low level vibrations as a power source for wireless sensor nodes. Comput Commun 26:1131–1144
2. DuToit NE, Wardle BL, Kim SG (2005) Design considerations for MEMS-scale piezoelectric mechanical vibration energy harvesters. Integr Ferroelectr 71(1):121–160
3. Jiang Y, Masaoka S, Fujita T, Uehara M, Toyonaga T, Fujii K, Higuchi K, Maenaka K (2011) Fabrication of a vibration-driven electromagnetic energy harvester with integrated NdFeB/Ta multilayered micro-magnets. J Micromech Microeng 21(9):095015
4. Khan F, Sassani F, Stoeber B (2010) Copper foil-type vibration-based electromagnetic energy harvester. J Micromech Microeng 20(12):125006
5. Tvedt LGW, Nguyen DS, Halvorsen E (2010) Nonlinear behavior of an electrostatic energy harvester under wide- and narrowband excitation. J Microelectromech Syst 19:305–316
6. Beeby SP, Tudor MJ, White NM (2006) Energy harvesting vibration sources for microsystems applications. Meas Sci Technol 17(12):175–195
7. Paci D, Schipani M, Bottarel V, Miatton D (2008) Optimization of a piezoelectric energy harvester for environmental broadband vibrations. In: 15th IEEE International conference on electronics, circuits and systems, 2008 (ICECS 2008), pp. 177–181
8. Miller L, Halvorsen E, Dong T, Wright P (2011) Modelling and experimental verification of low frequency MEMS energy harvesting from ambient vibrations. J Micromech Microeng 21
9. Daqaq MF (2010) Response of uni-modal duffing-type harvesters to random forced excitations. J Sound Vib 329(18):3621–3631
10. Mann BP, Sims ND (2009) Energy harvesting from the nonlinear oscillations of magnetic levitation. J Sound Vib 319:515–530
11. Sebald G, Kuwano H, Guyomar D, Ducharne B (2011) Experimental Duffing oscillator for broadband piezoelectric energy harvesting. Smart Mater Struct 20:102001
12. Umeda M, Nakamura K, Ueha S (1996) Analysis of transformation of mechanical impact energy to electrical energy using a piezoelectric vibrator. Jpn J Appl Phys 35(Part 1, 5B) 3267
13. Gu L, Livermore C (2011) Impact-driven, frequency up-converting coupled vibration energy harvesting device for low frequency operation. Smart Mater Struct 20(4):045004
14. Jacquelin E, Adhikari S, Friswell M (2011) A piezoelectric device for impact energy harvesting. Smart Mater Struct 20(10):105010
15. Harne RL, Wang KW (2012) A review of the recent research on vibration energy harvesting via bistable systems. Smart Mater Struct 22:023001
16. Babitsky VI (1998) Theory of vibro-impact systems and applications. Springer, Berlin
17. Vijayan K, Woodhouse J (2013) Shock transmission in a coupled beam system. J Sound Vib 332:3681–3695
18. Friswell MI, Ali SF, Bilgen O, Adhikari S, Lees A, Litak G (2012) Nonlinear piezoelectric vibration energy harvesting from a vertical cantilever beam with tip mass. J Intell Mater Syst Struct 23(13):1505–1521

Chapter 29
Spatiotemporal Sensing for Pipeline Leak Detection Using Thermal Video

Ganesh Sundaresan, Seung-Yeon Kim, Jong-Jae Lee, Ki-Tae Park, and Hae-Bum Yun

Abstract Auto Modulating Pattern Detection Algorithm (AMP) is a novel data processing technique to detect adverse hazards for various monitoring applications. This ongoing experimental study seeks to expand the one-dimensional "point-sensing" AMP to the two-dimensional "plane-sensing" case. AMP will be validated as an effective spatiotemporal technique for detecting leakage in fluid distribution pipeline networks.

Pipelines fail due to various causes, including external interference (mechanical damage) and corrosion caused by external environmental factors. These damage signatures are usually very tiny and are masked by other more dominant trends such as the ambient air temperature, making these patterns difficult to detect.

An experimental pipeline setup has been fabricated to simulate a real pipeline network. Damage is simulated through the use of holes that can be closed using watertight bolts. A stationary 360×240 resolution infrared camera will be used to measure spatiotemporal temperature signatures on the pipeline surface over time. AMP can be implemented on each pixel's time history to detect abnormal changes in temperature that are associated with hazards. Preliminary results show that AMP successfully provides spatiotemporal information related to adverse hazards.

Keywords Auto-Modulating pattern detection algorithm • Spatiotemporal analysis • Hilbert-Huang transform • Damage detection • Civil infrastructure monitoring

29.1 Introduction

As of 2009, the USA has about 600,000 bridges, 85,000 dams, 160,000 miles of national highway network, 140,000 miles of rail transportation network, 100,000 miles of levees, and 12,000 miles of navigable inland waterways [1]. The above mega infrastructure networks are continuously monitored for various operation and maintenance purposes using numerous monitoring technologies, such as structural health monitoring (SHM) systems [2–4], intelligent transportation systems (ITS) [5], road weather information systems (RWIS) [6], waste monitoring systems (WMS), and so on.

With recent advancements in sensing and networking technologies, quantitative data collected from various civil systems are becoming more available than ever. However, obtaining sensor data is necessary, but not sufficient, to understand the complicated spatiotemporal behavior of civil systems in infrastructure networks. The research community is overwhelmed with the extensive nature of data that is required to be collected from infrastructure networks comprised of a large number of heterogeneous civil systems. Future construction, operation and maintenance of infrastructure are envisioned to be

G. Sundaresan • H.-B. Yun (✉)
Department of Civil, Environmental and Construction Engineering, University of Central Florida, Orlando, FL, USA
e-mail: g.sundares@gmail.com; Hae-Bum.Yun@ucf.edu

S.-Y. Kim • J.-J. Lee
Civil and Environmental Engineering Department, Sejong University, Seoul, South Korea
e-mail: eswaiii@hanmail.net; jongjae@sejong.ac.kr

K.-T. Park
Korea Institute of Construction Technology, GoYang-Si, GyeongGi-Do, South Korea
e-mail: ktpark@kict.re.kr

A. Wicks (ed.), *Structural Health Monitoring, Volume 5: Proceedings of the 32nd IMAC, A Conference and Exposition on Structural Dynamics, 2014*, Conference Proceedings of the Society for Experimental Mechanics Series, DOI 10.1007/978-3-319-04570-2_29,

increasingly data-intensive and data-dependent for ubiquitous cities, the next-generation human dwellings. The voluminous, fast-growing, multi-modal sensor data generated related to the above large infrastructure networks are already beyond the ability of typical data management tools.

A data summarization framework to address the above technical challenges with extremely large datasets emanated from heterogeneous infrastructure networks is first presented in Sect. 29.2. For efficient data summarization, a novel model-free data processing algorithm is reviewed in Sect. 29.3. Section 29.4 presents the results of a preliminary MATLAB simulation analysis and an ongoing illustrates an experimental plan for pipeline leakage detection using AMP.

29.2 Data Summarization Framework and Associated Data Summarization Methodology

A comprehensive hazards detection methodology has been developed as an early warning detection system to detect adverse hazards by managing extremely large data from heterogeneous civil infrastructure networks. The framework and associated methodology is presented in Figs. 29.1 and 29.2, respectively.

This approach identifies two classes of data processing methods: ad hoc analysis and post hoc analysis. An ad hoc approach provides preliminary information by continuously processing streamed data from a sensor network to detect abnormal hazards or behaviors that can be encountered in construction, operation, and maintenance of the associated civil infrastructure system. If a potential hazard is detected, further evaluation can be done to determine whether a more rigorous post hoc analysis is required. A post hoc analysis refers to a comprehensive evaluation that is conducted to find physical causes of adverse behaviors of civil infrastructure systems through rigorous scientific investigation and additional inspections and testing, including visual inspections, destructive or non-destructive testing, and additional sensor-based monitoring.

The ad hoc approach can be further classified into two levels of data summarization: single-sensor analysis and multi-sensor analysis. Single-sensor analysis techniques summarize data from each sensor node by converting the complicated, nonlinear data into binary "spike trains" that are tuned to the hazards of interest. These spike trains provide temporal information related to when the hazard occurs.

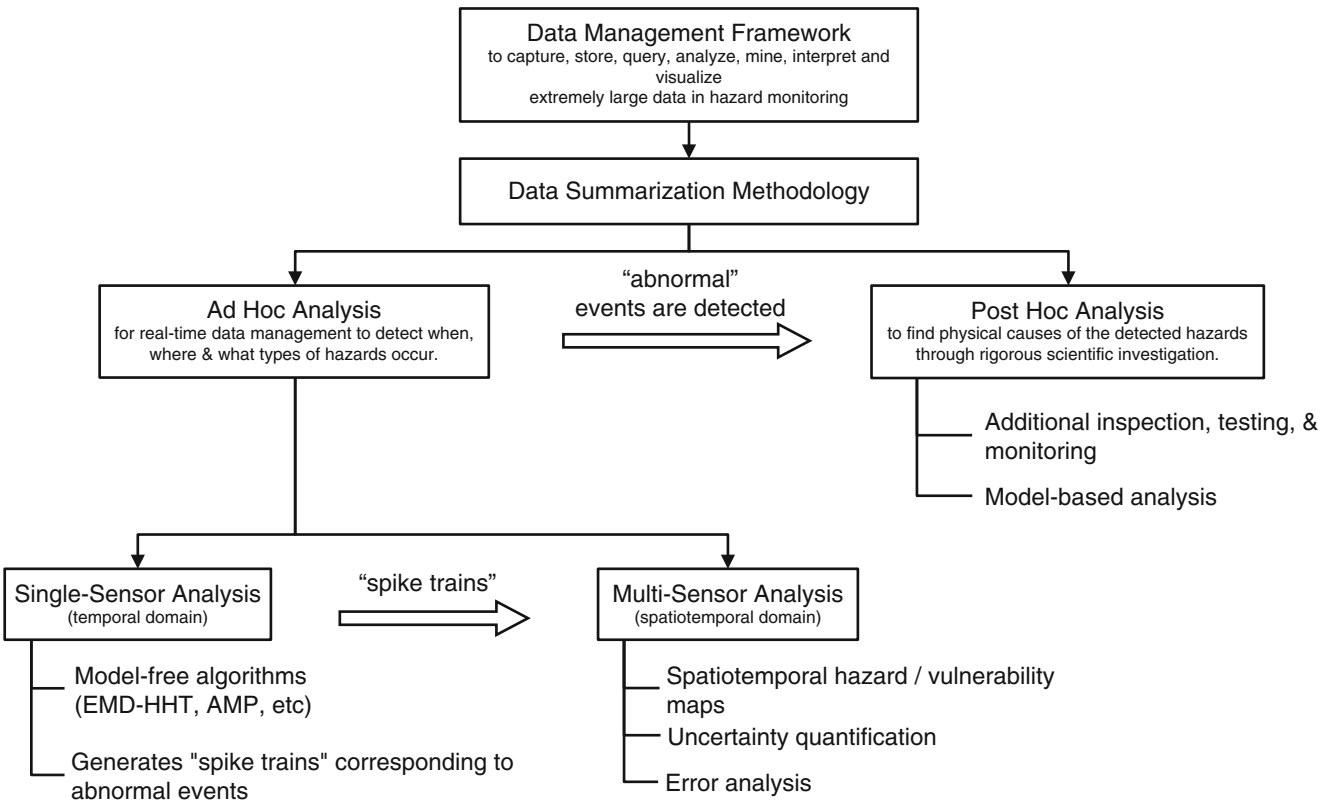

Fig. 29.1 Data management framework for extremely large data from heterogeneous infrastructure network for hazard monitoring

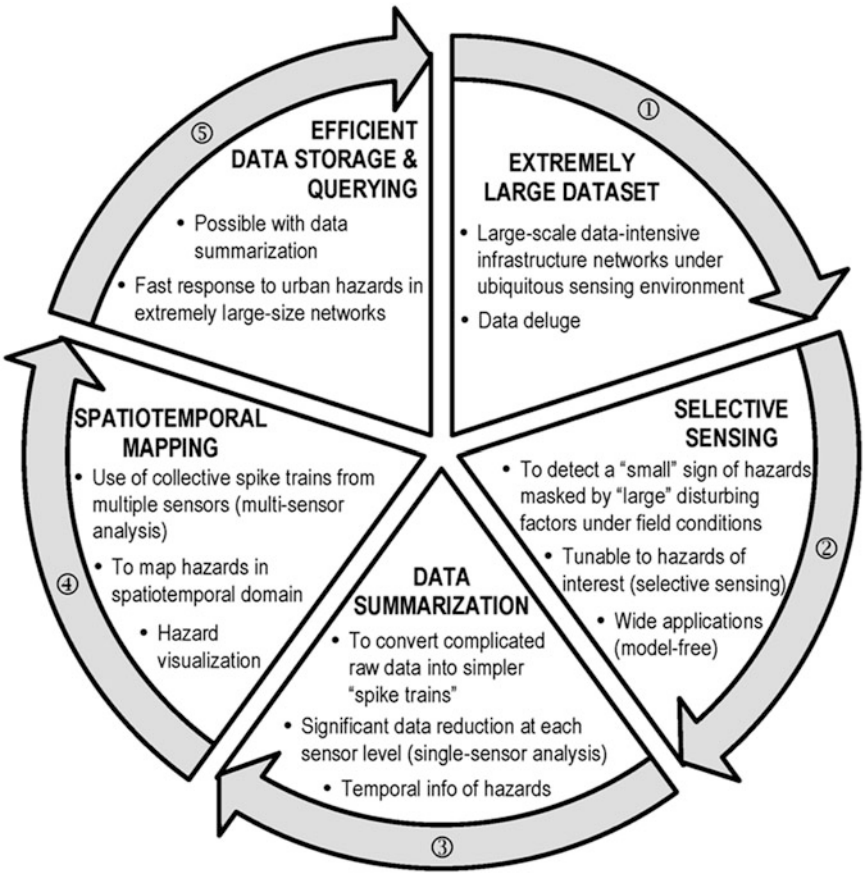

Fig. 29.2 Data summarization methodology associated with the data management framework in Fig. 29.1

In the *multi-sensor* analysis, the spike trains from multiple sensors are collectively processed to map the potential hazards or the corresponding vulnerabilities in spatiotemporal dimensions using known sensor location information. Thus, the dimension of hazard monitoring can be extended from the *temporal* domain to the *spatiotemporal* domain. Combined with well-established Bayesian estimation techniques, uncertainty quantification and error analysis of the detected hazard/vulnerability can be estimated in the spatiotemporal dimension [7].

29.3 AD-HOC Algorithm Using Single-Sensor Data

The Auto Modulating Pattern Detection Algorithm (AMP) is a novel data processing technique that is an extension of the original EMD-HHT algorithm to detect an abnormal event (or behavior) of interest, whose signature is overshadowed by other various dominant effects in nonlinear non-stationary signals [8]. AMP is particularly useful to detect the occurrence of intermittent events in field monitoring conditions that are entangled with a number of other disturbing factors. AMP is designed to utilize a unique property of EMD, known as *mode mixing*, to improve detectability of intermittence in a signal, which can be considered as an "abnormal" event compared to longer-period trends. Since EMD locally traces the highest frequency components in a given signal, the presence of intermittence distorts the shape of the IMF in the current and subsequent shifting processing. Consequently, different modes of oscillations could coexist in a single IMF. The effect of mode mixing due to intermittence is significant in EMD since its basis functions (i.e., intrinsic mode functions) are determined "empirically" from given data. Mode mixing is often considered an undesirable characteristic of EMD since "unique" source separation is preferable for many applications (i.e., one mode mixed with other oscillation modes in original signal is uniquely decomposed into one IMF). Thus, numerous techniques have been developed to reduce the mode mixing effects. AMP, on the contrary, the mode-mixing phenomenon is utilized desirably to improve the detectability of "tiny" intermittent patters from complicated non-stationary signals. Figure 29.1 summarizes the procedures of the AMP algorithm.

AMP improves the detectability of the hazardous events of interest in two ways: (1) the signal-to-noise ratio (SNR) is improved, and (2) the temporal resolution of detection can be tuned by the user to detect various events. As illustrated in

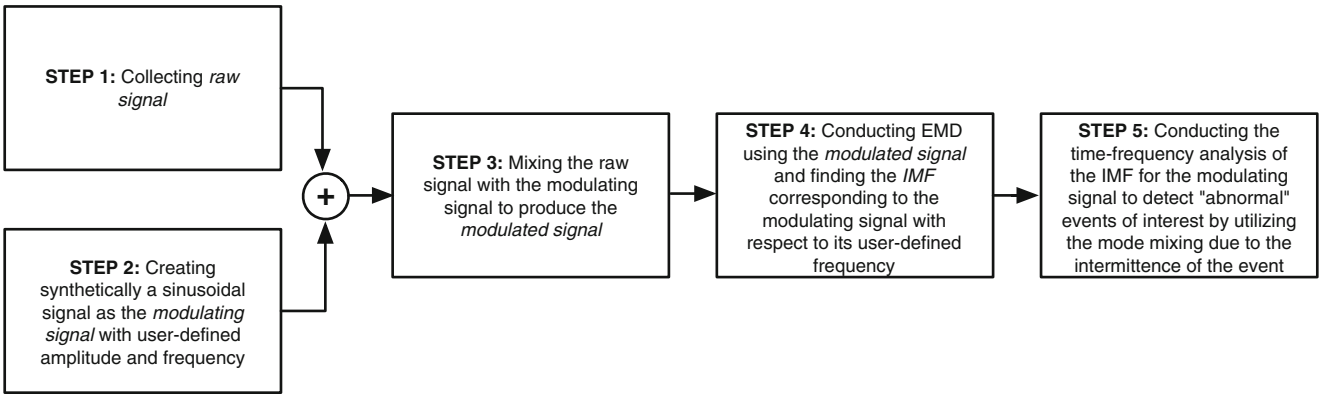

Fig. 29.3 The procedures of the Auto Modulating Pattern Detection Algorithm (AMP) [1]

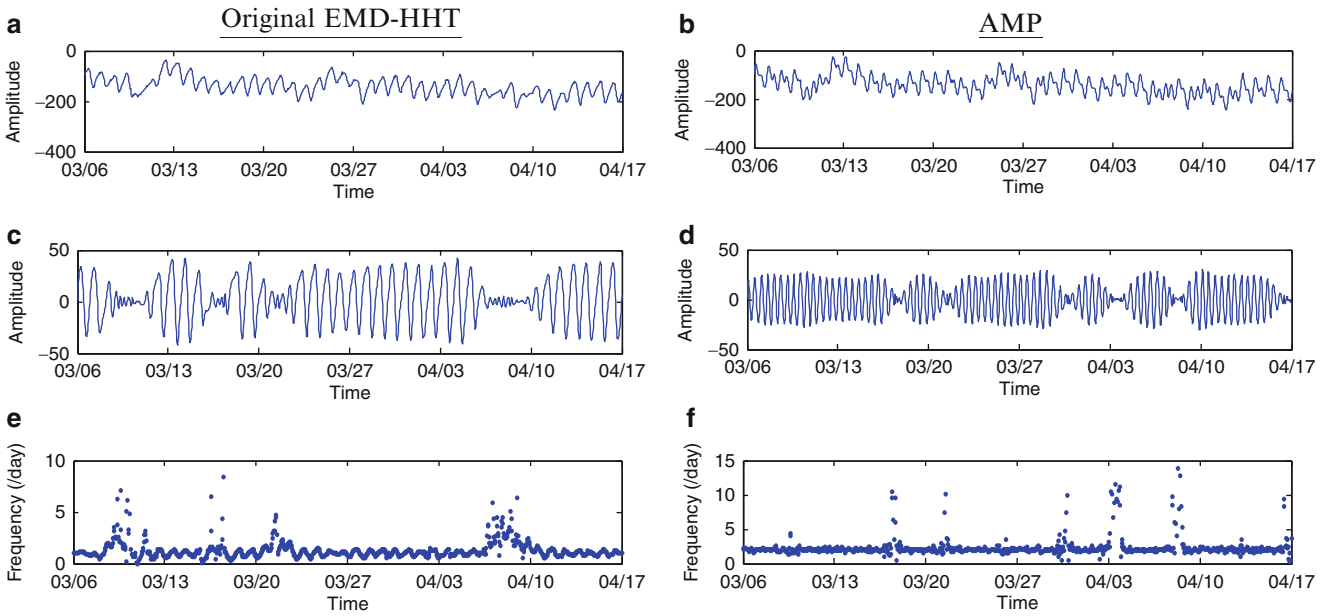

Fig. 29.4 Comparison of the original EMD-HHT and AMP [1]. (**a**) Raw sensor signal, (**b**) modulated signal, (**c**) raw signal after decomposition, (**d**) modulated signal after decomposition, (**e**) raw signal after time-frequency analysis and (**f**) modulated signal after time-frequency analysis

Fig. 29.2, the SNR can be improved by reducing the fluctuation of the baseline frequency or increasing the spike amplitude of the event. Using AMP, the baseline fluctuation decreases with the sinusoidal modulating signal and the spike amplitude increases due to the mode mixing (Fig. 29.3). The temporal resolution is also improved with the sharper peaks after AMP. These effects can be seen in Fig. 29.4.

AMP has successfully been implemented in two different field applications: (1) retaining wall monitoring for *structural safety*, and (2) ice monitoring on road pavement surface for *operational safety* [1]. The results show that AMP is successful as a *single-sensor* approach to detect the various hazards that adversely affect the respective civil systems.

29.4 Vision-Based Approach for Pipeline Leak Detection Using Thermal Video

This section presents the preliminary results of an ongoing study illustrating AMP's effectiveness as a spatiotemporal technique under realistic field conditions. The objective of this study is to (a) validate AMP under realistic field-like environment and (b) extend AMP application from temporal monitoring using a single sensor to spatiotemporal monitoring using multiple or surface sensors. The first part of this section shows the results of a preliminary simulation using MATLAB. The second section describes an experimental plan for pipeline leakage detection using AMP.

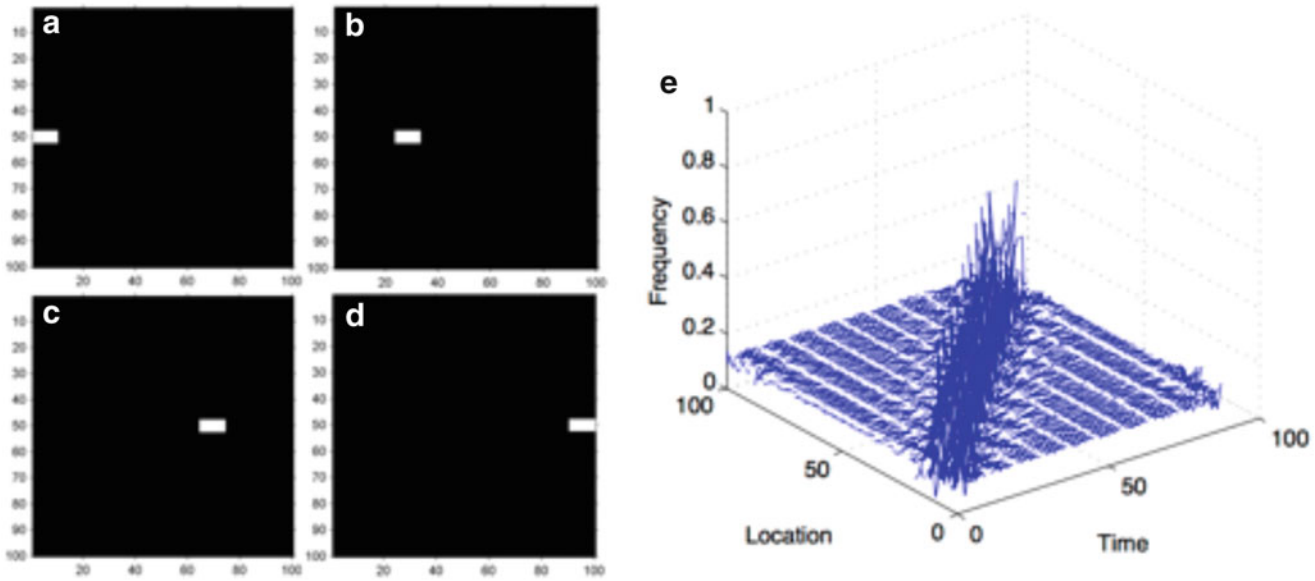

Fig. 29.5 (**a–d**) Video simulation generated using MATLAB showing the movement of a 10 × 10 pixel white block across a 100 × 100 pixel video frame at different times. The simulation lasted for 91 s, (**e**) AMP is implemented on each pixel from (50,1:100) to generate binary spike trains providing temporal and spatial information related to the movement of the block

29.4.1 MATLAB Video Simulation

A preliminary analysis was conducted using a 91 s MATLAB-generated video file to evaluate AMP's effectiveness as a spatiotemporal technique. The video consists of a completely black image with an aspect ratio of 100 × 100 pixels. A 10 × 10 pixel white block was propagated across the video frame at a 1 pixel/s rate. The purpose of this experiment was to detect the location of the block at a precise time as it moved across the video frame. Figure 29.5 depicts the results of the preliminary analysis. As seen in Fig. 29.5a, the white block originates at location (50,0) in the video frame. Figure 29.5b–d shows the movement of the block at different times.

Here, each pixel can be considered to be a "sensor node" with its own unique time history. For example, pixel (50,100) has a magnitude of zero at the time corresponding to Fig. 29.5a. At Fig. 29.5d, however, the value at pixel (50,100) becomes 255, corresponding to the color white. Thus, by utilizing each pixel, a dense sensor network of 100 × 100 "sensors" is simulated.

AMP was applied to the time history of each pixel; the results are shown in Fig. 29.5e. Here, the "location" axis refers to pixels (50, 1:100). As mentioned previously, the block is traveling at 1 pixel/s. A spike is generated each time the block advances to the next pixel. In other words, AMP successfully provides both spatial (pixels) and temporal information relative to the block's movement through the generation of each spike. Also note that if the block is not occupying a pixel at a given time, the signal is represented as a flat baseline. Thus, a spike containing both temporal and spatial information related to the block appears only if the block is occupying the corresponding pixels.

29.4.2 Pipeline Experiment

The Korean Institute of Construction and Technology (KICT) has provided a pipeline circulation system that will be used for the pipeline leakage experiment. A schematic of the pipeline experimental setup is illustrated in Fig. 29.6. The pipeline is attached with a water pump to flow water through the pipe. To experimentally simulate leakages at different places, the pipe will have holes that can be open or closed with watertight bolts.

In general, the surface temperature of the pipe is affected by ambient temperature, water temperature in the pipe, and temperature change due to water leakage:

$$T(t,x) = T_a(t,x) + T_w(t,x) + T_L(t,x) \tag{29.1}$$

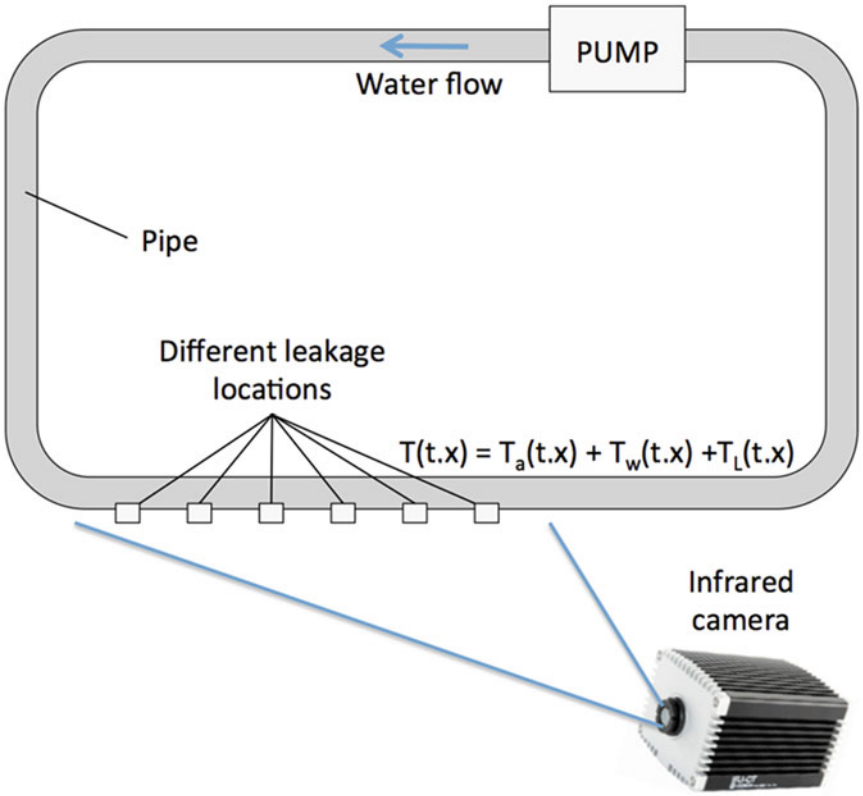

Fig. 29.6 Schematic of the pipeline test setup. The pipeline is attached with a water pump to flow water through the pipe. To experimentally simulate leakages at different places, the pipe will have holes that can be open or closed with watertight bolts. An infrared camera will be used to record a real-time streaming video that measures spatiotemporal temperature signatures on the pipeline surface

where t is time, x is location, T_a is the ambient temperature, T_w is the water temperature, and T_L is the temperature change due to leakage. Therefore, an important objective of the analytical program is to decompose the effect of T_L from the dominant effects of T_a and T_w to detect water leakage over time at different locations.

An infrared camera will be used to record a real-time streaming video that measures spatiotemporal temperature signatures on the pipeline surface. Similar to the MATLAB simulation, AMP will then be applied to each pixel in the infrared video frame to detect the precise time and location of the leakage by generating a spike corresponding to a change in temperature.

Figure 29.7a shows a thermal image of the actual pipeline setup using the infrared camera. Figure 29.7b then shows a thermal image after damage has been introduced in the pipeline. Note that the temperature signature of the pipe has changed after introduction of damage. AMP can then be applied to each pixel in the thermal image to capture the temperature signature changes in real time.

29.5 Conclusions

A comprehensive data management framework associated with an efficient data summarization methodology for extremely large datasets from infrastructure networks for hazard monitoring was presented. The Auto Modulating Pattern Detection Algorithm (AMP) is a novel data processing technique that is an extension of the original EMD-HHT algorithm to detect an abnormal event (or behavior) of interest, whose signature is overshadowed by other various dominant effects in nonlinear non-stationary signals. AMP was previously validated as a *single-sensor* approach for two different field applications: (1) retaining wall monitoring for *structural safety*, and (2) ice monitoring on road pavement surface for *operational safety*. This paper presented an ongoing study that seeks to expand AMP from a *single-sensor* technique that provides temporal information to a *multi-sensor* approach that provides spatiotemporal information related to hazards of interest.

AMP has previously been shown to summarize complicated raw time-history datasets into simpler *binary* "spike trains" for efficient data storage and querying (*data summarization*) at each sensor node; thus, combined with a distributed sensing configuration, the sensor network can be robust. The spike trains were tuned to the hazards of interest, whose detection is significantly disturbed by various known and unknown factors in field conditions (*selective sensing*). The data processing algorithms employed in the above examples can be applied to various monitoring applications for operation and maintenance

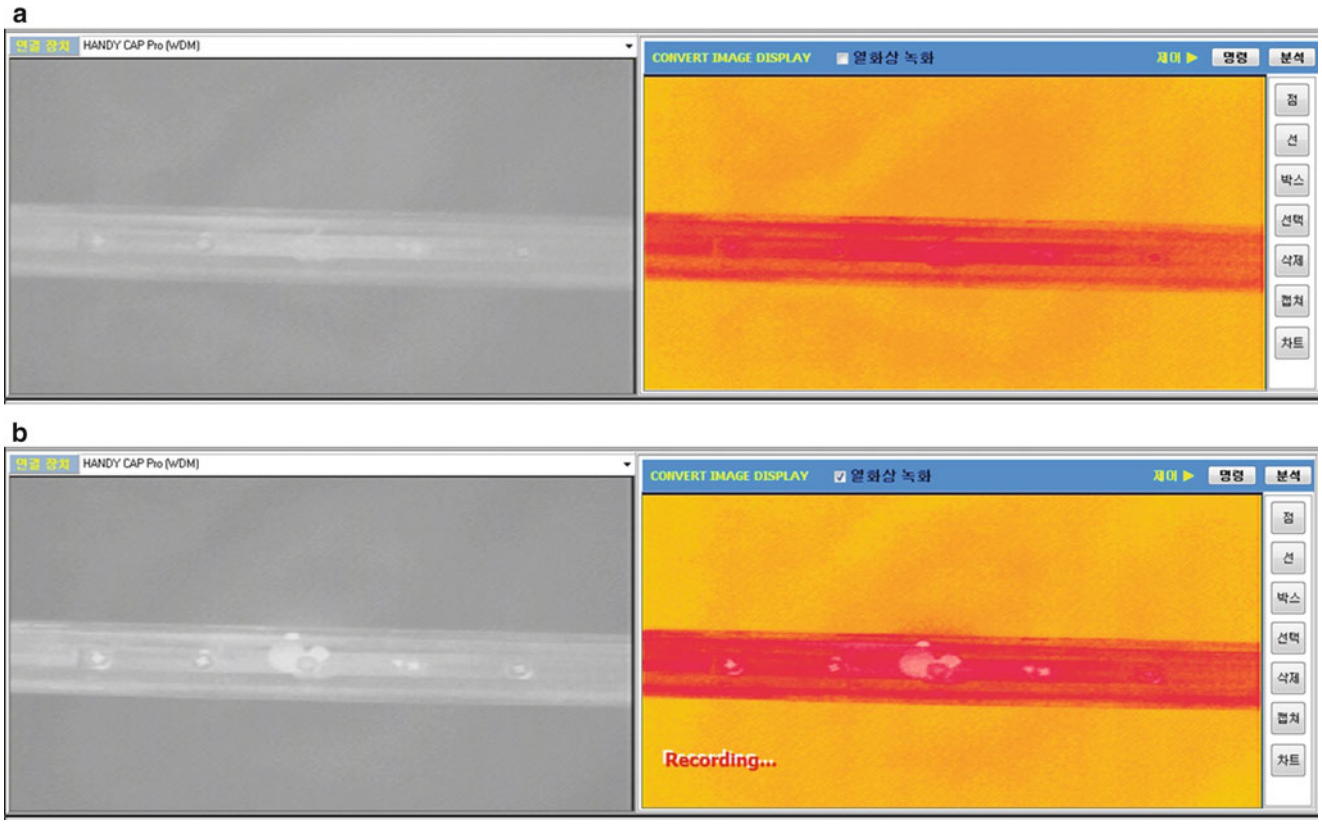

Fig. 29.7 (**a**) Thermal image of the pipeline setup using the infrared camera. (**b**) Thermal image of the pipeline setup after "damage" has been introduced. Note that the temperature signature of the pipeline has slightly changed, corresponding to the damage. AMP can be applied to each pixel of the thermal video to detect these changes in temperature using time-frequency analysis

without modifying the associated data processing algorithms since those algorithms are model-free (*wide applicability*). Also note that the multi-source, multi-modal sensor data collected in different monitoring applications were regulated into the form of the spike trains that have the comparable information of when, where and what type of hazards occur (*data standardization*).

The advantage of having such a data processing technique is that accurate detection of hazards of interest can be made with a very small number of sensors, meaning that sensing costs can be reduced without sacrificing accuracy (*low sensing cost*). This is particularly important in monitoring for extremely large infrastructure networks.

References

1. ASCE (2009) Report card for America's infrastructure, vol 1. ASCE, Washington, DC. doi:10.1126/science.1.3.84
2. Friedland IM, Ghasemi H, Chase SB (2008) The FHWA long-term bridge performance program. In: Fourth US-Taiwan bridge engineering workshop, Princeton. Retrieved from http://mceer.buffalo.edu/research/HighwayPrj/Workshops/2008_US_Taiwan_Workshop/default.asp
3. Saiidi MS, Ghasemi H, Hook J (eds) (2008) FHWA/NSF workshop on future directions for long term bridge performance monitoring, assessment & management, Las Vegas. Retrieved from http://mceer.buffalo.edu/publications/workshop/09-0011/default.asp
4. FHWA (2010) Long-Term pavement performance program: accomplishments and benefits 1989–2009, McLean. Retrieved from http://www.fhwa.dot.gov/publications/research/infrastructure/pavements/ltpp/10071/10071.pdf
5. RITA (2011) Benefits of intelligent transportation systems (ITS). RITA, Washington, DC
6. FHWA (2011) A clear solution for road weather information. U.S. Department of Transportation, Road Weather Management, Washington, DC
7. Yun H-B, Masri SF, Wolfe RW, Benzoni G (2009) Data-driven methodologies for change detection in large-scale nonlinear dampers with noisy measurements. J Sound Vib 322(1–2):336–357. doi:10.1016/j.jsv.2008.11.022
8. Yun H-B, Sundaresan G, Jung Y, Kim J-W (2012) A novel pattern detection algorithm for monitoring snow and ice forming on pavement using surface temperature data only. ASCE J Comput Civ Eng

Chapter 30
Vibration-Based Continuous Monitoring of Tensile Loads in Cables and Rods: System Development and Application

C. Rainieri, D. Gargaro, L. Cieri, and G. Fabbrocino

Abstract The estimation of axial load in prismatic members using flexural vibrations has been investigated for long. Several methods are available in the literature. They take advantage of experimental estimates of the parameters of flexural modes to solve an inverse problem and identify the axial loads in the presence of a number of assumptions and eventual additional unknowns. These methods represent a valuable solution for the estimation of the tensile force in operation. A common drawback is the need to periodically carry out a modal identification test, usually exciting the member by an impact hammer and manually processing the collected dataset. This makes these techniques suitable for periodic checks rather than continuous monitoring. Taking advantage of the most recent developments in the field of Operational Modal Analysis (OMA), an automated system for continuous monitoring of axial loads based on dynamic measurements has been developed.

After a review of the methods for vibration-based axial load identification, the development of the monitoring system for continuous tensile load estimation is discussed in its relevant aspects. Some experimental results obtained after the installation of the monitoring system on one of the cables of a sample arch steel roof are finally illustrated for validation purposes.

Keywords Vibration based structural health monitoring • Automated operational modal analysis • Tensile load estimation • Cables • Rods

30.1 Introduction

The inverse problem of identifying from vibration measurements the tensile axial force in relevant metallic elements for the structural stability, such as cable and tie-rods, has been investigated in several studies. The in-situ assessment of the tensile load is of primary interest for cable-stayed bridges or large steel arches, and for ancient masonry vaults and arches. The main advantage of the indirect determination of cable forces from dynamic tests in operational conditions is related to the possibility to carry out accurate, cheap and fast quality checks in the construction phase (after pre-stressing), and safety checks and structural maintenance over the structure lifespan [1].

In the case of masonry elements (Fig. 30.1), such as vaults and arches, tie-rods ensure the overall stability through an effective connection of the parts constituting the structural element and the elimination of horizontal thrusts. In this context, the accurate evaluation of the axial force in operational conditions makes possible a more accurate, non-invasive safety and performance assessment of ancient masonry structures.

The main differences between the different applications of indirect tensile load estimation are related to the amplitude of vibration (much lower for tie-rods with respect to cables) and the possibility to derive closed form expressions based on simplified assumptions (eventually, with the definition of some correction factors [1]).

C. Rainieri (✉) • D. Gargaro • G. Fabbrocino
DiBT Department, Structural and Geotechnical Dynamics Laboratory StreGa, University of Molise,
Via Duca degli Abruzzi, 86039 Termoli, Italy
e-mail: carlo.rainieri@unimol.it; danilo.gargaro@unimol.it; giovanni.fabbrocino@unimol.it

L. Cieri
S2X s.r.l. – Spin Off Company of the University of Molise, Via Duca degli Abruzzi, 86039 Termoli, Italy
e-mail: info@s2x.it

A. Wicks (ed.), *Structural Health Monitoring, Volume 5: Proceedings of the 32nd IMAC, A Conference and Exposition on Structural Dynamics, 2014*, Conference Proceedings of the Society for Experimental Mechanics Series, DOI 10.1007/978-3-319-04570-2_30,

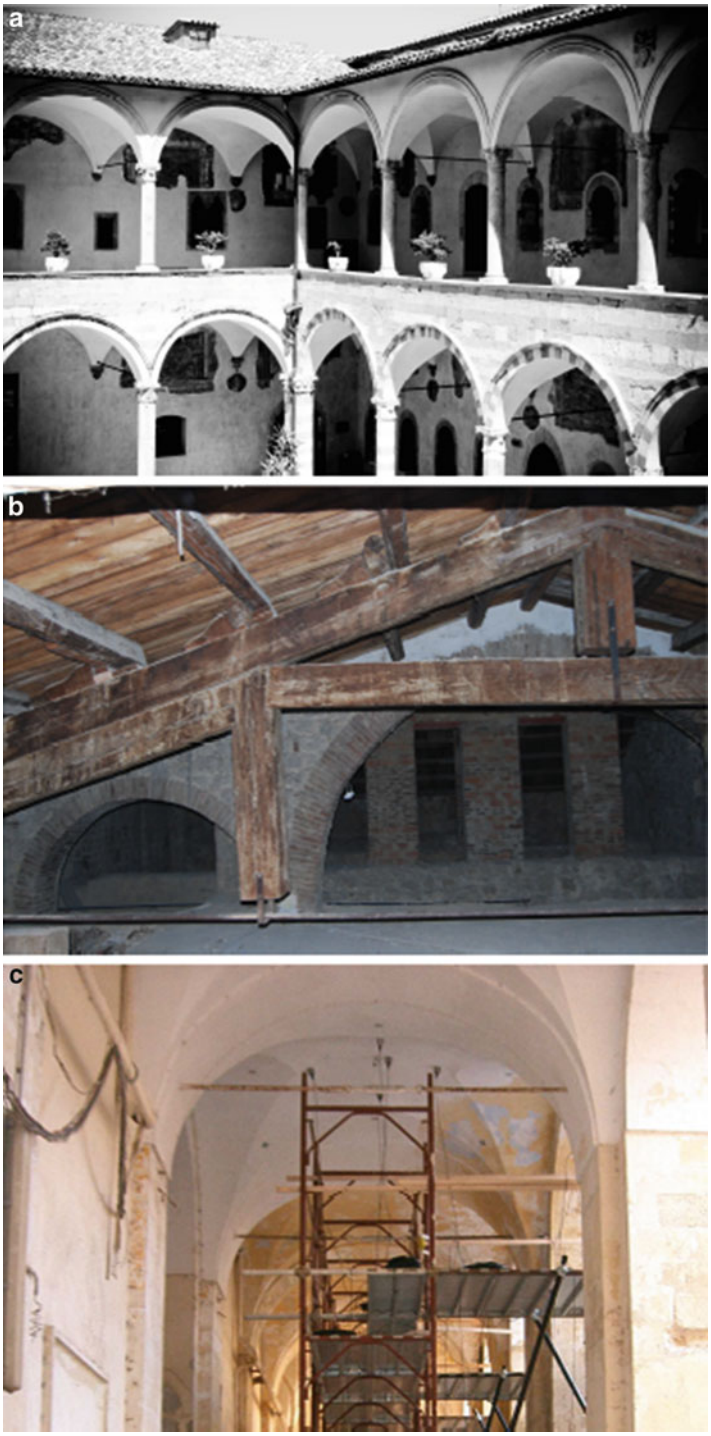

Fig. 30.1 Tie-rods ensure the stability and the elimination of horizontal thrusts in ancient masonry vaults, (**a**) and (**c**) [2], and wooden roofs, (**b**) [3]

Literature review about the available fast and accurate non-destructive methods for the estimation of tensile loads in cables and tie-rods from vibration measurements demonstrates that most of the methods developed over the years usually take advantage of the known input applied by an impact hammer [4–6] and eventually of the results of a numerical model [7]. The application of a known input by an impact hammer is theoretically more important in the case of tie-rods, since the reduced amplitude of vibration requires high performance sensors but the dimensions of the sensors (that determine their sensitivity) must be kept as small as possible to minimize the effect of the added mass on the dynamic behavior of the member.

However, a method able to take into account the effect of the mass of the sensors and the uncertain boundary conditions in the estimation of the tensile load has been recently developed [8], thus making the continuous monitoring of tensile loads in tie-rods based on vibration measurements more attractive.

On the other hand, the increasing availability of high performance accelerometers and the fast development of output-only modal identification techniques [9, 10] have revealed Operational Modal Analysis (OMA) as a profitable alternative for the estimation of tensile loads from dynamic measurements [11].

One of the main limitations to the extensive application of vibration-based tensile load estimation techniques in the field of Structural Health Monitoring (SHM) was represented by the lack of reliable and fully automated output-only modal identification procedures. However, significant research efforts have been spent in recent years in the automation of OMA methods. An extensive review about automated modal identification and tracking methods for SHM purposes can be found in the literature [12, 13]. An original hybrid approach to the automated output-only modal identification has also been recently proposed [14] to overcome the typical drawbacks of the available automated OMA methods [12], such as:

- threshold based peak and physical pole detection,
- need for a preliminary calibration phase at each new application,
- static settings of thresholds and parameters which may be unsuitable to track the natural changes in modal properties of structures due to damage or environmental effects,
- sensitivity to noise, problems of false or missed identification.

In the present paper, some methods for vibration-based axial load identification are briefly reviewed and the development of the monitoring system for continuous tensile load estimation is discussed in its relevant aspects. Some experimental results obtained after the installation of the monitoring system on one of the cables of a sample arch steel roof are finally illustrated for validation purposes.

30.2 Automated Output-Only Modal Identification

The developed system for tensile load estimation and monitoring takes advantage of an algorithm (Fig. 30.2) for automated output-only modal identification, which is based on the combination of different OMA techniques in order to simplify the analysis and interpretation of the stabilization diagram.

The modal parameter estimation is basically carried out according to the Stochastic Subspace Identification (SSI) method [15, 16], but the preliminary Blind Source Separation (BSS) [17], operated according to the Second Order Blind Identification (SOBI) [18, 19] procedure, simplifies the identification of the physical poles. In fact, as a result of the BSS phase, the raw data associated to the measured structural response are transformed into sources which can be well-separated (they show the contribution of a single mode to the structural response), not well-separated (noise or minor contributions from other modes could be superimposed to the contribution of the main mode) or noise sources [19].

The correlation of the sources can be interpreted as a free decay response of the equivalent Single Degree Of Freedom (SDOF) system corresponding to a mode, and covariance-driven modal identification algorithms, such as SSI, can process it. The preliminary, approximate separation of the modal contributions by BSS simplifies the analysis of the data and the interpretation of the stabilization diagram, since the modal information is extracted from the individual sources, which theoretically include information about one mode at the time (however, in the practice, noise or minor contributions from other modes can be present), and not the multivariate time series of raw data.

The analysis of the source correlations one-by-one according to the SSI method provides the physical poles for the individual mode present in each univariate time series and the spurious poles are easily separated by the physical ones by means of clustering techniques [20] and mode validation criteria. In fact, taking into account the stability of the physical information with respect to the spurious poles, the largest cluster is the one collecting the physical poles.

The final values of natural frequency and damping ratio for the identified modes are obtained by a sensitivity analysis with respect to the number of block rows i in SSI, for a fixed value of the maximum model order in the stabilization diagram.

The cluster characterized by the minimum variance of the estimates when i ranges in a certain interval with a certain step Δi is then selected as the one providing the best estimate of the modal parameters for a given structural mode [21]. Mode shape estimates are finally obtained from Singular Value Decomposition (SVD) of the output Power Spectral Density (PSD) matrix at the previously estimated frequency of the mode [22].

The key feature of the algorithm is the absence of any analysis parameter to be tuned at each new monitoring application. In fact, the results are insensitive to the setting of the two parameters governing the Joint Approximate Diagonalization (JAD)

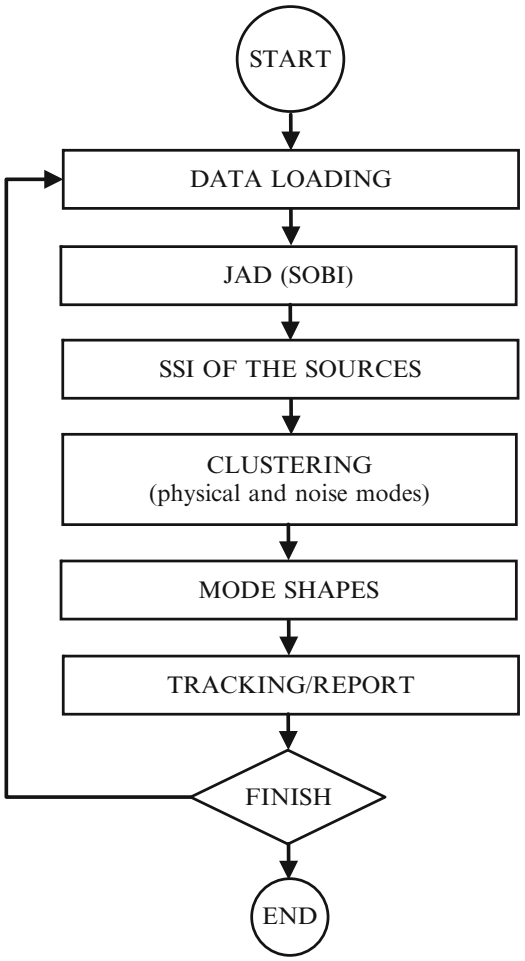

Fig. 30.2 Flowchart of the automated modal identification algorithm

[23] for source extraction, while the influence of the number of block rows is taken into account by sensitivity analyses. Moreover, the parameters governing the JAD play a primary role in the control of response time and computational burden.

The performance of the proposed algorithm in terms of accuracy and reliability of estimates has been investigated through extensive tests based on simulated data and real measurements [14]. The analysis of the obtained results has pointed out that the algorithm carries out automated output-only modal identification in a very robust way. In fact, a success rate larger than 99 % has been obtained.

Very accurate natural frequency and damping ratio estimates have been obtained for different values of the signal-to-noise ratio. Moreover, with an appropriate choice of sensor locations, it has been proved that the automated modal identification algorithm is able to accurately identify the modal parameters of the structure under investigation even in the case of a few measurement points.

30.3 Indirect Estimation of Axial Loads from Vibration Data

The solution of an inverse problem yields the tensile load from estimates of the dynamic parameters of bending modes of the cable or tie-rod under investigation. In the most general case of uncertain boundary conditions, the experimental identification of the tensile load is based on measurements of the mode shape of the member in at least five positions. In fact, from the equation governing the dynamic behavior of a beam with uniform section subjected to a constant axial tensile force [24]:

$$EI\frac{\partial^4 v(x,t)}{\partial x^4} + N\frac{\partial^2 v(x,t)}{\partial x^2} + \rho\frac{\partial^2 v(x,t)}{\partial t^2} = 0 \tag{30.1}$$

where EI represents the bending stiffness, ρ is the mass per unit length, v is the transversal displacement and N the tensile force, the partial differential equation given by Eq. (30.1) can be separated into two ordinary differential equations, providing natural frequencies and mode shapes respectively. In particular, the shapes of the vibrating beam are given by:

$$\phi(x) = C_1 \sin(\alpha x) + C_2 \cos(\alpha x) + C_3 \sinh(\beta x) + C_4 \cosh(\beta x) \tag{30.2}$$

where

$$\alpha^2 = \frac{N}{2EI}\left(\sqrt{1 + \frac{4\omega^2 \rho EI}{N^2}} - 1\right), \quad \beta^2 = \frac{N}{2EI}\left(\sqrt{1 + \frac{4\omega^2 \rho EI}{N^2}} + 1\right). \tag{30.3}$$

The coefficients C_1, C_2, C_3 and C_4 are determined from the known modal displacement in four points of the beam, while the last modal displacement is used, together with the estimate of the natural frequency of the mode, to compute the tensile load N. The number of unknowns and, therefore, of measurement points can be reduced if the boundary conditions are known. More details can be found elsewhere [4, 6].

When the influence of the bending stiffness EI and the end constraints is negligible with respect to the tensile load, the problem is reduced to that of the wire, whose frequencies are given in analytical form as follows:

$$f_n = \frac{n}{2l}\sqrt{\frac{N}{\rho}} \quad n = 1, 2, \ldots \tag{30.4}$$

where f_n in the natural frequency of the n-th mode of the wire and l its length. In this case, the experimental estimation of one natural frequency of the wire is sufficient to recover the tensile load N. A correction factor can be also applied to take into account the negligible but not null influence of bending stiffness and support conditions in real cases [1].

When only the rotational stiffness of the supports is negligible with respect to the bending stiffness EI, the problem is that of the pre-stressed pinned beam and the analytical expression of the natural frequency of the n-th mode is:

$$f_n = \frac{n}{2}\sqrt{\frac{n^2\pi^2 EI}{\rho l^4} + \frac{N}{\rho l^2}} \quad n = 1, 2, \ldots \tag{30.5}$$

In this case there are two unknown variables, N and EI, and two natural frequency estimates are necessary to solve the inverse problem. This has the following closed form solution:

$$N = 4\rho l^2\left(\frac{j^2 f_i^2}{i^2(j^2 - i^2)} - \frac{i^2 f_j^2}{j^2(j^2 - i^2)}\right), \quad EI = \frac{4\rho l^4}{\pi^2}\left(\frac{f_j^2}{j^2(j^2 - i^2)} - \frac{f_i^2}{i^2(j^2 - i^2)}\right) \tag{30.6}$$

where i and j represent the number of the modes, with $i < j$.

All the previously described methods for load estimation have been implemented into a software developed in LabView environment and integrated into the SHM system described in the next section.

30.4 The System for Continuous Monitoring of Axial Loads from Vibration Data

The developed SHM system for continuous monitoring of tensile loads in cables and tie-rods consists in a distributed measurement system based on programmable hardware and wireless modules, and in a centralized data processing system for the estimation of the tensile loads in the monitored elements starting from records of their dynamic response to ambient vibrations. The architecture of the system is depicted in Fig. 30.3.

A small number of piezoelectric accelerometers are installed on each cable. They are wired to a wireless data acquisition module from National Instruments™ and the distributed data acquisition modules (at least one module for each monitored element) are managed by a software developed in LabView environment.

The collected raw data are stored into a local MySQL database. Each monitored element has an individual table of its own in the database for data storage. When the number of monitored elements is very large, the data acquisition task can be fragmented among a number of local servers.

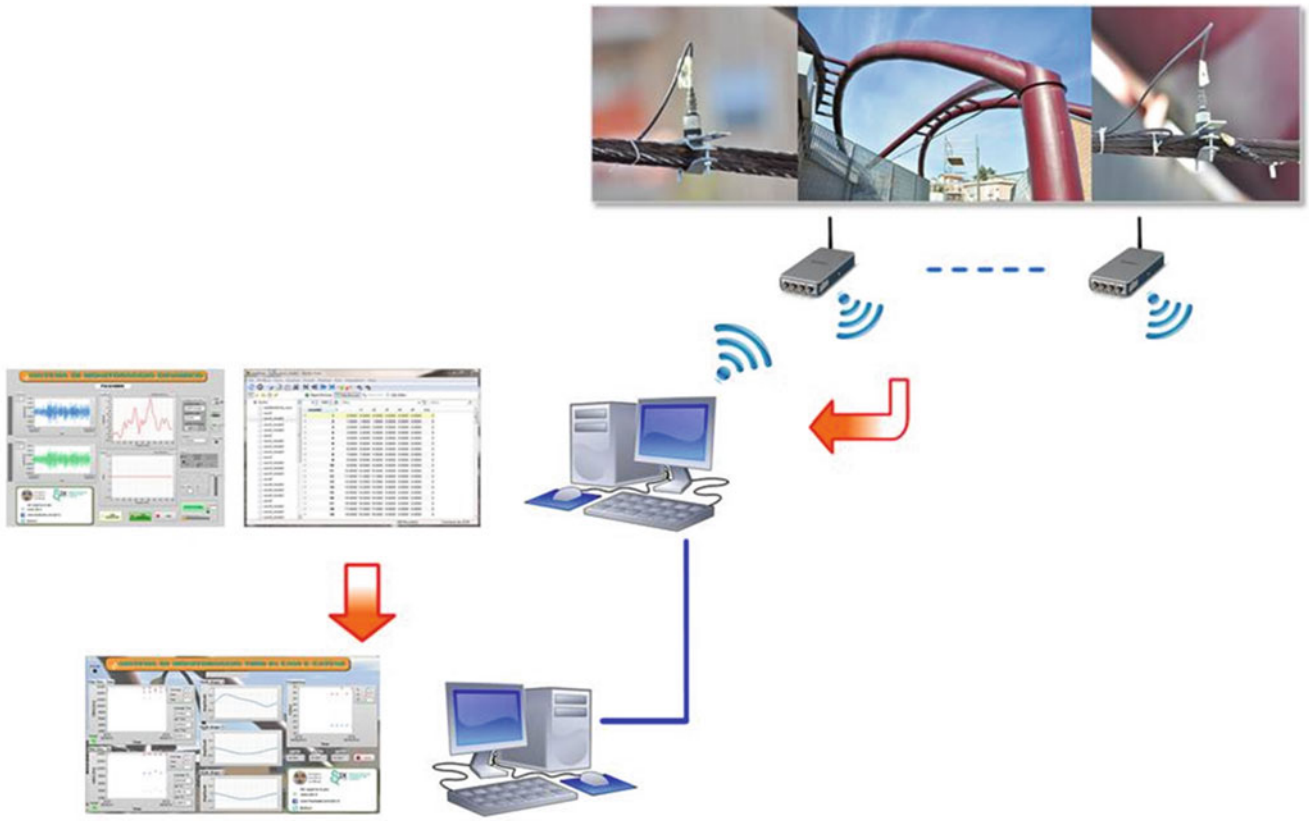

Fig. 30.3 Architecture of the axial force monitoring system

A centralized server collects time histories of the dynamic response of predefined durations and carries out the automated identification of the modal parameters. For each monitored element, the system provides estimates of the dynamic properties of its fundamental modes (natural frequencies, damping ratios and mode shapes, stored in a dedicated database) according to the previously described algorithm, and estimates of the tensile load according to the most appropriate procedure among those outlined in the previous section.

A prototype of the SHM system has been installed to monitor the tensile load in one of the cables of a sample arch steel roof (Fig. 30.4).

A set of experimental results obtained after the installation of the monitoring system are briefly illustrated for validation purposes.

Estimates of the tensile load close to the design value in operational conditions have been obtained. One-day monitoring results are shown in Fig. 30.5. Slight variations of the tensile load during the day can be observed. They can be probably addressed to environmental factors.

In fact, comparing the load estimates with the values of temperature in the city recorded by the local meteorological station, slight increases in the tensile load when the temperature decreases can be observed, and vice versa. However, for a more detailed characterization of the effect of environmental factors, the monitoring system has to be complemented by additional sensors, such as temperature sensors. Nevertheless, results are encouraging. A long-term validation of the performance of the system is in progress.

Fig. 30.4 Installation of the prototype of monitoring system on one of the cables of a sample arch steel roof

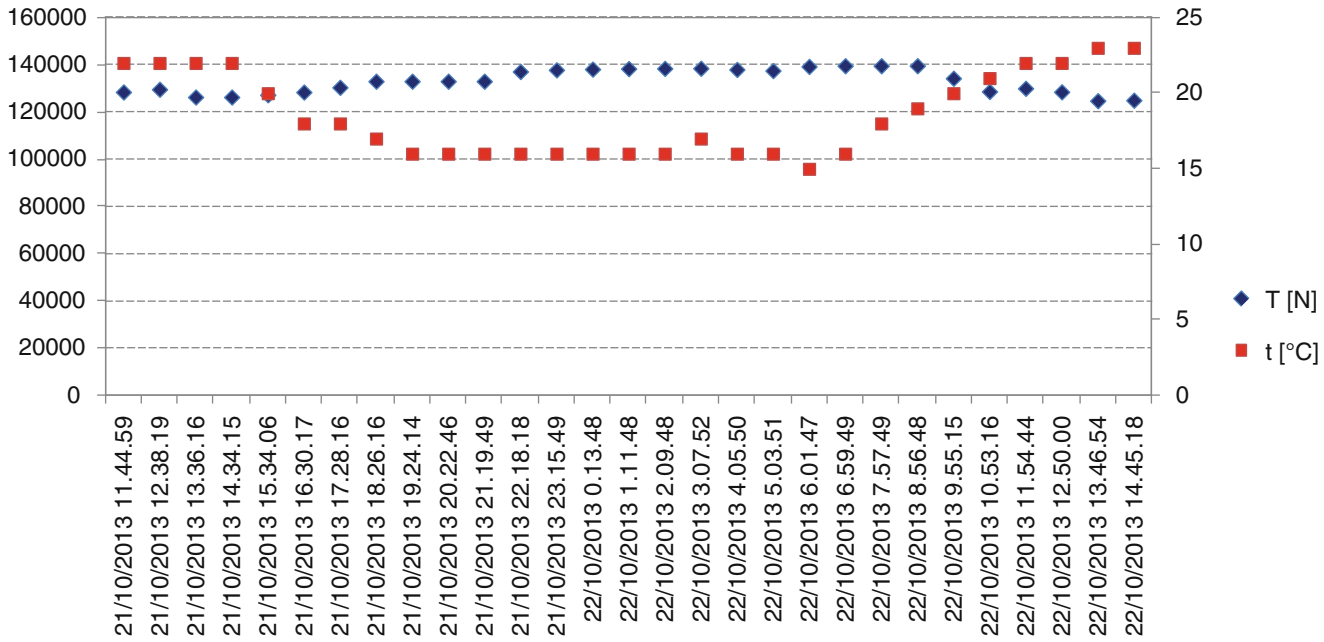

Fig. 30.5 One-day monitoring results—time window: 21.10.2013 (11:45) to 22.10.2013 (14:45)

30.5 Conclusions

The development of a reliable and robust algorithm for the accurate and fully automated estimation of the modal properties of civil structures under operational conditions enabled the development of a monitoring system for the continuous estimation of the tensile load in cables and tie rods.

It is based on the combination of a hybrid algorithm for automated output-only modal parameter identification and different procedures for tensile load estimation. The system can be profitably applied to both cable-stayed bridges or large steel arches, and ancient masonry vaults and arches.

The distributed architecture for data acquisition makes the developed SHM system fully scalable, so that it can be applied to monitor a large number of elements at the same time.

Encouraging results have been obtained from its application to a real test-case, pointing out the need to complement the system with sensors for the characterization of the effects of environmental factors on load estimates.

Acknowledgments The present work is carried out within the activities of AT2–LR 2–Task 3 of the ReLuis-DPC Executive Project 2010–2013, rep. 823. Support of ReLuis Consortium is therefore gratefully acknowledged.

References

1. Wenzel H, Pichler D (2005) Ambient vibration monitoring. Wiley, Chichester, p 291
2. Conte C, Rainieri C, Aiello MA, Fabbrocino G (2011) On-site assessment of masonry vaults: dynamic tests and numerical analysis. GEOFIZIKA 28:127–143
3. Marcari G, Fabbrocino G, Laorenza C, Cosenza E (2008) Structural analysis of timber connections of the Caserta Royal Palace. In: Proceedings of the 6th international conference on structural analysis of historic constructions (SAHC 08), Bath
4. Tullini N, Laudiero F (2008) Dynamic identification of beam axial loads using one flexural mode shape. J Sound Vib 318:131–147
5. Lagomarsino S, Calderini C (2005) The dynamical identification of the tensile force in ancient tie-rods. Eng Struct 27:846–856
6. Rebecchi G, Tullini N, Laudiero F (2011) Identificazione dello sforzo normale in elementi strutturali mediante prove dinamiche. In: Atti del Convegno Nazionale ANIDIS L'ingegneria sismica in Italia, Bari (in Italian)
7. Amabili M, Carra S, Collini L, Garziera R, Panno A (2010) Estimation of tensile force in tie-rods using a frequency-based identification method. J Sound Vib 329:2057–2067
8. Maes K, Peeters J, Reynders E, Lombaert G, De Roeck G (2013) Identification of axial force in beam members by local vibration measurements. J Sound Vib 332:5417–5432
9. Zhang L, Brincker R, Andersen P (2005) An overview of operational modal analysis: major development and issues. In: Brincker R, Moller N (eds) Proceedings of the 1st international operational modal analysis conference, Copenhagen, pp 179–190
10. Rainieri C, Fabbrocino G (2011) Operational modal analysis for the characterization of heritage structures. GEOFIZIKA 28:109–126
11. Lardies J, Ta M-N (2011) Modal parameter identification of stay cables from output-only measurements. Mech Syst Signal Process 25:133–150
12. Rainieri C, Fabbrocino G (2010) Automated output-only dynamic identification of civil engineering structures. Mech Syst Signal Process 24(3):678–695
13. Rainieri C, Fabbrocino G, Cosenza E (2011) Near real-time tracking of dynamic properties for standalone structural health monitoring systems. Mech Syst Signal Process 25(8):3010–3026
14. Rainieri C, Fabbrocino G (2013) Accurate damping estimation by automated OMA procedures. Conf Proc Soc Exp Mech Ser 39(4):1–9
15. Van Overschee P, De Moor B (1996) Subspace identification for linear systems: theory – implementation – applications. Kluwer Academic, Dordrecht, p 254
16. Peeters B (2000) System identification and damage detection in civil engineering. Ph.D. Thesis, Katholieke Universiteit Leuven, Leuven
17. Ans B, Hérault J, Jutten C (1985) Adaptive neural architectures: detection of primitives. In: Proceedings of COGNITIVA'85, Paris, pp 593–597
18. Belouchrani A, Abed-Meraim K, Cardoso JF, Moulines E (1997) A blind source separation technique using second-order statistics. IEEE Trans Signal Process 45:434–444
19. Poncelet F, Kerschen G, Golinval JC, Verhelst D (2007) Output-only modal analysis using blind source separation techniques. Mech Syst Signal Process 21:2335–2358
20. Tan P-N, Steinbach M, Kumar V (2006) Introduction to data mining. Pearson Addison-Wesley, Reading, p 769
21. Rainieri C, Fabbrocino G, Cosenza E (2010) Some remarks on experimental estimation of damping for seismic design of civil constructions. Shock Vib 17(4–5):383–395
22. Brincker R, Zhang L, Andersen P (2000) Modal identification from ambient responses using frequency domain decomposition. In: Proceedings of the 18th SEM international modal analysis conference, San Antonio
23. Cardoso JF, Souloumiac A (1996) Jacobi angles for simultaneous diagonalization. SIAM J Matrix Anal Appl 17:161–164
24. Clough RW, Penzien J (1993) Dynamics of structures, 2nd edn. McGraw-Hill, New York, p 738

Chapter 31
Non-Model-Based Crack Identification Using Measured Mode Shapes

Y.F. Xu, W.D. Zhu, J. Liu, and Y.M. Shao

Abstract Mode shapes (MSs) have been extensively used to detect structural damage. This paper presents two new non-model-based methods that use measured MSs to identify embedded horizontal cracks in beams. The proposed methods do not require any a priori information of the associated undamaged beams. Curvatures and continuous wavelet transform (CWT) coefficients of differences between a measured MS of a damaged beam and values of the associated polynomial that fits it are processed to yield curvature damage indices (CDIs) and CWT damage indices (CWTDIs), respectively, at each measurement point. It is shown that the polynomial can well approximate the measured MS and the associated curvature mode shape of the undamaged beam, provided that the fitted MS is extended beyond the boundaries of the beam and the order of the polynomial is properly chosen. The proposed CDIs of a measured MS are presented in multiple resolutions to alleviate negative effects caused by measurement noise, and the crack tips can be located near regions with high values of the indices. It is shown that the CWT of a measured MS with the n-th order Gaussian wavelet has a shape resembling that of the n-th order spatial derivative of the MS. The crack tips can also be located using the CWTs of the aforementioned MS differences with the second- and third-order Gaussian wavelets near the peaks and valleys of the resulting CWTDIs, respectively, which are presented in multiple scales. An finite element model of an acrylonitrile butadiene styrene uniform cantilever beam with an embedded horizontal crack is constructed to validate the proposed methods. Numerical crack identification can successfully identify the horizontal crack by locating its tips.

Keywords Non-model-based damage identification • Continuous wavelet transform • Curvature mode shape • Modal analysis • Embedded crack

31.1 Introduction

Vibration-based damage detection has become one of the major research topics in the application of structural dynamics in the past decades. Various methodologies have been developed to detect, locate, and characterize damage in structures based on vibration measurements, since the physical properties of a structure, i.e., mass, stiffness, and damping, directly determine the modal characteristics of the structure, i.e., natural frequencies, mode shapes (MSs), and modal damping ratios [1]. One criterion to categorize the methodologies is whether a model of the structure being monitored is needed. If it is needed, the methodology is model-based; otherwise, it is non-model-based. Model-based methods are capable of detecting the locations and extent of damage in structures with a small number of measurements [2, 3].

Y.F. Xu • W.D. Zhu (✉)
Department of Mechanical Engineering, University of Maryland, Baltimore Country, Baltimore, MD 21250, USA.
e-mail: yxu2@umbc.edu; wzhu@umbc.edu

J. Liu
Department of Mechanical Engineering, University of Maryland, Baltimore Country, Baltimore, MD 21250, USA

State Key Laboratory of Mechanical Transmission, Chongqing University, Chongqing 400030, People's Republic of China
e-mail: cqulj@163.com

Y.M. Shao
State Key Laboratory of Mechanical Transmission, Chongqing University, Chongqing 400030, People's Republic of China
e-mail: ymshao@cqu.edu.cn

A. Wicks (ed.), *Structural Health Monitoring, Volume 5: Proceedings of the 32nd IMAC, A Conference and Exposition on Structural Dynamics, 2014*, Conference Proceedings of the Society for Experimental Mechanics Series, DOI 10.1007/978-3-319-04570-2_31,

However, model-based methods could have problems due to inaccuracy of the model, environmental and other non-stationary effects on measurements, and lack of data in suitable frequency ranges [4]. In fact, it is difficult to construct models of most existing structures with high accuracy. Hence, methods that only analyze MSs or operating deflection shapes (ODSs) without the aid of a model can be good alternatives to model-based methods to locate damage, and they are non-model-based ones [5]. Since MSs are not sensitive to damage of small extent, curvatures of MSs, or curvature mode shapes (CMSs), are used to locate damage [6]. Differences between CMSs of a damaged beam and an undamaged one are localized in the region of damage and increase as the damage size increases [7]. A gapped-smoothing method was used to locate delamination in a composite beam by inspecting the smoothnesses of CMSs [8], and the method was extended to use broad-band ODS data [9]. It was applied to locate damage in a beam using a global fitting method, where generic MSs were used to fit measured MSs of a damaged beam [10], and the global fitting method was extended to ODS data to conduct damage detection on beams and plates [11]. A crucial aspect of the damage detection methods using CMSs is calculation of spatial derivatives of MSs. Optimal spatial sampling intervals were proposed for CMSs to avoid undersampling and oversampling of MS measurements, both of which have adverse effects on the quality of damage detection [12]. A novel Laplacian scheme was developed and experimentally validated in [13] to locate a delamination zone in a composite beam using associated modal curvatures with multiple resolutions. Besides CMSs, wavelet transforms of MSs can also be used in damage detection, since they are sensitive to localized abnormalities in MSs and can be presented in multiple scales. Cracks were identified in beams using a "symmetrical 4" wavelet; the position of a crack was accurately detected with the aid of a beam model [14]. Damage in the form of cracks in beams and thickness reductions in plates was identified using continuous wavelet transform (CWT), which was manifested as peaks in associated CWT coefficients [15]. The CWT of differences between MSs of a damaged beam and those of the associated undamaged one can be used to locate cracks with high sensitivities [16].

Beams with horizontal embedded cracks are studied in this work; they are similar to composite beams with delaminations. Natural frequencies of beams and plates will decrease if delaminations occur; the larger a delamination, the larger the reductions of the natural frequencies [17]. Free vibration analysis of a laminated beam was studied using a layerwise theory. Effects of the lamination angle, location, and size, and the number of delaminations on the natural frequencies of beams were addressed in [18]. A generalized variational principle was used to formulate equations of motion and associated boundary conditions for the free vibration of a delaminated composite beam; the coupling effect of longitudinal and bending vibrations was shown to be significant for the calculated natural frequencies and MSs [19]. Modal tests were conducted in [20] using polyvinylidene fluoride film sensors and piezoceramic patches with sine sweep actuation; backpropagation neural network models were developed using results from the beam theory and used to predict a delamination size. A spatial wavelet analysis was used in [21] to process static deformation profiles of cantilever beams to numerically and experimentally locate delaminations; the deformation profiles obtained by dense measurements were smoothed before applying the spatial wavelet analysis.

Two non-model-based crack identification methods are proposed in this work. CMSs are presented in multiple resolutions in order to reduce the adverse effects of measurement noise. The relationship between CWTs and CMSs is shown. Polynomials of MS-dependent orders are used to fit MSs of a damaged beam, which can be considered as MSs of the associated undamaged one; the fitted MSs are virtually extended beforehand beyond the boundaries of the beam in order to enhance the similarity of the CMSs obtained from the resulting polynomials to those of the associated undamaged ones near the boundaries. Differences between MSs of the damaged beam and those from the resulting polynomials are used to yield two damage indices: the curvature damage index (CDI) and the CWT damage index (CWTDI) with a Gaussian wavelet function. A cantilever beam made of acrylonitrile butadiene styrene (ABS) with an embedded horizontal crack is modeled, and the crack tips can be successfully located using the two proposed damage indices; they are located near the peaks of CDIs and CWTDIs with the second-order Gaussian wavelet, and the valleys of CWTDIs with the third-order Gaussian wavelet. The proposed methods can not only identify embedded horizontal cracks but also edge cracks and slant cracks.

31.2 Damage Identification Using CDIs and CWTDIs

The finite element (FE) model of a cantilever beam made of steel with an elastic modulus $E = 210\,\text{GPa}$ and Poisson's ratio $\mu = 0.3$, with an embedded horizontal crack, is constructed using FE software. The dimensions of the beam and the crack are shown in Fig. 31.1. An analytical model of the undamaged beam with the same material properties and dimensions as the damaged beam is also constructed for comparison purposes. In this section, MSs of the damaged and undamaged beams, denoted by f^d and f^u, respectively, are used to illustrate the proposed methodologies. The j-th MSs of the damaged and undamaged beams are denoted by $f^{d,j}$ and $f^{u,j}$, respectively, and the MSs are normalized so that their maximum absolute values are one. White noise is added to the MSs with a signal-to-noise ratio (SNR) of 60 to simulate measurement noise.

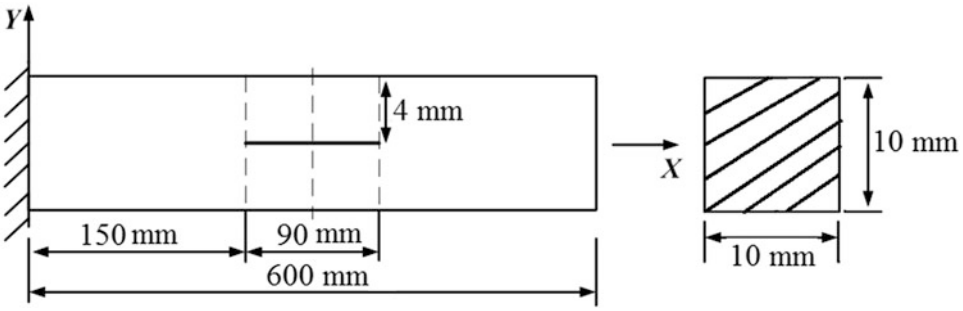

Fig. 31.1 Dimensions of a cantilever beam with an embedded horizontal crack

31.2.1 Curvature Mode Shapes

A CMS is the second-order spatial derivative of a MS. It can be used to identify structural damage because changes in CMSs are localized in damage regions [7], which can be manifested by the gapped-smoothing method [8, 9]. Assuming the measurement points are equally spaced, the CMS at a measurement point i can be calculated from the MS f using the central finite difference scheme of second-order accuracy:

$$f_i'' = C_i = \frac{f_{i-1} - 2f_i + f_{i+1}}{h^2} \tag{31.1}$$

where f_i is the MS at the measurement point i, and h is the distance between two neighboring measurement points. The gapped-smoothing method assumes that the CMSs are smooth in undamaged regions and unsmooth elsewhere. A crucial aspect of the gapped-smoothing method is that the minimum size of the detectable damage is determined by the density of the measurement grid since the effects of damage on CMSs are localized. Hence, a dense measurement grid becomes necessary to detect damage of a small size. However, measurement noise of MSs will become dominant in the resulting CMSs with a spatially dense measurement grid, since the difference between noise-free MSs at two neighboring measurement points is small compared with that between noisy MSs at the two points. Figure 31.2a shows that measurement noise is amplified when the CMSs are calculated using Eq. (31.1), and they cannot be used to identify damage.

In order to reduce adverse effects of measurement noise, the central finite difference scheme in Eq. (31.1) is modified to be

$$f_i'' = C_i^m = \frac{f_{i-m} - 2f_i + f_{i+m}}{(mh)^2} \tag{31.2}$$

where m is the number of measurement points from point i to either end of the derivative interval, which determines the width of the derivative interval and the resolution of the resulting derivative. This formulation is similar to the à trous Laplace operator in [13], and enables observation of CMSs with different resolutions: the lower the value of m, the higher the resolution of the resulting derivative. Note that Eq. (31.1) is the case with $m = 1$. Figure 31.2b–d show that $\left(f^{d,4}\right)''$ can be obtained with a lower noise level with a larger m. It can be seen from Fig. 31.2b–d that while the CMSs at a same point slightly vary for different m values, the singularities of the CMSs near the crack tips are retained. In practice, a suitable value of m can be obtained by increasing it from one until CMSs with a low noise level are observed.

31.2.2 Continuous Wavelet Transform

A linear transformation is defined by

$$W_w f(u,s) = \int_{-\infty}^{+\infty} f(x) w_{u,s}^*(x) dx \tag{31.3}$$

where W_w denotes the linear transformation operator with the weight function

$$w_{u,s}(x) = \frac{1}{\sqrt{s}} w\left(\frac{x-u}{s}\right) \tag{31.4}$$

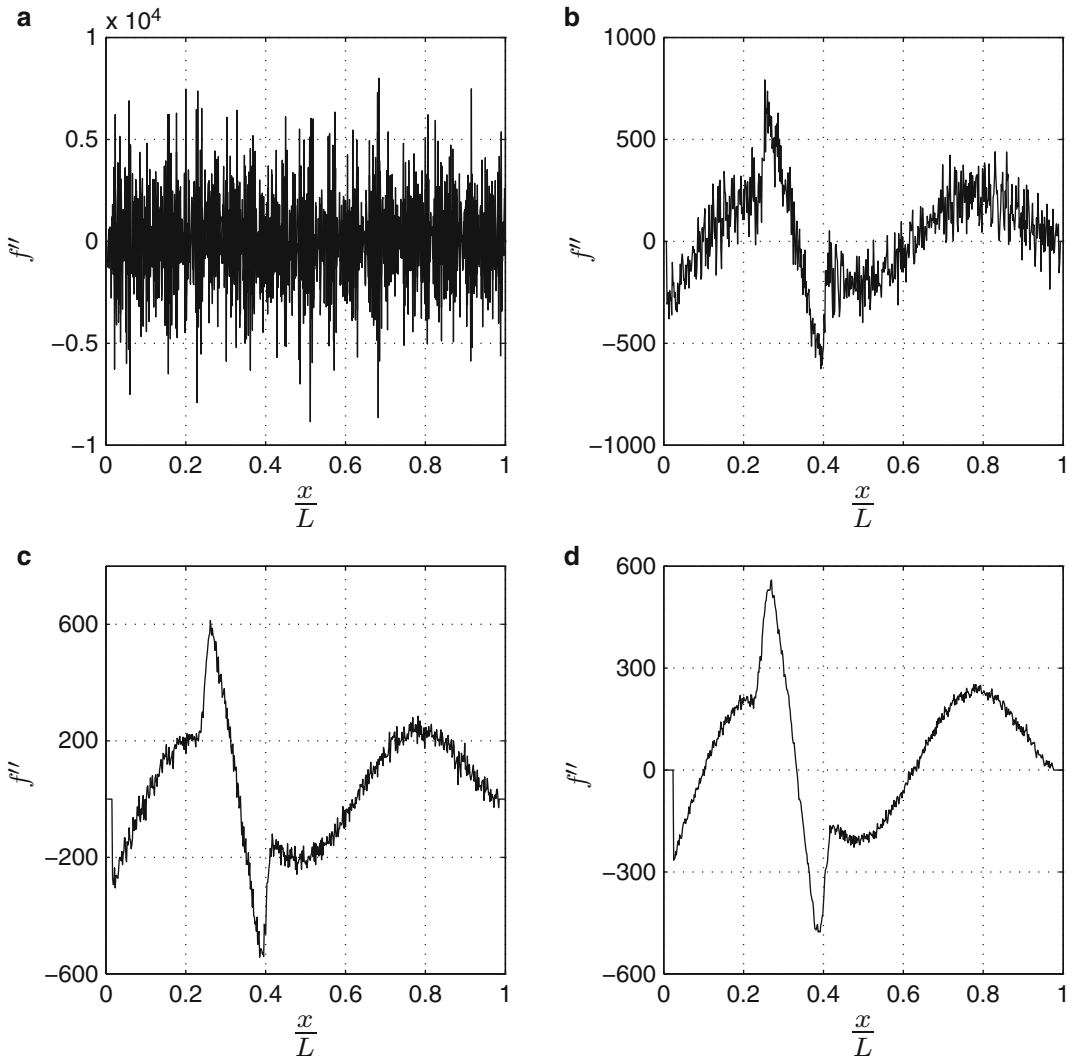

Fig. 31.2 (**a**) The CMS of the fourth mode of the damaged beam from Eq. (31.1), and those of the mode with different values of m: (**b**) $m = 5$, (**c**) $m = 10$, and (**d**) $m = 15$

in which u and s are the spatial and scale parameters of the weight function, respectively, and the superscript $*$ denotes complex conjugation. In this work, the weight function is defined in the real domain, and the superscript $*$ can be dropped. When the weight function is a wavelet function ψ, the transformation in Eq. (31.3) becomes a CWT [22]. The wavelet function ψ has a zero average, i.e.,

$$\int_{-\infty}^{+\infty} \psi(x)dx = 0 \tag{31.5}$$

and $W_\psi f(u, s)$ measures the variation of $f(x)$ in the neighborhood centered at u with an interval size proportional to s. The L^2-norm of $\psi(x)$ is one, i.e.,

$$\|\psi\|_2 = \left(\int_{-\infty}^{+\infty} |\psi(x)|^2 \, dx\right)^{\frac{1}{2}} = 1 \tag{31.6}$$

The CWT can be considered as a convolution:

$$W_\psi f = \frac{1}{\sqrt{s}} \int_{-\infty}^{+\infty} f(x)\bar{\psi}\left(\frac{u-x}{s}\right)dx = f \star \bar{\psi} \tag{31.7}$$

where $\bar{\psi}(x) = \psi(-x)$.

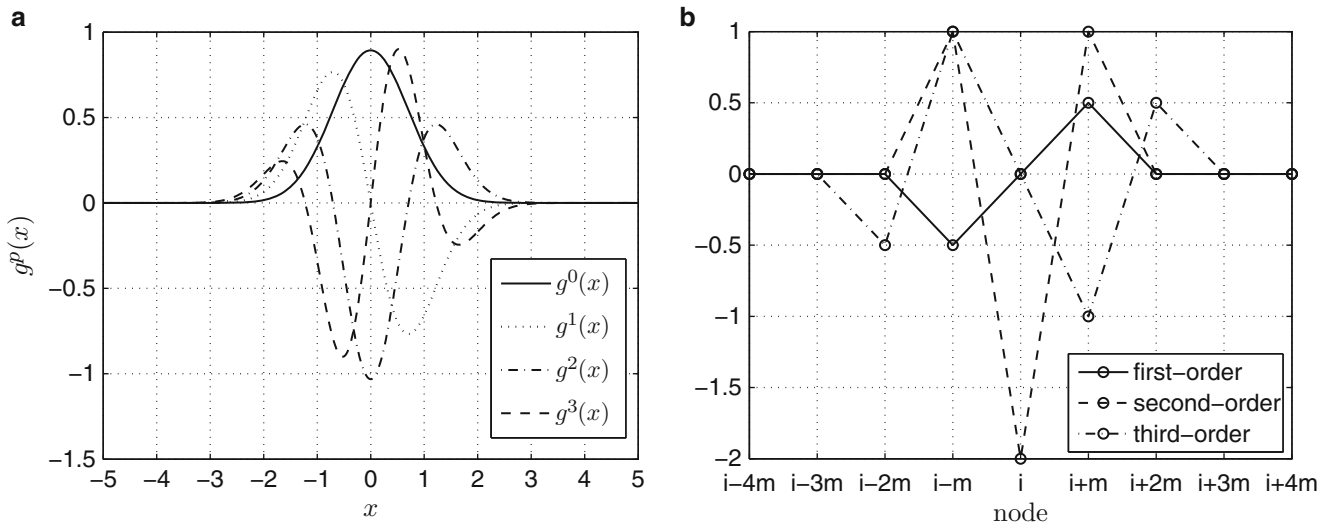

Fig. 31.3 (**a**) The Gaussian function $g^0(x)$ and the Gaussian wavelet functions of orders one through three, and (**b**) the finite difference coefficients of the central finite difference scheme of second-order accuracy for the first- through third-order derivatives

In this work, a p-th-order ($p \geqslant 1$) Gaussian wavelet function, denoted by $g^p(x)$, is used as the wavelet function, since it is smooth and differentiable, and can capture local changes in a transformed function [23]. Gaussian wavelet functions are derived from the Gaussian function $g^0(x)$ with a unit L^2-norm:

$$g^0(x) = \sqrt[4]{\frac{2}{\pi}} e^{-x^2} \tag{31.8}$$

The p-th-order Gaussian wavelet function can be written as

$$g^p(x) = C_p \left[g^0(x)\right]^{(p)} \tag{31.9}$$

where C_p is a constant such that $g^p(x)$ has a unit L^2-norm. The relationship between $\bar{g}^q(x)$ and $\bar{g}^{p+q}(x)$ can be expressed by

$$\frac{d^p \bar{g}^q}{dx^p} = \frac{C_q}{C_{p+q}\,(-1)^p}\,\bar{g}^{p+q} \tag{31.10}$$

The Gaussian function $g^0(x)$ and the Gaussian wavelet functions of orders one through three are shown in Fig. 31.3a.

Due to the commutative property of the convolution, i.e., $f \star \bar{\psi} = \bar{\psi} \star f$, a differentiation operation on $W_\psi f$ with respect to u can be expressed by

$$\frac{\partial^q}{\partial u^q} W_\psi f = f \star \bar{\psi}^{(q)} = \bar{\psi} \star f^{(q)} = f^{(q)} \star \bar{\psi} \tag{31.11}$$

Equation (31.11) shows that the differentiation operation on $\bar{\psi}$ in the CWT can be transferred onto f if $\bar{\psi}$ is differentiable. Hence, the variation of f'' can be measured without calculating f'':

$$W_\psi f'' = f'' \star \bar{\psi} = f \star \bar{\psi}'' \tag{31.12}$$

and the CWT can be used to inspect the variation of f'' and identify damage, which can reduce the adverse effects of measurement noise on $f(x)$. Similarly, when the $(p+q)$-th-order Gaussian wavelet function is used in the CWT, one has [23]

$$W_{g^{p+q}} f = f \star \bar{g}^{p+q}_{u,s} = \frac{C_q}{C_{p+q}\,(-s)^p} f^{(p)} \star \bar{g}^q_{u,s} = \frac{C_q}{C_{p+q} s^p} W_{(-1)^p g^q} f^{(p)} \tag{31.13}$$

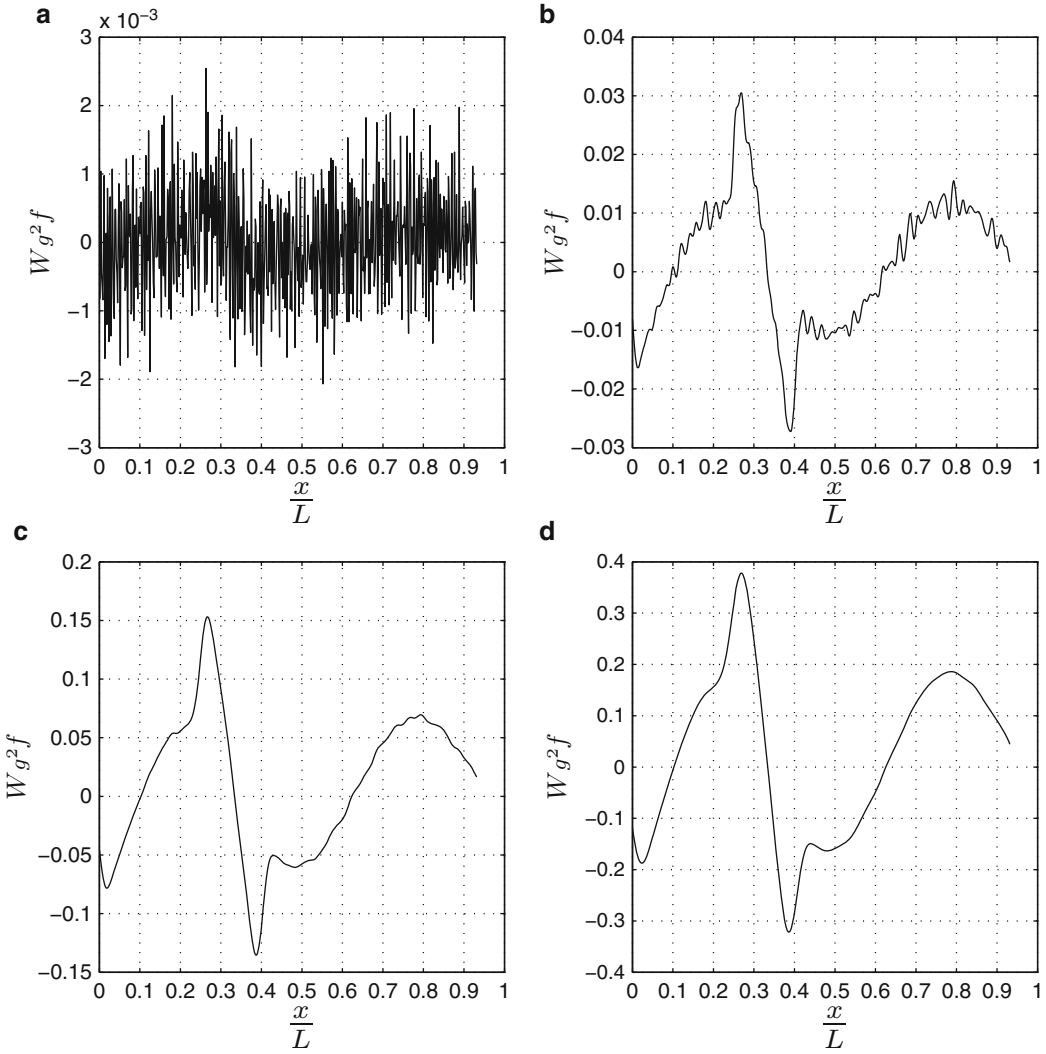

Fig. 31.4 The CWTs of the fourth measured MS of the damaged beam with $g^2(x)$ of different scales as the wavelet functions with: (**a**) $s = 1$, (**b**) $s = 5$, (**c**) $s = 10$, and (**d**) $s = 15$

When $q = 0$, Eq. (31.13) becomes

$$W_{g^p} f = \frac{C_0}{C_p s^p} f^{(p)} \star \left[(-1)^p \bar{g}^0{}_{u,s}\right] = \frac{C_0}{C_p s^p} W_{(-1)^p g^0} f^{(p)} = \frac{C_0}{C_p s^p} W_{g^0}\left[(-1)^p f^{(p)}\right] \tag{31.14}$$

Equation (31.14) shows that the CWT of f with the p-th order Gaussian wavelet function has the same shape as the linear transformation of $(-1)^p f^{(p)}$ with g^0 as the weight function, and they differ by a factor $\frac{C_0}{C_p s^p}$. The linear transformation of f with g^0 as the weight function is equivalent to applying a Gaussian filter g^0 to f, which smoothes the shape of f. Hence, $W_{g^p} f$ yields the smoothed shape of $(-1)^p f^{(p)}$. Figure 31.3b shows the finite difference coefficients of the central finite difference scheme of second-order accuracy for the first- through third-order derivatives. Note that the coefficients should be divided by $(mh)^k$, where k is the order of the derivatives. It can be observed that the plot of the coefficients of the p-th-order derivative in Fig. 31.3b resembles that of $(-1)^p g^p(x)$ in 31.3a; the latter is smoother than the former, and they have the same numbers of vanishing moments.

The CWTs of $f^{d,4}$ with $g^2(x)$ and $g^3(x)$ of different scales as the wavelet functions are shown in Figs. 31.4 and 31.5, respectively. In Fig. 31.4b–d, the shapes of the CWTs resemble those of the CMSs shown in Fig. 31.2b–d, where the two peaks are caused by the two crack tips. However, the peaks caused by the crack tips cannot be found in the case with $g^3(x)$ as

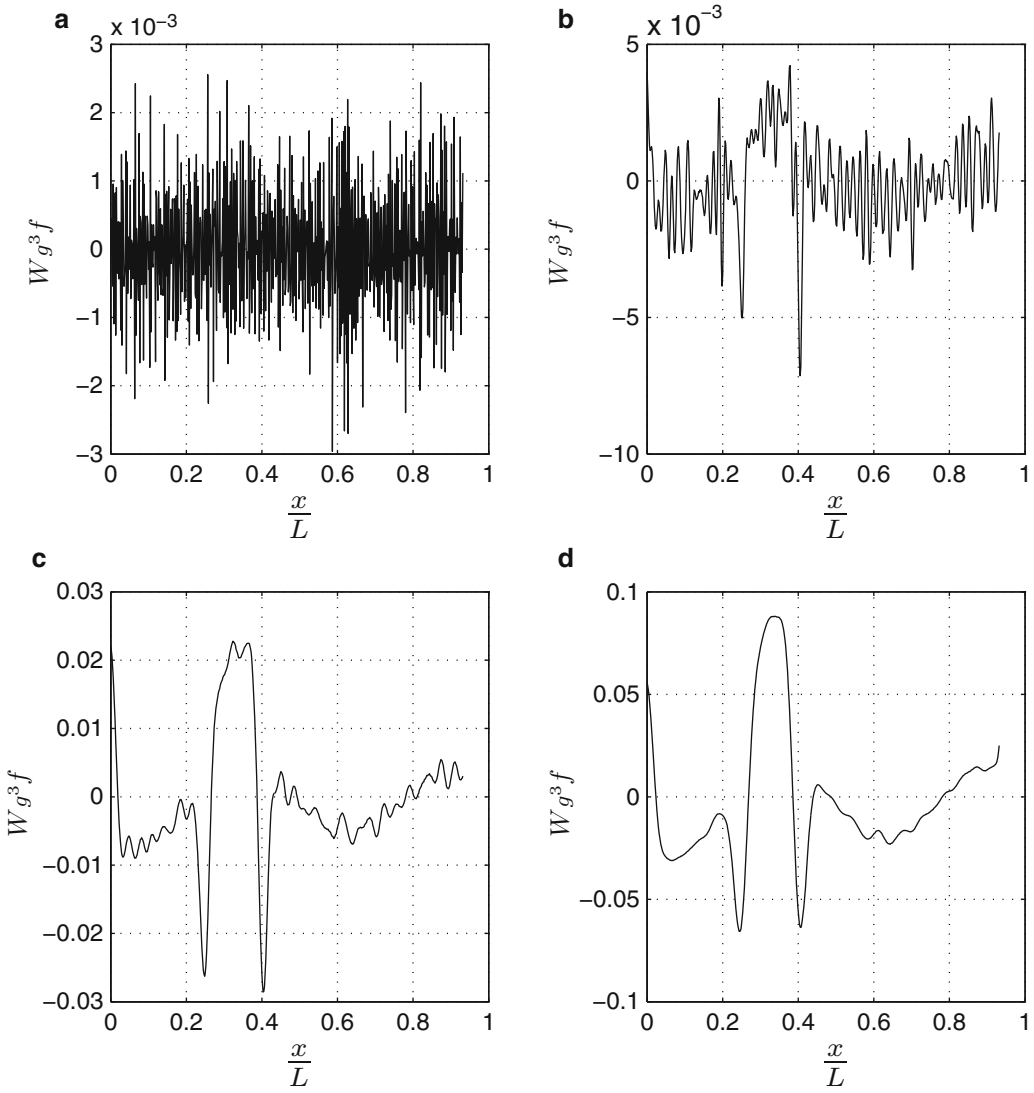

Fig. 31.5 The CWTs of the fourth measured MS of the damaged beam with $g^3(x)$ of different scales as the wavelet functions with: (**a**) $s = 1$, (**b**) $s = 5$, (**c**) $s = 10$, and (**d**) $s = 15$

the wavelet function, as shown in Fig. 31.5, where the CWT coefficients are zero near the crack tips, which can be explained by using Eq. (31.13):

$$W_{g^2} f = f \star \bar{g}^2_{u,s} = \frac{C_0}{C_2 s^2} f'' \star \bar{g}^0_{u,s} \tag{31.15}$$

$$W_{g^3} f = f \star \bar{g}^3_{u,s} = \frac{C_1}{C_3 s^2} f'' \star \bar{g}^1_{u,s} = -\frac{C_0}{C_3 s^3} f''' \star \bar{g}^0_{u,s} \tag{31.16}$$

The CWTs of f with $g^2_{u,s}(x)$ and $g^3_{u,s}(x)$ as the wavelet functions have the same shapes as the linear transformations of f'' and f''' with $g^0_{u,s}(x)$ and $-g^0_{u,s}(x)$ as the wavelet functions, respectively. Since f''' is the derivative of f'', $f''' = 0$ at local extrema of f''. Hence, the crack tips are located in the neighborhoods of the zero values of the CWTs of f with $g^3(x)$ as the wavelet function rather than their peak values.

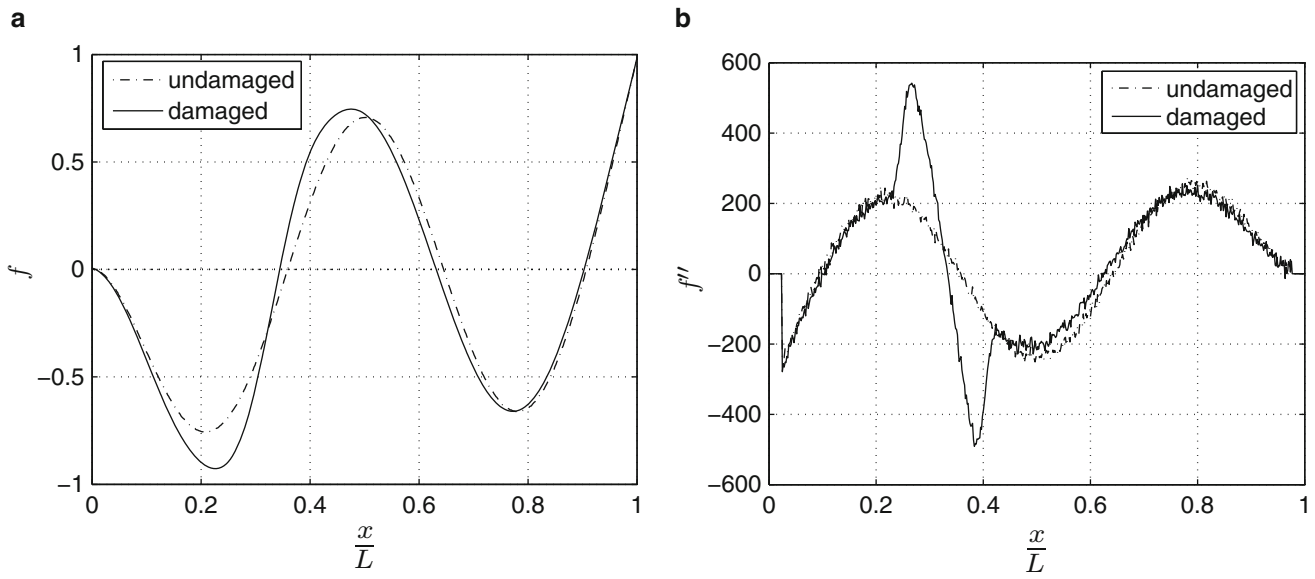

Fig. 31.6 (**a**) The fourth MSs of the undamaged and damaged beams, and (**b**) the associated CMSs with $m = 15$

31.2.3 Identification of an Embedded Horizontal Crack

When the MSs of the associated undamaged beam are known a priori, an embedded horizontal crack can be identified using the CMSs or the CWTs of the measured MSs. The reason is that local features caused by the crack occur along with global trends of the CMSs and the CWTs of the measured MSs of the damaged beam, and the measured MSs of the undamaged beam can provide references of the global trends to identify the crack. The gapped-smoothing method in [8] and [9] is able to locally diminish the global trends in a pointwise way by calculating a damage index, which is the squared value of the difference between the CMS at a measurement point and the corresponding value calculated from the polynomial fitting the CMS at four neighboring points of the measurement point. For each measurement point, a relatively large damage index indicates a high possibility of existence of damage. However, for a dense measurement grid, the CMSs of a damaged beam can be locally smooth, and there may not be large differences between the CMSs and those from local polynomial fits, and measurement noise can affect the application of the method.

When the MSs of both the damaged and undamaged beams are known, similar to the gapped-smoothing method, the CDI for a measured MS at a measurement point i with the resolution parameter m can be defined by

$$\delta_i^m = \left| \left(f_i^d\right)'' - \left(f_i^u\right)'' \right|^2 = \left[\frac{\triangle_{d,u} f_{i+m} + \triangle_{d,u} f_{i-m} - 2\triangle_{d,u} f_i}{(mh)^2} \right]^2 \tag{31.17}$$

where $\triangle_{d,u} f_i = f_i^d - f_i^u$ is the difference between f^d and f^u at point i. Figure 31.6a shows the plots of $f^{u,4}$ and $f^{d,4}$. Figure 31.6b shows the plots of $\left(f^{u,4}\right)''$ and $\left(f^{d,4}\right)''$ with $m = 15$; two extra peaks can be observed in the neighborhoods of the crack tips in $\left(f^{d,4}\right)''$, as opposed to $\left(f^{u,4}\right)''$. The CDIs associated with $f^{d,4}$ are shown in Fig. 31.7; two peaks can be clearly observed in the neighborhoods of the crack tips.

The CWTDI for a measured MS with the wavelet function ψ with scale s at a measurement point i can be defined by

$$\varpi_i^s = \left| W_\psi \triangle_{d,u} f(u_i, s) \right| \tag{31.18}$$

The plots of the CWTDIs for $f^{d,4}$ with the wavelet functions $g^2(x)$ and $g^3(x)$ with $s = 15$ are shown in Fig. 31.8a,b, respectively, whose peaks and valleys are located near the crack tips, respectively. However, the two damage indices defined above require use of MSs of the associated undamaged beam f^u as baseline information, which are not always available in practice.

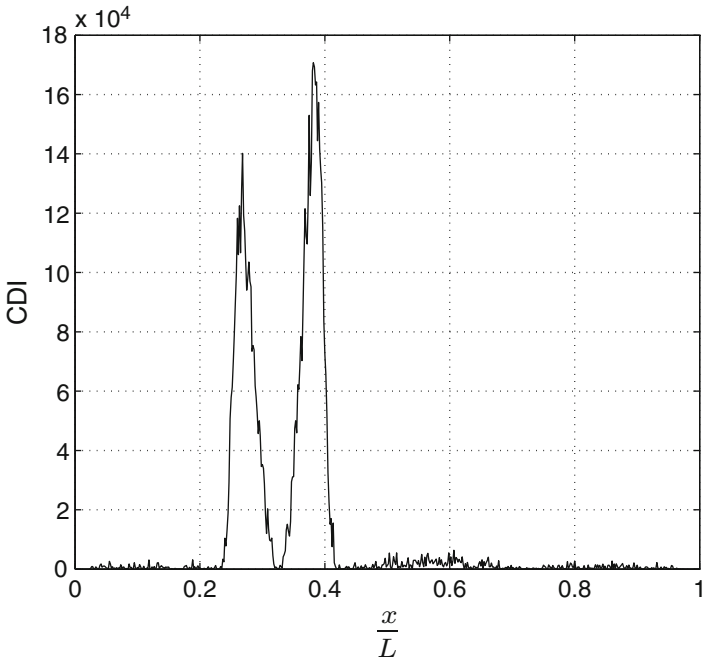

Fig. 31.7 CDIs using differences of the fourth MSs of the damaged and undamaged beams

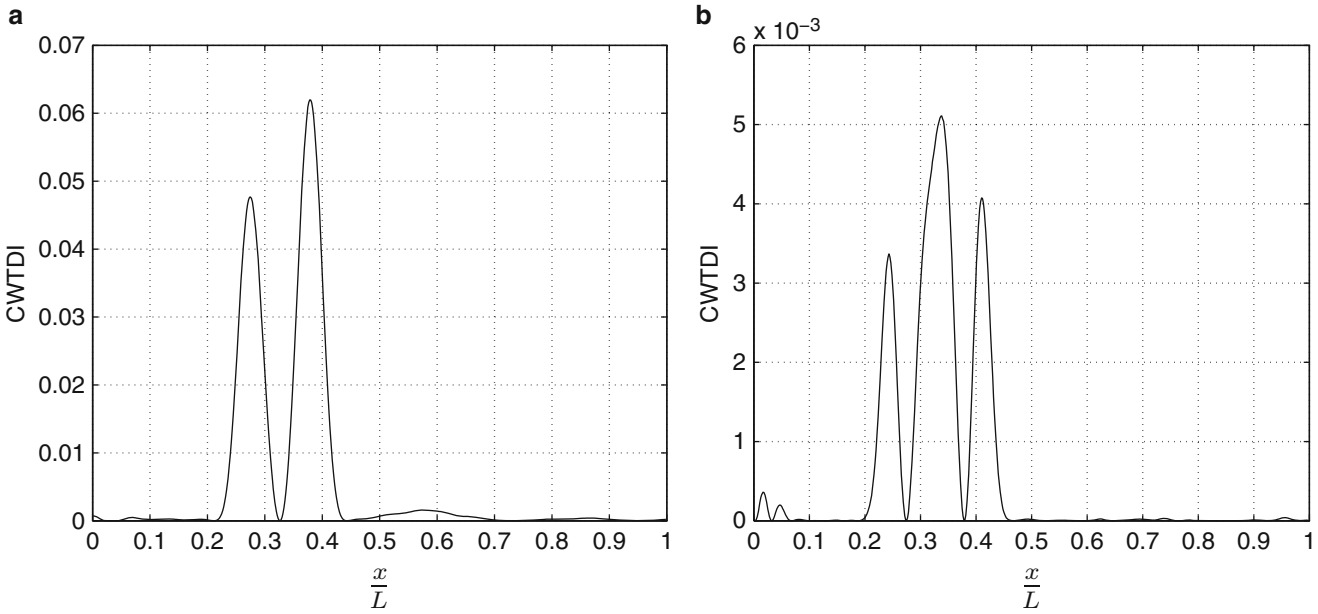

Fig. 31.8 (**a**) CWTDIs with the wavelet function $g^2(x)$ with $s = 15$ using differences between the fourth MSs of the damaged and undamaged beams, and (**b**) those with the wavelet function $g^3(x)$ with $s = 15$ using differences between the fourth MSs of the damaged and undamaged beams

While the MSs of the associated undamaged beam are not available, they can be constructed using polynomial fits based on the MSs of the damaged beam under the assumption that the presence of a crack in a beam does not cause prominent changes in its MSs in the neighborhood of the crack, which is valid for a crack of a small size. The MSs of an undamaged beam are not measured in this work, and it is proposed that the j-th MS of the undamaged beam be obtained from a polynomial of order $n + k$ that fits the j-th MS of the damaged beam:

$$f^{p,j}(x) = \sum_{i=0}^{n+k} a_i x^i \tag{31.19}$$

Table 31.1 MAC numbers in percentage between the first four measured MSs of the damaged and undamaged beams, and those between the associated CMSs with $m = 15$

Mode	1	2	3	4
MS	100	100	100	97
CMS	94	94	83	85

Table 31.2 (a) MAC numbers in percentage between the fourth MS of the undamaged beam and that obtained from the polynomial for different k values, and those between the associated CMSs; and (b) MAC numbers in percentage between the fourth MS of the damaged beam and that obtained from the polynomial, and those between the associated CMSs

(a)								(b)							
k	0	1	2	3	4	5	6	k	0	1	2	3	4	5	6
MS	87	86	99	98	98	98	98	MS	83	84	98	99	99	100	100
CMS	15	13	68	69	82	79	70	CMS	9	7	51	55	67	72	66

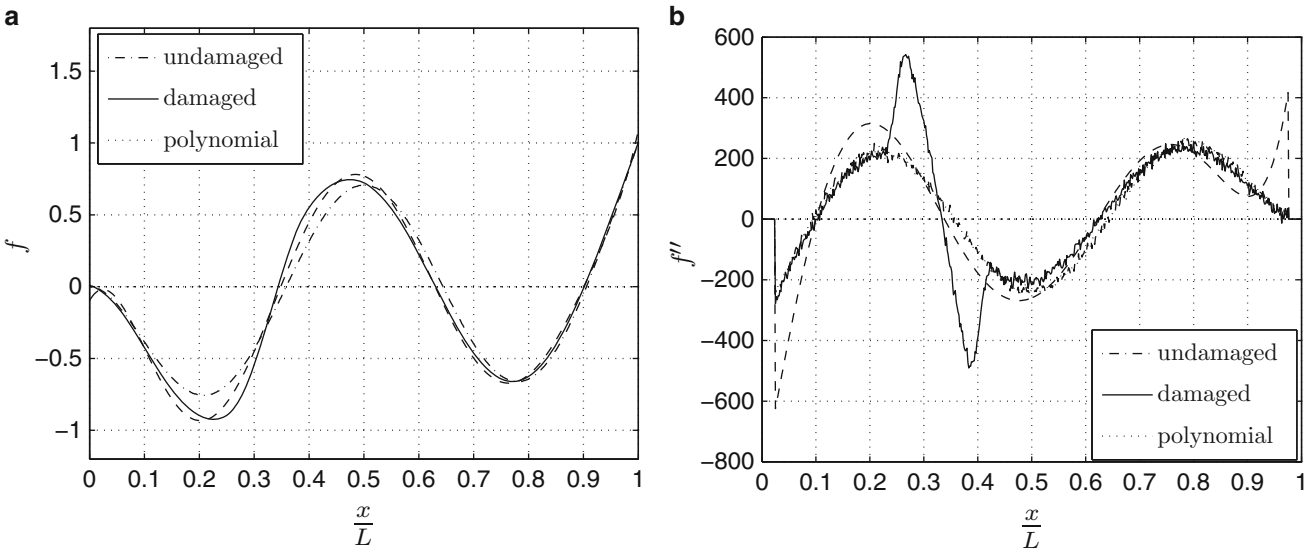

Fig. 31.9 (**a**) The fourth MSs of the undamaged and damaged beams and that obtained from the polynomial, and (**b**) the associated CMSs with $m = 15$

where n is the number of nodal points of the MS, k is a parameter that controls the level of approximation of the polynomial to the MS to be fitted, and a_i are the coefficients of the polynomial. As shown in Table 31.1, modal assurance criterion (MAC) values in percentage between the first four measured MSs of the undamaged and damaged beams are all above 97 %, which indicates that they are almost identical to each other [24]; this validates the assumption on the effects of a small crack on MSs. Hence, a MS f^p obtained from a polynomial that fits the MS of a damaged beam f^d well can approximate well that of a damaged beam f^u. On one hand, a CMS $(f^p)''$ with a properly chosen value of k in Eq. (31.19) cannot capture local features of $\left(f^d\right)''$ in the neighborhood of the crack, which are caused the crack, even though f^p is constructed based on f^d. On the other hand, the resulting $(f^p)''$ can approximate well $(f^u)''$ since the former is smooth as the latter without any blunt changes. With different k values in Eq. (31.19), MAC numbers in percentage between $f^{u,4}$ and $f^{p,4}$ and those between $\left(f^{u,4}\right)''$ and $\left(f^{p,4}\right)''$ are shown in Table 31.2a; MAC numbers in percentage between $f^{d,4}$ and $f^{p,4}$ and those between $\left(f^{d,4}\right)''$ and $\left(f^{p,4}\right)''$ are shown in Table 31.2b. When $k \geqslant 2$, the MAC numbers between $f^{u,4}$ and $f^{p,4}$ and those between $f^{d,4}$ and $f^{p,4}$ are above 98 %. However, the MAC values between $\left(f^{u,4}\right)''$ and $\left(f^{p,4}\right)''$ and those between $\left(f^{d,4}\right)''$ and $\left(f^{p,4}\right)''$ are relatively low. Figure 31.9a,b show $f^{u,4}$, $f^{d,4}$, and $f^{p,4}$ obtained from the polynomial with $k = 4$ and the associated CMSs, respectively. It can be seen that there are large discrepancies between $\left(f^{u,4}\right)''$ and $\left(f^{d,4}\right)''$ in the boundary

Table 31.3 With different k values, (a) the MAC values in percent between the MS of the undamaged beam and that from the polynomial that fits the extended MS of the damaged beam, and those between the associated CMSs with $m = 15$, and the MAC values in percent between the MS of the damaged beam and that from the polynomial that fits the extended MS of the damaged beam, and those between the associated CMSs with $m = 15$

(a)

k	0	1	2	3	4	5	6
MS	8	12	89	89	99	98	99
CMS	7	9	62	64	95	93	96

(b)

k	0	1	2	3	4	5	6
MS	9	12	86	86	97	98	99
CMS	4	6	40	43	70	71	76

intervals $[0, 0.1]$ and $[0.9, 1]$. The reason is that the coefficients a_i of $f^p(x)$ are determined by solving the unconstrained least-squares problem:

$$\min \sum_{i=1}^{N} \left[f^p(x_i) - f^d(x_i) \right]^2 \tag{31.20}$$

where N is the number of measurement points, and there are no constraints applied on the boundaries. For MSs of a cantilever beam defined on $[0, 1]$, for instance, the boundary conditions that the polynomials should satisfy are

$$\begin{cases} f^p(0) &= 0 \\ [f^p]'(0) &= 0 \\ [f^p]''(1) &= 0 \\ [f^p]'''(1) &= 0 \end{cases} \tag{31.21}$$

With the boundary conditions in Eq. (31.21), the least-squares problem in Eq. (31.20) becomes a constrained one, which can be solved by a numerical method [25]. However, the boundary conditions can be unknown or it can be difficult to accurately define them in practice; the polynomials that can fit f^d well near the boundaries may not be constructed.

To eliminate discrepancies between CMSs of a damaged beam and those obtained from the corresponding polynomials near the boundaries without use of any a priori knowledge of boundary conditions, it is proposed that MSs of the beam be extended to virtual intervals $[-0.2, 0]$ and $[1, 1.2]$, which are of twice the length of the boundary intervals indicated above, and the extended portions of the MSs on $[-0.2, 0]$ and $[1, 1.2]$ be obtained using polynomials of order three that fit the MSs in the boundary intervals $[0, 0.1]$ and $[0.9, 1]$, respectively. The extended MSs are obtained by correspondingly stitching the two extended portions onto the boundaries of the original MSs. With construction of the extended MSs, discrepancies between CMSs of the damaged beam and those obtained from the corresponding polynomials are transferred to the virtually extended portions. The polynomial that fits the j-th extended MS in $[-0.2, 1.2]$ can be obtained, and the MS obtained from the polynomial in $[0, 1]$ can be extracted and is denoted by $\widetilde{f^{p,j}}$, which can be used as the j-th MS of the undamaged beam. With different k values, MAC values in percentage between $f^{u,4}$ and $\widetilde{f^{p,4}}$ and those between $\left(f^{u,4}\right)''$ and $\left(\widetilde{f^{p,4}}\right)''$ are shown in Table 31.3a, and MAC values between $f^{d,4}$ and $\widetilde{f^{p,4}}$ and those between $\left(f^{d,4}\right)''$ and $\left(\widetilde{f^{p,4}}\right)''$ are shown in Table 31.3b. When $k \geqslant 4$, the MAC values between $f^{u,4}$ and $\widetilde{f^{p,4}}$ and those between $\left(f^{u,4}\right)''$ and $\left(\widetilde{f^{p,4}}\right)''$ are all above 98 and 92 %, respectively, indicating that the resulting $\widetilde{f^{p,4}}$ and $\left(\widetilde{f^{p,4}}\right)''$ can approximate well $f^{d,4}$ and $\left(f^{d,4}\right)''$ in $[0, 1]$, respectively. A proper k value for a certain MS is proposed to be two plus the least k value with which the MAC value between the MS to be fitted and that from the corresponding polynomial is above 90 %. Two is added here in order to preserve the smoothness of the CMSs from the corresponding polynomials, since calculation of the curvatures incurs second-order spatial differentiation, which reduces the orders of the polynomials by two. Since the MAC value between $f^{d,4}$ and $\widetilde{f^{p,4}}$ is above 90 % with $k = 4$, the k value for the polynomial is chosen to be six. The extended $f^{u,4}$, $f^{d,4}$ and the resulting $f^{p,4}$, and the associated CMSs are shown in Fig. 31.10a,b, respectively. The MAC value between $\left(f^{d,4}\right)''$ and $\left(\widetilde{f^{p,4}}\right)''$ is 75 %; such a low value is expected and mainly attributed to the presence of the crack, and the MAC value between $\left(f^{u,4}\right)''$ and $\left(\widetilde{f^{p,4}}\right)''$ is 99 %.

Combined with the above approximation technique for MSs of an undamaged beam, the proposed methods can identify a crack, including one near a boundary. The CDIs of the damaged beam using the difference between $f^{d,4}$ and $\widetilde{f^{p,4}}$, denoted by $\triangle_{d,p} f$, are shown in Fig. 31.11, where the crack tips can be located near the peaks of the CDIs. The CWTDIs using $\triangle_{d,p} f$ with the wavelet functions $g^2(x)$ and $g^3(x)$ with $s = 15$ are shown in Fig. 31.12a,b, where the crack tips can be located near the peaks and valleys of the CWTDIs, respectively.

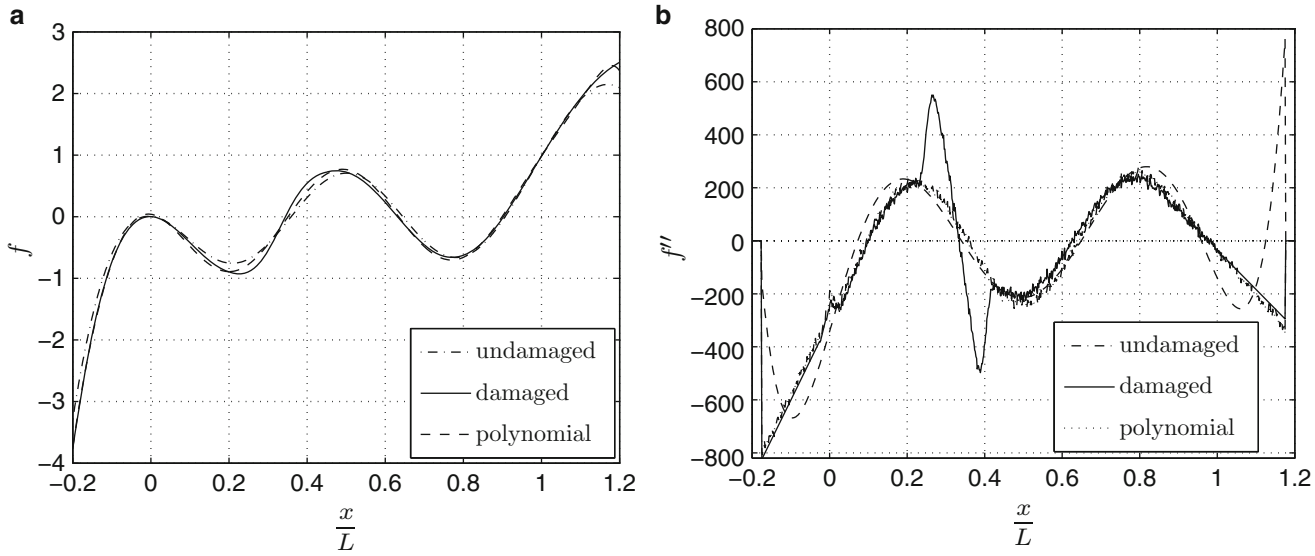

Fig. 31.10 (**a**) Extended fourth MSs of the undamaged and damaged beams and the MS obtained from the polynomial; and (**b**) the associated CMSs with $m = 15$

Fig. 31.11 CDIs using the difference between $f^{d,4}$ and $\widetilde{f^{p,4}}$ with $m = 15$

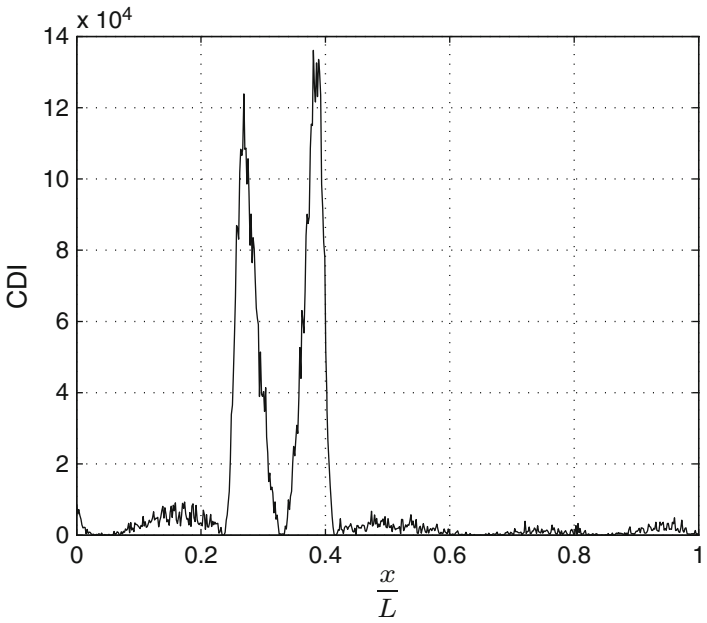

In order to validate the robustness of the proposed methods on identifying a crack near a boundary, the crack in the damaged beam shown in Fig. 31.1 is translated to the position where its left tip is 30 mm away from the fixed end of the beam, and its vertical position and length remain unchanged. The FE model of the beam is constructed, from which its fourth MS is calculated and used to identify the crack. The fourth MSs of the associated undamaged beam are obtained from the fitted polynomials with different values of k. The MAC values between the fourth MS of the damaged beam and the fitted ones and those between the associated CMSs are shown in Table 31.4; the optimal value of k is chosen to be six for this MS, according to the proposed criterion. The associated CDIs and CWTDIs with the wavelet functions $g^2(x)$ and $g^3(x)$ with $s = 15$ are shown in Figs. 31.14 and 31.15a,b, from which the crack tips can be located near the peaks of the CDIs, and the peaks and valleys of the CWTDIs, respectively.

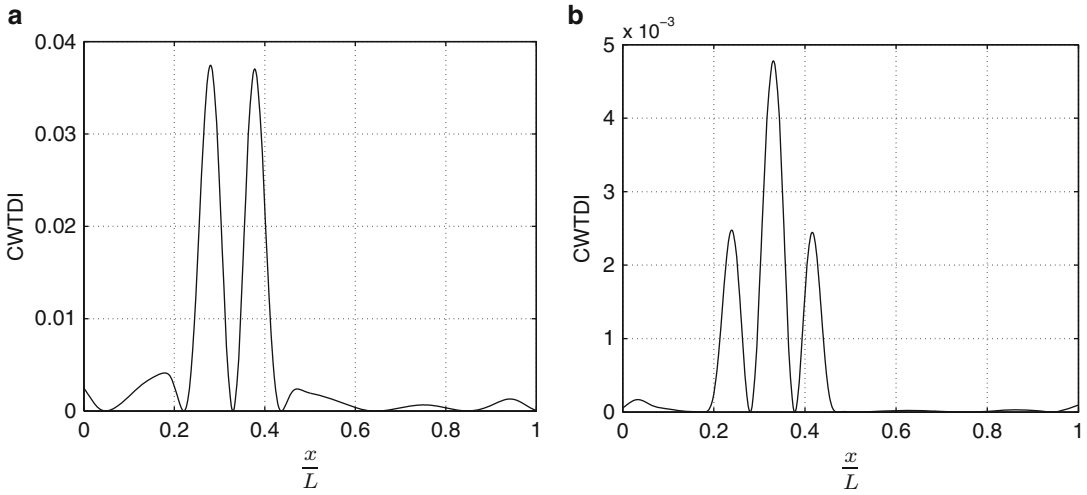

Fig. 31.12 (**a**) CWTDIs with the wavelet function $g^2(x)$ with $s = 15$ using the difference between $f^{d,4}$ and $\widetilde{f^{p,4}}$, and (**b**) those with the wavelet function $g^3(x)$ with $s = 15$ using the difference between $f^{d,4}$ and $\widetilde{f^{p,4}}$

Table 31.4 (a) The MAC values in percent between $\widetilde{f^{p,4}}$ and $f^{u,4}$, and those between $\left(\widetilde{f^{p,4}}\right)''$ and $\left(f^{u,4}\right)''$; and (b) the MAC values in percent between $\widetilde{f^{p,4}}$ and $f^{d,4}$, and those between $\left(\widetilde{f^{p,4}}\right)''$ and $\left(f^{d,4}\right)''$

(a)

k	0	1	2	3	4	5	6
MS	17	23	89	87	98	97	98
CMS	10	12	58	57	94	92	97

(b)

k	0	1	2	3	4	5	6
MS	21	25	89	89	94	99	100
CMS	8	9	47	47	81	83	87

31.2.4 Denoising of MSs

The above crack identification methods rely on MS measurement quality, which is usually subject to measurement noise that can deteriorate the resulting CMSs and CWTs, as shown in Figs. 31.2a and 31.4a, respectively. Suitable values of the resolution parameter m for a CMS and scale s for a CWT can relieve the negative effects of measurement noise. One needs to progressively test different values of m and s to get useful results. A numerical smoothing technique, which is local regression using weighted linear least squares and a second degree polynomial model, is applied to directly reduce measurement noise in MSs, and it is performed using the Matlab function "smooth" [26]. The method calculates a weighted quadratic least squares on every measurement point within an interval that consists of a certain number of its neighboring points, which is 15 % of the total number of measurement points herein. The CMS with $m = 1$ and CWT with the wavelet function $g^2(x)$ with $s = 1$ of the denoised $f^{d,4}$ are shown in Fig. 31.16a,b, respectively, where both the CMS and CWT have a lower noise level and are smooth, and their shapes are similar to the CMSs and CWTs before denoising with higher values of m and s, as shown in Fig. 31.2b–d and Fig. 31.4b–d, respectively.

31.3 Numerical Crack Identification

The FE model of an ABS uniform cantilever beam of length 114.4 mm, height 5.2 mm, and width 10.5 mm with an embedded horizontal crack was constructed, whose dimensions are shown in Fig. 31.17a; the shape of the crack was a rectangle, and its length, width, and height were 16.6, 10.5, and 0.3 mm, respectively, as shown in Fig. 31.17b. The distance between the left tip of the crack and the fixed end of the beam was 53.1 mm, and that between the crack and the top surface of the beam was 2.6 mm. The mass density and elastic modulus of the ABS were 1,000 kg/m^3 and 2.10 GPa, respectively. White noise is added to the MSs with a SNR of 60 to simulate measurement noise.

MSs are denoised using the technique in Sect. 31.2.4. Table 31.5a–d show the MAC values between the first four MSs from the FE model and those from the polynomial fits with different values of k, which are obtained using the approximation

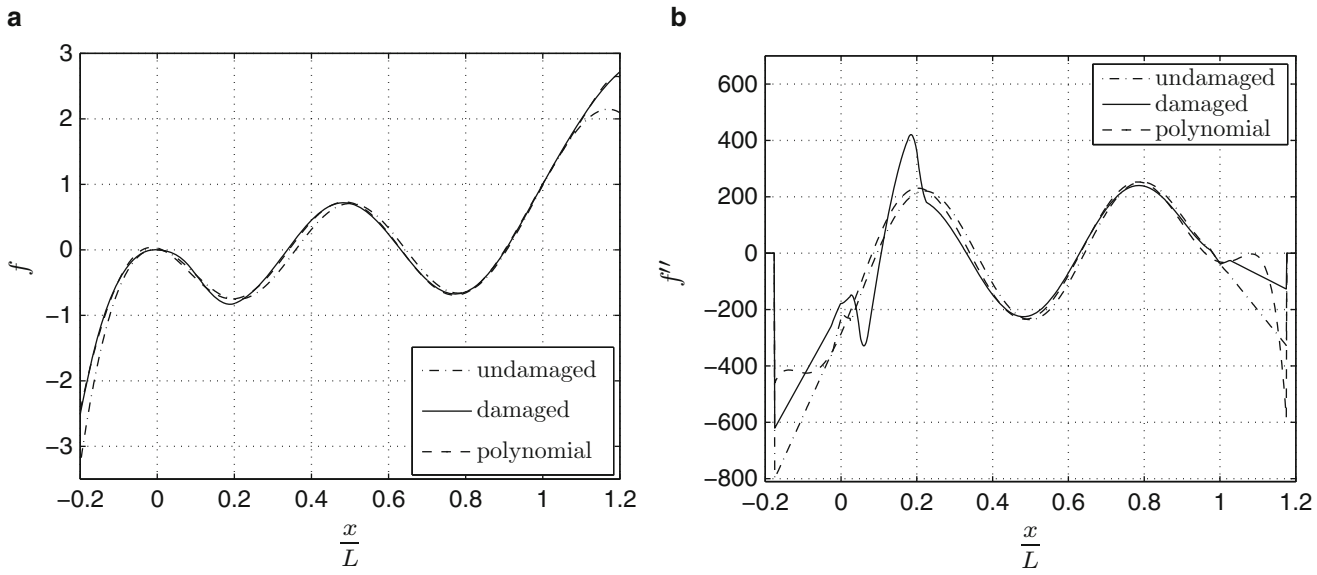

Fig. 31.13 (**a**) The plots of $f^{u,4}$, $f^{d,4}$, and $\widetilde{f^{p,4}}$; and (**b**) those of $\left(f^{u,4}\right)''$, $\left(f^{d,4}\right)''$, and $\left(\widetilde{f^{p,4}}\right)''$ with $m = 15$

Fig. 31.14 CDIs using the difference between $f^{d,4}$ and $\widetilde{f^{p,4}}$ with $m = 15$

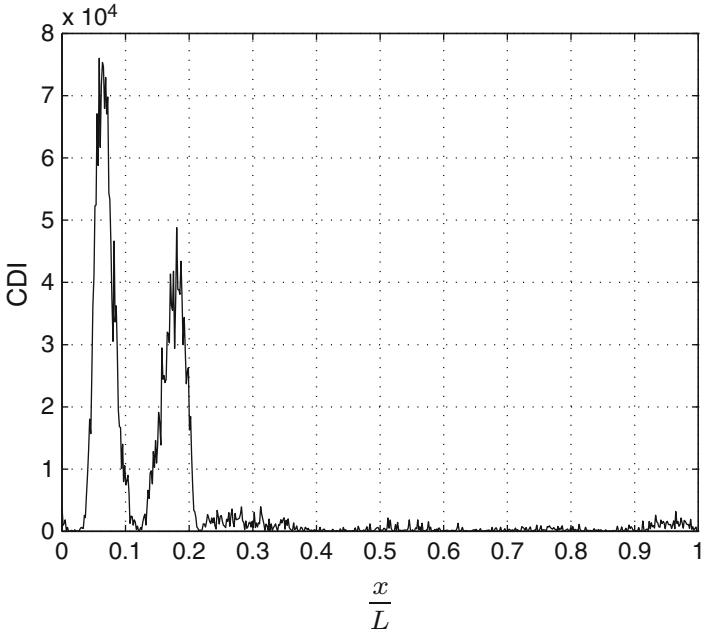

technique for MSs of the associated undamaged beam described in Sect. 31.2.3; the MAC values between the associated CMSs are also shown. The optimal k values for modes one through four are chosen to be two, three, four, and six, respectively. Figure 31.18a–d show the resulting CDIs with resolution up to 20 for the first four modes of the beam from the FE model; two ridges can be observed in the CDIs from each mode, from which the crack tips can be correspondingly identified. In Fig. 31.18a, the right crack tip, which is located at $\frac{x}{L} = 0.61$, can be more clearly identified than the left one, which is located at $\frac{x}{L} = 0.46$; in Fig. 31.18b, the ridges corresponding to the two crack tips are both weak. The reason is that the CMS of mode two, shown in Fig. 31.19b, is insensitive to the crack, since its abnormalities caused by the crack are weaker than those of the CMSs of the other three modes, as shown in Fig. 31.19a,c, and d; it can also be observed that modes three and four are more sensitive to the crack. Hence, in Fig. 31.18c, d, the CDIs of modes three and four can be used to more clearly identify the crack than the first two modes.

Figures 31.20 and 31.21 show the CWTDIs for the first four MSs of the damaged beam from the FE model with $g^2(x)$ and $g^3(x)$ as the wavelet functions with scale up to 50, respectively. Similar to the results for the CDIs, relatively high CWTDIs

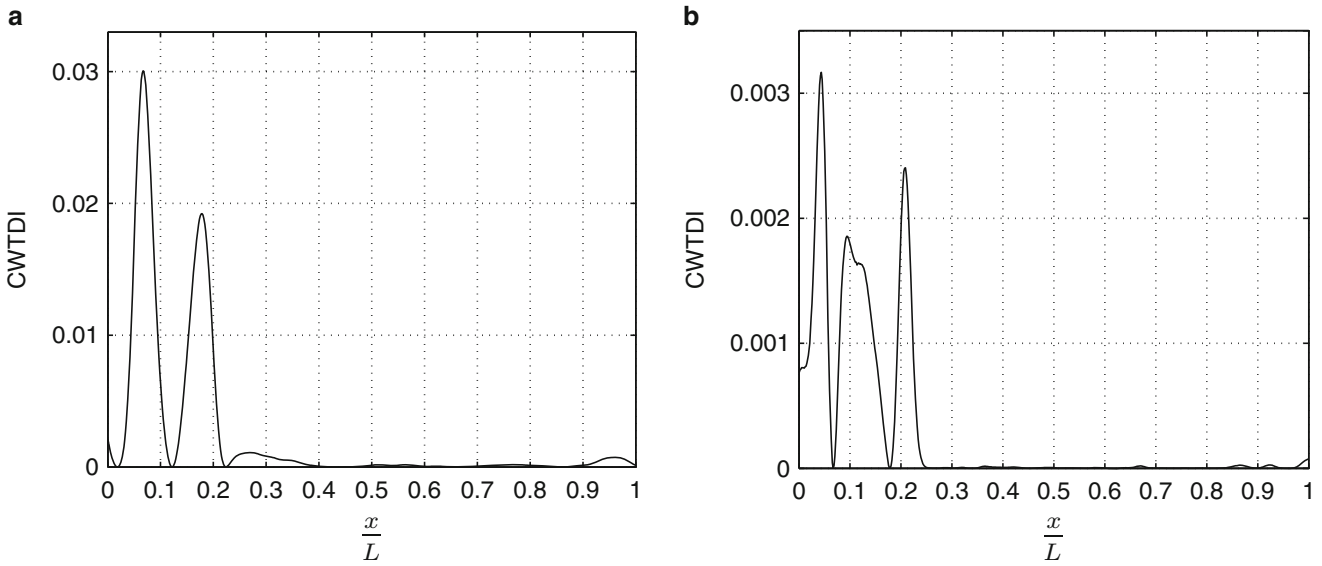

Fig. 31.15 (**a**) CWTDIs with the wave function $g^2(x)$ with $s = 15$ using the difference between $f^{d,4}$ and $\widetilde{f^{p,4}}$, and (**b**) CWTDIs with the wave function $g^3(x)$ with $s = 15$ using the difference between $f^{d,4}$ and $\widetilde{f^{p,4}}$

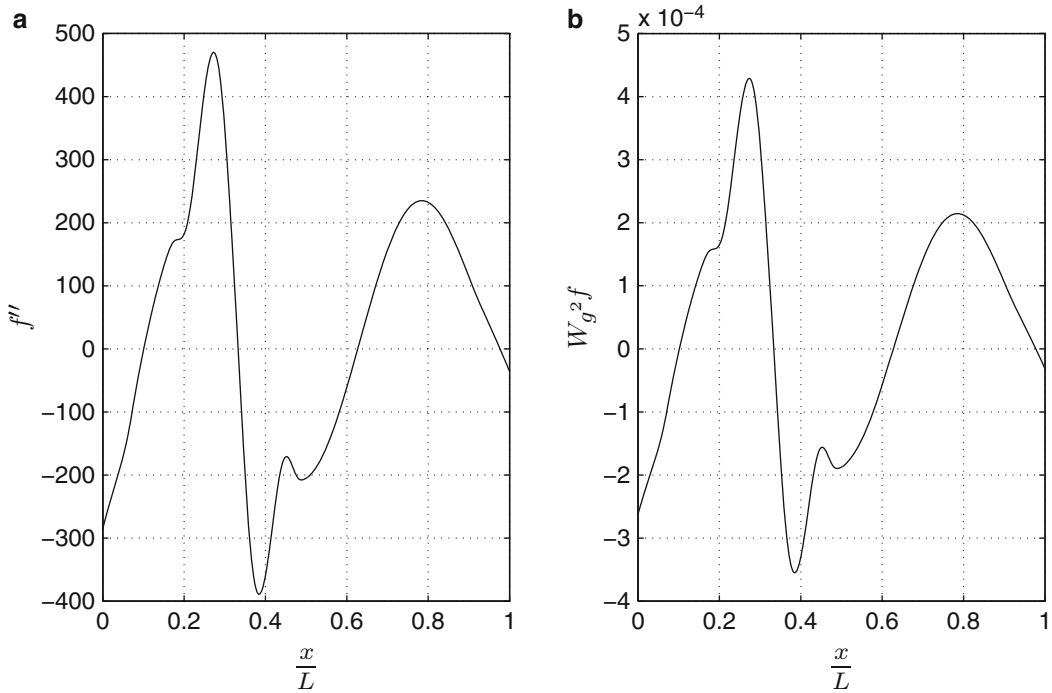

Fig. 31.16 (**a**) Curvature of the denoised fourth MS of the damaged beam with $m = 1$, and (**b**) the CWT of the denoised fourth MS of the damaged with the wavelet function $g^2(x)$ with $s = 1$

with the wavelet function $g^2(x)$ can be more clearly observed from modes three and four near the tips of the crack than from the first two modes, which is shown in Fig. 31.20a–d, since modes three and four are more sensitive to the crack. With the CTWDIs with the wavelet function $g^3(x)$, the crack tips can be located near the valleys of modes one through four, as shown in Fig. 31.21a–d, respectively. The crack tips can be more clearly and accurately identified near the valleys of modes one, three, and four than those of mode two.

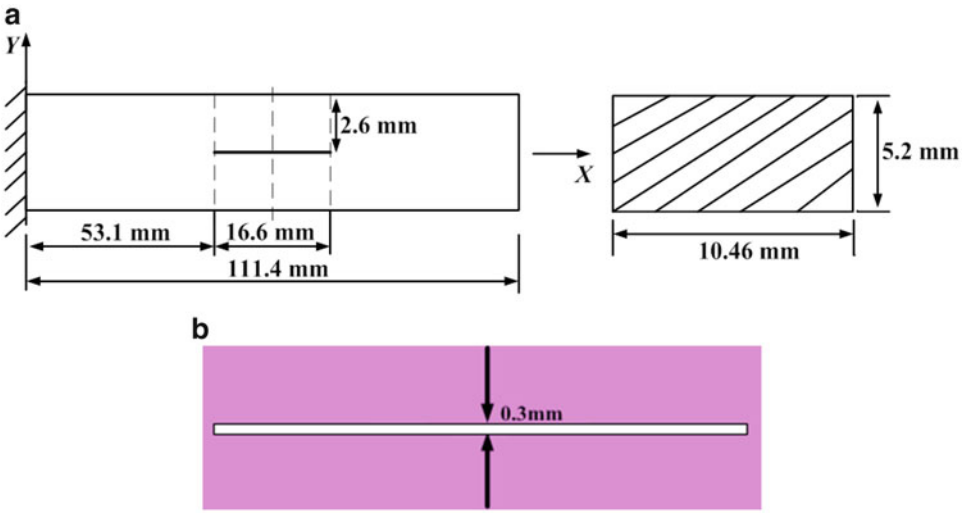

Fig. 31.17 (**a**) Dimensions of the ABS cantilever beam with an embedded horizontal crack, and (**b**) an enlarged view of the crack region

Table 31.5 The MAC values in percent between the numerical MSs f^d of the damaged beam shown in Fig. 31.17 and the associated $\widetilde{f^p}$ with different k values, and those between the CMSs of f^d and $\widetilde{f^p}$ with different k values; (a) through (d) correspond to modes one through four, respectively

(a)

k	0	1	2
MS	98	100	100
CMS	0	60	98

(b)

k	0	1	2	3
MS	85	93	100	100
CMS	19	36	98	98

(c)

k	0	1	2	3	4
MS	52	66	97	97	100
CMS	14	18	73	73	85

(d)

k	0	1	2	3	4	5	6
MS	11	14	87	87	97	98	99
CMS	8	5	52	52	82	83	89

31.4 Conclusion

Two new non-model-based crack identification methods are developed to identify embedded horizontal cracks in beams. Differences between MSs of a damaged beam with a crack and those obtained from polynomials that fit the MSs of the damaged beam are converted to CDIs and CWTDIs, which are used to locate the crack tips. MSs from polynomials that fit the MSs of a damaged beam, with properly selected parameters, can approximate those of the associated undamaged beam. CDIs for a MS are presented in multiple resolutions to relieve negative effects of measurement noise, and the crack tips can be located near the peaks of the CDIs. It is shown that the CWT of a MS with the n-th-order Gaussian wavelet function resembles that of the n-th-order spatial derivative of the MS. Crack tips can be located near the peaks and valleys of CWTDIs with multiple scales using the second- and third-order Gaussian wavelet functions, respectively. The proposed methods are numerically applied to an ABS cantilever beam with an embedded horizontal crack. An experimental investigation of the proposed methods will be performed to further validate the proposed methods.

Acknowledgements The authors are grateful for the financial support from the National Science Foundation under Grant Numbers CMMI-1229532 and CMMI-1335024 and the National Natural Science Foundation of China under Grant Number 51035008.

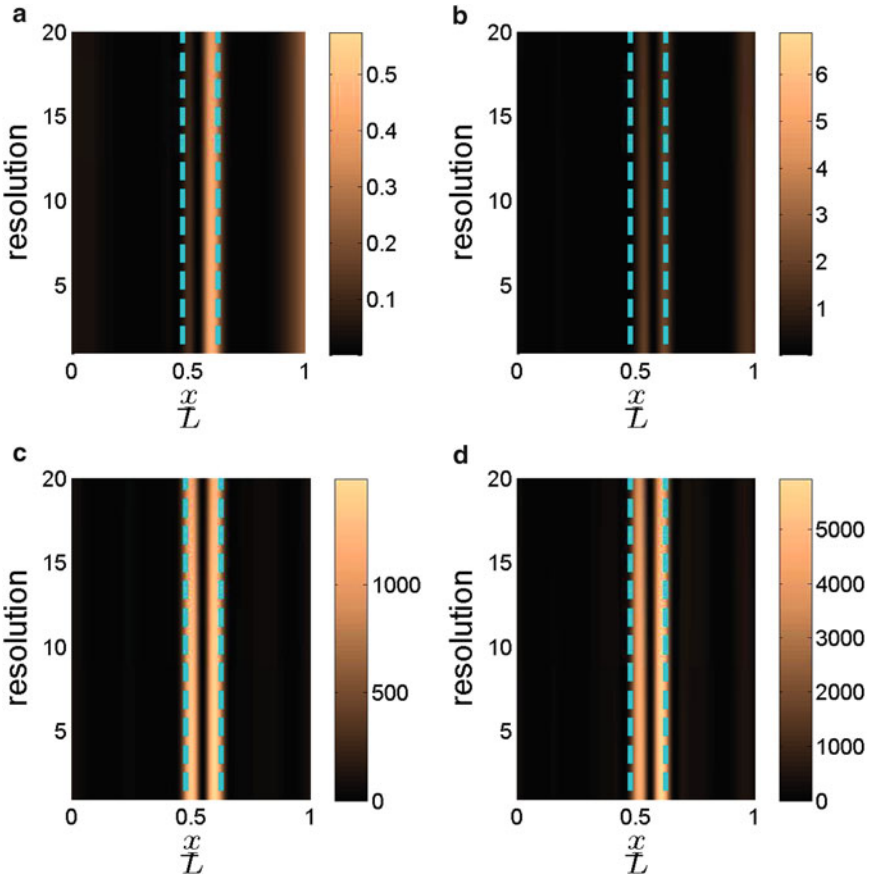

Fig. 31.18 Numerical crack identification by tracking the ridges of the CDIs with resolution up to 20. The locations of the crack tips are indicated using *thick dashed lines*; the CDIs associated with modes one through four are shown in (**a**) through (**d**), respectively

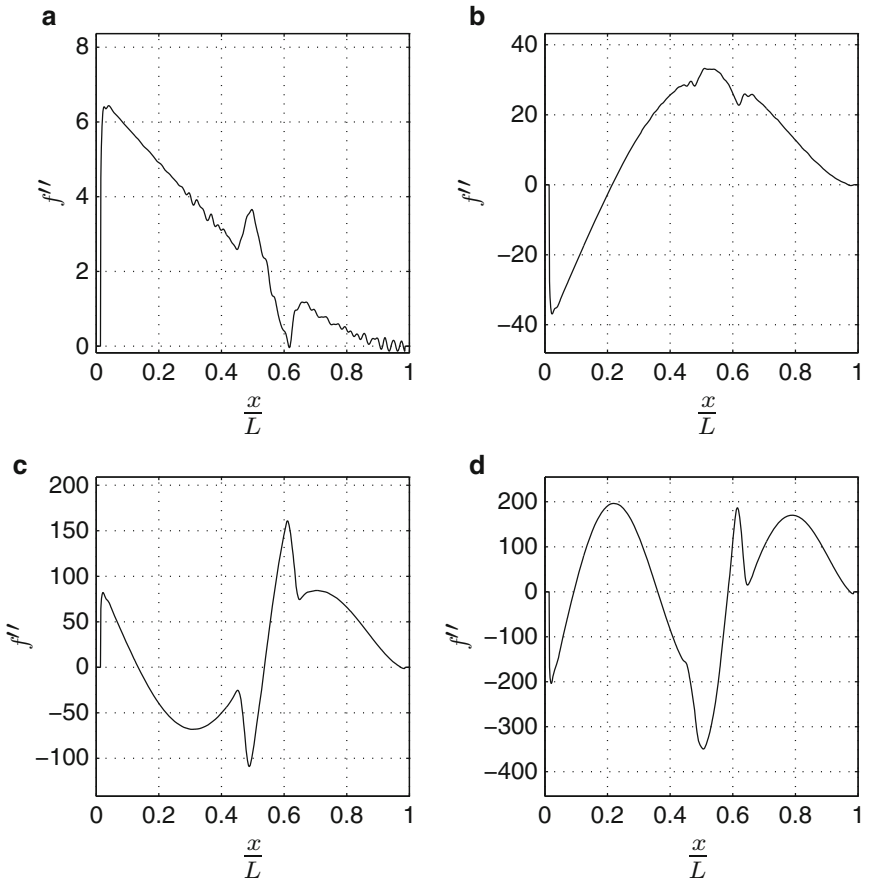

Fig. 31.19 CMSs of the first four modes of the damaged ABS beam shown in Fig. 31.17 with $m = 15$

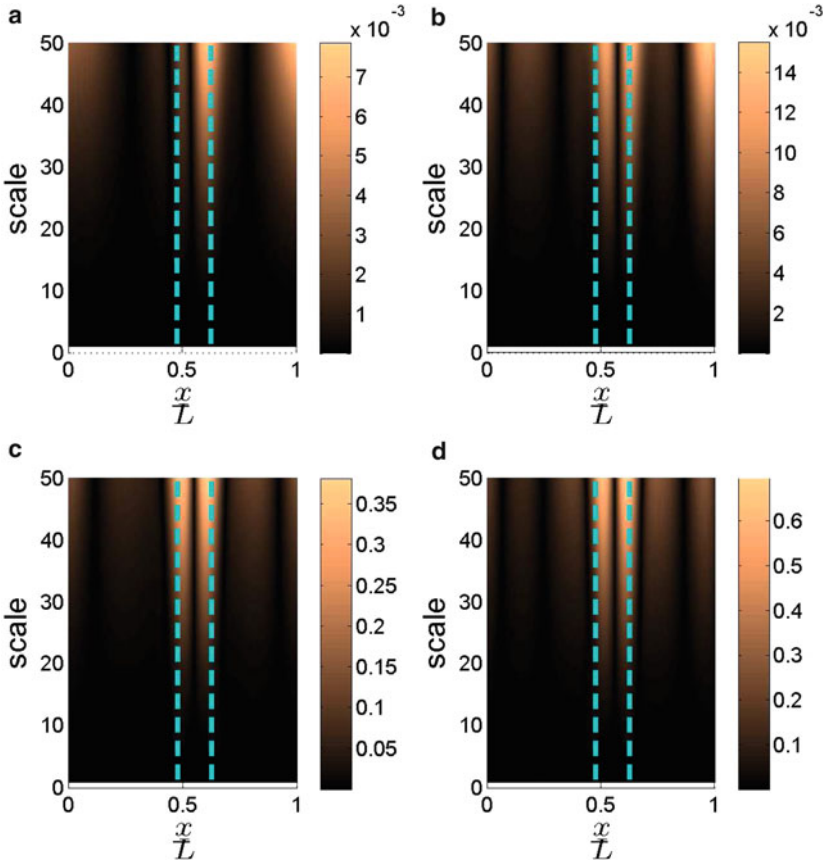

Fig. 31.20 Numerical crack identification by tracking the peaks of the CWTDIs with the wavelet function $g^2(x)$ with scale up to 50. The locations of the crack tips are indicated using *thick dashed lines*; the CWTDIs associated with modes one through four are shown in (**a**) through (**d**), respectively

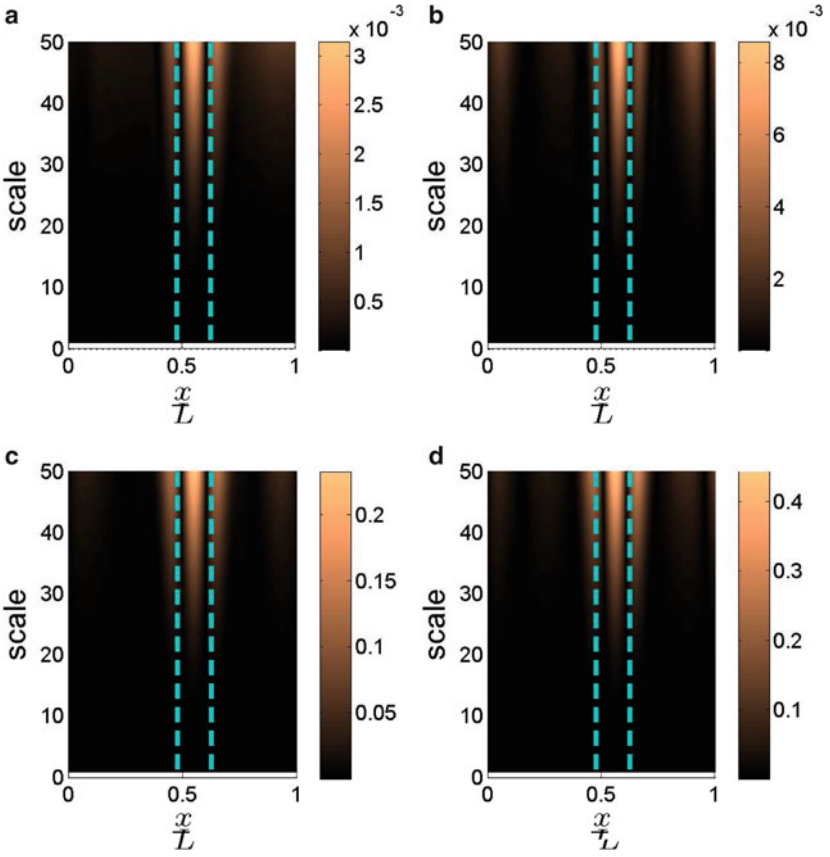

Fig. 31.21 Numerical crack identification by tracking the valleys of the CWTDIs with the wavelet function $g^3(x)$ with scale up to 50. The locations of the crack tips are indicated using *thick dashed lines*; the CWTDIs associated with modes one through four are shown in (**a**) through (**d**), respectively

References

1. Doebling SW, Farrar CR, Prime MB (1998) A summary review of vibration-based damage identification methods. Shock Vib Dig 30:91–105
2. He K, Zhu WD (2010) Detection of damage and loosening of bolted joints in structures using changes in natural frequencies. ASNT Mater Eval 2010:721–732
3. He K, Zhu WD (2011) Damage detection of space frame structures with L-shaped beams and bolted joints using changes in natural frequencies. ASME J Vib Acoust 135:051001 (13 pages)
4. Friswell MI (2007) Damage identification using inverse methods. Philos Trans Math Phys Eng Sci 365:393–410
5. Surace C (2013) Damage assessment of structures using only post-damage vibration measurements. Key Eng Mater 569–570:11–22
6. Fan W, Qiao P (2011) Vibration-based damage identification methods: a review and comparative study. Struct Health Monit 10:83–111
7. Pandey AK, Biswas M, Samman MM (1991) Damage detection from changes in curvature mode shapes. J Sound Vib 145:321–332
8. Ratcliffe CP, Bagaria WJ (1998) Vibration technique for locating delamination in a composite beam. AIAA J 36:1074–1077
9. Ratcliffe CP (2000) A frequency and curvature based experimental method for locating damage in structures. J Vib Acoust 122:324–329
10. Yoon M-K, Heider D, Gillespie JW Jr, Ratcliffe CP, Crane RM (2009) Local damage detection with the global fitting method using mode shape data in notched beams. J Nondestruct Eval 38:63–74
11. Yoon M-K, Heider D, Gillespie JW Jr, Ratcliffe CP, Crane RM (2010) Local damage detection with the global fitting method using operating deflection shape data. J Nondestruct Eval 29:25–37
12. Szzonov E, Klinkhachorn P (2005) Optimal spatial sampling interval for damage detection by curvature or strain energy mode shapes. J Sound Vib 285:783–801
13. Cao M, Qiao P (2009) Novel Laplacian scheme and multiresolution modal curvatures for structural damage identification. Mech Syst Signal Process 23:1223–1242
14. Douka E, Loutridis S, Trochidis A (2003) Crack identification in beams using wavelet analysis. Int J Solids Struct 40:357–3569
15. Rucka M, Wilde K (2006) Application of continuous wavelet transform in vibration based damage detection method for beams and plates. J Sound Vib 297:536–550
16. Solis M, Algaba M, Galvin P (2013) Continuous wavelet analysis of mode shapes differences for damage detection. Mech Syst Signal Process 40:645–666
17. Zak A, Krawczuk M, Ostachowicz W (2000) Numerical and experimental investigation of free vibration of multilayer delaminated composite beams and plates. Comput Mech 26:309–315
18. Lee J (2000) Free vibration analysis of delaminated composite beams. Comput Struct 74:121–129
19. Shen M-HH, Grady JE (1992) Free vibrations of delaminated beams. AIAA J 30:1361–1370
20. Okafor AC, Chandrashekhara K, Jiang YP (1996) Delamination prediction in composite beams with built-in piezoelectric devices using modal analysis and neural network. Smart Mater Struct 5:338–347
21. Wang Q, Wu N (2002) Detecting the delamination location of a beam with a wavelet transform: an experimental study. Smart Mater Struct 20:01202 (7 pages)
22. Mallet S (1998) A wavelet tour of signal processing. Academic, London
23. Cao M, Cheng L, Su Z, Xu H (2012) A multi-scale pseudo-force model in wavelet domain for identification of damage in structural components. Mech Syst Signal Process 28:638–659
24. Ewins DJ (2000) Modal testing: theory, practice and application, 2nd edn. Research Studies Press, Hertfordshire
25. Nocedal J, Wright SJ (1999) Numerical optimization. Springer, New York
26. The Mathworks Inc. (2010) MATLAB user's guide, Natick